Development and application of laser diagnostics - from laboratory devices towards practical combustion engines

Wang, Zhenkan

2018

Document Version:
Publisher's PDF, also known as Version of record

Development and application of laser diagnostics - from laboratory devices towards practical combustion engines

Development and application of laser diagnostics

- from laboratory devices towards practical combustion engines

Zhenkan Wang

LUND
UNIVERSITY

DOCTORAL DISSERTATION
by due permission of the Faculty of Engineering, Lund University, Sweden.
To be defended at Rydbergsalen, Fysicum, Professorsgatan 1. 4th May 2018, at 9:15.

Faculty opponent
Dr. James Gord, Air Force Research Laboratory, Aerospace Systems Directorate,
Wright-Patterson AFB, Dayton, Ohio, USA

Organization	Document name
LUND UNIVERSITY Division of Combustion Physics, Department of Physics P.O. Box 118, SE-211 00, Lund, Sweden	Doctoral Dissertation
	Date of issue 2018-04-03
Author: Zhenkan Wang	Sponsoring organization
	ISRN: LUTFD2/TFCP-211-SE

Title and subtitle: Development and application of laser diagnostics - from laboratory devices towards practical combustion engines

Abstract

For many decades, research work on combustion has been focused on improving combustion efficiency and reducing harmful emissions. Laser diagnostics is one of the best ways to investigate the combustion process and emission formation as it is non-intrusive and it has high spatiotemporal resolution. In this thesis work, many laser diagnostics have been developed and employed for combustion research. The laser-based optical methods cover ballistic imaging (BI), multi-scaler laser introduced fluorescence (LIF) imaging, particle imaging velocimetry (PIV), laser Doppler anemometry (LDA), and high speed LIF measurement (up to 140 kHz).

Two BI systems were developed and compared, together with ultrafast shadow imaging (USI) for better imaging through a high optical depth (OD) substance, *e.g.* a spray. In addition, multi-scaler planar laser introduced fluorescence (PLIF) measurements were developed in Lund University Piloted Jet (LUPJ) burners including simultaneous measurement of temperature, CH radicals and OH radicals distribution, and simultaneous measurement of CH_2O radicals, CH radicals and OH radicals distribution. Key parameters, such as Damköhler number, Karlovitz number, and Kolmogorov time scale, were calculated and are listed in this thesis based on LDA measurements. Moreover, high speed PLIF measurements were developed in an LUPJ burner including simultaneous OH/CH_2O PLIF at 50 kHz, OH PLIF at 100 kHz and CH_2O PLIF at 140 kHz, with more than 100 consecutive images for the first ever time. That was achieved by using a burst-mode laser pumped OPO system synchronised with high speed cameras and high speed intensifiers. The diagnostics approaches were capable of following the temporal evolution of the reacting flow down to the Kolmogorov scale for better understanding of the transient behaviour of the eddy/flame interaction in highly turbulent premixed flames.

The developed laser diagnostics have also been applied in a diesel spray in an HTHP constant volume vessel, in a pulsed plasma discharge and in practical combustion devices, *e.g.* internal combustion engines. The developed 2f-BI system has been successfully employed for investigation of the spray formation region of a diesel spray, *i.e.* ECN Spray A, and the supercritical phenomenon has been observed with cellular structures of the spray for the first time. It's also the first time that a burst-mode laser system has been applied for high-speed OH PLIF imaging in pulsed plasma discharges at tens of kHz repetition rate. The changing of OH radical distribution during post discharge was captured at 27 kHz, *e.g.* the deformation of the OH PLIF intensity from toroidal shape to a filled circle was observed. In addition, the decay rate of OH distribution at the outer layer of the plasma column and the increasing rate of that in the plasma column were calculated.

The mixing process of gasoline/diesel and air in HCCI/PPC engines was visualised and investigated by 10 Hz fuel-tracer PLIF measurements and, also, the developed high-speed PLIF techniques with the burst-mode laser system. In addition, the mixture formation and evolution of low temperature combustion, *i.e.* CH_2O distribution, together with the auto-ignition, *i.e.* high temperature combustion, were captured and followed in one engine cycle. To the best of my knowledge, no one has ever achieved this before. The results are also of significant value for computational fluid dynamics of internal combustion engines. An extended conceptual model for gasoline PPC combustion with EGR-dilution and single-injection strategy is proposed. Furthermore, cycle-resolved PIV measurement was performed in a light-duty optical diesel engine with single, double and triple injection strategies. Last but not least, the experimental equipment and setups are introduced in this thesis, together with some practical experience and hands-on advice not mentioned in the attached papers.

Key words: Combustion Diagnostics, Laser induced fluorescence, Ultra-high-speed, Burst-mode laser; Ballistic imaging, Particle imaging velocimetry, Laser Doppler anemometry, Turbulent premixed combustion, Plasma, Internal combustion engine, Partially premixed combustion, Auto-ignition, OH, CH_2O

Classification system and/or index terms (if any)

Supplementary bibliographical information		Language: English
ISSN and key title: 1102-8718		ISBN: 978-91-7753-653-6 (print) ISBN: 978-91-7753-654-3 (pdf)
Recipient's notes	Number of pages: 387	Price
	Security classification	

Development and application of laser diagnostics

- from laboratory devices towards practical combustion engines

Zhenkan Wang

Division of Combustion Physics,
Department of Physics, Faculty of Engineering

Lund, Sweden
May 2018

Coverphoto by Zhenkan Wang

Lund University, Faculty of Engineering, Department of Physics
Lund Reports on Combustion Physics, LRCP-211

ISBN 978-91-7753-653-6 (print)
ISBN 978-91-7753-654-3 (pdf)
ISSN 1102-8718
ISRN LUTFD2/TFCP-211-SE

Printed in Sweden by Media-Tryck, Lund University
Lund 2018

MADE IN SWEDEN

To my family

天之道，损有余而补不足，因顺其自然。

Table of Contents

Abstract

For many decades, research work on combustion has been focused on improving combustion efficiency and reducing harmful emissions. Laser diagnostics is one of the best ways to investigate the combustion process and emission formation as it is non-intrusive and it has high spatiotemporal resolution. In this thesis work, many laser diagnostics have been developed and employed for combustion research. The laser-based optical methods cover ballistic imaging (BI), multi-scaler laser introduced fluorescence (LIF) imaging, particle imaging velocimetry (PIV), laser Doppler anemometry (LDA), and high speed LIF measurement (up to 140 kHz).

Two BI systems were developed and compared, together with ultrafast shadow imaging (USI) for better imaging through a high optical depth (OD) substance, *e.g.* a spray. In addition, multi-scaler planar laser introduced fluorescence (PLIF) measurements were developed in Lund University Piloted Jet (LUPJ) burners including simultaneous measurement of temperature, CH radicals and OH radicals distribution, and simultaneous measurement of CH_2O radicals, CH radicals and OH radicals distribution. Key parameters, such as Damköhler number, Karlovitz number, and Kolmogorov time scale, were calculated and are listed in this thesis based on LDA measurements. Moreover, high speed PLIF measurements were developed in an LUPJ burner including simultaneous OH/CH_2O PLIF at 50 kHz, OH PLIF at 100 kHz and CH_2O PLIF at 140 kHz, with more than 100 consecutive images for the first ever time. That was achieved by using a burst-mode laser pumped optical parametric oscillator (OPO) system synchronised with high speed cameras and high speed intensifiers. The diagnostics approaches were capable of following the temporal evolution of the reacting flow down to the Kolmogorov scale for better understanding of the transient behaviour of the eddy/flame interaction in highly turbulent premixed flames.

The developed laser diagnostics have also been applied in a diesel spray in a high temperature high pressure (HTHP) constant volume vessel, in a pulsed plasma discharge and in practical combustion devices, *e.g.* internal combustion engines with elevated pressure and temperature (>90 bar and >1000 ^{o}C).

The developed 2f-BI system has been successfully employed for investigation of the spray formation region of a diesel spray, *i.e.* engine combustion network (ECN) Spray A, and the supercritical phenomenon has been observed with cellular structures of the spray for the first time. It's also the first time that a burst-mode

laser system has been applied for high-speed OH PLIF imaging in pulsed plasma discharges at tens of kHz repetition rate. The changing of OH radical distribution during post discharge was captured at 27 kHz, *e.g.* the deformation of the OH PLIF intensity from toroidal shape to a filled circle was observed. In addition, the decay rate of OH distribution at the outer layer of the plasma column and the increasing rate of that in the plasma column were calculated.

The mixing process of gasoline/diesel and air in homogeneous charge compression ignition (HCCI) and partially premixed combustion (PPC) engines was visualised and investigated by 10 Hz fuel-tracer PLIF measurements and, also, the developed high-speed PLIF techniques with the burst-mode laser system. In addition, the mixture formation and evolution of low temperature combustion, *i.e.* CH_2O distribution, together with the auto-ignition, *i.e.* high temperature combustion, were captured and followed for more than ten crank angle degrees (CADs) in one engine cycle at 36 kHz. To the best of my knowledge, no one has ever achieved this before. The results are also of significant value for computational fluid dynamics of internal combustion engines. An extended conceptual model for gasoline PPC mode with exhaust gas recirculation (EGR)-dilution and single-injection strategy is proposed. Furthermore, cycle-resolved PIV measurement was performed in a light-duty optical diesel engine with single, double and triple injection strategies. Last but not least, the experimental equipment and setups are introduced in this thesis, together with some practical experience and hands-on advice not mentioned in the attached papers.

Popular Science

Combustion is commonly applied in our daily life, cooking, driving, heating, manufacturing, *etc.* When fuel is mixed with air above a critical temperature, *e.g.* several hundred degrees Celsius, the combustion begins. This start of combustion can be termed ignition. Usually, the combustion gives out intensive heat and light. In this way, it also produces emissions, not only visible ones such as soot but also transparent ones such as water vapour and carbon dioxide. Some emissions are harmful, toxic, and have been linked to human cancers, *e.g.* NOx, CO, HCN, polycyclic aromatic hydrocarbons, soot and so on. Furthermore, these pollutant emissions are nowadays considered by many countries to be an increasingly severe problem. As a result, there is significant research effort focusing on how to reduce harmful emissions from the combustion process.

The majority of fuel used today is fossil fuel, which is a non-renewable resource. Sooner or later, we will face shortages of such resources. Improvement of combustion efficiency could save a great deal of energy and also the corresponding resources. Therefore, it is very important to know what combustion is and how to manipulate it in order to improve combustion efficiency and reduce harmful emissions.

Laser diagnostics is one of the best ways to investigate the combustion process and emission formation as it is in situ and non-intrusive with high spatiotemporal resolution. Many features such as temperature and species concentrations during the combustion can be captured by advanced laser techniques. In these measurements, a laser source is used as it has a very high intensity and short duration, *e.g.* several nanoseconds, which provides the possibility to 'freeze' the motion of the object in the region of interest. The objects of study in the flame, for example, mixture gas which contains fuel and oxidiser, intermediate species which are produced during the combustion and are not stable, other combustion products and so on, can sometimes be a molecule, an atom or a kind of tracer. In short, when a laser beam reaches the object, it can 'illuminate' the object which could then be detected by a device, for instance, a camera. To use a metaphor, it is like using a torch in a dark room to find something.

However, in many practical machines such as diesel or gasoline engines, gas turbines and heat guns, the flame propagates at a very high rate and in a very turbulent environment. Such turbulence can increase the mixing rate between fuel

and air which contributes to high combustion efficiency. Therefore, high speed laser diagnostics should be developed and applied to the investigation of such combustion processes that have highly transient behaviours. It is extremely capable of following and resolving the development of the turbulent combustion. Once more information about the combustion is known, it is easier for us to manipulate and control the processes involved, which will result in a more efficient and cleaner combustion.

In this thesis work, many laser diagnostics have been developed. The laser-based optical methods cover ballistic imaging (BI), multi-scaler laser introduced fluorescence (LIF) imaging, particle imaging velocimetry (PIV), laser doppler anemometry (LDA), laser introduced exciplex fluorescence (LIEF) imaging, high speed LIF measurement (up to 140 kHz) and so on. The development work was conducted in laboratorial environments and different laboratorial jet burners, which were scaled from gas-turbine combustors.

The developed laser diagnostics have also been applied in a diesel spray with a high temperature high pressure (HTHP) constant volume vessel and in practical combustion devices, *e.g.* internal combustion engines with elevated pressure and temperature (>90 bar and >1000 ^{o}C). The mixing process of gasoline/diesel and air in engines was visualised and investigated. In addition, the combustion process using advanced combustion concepts, *e.g.* partially premixed combustion, in combustion engines was also monitored and studied. Furthermore, the mixture formation and evolution of low temperature combustion as well as high temperature combustion, *i.e.* auto-ignition, were captured and followed in one engine cycle. To the best of my knowledge, no one has ever achieved this before. The understanding of these processes is crucial for increasing engine efficiency and reducing harmful emissions. Therefore, with the research study in this thesis more efficiency and cleaner automotive engines will be developed for the society.

List of papers

I. M. Rahm, M. Paciaroni, **Z. Wang**, D. Sedarsky, and M. Linne, *Evaluation of Optical Arrangements for Ballistic Imaging in Sprays*, Optics Express, Volume 23, Issue 17, Pages 22444-22462, 2015.

II. Z. Falgout, M. Rahm, **Z. Wang**, and M. Linne, *Evidence for Supercritical Mixing Layers in the ECN Spray A*, Proceedings of the Combustion Institute, Volume 35, Issue 2, Pages 1579–1586, 2015.

III. B. Zhou, C. Brackmann, Q. Li, **Z. Wang**, P. Petersson, Z. Li, M. Aldén, and X. Bai. *Distributed reactions in highly turbulent premixed methane/air flames: Part I. Flame structure characterization*, Combustion and Flame, Volume 162, Issue 7, Pages 2937–2953, 2015.

IV. **Z. Wang**, S. Tanov, H. Wang, M. Richter, B. Johansson, and M. Aldén, *High-Speed Particle Image Velocimetry Measurement of Partially Premixed Combustion (PPC) in a Light Duty Engine for Different Injection Strategies*, No. 2015-24-2454, SAE Technical Paper, 2015.

V. **Z. Wang**, S. Lönn, A. Matamis, Ö. Andersson, M. Tuner, M. Aldén, and M. Richter, *Transition from HCCI to PPC: Investigation of Fuel Distribution by Planar Laser Induced Fluorescence (PLIF)*, SAE International Journal of Engines 10, No. 2017-01-0748, 2017.

VI. **Z. Wang**, P. Stamatoglou, Z. Li, M. Aldén, and M. Richter, *Ultra-high-speed PLIF imaging for simultaneous visualization of multiple species in turbulent flames*, Optics Express, Volume 25, Issue 24, Pages 30214-30228, 2017.

VII. **Z. Wang**, P. Stamatoglou, M. Lundgren, L. Luise, B. Vaglieco, A. Andersson, Ö. Andersson, M. Aldén, and M. Richter, *Ultra-high-speed fuel tracer PLIF imaging in a heavy-duty optical PPC engine*, No. 2018-01-0904, SAE Technical Paper, 2018.

VIII. **Z. Wang**, P. Stamatoglou, M. Lundgren, L. Luise, B. Vaglieco, A. Andersson, Ö. Andersson, M. Aldén, and M. Richter, *Simultaneous 36 kHz PLIF/Chemiluminescence imaging of fuel, CH_2O and combustion in a PPC engine*, accepted for oral presentation at the 37th International Symposium on Combustion, 2018.

IX. **Z. Wang**, B. Zhou, S. Yu, C. Brackmann, Z. Li, M. Richter, M. Aldén, and X. Bai, *Structure and burning velocity of turbulent premixed methane/air jet flames in thin-reaction zone and distributed reaction zone regimes*, accepted for oral presentation at the 37th International Symposium on Combustion, 2018.

X. **Z. Wang**, P. Stamatoglou, B. Zhou, M. Aldén, X. Bai, and M. Richter, *Investigation of OH and CH_2O at ultra-high repetition rates by planar laser induced fluorescence imaging in highly turbulent jet flames*, submitted to Fuel, in minor revision.

XI. **Z. Wang**, P. Stamatoglou, C. Kong, J. Gao, Z. Li, M. Aldén, M. Richter, and A. Ehn, *PLIF imaging at 27 kHz of OH radicals - applications in pulsed plasma discharges*, to be submitted .

Related work

A. Z. Falgout, M. Rahm, D. Sedarsky, **Z. Wang**, and M. Linne, *Transcritical Mixing Layers at ECN Spray A Conditions*, 26th European Conference on Liquid Atomization and Spray Systems (ILASS – Europe), Bremen, Germany, September 8-10, 2014.

B. M. Rahm, M. Paciaroni, **Z. Wang**, D. Sedarsky, and M. Linne, *Optical Arrangements for Time-Gated Ballistic Imaging*, Laser Applications to Chemical, Security and Environmental Analysis (LACSEA), Seattle, USA, July 13 – 17, 2014.

C. Q. Li, B. Zhou, **Z. Wang**, P. Petersson, C. Brackmann, Z. Li, M. Richter, M. Aldén, and X. Bai, *Experimental study of reactive turbulent jet flows at high Reynolds numbers*, International Conference on Jets, Wakes and Separated Flows (ICJWSF), Stockholm, Sweden, June 15-18, 2015.

D. S. Tanov, **Z. Wang**, H. Wang, M. Richter, and B. Johansson, *Effects of Injection Strategies on Fluid Flow and Turbulence in Partially Premixed Combustion (PPC) in a Light Duty Engine*, No. 2015-24-2455, SAE Technical Paper, 2015.

E. H. Wang, S. Tanov, M. I. Najafabadi, **Z. Wang**, and B. Johansson, *Time-Resolved In-cylinder PIV Measurement in a Light Duty Optical Engine under PPC Conditions*, 18th International Symposium on the Application of Laser and Imaging Techniques to Fluid Mechanics, Lisbon, Portugal, July 4 – 7, 2016.

F. B. Zhou, C. Brackmann, **Z. Wang**, Z. Li, M. Richter, M. Aldén, and X. Bai, *Thin reaction zone and distributed reaction zone regimes in turbulent premixed methane/air flames: Scalar distributions and correlations*, Combustion and Flame, Volume 175, Pages 220–236, 2017.

G. M. Lundgren, **Z. Wang**, A. Matamis, Ö. Andersson, M. Richter, M. Tuner, M. Aldén, and A. Arne, *Effects of Post-Injections Strategies on UHC and CO at Gasoline PPC Conditions in a Heavy-Duty Optical Engine*, No. 2017-01-0753, SAE Technical Paper, 2017.

H. R. Joakim, X. Bai, J. Sjöholm, B. Zhou, Z. Li, **Z. Wang**, P. Pettersson, Z. Li, M. Richter, and M. Aldén, *Multi-species PLIF study of the structures of turbulent premixed methane/air jet flames in the flamelet and thin-reaction zones regimes*, Combustion and Flame Volume 182, Pages 324-338, 2017.

I. **Z. Wang**, P. Stamatoglou, B. Zhou, M. Aldén, and M. Richter, *Investigation of OH and CH_2O at ultra-high repetition rates by planar laser induced fluorescence imaging in highly turbulent jet flames*, 13th International Conference on Energy for a Clean Environment, São Miguel, Azores, Portugal, July 2-6, 2017.

J. S. Tanov, L. Pachano, Ö. Andersson, **Z. Wang**, M. Richter, J. V. Pastor, J. M. García-Oliver, and A. García, *Influence of spatial and temporal distribution of Turbulent Kinetic Energy on heat transfer coefficient in a light duty CI engine operating with Partially Premixed Combustion*, Applied Thermal Engineering, Volume 129, Pages 31-40, 2018.

K. Y. Tong, X. Liu, **Z. Wang**, M. Richter, and J. Klingmann, *Experimental and Numerical Study of Bluff-body and Swirl Stabilized Diffusion Flames*, Fuel, Volume 217, Pages 352-364, 2018.

L. M. Lundgren, A. Matamis, **Z. Wang**, P. Valladolid, M. Richter, Ö. Andersson, and A. Andersson, *Lift-off Lengths of Gasoline and Diesel at High Load Operation in an Optical Heavy-Duty Engine*, No. 2018-01-0245, SAE Technical Paper, 2018 .

M. M. Denny, H. Persson, **Z. Wang**, A. Matamis, M. Richter, and Ö. Andersson, *Optical Investigation on the Combustion Process Differences between Double-Pilot and Closely-Coupled Triple-Pilot Injection Strategies in a LD Diesel Engine*, submitted to SAE International Powertrains, Fuels & Lubricants Meeting, Heidelberg, Germany, 2018.

N. **Z. Wang**, P. Stamatoglou, M. Lundgren, A. Andersson, Ö. Andersson, M. Aldén, and M. Richter, *Ultra high-speed CH_2O PLIF imaging in a heavy-duty optical PPC engine*, manuscript in preparation, to be submitted to Measurement of Science and Technology.

Abbreviations

AOM	Acousto-Optic Modulator
ASE	Amplified Spontaneous Emission
ASOC	After Start Of Combustion
ATDC	After Top Dead Centre
BBO	β-Barium Borate
BI	Ballistic Imaging
BTDC	Before Top Dead Centre
CAD	Crank Angle Degree
CCD	Charge-Coupled Device
CCV	Cycle-to-Cycle Variations
CH2O	Formaldehyde
CMOS	Complementary Metal–Oxide–Semiconductor
CO	Carbon monoxide
CS2	Carbon disulphide
CW	Continuous Wave
DPSS	Diode Pumped Solid State
DRZ	Distributed Reaction Zone
ECN	Engine Combustion Network
EGR	Exhaust Gas Recirculation
EOI	End of Injection
EOM	Electro-Optic Modulator
FHG	Fourth Harmonic Generation
FOV	Field Of View

FWHM	Full Width at Half Maximum
HCCI	Homogeneous Charge Compression Ignition
HRR	Heat Release Rate
HTHP	High Temperature High Pressure
IA	Interrogation Area
ICCD	Intensified Charge-Coupled Device
ICE	Internal Combustion Engine
IEA	International Energy Agency
KDP	Potassium Dihydrogen Phosphate
LDA	Laser Doppler Anemometry
LDV	Laser Doppler Velocimetry
LED	Light-Emitting Diode
LIF	Laser Induced Fluorescence
LTC	Low Temperature Combustion
LUPJ	Lund University Piloted Jet burner
MCP	Microchannel Plate
NOx	Nitrogen Oxides
OD	Optical Depth
OH	Hydroxyl
OKE	Optical Kerr Effect
OPO	Optical Parametric Oscillator
PAH	Polycyclic Aromatic Hydrocarbon
PD	Photodiode
PDI	Phase Doppler Interferometry
PIV	Particle Imaging Velocimetry
PLIF	Planar Laser Induced Fluorescence
PMT	Photomultiplier Tube
PPB	Parts Per Billion

PPC	Partially Premixed Combustion
PPCI	Partially Premixed Compression Ignition
PPM	Parts Per Million
RMS	Root-Mean-Square
RPM	Rounds Per Minute
SHG	Second Harmonic Generation
SLIPI	Structured Laser Illumination Planar Imaging
SNR	Signal-to-Noise Ratio
SOC	Start of Combustion
SOI	Start of Injection
TDC	Top Dead Centre
THC	Total hydrocarbon
THG	Third Harmonic Generation
TRZ	Thin Reaction Zone
TTL	Transistor-Transistor Logic
USI	Ultrafast Shadow Imaging
UV	Ultraviolet

1. Introduction

Combustion has a long history and it plays a very important role in the lives of human beings. In addition, combustion has been used for over 100 centuries and it will continue to be important for the foreseeable future. As can be seen in the data from International Energy Agency (IEA) [1] in Figure 1.1, the major part of energy consumption is from combustible fuel, both in the past and in the future. Thus, improvement of combustion efficiency could save huge amounts of energy and the corresponding resources.

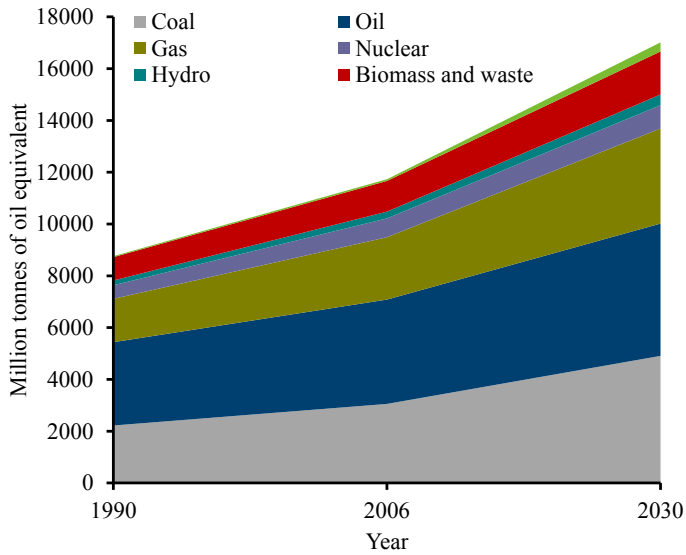

Figure 1.1. Global total primary energy consumption by fuel from IEA [1].

Transportation has a high demand of energy from fuels and today transportation mainly relies on the oil-type of fuel, demand for which is estimated to grow from 2015 to 2040 as shown in Figure 1.2. Moreover, light-duty and heavy-duty engines will be major parts of the transportation sector as shown in Figure 1.3. Therefore, investigation into them and improvement of their efficiency in the near future is of utmost importance for saving energy in the world. In addition, it is essential to investigate and understand the combustion process in light-duty and heavy-duty engines, in order to reduce the harmful emissions.

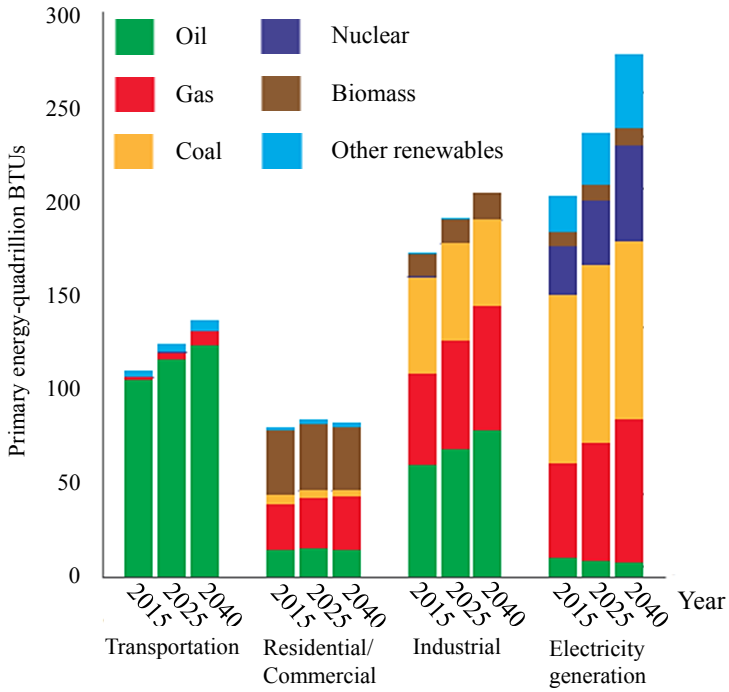

Figure 1.2. Energy demand for different usages [2].

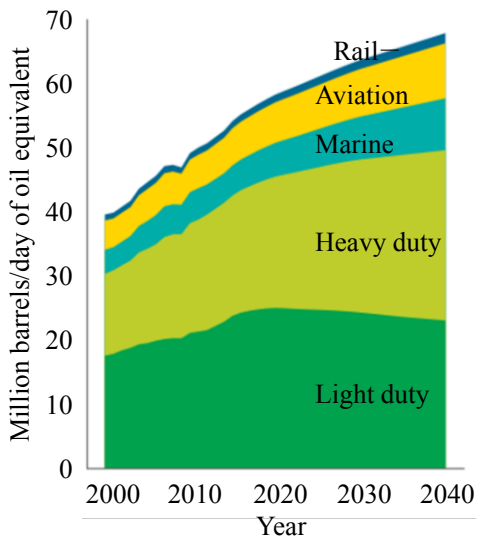

Figure 1.3. Outlook of energy for transportation [2].

Running an engine for transportation usually includes the following processes: fuel injection, mixing with oxidiser and combustion for output work. Laser diagnostics is one of the best ways to investigate these processes and emission formation as it is in situ and non-intrusive with high spatiotemporal resolution [3, 4]. Diagnostics for experimental combustion research have received considerable attention since the 1970s, *e.g.* in May 1975, project SQUID conducted a workshop lasting several days which focused on combustion measurements in jet propulsion systems [5].

As regards the fuel injection process, combustion devices with liquid fuel and high pressure injection systems are very common in order to provide better atomisation in a very short time (~ms). The atomisation of the spray largely affects the combustion behaviour. Therefore, it is important to investigate the spray breakup and atomisation. In dense sprays, *e.g.* diesel sprays, ballistic imaging (BI) with ultra-short laser pulses is a technique to visualise the liquid core in the spray formation region through the droplet clouds [6]

Turbulent combustion commonly occurs in most practical advanced combustors, such as internal combustion engines (ICEs) and gas turbines. Comprehensive understanding of turbulent combustion calls for more advanced modelling and diagnostic techniques. Detailed measurements of flame structure at high spatial and temporal resolution helps to understand the transient behaviour, *e.g.* eddies in the flow field of a turbulent flame can form, interact and propagate rapidly. However, it is still challenging to perform such measurements in highly turbulent flames, especially at ultra-high repetition rates.

With the development of high speed techniques, it becomes feasible to facilitate the acquisition of multiple images at high repetition rates and high signal-to-noise ratio (SNR) [7-29]. In addition, the presence of cycle-to-cycle variations (CCV) and the need to temporally resolve events within a single cycle have led to the application of high-repetition rate laser diagnostic for cycle-resolved imaging in ICEs.

In this thesis, laser diagnostics for investigation of spray and combustion in practical engines as well as turbulent flames are studied. In particular, high speed diagnostics are developed and employed.

The structure of this thesis will be as follows:

Chapter 1 briefly describes the need for the research work in the thesis and gives a short introduction of the thesis.

Chapter 2 illustrates the experimental equipment and setups used in the research work.

Chapter 3 introduces the laser diagnostic methods involved in the experiments in this thesis, such as ballistic imaging, laser induced fluorescence (LIF), particle imaging velocimetry (PIV), laser Doppler anemometry (LDA) *etc.*

Chapter 4 summarises the results including the development of different laser diagnostics for spray imaging and combustion investigation in laboratorial environment as well as the application of the developed laser diagnostics in a diesel spray with a high temperature high pressure (HTHP) constant volume vessel, in a plasma discharge system and in combustion engines.

Chapter 5 sums up the work in the thesis and gives an outlook on the future.

2. Experimental equipment and setups

The experimental equipment and setups for the studies in this thesis are illustrated in this chapter. The equipment includes laser systems, detectors, an HTHP vessel, burners, optical engines, a plasma discharge system and other accessories. The experimental setups include BI measurements in turbid media, an LDA measurement in a burner, high speed planar laser induced fluorescence (PLIF) measurements in a burner, high speed PLIF measurements in a plasma discharge system, high speed PIV measurement in an optical engine and high speed PLIF measurement in an optical engine.

2.1. Lasers

2.1.1. Femtosecond pulsed laser

A mode-locked Ti:Sapphire oscillator (*e.g.* Spectra-Physics Mai Tai) is usually used in order to generate ultra-short laser pulses, *e.g.* generating ~100 fs pulses at full width at half maximum (FWHM). The oscillator seeds a chirped-pulse regenerative amplifier (*e.g.* Spectra-Physics Spitfire) to produce amplified pulses with 4 mJ/pulse and centred wavelength at 800 nm. The beam diameter is about 8 mm.

2.1.2. 10 Hz Nd:YAG laser

Generally, an Nd:YAG laser contains yttrium aluminium garnet (YAG) and neodymium(Nd^{3+}) solid-state material as gain materials from which a laser beam absorbs and accumulates energy before emitting from a cavity triggered by Q switching. A Q-switch is usually made of a high voltage Pockels cell and the Q switching technique is used in a solid-state laser which has long upper-state lifetimes to easily store a great deal of energy in the crystal, like a dam. In the history of PLIF, Nd:YAG lasers are employed in almost all measurements for

detection of species, concentration, temperature and so on [4]. The principle of LIF will be introduced in the next chapter. The pulse width of such lasers is typically on the order of 10 ns, which provides the possibility to 'freeze' the motion of the object in the region of interest. In addition, the power density or the laser intensity can be sufficiently high due to short pulse duration. The wavelength of the laser is commonly 1064 nm where it reaches best efficiency [30, 31]. Usually, second harmonic generation (SHG), third harmonic generation (THG) and fourth harmonic generation (FHG) are used to convert the fundamental wavelength, *i.e.* 1064 nm, into 532 nm, 355 nm and 266 nm, respectively. They are made by non-linear crystals such as beta barium borate (BBO) or potassium dihydrogen phosphate (KDP). These wavelengths are more useful for LIF measurements. Moreover, an Nd:YAG laser cluster provides the opportunities to achieve high speed measurements, *e.g.* > 10 kHz, with 8 images. More detailed information on the laser cluster can be found in references [4, 32-34].

2.1.3. High speed Nd: YLF laser

Lasers with solid-state gain media are also often used for PIV measurement to obtain the velocity field. The principle of PIV will be introduced in the next chapter. An Nd:YLF (neodymium-doped yttrium lithium fluoride) solid-state laser pumped by diodes, *i.e.* a diode pumped solid state (DPSS) laser, has better performance as regards power efficiency, long lifetime, thermal effects and beam quality than those optically pumped with flash lamps. In this thesis work, a Q-switched Nd:YLF laser (Litron LD30-527) was used which is capable of producing an average output power of ~30 W at 527 nm and pulse repetition rates from 1 kHz to 20 kHz. Furthermore, such lasers are also used for pumping the amplifiers such as the Spectra-Physics Spitfire in the aforementioned femtosecond pulsed laser system.

2.1.4. Burst-mode laser

Figure 2.1 and Figure 2.2 show a photo and a schematic drawing of the layout inside the burst-mode laser system (Quasimodo, Spectral Energies) used in this thesis work, and the layout of harmonic generations for the burst-mode laser. The optical setup for frequency conversion, *i.e.* harmonic generations, is similar to commonly-used 10 Hz Nd:YAG lasers.

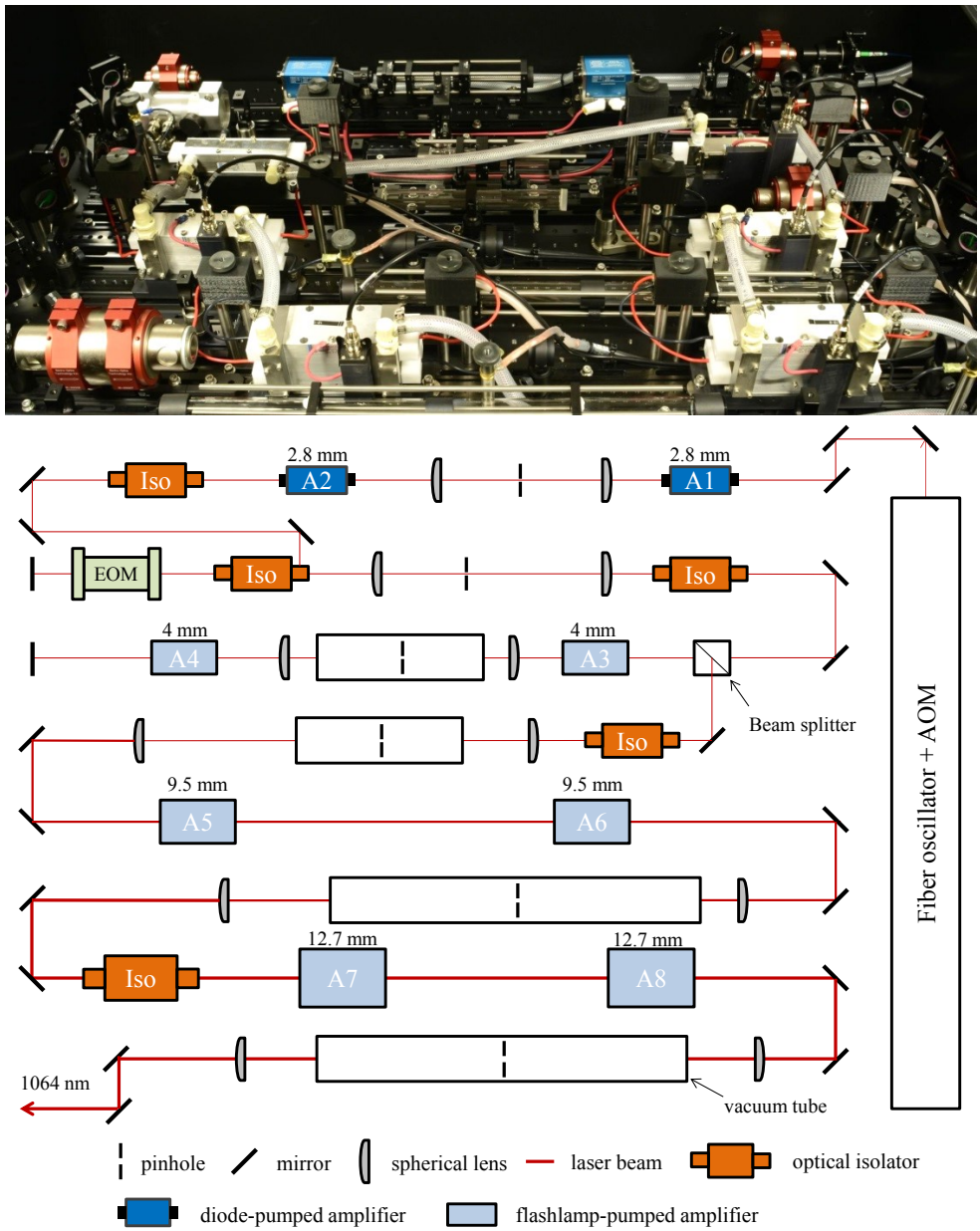

Figure 2.1. Photo (courtesy of M. Richter) and schematic drawing of the layout inside a burst-mode laser.

A single mode (spectral linewidth <100 MHz) laser (*e.g.* IPS 1064SU0120PA) produces a continuous wave (CW) laser beam at 1064 nm as shown in Figure 2.3(a). The laser beam is guided through optical fibers to an acousto-optic modulator (AOM) and two fiber amplifiers. The AOM slices the CW laser into a pulse train as shown in Figure 2.3(b). The gate time of AOM is 10 ns which creates pulses of 10 ns width. However, using the first order of diffraction of the AOM cannot block all the background noise. Furthermore, the background noise, which is located between two pulses, is not coherent. When that light passes through the next stages of amplifiers it will consume the gain that is used for amplifying the coherent light. This is usually defined as amplified spontaneous emission (ASE). An electro-optic modulator (EOM) is employed to suppress the ASE, which will be discussed later. The repetition rate of the laser pulse is adjustable and is controlled by the AOM. For instance, the repetition rate can cover from 10 kHz up to 1000 kHz. However, a consequence of higher repetition rates is a decrease in laser pulse energy, as the total burst power is nearly constant. The AOM-frequency in this thesis was set to generate, for example a 27 kHz, 36 kHz, 50 kHz, 100 kHz or 140 kHz pulse train.

In this burst-mode laser, there are four amplification stages including two diode-pumped amplifiers and six flashlamp-pumped amplifiers. After the AOM, the

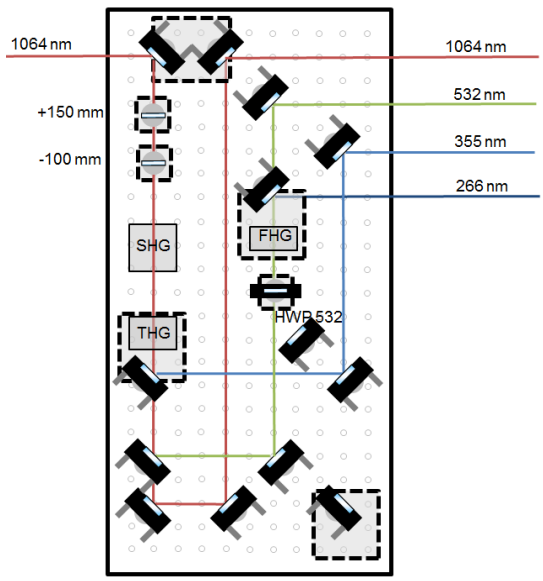

Figure 2.2. Layout of harmonic generations for a burst-mode laser (courtesy of M. Slipchenko).

pulse train is guided by optical fibers and several mirrors towards the first amplification stage. In this stage, the pulse train is amplified by two 2.8-mm-diameter Nd:YAG-rod diode-pumped amplifiers (A1 and A2 in Figure 2.1). An optical relay including two convex spherical lenses is placed between the amplifiers. A spatial filter is positioned at the focus point of the lens to reduce high spatial frequency noise and to produce a uniform Gaussian beam profile. After the diode-pumped amplifiers, a Faraday-rotation optical isolator is used to prevent any back reflected light entering into the amplifiers, being amplified again and damaging the upstream optical components afterwards. The pulse energy after the first amplification stage is below 1 mJ at 27 kHz.

After the isolator, there is a double-pass of the laser beam including another optical isolator and the EOM. This configuration enables a dramatic reduction of

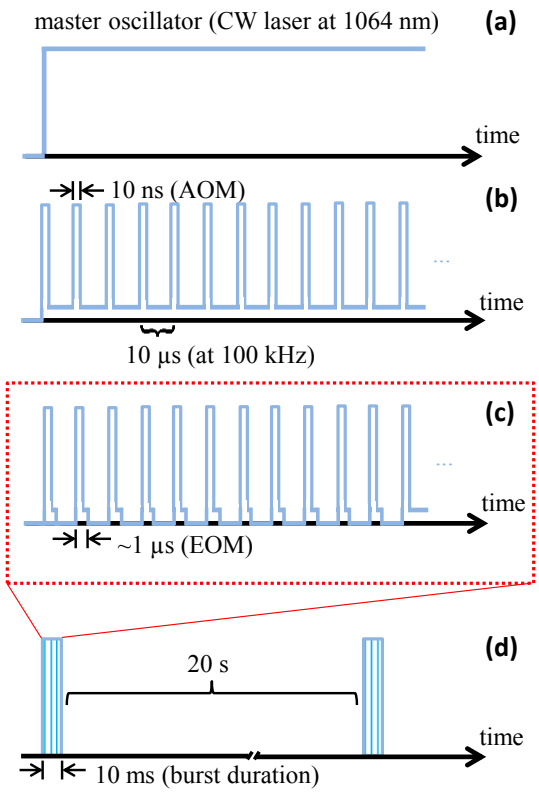

Figure 2.3. The producing strategy of pulse trains for the burst-mode laser with fundamental wavelength at 1064 nm. (a) – (c) represent the pulse train at different locations of the beam path, *i.e.* from the master oscillator to the EOM; (d) shows pulse trains between two bursts.

the ASE as shown in Figure 2.3(c). The gate width of the EOM is around 1 μs, whereas the envelope of the EOM waveform in a burst is adjustable as well, providing freedom to control the pulse energy distribution within a burst so that it is as uniform as possible. For example, if the pulse energy is higher at the beginning of the burst, the voltage of the EOM can be lowered for these initial pulses to achieve small pulse energy variation throughout the burst.

After the double-pass of the isolator and EOM, another optical relay and spatial filter are utilised to reduce the noise. An optical isolator is employed before the pulse train passes through the second amplification stage. In this stage, two 4-mm-diameter flashlamp-pumped amplifiers A3 and A4 are used in a double-pass configuration. An optical relay is placed between the amplifiers. Moreover, a spatial filter is installed in a vacuum tube to prevent any ionisation by the laser at the focus point of the lens. Due to higher and higher laser pulse energy, spatial filters in downstream optics are also placed in vacuum tubes. After the double-pass of two amplifiers, the pulse train is guided by a beam splitter to the next amplification stage.

Two xenon flashlamps are exerted to optically pump an Nd:YAG gain medium in each flashlamp-pumped amplifier in this laser system. The amplifier employs water cooling systems to remove the heat created by the flashlamps. However, the burst duration is at an order of several milliseconds. Therefore, even with thermal management, the huge amounts of heat cannot transfer promptly and sufficiently during the burst, which can result in some undesired effects *e.g.* thermal lensing. In order to compensate for the thermal lensing effect, amplifier A3 is rotated 90 degrees around the laser beam direction compared to amplifier A4. Another approach to mitigate the adverse effect is to setup a sufficiently long time interval between the two bursts, *e.g.* ≥20 seconds, as shown in Figure 2.3(d).

Another set of optical relay and spatial filter (with vacuum tube), and an optical isolator are used before the pulse train passes through two 9.5-mm-diameter flashlamp-pumped amplifiers, A5 and A6. After the amplification by A5 and A6, similar to the previous stage, optical relay, spatial filter (with vacuum tube) and isolator are used before the pulse train enters into the next amplification stage.

Two 12.7-mm-diameter flashlamp-pumped amplifiers are employed in the last amplification stage. The last set of optical relay and spatial filter (with vacuum tube) are placed after the amplifiers A7 and A8. The usage of this spatial filter is mainly to block the back reflection light as the size of the pinhole is fairly large, *e.g.* ≥3 mm. The output of the burst-mode laser is approximately 1.4 J per pulse at 10 kHz. Each pulse in a burst is comparable to that produced by commonly-used 10 Hz Nd:YAG laser as regards pulse energy.

2.1.5. Continuous wave solid-state laser

The development of DPSS lasers meant that they recently become available with power levels suitable for LDA or laser Doppler velocimetry (LDV). Two coherent beams from the DPSS lasers are focused at the same point in space, which is called 'probe volume' where velocity information can be obtained, when a particle or droplet passes through it. Usually, two pairs of lasers are used at two wavelengths, *e.g.* 488 nm and 515 nm, to measure the velocity component in two dimensions. In this thesis, backscatter operating mode of an LDA was used to obtained high temporal resolution velocity information in a jet flame. A Bragg cell is used in LDA systems to make a frequency shift for one laser beam out of a pair to be able to detect the Doppler effect when a particle passes through the probe volume and consequentially changes the scattered frequency. More details about the principle of LDA will be described in the next chapter.

2.1.6. OPO

Nd:YAG lasers have fixed output wavelength with harmonic generations, *e.g.* 1064 nm, 532 nm, 355 nm, 266 nm, *etc.*, while they are 527 nm, 264 nm, *etc.* for Nd:YLF lasers with harmonic generations. However, there are several ways to have a tunable laser radiation, *e.g.* a dye laser which contains large organic molecules dissolved in alcohol to work as gain media. Another way to generate a tunable laser beam is to use an optical parametric oscillator (OPO).

Figure 2.4 illustrates the schematic sketch of the OPO (GWU, PremiScan/ MB) system used in this thesis work. A telescope is used to reduce the size of the laser beam in order to have higher laser irradiance and better conversion efficiency. A 355 nm wavelength laser is used as a pumping beam and is guided by two mirrors into a resonator cavity, including two resonator mirrors and a BBO crystal. The angle of the BBO crystal controls the output wavelength which is, for example, tuned to 568 nm in hydroxyl (OH) PLIF measurements. By adjusting the resonator mirrors, the optimal output can be achieved. An ultraviolet (UV) filter is used only to absorb the residual 355 nm laser. The offset of the beam path caused by rotating the BBO crystal is controlled with a compensator. After the resonator cavity, the desired laser, *e.g.* at 568 nm wavelength, and idler laser (*e.g.* at 947 nm) beams are separated by a dichroic mirror. The idler beam is terminated with a beam dump. A beam splitter is used in the beam path of the desired laser before the OPO outlet. After the beam splitter, a fraction of the desired laser enters a wavemeter (GWU, LambdaScan) for monitoring the output wavelength. Several neutral density filters are used to reduce the laser power in order to protect the wavemeter. Such OPO can also be pumped by lasers at other wavelengths depending on the choice of BBO crystal.

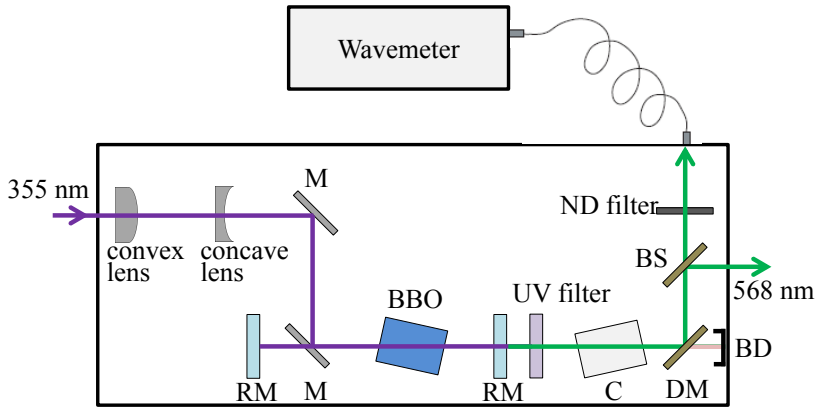

BBO: beta barium borate (BBO) crystal
BS: beam splitter
BD: beam dump
C: compensator
DM: dichroic mirror
M: HR 355 nm mirror
ND filter: neutral density filter
RM: resonator mirror

Figure 2.4. Schematic sketch of the OPO.

2.2. Detectors

In order to capture the signal generated by laser techniques, *e.g.* laser induced fluorescence, Mie scattering, Rayleigh scattering, ballistic photons, *etc.*, detectors such as a charge-coupled device (CCD), complementary metal–oxide–semiconductor (CMOS) and photomultiplier tube (PMT) are usually employed. Intensified CCD (ICCD) cameras and high speed intensifiers combined with high speed CMOS cameras are able to achieve very fast gate times, *e.g.* orders of nanoseconds. The intensifier has an evacuated tube which contains a photocathode, a microchannel plate (MCP) and a phosphor screen. The photocathode is for converting light to an electron current which will be amplified by MCP and will generate phosphorescence afterwards on the phosphor screen. Therefore, not only the signal is amplified, but it is also possible to detect UV light which cannot be easily detected by a CCD or a CMOS chip. One of the drawbacks is that with an intensifier, the spatial resolution is diminished. More detailed information on intensifiers can be found in [35].

2.3. An HTHP vessel with spray injection system

A high temperature high pressure vessel is used to control the environment pressure and temperature. Figure 2.5 shows a photo of it at Chalmers University. It is a constant volume chamber with four optical quartz windows, which are at 90-degree angles to each other, at each side of it to allow the optical access. In addition, a compressor is used to pressurise the gas, *e.g.* air, N2 *etc.* The pressurised air is fed from the top of the vessel with an electrical resistance heater to heat up the gas. The injector is mounted on the top of the vessel. It is also possible to replace a side window with a metal holder to mount an injector at the side of it. There is cooling water running in the water jacket of the vessel to cool down the surface. The fuel temperature of the injector can be adjusted by the cooling water with a separated water jacket.

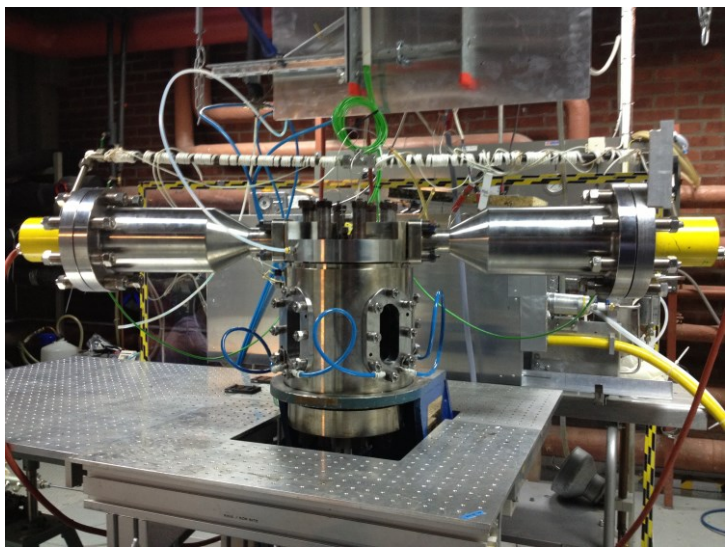

Figure 2.5. Photo of the HTHP vessel at Chalmers University.

The air is a steady flow which also purges the environment inside the vessel. During the work in this thesis, the pressure went up to 60 bar and the temperature increased to 900 K in the vessel.

The diesel injector for spray investigation is a standard engine combustion network (ECN) Spray A injector. More detailed information about the configuration of the injector and the experiment's conditions can be found in reference [36].

2.4. LUPJ burners

In this thesis work, a Lund University Piloted Jet (LUPJ) burner was used, which is a hybrid porous-plug/jet type burner, with a 1.5-mm-diameter nozzle, a 2.2-mm-diameter tube or a 4.5-mm-diameter tube in the center utilised for the creation of a jet flame. The premixed methane/air jet flame was stabilised by a reacting co-flow above the porous sintered stainless steel plug burner that has a diameter of 61 mm. The reacting co-flow was generated from a premixed methane/air flat-flame at 0.9 equivalence ratio to sustain the jet flame by supporting enough heat. The piloted co-flow flame was set to a slightly leaner condition to avoid soot and the combustion of the jet flame being affected by the unburnt reactants from the co-flow. The equivalence ratio of the jet flame and the flow speeds of the jet flame and co-flow were varied in this thesis work in order to investigate the turbulent flame characteristics. More detailed information on the LUPJ burner can be found in references [37-40].

Figure 2.6 shows a turbulent jet flame (Figure 2.6a) and a laminar jet flame (Figure 2.6b) in the burner with 1.5-mm-diameter nozzle. The blue color in the figure is from the CH*, C_2 and hot H_2O emission.

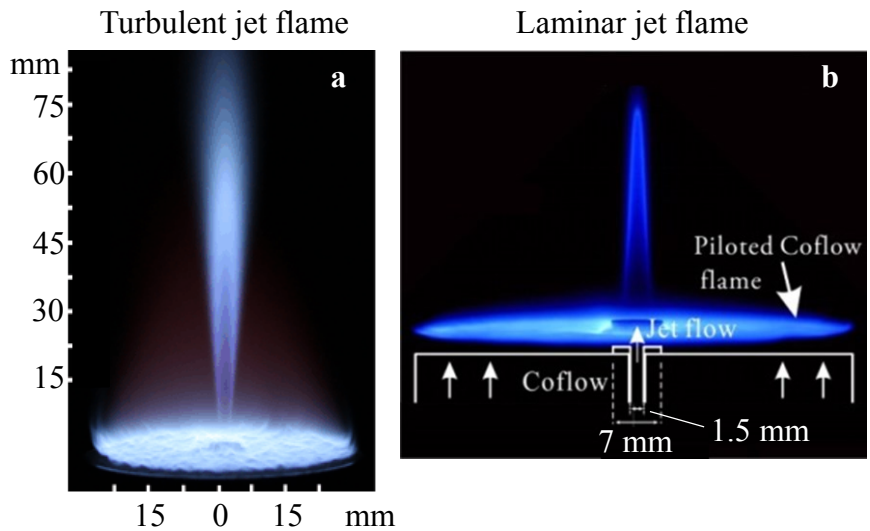

Figure 2.6. Photos of LUPJ burners with a turbulent jet flame (a) and a laminar jet flame (b). The figure is adapted from the reference [38].

2.5. Optical engines

An optical engine with windows and an optical piston usually provides optical access into the combustion chamber for the investigation of the atomisation, mixture process, combustion behaviour and emissions. At Lund University, optical engines are modified based on standard production engines. One cylinder is equipped with a piston extension, while tungsten weights are added to the other pistons in order to maintain balance. In this thesis work, the layout of optical engines is based on the traditional Bowditch design [41] with several side windows or a full quartz liner and a hollow piston extension with a quartz piston in a titanium retainer. That allows optical access from the sides and from below into the combustion chamber.

Figure 2.7 shows a sketch of a light-duty optical engine. At the top of the figure, there is a cylinder head which is the same as the original engine. Below it, extended liner and piston are installed which are not present in metal test engines or in production engines. Inside the extended piston, a 45-degree mirror, which is usually an aluminium mirror with UV enhanced coating, is mounted to reflect the light from the combustion chamber through the optical piston to the detectors.

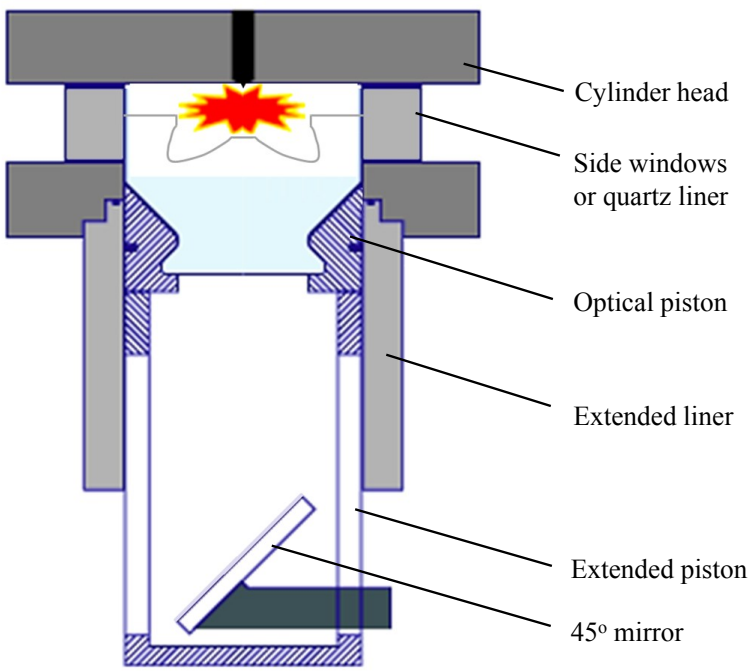

Figure 2.7. Sketch of a light-duty optical engine.

Figure 2.8 displays the optical piston with quartz piston crown. The piston can be made with a complicated piston bowl shape, *e.g.* re-entrant bowl shape, which is the same as the standard diesel combustion chamber design for a commercial passenger car engine. Figure 2.9 presents a photo of a light-duty optical engine at Lund University.

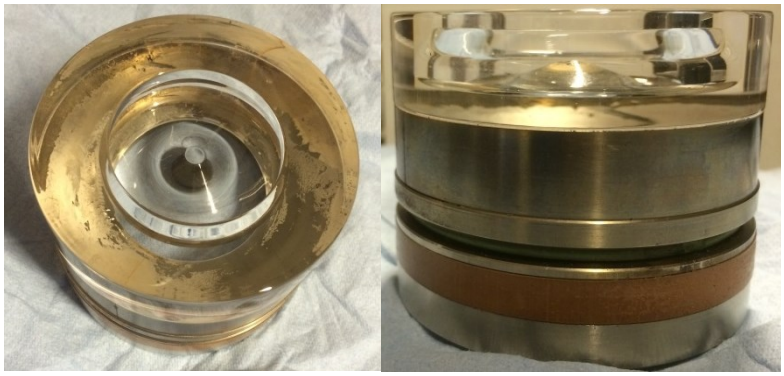

Figure 2.8. Photos of an optical piston.

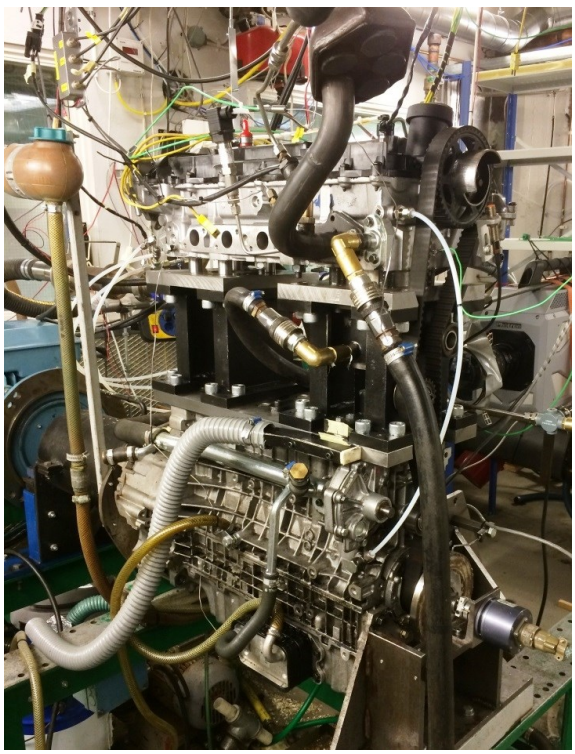

Figure 2.9. Photo of a light-duty optical engine at Lund University.

2.6. Plasma discharge systems

Figure 2.10 shows a photo of a plasma discharge system at Lund University, *i.e.* a gliding arc discharge system. A schematic diagram of the gliding arc discharge system is shown in Figure 2.11. Similar configurations are detailed in references [42-50].

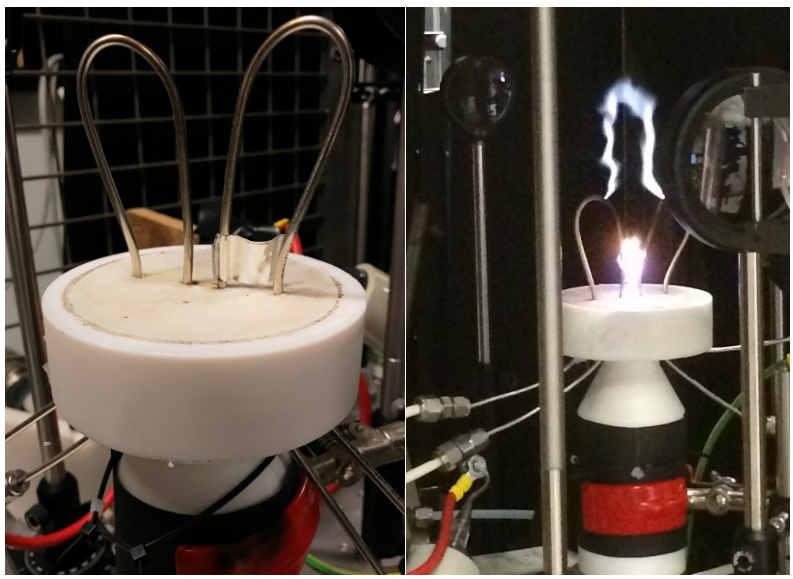

Figure 2.10. Photos of a plasma discharge system at Lund University.

The pulsed discharge is driven by an AC power supply at a frequency of 35 kHz (Generator 9030E, SOFTAL Electronic GmbH, Germany), corresponding to a full cycle period of 28 μs. The power supply is triggered by a programmable pulse generator (BNC 575) in a burst mode. The time duration of the high-voltage burst is adjustable, *e.g.* >10 ms, which is enough to make the gliding arc propagate into the field-of-view.

In addition, afterglow studies can be performed with synchronisation between the discharge system and a camera. Details about synchronisation, data acquisition, plasma ignition and burst-mode operation for this setup were described by Sun *et al.* [42].

The input power to the gliding arc can be adjusted, *e.g.* 600 - 1200 W. The effective electrical circuit driving the gliding arc discharge is shown in Figure 2.11. The high voltage output of the power supply is connected to one electrode

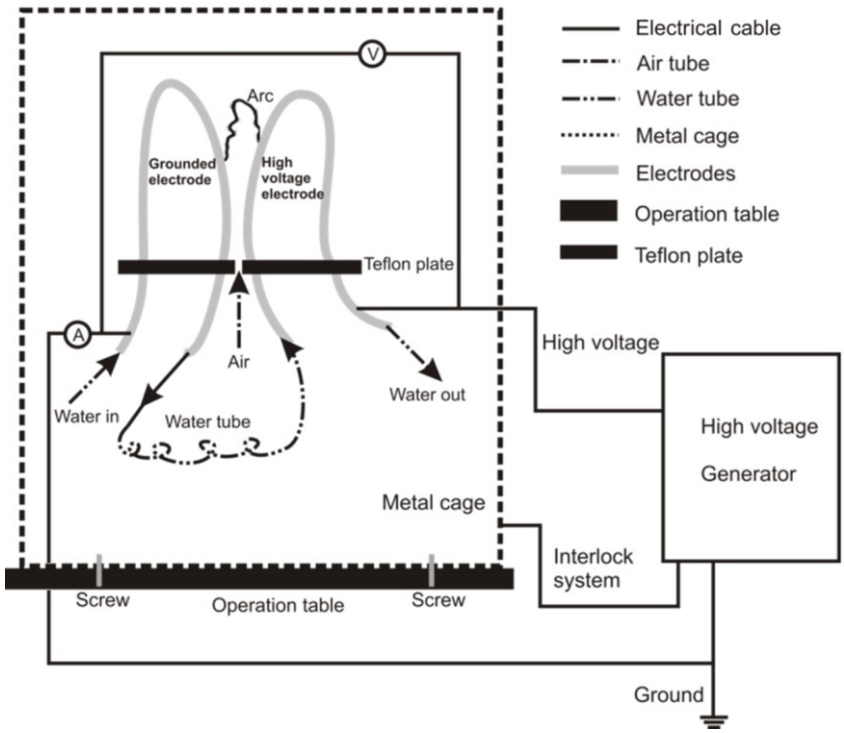

Figure 2.11. Schematic diagram of the gliding arc discharge system.

and the other electrode is grounded. Both the grounded and high voltage electrode are made of hollow stainless steel tubes with an outer diameter of 3 mm, where cooling water can be circulated. The electrodes are fixed on a Teflon plate with a closest gap separation of approximately 5 mm.

An air jet is ejected from a circular channel (with a diameter of 3 mm) that is located in the centre of the Teflon plate. The jet flow is controlled by mass flow controllers which provide a mass flow corresponding to several standard litres per minute. The plasma channel is first established at the narrowest gap between the two diverging electrodes and starts elongating and propagating upwards due to the jet flow as shown in Figure 2.10.

2.7. Experimental setups

Figure 2.12 shows a photo of BI experiment setup on an optical table including an optical time delay which consists of two mirrors at 90 degrees, mirrors, a

resolution test chart, a container for polystyrenes as turbid media, Glan polarisers, waveplates, convex spherical lenses, a cell for carbon disulfide (CS_2) liquid, a screen for monitoring BI, a camera with objective lens, translation stages and some accessories. More detailed comparison between two BI setups will be described and discussed in Chapter 4.

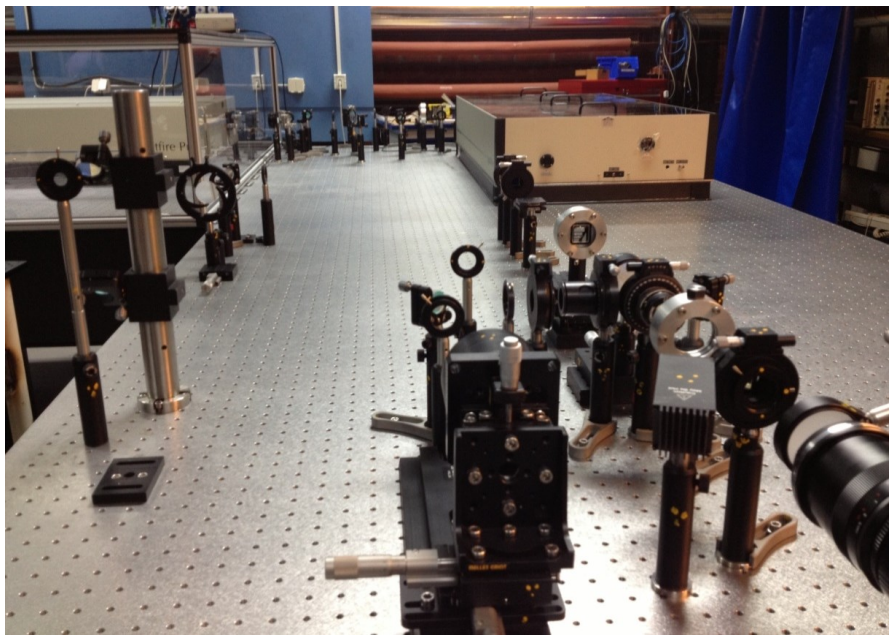

Figure 2.12. Photo of the BI experimental setup.

Figure 2.13 shows photos of the PIV experiment with an optical engine. The laser light was at 527 nm wavelength and coming from the right side of the figure. The full quartz liner is illuminated by the laser as seen by the part with shining green colour in the figure. A protection glass is used in front of the camera lens. In the event of the full quartz liner exploding due to a failure, this can protect the camera lens and the camera which are quite expensive. A quartz window is utilised instead of a glass one if detection of UV signal is needed.

Figure 2.14 shows a photo of LDA experimental setup with an LUPJ burner. In addition, Figure 2.15 shows a photo of four laser beams from the LDA crossing over in a jet flame to obtain 2D velocity information. The LDA system is a commercial product (Flow Explorer DPSS & BSA F80 processor unit) from Dantec Dynamics Company.

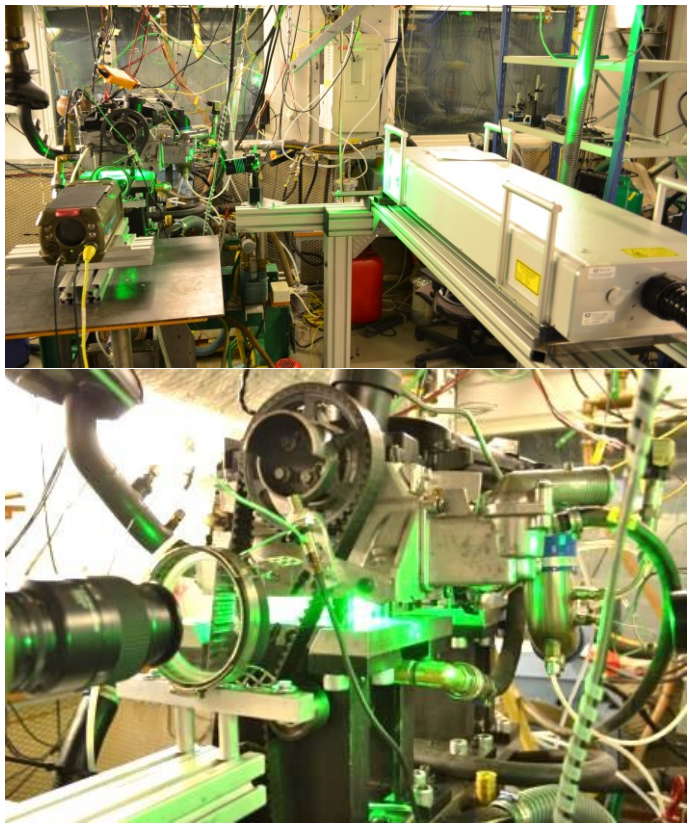

Figure 2.13. Photos of the PIV experiment with an optical engine.

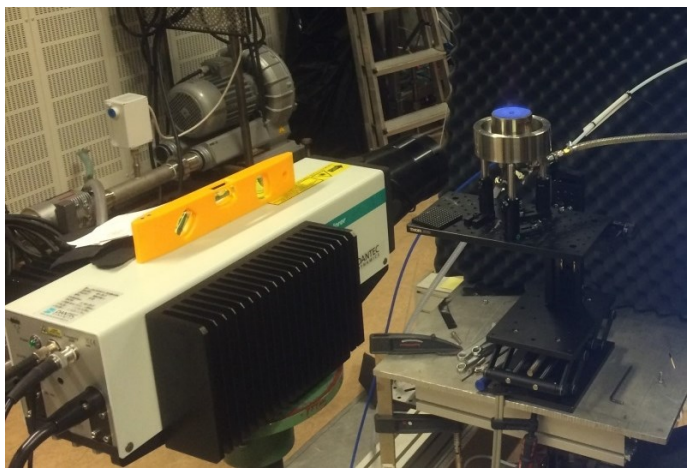

Figure 2.14. Photo of the LDA experiment with an LUPJ burner.

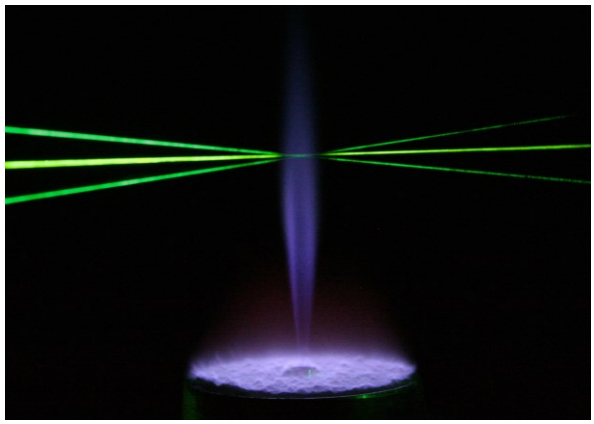

Figure 2.15. Photo of the crossing beams of LDA with an LUPJ burner.

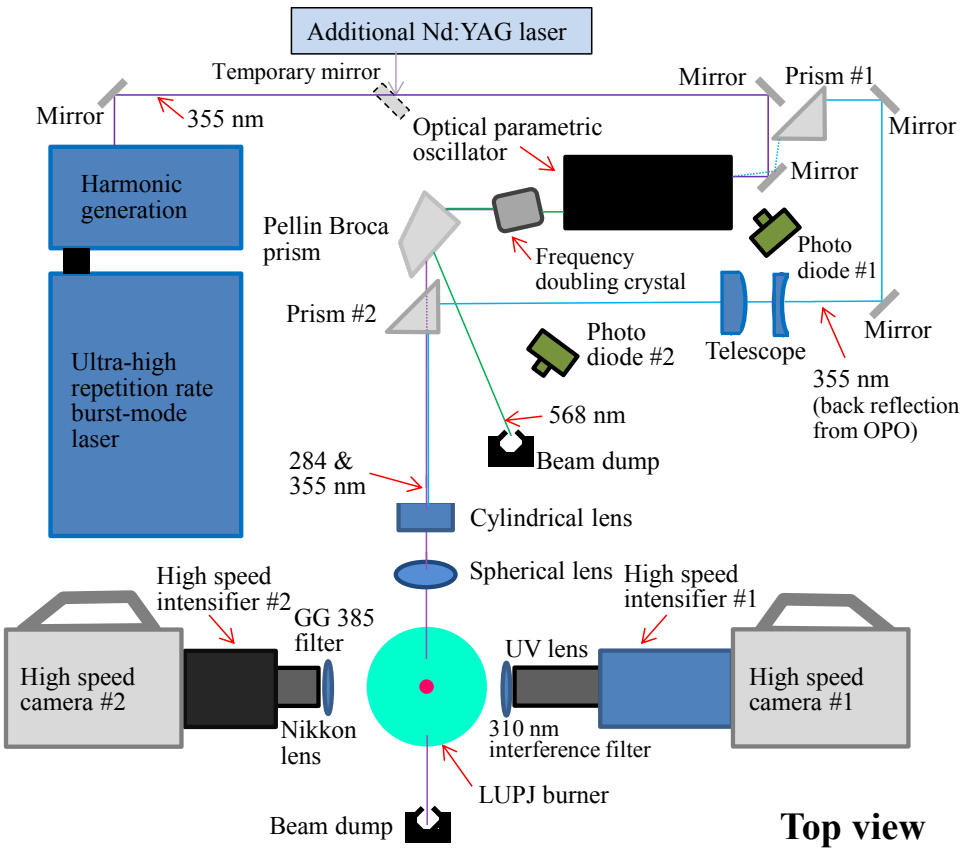

Figure 2.16. Sketch of experimental setup for simultaneous OH/CH_2O PLIF measurements at 50 kHz. The figure is adapted from Paper VI.

Figure 2.16 shows a sketch of simultaneous OH/CH_2O PLIF measurements at 50 kHz, which is adapted from Paper VI. The alignment with the burst-mode laser is a little troublesome. It takes about 12 seconds to generate a pulse train at 355 nm. If the idle time is too short, the laser beam becomes smaller due to thermal lensing effect. The increased fluence could damage the BBO crystal (damage threshold at 700 mJ/cm^2) in OPO. Also, within a burst, the interval between laser pulses is very short, *e.g.* 20 μs, which leads to a rapid accumulation of heat on the optics surface. That could damage the mirrors in the beam path. Figure 2.17 displays a failure of an HR at 355 nm mirror. The burn mark on the mirror can be seen distinctly.

Nevertheless, if the energy of the pumping pulse is too low, the output of OPO at 568 nm has quite high fluctuations as seen in Figure 2.18. That results in fluctuations of 284 nm beam after KDP (a frequency doubling crystal) as well. It is a trade-off. The optimal pumping energy density should be approximately 630 mJ/cm^2 given the pulse to pulse variation of 355 nm is less than 10%.

For the alignment of OPO with burst-mode laser, an additional 10 Hz Nd:YAG laser with harmonic generations would be of great help. If the beam paths of both lasers for pumping the OPO are overlapped, the beam path after OPO for the 10 Hz laser and the burst-mode laser should theoretically be the same. Therefore the alignment for the OPO and OH PLIF measurements as well as OH excitation scan can be performed with the 10 Hz laser first and with the burst-mode laser afterwards. That procedure can make the alignment of the measurements with the burst-mode laser much easier and more efficient. The left-hand side of Figure 2.19 shows an ICCD camera (PI MAX2) for the 10 Hz Nd:YAG laser while the right side of the figure displays a high speed CMOS camera (Photron Fastcam SA-Z) with a high speed intensifier (Lavision HS-IRO) for the burst-mode laser. OH PLIF result is shown on the screen of the computer in the illustration.

Figure 2.17. Photo of a damaged mirror in the OPO.

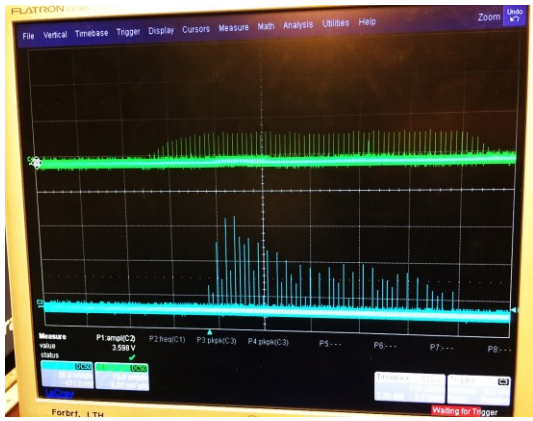

Figure 2.18. Photo of PD signals for the burst-mode laser system on an oscilloscope. The green one represents a 355 nm laser (input of the OPO) and the blue one indicates a 568 nm (output of the OPO) laser.

In practice, it is almost impossible to perfectly overlap the 10 Hz laser with the pulse train of the burst-mode laser due to the long idle time. The difference of incident angle to OPO leads to a difference of output wavelength from OPO. However, such difference is quite small, *e.g.* 1 nm, thus it is still easier to find the right wavelength for OH PLIF measurement with the burst-mode laser after switching the 10 Hz laser to the burst-mode laser in the beam path during the alignment.

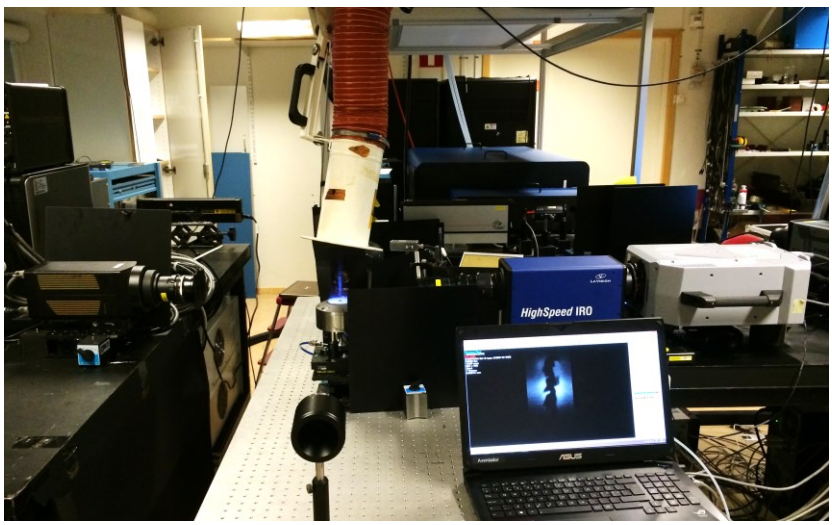

Figure 2.19. Photo of simultaneous OH/CH_2O PLIF measurements at 50 kHz with an LUPJ burner.

Although the direction of back reflection at 355 nm from the OPO is horizontally offset to the incident laser to the OPO as shown in Figure 2.16, it is for the purpose of clearly distinguishing two beams. In reality, the back reflection laser is offset only in the vertical direction. Moreover, the distance from Prism #1 (to guide back reflection laser) to the OPO seems very short according to the figure. This is for a better layout of the sketch. In fact, Prism #1 was placed near the harmonic generation of the burst-mode laser and the distance between Prism #1 and the OPO is larger than 1 metre. In the design of the harmonic generation, dichroic mirrors are used to prevent the back reflection of the pumping laser at 266 nm, 355 nm or 532 nm reentering the burst-mode laser system, which could severely damage the upstream optics.

Figure 2.20 present a sketch of experimental setup for 27 kHz OH PLIF in a plasma discharge. The optical setup is similar to the OH PLIF experiments presented in Paper VI and X. Since the repetition of the pulse train for OH PLIF in

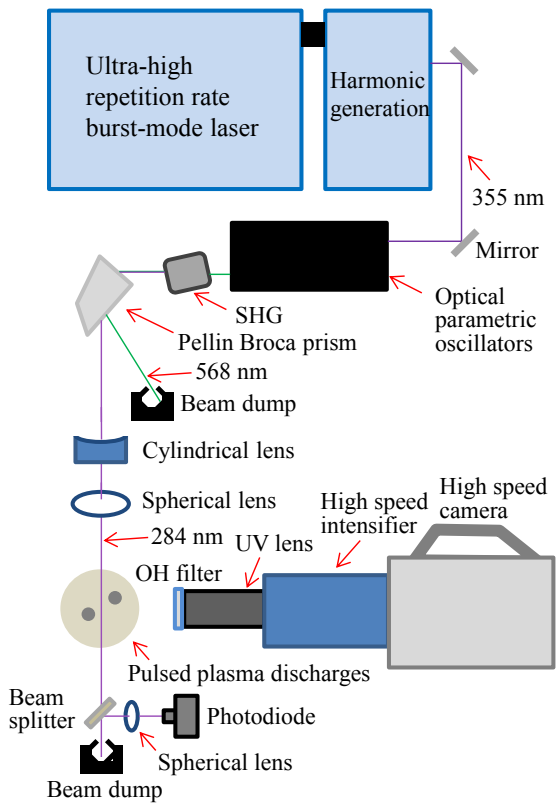

Figure 2.20. Sketch of experimental setup for 27 kHz OH PLIF in a plasma discharge.

the plasma discharge is lower than that for OH PLIF in the LUPJ burner, the pulse energy is higher. The lens set for the telescope in the OPO was then adjusted accordingly to make the fluence of the pumping beam at optimal value.

Figure 2.21 and Figure 2.22 show photos of both 10 Hz and 36 kHz PLIF measurements in optical engines. There is a distance between the output of the laser and the optical engine. Aluminium beams were used for support of optical alignment. Here, by combining the laser system, detectors and other accessory devices, the PLIF measurement in optical engines can be performed. More practical experience and solutions will be introduced in Chapter 4.

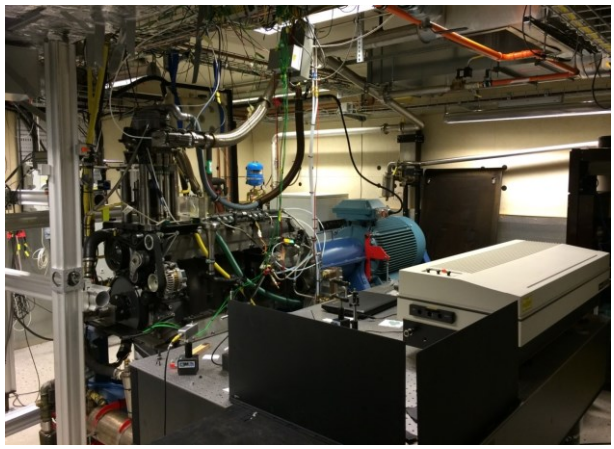

Figure 2.21. Photo of 10 Hz PLIF measurements in an optical engine.

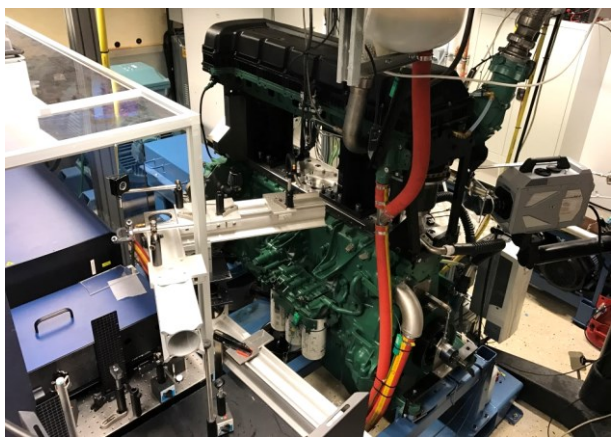

Figure 2.22. Isometric view of 36 kHz PLIF measurements in an optical engine.

3. Methods

The principle and methods used in this thesis work will be introduced in this chapter. Ballistic imaging will be described first, followed by Mie scattering and Rayleigh scattering. The laser-based methods, *e.g.* laser Doppler anemometry, laser induced fluorescence, and particle imaging velocimetry will be presented in the later part of this chapter.

3.1. Ballistic imaging

Ballistic imaging is a technique in which only ballistic photons (unscattered light) and some single scattered light are captured by the detectors when a laser beam passes through a very dense media *e.g.* optical depth (OD) >10. The ballistic photons and some single scattered are called ‘‘useful imaging light’’. Linne pointed out that BI is a transillumination (line-of-sight imaging) technique which is similar to laser shadowgraphy [6]. The difference between conventional shadowgraphy and BI is that shadowgraphy allows all the light to come into the detector sensor - including useful imaging light and multiple scattering light - with a fairly long exposure time, typically > 1 μs. When seen through a droplet cloud,

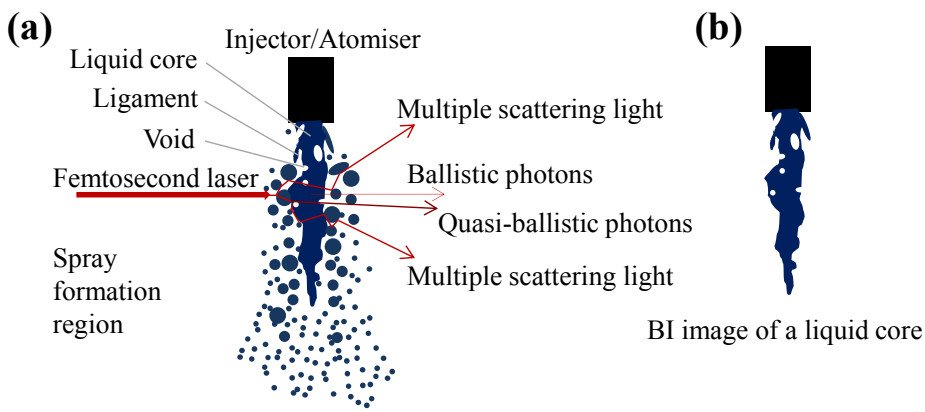

Figure 3.1. Principle of BI for a dense spray in the spray formation region. Spatial separation between useful imaging light (ballistic photons and quasi-ballistic photons) and multiple scattering light is illustrated.

the multiple scattering light blurs the image. Berrocal and co-workers invented and developed structured laser illumination planar imaging (SLIPI) to minimise the effect of multiple scattering in a slightly or moderately dense spray, *e.g.* OD<6 [51-57].

For highly dense spray (OD>10), *e.g.* a diesel spray, it is possible to 'see' through the spray formation region in the vicinity of the nozzle with the BI technique. For example, once an input laser pulse passes through a spray, the output contains various classes of photons including ballistic photons (photons do not scatter), quasi-ballistic photons (photons scatter into the forward lobe of the droplet) and multiple scattering light as shown in Figure 3.1(a). They arrive at the camera sensor at different times since multiple scattering light travels a longer distance than ballistic photons. Also, the multiple scattering lights spatially separate with the useful light. If only useful imaging light is captured by the detector, one can see through the droplet cloud and the liquid core information can be observed as shown in Figure 3.1(b). However, the time separation between the useful imaging light and multiple scattering light is very short, *e.g.* on the order of picoseconds [58, 59]. A fast time gate is one way to separate them. This means that useful imaging useful imaging light can pass through the gate while the later arriving multiple scattering light is blocked.

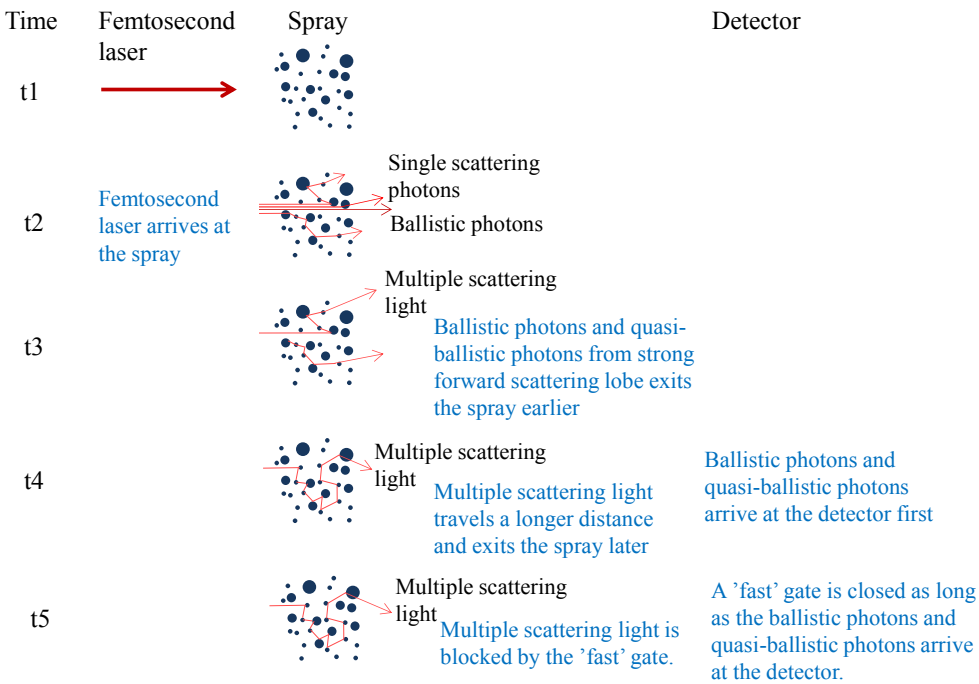

Figure 3.2. Various classes of photons pass through a spray at different times.

Figure 3.2 illustrates various classes of photons passing through a spray at different times. It explains temporal separation between useful imaging light and multiple scattering light, as multiple scattering light travels a longer distance than the useful imaging light before it arrives at the detector. Here, it is simplified in two dimensions. However, we need to remember it is more complicated than this as in reality it is three dimensional.

In order to achieve a fast time gate for BI, an optical Kerr effect (OKE) gate is used, like a Pockels cell but much faster. In this thesis work, liquid CS_2 was placed in an optical cell with two polarisers as an OKE [60, 61] time gate as shown in Figure 3.3. When a switching pulse arrives at the cell, the CS_2 changes the polarisation due to birefringence. It is worth mentioning that polariser 1 and 2 have opposite polarisation, *i.e.* the imaging beam with the same polarisation of polariser 1 will be blocked by the polariser 2. When CS_2 works, *i.e.* pumped by a switching pulse, it changes the polarisation of the imaging pulse to the same as polariser 2. Hence, the imaging pulse can pass through it. The relaxation time of CS_2 is usually ~2 ps [62-64] if pumping by a ~100 fs pulse. After the relaxation time, it acts as a normal transparent media that cannot change the polarisation. As a result, the light, *e.g.* the tail of the useful imaging light and multiple scattering light is blocked at polariser 2 due to the opposite polarisation of polariser 1 and 2.

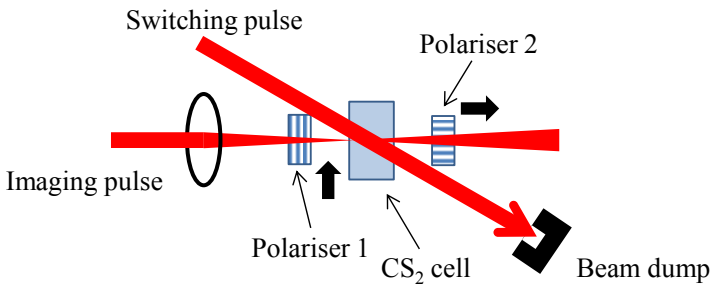

Figure 3.3. An OKE with a CS_2 cell and two polarisers at opposite polarization, *i.e.* a fast shutter.

The OKE can act as a spatial filter which cuts off the high spatial frequency components of the image (those components resolve small structures for good spatial resolution). The high frequency components are scattered at steeper angles and hence propagate a longer distance than ballistic photons. They can occupy the same angles and propagate the same distance as second order or third order multiple-scattering light. If the OKE time gate is opened for a longer time or the time gate is moved towards the high frequency components which arrive at the camera later than ballistic photons, the spatial resolution is improved. But in the

meantime, more multiple scattering light will arrive at the camera, which adds to the background and degrades contrast. Thus, there is a trade-off between better spatial resolution and more multiple scattering light. In practice, by playing with the optical delay in the BI system, it is possible to find an optimal point. In other words, the spatial resolution of BI is worse than the BI shadowgraphy without OKE, *i.e.* ultrafast shadow imaging (USI), when OD=0.

3.2. Mie scattering

Mie scattering occurs where there are many particles with diameters equal to or larger than the size of the wavelength of the incident laser. It is used for many laser diagnostics, *e.g.* PIV, LDA, phase Doppler interferometry (PDI), *etc.*

Figure 3.4 illustrates the single light scattering by a spherical droplet. The refractive index n_1 is smaller than that of a particle or droplet, n_2. The directions of the new refracted light can be calculated from the Snell–Descartes law [65],

$$n_1 \cdot sin\theta_1 = n_2 \cdot sin\theta_2 \tag{3.1}$$

Where θ_1 is the angle between incident light and normal direction of the particle surface at the point of intersection between the incident light and the particle surface; and θ_2 represents the angle between the new refracted light and the normal direction. The refracted light of the particle has many orders of refraction but the higher order, the less light intensity it will have. All the refraction light and reflection light contribute to Mie scattering light. If many particles exist in the

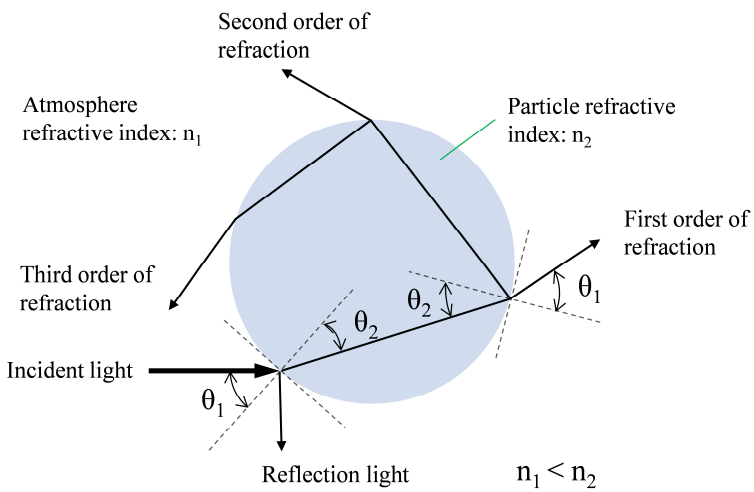

Figure 3.4. The light scattering by a spherical droplet.

beam path, the refraction and reflection light between them will introduce a great deal of multiple scattering light which corrupts the result image, as previously mentioned.

3.3. Rayleigh scattering

Different from the Mie scattering, if the wavelength of the radiation is much larger than the particle, *e.g.* a molecule, elastic scattering of the light will be generated, *i.e.* Rayleigh scattering.

Rayleigh scattering depends on the number density of molecules in the gas. All molecules from different species contribute to the scattering process in the gas. When the temperature of the gas increases at a constant pressure, the number density and sequentially the intensity of Rayleigh scattering will decrease. Therefore, Rayleigh scattering thermometry is usually used to determine temperature distribution in flames by measuring Rayleigh scattering intensity. A calibration is needed to obtain the reference Rayleigh scattering intensity, *i.e.* I_{ref}, at a known temperature, T_{ref}. The measured Rayleigh scattering intensity can be expressed as:

$$I = I_{ref} \frac{T_{ref}}{T} \frac{\sigma_{ref}}{\sigma} \tag{3.2}$$

where σ_{ref} and σ are the Rayleigh scattering cross section of the gas mixture in reference condition and in the measured flame, respectively. Hence, the gas temperature, T can be derived by equation 3.2.

3.4. LDA

In an LDA system, two parallel coherent laser beams are focused at the same point, called probe volume, and consequently fringes are created in the probe volume as shown in Figure 3.5. The distance between two fringes, *i.e.* fringe spacing, can be expressed as:

$$d_f = \frac{\lambda}{2sin\theta} \tag{3.3}$$

where λ is the wavelength of the laser and θ represents half of the angle between two laser beams. As a particle or droplet passes through the probe volume, it generates scattering light to the detector and its velocity can be determined as:

$$U_y = f_{Doppler} \cdot d_f = f_{Doppler} \frac{\lambda}{2sin\theta} \tag{3.4}$$

where $f_{Doppler}$ is the shifted signal frequency by Doppler effect.

A Bragg cell is used to produce two beams of equal intensity with frequencies f_0 and f_{shift} to avoid the ambiguity of the velocity direction. More detailed information about LDA theory can be found in reference [66].

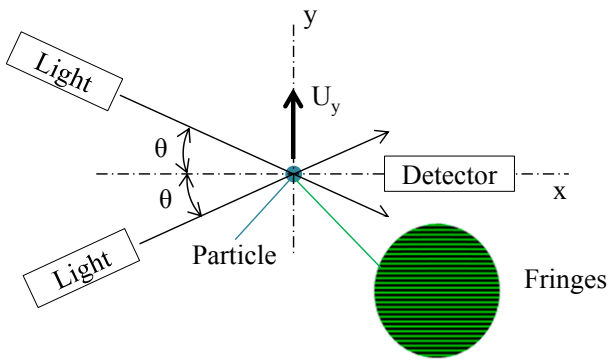

Figure 3.5. Principle of an LDA measurement.

3.5. LIF

LIF is widely used in detecting species in flames [3]. The concentration level of the species can be down to hundreds of ppb. Both qualitative and quantitative measurements, which show the species distribution and concentration in 2D [67, 68], 3D [69-72], or even in 4D [73, 74], can be performed.

Max Planck theorised that energy is transferred in discrete packets, called 'quanta', and they equal hν where h is a constant ($6.63 \times 10^{-34}\, J \cdot s$) and ν represents the frequency of a wave or a light [75]. When the energy of a light equates to the energy between two energy levels of an atom or a molecule, the atom or molecule absorbs the light energy as an input energy and transfers from ground state to excited state. However, the excited state is not stable and after a while the atom or molecule will return to a stable energy level, *e.g.* the ground state. In the meantime, the atom or molecule emits fluorescence during such a relaxation process (from excited state to ground state). More details can be found in the reference [3].

Figure 3.6 shows different transitions including electronic transition, vibrational transition and rotational transition between ground state and excited state for a diatomic molecule, *e.g.* OH, CH, NH, *etc.*

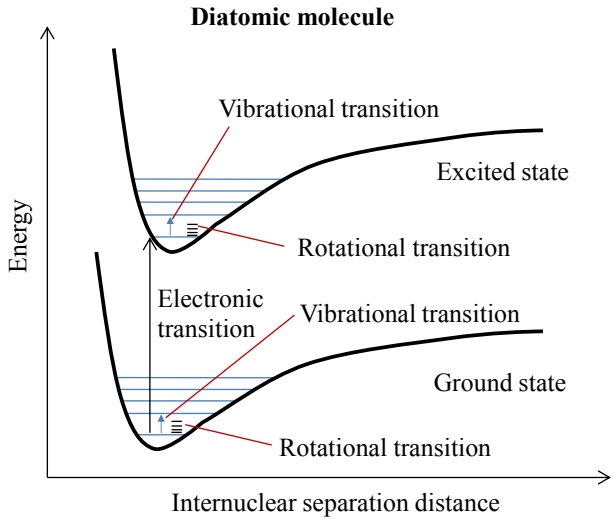

Figure 3.6. Different transitions of a diatomic molecule.

A tunable laser source is employed to change the wavelength of the laser in order to fit the energy gap between transitions to excite a molecule. Table 3.1 summarises the excitation wavelength and detection wavelength of various molecules (species) in flames investigated in this thesis work. The filters used for LIF of each species are listed in Table 3.1 as well.

Table 3.1. The excitation wavelength, the detection wavelength and filters used for LIF measurements in this thesis work.

Species	**Excitation wavelength**	**Detection wavelength**	**Filter**
CH	~387 nm	~430 nm	Long pass filter, GG400
CH_2O	355 nm	380-550 nm	Long pass filter, GG385
OH	~284 nm	~308 nm	Interference filter, 310±10 nm
Acetone	266 nm	>330 nm	Long pass filter, liquid N,N-Dimethylformamide

3.6. PIV

In brief, PIV is based on tracking the movement of particles. For example, Figure 3.7 illustrates two frames in a PIV measurement as a simplified model. Frame 1 is taken at time t_0 at which point particles are marked as solid circles. In frame 2, the particles at time t_0 are marked as hollow circles while the particles at time $t_0+\Delta t$ are marked as solid circles. Therefore, the velocity can be derived by the ratio of the distance, that particles move, to the time difference between frames, Δt. The velocity vectors are marked in frame 2 between hollow circles and solid circles. Some particles move out of the measurement plane (usually illuminated by a laser sheet) while some particles move into the measurement plane from outside of the plane due to out of plane motion (the direction of which is perpendicular to the measurement plane).

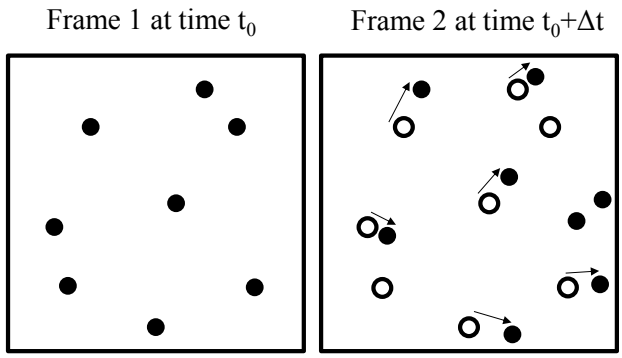

Figure 3.7. Two frames of a PIV measurement in a simplified model.

For a real case, the particle number density is high as shown in Figure 3.8 and hence a spatial cross-correlation map is calculated from sub-sections of the target area in order to get the movement of the sub-sections. The sub-sections selected to calculate the cross-correlation is called interrogation area (IA), *e.g.* 32 by 32 pixels. More details can be found in references [76, 77].

As a rule of thumb, the particles in an IA should move no more than a quarter of the IA size and no more than a quarter of the laser sheet thickness between two frames [78, 79]. If the flow field is highly dynamic and these requirements cannot be met, an alternative approach referred to as adaptive PIV [80] can be employed. In this technique, the size and shape of the IA are changed. There are iterations until the optimal size and shape of each IA is achieved.

(a) Frame 1 at time t_0

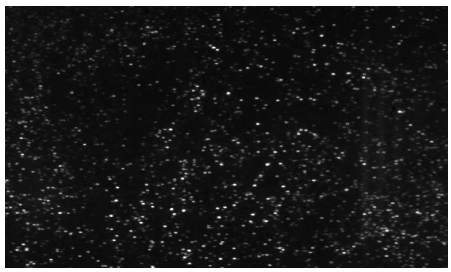

(b) Frame 2 at time $t_0+\Delta t$

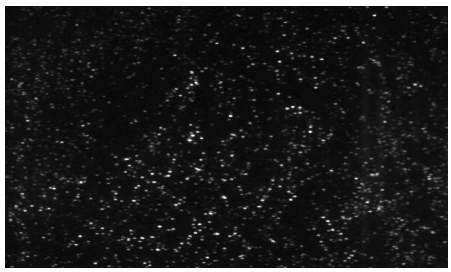

Figure 3.8. Two frames of the PIV measurement in an optical engine.

4. Results

This chapter provides a summary of the development of laser diagnostics in laboratory devices and its application in practical combustors. First, BI was developed for better imaging through high OD substances, *e.g.* droplet clouds. The developed BI was used for investigation of the spray formation region of ECN Spray A in an HTHP chamber. Second, PLIF measurements were developed in LUPJ burners including multi-scalar PLIF, *e.g.* OH/CH/CH_2O and OH/CH/T PLIF, and high speed PLIF, *e.g.* simultaneous OH/CH_2O PLIF at 50 kHz, OH PLIF at 100 kHz and CH_2O PLIF at 140 kHz. Third, the developed high speed OH PLIF imaging has been applied in pulsed plasma discharges. A decay of OH PLIF intensity during a plasma afterglow was distinctly observed using this technique. Last, different laser diagnostics including the newly developed ones were carried out in optical combustion engines with advanced combustion concepts, *e.g.* homogeneous charge compression ignition (HCCI) and partially premixed combustion (PPC), to improve the understanding of the mixing process of fuel and air, combustion behaviour and emission formation.

4.1. Ballistic imaging

This section provides a summary of the results obtained in the work related to BI, including the development of BI and its application in a diesel spray. Results are from Paper I and Paper II. Some practical experience and hands-on advice not mentioned in the attached papers are described.

The BI used in the spray was developed by Linne and Paciaroni [6, 62]. To understand BI better and to make a comparison with the Monte-Carlo simulation performed by Sedarsky *et al.* [81], Linne's group built and compared two BI setups at Chalmers University.

Figure 4.1 shows the two BI experimental setups. The imaging pulse and switching pulse are about 100 fs. They are from a mode-locked Ti:Sapphire femtosecond pulsed laser system. A beam splitter was used to split one laser beam into two beams with equal power. Afterwards the power of both image pulse and gate pulse were adjustable via a waveplate/polariser combination, *i.e.* there is a

polariser directly after a waveplate. When the polarisation of the laser beam, which can be adjusted by the waveplate, is the same as the polarisation of the polariser, output of the laser beam after the polariser reaches maximum intensity. Otherwise, the output intensity decreases by changing the polarisation (by the waveplate) down to zero when the polarisation of the laser beam is opposite to that of the polariser. In the experiments in this thesis, the polarisation of the polariser was fixed.

The test chart in the experiment is a USAF 1951 resolution test chart. A photo of the test chart is shown in Figure 4.2. It has different line pairs per mm and the contrast between black lines and white lines is 100%, in theory. Use of the test chart can judge the detection limit of high spatial frequency components of the resulting image, *i.e.* how small size the current optical setup can resolve/visualise.

The resolution test chart was embedded in the centre of a cell containing turbid media. However, since the test chart was in the middle of the turbid media, the incoming light, *i.e.* the light reaching the test chart, did not have perfect polarisation as the turbid media changes the polarisation by multiple scattering as discussed in Chapter 3. Only the ballistic photons have unchanged coherence, directional and polarisation properties compared to the input beam.

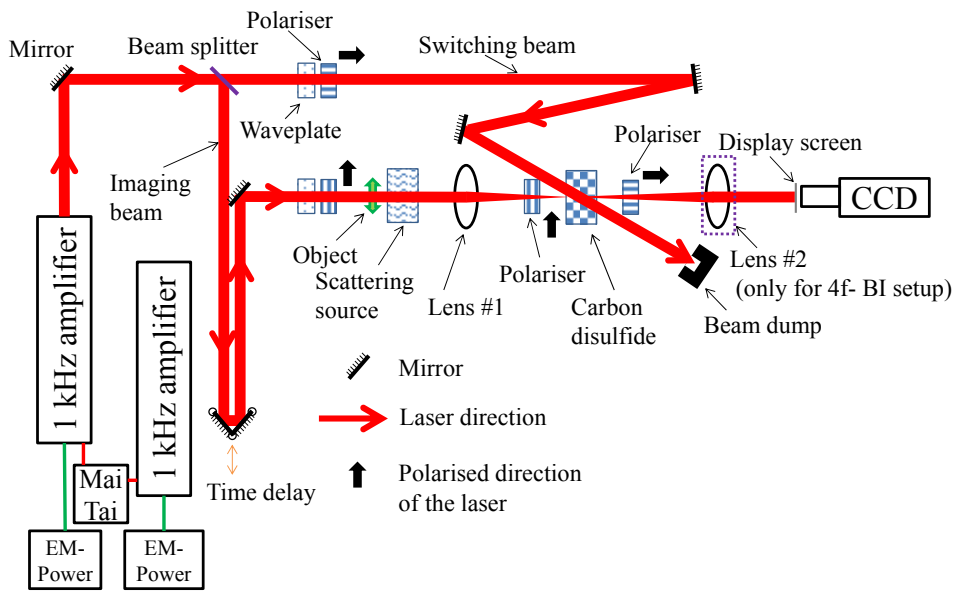

Figure 4.1. Sketch of 2f-BI/4f-BI experimental setup. For 4f-BI setup, Lens #2 is used while there is not Lens #2 for 2f-BI setup.

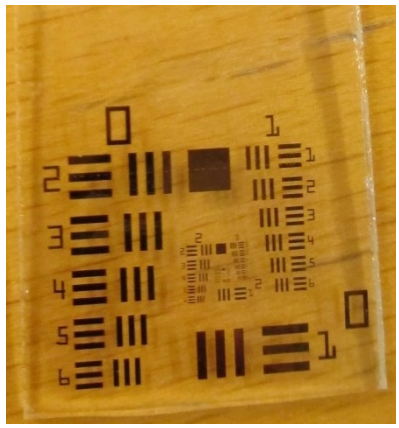

Figure 4.2. Photo of the test chart used in the experiment.

Paper I illustrates the experimental setup in detail. In addition, the effects of varying the switching beam energy were investigated in the paper. The switching beam energy decreased from approximately 0.7 mJ to about 0 mJ, which leads to a worse mean contrast. However, the influence of increasing switching beam energy on the mean contrast was not discussed. It is worth mentioning that if the pulse energy for the switching beam is too strong, *e.g.* above several mJ, it will not improve the image quality. On the contrary, due to too much input energy into the CS_2 medium, it will 'cook' the liquid which leads to a worse situation. The thermal gradient in CS_2 liquid results in turbulence and movement of the liquid. Moreover, the switching beam and imaging beam are from one laser system split by the beam splitter. Therefore, more energy in the switching beam results in less energy in the imaging beam. Due to only a few ballistic photons being able to pass through the turbid media, more imaging beam energy can increase the number of passable ballistic photons to improve the image quality. A suggested feasible proposal is that the switching beam should be expanded and trimmed, and hence when the imaging beam passing through the OKE, it can overlap a more uniform beam profile of the switching beam. The time gate of OKE can consequently perform more stably and robustly.

The imaging beam which is focused by lens #1 is usually smaller than the switching beam in the OKE. It is found that due to the Gaussian shape of the switching beam, the overlap position of the imaging beam and switching beam affects the resulting imaging. In practice, the position of them should be adjusted to achieve an optimal value. Furthermore, the focal point of the imaging beam should be positioned a distance away, *e.g.* 2 cm depending on the focal length of the first lens (lens #1), from the CS_2 cell in order to avoid unwanted non-linear lensing effects as discussed in Paper I and in reference [82].

The OKE plays a role as not only a time filter but also as a spatial and polarisation filter mentioned in Paper I. The size of the overlap between imaging beam and switching beam is the size of the spatial aperture. Since the focal point of the imaging beam is outside of the CS_2 cell, the aperture size is not extremely small, *e.g.* > 1 mm.

In practice, 2f is easier to realise by adjusting the position of the lens #1 and the display screen to achieve a high quality image, whereas 4f is complicated in practice - it is hard to achieve the best point that has better image quality, in theory, than the 2f system. There are three parameters, *i.e.* the positions of lens #1, lens #2 and the screen in 4f system. Moreover, when the OD of the turbid media or the spray is small, *e.g.* OD<4, it is better to use USI than BI techniques. The advantage of the 4f system is that the image can be magnified on the screen by selecting the corresponding focal length of lens #1 and lens #2.

It is also worth mentioning several practical issues for the BI experiments here.

1) Lens #1 should be placed in a translation stage and its position should be adjusted to obtain a sharp image.

2) The image containing pure ballistic photons has lower quality than that including useful image light (ballistic photons and snake photons). Therefore, the time delay should be optimised. The OKE gate should be positioned at the beginning of the pulse (capturing ballistic photons) at first. Then the OKE gate should be slightly delayed in order to capture ballistic photons and useful image light at the same time when the image quality is the best.

3) CS_2 medium has birefringent properties, which leads to the BI results having a birefringent effect, *i.e.* the focus of horizontal lines cannot occur at the same time as vertical lines. There is a compromise position where both horizontal lines and vertical lines are close to their sharpest situations.

4) A screen is placed in front of the camera lens to protect the camera chip from directly strong input energy and overwhelming saturation, and consequently damaging the camera if mistakes happen. Owing to the BI directly capturing ballistic photons, in some situations, like the second polariser in the OKE being opened (the polarisation of the first polariser and the second one is not 90 degrees, *i.e.* not opposite polarisation), the camera can be straight exposed to the laser beam. Furthermore, it is also easier to find the image with the screen, *e.g.* in 4f setup, the object was transformed from Fourier image plane to the image plane on the screen by lens #2.

5) The angle of switching beam and imaging beam should be as small as possible.

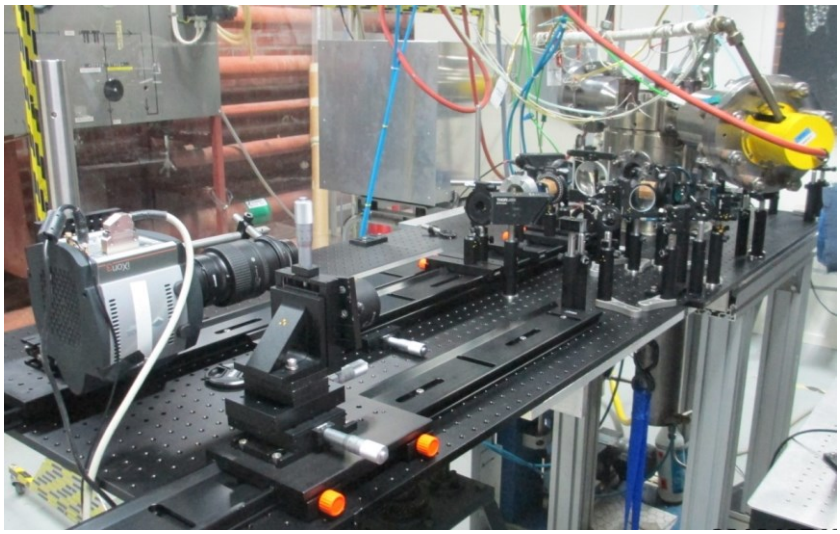

Figure 4.3. Photo of the BI experimental setup for ECN Spray A in the HTHP vessel at Chalmers University.

Figure 4.3 and Figure 4.4 show the photo and sketch of BI experimental setup for ECN Spray A in the HTHP vessel at Chalmers University. The BI setup was the aforementioned 2f- BI system. Due to the early installation of the HTHP vessel and the optical table for mode-locked Ti:Sapphire femtosecond pulsed laser system in the lab, they are located 5 m away from each other. Neither of them is movable. Therefore the laser beam had to pass across the lab. A telescope was built to make sure the laser beam doesn't expand too much. The position of the beam slightly changes day by day. Several apertures were used to realign the laser beam into the right position before the experiment at the beginning of the day. Similar to the previously mentioned development of BI setup, *i.e.* 2f-BI system, the imaging beam and switching beam were generated by a beam splitter and only one femtosecond laser system was used. Because the imaging beam had to pass through quartz windows and the spray, which leads to a longer beam path than switching beam, the optical time delay was installed in the switching beam path.

It can be noticed that the 2f BI setup was installed on an aluminium breadboard as a modulator. It will be easier and faster to install the BI setup when access to the HTHP vessel is available for BI experiments. The alignment of the setup was done by inserting the test chart (USAF 1951) below the injector tip without a quartz window. Due to the steady flow and the turbulence, the thermal gradient of the hot ambient gas changes the refractive index along the beam path in the vessel during the experiment. Therefore the background outside the spray is not uniform as shown in Figure 4.5.

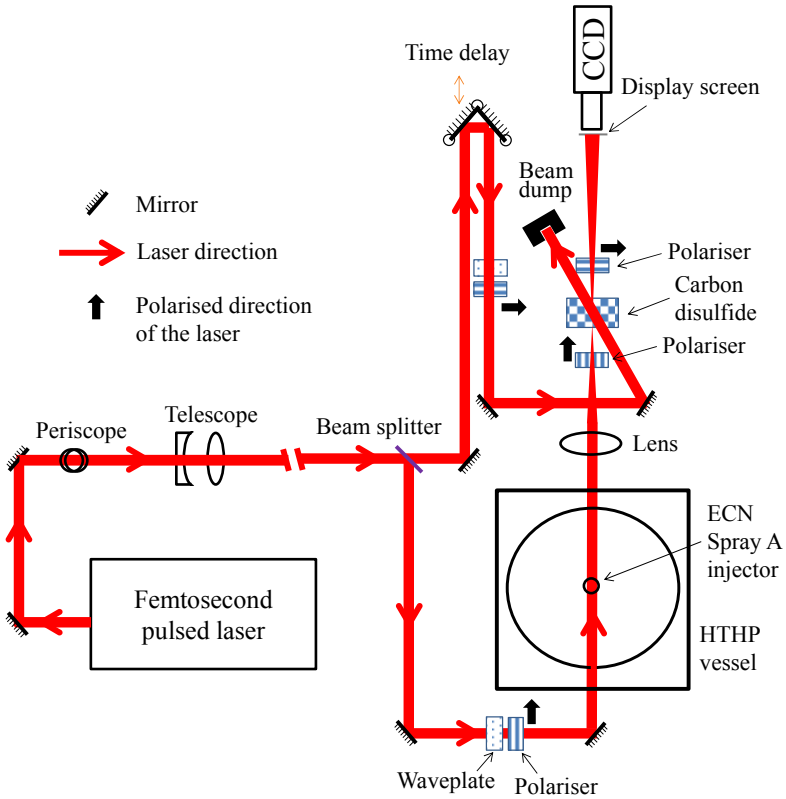

Figure 4.4. Sketch of the BI experimental setup for ECN Spray A in the HTHP vessel at Chalmers University.

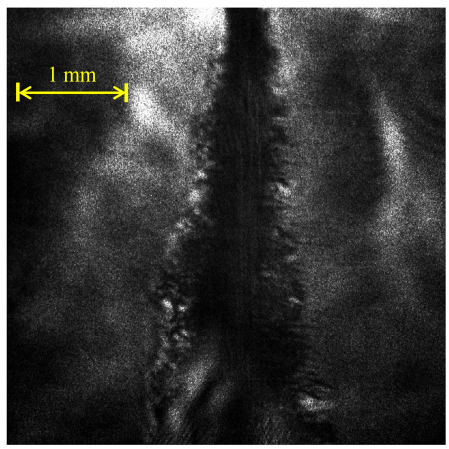

Figure 4.5. BI of the jet at ECN Spray A condition taken 0.8 ms after start of injection (steady regime), at 1 mm to 5 mm downstream of the injector tip.

4.2. Diagnostics in LUPJ burners

This section provides a summary of the results obtained in the work related to laser diagnostics in LUPJ burners. Multi-scaler PLIF measurements were conducted in three LUPJ burners with different nozzle/tube diameters, *i.e.* 1.5 mm, 2.2 mm and 4.5 mm. The turbulent burning velocity was calculated based on mean progress variables. Moreover, high speed PLIF was developed and employed in an LUPJ burner with the burst-mode laser system. Some details of post-processing are described. More results can refer to Paper III, Paper VI, Paper IX and Paper X.

4.2.1. Multi-scalar PLIF

The multi-scaler PLIF measurements in LUPJ burners includes simultaneous measurement of temperature, CH radicals and OH radicals distribution, and simultaneous measurement of CH_2O radicals, CH radicals and OH radicals distribution. More detailed information on the experimental setup can be found Paper III and in reference [37].

The experimental conditions and key parameters are shown in Table 4.1 in which Φ indicates the equivalence ratio of the jet flame.

In Table 4.1, the laminar flame speed (S_L) and laminar flame thickness (δ_L) are derived based on the measurement in LUPJ flames at jet velocity of 11 m/s described in Paper III. Jet Reynolds number, Re_{jet}, is calculated as the following equation:

$$Re_{jet} = \frac{U_0 \cdot d}{\nu} \tag{4.1}$$

where ν is the kinematic viscosity at 298 K, U_0 is the jet velocity and d is the diameter of the jet nozzle.

From N. Peters' text book [83], Lewis number is defined as

$$Le = \frac{D}{D_i} \tag{4.2}$$

where D is thermal diffusivity and D_i represents mass diffusivity. When Le=1, D equals to D_i.

The Schmidt number, Sc, is defined as

$$Sc = \frac{\nu}{D} \sim \frac{diffusive\ momentum\ transfer}{diffusive\ mass/heat\ transfer} \tag{4.3}$$

where D is mass diffusivity or thermal diffusivity as they are equal for unity Lewis number flow. ν is the kinematic viscosity.

Suppose the Schmidt number is unity for scaling law, *i.e.* the diffusion of mass/heat and diffusion of momentum are at the same rate. The laminar flame thickness, δ_L, and laminar flame speed, S_L, can be related to thermal diffusivity.

$$D \sim S_L \cdot \delta_L \sim \nu \tag{4.4}$$

Therefore, for a turbulent flow, the Reynolds number can be expressed similar to jet Reynolds number:

$$Re = \frac{u'_l \cdot l}{S_L \cdot \delta_L} \tag{4.5}$$

where u'_l is the turbulent velocity of eddies with size, l. The eddies size ranges from integral scale, l_0 to Kolmogorov scale, η.

Then the turbulent Reynolds number can be presented as:

$$Re_t = \frac{u' \cdot l_0}{S_L \cdot \delta_L} \tag{4.6}$$

where u' is considered as the root-mean-square (RMS) of the flow velocity at integral length scale as turbulence makes the flow fluctuate around its mean value. u'/S_L is termed as turbulence intensity.

According to Kolmogorov's 1941 theory, the energy transfer from the large eddies is equal to the dissipation of energy of the smallest eddies at Kolmogorov length scale η [83].

$$\varepsilon \sim \frac{u'^3}{l_0} \sim \frac{u'^3_\eta}{\eta} \tag{4.7}$$

where ε represents the dissipation rate of turbulent kinetic energy and u'_η is the turbulent velocity of the smallest eddies at Kolmogorov length scale.

The Reynolds number becomes unity for eddies at Kolmogorov length scale as the eddies at this small scale will not break up further and energy at the Kolmogorov scale is quickly dissipated to heat by viscous dissipation.

$$Re_\eta = \frac{u'_\eta \cdot \eta}{\nu} = 1 \tag{4.8}$$

By combining equation 4.7 and 4.8, we get the following expression:

$$\varepsilon \sim \frac{u'^3}{l_0} = \frac{(\frac{\nu}{\eta})^3}{\eta} = \frac{\nu^3}{\eta^4} \tag{4.9}$$

Therefore, by combining equation 4.4 and 4.6 with 4.9, Kolmogorov length scale can be expressed as

$$\eta = (l_0 \cdot \frac{\nu^3}{u'^3})^{\frac{1}{4}} = l_0 \cdot Re_t^{-\frac{3}{4}} \tag{4.10}$$

In order to investigate the interaction between turbulence and flame, two non-dimensional numbers are introduced, *i.e.* Damköhler number, Da and Karlovitz number, Ka.

Damköhler number is defined as the ratio of time scale of eddies at integral length scale, τ_0, to the time scale of chemical reaction, τ_c, while Karlovitz number is defined as the ratio of τ_c to the time scale of eddies at Kolmogorov length scale, τ_η.

$$Da = \frac{\tau_0}{\tau_c} \tag{4.11}$$

$$Ka = \frac{\tau_c}{\tau_\eta} \tag{4.12}$$

where the time scale of chemical reaction can be derived from the laminar flame speed and the width of the reaction zone, *i.e.* laminar flame thickness.

$$\tau_c \sim \frac{\delta_L}{S_L} \tag{4.13}$$

The Kolmogorov time scale, τ_η, can be defined as

$$t_\eta \sim (\frac{\nu}{\epsilon})^{\frac{1}{2}} \tag{4.14}$$

Using the definitions 4.11- 4.14 and equations 4.4 and 4.9, the following relations can be derived.

$$Ka = \frac{\frac{\delta_L}{S_L}}{(\frac{\nu}{\epsilon})^{\frac{1}{2}}} = \frac{\frac{\delta_L}{S_L}}{(\frac{\delta_L \cdot S_L}{\frac{u'^3}{l_0}})^{\frac{1}{2}}} = \frac{(\frac{u'}{S_L})^{\frac{3}{2}}}{(\frac{l_0}{\delta_L})^{\frac{1}{2}}} \tag{4.15}$$

$$Da = \frac{\frac{l_0}{u'}}{\frac{\delta_L}{S_L}} = \frac{S_L}{u'} \cdot \frac{l_0}{\delta_L} \tag{4.16}$$

$$Ka \cdot Da = (\frac{u' \cdot l_0}{S_L \cdot \delta_L})^{\frac{1}{2}} = Re_t^{\frac{1}{2}} \tag{4.17}$$

In Table 4.1, the turbulence intensity and integral scale use the values at x/d=30 and integral scale is derived from the formula $\frac{l_0}{d} = 3.74 \times 10^{-4}(\frac{x}{d})^2 + 3.9 \times 10^{-2}\left(\frac{x}{d}\right) + 4.6 \times 10^{-1}$ presented in Paper III. x is the height above the burner surface and d is the nozzle diameter of the LUPJ burner.

From the LDA data of the flame series presented in Paper III, it is seen that, for the flame height x/d ~15 to 40, the variation of u' is not significant. The value of l_0 is however increasing monotonically along the flame height. As shown in Figure 4.6 the reaction zone and preheat zone in these flames are within x/d<32. Thus, the data at x/d=30 reasonably characterises the mean turbulent data in the flame.

Table 4.1. Experimental cases of the LUPJ burner with 1.5-mm-diameter nozzle and the corresponding key parameters.

Flame cases	Φ	U_0 (m/s)	Re_{jet}	Re_t	η (μm)	u'/S_L	Ka	Da
LUPJ10-66	1.0	66	6306	95	96	16	26	0.38
LUPJ07-66	0.7			97	95	20	41	0.24
LUPJ06-66	0.6			99	93	21	44	0.22
LUPJ04-66	0.4			107	89	31	93	0.11
LUPJ10-110	1.0	110	10510	190	57	31	70	0.19
LUPJ07-110	0.7			195	56	40	115	0.12
LUPJ06-110	0.6			199	56	42	126	0.11
LUPJ04-110	0.4			214	53	62	264	0.06
LUPJ10-165	1.0	165	15764	238	49	39	99	0.15
LUPJ07-165	0.7			244	48	50	161	0.10
LUPJ06-165	0.6			248	47	52	173	0.09
LUPJ04-165	0.4			267	45	77	366	0.04
LUPJ10-220	1.0	220	21019	317	39	52	153	0.12
LUPJ07-220	0.7			325	38	66	244	0.07
LUPJ06-220	0.6			331	38	70	270	0.07
LUPJ04-220	0.4			356	36	103	566	0.03
LUPJ10-330	1.0	330	31529	476	26	78	280	0.08
LUPJ07-330	0.7			487	26	99	448	0.05
LUPJ06-330	0.6			496	26	105	496	0.04
LUPJ04-330	0.4			534	24	154	1035	0.02
LUPJ10-418	1.0	418	39936	603	22	98	395	0.06
LUPJ07-418	0.7			617	21	126	643	0.04
LUPJ06-418	0.6			629	21	133	708	0.04
LUPJ04-418	0.4			676	20	196	1486	0.02

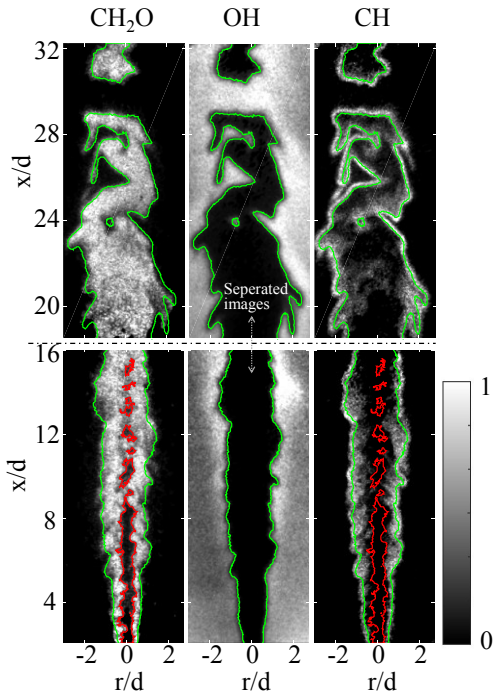

Figure 4.6. From left to right, distributions of CH_2O, OH and CH in flame LUPJ10-220 are presented. Green contour is OH isosurface $<s_{OH}>=0.2$ while red one is CH_2O isosurface $<S_{CH2O}>=0.30$.

Namely, the use of x/d=30 flame height to characterise the integral length is owing to the fact that this is the key flame height, downstream of which the oxidation of fuel and CH_2O is nearly complete.

Figure 4.7 shows the mean thickness of the CH layer and the overlapping layer of OH and CH_2O along the flame height for LUPJ10-110 and LUPJ10-220 flames, respectively. The CH layer is broadening with increasing Ka number as shown in the figure. However, the broadening of the overlapping region of OH and CH_2O is not sensitive to U_0 and Ka, and the mean thickness of this 'heat release' layer (the overlapping region of OH and CH2O) is still considerably thinner than the CH layer.

The SNR and quality of the images largely affects the evaluation [38]. The overlapping layer of OH and CH2O locates either at the high OH concentration area with low CH_2O concentration or vice versa. Other species such as CH3, HCO, and HO_2 may be a better marker of heat release rate (HRR) than the production of OH and CH_2O although the laser diagnostics for them to achieve a decent SNR is not an easy task.

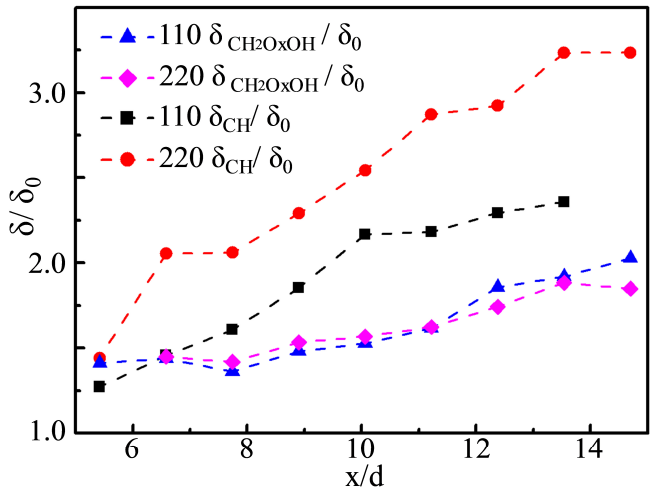

Figure 4.7. Mean thickness of CH layer and the overlapping layer of OH and CH_2O along the flame height for two flames, LUPJ10-110 and LUPJ10-220. The figure is adapted from Paper IX.

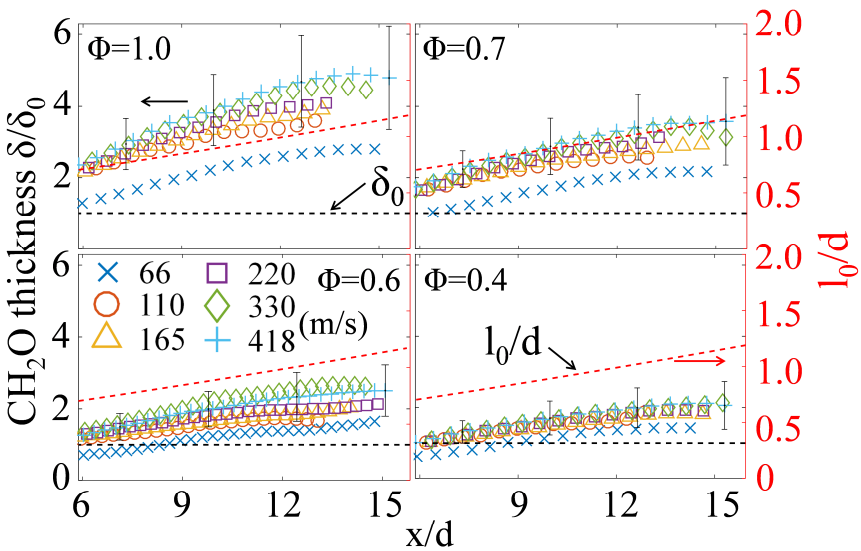

Figure 4.8. Thickness of the CH_2O layer along the flame height for the flames listed in Table 4.1. δ_0 and l_0 are the laminar flame thickness and integral length scale, determined from the experiments in Paper III; d is the nozzle diameter.

The CH_2O layer is often used as the preheat zone marker while the OH formation is a marker of the reaction zone [84]. The broadening of the preheat zone increases

along the flame height as shown in Figure 4.8. At around x/d=15, the thickness of the preheat zone decreases along the flame height in some cases because at that height it is close to the flame tip, where most fuel has been consumed. For leaner cases, the flame is higher due to lower laminar flame velocity compensated by increasing flame surface area.

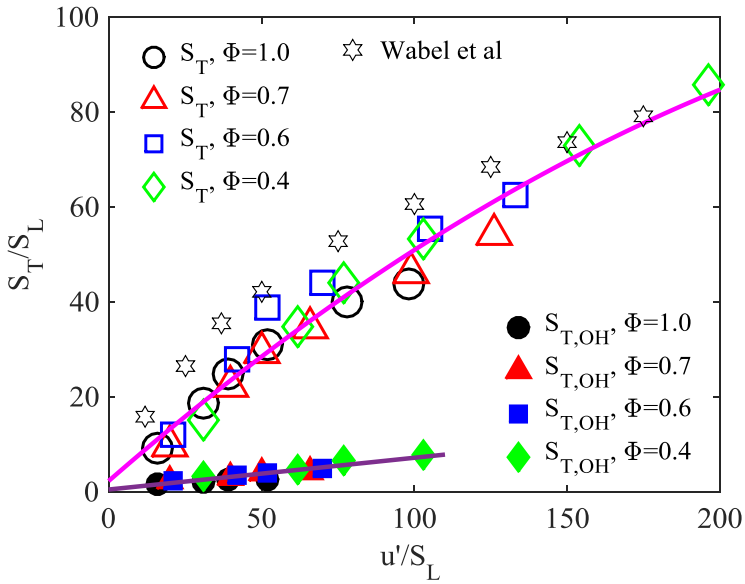

Figure 4.9. Turbulent burning velocity normalised with the corresponding laminar flame speed (S_T/S_L) as a function of turbulent intensity, u'/S_L, for a series of the turbulent flames listed in Table 4.1. Two mean flame surface areas are used, a CH_2O based reaction progress variable $c_{CH2O} = 0.5$, and a OH based reaction progress variable $c_{OH} = 0.2$. The figure is adapted from Paper IX.

In Figure 4.9, flow velocity causes flame blow off, *i.e.* CH_2O leaks out from OH layer, which is why the OH dataset has no data for large u'/S_L. The present data shows a similar trend of turbulent burning velocity in the thin reaction zone (TRZ) and distributed reaction zone (DRZ) regimes as it does in Wabel *et al.* [85], *i.e.* turbulent burning velocity increases monotonically with the turbulent intensity, first linearly and then it increases at a slower rate.

In order to obtain the reaction progress variable of CH_2O, post-processing was conducted on the CH_2O PLIF results in MATLAB© (The Matworks, Massachusetts, USA), including background subtraction, energy distribution correction of laser beam profile, normalisation of signal intensity (the maximum intensity in the image is unity), median filtering of 2×2 pixels area, binarisation

with a threshold, 30% of the maximum, below which the pixel intensity was set to zero for each pixel in the image and edge detection. Wabel *et al.* mentioned that the preheat zone begins where formaldehyde is around 35% of its maximum value [85]. Thus, for a binarised image, the CH_2O layer is unity while inside the CH_2O layer is unburnt fuel, *i.e.* CH_4. The area outside the CH_2O layer is the reaction zone and production zone of the combustion as well as the co-flow flame and ambient air. A similar procedure was applied for the reaction progress variable of OH.

In order to investigate the influence of integral scale on the turbulent burning velocity, the CH_2O PLIF measurements were conducted on two LUPJ burners with the same jet speed. The jet diameter is 1.5 mm and 4.5 mm, respectively.

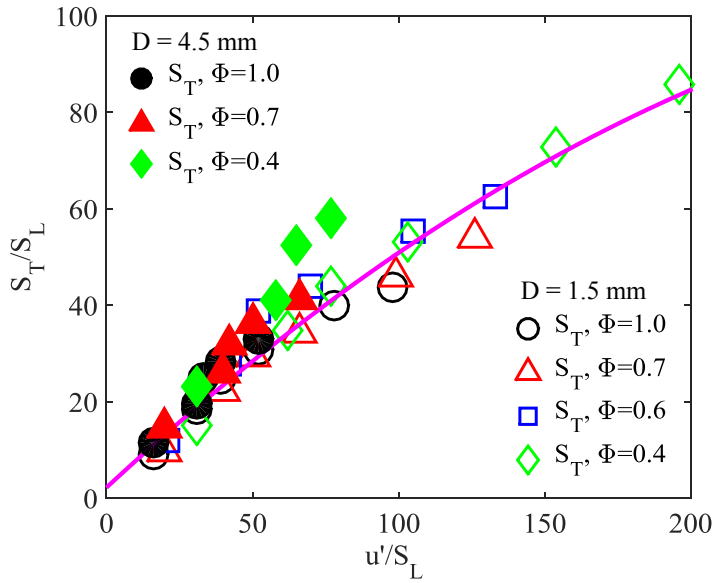

Figure 4.10. Turbulent burning velocity normalised with the corresponding laminar flame speed (S_T/S_L) as a function of turbulent intensity, u'/S_L, for flames listed in Table 4.1 and 4.2 with different LUPJ burners, *i.e.* the jet diameter is 1.5 mm and 4.5 mm, respectively. A mean reaction progress variable $c_{CH2O} = 0.5$ is used.

Turbulent burning velocity from two LUPJ burners is compared, as shown in Figure 4.10. It can be seen that similar to the data from the 1.5-mm-diameter burner, the turbulent burning velocity of 4.5-mm-diameter burner increases linearly at low turbulent intensity, *e.g.* $u'/S_L < 40$. With further increase of

turbulent intensity, the turbulent burning velocity increases at a slower rate for cases of equivalence ratio equal to 1 and 0.7. However, for the case of equivalence ratio equal to 0.4, the turbulent burning velocity increases monotonically all the way to $u'/S_L = 64$. Except that, the turbulent burning velocity calculated from two LUPJ burners overlap with each other. It can be concluded that under low turbulent intensity, *e.g.* $u'/S_L < 40$, the turbulent burning velocity is independent of the integral scale, l_0. Table 4.2 depicts the experimental cases of 4.5-mm-diameter LUPJ burner and corresponding key parameters, *e.g.* jet Reynolds numbers are three times larger than those in Table 4.1 as the integral scale is in proportion to the jet diameter.

Table 4.2. Experimental cases of the LUPJ burner with 4.5 mm jet diameter and the corresponding key parameters.

Flame cases	Φ	U_0 (m/s)	Re_{jet}	η (μm)	Ka
LUPJ45-10-66	1.0			126	43
LUPJ45-07-66	0.7	66	18918	125	69
LUPJ45-04-66	0.4			117	159
LUPJ45-10-110	1.0			75	121
LUPJ45-07-110	0.7	110	31530	74	196
LUPJ45-04-110	0.4			70	452
LUPJ45-10-165	1.0			64	170
LUPJ45-07-165	0.7	165	47292	63	274
LUPJ45-04-165	0.4			59	632
LUPJ45-10-220	1.0			51	262
LUPJ45-07-220	0.7	220	63057	50	423
LUPJ45-04-220	0.4			47	972

4.2.2. High speed PLIF

4.2.2.1 Time scale

For the jet flame at high turbulence intensity and high Ka conditions, time scale of the flow is rather small. Therefore, if the temporal resolution of the laser/camera can be better than the time scale of the flow, the movement of the eddies can be

captured by the high speed PLIF imaging. Table 4.3 depicts the time scale of jet flames at x/d=10 and x/d=30 in the LUJP burner with 1.5-mm-diameter nozzle, respectively. The Kolmogorov time scale in Table 4.3 can be properly resolved for the measurement of instantaneous hydroxyl radicals and formaldehyde distributions at 140 kHz.

Table 4.3. Time scale of jet flames at two heights above the burner surface in the LUJP burner with 1.5-mm-diameter nozzle.

Cases	**LUPJ10-66**	**LUPJ10-110**	**LUPJ10-165**	**LUPJ10-220**
Integral time scale at x/d=10 (μs)	288	161	115	93
Integral time scale at x/d=30 (μs)	447	223	179	134
Kolmogorov time scale at x/d=10 (μs)	52	22	13	10
Kolmogorov time scale at x/d=30 (μs)	46	16	11	7.5

However, due to laser sheet thickness and poor spatial resolution of the CMOS camera combined with a high speed intensifier, we unfortunately cannot resolve Kolmogorov length scale for all the flames listed in the table. Therefore even if high temporal resolution is achieved, we cannot see the turnover of the smallest eddies. It is worth pointing out that even with a higher jet velocity and Reynolds number, the ultra-high repetition rates, *e.g.* 140 kHz, PLIF can still be useful since it resolves a large portion of time scales in the turbulence spectrum.

Figure 4.11. Image of a test chart to evaluate the spatial resolution of the optical setup.

Figure 4.11 presents an image of a test chart (USAF 1951) with the high speed camera and intensifier. The intensifier was operated in the middle of its gain range. It is obvious that 8 line pairs per mm is marginally resolvable, which corresponds to 62.5 μm spatial resolution.

4.2.2.2 Influence of PAH on high speed CH_2O and OH PLIF measurements

Both CH_2O and polycyclic aromatic hydrocarbon (PAH) can co-exist in the fuel-rich regions of the flame. In addition, both of them can be excited at 355 nm. During the high speed PLIF measurement, it may be possible that PAH will contribute to the resulting signal being presented as CH_2O images.

In order to evaluate the influence of PAH, a PLIF measurement was conducted in a CH_4-air flame at stoichiometric conditions with lasers at 266 nm and 355 nm wavelengths respectively to check the contribution of PAH fluorescence on the CH_2O signal. Figure 4.12(a) shows the fluorescence created only by PAH as 266 nm laser doesn't excite CH_2O and Figure 4.12(b) presents the signal generated by both PAH and CH_2O. In the figure, the PAH signal in the flame is hard to detect as it is similar to the background noise while the CH_2O signal is very distinguishable. For leaner cases, it will be better as PAH concentration is even lower. Therefore, the influence of PAH is considered to be negligible in the high speed PLIF experiment.

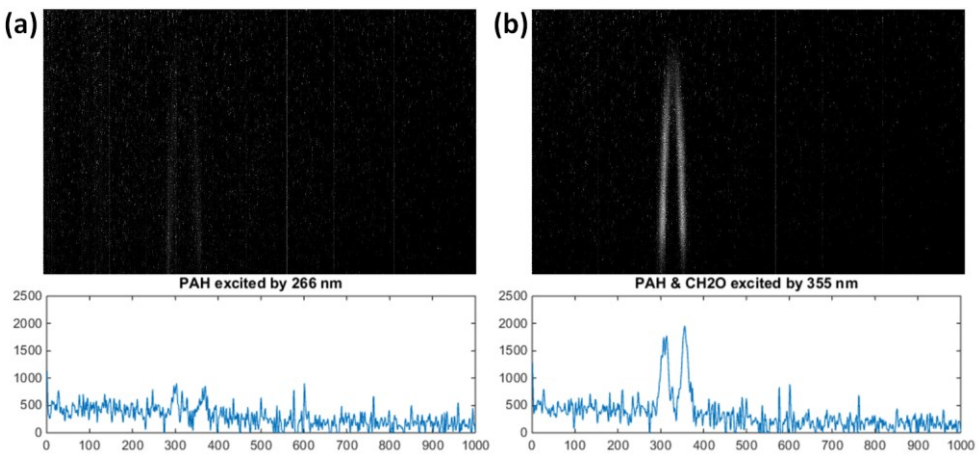

Figure 4.12. (a) Signal from PAH excited by 266 nm laser at stoichiometric conditions; (b) Signal from both PAH and CH_2O excited by 355 nm laser in a CH_4-air flame at stoichiometric condition.

Moreover, from numerical simulations of CH_4-air flames, the CH_2O concentration is about one thousand ppm while PAH concentration is much lower (<10 ppm) for stoichiometric conditions [86]. It would be even better if a dye laser is used to tune the wavelength to be slightly offset at 355 nm, *e.g.* 0.1 nm, so that CH_2O cannot be excited at such a wavelength while PAHs are excited to check the influence of PAHs more precisely. Sjöholm [33] used an on-off resonance technique to distinguish fluorescence between formaldehyde and PAH excited by 355 nm laser in a premixed flame. The results show a good separation between them.

In addition, the possible role of the 284-nm OH excitation laser beam may also act on the excitation of PAH, which is hard to distinguish from the CH_2O image. Normally, the OH excitation beam needs to be delayed significantly (on the order to 30–50 ns) with respect to the CH_2O excitation beam to avoid the resulting cross talk and interference. However, the possible cross talk was evaluated by blocking one laser in turn, which revealed no detectable crosstalk for the high speed PLIF measurements in the jet burner. Admittedly, the influence of PAH on CH_2O image will be mitigated if a delay system (30-50 ns) of the OH beam path was set up to avoid the influence of PAH excited by 284 nm laser.

4.2.2.3 Synchronization for simultaneous high speed CH_2O/OH PLIF measurement

The synchronisation of the burst-mode laser, two cameras and two intensifiers in simultaneous high speed CH_2O/OH PLIF measurement will be described in this sub-section. The jet flame is a steady flow which doesn't need any triggering.

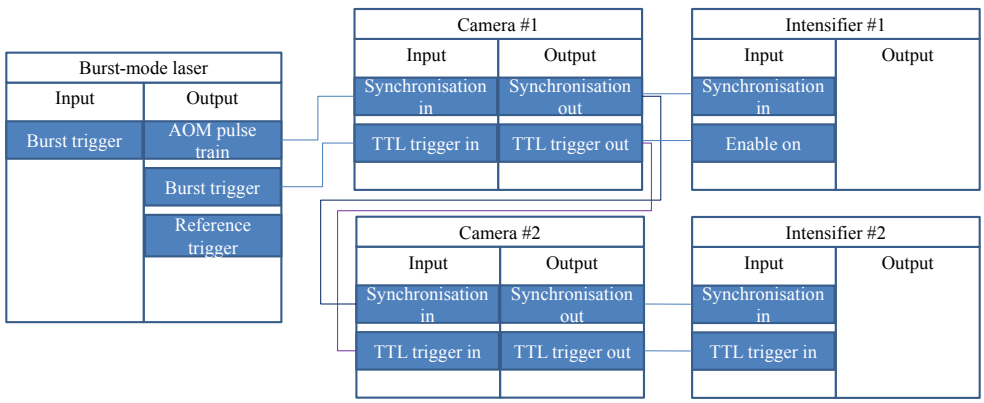

Figure 4.13. Connections of the input and output among the burst-mode laser, two cameras and two intensifiers.

Figure 4.13 shows the connection of the input and output among the burst-mode laser, two cameras and two intensifiers. The burst-mode laser was operating in an internally triggered pulse train and internally triggered burst. The internally triggered pulse train was set to 50 kHz and the burst trigger was activated every 20 seconds.

When the camera received the burst trigger signal, the camera started to record the image. The buildup time of the pulse train is about 0.5 ms which results in the delay between the burst trigger and the start of the LIF signal. Because the camera can capture images for a longer time than the burst duration, it can always record the LIF signal without changing the trigger timing. In the burst-mode laser system, a reference trigger is able to generate an arbitrary trigger before or after and synchronised with the burst trigger. Therefore, it can be an option that the reference trigger, which is delayed to compensate that 0.5 ms delay, is used to trigger the camera.

4.3. Applications in pulsed plasma discharges

This section provides a summary of the developed laser diagnostics applied in pulsed plasma discharges. 27 kHz OH PLIF was conducted in a gliding arc discharge system with the burst-mode laser system. Results are from Paper XI. More results can be found in that manuscript.

4.3.1 Synchronisation for high speed OH PLIF measurement in a pulsed plasma discharge

Figure 4.14 presents the signal connections in the application of high speed OH PLIF measurement on pulsed plasma discharges. The burst-mode laser acts as a masterclock while the reference trigger was set to 80 ms prior to the burst trigger. Therefore, the pulsed discharger system started 80 ms before the onset of the pulse train from the burst-mode laser. As mentioned in the previous section, there is a delay between the burst trigger and the start of the LIF signal, which was about 0.7 ms in this experiment.

In order to reduce the influence of ozone on the OH radicals during afterglow, a 10 Hz Nd:YAG laser is used to have the photodissociation of the ozone. Ozone discomposes into singlet state O atom which is very active. OH radicals can be produced by the reaction of O atom and water. Since the ozone has a very long life time, several milliseconds [87], the Nd:YAG laser is used to photolysis the Ozone immediately after the plasma discharge is turned off. In such approach, the OH produced by ozone during afterglow is excluded. The synchronisation is shown in

Figure 4.15. Due to the fact that a 10 Hz Nd:YAG laser needs a continual pulsed input with 100 ms time interval (*i.e.* 10 Hz), a second pulse generator was used to create a pulse train with the 100 ms time interval as input signal to the Q-switch input channel of the Nd:YAG laser. By adjusting the time delay in the programmable pulse generator #2, the laser pulse of Nd:YAG laser arrives at the plasma discharge at the beginning of the afterglow.

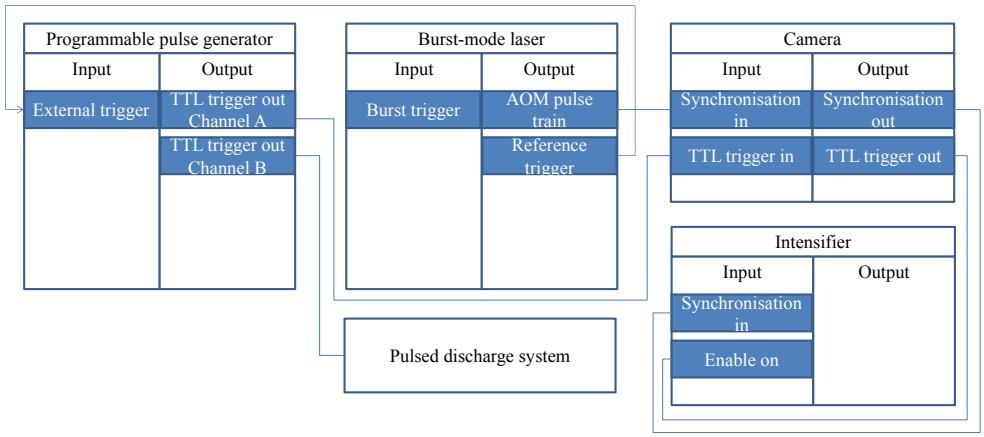

Figure 4.14. Connections of the input and output among the burst-mode laser, the high speed camera, the high speed intensifier, a programmable pulse generator and the plasma discharge system.

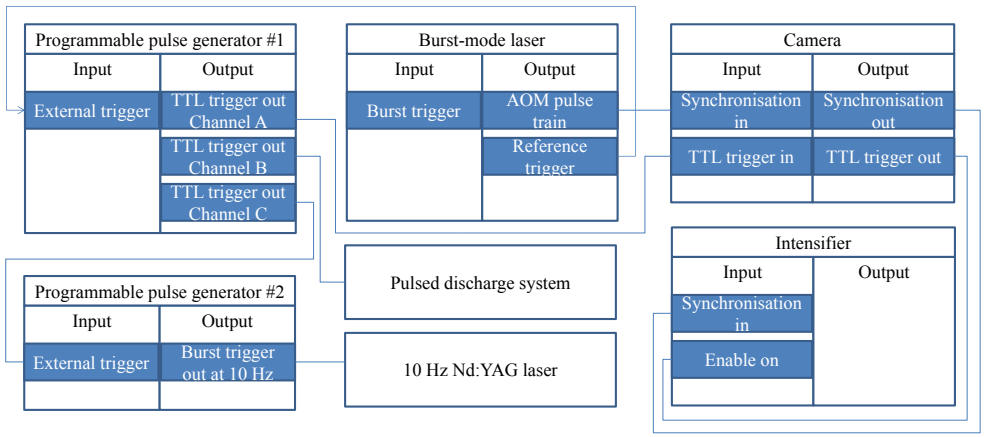

Figure 4.15. Connections of the input and output among the burst-mode laser, a 10 Hz Nd:YAG laser (as a photolysis laser), the high speed camera, the high speed intensifier, programmable pulse generators and the plasma discharge system.

4.3.2 Post-processing

The procedure of post-processing for the OH PLIF images was done in MATLAB©. A background image was recorded without the presence of plasma while the laser was on. The background image was subtracted from each OH PLIF image as the first step in the post-processing procedure.

The processing also included compensation for vertical variations in the energy distribution of the laser sheet in the OH PLIF images. This was carried out by using a Bunsen burner with a CH_4 and air premixed flame to record the corresponding PLIF images. The OH PLIF image of the flame and the intensity along the laser sheet is shown in Figure 4.16. In the figure, the intensity is a sum of all the intensities at each pixel along the horizontal direction and it is then normalised by the maximum intensity along the laser sheet, *i.e.* vertical direction.

It is worth mentioning that this approach only compensates for average energy distributions, whereas pulse-to-pulse or burst-to-burst variations are not compensated for. In addition, the OH distribution in the flame is not perfectly homogeneous. However, the OH PLIF image was captured in the production zone at the side of the flame and the flame height was over 10 cm, where the OH distribution is relatively homogeneous. Therefore, the influence of the homogeneity of the OH distribution was minimized. Admittedly, it would be much better to use a beam splitter and a dye cell with an additional high speed camera to monitor the in-site pulse-to-pulse variations in the energy distribution of the laser.

The compensation of energy variations was achieved by normalising each OH PLIF image in the plasma discharge by the laser sheet energy distribution, *i.e.* the intensity curve in Figure 4.16.

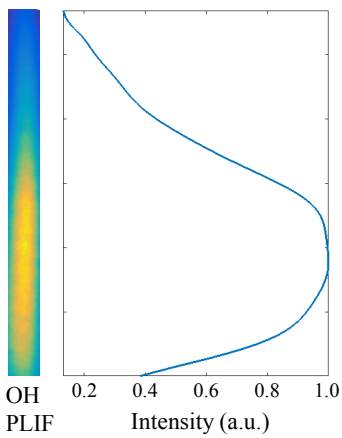

Figure 4.16. OH PLIF image of a CH_4- air premixed flame and the normalisation intensity along the laser sheet.

As a last step, each image was normalised by the laser pulse energy measured by a photodiode, as shown in Figure 4.17.

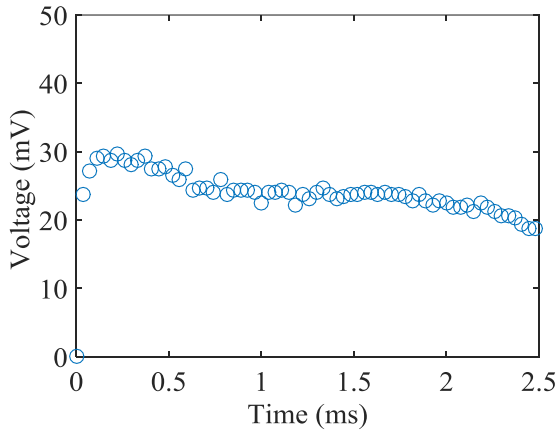

Figure 4.17. Voltage signals of the photodiode for 284 nm laser.

4.3.3 Results and discussion

Figure 4.18 represents an OH PLIF image of the gliding arc after post-processing. A toroidal shape can be observed because ground state OH is mostly located at the outer layer of the plasma column, which has good agreement with the studies in references [42, 44]. Inside the hollow structure the excited state OH, *i.e.* OH*, predominately exists, rather than ground state OH because of the higher temperature which was measured by Zhu *et al.* [50] and because ionisation of the OH is present in the core of the discharge. As a result, the OH PLIF signal inside the torus is very weak, *i.e.* similar to the background. The time information and dimension scale are indicated in the bottom-left and bottom-right corner of the

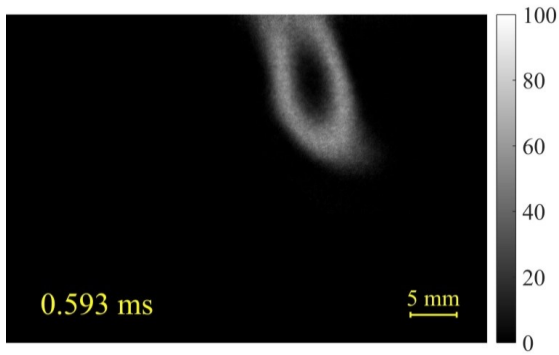

Figure 4.18. An OH PLIF image of the plasma discharge after post-processing.

figure, respectively. The intensity is normalised to the maximum among all the OH PLIF images. A greyscale bin ranging from 0 to 100 is displayed to the right side of the image.

Figure 4.19 displays a number of high speed OH PLIF images including before and during the post discharge, *i.e.* afterglow. The dynamic feature of OH distribution can be captured solely by high speed PLIF imaging. In the first two sub-figures, t=0.37 ms and t= 0.741 ms, the toroidal structure of OH distribution is clearly observed. After switching off the plasma at approximately t=0.8 ms, the hollow structure gradually turns to a solid circle as seen from the last five sub-figures (from t=0.926 ms to t=2.222 ms) in Figure 4.19. A possible explanation can be that once the power supply of discharge is turned off, the balance between producing excited state OH and consuming OH* ,*e.g.* quenching, collapses. As a consequence, consumption of OH* becomes more dominant due to a lack of support of energy from glow discharge and chemical reactions. More OH* becomes ground state OH, which can be excited by the laser and emits fluorescence light. The results from OH chemiluminescence show that plenty of OH* exists inside the hollow structure of the OH PLIF image, where the plasma column is before switching off the power supply, and the decay time of OH* is quite long, *e.g.* >1 ms [46]. It can also been seen that after the ground-state OH

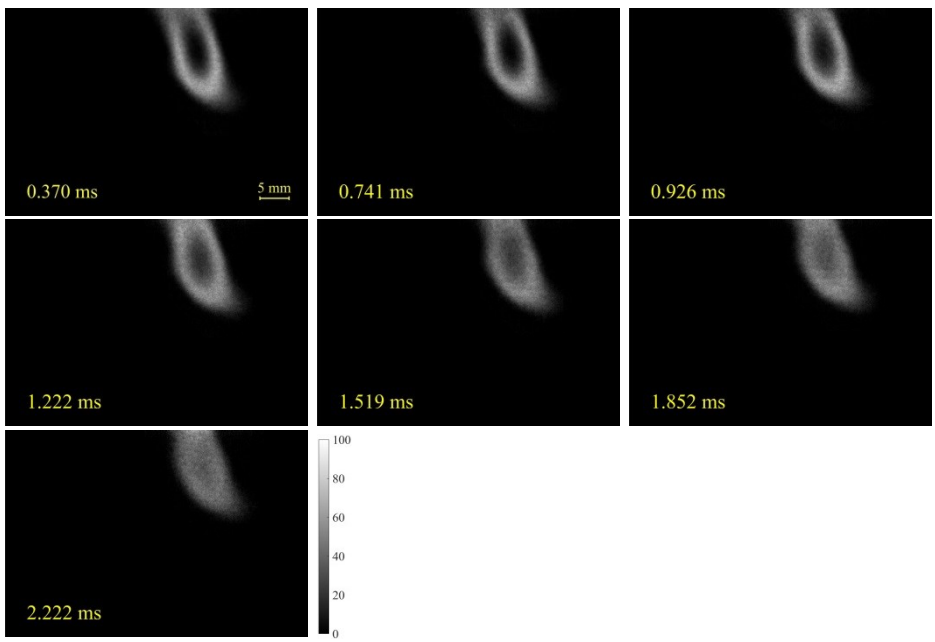

Figure 4.19. OH PLIF images versus time during post discharge. The distribution of OH radicals looks like a torus.

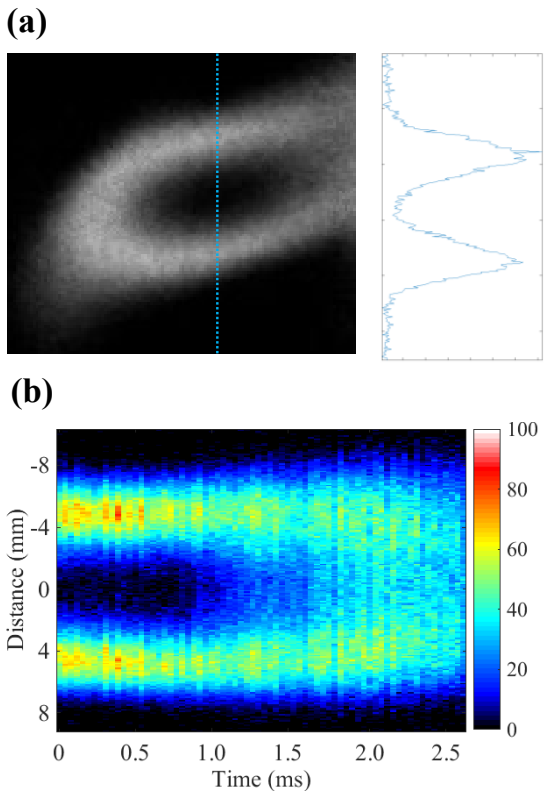

Figure 4.20. The signal profile of OH PLIF images across the centre of the plasma column (a) versus time (b).

radical is formed at the outer layer of the plasma column, the life time of OH is quite long, *e.g.* > 2 ms, in the study. More consecutive high speed OH PLIF images are included in the appendix section of Paper XI.

In order to obtain the relation between OH distribution and time, the intensity profile across the centre of the toroidal structure is calculated as shown in Figure 4.20. The intensity profile along the blue line of the OH PLIF image is illustrated in Figure 4.20(a). Afterwards, the intensity profile at different times is plotted in Figure 4.20(b) where the horizontal axis indicates the time from 0 ms to 2.7 ms and the vertical axis represents the position of OH PLIF intensity which is displayed by a pseudo colour scale. In the centre of Figure 4.20(b) where the plasma column is located, the OH PLIF intensity keeps constantly low until t=0.8 ms. Similarly, the OH PLIF intensity at the outer layer of the plasma column remains almost steady during that period. After t=0.8 ms, the intensity drops at the outer layer of the plasma column while it increases rapidly in the plasma column.

Since the OH PLIF intensity is roughly (assuming same quenching rate) proportional to the number density of OH radical in a plasma [88, 89], OH concentration is increasing in the plasma column while it is decreasing at the outer layer of the plasma column during post discharge.

The averaged intensity in the plasma column and at the outer layer of the plasma column, *i.e.* at the cross section of either side of the torus, is calculated based on Figure 4.20. Figure 4.21 shows how they change with time and the intensity is normalised to unity. The circle, square and triangle symbols indicate the experimental results while the solid and dashed lines represent the corresponding curve fittings.

An exponential function $I = I_0 e^{-\frac{t}{\tau}}$ is used for fitting the intensity decay (or the increase of intensity). I and I_0 are instantaneous intensity and initial intensity, respectively. t indicates time and τ is the exponential time constant which represents the lifetime. According to calculations, the lifetime of OH at the outer layer of plasma column is around 3 ms from the exponential fitting (solid line) during the post discharge. In the same period, τ for the increment of OH intensity in the plasma column (dashed line) is approximately -1 ms. That means the growth-rate is 1 ms^{-1}, *i.e.* the rate for producing OH radicals is 3 times faster in the plasma column than the OH extinction outside the plasma column from t=0.8 ms to t= 2.1 ms.

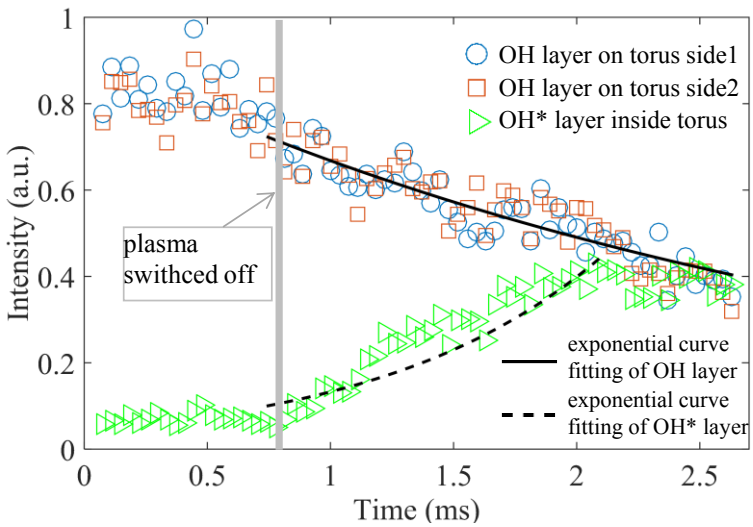

Figure 4.21. Intensity of OH PLIF on both sides of the torus and inside it versus time. The circle, square and triangle markers show the experimental results while the solid and dashed lines indicate the corresponding exponential fittings. The intensity is obtained as shown in Figure 4.20.

The decay of OH number density attributes to the depletion reactions and diffusion effect of turbulence while the production of OH by radical chemistry and ionic reactions as well as OH* relaxation into OH by quenching contributes to the increase of OH. A plausible conclusion is made that the impacts causing the increment of OH number density are dominant rather than the destructions leading to an increase of OH number density in the plasma column region. In addition, owing to low diffusion rate by the turbulence, even though the OH number density is rising in the plasma column, it is still declining at the outer layer of the plasma column as depletion reactions dominate.

Because the OH* is used up at about t=2.1 ms as its chemiluminescence disappeared, OH number density is not able to be escalated by OH* relaxation. After that time, the intensity in and around the plasma column converges to the same level and the decay rate of OH number density also becomes the same as shown in Figure 4.21.

4.4. Diagnostics in combustion engines

This section provides a summary of the results obtained in the work related to the applications of laser diagnostics on practical combustors. Some practical experience and hands-on advice not mentioned in the papers, as well as some procedures of post-processing, are described. Tests of different quartz material will be introduced in order to improve the SNR for the LIF measurement in optical engines. In addition, the developed high speed PLIF techniques with the burst-mode laser system which are mentioned in Section 4.2 are used in a heavy-duty PPC engine. Furthermore, high speed PIV measurement is employed to obtain in-cylinder flow field in a light-duty PPC engine. More results are presented in Paper IV, Paper V, Paper VII and Paper VIII.

4.4.1. Quartz fluorescence study

In an earlier measurement campaign, in which fuel concentration and the mixing process were investigated by PLIF in PPC, was unsatisfactory due to the fluorescence from the quartz glass being much stronger than the useful fluorescence signal from the PLIF tracer, acetone. In other words, the signal to noise ratio was extremely low in this measurement. In addition, because the spectrum of fluorescence from quartz components, *e.g.* optical piston and cylinder liner, overlaps with that from the acetone (both are around 400 nm as shown in Figure 4.22), it is almost impossible to remove fluorescence using only optical filters. Therefore, an investigation of different quartz materials was performed and

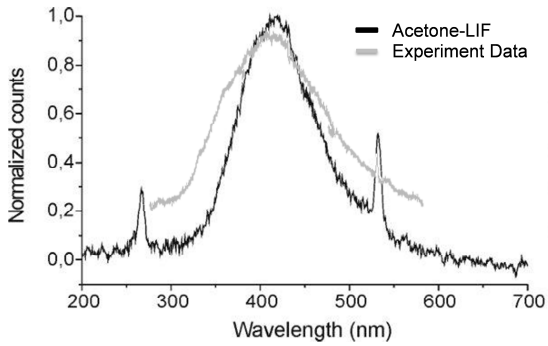

Figure 4.22. Spectrum of the acetone LIF [90-92].

new optical parts should be made of the optimal material, which should possess as low fluorescence as possible at a reasonable price.

Figure 4.23 and Figure 4.24 show the sketch and photo of the experimental setup for the fluorescence responses of different quartz samples. A Nd:YAG (Quantel Brilliant B) laser was used combining SHG and FHG. The power of the laser beam can be controlled by a laser power attenuator. A cylindrical lens (f=-150 mm) and a spherical lens (f=+250 mm) were utilised to create a 10 mm height laser sheet. The quartz sample was placed at almost 45 degrees to the laser sheet and reflected the fluorescence signal to an ICCD camera (PIMAX II). Several filters including a long pass filter (>270 nm) and a short pass filter (<450 nm) were used to cut off the 266 nm wavelength and 532 nm wavelength laser radiations.

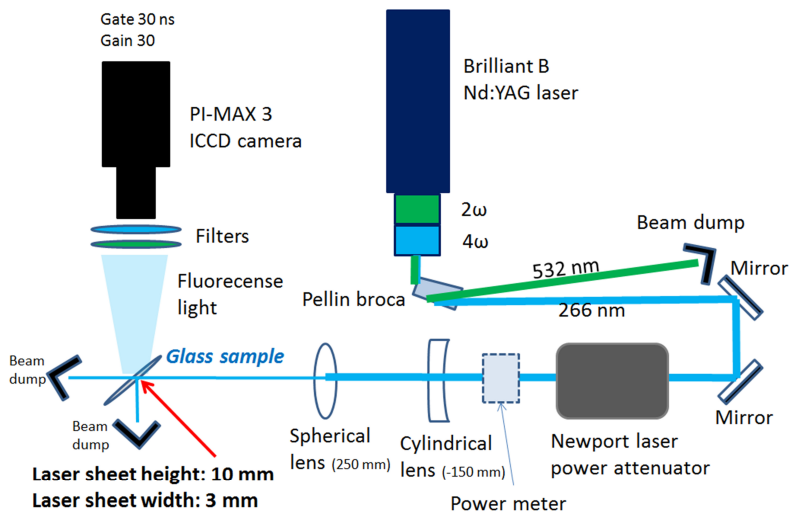

Figure 4.23. Experimental setup of the quartz fluorescence study.

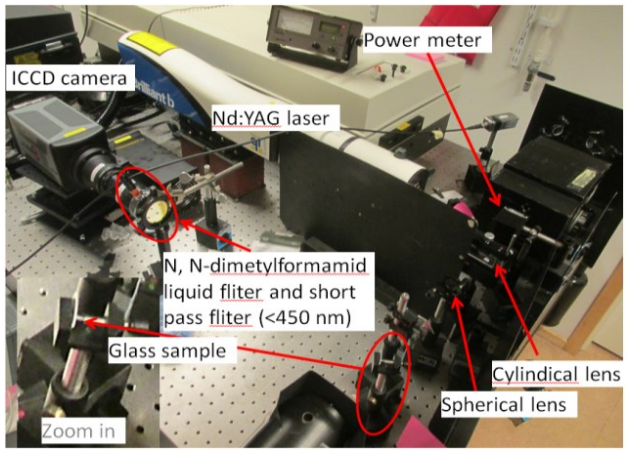

Figure 4.24. Photo of the experimental setup for quartz fluorescence study.

Table 4.4 depicts the material and supplier of different quartz samples. 100 images were captured for each quartz sample and fluorescence data was averaged to minimise the influence of the laser fluctuation.

Table 4.4. Test quartz specifications.

Company	**Test sample**
Impex	CaF2 (Calcium Flourid)
	MgF2 (Magnesium Flourid)
	Sapphire (UV Qualität)
Aachener Quarzglas	Suprasil 1
	Suprasil 2A
	Suprasil 2B (S2B)
	SQ1
J-Plasma GmbH	SQ1 – 7
	SQ1 – E248
	SQ – E193
Heraeus	Suprasil UVL
From GenDies lab	Cylinder head side windows

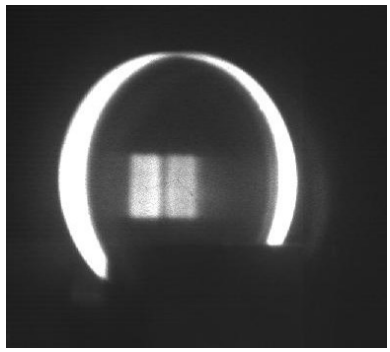

Figure 4.25. Fluorescence on the quartz surface.

Figure 4.25 shows the averaged fluorescence of CaF_2 quartz. The two white rectangles in the middle of the quartz sample are the fluorescence on the front surface and back surface of the quartz. The rectangular shape is the same as the laser sheet. The white on the edge of quartz sample is a result of the scattering light due to the roughness.

The averaged fluorescence intensity was evaluated and compared for all quartz samples. According to the experiment results (see references [93, 94]), there was no fluorescence signal inside the quartz samples such as Suprasil 2, Sapphire, CaF_2 and MgF_2 while there were similar but non-conclusive results for the quartz samples such as SQ1, Suprasil 1 and S2B since these samples are very thin. SQ1, Suprasil 1 and S2B were found to be superior in terms of surface fluorescence. Namely, they have ultra-low laser induced fluorescence by 266 nm laser. In addition, S2B is reasonably priced in relation to its optical performance. Thus, the optical piston and optical windows used in the experiments in this thesis are made of Suprasil 2B (S2B).

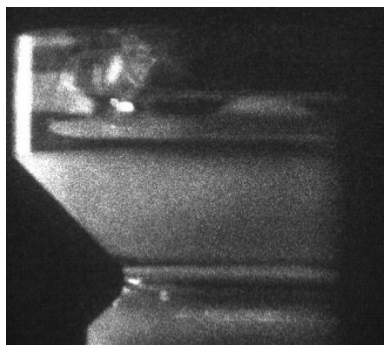

Figure 4.26. Fluorescence of the original quartz piston. The laser sheet passes through the centre of the piston.

Figure 4.26 shows the fluorescence from the original quartz piston which has a fairly strong fluorescence inside the quartz material. Moreover, it has at least 5 times higher fluorescence intensity than S2B material. More detailed information can be found in the references [93, 94].

4.4.2. 10 Hz fuel-tracer PLIF

In Paper V, fuel distribution was investigated in an optical heavy-duty engine with advanced combustion concepts, *i.e.* from HCCI to PPC mode. Both of them share the capability of producing low NOx and soot emissions without adverse effects on engine efficiency [95-104]. In HCCI engines, the fuel mixture is homogeneously distributed in the combustion chamber before the start of combustion and the charge is usually highly diluted in order to keep the pressure rise rate at acceptable levels.

In PPC engines, there is a prolonged time delay between the end of injection (EOI) and the start of combustion (SOC) leading to the mixture being partially premixed before the combustion process. Therefore, different from HCCI, the degree of mixing of fuel and air before the onset of combustion is crucial for the combustion behaviour and emission production in the PPC mode.

In the study performed by Li *et al.* [102], it is found that emissions such as CO and total hydrocarbon (THC) increase tremendously during the transition from HCCI to PPC in a single cylinder heavy-duty all-metal diesel engine. This transition behaviour was realised by varying the start of injection (SOI) timing with constant CA50 (at which 50% heat release generates from the combustion of fuel). Varying the SOI timing, *e.g.* from 100 crank angle degree (CAD) before top dead centre (BTDC) to 15 CAD BTDC, leads to different fuel distribution and mixing process in the combustion chamber before the SOC. In order to understand the influence of stratified fuel distribution on the combustion performance and deteriorated emissions, fuel-tracer PLIF measurement was performed.

Figure 4.27 shows the fuel distribution at about 10 CADs after SOI for three cases. For the case of SOI at 35 CAD BTDC, when the injection hits the vertical wall of the piston bowl, most of the fuel is injected inside the piston bowl and that is where all of the mixing process takes place. The earlier the injection, the more homogeneous it can become before the onset of combustion due to the longer time for mixing.

For the cases of SOI at 46 CAD and 54 CAD BTDC, the injection hits on the rim of the piston bowl. It splits the mixture moving into two directions: inside the piston bowl and towards the squish region, as shown by the arrows in the figure. During the mixing process, part of the fuel mixture dissipates into the crevice areas above the ring pack and fuel is trapped on the piston top-land and in the

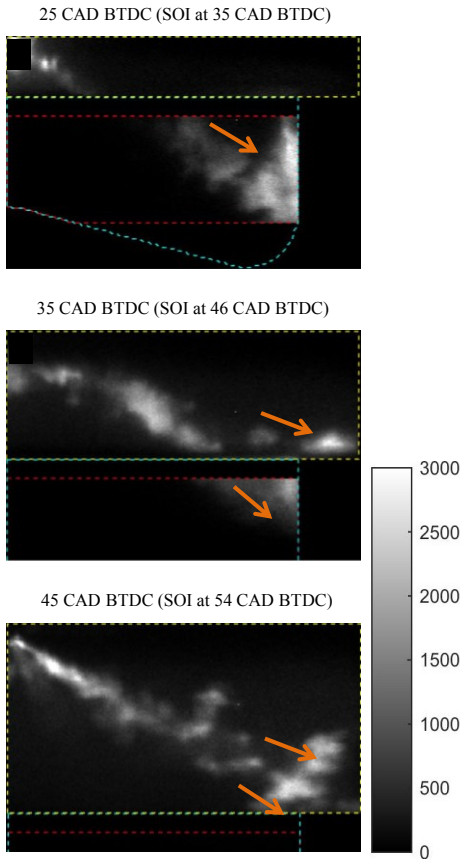

Figure 4.27. Instantaneous PLIF images at about 10 CADs after SOI for cases of SOI at 35, 46 and 54 CAD BTDC, respectively.

squish volume. This leads to poor combustion efficiency and high harmful emissions [105].

Figure 4.28 plots the emissions against the intensity of fuel in squish/crevices region. Fuel trapped in the squish/crevice region can be one of the reasons for deteriorated emissions. Some of the fuel films are attached on the surface of the crevice region which increases CO/THC emission while the PLIF intensity doesn't increase by the same amount.

Therefore, in order to increase combustion efficiency and to reduce THC, the majority of the fuel should be injected into the piston bowl where most of the mixture formation takes place. If a split injection scenario is employed, *e.g.* a double injection strategy, the first injection has to be injected early in a small quantity to provide enough time for evaporation, although the in-cylinder pressure

is low which leads to a long penetration. The worst case is that the majority of the fuel is injected on the top of the piston crown and penetrates into the crevice areas. Optimal injection timings need to be considered together with the geometry of the combustion chamber coupled with the configuration of the injector in order to prevent fuel being injected into the crevice areas.

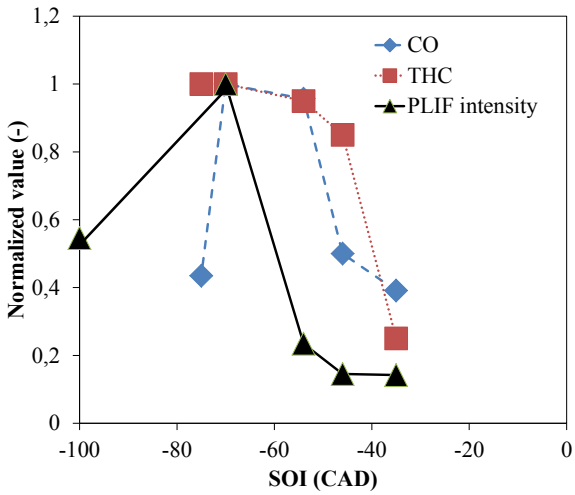

Figure 4.28. Comparison between averaged PLIF intensity in the squish region and emissions data from the reference [102].

4.4.3. High speed PLIF

4.4.3.1 High speed fuel-tracer PLIF and CH_2O PLIF

The PLIF intensity profiles presented in Paper V were obtained from 50 different engine cycles. However, in order to obtain the dynamic features of the mixing process and minimise the influence of CCV, high speed techniques which were developed in a laboratorial burner were employed in a heavy-duty PPC engine.

Simultaneous high-speed fuel tracer PLIF and chemiluminescence imaging as well as simultaneous high-speed formaldehyde PLIF and chemiluminescence imaging were employed for investigation of auto-ignition events with a high temporal resolution, *i.e.* 5 frames/CAD at 1200 rpm. The work demonstrates for the first time the application of the burst-system in an optical engine at tens of kHz repetition rate with a large number of consecutive images, *i.e.* >100 frames. In addition, it is also possible to measure fuel distribution and CH_2O distribution in multiple engine cycles after the idling time of the burst-mode laser system.

Therefore, in a short amount of time more frames can be captured before the windows need cleaning. This is especially valuable under sooty conditions where window fouling can be a major obstacle for optical diagnostics. By comparing the data from multiple engine cycles, the cycle-to-cycle variations can be studied in a time-resolved manner.

The development of auto-ignition together with fuel or CH_2O distribution were investigated in Paper VII and paper VIII. Due to the symmetric feature of the injector and combustion chamber, only part of the combustion chamber and 3 out of 6 spray plumes were captured in the field of view (FOV) as shown in Figure 4.29. For high-speed CMOS cameras, the pixel resolution is reduced with increasing repetition rate. This results in a trade-off between the field of view and the spatial resolution. The present 65 x 60 mm^2 FOV with 512 x 480 pixels resolution was the optimal one after trying different extension rings and camera objectives.

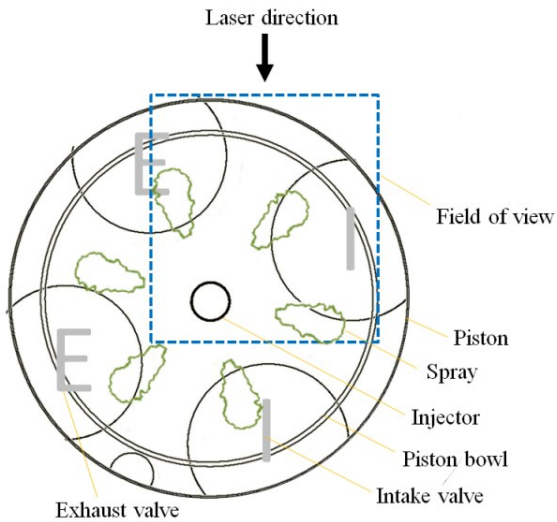

Figure 4.29. Field of view for high speed PLIF measurements in a PPC engine at 36 kHz.

A merit of the developed high speed technique is that the fuel distribution and CH_2O distribution from the SOI can be followed over time and it can thus be observed what happens to them. Prior to the onset of combustion (high temperature combustion) the majority of both fuel and CH_2O are located in the recirculation zone, where the first auto-ignition also occurs.

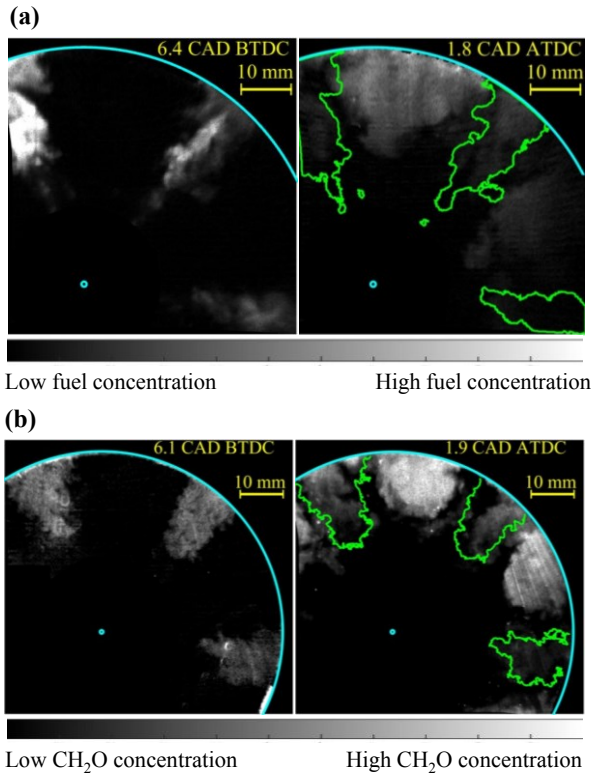

Figure 4.30. (a) Fuel distribution before SOC at 1.8 CAD ATDC together with the outer boundary of fuel distribution at 6.4 CAD BTDC (green lines) in one cycle; (b) CH_2O distribution before SOC at 1.9 CAD ATDC together with the outer boundary of CH_2O distribution at 6.1 CAD BTDC (green lines) in one cycle.

Figure 4.30 shows the comparison of both fuel distribution and CH_2O distribution at around 6 CAD BTDC and at about 2 CAD after top dead centre (ATDC), respectively. It is close to the end of injection at 6 CAD BTDC while it is just before ignition occurs at 2 CAD ATDC. The green boundary in Figure 4.30 (a) or (b) represents the envelope of the fuel distribution and CH_2O distribution recorded at 6 CAD BTDC. It is distinctly evident that after EOI, the majority of the charge ends up in the recirculation zone before the onset of combustion while the area along the spray axis is highly leaned out. CH_2O distribution has similar characteristics. It is worth mentioning that no swirl was used in this engine.

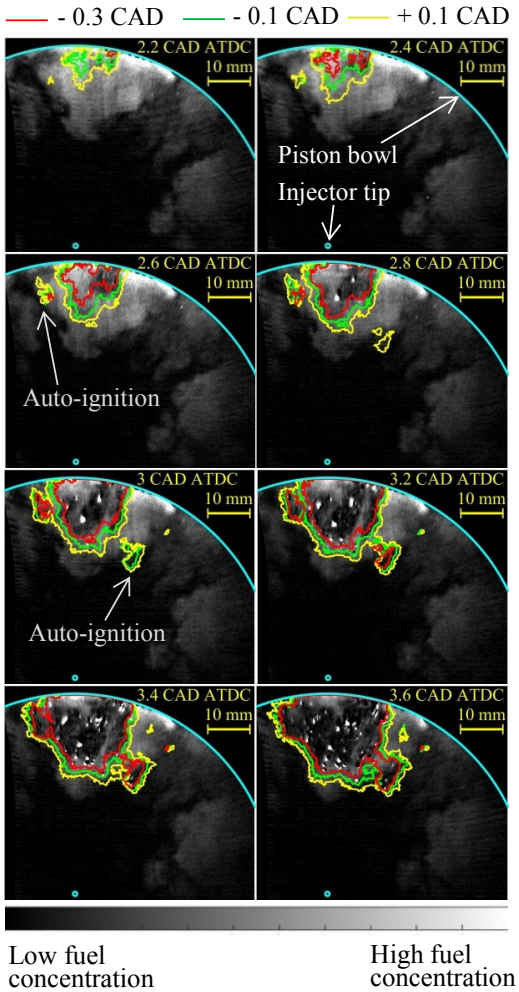

Figure 4.31. Fuel distribution after SOC, *i.e.* high temperature combustion, together with the envelope of auto-ignition zones. Red, green and yellow lines indicate the envelope of flame luminosity at 0.3 CAD, 0.1 CAD before the PLIF image and 0.1 CAD after the PLIF image, respectively.

Due to cycle-to-cycle variation and strong turbulence in the cylinder, the auto-ignition timing and position are variable and predicting them a priori is not easy. Hence, it is very difficult to obtain such simultaneous results with the commonly-used 10 Hz lasers. The long burst duration of this ultra-high-speed technique makes the measurement far more feasible. Nevertheless, both single-shot imaging at 10 Hz and high speed techniques provide different types of data and thus complement each other.

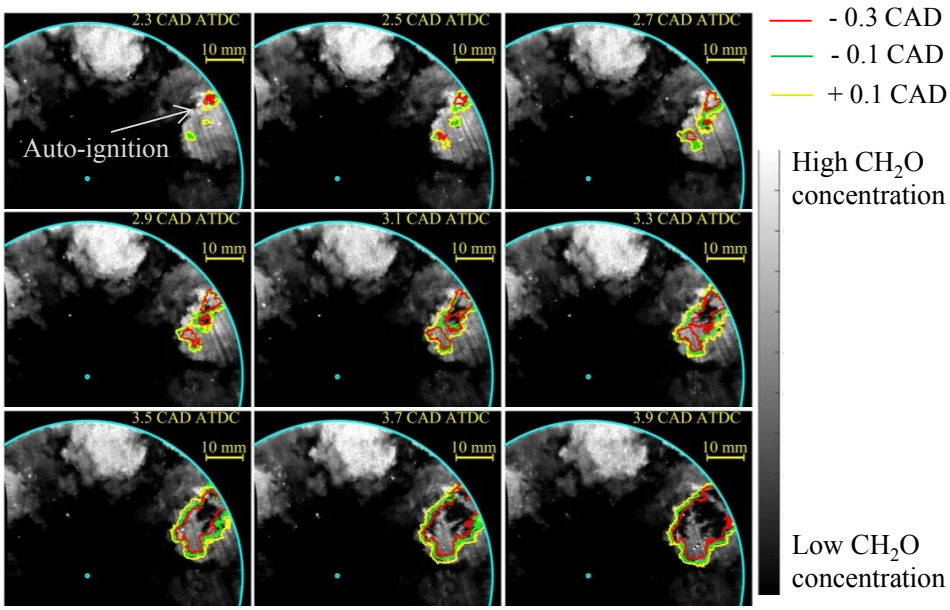

Figure 4.32. CH_2O distribution after SOC, *i.e.* high temperature combustion, together with the envelope (curve notation, see Figure 4.31) of auto-ignition zones.

Figure 4.31 shows the outer boundary of simultaneously recorded chemiluminescence which is imposed on the fuel PLIF images with 0.2 CAD temporal resolution. The timing of the fuel PLIF image is indicated in the upper right corner of the image. It can be seen that the initial auto-ignition (left image in the upper row of Figure 4.31) is located close to the bowl rim in the centre of the recirculation zone where most of the mixture resides after the ignition delay (ID).

Similar to Figure 4.31, the outer boundary of chemiluminescence is overlaid on the CH_2O PLIF image and presented in Figure 4.32 from 0.3 CAD after start of combustion (ASOC) to 1.9 CAD ASOC. The initial auto-ignition (images in the top row of Figure 4.32) is located in the recirculation zone. The obvious difference between the chemiluminescence boundary and the 'holes' in CH_2O distribution in the recirculation zone (in the bottom row of Figure 4.32) is a result of the PLIF images showing true two-dimensional cross-sections whereas the chemiluminescence signal is integrated along the line of sight. The outer border of the chemiluminescence thus represents the largest possible extent of the three-dimensional flame as viewed by the camera. Thus, the flame expansion speed cannot be calculated based on the expansion of the chemiluminescence region. Taking an extreme case as an example, the flame can propagate along the z-axis which is perpendicular to the image plane. In such a case, the area of

chemiluminescence doesn't change on the camera while the flame is growing. A three-dimensional LIF imaging is greatly needed, *e.g.* tomography LIF imaging.

During the injection event the leading edge of the spray is heated as it propagates towards the recirculation zone with the heat exchange with the surrounding hot air while the wake along the spray axis has a relatively cold environment due to the cooling effect from the spray vaporisation. In addition, an entrainment wave leans out the equivalence ratio along the spray axis after EOI. Consequently, the mixture in the recirculation zone is more likely to be ignited (high temperature combustion) first. At the early phase of injection in PPC, the velocity of the leading edge of the spray is too high and due to the early injection timing the local temperature is not high enough for auto-ignition to occur. However, after impingement of neighbouring sprays in the recirculation zone, the flow velocity becomes low and the mixture is further heated which results in a favourable condition for auto-ignition. The ignition precursor CH_2O is formed in the recirculation zone well before the SOC. Once ignition occurs, the reaction front

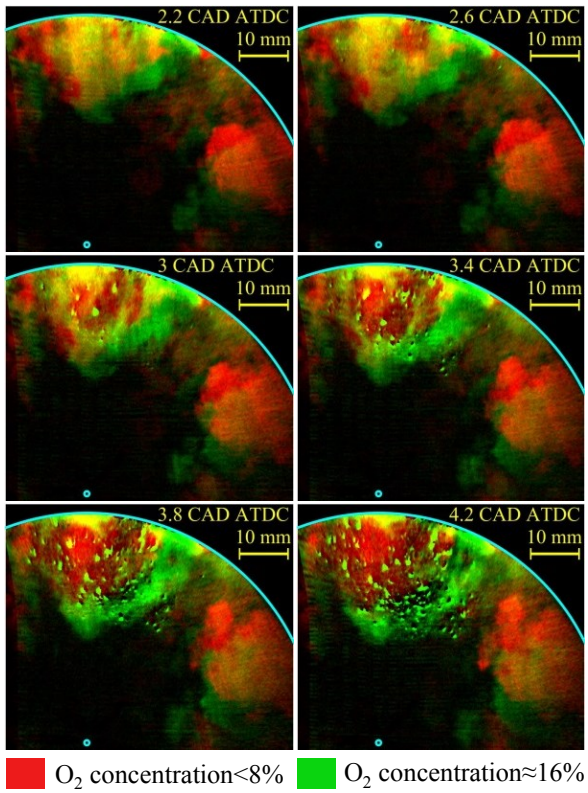

Figure 4.33. Fuel distribution for combusting case (green) after high temperature combustion and high EGR case (red) at several CADs ATDC.

propagation speed is very high and is driven by sequential auto-ignition and hot gas expansion. Whether the initial auto-ignition occurs in the centre or at the periphery of the recirculation zone is a competition between the local equivalence ratio and temperature. Equivalence ratio is higher inside recirculation zone while temperature is higher at the periphery due to less vaporisation and more heat exchange with the hot ambient air.

Figure 4.33 and Figure 4.34 show how the expanding hot gases in the early flame kernel push the fuel and CH_2O in the recirculation zone along the tangential direction (circumferencial direction) and towards the centre of the piston bowl. Since CH_2O is present also slightly after the fuel (tracer) has decomposed, the push from the burnt gases is even more pronounced here.

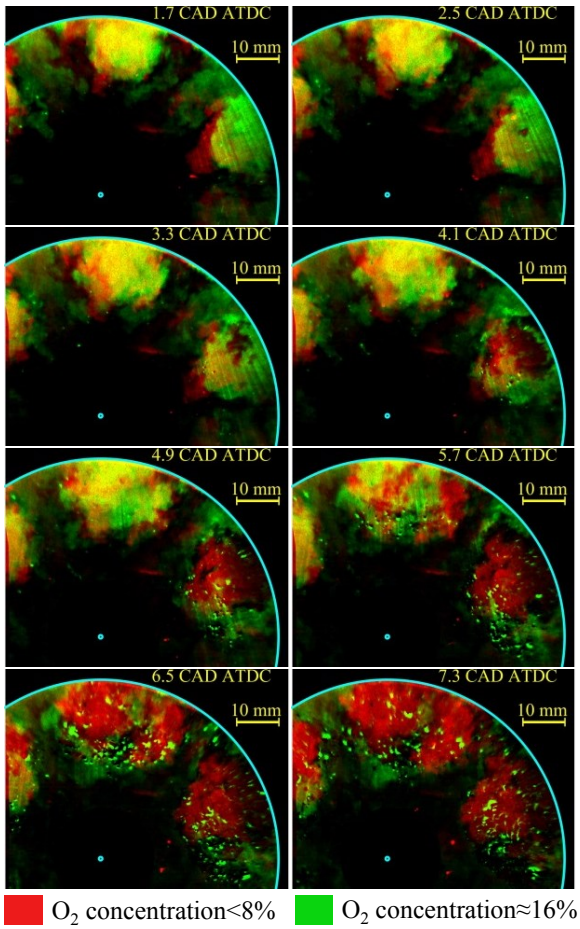

Figure 4.34. CH_2O distribution for combusting case (green) after high temperature combustion and high EGR case (red) at several CADs ATDC.

More frames and movies are included in Paper VII and Paper VIII, by which a more vivid visualisation of the mixing process and evolution of CH_2O can be realised. The ability to record, in excess of 100 PLIF images, in a single cycle brings unique possibilities to follow the in-cylinder processes without the averaging effects caused by cycle-to-cycle variations.

4.4.3.2 An extended conceptual model for gasoline PPC mode

According to Musculus's conceptual model [106], the start of low temperature combustion occurs along the spray axis marked as CH_2O radicals and the second stage combustion (high temperature combustion represented by OH radicals) occurs near the piston bowl wall and spray axis. Figure 4.35 shows a sketch of the conceptual model during the second stage combustion. In their study diesel fuel, which has shorter ID than gasoline fuel, is used for PPC or partially premixed compression ignition (PPCI) mode. Nevertheless, gasoline-like fuel, *i.e.* PRF 87, was used in this thesis work. Therefore, an extended conceptual model for gasoline PPC mode with exhaust gas recirculation (EGR) dilution and single-injection strategy is proposed based on Musculus's one and the results obtained by the developed high speed techniques.

First, the area along the spray axis is highly leaned out. Namely, the fuel concentration and the concentration of low temperature combustion (LTC) products like CH_2O there are low. Secondly, before the onset of second-stage ignition, fuel and CH_2O have a higher concentration in the recirculation zone. Thirdly, the second-stage ignition occurs at the recirculation zone. It is a competition between the local equivalence ratio and temperature as to whether the second-stage ignition starts in the centre or at the periphery of the recirculation zone. In addition, sequential second-stage ignition may occur in the same recirculation zone or in other recirculation zones. The expansion speed of the sequential second-stage ignition in other recirculation zones is significantly faster

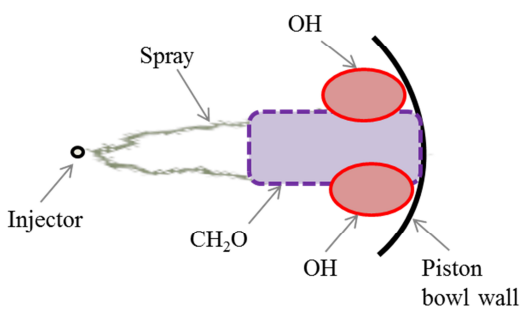

Figure 4.35. Conceptual model for low-load, single-injection, EGR-diluted, PPCI low-temperature heavy-duty DI diesel combustion, proposed by Musculus *et al*.

than the corresponding expansion in the recirculation zone that ignited first. Fourthly, when the second-stage ignition occurs, the expansion of the flame kernels pushes the surrounding fuel and CH_2O in the recirculation zone away tangentially and towards the centre of the piston bowl. Finally, since the flame is three-dimensional, the area of consumed fuel or CH_2O in the laser sheet plane is less than or equal to the area of chemiluminescence from the second-stage ignition, *i.e.* 3D flame may initiate outside the PLIF plane. Figure 4.36 illustrates the aforementioned proposed model.

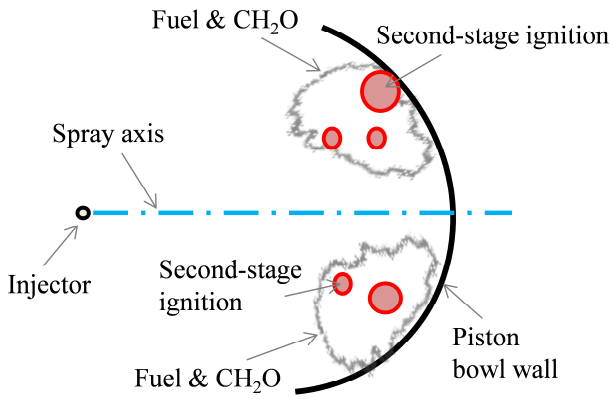

Figure 4.36. An extended conceptual model for low-load, single–injection, EGR-diluted gasoline PPC mode in a heavy-duty diesel engine.

4.4.3.3 Synchronisation

Figure 4.37 shows the connection among the optical engine, the burst-mode laser, the high speed camera and a programmable pulse generator. A crank angle encoder and a top dead centre (TDC) sensor provide instantaneous position of the piston and TDC signal for each engine cycle. The output of the encoder can be connected to the synchronisation of the camera input as shown in the figure or it can be connected to the AOM pulse train input of the burst-mode laser. However, in the configuration shown in Figure 4.37, the synchronisation of the camera output can be adjusted to half frequency or double frequency of the input synchronization signal. Therefore, in simultaneous high-speed fuel tracer PLIF and chemiluminescence imaging measurements as well as simultaneous high-speed formaldehyde PLIF and chemiluminescence imaging measurements presented in Paper VIII, the repetition rate of the high speed camera is twice that of the pulse train from the burst-mode laser.

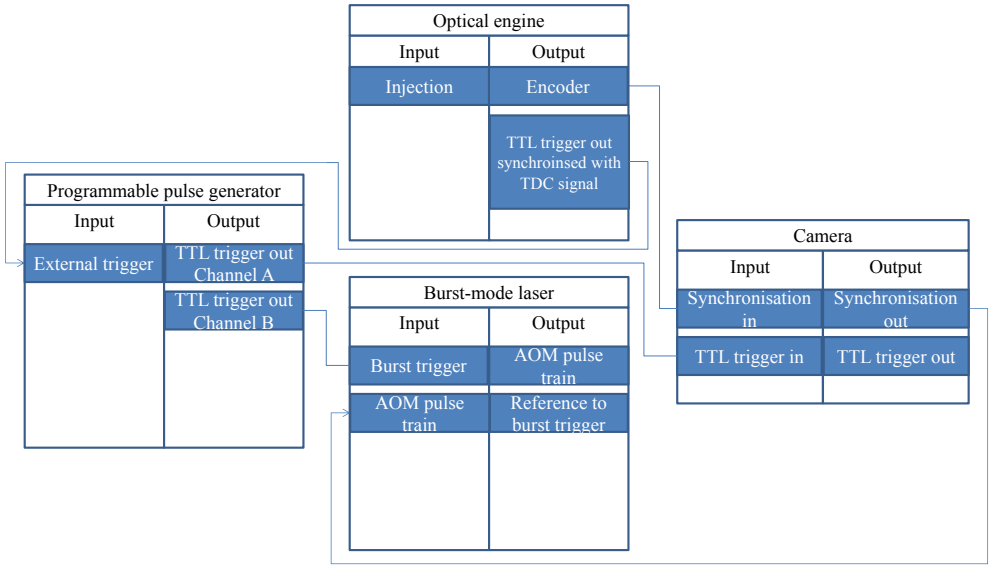

Figure 4.37. Connections of the input and output among the optical engine, the burst-mode laser, the high speed camera and a programmable pulse generator.

4.4.4. PIV

The influence of different injection strategies on in-cylinder flow field and fuel air interaction and mixing with a re-entrant piston bowl design has been investigated by high speed PIV measurements in an optical light-duty PPC engine. In this sub-section, the characteristics of seedings for PIV measurement will be discussed. Moreover, the synchronisation of the high speed Nd:YLF laser, the high speed camera and the optical engine will be described. At the end, the post-processing of the results and cycle-resolved turbulence in the engine will be introduced and discussed. In the beginning of the experiment, the laser was performing at 4.8 kHz in order to obtain PIV images at every CAD. However, because the pulse energy was too low, *e.g.* <4 mJ, and the aperture of the camera lens was set to f#16, the signal was too weak to calculate the velocity field. The repetition rate then decreased to 2.4 kHz to achieve higher pulse energy.

4.4.4.1 Seedings

In PIV measurements, the particle number density in an IA should be larger than 10 [78, 79]. In this thesis work, metal oxide particles *e.g.* TiO_2 and Al_2O_3 are used as seedings for PIV (and LDA) measurements. Stokes number (St), which is defined as the ratio of the particle relaxation time (t_p) to a characteristic time of the

flow (t_f), is calculated to check whether the particle is well-suited to follow the flow or not.

$$St = \frac{t_p}{t_f} = \frac{t_p}{\frac{L_0}{U_0}} = \frac{t_p U_0}{L_0} \tag{4.18}$$

where U_0 is flow velocity and L_0 is the characteristic dimension of the flow, *i.e.* the size of an eddy. Particle relaxation time, t_p can be expressed as the following.

$$t_p = \frac{\rho_p d_p^2}{18\mu_f} \tag{4.19}$$

where ρ_p and d_p represent the particle density and particle diameter; μ_f is dynamic viscosity of the flow.

For example, in a diesel engine at TDC condition, the flow temperature is about 900 K. The diameter of the TiO_2 particle is around 2.5 μm and its density is 4260 kg/m3. The particle relaxation time is approximately 40 μs. If the flow time scale t_f is larger than 0.4 ms, the Stokes number is less than 0.1 which represents accuracy errors of particle tracing below 1% [107].

4.4.4.2 Synchronisation

A timing box (cyclic synchroniser from Dantec Dynamics) was used to synchronise the engine and the high speed PIV system as shown in Figure 4.38.

The timing box receives a TDC signal and crank angle signal from a TDC sensor and an encoder, respectively. Meanwhile, the timing box triggers the high speed laser (DualPower 30-1000) and high speed camera (SpeedSense 710) for every two CADs at 1200 rpm, *i.e.* 2.4 kHz. The laser continuously generates laser beams

Figure 4.38. A timing box used for synchronisation in PIV measurement.

at this repetition rate with about 11 mJ per pulse while the camera receives the PIV signal but does not proceed to readout of the signal. A transistor-transistor logic (TTL) trigger synchronised with the TDC signal from the optical engine triggers the recording of the PIV images.

4.4.4.3 Post-processing

The procedure of post-processing was conducted in MATLAB© for image processing and DynamicStudio software from Dantec Dynamics for the evaluation of PIV data.

The application of a re-entrant piston bowl in the optical engine, inevitably results in severe image distortions. However, the geometrical distortions could be minimised through the recording of reference targets and careful dewarping of the images. In order to test the possibility of distortion correction for this piston, several targets were used together with, at first, a digital camera.

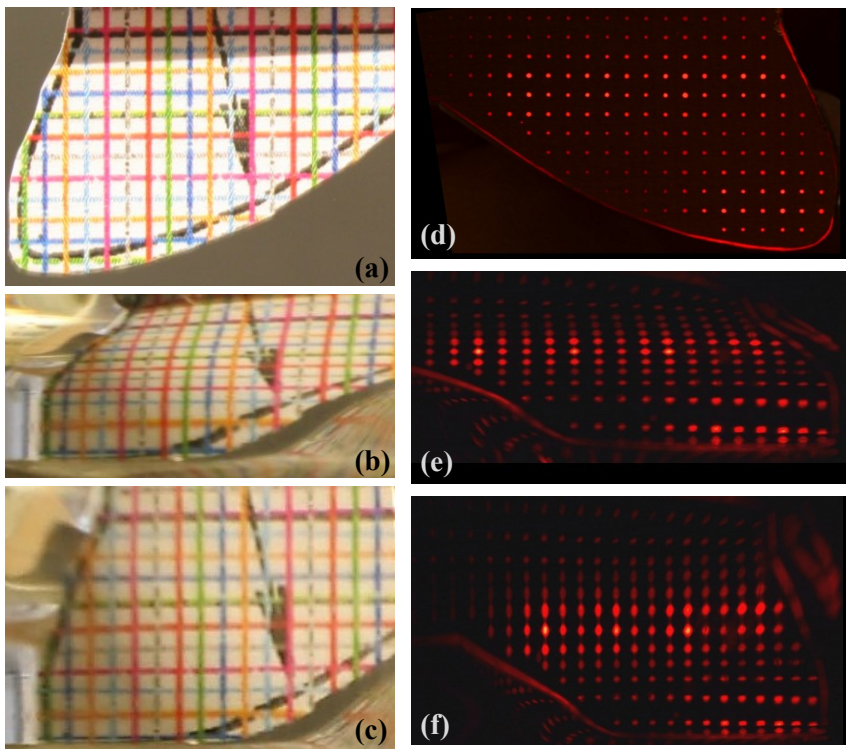

Figure 4.39. A target image without the optical piston (a), with the optical piston (b) and after distortion correction (c); an LED array without the optical piston (d), with the optical piston (e) and after distortion correction (f).

Figure 4.39(a) shows a target with 1 mm distance between each line. After putting the target into the optical piston, it can be seen the target image is distorted as shown in Figure 4.39(b). Due to birefringence effect and because the thickness of the piston wall is not uniformly thick, some parts of the image are in focus while other parts are out of focus. Therefore, the aperture of the camera lens was adjusted to be quite small, *e.g.* focal ratio (F#) is 16, to obtain a large depth of focus. It can be seen that the horizontal lines are squeezed in vertical direction while the vertical lines are skewed. After the image distortion correction, the corrected image looks identical to the original target in most parts of the image as shown in Figure 4.39(c).

In addition, a light-emitting diode (LED) array was used to simulate the particles in PIV measurement for image distortion correction. Similarly, after the image distortion correction, the corrected image seems to be the same as the original LED array as shown in Figure 4.39(d)-(f).

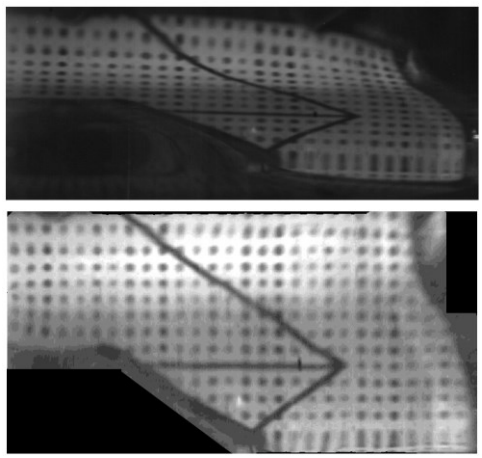

Figure 4.40. Target image before dewarping and after dewarping with a high speed camera.

Then the distortion correction was evaluated in the optical engine with a high speed camera as shown in Figure 4.40. Other post-processing procedures include normalisation, image masking and vector masking. The normalisation of the PIV results improves the contrast of the image as shown in Figure 4.41. In the post-processing of image masking and vector masking, a mask was selected. Outside of it the intensity of PIV images and the velocity of the velocity vector map were set to zero.

Before normalisation

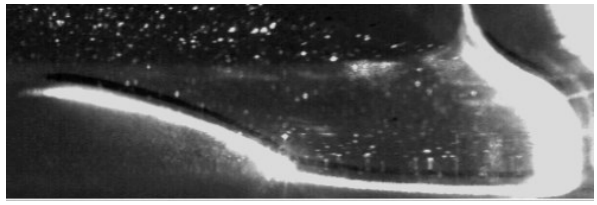

After normalisation

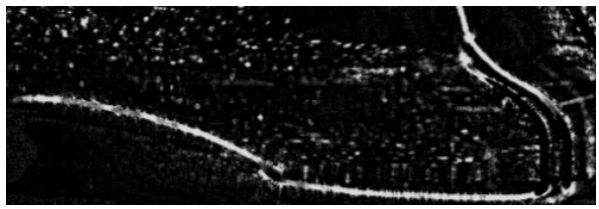

Figure 4.41. PIV images before normalisation and after normalisation in the post-processing.

4.4.4.4 Results and discussion

The turbulence can be obtained by measuring the fluctuation around the averaged value. Because the turbulence cannot suddenly be created and it cannot disappear instantly, it has some relations with the turbulence in the former time and it will affect the turbulence in the later time. In other words, we can think of the turbulence in the time domain. The turbulence at a certain time will be influenced by the upstream time and it will affect the turbulence at the downstream time. The way to make such a connection between them is to use this sine weighted moving average function which is described in Paper VI. The closer the time to the instantaneous velocity, the more influence or the more weight of the turbulence at that time has to affect the turbulence of the instantaneous velocity.

In the PIV measurement in this thesis, the averaged value was calculated based on cycle-resolved PIV data with a 10 CADs window for sine weighted moving average function, *i.e.* five PIV images in one engine cycle. The difference between the instantaneous velocity and the averaged one (by the 10 CADs window) in an IA is considered to be the turbulence velocity. In such a way, the influence of CCV is reduced. More than forty consecutive cycles were recorded with cycle-resolved data in the experiment. Therefore, the averaged turbulent kinetic energy can be calculated by averaging the data from different cycles while CCV is not introduced.

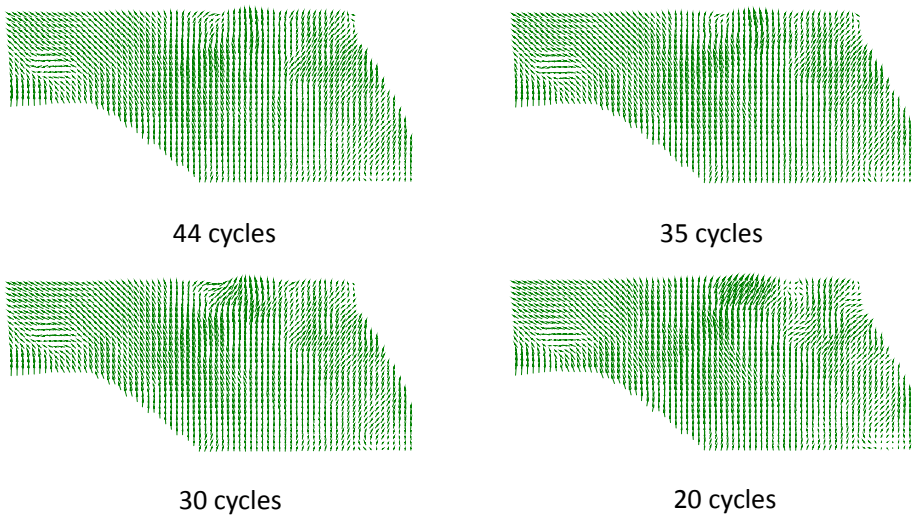

Figure 4.42. Ensemble averaged flow field in the piston bowl calculated based on different numbers of cycles.

Figure 4.42 shows the convergence check of the ensemble averaged results. As long as the number of cycles for calculation of ensemble averaged flow field is above 35, the averaged flow field is almost identical.

More interpretion of the PIV result can be found in Paper VI. A delimitation of the experiment is that it is only two dimensional data. Therefore, in order to obtain the turbulent kinetic energy more accurately, *i.e.* in order to contain three dimensional turbulence velocity components, a stereoscope PIV measurement would be a good future investigation.

5. Summary and outlook

In this thesis, many laser diagnostics have been developed, such as BI, high speed LIF and multi species LIF. Moreover, the developed laser diagnostics have been applied in laboratory jet burners, in diesel sprays, in an HTHP constant volume vessel, in a pulsed plasma discharge and in practical combustion devices, *e.g.* internal combustion engines with elevated pressure and temperature. The experimental equipment and setups are introduced together with some practical experience and hands-on advice not mentioned in the attached papers.

In the first part of the thesis, BI was developed for better imaging through a high OD substance. Two BI systems, 2f-BI system and 4f-BI system, have been developed and compared with scattered media, *e.g.* different sizes of polystyrenes. In addition, USI and BI were also compared based on the contrast transfer functions. The results show that 2f-BI is easier to realise by adjusting the position of the lens and the display screen to achieve a high quality image while 4f is complicated and less robust in practice. Moreover, when the OD of the turbid media or the spray is small, *e.g.* OD<4, it is better to use USI rather than BI techniques. Furthermore, several pieces of practical advice for the BI experiments were put forward, *e.g.* the energy of switching beam for the OKE should not be high, *i.e.* not above several mJ/pulse, while the switching beam can be expanded so that the imaging beam can overlap a more uniform beam profile of it; the time gate of OKE can be adjusted, slightly retarded towards the ballistic photons so that more useful imaging light can be captured so as to improve the image quality, although part of the multiple scattering light would be received as well. Additionally, the developed 2f-BI system has been successfully employed for investigation of the spray formation region of a diesel spray, *i.e.* ECN Spray A, and the supercritical phenomenon has been observed with cellular structures of the spray for the first time.

In the second part of the thesis, multi-scaler PLIF measurements were developed in LUPJ burners including simultaneous measurement of temperature, CH radicals and OH radicals distribution, and simultaneous measurement of CH_2O radicals, CH radicals and OH radicals distribution. Key parameters, such as Damköhler number, Karlovitz number, and Kolmogorov time scale, were calculated and are listed in this thesis based on LDA measurements. The results show that the mean thickness of the CH layer was broadening with an increasing Ka number while the

overlapping layer of OH and CH_2O was not. In addition, the thickness of the CH_2O layer, *i.e.* the preheat zone, rises along the flame height for all the flames investigated. The reaction progress variable of CH_2O was calculated in order to evaluate the turbulent burning velocity, which increases monotonically with the turbulent intensity, first linearly and then at a slower rate. Two LUPJ burners with jet diameter 1.5 mm and 4.5 mm were utilised to investigate the influence of integral scale on the turbulent burning velocity with the same jet speed. It is found that under low turbulent intensity, *e.g.* $u'/S_L < 40$, the turbulent burning velocity is independent of the integral scale, l_0.

In the third part of the thesis, high speed PLIF measurements were developed in an LUPJ burner including simultaneous OH/CH_2O PLIF at 50 kHz, OH PLIF at 100 kHz and CH_2O PLIF at 140 kHz, with more than 100 consecutive images for the first ever time. This was achieved by using a burst-mode laser pumped OPO system synchronised with high speed cameras and high speed intensifiers. The diagnostics approaches were capable of following the temporal evolution of the reacting flow down to the Kolmogorov scale for better understanding of the transient behaviour of the eddy/flame interaction in highly turbulent premixed flames. In addition, it is proved that PAH had negligible influence on high speed PLIF measurements. The synchronisation of the burst-mode laser, two cameras and two intensifiers was described in detail.

In the fourth part of the thesis, the developed high speed PLIF technique was applied in a pulsed plasma discharge, *i.e.* a gliding arc system. It's the first time that a burst-mode laser system is applied for high-speed OH PLIF imaging in pulsed plasma discharges at tens of kHz repetition rate. The changing of OH radical distribution during post discharge, *i.e.* afterglow, was captured at 27 kHz, *e.g.* the deformation of the OH PLIF intensity from a toroidal shape to a filled circle was observed. Furthermore, the decay rate of OH distribution at the outer layer of the plasma column and the growth rate of that in the plasma column were calculated. The results indicate that the decay time of OH at the outer layer of the plasma column is about 3 ms while the increasing rate in the plasma column is 3 times faster than it, which is partially contributed to by the relaxation of OH* into OH.

In the last part of the thesis, varied laser diagnostics have been performed in internal combustion engines with advanced combustion concepts, *e.g.* HCCI and PPC. The laser-based optical methods cover 2.4 kHz PIV, 10 Hz fuel-tracer PLIF and simultaneous high-speed fuel-tracer PLIF and chemiluminescence imaging as well as simultaneous high-speed formaldehyde PLIF and chemiluminescence imaging at 36 kHz repetition rate.

Different quartz samples were tested for PLIF measurements in optical engines. It is found SQ1, Suprasil 1 and S2B are superior in terms of surface fluorescence.

Namely, they have ultra-low laser induced fluorescence by 266 nm laser. In addition, S2B is reasonably priced in relation to its optical performance. Thus, the optical piston and optical windows used in the experiments in this thesis are made of S2B.

The cycle-resolved PIV measurement was performed in a light-duty optical diesel engine with single, double and triple injection strategies. The geometry of the quartz piston crown is based on the standard diesel combustion chamber design for this passenger car engine, including a re-entrant bowl shape. The severe distortions caused by the piston shape could be minimised through the recordings of reference targets and careful dewarping of result images. The influence of CCV is reduced by evaluation of cycle-resolved PIV data with a 10 CADs window for sine weighted moving average function.

10 Hz fuel-tracer PLIF measurements were employed in a heavy-duty optical engine with the transition from HCCI to PPC mode. Different fuel distributions and mixing schemes can be distinguished as the SOI timings are varied during the transition. It is linked to the results presented in the reference, where THC and CO emissions of an all-metal engine were measured at different SOI timings. In the worst case, where the CO/THC emission is considerably high, the majority of the fuel is injected on the top of the piston crown and penetrates into the crevice areas. Therefore, optimal injection timings need to be considered together with the geometry of the combustion chamber coupled with the configuration of the injector in order to prevent deteriorated emissions.

The developed high-speed PLIF techniques have been successfully applied in a heavy-duty PPC engine and that demonstrates for the first time the application of the burst-system in an optical engine with a high temporal resolution, *i.e.* 5 frames/CAD at 1200 rpm and a large number of consecutive images, *i.e.* >100 frames. The mixture formation and evolution of low temperature combustion, *i.e.* CH_2O distribution, together with the auto-ignition were captured and followed in one engine cycle. Since the auto-ignition timing and position are variable and predicting them a priori is not easy, the long burst duration of these ultra-high-speed technique makes the measurement far more feasible. It is found that prior to the onset of combustion the majority of both fuel and CH_2O are located in the recirculation zone, where the first auto-ignition occurs, *i.e.* high temperature combustion. Meanwhile, the concentration of fuel and CH_2O is comparably low along the spray axis. In addition, the expanding hot gases in the early flame kernel push the fuel and CH_2O in the recirculation zone along the tangential direction (circumferencial direction) and towards the centre of the piston bowl. An extended conceptual model for gasoline PPC mode with EGR-dilution and single-injection strategy is proposed based on the results obtained by the developed high speed techniques.

For future study, frequency mixing crystals can be utilised in the development of high speed PLIF imaging with the burst-mode laser pumped OPO system. For instance, by tuning the output of the current OPO system at 606 nm and mixing with a 532 nm laser in a sum frequency generation, 283 nm laser can be consequently generated for OH PLIF measurement. Since the residual 532 nm laser from the harmonic generations of the burst-mode laser has quite high pulse energy, the resulting 283 nm is able to achieve high pulse energy as well. The configuration of this combination and the setup mentioned in this thesis can hence be compared. Moreover, the combination of 609 nm and 1064 nm can produce 387 nm laser which is suitable for CH PLIF measurement in a flame.

The developed simultaneous high speed OH/CH_2O PLIF presented in this thesis can be used in optical engines. Furthermore, it is also possible to perform simultaneous high speed OH/CH_2O PLIF and PIV measurements in optical engines with cycle-resolved resolution. The calibration of fuel distribution will be conducted as well in order to obtain the distribution of equivalence ratio and the link between the equivalence ratio and auto-ignition positions in PPC engines.

An interesting development for high speed imaging techniques is towards four-dimensional tomographic measurements in turbulent flames for the purpose of investigating combustion dynamics. In addition, quantitative 4D measurement with high spatiotemporal resolution for temperature field, flow field and concentration distribution of varied species would be of benefit to fundamental combustion models.

6. References

[1] *World Energy Outlook 2013*, International Energy Agency, OECD/IEA, ISBN: 978-92-64-20130-9, 2013.

[2] *The Outlook for Energy: A View to 2040*, Exxon Mobil Corporation, 2017.

[3] Eckbreth, Alan C., *Laser diagnostics for combustion temperature and species*, Vol. 3. CRC Press, 1996.

[4] Aldén M, Bood J, Li Z and Richter M., *Visualization and understanding of combustion processes using spatially and temporally resolved laser diagnostic techniques*, Proceedings of the Combustion Institute, 33(1), pp.69-97, 2011.

[5] Goulard R., *Combustion measurements: modern techniques and instrumentation*, Project SQUID workshop proceedings, (No. CONF-750569-), Academic Press, New York, 1976.

[6] Linne M., *Imaging in the optically dense regions of a spray: A review of developing techniques*, Progress in Energy and Combustion Science, 39(5), pp.403-440, 2013.

[7] Lempert W., Wu P.F., Miles R., Zhang B., Lowrance J., Mastrocola V. and Kosonocky W., *Pulse-burst laser system for high-speed flow diagnostics*, In 34th Aerospace Sciences Meeting and Exhibit (p. 179), 1996.

[8] Kaminski C.F., Hult J. and Aldén M., *High repetition rate planar laser induced fluorescence of OH in a turbulent non-premixed flame*, Applied Physics B: Lasers and Optics, 68(4), pp.757-760, 1999.

[9] Miller J.D., Slipchenko M., Meyer T.R., Jiang N., Lempert W.R. and Gord J.R., *Ultrahigh-frame-rate OH fluorescence imaging in turbulent flames using a burst-mode optical parametric oscillator*, Optics letters, 34(9), pp.1309-1311, 2009.

[10] Sjöholm J., Kristensson E., Richter M., Aldén M., Göritz G. and Knebel K., *Ultra-high-speed pumping of an optical parametric oscillator (OPO) for high-speed laser-induced fluorescence measurements*, Measurement Science and Technology, 20(2), p.025306, 2009.

[11] Jiang N., Patton R.A., Lempert W.R. and Sutton J.A., *Development of high-repetition rate CH PLIF imaging in turbulent nonpremixed flames*, Proceedings of the Combustion Institute, 33(1), pp.767-774, 2011.

[12] Boxx I., Arndt C.M., Carter C.D. and Meier W., *High-speed laser diagnostics for the study of flame dynamics in a lean premixed gas turbine model combustor*, Experiments in fluids, 52(3), pp.555-567, 2012.

[13] Gabet K.N., Patton R.A., Jiang N., Lempert W.R. and Sutton J.A., *High-speed CH2O PLIF imaging in turbulent flames using a pulse-burst laser system*, Applied Physics B, 106(3), pp.569-575, 2012.

[14] Slipchenko M.N., Miller J.D., Roy S., Gord J.R., Danczyk S.A. and Meyer T.R., *Quasi-continuous burst-mode laser for high-speed planar imaging*, Optics Letters, 37(8), pp.1346-1348, 2012.

[15] Sick V., *High speed imaging in fundamental and applied combustion research*, Proceedings of the Combustion Institute, 34(2), pp.3509-3530, 2013.

[16] Miller J.D., Michael J.B., Slipchenko M.N., Roy S., Meyer T.R. and Gord J.R., *Simultaneous high-speed planar imaging of mixture fraction and velocity using a burst-mode laser*, Applied Physics B, 113(1), pp.93-97, 2013.

[17] Slipchenko M.N., Miller J.D., Roy S., Gord J.R. and Meyer T.R., *All-diode-pumped quasi-continuous burst-mode laser for extended high-speed planar imaging*, Optics express, 21(1), pp.681-689, 2013.

[18] Hsu P.S., Kulatilaka W.D., Roy S. and Gord J.R., *Investigation of optical fibers for high-repetition-rate, ultraviolet planar laser-induced fluorescence of OH*, Applied optics, 52(13), pp.3108-3115, 2013.

[19] Thurow B., Jiang N. and Lempert W., *Review of ultra-high repetition rate laser diagnostics for fluid dynamic measurements*, Measurement Science and Technology, 24(1), p.012002, 2013.

[20] Michael J.B., Venkateswaran P., Miller J.D., Slipchenko M.N., Gord J.R., Roy S. and Meyer T.R., *100 kHz thousand-frame burst-mode planar imaging in turbulent flames*, Optics letters, 39(4), pp.739-742, 2014.

[21] Slipchenko M.N., Miller J.D., Roy S., Meyer T.R., Mance J.G. and Gord J.R., *100 kHz, 100 ms, 400 J burst-mode laser with dual-wavelength diode-pumped amplifiers*, Optics letters, 39(16), pp.4735-4738, 2014.

[22] Roy S., Miller J.D., Slipchenko M.N., Hsu P.S., Mance J.G., Meyer T.R. and Gord, J.R., *100-ps-pulse-duration, 100-J burst-mode laser for kHz–MHz flow diagnostics*, Optics letters, 39(22), pp.6462-6465, 2014.

[23] Miller J.D., Gord J.R., Meyer T.R., Slipchenko M.N., Mance J.G. and Roy S., *Development of a diode-pumped 100-ms quasi-continuous burst-mode laser for high-speed combustion diagnostics*, In 30th AIAA Aerodynamic Measurement Technology and Ground Testing Conference (p. 2524), 2014.

[24] Roy S., Hsu P.S., Jiang N., Slipchenko M.N. and Gord J.R., *100-kHz-rate gas-phase thermometry using 100-ps pulses from a burst-mode laser*, Optics letters, 40(21), pp.5125-5128, 2015.

[25] Miller J.D., Jiang N., Slipchenko M.N., Mance J.G., Meyer T.R., Roy S. and Gord J.R., *Spatiotemporal analysis of turbulent jets enabled by 100-kHz, 100-ms burst-mode particle image velocimetry*, Experiments in Fluids, 57(12), p.192, 2016.

[26] Halls B.R., Gord J.R., Jiang N., Splichenko M., Roy S. and Meyer T.R., *High-speed three-dimensional tomographic measurements for combustion systems*, In 32nd AIAA Aerodynamic Measurement Technology and Ground Testing Conference (p. 4027), 2016.

[27] Meyer T.R., Halls B.R., Jiang N., Slipchenko M.N., Roy S. and Gord J.R., *High-speed, three-dimensional tomographic laser-induced incandescence imaging of soot volume fraction in turbulent flames*, Optics express, 24(26), pp.29547-29555, 2016.

[28] Miller J.D., Peltier S.J., Slipchenko M.N., Mance J.G., Ombrello T.M., Gord J.R. and Carter C.D., *Investigation of transient ignition processes in a model scramjet pilot cavity using simultaneous 100 kHz formaldehyde planar laser-induced fluorescence and CH* chemiluminescence imaging*, Proceedings of the Combustion Institute, 36(2), pp.2865-2872, 2017.

[29] Aldén M. and Richter M., *Development and Application of High-Speed Laser Visualization Techniques in Combustion Research*, In the Micro-World Observed by Ultra High-Speed Cameras (pp. 241-259). Springer, Cham, 2018.

[30] Geusic J.E., Marcos H.M. and Van Uitert L., *Laser oscillations in Nd‐doped yttrium aluminum, yttrium gallium and gadolinium garnets*, Applied Physics Letters, 4(10), pp.182-184, 1964.

[31] Kiss Z.J. and Pressley R.J., *Crystalline solid lasers*. Applied optics, 5(10), pp.1474-1486, 1966.

[32] Hult J., *Development of time resolved laser imaging techniques for studies of turbulent reacting flows*, Doctoral thesis, Department of Physics, Lund University, Lund, 2002.

[33] Sjöholm J., *High Repetition Rate Laser Diagnostics for Combustion Applications*, Doctoral thesis, Department of Physics, Lund University, Lund, 2012.

[34] Li Z., *OH and Soot Optical Diagnostics for Combustion Applications for Combustion Applications*, Doctoral thesis, Department of Physics, Lund University, Lund, 2016.

[35] Wellander R., *Multi-Dimensional Quantitative Laser-based Diagnostics-Development and Practical Applications*, Doctoral thesis, Department of Physics, Lund University, Lund, 2014.

[36] Engine Combustion Network, ECN, website: https://ecn.sandia.gov/.

[37] Zhou B., Brackmann C., Li Z., Aldén M. and Bai X.S., *Simultaneous multi-species and temperature visualization of premixed flames in the distributed reaction zone regime*, Proceedings of the Combustion Institute, 35(2), pp.1409-1416, 2015.

[38] Zhou B., *Advanced laser-based multi-scalar imaging for flame structure visualization towards a deepened understanding of premixed turbulent combustion*, Doctoral thesis, Department of Physics, Lund University, Lund, 2015.

[39] Zhou B., Brackmann C., Wang Z., Li Z., Richter M., Aldén M. and Bai X.S., *Thin reaction zone and distributed reaction zone regimes in turbulent premixed methane/air flames: scalar distributions and correlations*, Combustion and Flame, 175, pp.220-236, 2017.

[40] Rosell J., Bai X.S., Sjöholm J., Zhou B., Li Z., Wang Z., Pettersson P., Li Z., Richter M. and Alden M., *Multi-species PLIF study of the structures of turbulent premixed methane/air jet flames in the flamelet and thin-reaction zones regimes*, Combustion and Flame, 182, pp.324-338, 2017.

[41] Bowditch F.W., *A new tool for combustion research a quartz piston engine* (No. 610002), SAE Technical Paper, 1961.

[42] Sun Z., Zhu J., Li Z., Aldén M., Leipold, F., Salewski, M. and Kusano, Y., *Optical diagnostics of a gliding arc*, Optics express, 21(5), pp.6028-6044, 2013.

[43] Zhu J., Gao J., Li Z., Ehn A., Aldén M., Larsson A. and Kusano Y., *Sustained diffusive alternating current gliding arc discharge in atmospheric pressure air*, Applied Physics Letters, 105(23), p.234102, 2014.

[44] Zhu J., Sun Z., Li Z., Ehn A., Aldén M., Salewski M., Leipold F. and Kusano Y., *Dynamics, OH distributions and UV emission of a gliding arc at various flow-rates investigated by optical measurements*, Journal of Physics D: Applied Physics, 47(29), p.295203, 2014.

[45] Zhu J., Gao J., Ehn A., Aldén M., Li Z., Moseev D., Kusano Y., Salewski M., Alpers A., Gritzmann P. and Schwenk M., *Measurements of 3D slip velocities and plasma column lengths of a gliding arc discharge*, Applied Physics Letters, 106(4), p.044101, 2015.

[46] Zhu J., *Optical diagnostics of non-thermal plasmas and plasma-assisted combustion*, Doctoral thesis, Department of Physics, Lund University, Lund, 2015.

[47] Zhu J., Kusano Y. and Li Z., *Optical Diagnostics of a Gliding Arc Discharge at Atmospheric Pressure*, In Atmospheric Pressure Plasmas: Processes, Technology and Applications. Nova Science Publishers, Incorporated, 2016.

[48] Zhu J., Gao J., Ehn A., Aldén M., Larsson A., Kusano Y. and Li Z., *Spatiotemporally resolved characteristics of a gliding arc discharge in a turbulent air flow at atmospheric pressure*, Physics of Plasmas, 24(1), p.013514, 2017.

[49] Gao J., Zhu J., Ehn A., Aldén M. and Li Z., *In-Situ Non-intrusive Diagnostics of Toluene Removal by a Gliding Arc Discharge Using Planar Laser-Induced Fluorescence*, Plasma Chemistry and Plasma Processing, 37(2), pp.433-450, 2017.

[50] Zhu J., Ehn A., Gao J., Kong C., Aldén M., Salewski M., Leipold F., Kusano Y. and Li Z., *Translational, rotational, vibrational and electron temperatures of a gliding arc discharge*, Optics express, 25(17), pp.20243-20257, 2017.

[51] Kristensson E., Richter M., Pettersson S.G., Aldén M. and Andersson-Engels S., *Spatially resolved, single-ended two-dimensional visualization of gas flow phenomena using structured illumination*, Applied optics, 47(21), pp.3927-3931, 2008.

[52] Berrocal E., Kristensson E., Richter M., Linne M. and Aldén M., *Application of structured illumination for multiple scattering suppression in planar laser imaging of dense sprays*, Optics express, 16(22), pp.17870-17881, 2008.

[53] Kristensson E., Berrocal E., Richter M., Pettersson S.G. and Aldén M., *High-speed structured planar laser illumination for contrast improvement of two-phase flow images*, Optics letters, 33(23), pp.2752-2754, 2008.

[54] Kristensson E., Araneo L., Berrocal E., Manin J., Richter M., Aldén M. and Linne M., *Analysis of multiple scattering suppression using structured laser illumination planar imaging in scattering and fluorescing media*, Optics express, 19(14), pp.13647-13663, 2011.

[55] Kristensson E., Berrocal E. and Aldén M., *Quantitative 3D imaging of scattering media using structured illumination and computed tomography*, Optics express, 20(13), pp.14437-14450, 2012.

[56] Berrocal E., Kristensson E., Hottenbach P., Aldén M. and Grünefeld G., *Quantitative imaging of a non-combusting diesel spray using structured laser illumination planar imaging*, Applied physics b, 109(4), pp.683-694, 2012.

[57] Kristensson E., *Structured laser illumination planar imaging SLIPI applications for spray diagnostics*, Doctoral thesis, Department of Physics, Lund University, Lund, 2012.

[58] Berrocal E., Sedarsky D., Paciaroni, M. and Linne M., *Propagation of ultra-short laser light pulses within spray environments*, In ILASS Americas, 20th Annual Conference on Liquid Atomization and Spray Systems, Chicago, IL. 2007.

[59] Berrocal E., Sedarsky D., Paciaroni, M., Meglinski, I. and Linne, M., *Laser light scattering in turbid media Part II: Spatial and temporal analysis of individual scattering orders via Monte Carlo simulation*, Optics express, 17(16), pp.13792-13809, 2009.

[60] Ho, P.P. and Alfano, R.R., *Optical Kerr effect in liquids*, Physical Review A, 20(5), p.2170, 1979.

[61] Demos, S.G. and Alfano, R.R., *Temporal gating in highly scattering media by the degree of optical polarization*, Optics letters, 21(2), pp.161-163, 1996.

[62] Paciaroni M, *Time-gated ballistic imaging through scattering media with applications to liquid spray combustion*, Doctoral thesis, Division of Engineering, Colorado School of Mines, Colorado, 2004.

[63] Paciaroni M. and Linne M., *Single-shot, two-dimensional ballistic imaging through scattering media*, Applied optics, 43(26), pp.5100-5109, 2004.

[64] Rahm M., *Temporally Gated Imaging for Investigation of Atomizing Sprays*, Doctoral thesis, Department of Applied Mechanics, Chalmers University of Technology, Gothenburg, 2016.

[65] Van de Hulst, H.C., *Light scattering by small particles*, Wiley & Sons, New York, 1957.

[66] Wilson, R.E. and Bodapati, S., *Steady flow field measurements using Laser Doppler Velocimetry*, Doctoral thesis, Naval Postgraduate School, Monterey, California, 1987.

[67] Aldén M., Edner H., Holmstedt G., Svanberg S. and Högberg T., *Single-pulse laser-induced OH fluorescence in an atmospheric flame, spatially resolved with a diode array detector*, Applied optics, 21(7), pp.1236-1240, 1982.

[68] Kychakoff G., Howe R.D., Hanson R.K., Drake M.C., Pitz R.W., Lapp M. and Penney C.M., *Visualization of turbulent flame fronts with planar laser-induced fluorescence*, Science, 224(4647), pp.382-384, 1984.

[69] Nygren J., Hult J., Richter M., Aldén M., Christensen M., Hultqvist A. and Johansson B., *Three-dimensional laser induced fluorescence of fuel distributions in an HCCI engine*, Proceedings of the Combustion Institute, 29(1), pp.679-685, 2002.

[70] Wellander R., Richter M. and Aldén M., *Time resolved, 3D imaging (4D) of two phase flow at a repetition rate of 1 kHz*, Optics express, 19(22), pp.21508-21514, 2011.

[71] Halls B.R., Thul D.J., Michaelis D., Roy S., Meyer T.R. and Gord J.R., *Single-shot, volumetrically illuminated, three-dimensional, tomographic laser-induced-fluorescence imaging in a gaseous free jet*, Optics express, 24(9), pp.10040-10049, 2016.

[72] Kristensson E., Li Z., Berrocal E., Richter M. and Aldén M., *Instantaneous 3D imaging of flame species using coded laser illumination*, Proceedings of the Combustion Institute, 36(3), pp.4585-4591, 2017.

[73] Wellander R., Richter M. and Aldén M., *Time-resolved (kHz) 3D imaging of OH PLIF in a flame*, Experiments in fluids, 55(6), p.1764, 2014.

[74] Halls B.R., Hsu P.S., Jiang N., Legge E.S., Felver J.J., Slipchenko M.N., Roy S., Meyer T.R. and Gord J.R., *kHz-rate four-dimensional fluorescence tomography using an ultraviolet-tunable narrowband burst-mode optical parametric oscillator*, Optica, 4(8), pp.897-902, 2017.

[75] Banwell C.N. and McCash E.M., *Fundamentals of molecular spectroscopy* (Vol. 851), New York: McGraw-Hill, 1994.

[76] Adrian R.J. and Westerweel J., *Particle image velocimetry* (No. 30), Cambridge University Press, 2011.

[77] Raffel M., Willert C.E., Wereley S.T. and Kompenhans J., *Particle image velocimetry: a practical guide*, Springer, 2013.

[78] Keane R.D. and Adrian R.J., *Theory of cross-correlation analysis of PIV images*, Applied scientific research, 49(3), pp.191-215, 1992.

[79] Keane R.D. and Adrian R.J., *Theory of cross-correlation analysis of PIV images*, In Flow visualization and image analysis (pp. 1-25). Springer, Dordrecht, 1993.

[80] Theunissen R., Scarano F. and Riethmuller M.L., *An adaptive sampling and windowing interrogation method in PIV*, Measurement Science and Technology, 18(1), p.275, 2006.

[81] Sedarsky D., Berrocal E. and Linne M., *Quantitative image contrast enhancement in time-gated transillumination of scattering media*, Optics express, 19(3), pp.1866-1883, 2011.

[82] Campillo A.J., Shapiro S.L. and Suydam B.R., *Relationship of self‐focusing to spatial instability modes*, Applied Physics Letters, 24(4), pp.178-180, 1974.

[83] Peters, N., *Turbulent combustion*, Cambridge university press, 2000.

[84] Li Z., Li B., Sun Z., Bai X.S. and Aldén M., *Turbulence and combustion interaction: High resolution local flame front structure visualization using simultaneous single-shot PLIF imaging of CH, OH, and CH2O in a piloted premixed jet flame*, Combustion and Flame, 157(6), pp.1087-1096, 2010.

[85] Wabel T.M., Skiba A.W. and Driscoll J.F., *Turbulent burning velocity measurements: Extended to extreme levels of turbulence*, Proceedings of the Combustion Institute, 36(2), pp.1801-1808, 2017.

[86] D'Anna, A. and Violi, A., *A kinetic model for the formation of aromatic hydrocarbons in premixed laminar flames*, In Symposium (International) on Combustion Vol. 27, No. 1, pp. 425-433, 1998.

[87] Larsson K., *Development of photofragmentation-based diagnostics*, Doctoral thesis, Department of Physics, Lund University, Lund, 2018.

[88] Ono R. and Oda T., *Measurement of gas temperature and OH density in the afterglow of pulsed positive corona discharge*, Journal of Physics D: Applied Physics, 41(3), p.035204, 2008.

[89] Zheng C., Shen X., Gao X., Li Z., Zhu X., Luo Z. and Cen K., *Planar laser-induced fluorescence diagnostics for spatiotemporal oh evolution in pulsed corona discharge*, IEEE Transactions on Plasma Science, 41(3), pp.485-493, 2013.

[90] Bryant R.A., Donbar J.M. and Driscoll J.F., *Acetone laser induced fluorescence for low pressure/low temperature flow visualization*, Experiments in Fluids, 28(5), pp.471-476, 2000.

[91] Tran T., Kochar Y. and Seitzman J., *Measurements of liquid acetone fluorescence and phosphorescence for two-phase fuel imaging*, In AIAA Paper 2005-0827, 43rd AIAA Aerospace Sciences Meeting and Exhibit, 2005.

[92] Schulz C. and Sick V., *Tracer-LIF diagnostics: quantitative measurement of fuel concentration, temperature and fuel/air ratio in practical combustion systems*, Progress in Energy and Combustion Science, 31(1), pp.75-121, 2005.

[93] *KCFP Annual Report 2014*, Centre of Competence Combustion Processes (KCFP), Faculty of Engineering, Lund University, 2014. Online available: https://www.lth.se/fileadmin/kcfp/Reports/KCFP_AR_2014_SV.pdf.

[94] *Activity Report from the Division of Combustion Physics 2012-2014*, Lund Reports on Combustion Physics, Lund University, 2015. Online available: http://www.forbrf.lth.se/fileadmin/forbrf/Documents/Activity_reports/Activity_report_2012_2014.pdf.

[95] Kalghatgi G.T., Risberg P. and Ångström H.E., *Advantages of fuels with high resistance to auto-ignition in late-injection, low-temperature, compression ignition combustion* (No. 2006-01-3385), SAE Technical Paper, 2006.

[96] Hildingsson, L., *Laser Diagnostics of HCCI and Partially Premixed Combustion*, Doctoral thesis, Department of Energy Sciences, Lund University, Lund, 2006.

[97] Kalghatgi G.T., Risberg P. and Ångström H.E., *Partially pre-mixed auto-ignition of gasoline to attain low smoke and low NOx at high load in a compression ignition engine and comparison with a diesel fuel* (No. 2007-01-0006), SAE Technical paper, 2007.

[98] Manente V., Johansson B. and Tunestal P., *Partially premixed combustion at high load using gasoline and ethanol, a comparison with diesel* (No. 2009-01-0944), SAE Technical Paper, 2009.

[99] Dec J.E., *Advanced compression-ignition engines—understanding the in-cylinder processes*, Proceedings of the combustion institute, 32(2), pp.2727-2742, 2009.

[100] Manente V., *Gasoline partially premixed combustion-an advanced internal combustion engine concept aimed to high efficiency, low emissions and low acoustic noise in the whole load range*, Doctoral thesis, Department of Energy Sciences, Lund University, Lund, 2010

[101] Dempsey A.B., Curran S.J. and Wagner R.M., *A perspective on the range of gasoline compression ignition combustion strategies for high engine efficiency and low NOx and soot emissions: Effects of in-cylinder fuel stratification*, International Journal of Engine Research, 17(8), pp.897-917, 2016.

[102] Li C., Yin L., Shamun S., Tuner M., Johansson B., Solsjo R. and Bai X.S., *Transition from HCCI to PPC: the Sensitivity of Combustion Phasing to the Intake Temperature and the Injection Timing with and without EGR* (No. 2016-01-0767), SAE Technical Paper, 2016.

[103] Shen M., *Particulate matter emissions from partially premixed combustion with diesel, gasoline and ethanol*, Doctoral thesis, Department of Energy Sciences, Lund University, Lund, 2016.

[104] Lundgren M., *Optical Diagnostics of Gasoline Compression Ignition: HCCI-PPC-Diffusion Combustion*, Doctoral thesis, Department of Energy Sciences, Lund University, Lund, 2017.

[105] Aronsson U., Andersson Ö., Egnell R., Miles P.C. and Ekoto I.W., *Influence of spray-target and squish height on sources of CO and UHC in a HSDI diesel engine during PPCI low-temperature combustion* (No. 2009-01-2810), SAE Technical Paper, 2009.

[106] Musculus M.P., Miles P.C. and Pickett L.M., *Conceptual models for partially premixed low-temperature diesel combustion*, Progress in Energy and Combustion Science, 39(2-3), pp.246-283, 2013.

[107] Tropea C. and Yarin A.L., *Springer handbook of experimental fluid mechanics* (Vol. 1). Springer Science & Business Media, 2007.

7. Acknowledgements

My sincere thanks go to everyone who has helped, supported and taught me during my PhD study. It's been a long-term endeavour, a marathon race with obstacles and difficulties, that I definitely could not have finished without you. There are too many people for me to name all of you. However, even if you are not mentioned by name here, your help and support are still greatly appreciated.

First, I would like to express my significant gratitude to my main supervisor Prof. Mattias Richter. You always forgive my mistakes and faults. One of the most memorable things is that once I was changing a flash-lamp in the burst-mode laser without turning off the laser, as a result, the cooling water splashed everywhere including the optics inside the burst-mode laser. You were just beside me and put me at ease afterwards. Another example is that during the submission period for the 36th Combustion Symposium, I sent you the manuscript for review at a very late stage, maybe one or two days before the deadline. Despite this, you still worked very late to correct the mistakes I had made and gave me excellent suggestions and advice. Thank you very much not only for supervising my PhD study but also for those discussions about all those things outside of it, for example, where to buy a snowboard or where to rent a van for moving. I very much appreciate the invitation to your house for a barbecue and to look at your fancy handmade sports cars.

I would also like to thank my co-supervisor, Prof. Marcus Aldén. As a division head you are extremely busy, however, you have spent quite a lot of time discussing the paper, research and holidays with me. Your questions are sharp but worth pondering. Furthermore, your garden and spare-time life have made a deep impression on me and have inspired me a great deal in terms of how to be an excellent researcher while having a fully rounded and exciting life. You are a good example for me forever.

In addition, I am incredibly grateful to Prof. Mark Linne. You opened a door to a new world for me and changed my life completely. You were the first person I got to know in Sweden when I came here. Also, you were a distinguished supervisor while I was at Chalmers University. However, you treated me as a good friend as well. I could not have imagined how kind you were and how knowledgeable you

were. I deeply and sincerely appreciate your help, education, support, guidance, conversation and great times that we spent together. When I was alone in Göteborg, you invited me to your home for dinner, barbecues and most especially that Thanksgiving Day's banquet where for the first and only time I tried a whole home-cooked turkey. It was amazingly delicious. Moreover, whenever I was in trouble, you were always willing to offer to help. So I sincerely appreciate all those things.

Many thanks also go to Prof. Xuesong Bai, Prof. Öivind Andersson and Prof. Bengt Johansson for your help and support. I was especially moved by Bai's hard work. I sincerely appreciate your efforts on my thesis work and my papers. Thank you very much indeed for spending huge amounts of time on teaching me turbulent combustion with your profound knowledge. Your invitation to your house is much appreciated and the Chinese food was the best I ever had in Sweden. Öivind and Bengt taught me a lot about advanced combustion concepts and structures of combustion engines. Moreover, Öivind's courses 'Design of Experiment' and 'Academic Writing' hugely helped me with my thesis work, for which I am very grateful.

Furthermore, special gratitude should go to Dr. Bo Zhou, Dr. Jiajian Zhu and Dr. Zheming Li. I will never forget the happiness and arguments that we had. Bo not only taught me about laser techniques and turbulent combustion but also finance, jobs, computer games and so on. Jiajian has always supported me and invited me into his home. We have had many great times together in USA, Europe and China. Zheming helped me hugely when I came to Lund. I also appreciated being accompanied and helped by other colleagues, *e.g.* Dr. Chengdong Kong, Dr. Wubin Weng, Alexios Matamis, Panagiota Stamatoglou, Dr. Marcus Lundgren, Dr. Slavey Tanov, Sara Lönn, Michael Denny, Yupan Bao, Jianfeng Zhou, Jinlong Gao, Dr. Pengji Ding, Qingshuang Fan, Xin Liu, Dr. Yiheng Tong, Senbin Yu, Dr. Yogeshwar Mishra, Dr. Joakim Rosell, Dr. Fahed Abou Nada, Dina Hot, Joakim Jönsson, Dr. Kajsa Larsson, Dr. Arman Subash, Dr. Jesper Borggren, Dr. Qing Li, Dr. Vladimir Alekseev, Lianhao Yin, Changle Li, Dr. Guillaume Lequien, Manu Mannazhi, Jian Wu, Rui Li, Christoffer Pichler, Gianluca Capriolo, Christian Binder, Saeed Derafshzan, Dr. Qiang Gao, Dr. Rikard Wellander, Dr. Per Petersson, Jim Larsson, Elin Malmqvist, Maria Ruchkina, Pär Samuelsson, Dr. Anna-Lena Sahlberg, Dr. Elias Kristensson, Johan Simonsson, Sandra Török, David Sanned, *etc.* It was fantastic to share an apartment with Chengdong for one year and nine months. Thank you for helping me - your lifestyle, hard work and intelligence have made a deep impression. I sincerely appreciate the immense hospitality from Qingshuang and Xin. I also exceptionally appreciated the help and support from seniors and the administration at Lund University, *e.g.* Dr.

Edouard Berrocal, Minna Ramkull, Cecilia Bille, Igor Buzuk, Dr. Andreas Ehn, Dr. Zhongshan Li, Dr. Elna Heimdal Nilsson, Prof. Per-Erik Bengtsson, Prof. Alexander Konnov and so on.

It's truly lucky for me that I share an office with Dr. Christian Brackmann. You are calm and quiet, and you always help me a lot whenever I need it. I am also immensely grateful for the help from Dr. Mattias Rahm, Dr. Zachary Falgout, Dr. Megan Paciaroni, Dr. Chengjun Du, Dr. Zhiqin Jia, Dr. Mats Andersson, Dr. Alf Magnusson, Prof. Sven Andersson, Prof. Michael Oevermann, Elenor Norberg and so on when I was studying at Chalmers University.

I am also grateful to my friends, Dr. Hua Wang, Haoran Yu, Jie Niu, Dr. Siyuan Hu, Xi Kang, Qi Shi, Dr. Mengqin Shen, Dr. Zhen Li, Mengshu Hao, Lai Wei, Dr. Fangfang Yang, Dr. Xiaoming Shen, Zhongyuan Zhang, Dr. Fangkun Yang, Di Shen, Shijie Zhong, Yanfei Hu, Dr. Xiang Chai, *etc.* and to those in the Butterfly Club for teaching me snowboarding - although I don't know your names you made my PhD life more colourful and wonderful. Many thanks to Hua for your support and encouragement when we were conquering Mont Blanc together.

Additionally, I would like to thank Prof. Mario Costa from IST, Dr. Jason Mance, Dr. Mikhail Slipchenko, Dr. Naibo Jiang, Dr. Sukesh Roy from Spectral Energies, Dr. Kan Zha, Dr. Paul Miles from SNL, Prof. Shuncong Zhong, *etc.* for your help and support during my PhD study.

Last but not least, my deepest gratitude goes eternally to my supportive and considerate family.

8. Summary of papers

Paper I

In this paper, two BI systems, 2f-BI system and 4f-BI system, have been developed and compared with different ODs realised by scattered media, *e.g.* different sizes of polystyrenes. It is shown that the two setups generate similar spatial resolution in the presence of scattered media. Moreover, the results show that 2f-BI is easier to realise by adjusting the position of the lens and the display screen to achieve a high quality image while 4f is complicated and more sensitive to component misalignments and time-gate induced aberrations. In addition, USI and BI were also compared based on the contrast transfer functions. It is shown that the time-gated setup, *i.e.* 2f-BI, generates higher contrast under almost all of the scattering conditions tested, while the non-time-gated setup, *i.e.* USI, generates higher spatial resolution only in the lower scatterer size range at the low concentrations, *e.g.* OD<4.

M. Rahm took responsibility for the paper. M. Rahm, M. Paciaroni and M. Linne planned and designed the experiments. M. Rahm, M. Paciaroni and I built the experimental setup together. M. Rahm and I took the data and analysed the results. I participated in the discussion with M. Rahm, M. Paciaroni and M. Linne. M. Rahm and D. Sedarsky did the modelling. M. Rahm, D. Sedarsky and M. Linne wrote the paper to which I also contributed.

Paper II

Ballistic imaging has been applied in the spray formation region of a diesel spray under ECN Spray A condition, and it is found that a structural change occurs at the thickened turbulent mixing layer when going from subcritical to supercritical conditions. Under subcritical conditions a well-defined liquid/gas interface, surface wave structure, and formation of ligaments and voids was observed while under supercritical conditions the interface transitions into a continuous, turbulent mixing layer. Images of this layer include the cellular structure characteristic of gas jets. These changes are consistent with experimental literature on cryogenic supercritical jets and with DNS modelling of supercritical mixing layers.

Z. Falgout took responsibility for the paper. The idea was proposed by M. Linne. I took responsibility for the BI experiment setup. Z. Falgout modified the injector adapter and installed it in the HTHP chamber. Z. Falgout and I took the data and analysed the results. I did the post-processing of the images and participated in the discussion of the paper. Z. Falgout and M. Linne wrote the paper.

Paper III

The paper reports an experimental investigation of a series of premixed methane/air flames with different jet speeds and equivalence ratios, covering the laminar flamelet regime, the TRZ regime, and the DRZ regime. The jet Reynolds number ranges from 6000 to 40,000 and the resulting Karlovitz number varies from 25 to 1500. Three series of simultaneous laser-induced planar measurements of reactive scalars and temperature, *i.e.* CH/CH_2O/OH, HCO/CH_2O/OH and T/CH_2O/OH, have been performed. The flow field of the investigated flames was characterised using LDA measurements. The flame structures, layers of different radicals and temperature distribution were analysed and compared.

B. Zhou took responsibility for the paper. B. Zhou and C. Brackmann did the PLIF measurement. B. Zhou, Q. Li and I set up the LDA measurement and took the results. I participated in the post-processing of LDA and discussion of the paper.

Paper IV

In the paper, a light-duty optical PPC engine was used to conduct cycle-resolved high speed PIV measurements with different fuel injection strategies, *i.e.* single, double and triple injections with different timings which could affect the fuel air mixing and combustion behaviour. The geometry of the quartz piston crown is based on the standard diesel combustion chamber design for this commercial passenger car engine, including a re-entrant bowl shape. The severe image distortions caused by the optical piston shape are minimised through recordings of reference targets and an image dewarping algorithm. With cycle-resolved evaluation, CCV could be minimised. The TKE was calculated for all the cases and its changing with time was analysed and discussed. The results generated also constitute an experimental database which provides quantitative validation data to the computational fluid dynamics modelling of PPC.

I took responsibility for the paper. H. Wang and I set up the high speed PIV system and synchronised with the engine. The laser and camera were aligned by H. Wang and me. S. Tanov took responsibility for the optical engine and operated the

engine. B. Johansson, S. Tanov and I designed the experiment points. In addition, S. Tanov, H. Wang and I took the data. H. Wang taught us how to use Dantec software, DynamicStudio. Matlab scripts for the post-processing were developed by H. Wang and me. I wrote the paper with supervision from M. Richter.

Paper V

Fuel-tracer PLIF measurements were employed in a heavy-duty optical PPC engine in order to obtain better knowledge about the mixing process in the transition from HCCI to PPC mode. The operating conditions were kept the same as the reference all-metal engine for comparison. To the best of the authors' knowledge, this is the first time performing fuel-tracer PLIF measurements in an optical engine with a close to production bowl in a piston combustion chamber, under transition conditions from HCCI to PPC mode. Results show that four mixing schemes can be distinguished as the SOI timings are varied during the transition. They are linked to the results presented in the reference all-metal engine, where emissions were measured in different zones. In some scenarios, a significant part of the fuel mixture was trapped in the squish region and crevice area before start of combustion as shown by PLIF results. The observations in the reference all-metal engine were confirmed by this measurement. Results are also in good agreement with computational fluid dynamics simulations performed for this engine.

I took responsibility for the paper. A. Matamis and I set up the PLIF system and aligned the laser and camera. I did synchronisation of the PLIF system with the engine. S. Lönn took responsibility for the optical engine and operated the engine. Ö. Andersson, M. Richter, S. Lönn and I designed the experiment points. S. Lönn and I took the data. In addition, I developed Matlab scripts for the post-processing and I did all the post-processing. A. Matamis and I participated in the discussion on the paper. I plotted all the figures in the paper except figure 2 and I wrote the paper with supervision from M. Richter.

Paper VI

In the paper, the development of the first ultra-high-speed diagnostic technique capable of simultaneous probing of hydroxyl radicals and formaldehyde distributions at a repetition rate of 50 kHz is outlined. This has been achieved by employing a burst laser pumped OPO system for the simultaneous detection of CH_2O excited at 355 nm and OH-radicals excited at 284 nm, where the interference of scattering laser light can be avoided. Using appropriate filters in

front of two intensified CMOS detectors the feasibility of this ultra-high-speed diagnostics technique could be successfully demonstrated in a premixed turbulent jet flame featuring flow velocities in excess of 60 m/s. Moreover, by applying a 2 ms long burst at 50 kHz, a pulse train of 100 individual pulses could be generated from the burst laser. Due to the high temporal resolution, the movement of CH_2O pockets enclosed by OH at the flame tip can be clearly captured. The transport velocity of the CH_2O pocket was calculated and found to be in good agreement with our previous LDA results.

I took responsibility for the paper. The combination of burst-mode laser system and the OPO was set up by myself. Z. Li taught me how to use the OPO. I also aligned OH PLIF, CH_2O PLIF and cameras, and I implemented synchronisation of them. In addition, the experiment points were designed by me. P. Stamatoglou and I took the data. I developed Matlab scripts for the post-processing and I did all the post-processing. Moreover, all the figures in the paper were plotted by myself. I wrote the paper with supervision from M. Richter and P. Stamatoglou corrected the grammar mistakes. M. Richter, P. Stamatoglou and I participated in discussion of the comments from reviewers and I wrote the rebuttal and revised the manuscript.

Paper VII

In the paper, ultra-high-speed fuel-tracer PLIF imaging has been successfully performed in an optical heavy-duty diesel engine. About 90 consecutive PLIF images were obtained from one engine cycle. The fuel distribution was imaged in a relatively large field of view (~70 x 80 mm) inside the combustion chamber with high temporal resolution, *i.e.* 0.2 CAD. To the best of the authors' knowledge, this is the first time demonstrating the applicability of ultra-high-speed burst lasers in an internal combustion engine. In addition, the temporally resolved fuel distribution and mixing process were captured and studied within one single cycle. This capability eliminates the influence from CCV that is inherent to conventional 10 Hz diagnostics. Moreover, auto-ignition was studied together with the fuel distribution in the combustion chamber using this technique. The luminosity of the auto-ignition and the fluorescence signal of the fuel-tracer by PLIF prior to SOC were captured.

I took responsibility for the paper. I aligned and set up the burst-mode laser system in the engine lab after the movement of the laser system from the combustion physics division to the combustion engine division. The PLIF setup and alignment of the camera were done by P. Stamatoglou and me. M. Lundgren took responsibility for the optical engine and operated the engine. M. Richter, Ö. Andersson, M. Lundgren, P. Stamatoglou and I designed the experiment points. M.

Lundgren, P. Stamatoglou, L. Luise and I took the data. Synchronisation of the laser system and the camera with the engine was conducted by me. I developed Matlab scripts for the post-processing and I did all the post-processing. In addition, all the figures except the figure of the pressure tracer in the paper were plotted by me. I wrote the paper with supervision from M. Richter and P. Stamatoglou corrected the grammar mistakes. M. Richter, M. Lundgren, P. Stamatoglou and I participated in discussion of the comments from reviewers and I wrote the rebuttal and revised the manuscript.

Paper VIII

The paper constitutes the application of a high-speed, high-power burst-mode laser system for diagnostics in an optical engine. To the best of the authors' knowledge, this is the first time to achieve a combination of simultaneous fuel tracer PLIF and chemiluminescence imaging as well as CH_2O PLIF and chemiluminescence imaging in an optical engine, at 36 kHz repetition rate, *i.e.* temporal resolution of 0.2 CAD at 1200 rpm. The development of auto-ignition together with fuel or CH_2O distribution are visualised simultaneously. It is observed that the equivalence ratio of fuel along the spray axis decreases rapidly after the EOI, which is consistent with the occurrence of the entrainment wave proposed by Musculus *et.al*. Prior to the onset of combustion the majority of both fuel and CH_2O are located in the recirculation zone, where the first auto-ignition also occurs. The ability to record in excess of 100 PLIF images in a single cycle brings unique possibilities to follow the in-cylinder processes without the averaging effects caused by CCV.

I took responsibility for the paper. I aligned and set up the burst-mode laser system in the engine lab after the movement of the laser system from the combustion physics division to the combustion engine division. The PLIF setup and alignment of the camera was done by P. Stamatoglou and me. M. Lundgren took responsibility for the optical engine and operated the engine. M. Richter, Ö. Andersson, M. Lundgren, P. Stamatoglou and I designed the experiment points. M. Lundgren, P. Stamatoglou and I took the data. Synchronisation of the laser system and the camera with the engine was conducted by myself. I developed Matlab scripts for the post-processing and I did all the post-processing. Moreover, all the figures except Figure 1 in the paper were plotted by me. I wrote the 'results and discussion' section and 'summary' section of the paper with supervision from M. Richter. P. Stamatoglou wrote the 'introduction' section and part of the 'experimental details' section. M. Lundgren and L. Luise wrote part of the 'experimental details' section. M. Richter, Ö. Andersson, M. Lundgren, P.

Stamatoglou and I participated in discussion of paper and the comments from reviewers. M. Richter wrote the rebuttal.

Paper IX

A series of turbulent methane/air premixed jet flames with different jet speeds and equivalence ratios were studied using simultaneous OH/CH/T and CH/OH/CH_2O planar imaging measurements. Simultaneous OH/CH/T PLIF measurements, reported for the first time, directly correlate the temperature with CH PLIF and OH PLIF. It was found that CH and OH PLIF overlap in a wide range of temperatures at high Karlovitz number conditions. The reaction zone characterised using the CH PLIF signal shows increased broadening with increasing jet velocity or Karlovitz number. The heat release zone characterised by the overlapping region of OH PLIF and CH_2O PLIF is however not as significantly broadened as the CH layer. In addition, the preheat zone characterised with the CH_2O PLIF signal shows increased broadening with increasing turbulent eddy viscosity ($u'l_0$). The broadening of this layer at high Ka flames is on the order of the turbulent integral length scale. Moreover, the turbulent burning velocity is shown to increase monotonically with the turbulence intensity (u'/S_L).

X. Bai and I took responsibility for the paper. The paper was initially written by B. Zhou with the initial data taken by B. Zhou and C. Brackmann. B. Zhou and I did additional experiments and took new data. B. Zhou did the post-processing of all the PLIF images. Senbin post-processed the mean thickness of CH layer and the overlapping of OH and CH_2O layer to plot Figure 3 with the initial data. I post-processed the initial data as well as new data to obtain thickness of the CH_2O layer, turbulent burning velocity and flame surface wrinkle ratio for Figures 4-6. X. Bai wrote the final paper to which I also contributed. X. Bai, B. Zhou and I participated in the discussion of the paper. X. Bai wrote the rebuttal to which I also contributed.

Paper X

Using a burst-mode laser pumped optical parametric oscillator system, the work in the paper demonstrated an ultra-high-speed diagnostic, capable, for the first time, of visualising hydroxyl radicals and formaldehyde distributions in a highly turbulent flame at repetition rates up to 140 kHz (*i.e.* with a temporal resolution of 7.1 μs) to access the Kolmogorov time scales of flames in the distributed/broken reaction zone regime (Ka $\geqslant$ 100). More than 100 consecutive images were recorded in the paper for OH PLIF measurement at 100 kHz. Systematic temporal

and spatial evolution of the flame structure was clearly resolved over long sequences, *e.g.* 1.2 ms for OH PLIF and 10 ms for CH_2O PLIF respectively. In addition the Kolmogorov time scale for all the cases at x/d=10 and x/d=30 were estimated and the resulting minimum Kolmogorov time scale of 7.5 μs indicates that nearly all time-scales of the flow are resolved with the experimental setup. The axial velocity of the CH_2O structure at its outer layer at different x/d positions was obtained and it shows a good agreement with LDA measurements. By comparing that velocity with the local axial velocity, different mechanisms responsible for the large-scale wrinkle structures in the reaction zone and the propagation of CH_2O structure along the flame height were discussed. Frequency spectrum, autocorrelation function and power spectral density of the CH_2O radial fluctuation were calculated and presented as well. Furthermore, in the high frequency range, *e.g.* >10 kHz, the PSD distribution follows -5/3 Kolmogorov law while the PSD from the large structures starts to decrease towards smaller eddies at integral scale which is similar to the calculated value.

I took responsibility for the paper. The burst-mode laser system at Lund University was setup by Spectral Energies to which I also contributed, and the OPO was set up by myself. I organised and B. Zhou and P. Stamatoglou participated in the alignment of the burst-mode laser during the OH PLIF measurement. I aligned the OH PLIF setup and CH2O PLIF setup. Synchronisation of the camera with the laser system was conducted by myself as well. Moreover, I designed the experiment points and took the data, and CH_2O PLIF measurements were performed by myself. In addition, I performed OH PLIF measurements while P. Stamatoglou took the notes during the experiments. I developed Matlab scripts for the post-processing and I did all the post-processing. Furthermore, all the figures in the paper were plotted by myself. I wrote the paper with supervision from M. Richter and X. Bai. M. Richter, X. Bai and I participated in discussion of the paper.

Paper XI

In the paper, the optical system is described in detail including the state-of-the-art burst-mode laser system and the OPO. By using the burst-mode laser system combined with the OPO, the dynamic feature of the pulsed discharge, *i.e.* a gliding arc discharge, has been successfully studied which is not possible with the commonly-used 10 Hz laser system. The changing of OH radical distribution during post discharge/afterglow was captured at 27 kHz, *e.g.* the deformation of the OH PLIF intensity from a toroidal shape to a filled circle was observed. In addition, the decay rate of OH distribution at the outer layer of the plasma column and the increasing rate of that in the plasma column were calculated. Furthermore,

the thickness of the OH layer and the thickness between two OH layers, *i.e.* OH* layer, altering with the time, was obtained. It's the first time that burst-mode laser system is applied for high-speed OH PLIF imaging in pulsed plasma discharges at tens of kHz repetition rate.

I took responsibility for the paper. P. Stamatoglou and I set up OH PLIF. C. Kong and J. Gao took charge of the plasma discharge system. The idea was proposed by A. Ehn and M. Richter. M. Richter, A. Ehn, P. Stamatoglou, C. Kong, J. Gao and I participated in the discussion of the results and content of the manuscript. Synchronisation of the camera with the laser system and plasma discharge was conducted by C. Kong and me. P. Stamatoglou, C. Kong, J. Gao and I designed the experiment points and took the data. I developed Matlab scripts for the post-processing and I did all the post-processing. Moreover, all the figures in the paper were plotted by me except the voltage and current information in Figure 7 and Figure 8. I wrote the manuscript with supervision from M. Richter and A. Ehn. P. Stamatoglou corrected the grammar mistakes in the manuscript.

Paper I

Evaluation of optical arrangements for ballistic imaging in sprays

Mattias Rahm,[1,*] **Megan Paciaroni,**[2] **Zhenkan Wang,**[3] **David Sedarsky,**[1] **and Mark Linne**[1,4]

[1]*Division of Combustion, Department of Applied Mechanics, Chalmers University of Technology, Gothenburg, Sweden*
[2]*Department of Physics & Engineering, Fort Lewis College, Durango, Colorado, 81301, USA*
[3]*Combustion Physics, Lund University, Lund, Sweden*
[4]*School of Engineering, University of Edinburgh, Edinburgh, UK*
[*]*mattias.rahm@chalmers.se*

Abstract: This work investigates the imaging performance, in terms of contrast and resolution, of two different time-gated ballistic imaging setups commonly used in spray research. It is shown that the two setups generate similar spatial resolution in the presence of scattering media. The simpler ($2f$) setup, however, is less sensitive to component misalignments and time-gate induced aberrations than the commonly used ($4f$) system. Measurements comparing both arrangements indicated slightly higher contrast for the $2f$ system under the densest conditions for small scatterers. Subsequent computational modeling confirmed the observed tolerance of the $2f$ system to misalignment and gate effects. The best performing setup was also compared experimentally to its non-time-gated shadow-imaging equivalent, to establish when the time-gate enhances imaging performance. It is shown that the time-gated setup generates higher contrast under almost all of the scattering conditions tested, while the non-time-gated setup generates higher spatial resolution only in the lower scatterer size range at the lowest scatterer concentrations.

OCIS codes: (110.0113) Imaging through turbid media; (190.3270) Kerr effect.

References and links

1. T. Fansler and S. Parrish, "Spray measurement technology: a review," Meas. Sci. Technol. **26**, 012002 (2015).
2. M. Linne, "Imaging in the optically dense regions of a spray: a review of developing techniques," Prog. Energy Combust. Sci. **39**, 403–440 (2013).
3. L. Wang, P. P. Ho, C. Liu, G. Zhang, and R. R. Alfano, "Ballistic 2-d imaging through scattering walls using an ultrafast optical kerr gate," Science **253**, 769–771 (1991).
4. L. Wang, P. P. Ho, X. Liang, H. Dai, and R. R. Alfano, "Kerr-fourier imaging of hidden objects in thick turbid media," Opt. Lett. **18**, 241–243 (1993).
5. L. Wang, P. P. Ho, and R. R. Alfano, "Time-resolved fourier spectrum and imaging in highly scattering media," Appl. Opt. **32**, 5043–5048 (1993).
6. E. Berrocal, D. L. Sedarsky, M. E. Paciaroni, I. V. Meglinski, and M. A. Linne, "Laser light scattering in turbid media part I: experimental and simulated results for the spatial intensity distribution," Opt. Express **15**, 10649–10665 (2007).
7. E. Berrocal, D. L. Sedarsky, M. E. Paciaroni, I. V. Meglinski, and M. A. Linne, "Laser light scattering in turbid media part II: spatial and temporal analysis of individual scattering orders via monte carlo simulation," Opt. Express **17**, 13792–13809 (2009).
8. M. Paciaroni, M. Linne, T. Hall, J. P. Delplanque, and T. Parker, "Single-shot two-dimensional ballistic imaging of the liquid core in an atomizing spray," Atomization Sprays **16**, 51–69 (2006).

9. J. B. Schmidt, Z. D. Schaefer, T. R. Meyer, S. Roy, S. A. Danczyk, and J. R. Gord, "Ultrafast time-gated ballistic-photon imaging and shadowgraphy in optically dense rocket sprays," Appl. Opt. **48**, B137–B144 (2009).
10. D. Sedarsky, E. Berrocal, and M. Linne, "Quantitative image contrast enhancement in time-gated transillumination of scattering media," Opt. Express **19**, 1866–1883 (2011).
11. D. Barnhart, "Optica software," (www.opticasoftware.com).
12. M. Paciaroni and M. Linne, "Single-shot, two-dimensional ballistic imaging through scattering media," Appl. Opt. **43**, 5100–5109 (2004).
13. E. Hecht, *Optics*, 4th ed. (Addison Wesley Longman Inc., 1998).
14. D. Sedarsky, "Ballistic imaging of transient phenomena in turbid media" (Ph.D. Thesis, Department of Physics, Lund University, 2009).
15. T. Parker and J. Labs, "Diesel fuel spray droplet sizes and volume fractions from the region 25 mm below the orifice," Atomization Sprays **13**, 18 (2003).
16. A. Campillo, S. Shapiro, and B. Suydam, "Relationship of self-focusing to spatial instability modes," Appl. Phys. Lett. **24**, 178–180 (1974)
17. G. Lawrence, "GLAD theory manual, ver. 5.5," (2009). Applied optics research. See www.aor.com.
18. S. Spuler and M. Linne, "Numerical analysis of beam propagation in pulsed cavity ring-down spectroscopy," Appl. Opt. **41**, 2858–2868 (2002).
19. M. Linne, "Analysis of x-ray phase contrast imaging in atomizing sprays," Exp. Fluids **52**, 1201–1218 (2012).
20. M. Linne, "Analysis of x-ray radiography in atomizing sprays," Exp. Fluids **53**, 655–671 (2012).
21. R. A. Ganeev, A. I. Ryasnyansky, N. Ishizawa, M. Baba, M. Suzuki, M. Turu, S. Sakakibara, and H. Kuroda, "Two- and three-photon absorption in CS_2," Opt. Commun. **231**, 431–436 (2004).
22. S. Couris, M. Renard, O. Faucher, B. Lavorel, R. Chaux, E. Koudoumas, and X. Michaut, "An experimental investigation of the nonlinear refractive index (n_2) of carbon disulfide and toluene by spectral shearing interferometry and z-scan techniques," Chem. Phys. Lett. **369**, 318–324 (2003).
23. E. Reynoso Lara, Z. Navarrete Meza, M. D. Iturbe Castillo, C. G. Trevino Palacios, E. Marti Panameno, and M. L. Arroyo Carrasco, "Influence of the photoinduced focal length of a thin nonlinear material in the z-scan technique," Opt. Express **15**, 2517–2529 (2007).
24. H. Kogelnik and T. Li, "Laser beams and resonators," Appl. Opt. **5**, 1550–1567 (1966).
25. A. Samoc, "Dispersion of refractive properties of solvents: chloroform, toluene, benzene, and carbon disulfide in ultraviolet, visible, and near-infrared," J. Appl. Phys. **94**, 6167–6174 (2003).
26. R. A. Ganeev, A. I. Ryasnyansky, M. Baba, M. Suzuki, N. Ishizawa, M. Turu, S. Sakakibara, and H. Kuroda, "Nonlinear refraction in CS_2," Appl. Phys. B **78**, 433–438 (2004).
27. S. Idlahcen, C. Roze, L. Mees, T. Girasole, and J. B. Blaisot, "Sub-picosecond ballistic imaging of a liquid jet," Exp. Fluids **52**, 289–298 (2012).
28. H. Purwar, S. Idlahcen, C. Roze, D. Sedarsky, and J. B. Blaisot, "Collinear, two-color optical kerr effect shutter for ultrafast time-resolved imaging," Opt. Express **22**, 15778–15790 (2014).

1. Introduction

Fuel sprays and the conversion of liquid fuel to combustible fuel vapor are critical factors in the performance of several types of combustion engines. Unfortunately, spray break-up and mixing processes are not well understood; the current state of understanding of primary spray breakup processes is limited. In order to address this problem several new experimental techniques have appeared, providing quantitative information on break-up in the dense spray formation region [1, 2]. Ballistic Imaging (BI) is one such technique.

BI is a line-of-sight optical imaging technique providing high-resolution images of structures hidden within turbid media. This diagnostic is most commonly implemented using commercially available short pulse (*e.g.* $\sim$ 100 fs pulsewidth) lasers and low light level imaging systems. Ballistic imaging was originally developed for imaging through human tissue, and the time-gated approach was reported by the group of Alfano at the City University of New York (see *e.g.* [3–5]). Time-gated ballistic imaging (TGBI) for spray studies has recently been reviewed in detail [2]; therefore, these introductory comments will simply provide context for the current work.

Ballistic imaging passes a laser beam through the spray utilizing specialized optics to filter the light exiting the spray, to extract a high-resolution image of larger liquid structures. BI takes advantage of the very small amount of light passing directly through a dense spray without scattering off-axis from the droplets. Light that passes straight through the droplet cloud surround-

ing the spray formation region, without droplet interactions, is termed ballistic light. This light exits the spray with unchanged coherence, directional and polarization properties compared to the input beam. Ballistic photons travel the shortest path and exit the spray first. Unfortunately, there are generally not enough ballistic photons to produce single-shot, time-resolved images in a dense spray [2]. The scattering phase functions of the typical droplets sizes (5-20 μm) in sprays have a very strong forward scattering lobe, however, and the bulk of these forward scattered photons are quasi-ballistic; exiting on or very near the centerline and they exit just after the ballistic photons [6, 7]. The combined ballistic and quasi-ballistic light (together called "useful imaging light") is refracted by the larger liquid structures inside the spray. Thus useful imaging light can be used to construct shadow images of larger fluid structures by suppressing the off-axis scattered light from drops that can corrupt more traditional forms of shadowgraphy. BI thus aims to reject almost all of the light headed towards the camera because it is corrupted by multiple scattering off-axis; it preserves only the useful imaging light.

In the current implementation, BI segregates the small amount of useful imaging light by filtering the light signal based on the following characteristic signatures. First, the useful imaging light is nearly co-linear with the input laser beam (soft spatial filtering is used). Second, it retains the polarization of the input beam (polarization filtering). Finally, the useful imaging light is first to exit because it travels the shortest path (time-gating). Time gated ballistic imaging commonly rejects the contribution of multiply scattered off-axis photons with a very fast optical Kerr effect (OKE) time-gate (a very fast external shutter). This allows transmission of useful imaging light while rejecting later arriving photons. The design of the OKE-gate also includes inherent spatial and polarization filtering. This contributes to further filtering of corrupted image light to produce a single-shot ballistic image.

Examples of two OKE-gated optical systems are shown in Figs. 1(a) –1(b). The main difference between the two setups is in the method of relaying the image to the camera. The setup in Fig. 1(a), here called the 4f setup, is similar to the arrangement used in earlier work by Alfano *et al.* [4] which was adapted and used in early BI spray studies [8]. The setup in Fig. 1(b), here called the 2f setup, was first described by Schmidt *et al.* [9] and is less complex. It generated what appeared to be similar image quality compared to the 4f setup. The double lens setup is referred to as 4f since it in principle is a standard 4f correlator used in Fourier optics. The single lens setup, on the other hand, is referred to as 2f since it is a more classical imaging setup and resembles the one-to-one magnification achieved when placing the collecting lens 2f behind the object. The results from Schmidt *et al.* indicated that for time-gated ballistic imaging in atomizing sprays the Fourier-imaging style used in the 4f is not the only option; simpler setups can be used for spray studies. In 2011 Sedarsky *et al.* published a detailed model comparing the 2f imaging setup to a 4f projection system [10]. Here, the 4f system was modeled as a non-focused system as opposed to the experimentally focused one. In the work of Sedarsky *et al.*, the output of a Monte Carlo code which modeled the light scattering in the turbid media was coupled with a commercial ray-tracing code used to model the optical system [11]. The modeling by Sedarsky *et al.*, which produced very good agreement with the experimental contrast transfer functions (CTF) by Paciaroni [12], demonstrated that the size of the scattering particles (*i.e.* their scattering phase function) determines the regimes in which each optical system performs best. In their comparison, contrast from a single spatial frequency (1 line pair/millimeter (lp/mm)) was investigated and the 2f system generated higher contrast than the non-focused 4f in the large-particle limit (15 μm polystyrene spheres (PS) in water). In the small-particle limit (0.7 μm PS spheres in water), on the other hand, the 2f system generated lower contrast. Sedarsky *et al.* argued that the reason for these results lies in the scattering phase function of the spheres. The 2f with its longer object-to-lens distance performs better in situations dominated by forward scattering than in the more diffuse scattering generated by small particles. The op-

posite can be said about the non-focused 4*f* projection system which preferentially transmits forward scattered light while suppressing diffusively scattered light and, hence, performs better in the small-particle limit. However, the resultant CTFs of the two modeled setups have not been investigated experimentally, neither has a comparison between a focused 4*f* setup and the 2*f* setup.

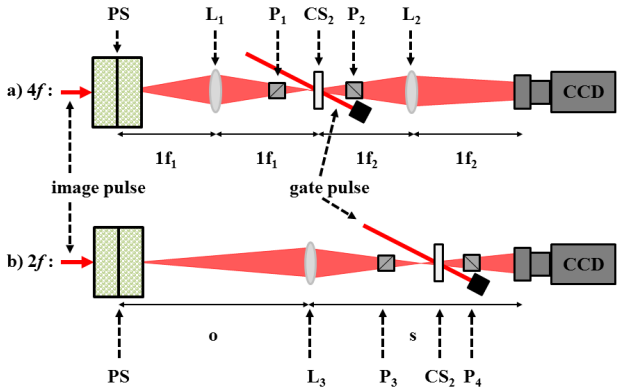

Fig. 1. Optical setups. Part a) shows the 4*f* setup and part b) the 2*f* setup. For USI the polarizers and the CS_2 cell (Kerr medium) were removed and the gate beam blocked.

In the wider ballistic imaging community, the OKE-gate is not always considered a necessity. Many techniques used to segregate high quality image light from corrupted light has been called 'ballistic imaging' in the biomedical literature. In our work, we have noticed that certain sprays with lower optical depths (OD) do not require the OKE-gate in order to generate images of large interior structures with reasonable resolution. In addition to the study of 4*f* and 2*f* setups, therefore, we have conducted a short study to evaluate the contribution of the OKE gate even at lower values of OD.

In this work, we compare the 4*f* and 2*f* TGBI setups. First they were compared experimentally under controlled scattering conditions. To increase understanding of the imaging differences between the two setups caused by aberrations, a series of experiments combined with computational modeling were conducted. Finally, the 2*f* TGBI setup was compared to its non-time-gated equivalent, under the same scattering conditions, to determine when and how the time-gate enhances imaging performance. It should be noted that the non-time-gated shadow imaging technique applied in this work uses the same short laser pulses as used in TGBI, as opposed to broad-band white light shadow images. Throughout this article, this technique will be referred to as ultrafast shadow imaging (USI).

2. Experimental methods

Two different types of experiments were carried out in the 4*f*-2*f* TGBI studies. First, the performance of the two optical systems was evaluated under varying scattering environments. Many of the results indicated that system-based aberrations were generated; therefore, a second style of experiment was focused on aberrations. For the aberration work, the scatterers were removed to make the outcomes more straightforward. All images were flatfield corrected with camera dark current and gate beam scattering subtracted.

The performance of the two imaging setups was quantified using contrast transfer functions. The CTF is related to the system optical transfer function [13], and serves as a metric for the

dynamic range and spatial resolution of the system [14]. A resolution test chart was imaged both through a series of scattering conditions designed to replicate those of typical diesel fuel sprays issuing into room-temperature air and through a series of non-scattering conditions to identify sources of aberrations. The contrast was measured for a range of single spatial frequencies (line patterns) and from these measurements the CTFs were constructed. Here the contrast for a specific spatial frequency was calculated according to $C = (I_{\max} - I_{\min})/(I_{\max} + I_{\min})$.

For experiments under scattering conditions, the scattering environment was simulated using monodisperse suspensions of polystyrene spheres (PS) mixed with distilled water in varying sizes and concentrations. The test chart (a USAF 1951 resolution test chart) was placed in the center of the scattering medium. The optical system collection angles were matched to compare setups with similar numerical aperture, *i.e.* setups with nominally similar resolution. Ten images under each condition were taken, and CTF mean and standard deviations were calculated.

Fuel spray droplets are formed in a distribution of sizes which roughly fall in the range of 5-20 μm [15]. Thus, 5 μm, 10 μm, 15 μm, and 20 μm fuel droplets in varying concentrations were investigated. Corresponding PS sphere sizes were determined by calculating the Mie scattering phase function for the diesel droplets surrounded by air using a light wavelength of 800 nm. The phase functions were then compared to those of the available PS spheres suspended in water and a nearest match was determined by choosing the sphere sizes yielding the smallest root-mean-square difference. This resulted in the following selection of PS sphere sizes: 3.5 μm, 8.0 μm, 9.7 μm, and 14.9 μm. Here, the standard deviation of the diameter in the different PS suspensions was around 0.1%. In Figs. 2(a) –2(d) the scattering phase functions of the fuel drops together with the phase functions of the corresponding PS spheres can be seen.

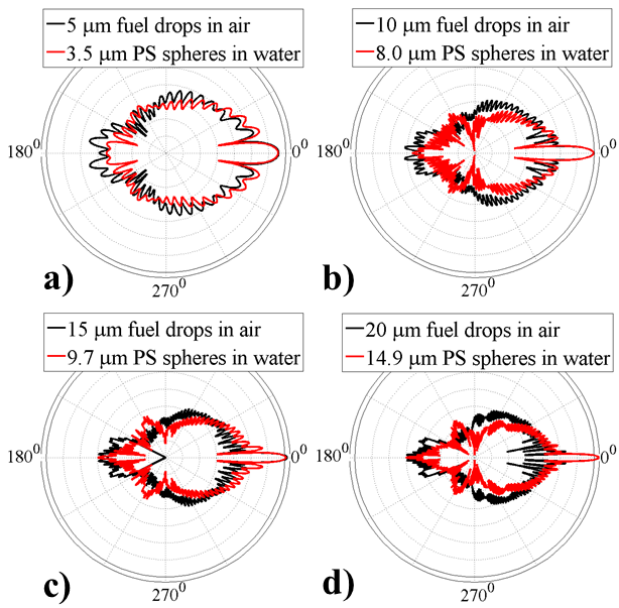

Fig. 2. a) – d) Logarithmic polar plots of the scattering phase functions for 5 μm, 10 μm, 15 μm, and 20 μm fuel drops in air with the corresponding phase functions for the PS spheres in water. 0° corresponds to strictly forward scattering.

Optical Depth (OD) was used to quantify sphere concentrations. OD is formally defined by

the Beer-Lambert law

$$\frac{I}{I_0} = e^{-\mathrm{OD}},\ OD = n\sigma_{ext}L. \tag{1}$$

Here n, σ_{ext} and L are the number density of spheres, total extinction cross-section, and path length through the scattering medium, respectively. Under the assumption of no absorption, the total extinction cross section can be replaced by the scattering cross-section (σ_{scatt}). $n\sigma_{scatt}$ represents the average number of scattering events taking place on a unit path length. As argued by Linne [2], experimentally measured values for transmission through a spray are a function of the scattering phase function of the particles and the collection angle of the experimental instrument. This complicates discussion of the measured OD for particular sprays or PS suspensions. For this reason, in the work reported here we equate the number of scattering events to the OD. This is justified by the fact that scattering events and OD are roughly similar for this particle size range [7]. Using the scattering cross-sections in Table 1, the relation between OD and number density can be calculated using Eq. (1).

Table 1. Scattering cross-sections for the used PS sphere sizes in water using 800 nm light.

Sphere size	σ_{scatt}
3.5 μm	1.7×10^{-5} mm^2
8.0 μm	1.2×10^{-4} mm^2
9.7 μm	1.4×10^{-4} mm^2
14.9 μm	4.0×10^{-4} mm^2

TGBI aberrations were investigated with a Siemens star chart, with spatial frequencies ranging from 5.7 lp/mm to 115 lp/mm, placed in the cell filled with distilled water. The same collection lens was used for both the 4f and 2f setups in order to match focal spot sizes and relative positions of the Kerr medium when isolating aberrations. Nine images under each condition were captured and a mean contrast for each condition was obtained from the CTFs. Data variation was calculated from contrast variance for each measured spatial frequency. Variances were subsequently summed and standard deviations calculated. Finally, the 2f system was used to compare TGBI and USI under similar conditions.

3. Experimental setups

The experimental configurations are shown in Figs. 1(a) –1(b). Here, the symbols represent the following; PS - a 10 mm path length optical cell for the scattering and non-scattering media with the test chart in the center, L_1-L_3 - achromatic lenses, P_1-P_4 - 15x15 mm^2 clear aperture Glan-Laser polarizers, CS_2 - a 40 mm clear aperture optical cell with 10 mm path length and filled with CS_2 (the Kerr medium), f_1-f_2 are the focal lengths for respective lens, and o and s are the object-to-lens and lens-to-image distances respectively. For the experiments in scattering environments, the following lenses where used: $L_1 = 3$ inch diameter with $f_1 = 250$ mm, $L_2 = 3$ inch diameter with $f_2 = 500$ mm, and $L_3 = 2$ inch diameter with $f_3 = 150$ mm. In the aberration experiments the 4f configuration used the same lenses used previously, but the 2f used a 3 inch diameter, $f = 250$ mm lens. Minimization of gate beam scattering onto the image plane was achieved through the use of a CS_2 cell with large enough clear aperture to mitigate cell wall scattering through the last OKE-gate polarizer.

In the 4f setup (Fig. 1(a)), the object plane is relayed through the Fourier plane and back to the image plane on the screen. The first lens (L_1) is placed a focal length, f_1, from the object plane, and the second lens (L_2) is placed an additional focal length, f_2, behind the Fourier

plane, or focus, of L_1. A real image displayed a focal length behind L_2 has a magnification, M, given by $M = f_2/f_1$. In TGBI, the OKE-gate is placed between the two lenses. Here the CS_2 cell is placed far enough away from the image beam focal plane for nonlinear distortion effects not to be noticed. Using the published data for the lenses, this setup resulted in an image magnification of two and a collection half angle of 8.7°.

The $2f$ system (Fig. 1(b)) uses a single lens to generate a real image of the object at the screen. A magnified, real image requires an object-to-lens distance of between 1 and 2 focal lengths. Matching the magnification and collection angle of the $4f$ configuration in the PS sphere experiments required the lens to be placed 225 mm behind the test chart. This resulted in an image magnification of two and a collection half angle of 6.4° degrees. In this scheme, the OKE-gate was placed between the lens and the camera. As before, the CS_2 cell was placed away from the focal plane to avoid unwanted nonlinear effects. In the aberration experiments the $2f$ used the same collecting lens as the $4f$. In this set of experiments both setups had a magnification of two, and for the $2f$ setup the corresponding object-to-lens distance was 375 mm.

A 1 kHz repetition rate chirped-pulse regenerative amplifier (Spectra-Physics Spitfire) providing 4 W of average optical power was used to generate source light for the experiments. It provided pulse widths around 180 fs (Full Width at Half Maximum (FWHM)) centered at 800 nm with a 10 nm (FWHM) bandwidth and a beam diameter of about 8 mm ($1/e^2$). The beam was split into an imaging beam and a gating beam. After the beam splitter, the gating beam was directed through a polarizer/waveplate combination and a retroreflecting time delay (TD) to control polarization, power and timing in relation to the image pulse. In the TGBI configuration, the gating beam was used to induce birefringence in the CS_2, creating an optical shutter time of around 1.5 ps FWHM. In the scattering experiments the gate beam used a pulse energy around 0.7 mJ. In the aberration experiments, on the other hand, the gate pulse energy was varied to investigate distortion effects. After the beam splitter the image beam was passed through a polarizer/wave plate combination providing polarization and power control. The resolution test chart embedded in the center of a cell containing either the PS sphere suspension or pure water, was placed after this first polarizer. In the scattering experiments, the image pulse energy was adjusted to achieve a suitable signal strength depending on the particular scattering condition, while in the aberration experiments it was varied to observe effects of changes to it. The image, for all configurations, was captured with an Andor iXon 885 EMCCD camera. In the USI configurations, the gating beam was blocked and the OKE-gate removed.

4. 4f setup compared with the 2f setup

4.1. TGBI experiments in scattering conditions

In Fig. 3 representative unprocessed raw images of the test chart generated by the TGBI setups can be seen. In the figure, images generated by the $4f$ and the $2f$ setups with 3.5 μm spheres at OD7, and 14.9μm spheres at OD10 are shown. The experimental TGBI results are shown in Figs. 4 and 5 as CTF plots. Based on the standard deviation in the data, a practically useful lower limit for a detectable contrast is ~ 0.15 (based on a 95% confidence interval). In the OD0 case, which was achieved using pure distilled water, the $4f$ and $2f$ setups exhibited ultimate resolutions of roughly 30 lp/mm and 50 lp/mm respectively. The $2f$ setup had notably better image resolution before the introduction of scatterers. With the introduction of scatterers, however, the highest resolvable spatial frequency is similar for both setups for all ODs and sphere sizes. This is an indication that certain finer features in the imaging setups are lost in the presence of scatterers, and scattering controls the ultimate resolution. One reason the two systems differ when there are no scatterers is that the OKE-gate affects the imaging performance of the two systems differently. Finer details are lost due to harder spatial filtering in the $4f$ setup. The

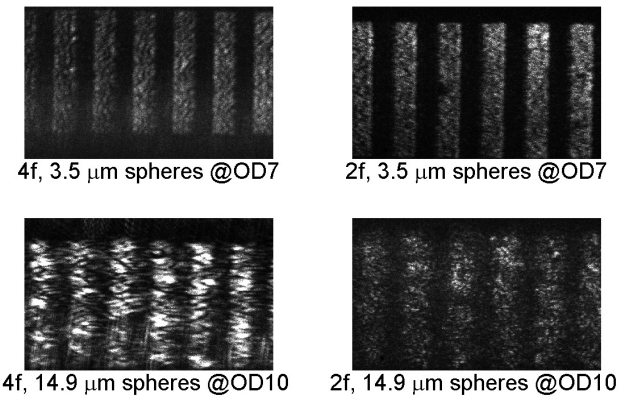

Fig. 3. Representative raw images of a 3.56 lp/mm line pattern for TGBI with 3.5 μm spheres at OD7, and 14.9μm spheres at OD10.

high frequency components visible in the 2*f* setup, on the other hand, are still present even with scatterers. However, due to the presence of noise introduced by scattered light, the background noise level is higher than the intensity of the high frequency components. Contrast is lost.

To continue the discussion on scattering results, the 2*f* setup generates higher contrast in the lower sphere size range and in the densest cases. Using larger sphere sizes at moderate ODs, the results are mixed. During the experiments, it was noted that the 4*f* setup was consistently more sensitive to alignment issues and to changes in the OKE-gate setup. This observation is evidenced in the oscillations of the CTFs, which indicate aberrations in the optical system. Here, one sees that they are present for both setups but more pronounced in the 4*f* case. The outlying CTFs are the ones from the 3.5 μm spheres at OD10. Here both the 4*f* and the 2*f* setups show increasing contrast with increasing spatial frequency up to around 10 lp/mm where the CTF starts to decay.

4.2. TGBI aberration experiments in non-scattering conditions

By examining the CTFs in Figs. 4 and 5, one can see that system aberrations play a noticeable role in image generation by TGBI. Their presence can be both inherent to the TGBI design or caused by optical misalignments. One speculation was that the OKE-gate could be a significant contributor to the aberrations. To further investigate the potential role of the OKE time-gate in the generation of aberrations, two sets of experiments were performed. The first set investigated the influence of image pulse energy coupled with position of the CS_2 cell along the image beam optical axis. The second set investigated the influence of the gate pulse energy. In both experiments, the imaging performance was quantified in terms of CTF, using a Siemens star chart placed in distilled water (a non-scattering environment). The observed changes in mean contrast was for both set of experiments statistically significant based on the Student's t-test, with *p*-values well below 0.0001.

To investigate the effects of image pulse energy and the position of the CS_2 cell, the gate beam was blocked and the second OKE-gate polarizer rotated to allow transmission. The CS_2 cell was translated along the optical axis as shown in Figs. 1(a) –1(b). Limited by the polarizers, the cell was moved between 10 cm and 45 cm behind the collecting lens (in both setups the image beam had a focal plane $\sim$25 cm behind the collecting lens). Image pulse energies of 10, 25, and 50 μJ were tested. Representative images generated with the 2*f* setup using 50 μJ image

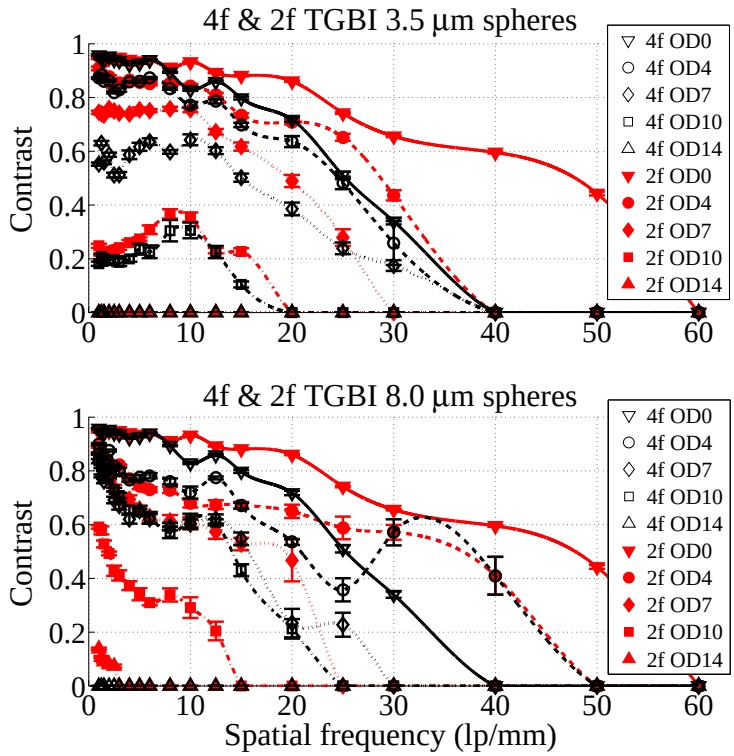

Fig. 4. Experimentally measured CTFs for 4*f* and 2*f* TGBI setups with sphere sizes of 3.5 μm and 8.0 μm. The error bars represent one standard deviation.

pulse energy and with the CS_2 cell placed 26 cm and 38 cm behind the collecting lens are shown in Fig. 6. Here, the effect of placing the CS_2 cell near the focal plane can be seen. The image at 26 cm is significantly distorted compared to the image at 38 cm. The distortion is caused by the higher intensity of the focused image beam. With sufficiently high light intensities, undesirable nonlinear effects in the CS_2 (*e.g.* self-focusing) are generated, which can distort the image information carried in the pulse [16]. The results of moving the CS_2 cell through the image beam focal plane in the 4*f* setup can be seen in Fig. 7. Only the 4*f* results are presented because the 2*f* setup exhibited the same trends. To ease interpretation of the data, and since finer details of the transfer functions are not needed to interpret the results, the mean contrast from between 6.1 - 32.0 lp/mm in each CTF was calculated. The spatial frequency range in the average was chosen to avoid the significantly distorted image center, since calculating contrast there does not provide useful information. Even with this restriction, a clear dependence on position can be observed. All three energy levels produce distortion, manifested by a decrease in mean contrast, with the CS_2 cell close to the focal plane.

In the second set of aberration experiments, effects of varying the gate pulse energy were investigated. Here, the gate beams in Figs. 1(a) –1(b) were unblocked and the OKE-gate polarizers were set with perpendicular transmission axes, *i.e.* the setups were in TGBI mode. For

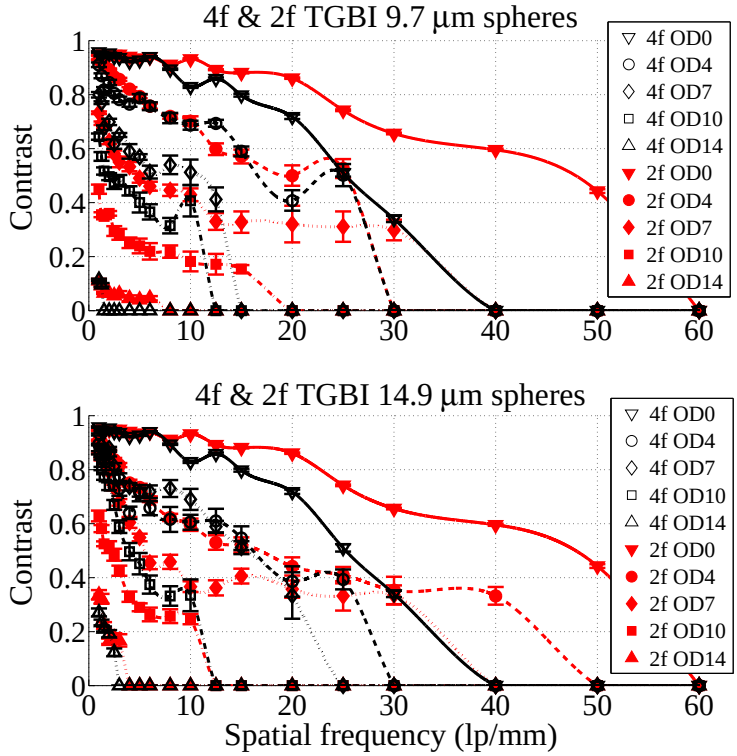

Fig. 5. Experimentally measured CTFs for 4*f* and 2*f* TGBI setups with sphere sizes of 9.7 μm and 14.9 μm. The error bars represent one standard deviation.

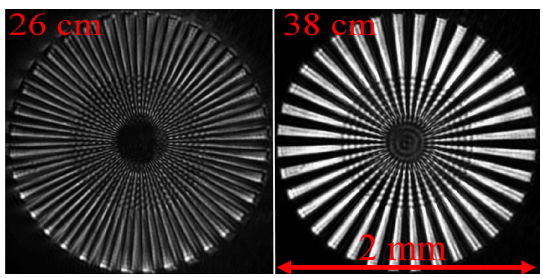

Fig. 6. Comparison of images of the Siemens star target generated with the 2*f* setup using an image pulse energy of 50 μJ with the CS_2 cell placed at 26 cm and 38 cm behind the collecting lens.

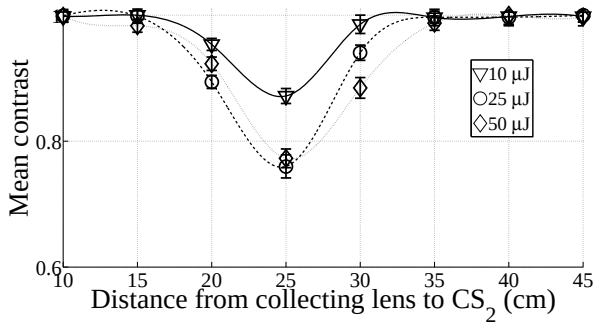

Fig. 7. Mean contrast (average over 6.1-32.0 lp/mm in the CTF) as function of distance between collecting lens and CS_2 cell with the gate beam blocked and the OKE-gate opened for the 4*f* setup. The normalized curves show significant degradation in mean contrast near the focal plane. The error bars represent one standard deviation.

both the 4*f* and 2*f* setups, the CS_2 cell was placed 50 cm behind the collecting lens, and the angle between the image and gate beams was $\sim 11^{\circ}$. The experiment was performed by first aligning and optimizing the image quality at maximum gate pulse energy for each setup. This corresponded to 0.66 mJ and 0.68 mJ gate pulse energies for the 4*f* and 2*f* respectively. The gate pulse energy was subsequently decreased in steps. The results can be seen in Fig. 8, presented again as the mean contrast over 6.1 - 32.0 lp/mm. In this set of experiments, a significant differ-

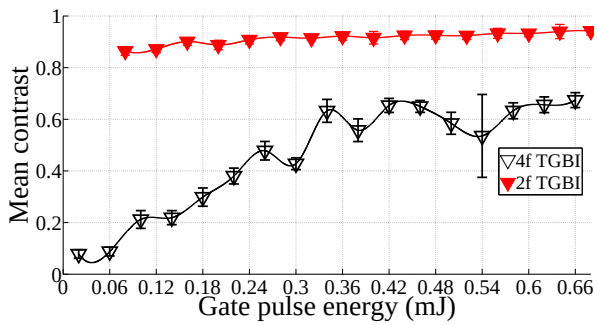

Fig. 8. Mean contrast (average over 6.1-32.0 lp/mm in the CTF) as function of gate pulse energy for 4*f* and 2*f* setups. The error bars represent one standard deviation.

ence between the two setups can be detected. The mean contrast of the 2*f* setup decreases only marginally when the gate pulse energy is decreased. The 4*f* setup, on the other hand, exhibits a significant reduction in mean contrast.

4.3. Computational modeling of the optical setups

The TGBI experiments indicate that there are differences between the two setups regarding how alignment and aberrations affect the images that are produced. To gain a better understanding, the two setups were modeled in GLAD which is a commercial physical optics code [17] that

has been used in the past to analyze cavity enhanced absorption [18] and x-ray based spray diagnostics [19, 20]. The code and its use are described in more detail in those papers. In short, GLAD solves the full electromagnetic wave propagation for nearly collimated beams. In this work, the response of the optical systems to lens misalignment and then the response to changes in the OKE-gate setup were modeled.

4.3.1. Model definition

Here, the light pulses were modeled as single wavelength beams (*i.e.* no bandwidth or temporal effects were included). The lenses were modeled as three-surface representations for the achromatic doublets used in the non-scattering experiments, and the polarizers were modeled as isotropic media with the correct dimensions and refractive indices. To approximate a point source, a diverging Gaussian beam with a waist radius of 4 μm and a wavelength of 800 nm was placed with the waist in the object plane, and propagated through the system to the image plane. In the image plane, a one-dimensional intensity pattern was recorded. Using this pseudo Point Spread Function (PSF), the CTF could be estimated by Fourier transformation of the PSF. It should be noted that, since an ideal point source was not used, the resulting CTFs cannot be directly compared with experimental data. Setup response and trends due to misalignments and inherent aberrations, however, will be captured within this approximation. The optical setups were aligned by minimizing spot sizes in the image plane while keeping the position of the collecting lens as described in section 3. In the case of the $2f$ setup, this is straightforward. However, in the case of the $4f$ setup, positioning of the last lens included re-collimation of an originally collimated beam emanating from the object plane.

To model image beam propagation through the CS_2, potential sources of aberration must be identified. Experimental observation established that both image and gate pulse energies can affect the CTF. If, however, the CS_2 cell is placed far enough from the image beam focal plane, non-linear effects from a focused beam can be neglected. This is representative of the experiment leading to Fig. 8. In this arrangement, the primary source of aberration is the gate beam.

CS_2has negligible linear absorption around 800 nm, and with pulse repetition rates of 1 kHz effects due to non-linear absorption are insignificant [21, 22]. Thus, thermal lensing effects are not significant. Another potential source of aberration is the OKE induced spatial refractive index change. Due to the intensity profile of the gate beam a change in the refractive index will be induced along its polarization axis. Since there is an angle between the relative polarization states of the image and gate beams (optimally the angle should be 45°), the image beam's two polarization components will experience different refractive indices and a polarization rotation of the image beam will occur. However, due to the intensity profile there will also be differences in the refractive index along the component of the image beam parallel to the polarization axis of the gate beam. This refractive index anisotropy has the potential to induce aberrations in an optical setup. It can be expressed as

$$n(r_g,t) = n_0 + n_2 I_g(r_g,t). \tag{2}$$

Here n is the refractive index profile, r_g the radial coordinate along the polarization axis of the gate beam, n_0 the linear refractive index, n_2 the non-linear refractive index, t time, and I_g the gate beam intensity.

An approximate analytical solution can be obtained by using the parabolic approximation for the gate beam by Lara *et al.* and the Gradient Index (GRIN) lens expressions by Kogelnik & Li [23, 24]. We assume a Gaussian beam profile of the form

$$I_g(r_g,t) = \frac{2P_p}{\pi\omega^2}\exp\left(-\frac{2r_g^2}{\omega^2} - \frac{\ln(2)t^2}{\tau^2}\right), \tag{3}$$

where $P_p \approx 0.94E_p/\tau$ is the peak power, E_p the total pulse energy, τ the FWHM length of the pulse, and ω the beam radius ($1/e^2$). Following the derivation by Lara *et al.* and taking the temporal dependence into account only through the magnitude of the peak power, the Gaussian shaped refractive index can be approximated as a parabolic function:

$$n(r_g) \approx n_0 + \frac{2n_2P_p}{\pi\omega^2} - \frac{4n_2P_p}{\pi\omega^4}r_g^2. \tag{4}$$

It can be shown that the induced refractive index anisotropy will act as a GRIN lens with a focal length given by

$$f_{\text{GRIN}} = \frac{1}{n_0'\gamma\sin(\gamma L)}. \tag{5}$$

Here $n_0' = n_0 + 2n_2P_p/(\pi\omega^2)$, $n_2' = 8n_2P_p/(\pi\omega^4)$, $\gamma = \sqrt{n_2'/n_0'}$, and L the path length inside the Kerr medium. Samoc has reported linear refractive index values of 1.6056 and Ganeev *et al.* reported a nonlinear index of $3\cdot10^{-19}$ m^2/W [25,26] for CS_2. Using these values together with a gate pulse energy of 0.7 mJ, a 100 fs pulse length, a 4 mm beam radius, and a CS_2 path length of 1 cm, the corresponding focal length can be calculated. We find that the induced refractive index anisotropy will have a focusing effect with a focal length around 5 m. This effect will act in a crossed-beam geometry and only be active along the polarization axis of the gate beam. Consequently, within this parabolic approximation in the crossed beam geometry, the image beam will experience a skewed cylindrical GRIN lens with a focusing power depending on the peak power of the gate pulse. Since this lensing effect is due to the nonlinear refractive index of the medium it is not restricted to CS_2, it will appear in solid-state Kerr media as well. This source of aberration was implemented in the models of the two TGBI setups. For simplicity, however, the cylinder-lens nature of the GRIN lens is ignored in the models; this effect is modeled as a spherical lensing.

In the GLAD model, the lensing effect was approximated as a series of transversely aligned and offset GRIN lenses with thickness Δz and a refractive index n_0. This implies that apart from offsetting the center of aberration for each GRIN slice, cosine effects due to the oblique gate beam angle are ignored. The initial center of the GRIN aberration is given by:

$$X_0 = X_{\text{offset}} + 0.5L\tan(\theta). \tag{6}$$

Here X_{offset} is the offset in the transverse x-direction and θ is the relative angle between the image and gate beams. In each step (j) the center of the GRIN lens (X_{dec}) is calculated according to

$$X_{\text{dec}}(j) = X_0 - \tan(\theta)\sum_1^j \Delta z. \tag{7}$$

Here it is apparent that if there is no offset Eqs. (6) and (7) yields a symmetric GRIN lens around the center of the Kerr medium ($L/2$). In Fig. 9 an illustration of how the GRIN effect was implemented is shown.

In the calculations, the radius of the GRIN lens was chosen to be large enough to cover the image beam, regardless of angle and transverse offset. The step size (Δz) was taken to be 40 μm which implies calculation of 250 steps in the GRIN model to achieve the 1 cm CS2 path length. The results were checked for grid size dependence and a sufficiently small grid was chosen to avoid that problem. In Fig. 10 the focal length of the GRIN model is compared with the analytical expression in Eq. (5). The computational model agrees fairly well with the analytical results. With gate pulse energies of 2 mJ and higher the differences between the focal lengths were less than 8%, but in the limit of low gate pulse energies the computational model tends to predict stronger focusing than the analytical model. Here, with a 0.1 mJ gate pulse the difference in focal lengths predicted by the models was around 25%.

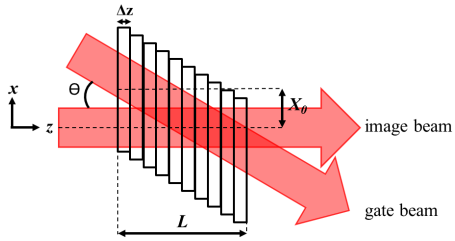

Fig. 9. Illustration of the GRIN effect model.

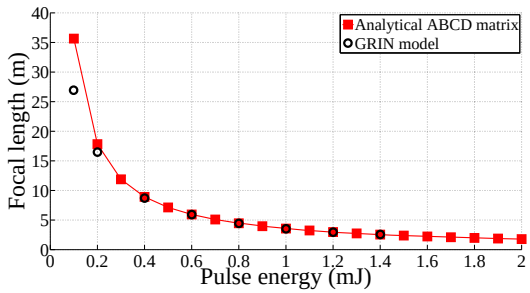

Fig. 10. Comparison of the GRIN model with the analytical ABCD matrix results from Eq. (5). In both cases a pulse length of 100 fs was assumed. In the computational model a 4 mm radius Gaussian beam was propagated through the GRIN model which here was implemented with $\theta = 0$ and no transverse offset.

4.3.2. Modeling results

The model defined in section 4.3.1 was used to observe changes in imaging performance when varying model dependent parameters. To investigate the response to lens misalignments, the collecting lens was displaced along the optical axis, in the transverse direction, and tilted with respect to the optical axis while keeping the other components unchanged from the aligned case. In these cases the GRIN effect of the Kerr medium was not applied (*i.e.* $E_p = 0$). The collecting lens was moved in steps from 0 mm to 0.3 mm along the optic axis, from 0 to 3 mm in the transverse direction, and tilted from 0 to 4 degrees around the optic axis. In Fig. 11 the results of misalignment of the collecting lens along the optic axis are shown. Here, the $4f$-system starts to display oscillations in the CTF with a 0.2 mm increase of the object to collecting lens distance. The magnitude of the oscillations in the $4f$ setup vary with changes in the lens displacement. The $2f$-system, on the other hand, shows smooth variations in contrast while being subject to the misalignments. The results for transverse misalignment of the collecting lens show the same behavior. The $4f$ setup starts to develop oscillations in the CTF with minor misalignments and the $2f$ setup undergoes a smooth decay in the CTF. In the case of tilting the collecting lens relative the optic axis, both systems show the same response and exhibit a smooth decay in the CTF up to 3° where oscillations start to become significant.

In Fig. 12 the results of changing the gate pulse energy (E_p) with the gate beam and image beam arranged in a collinear geometry are shown. In this case, the position of the image plane was optimized for each gate pulse energy value to achieve the best PSF possible. Here, at relatively low gate pulse energies (∼0.3 mJ) the GRIN effect introduces oscillations in the

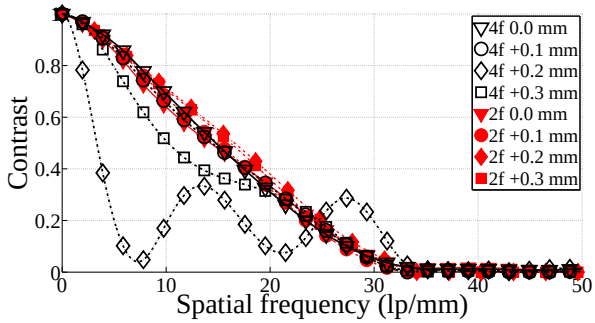

Fig. 11. Model CTFs showing effects of misalignment of the collecting lens along the optic axis in the computational model. The CS_2 is modeled as an isotropic medium ($E_p = 0$).

CTF which cannot be avoided completely by optimizing the image plane position. Both setups were affected by changes in gate pulse energy. If the image plane position was not optimized, the same behavior of the CTFs occurred but at lower gate pulse energies. This result could appear to disagree with Fig. 8. The mean contrast values plotted in Fig. 8 represent an average over a broad spatial frequency range; the same range across which the model and experiments disagree the most. The model is a simplified representation used to evaluate relative sensitivity to changes in various parameters like the gate pulse energy, but the model results cannot be directly compared with experiments. Differences between the model and experiment include re-optimization of the image plane position (done in modeling but not in experiments), the assumption of a steady state in the model OKE gate, and the finite size of the point source used in the model.

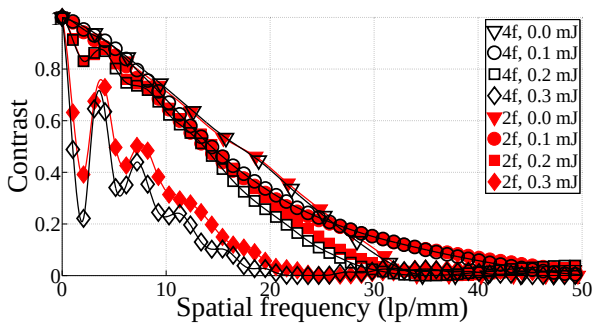

Fig. 12. Model CTFs showing effects of changes in the gate pulse energy (E_p) in the computational model with $\theta = 0$, $\tau = 100$ fs, and $X_{\text{offset}} = 0$.

Figure 13 shows the effect of changing the gate beam angle (θ). Here, the gate pulse energy was 0.2 mJ, the transverse offset 0 mm, and θ was varied between 0° and 30°. The position of the image plane was optimized for the 0.2 mJ gate pulse energy in a collinear geometry. Neither of the setups were significantly affected by the increase in θ, but as can be seen in the magnified part of the graph; there was no effect on the $2f$ setup but the $4f$ setup exhibited a small decrease

in the CTF with increasing gate beam angle.

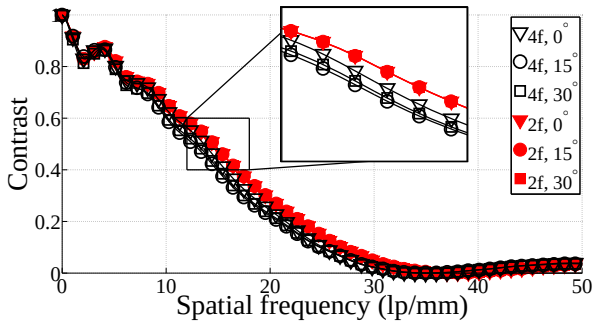

Fig. 13. Model CTFs showing effects of changes in the gate beam angle (θ) in the computational model with $E_p = 0.2$ mJ, $\tau = 100$ fs, and $X_{\text{offset}} = 0$.

In Fig. 14, changes in the CTF caused by variations of the gate beam offset (X_{offset}) can be seen. Here the gate pulse energy was 0.2 mJ, the gate beam angle was 20°, and the transverse offset was varied between 0 mm and 2 mm. In this case the image plane position was optimized for the gate pulse energy in a collinear geometry. A significant effect of increasing the offset can be seen for both setups. The 4*f*, however, was affected more strongly.

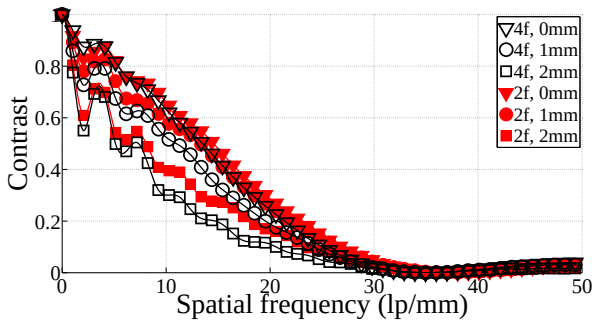

Fig. 14. Model CTFs showing effects of changes in the gate offset (X_{offset}) in the computational model with $E_p = 0.2$ mJ, $\theta = 20°$, $\tau = 100$ fs.

While very careful alignment of the 4*f* system can produce good results, for our cases the 2*f* system is more robust to misalignment and hence and more easily used. For that reason it was used for the study that follows.

5. TGBI compared with USI

In Figs. 15 and 16 the results of the comparison between the TGBI and USI setups are shown. The 2*f* setup was used in this comparison. Also here, the standard deviation in the data indicated a useful lower limit for detectable contrast ~ 0.15 (based on a 95% confidence interval). As expected the ultimate resolution of USI OD0 is superior to the TGBI case owing to softer

spatial filtering and lack of distortion introduced by the time gate. In this case, with scattering spheres present, TGBI generates higher contrast for most sphere sizes and OD's. Looking at the highest resolvable spatial frequency, one sees the same trend. It is only the 3.53 μm spheres at OD4 and OD7, and 9.7 μm at OD4 that generate higher spatial resolution for USI. A 2f USI data trend shows higher maximum resolvable spatial frequencies and lower overall contrast for the small sphere sizes than for the larger ones. The opposite is true for larger spheres; here, the overall contrast is higher but the ultimate resolution is lower than in the small sphere cases. This behavior can be attributed to differences in the scattering phase function which is more uniform for the smaller spheres while the probability for forward scattering increases with sphere size. The result is that while more uniform scattering introduces almost constant background noise uniformly decreasing contrast, the larger spheres with a dominant forward scattering lobe, hold the contrast to a higher level until angular spreading of the forward lobe interferes with the size of the line pattern. Here, the contrast is significantly reduced.

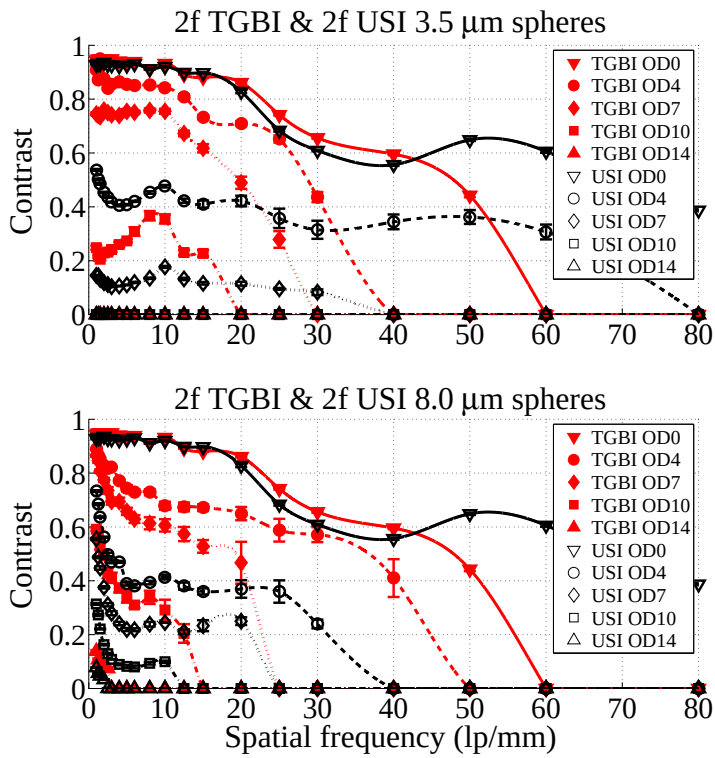

Fig. 15. Experimentally measured CTFs for 2f TGBI and USI setups with sphere sizes of 3.5 μm and 8.0 μm. The error bars represent one standard deviation.

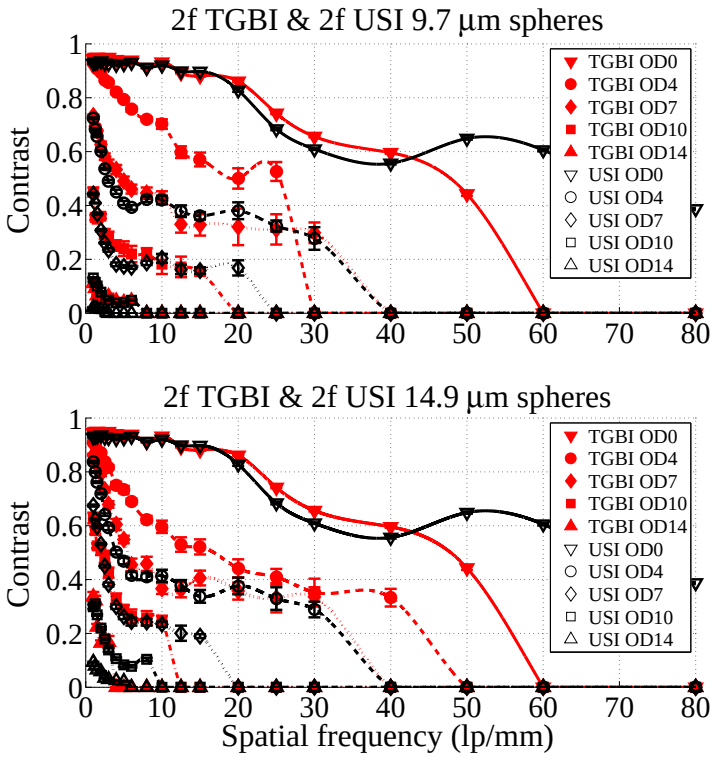

Fig. 16. Experimentally measured CTFs for 2f TGBI and USI setups with sphere sizes of 9.7 μm and 14.9 μm. The error bars represent one standard deviation.

6. Conclusion

In this work, we have investigated two different optical setups that have been used in TGBI of sprays in the past. The experimental results showed that, in terms of ultimate resolution, the two setups performed similarly in the presence of scatterers. In terms of contrast, the 2f setup performed better in the lower scatterer size range and in the densest cases. With larger scatterer sizes at moderate ODs, the results are mixed. Oscillations in the CTFs, which are indications of system aberrations, are present for both setups but more pronounced in the 4f case. The experiments indicated that the 2f setup is less sensitive to alignment issues and to variations and fluctuations in the OKE-gate setup.

To gain a better understanding of the sources of aberrations and the difference in sensitivity to them, a set of experiments combined with modeling were performed. It was shown that positioning of the Kerr medium along the optic axis is important since the image beam, when focused, can generate unwanted non-linear lensing effects. It should be noted that the experiments did not investigate spatial filtering effects of the image information due to the finite size of the gate beam. In experiments with an active OKE-gate, there will be a trade-off between mitigating unwanted non-linear effects and minimizing gate beam induced spatial filtering. It was also shown that variations in the gate energy affect the two setups differently. The experi-

mental results indicate that the 4f setup is more sensitive to variations in the gate pulse energy than the 2f setup.

An analytical investigation indicates that the gate pulse generates a focusing effect in the Kerr medium which induces image distortions. By modeling this lensing effect with a parabolic approximation, it was shown that both setups were affected by changes in the gate beam energy and by induced asymmetries introduced by moving the gate beam in the transverse direction. The 4f setup, however, exhibited a more significant degradation in imaging performance as a result of these factors. Furthermore, it appears that the relative angle between the gate beam and the image beam, or the 'skewedness' of the induced lens, is not significant. However, it should be pointed out that, in the model, the cylinder-lens nature of the induced lensing effect has been ignored. For simplicity, this effect was modelled as a spherical lensing process. Furthermore, spatio-temporal effects on image information transmission have not been considered within this approximation. These effects, however, typically only become significant at sub-picosecond OKE-gates. For further discussion on this issue see for example work published by the group at CORIA [27, 28].

The investigations of the two different optical setups indicate that the 2f system is more robust to misalignment and, hence, more easily used. It is less prone to image distortions caused by component misalignments, changes in object plane position, and variations in the OKE-gate setup.

When comparing the best performing TGBI setup to its USI equivalent, in order to determine cases when the OKE-gate enhances imaging performance, it was shown that the TGBI setup generated higher contrast for most PS sphere sizes and ODs. In terms of resolution it was only in the lower scatterer size range at low ODs that the USI generated higher spatial resolution than the TGBI setup.

Acknowledgments

The authors gratefully acknowledge the Swedish Research Council, the Swedish Energy Agency, and the Knut and Alice Wallenberg Foundation for funding the work.

Paper II

Available online at www.sciencedirect.com

ScienceDirect

Proceedings of the Combustion Institute 35 (2015) 1579–1586

Proceedings of the Combustion Institute

www.elsevier.com/locate/proci

Evidence for supercritical mixing layers in the ECN Spray A

Zachary Falgout [a], Mattias Rahm [a], Zhenkan Wang [b], Mark Linne [a,*]

[a] Division of Combustion, Institution for Applied Mechanics, Chalmers University, 41296 Gothenburg, Sweden
[b] Combustion Physics, Physics Institution, Lund University, 22100 Lund, Sweden

Available online 15 July 2014

Abstract

Prior work on an engine combustion network Diesel fuel injector led to the conclusion that under Diesel engine conditions (combustion chamber pressure and temperature) the jet was transitionally supercritical; meaning that the core of the jet would be condensed liquid while the edge of the jet would be supercritical. We report initial experiments aimed at observing the thickened turbulent mixing layer that would result if the jet were transitionally supercritical. We have applied ballistic imaging to the same Diesel fuel injector, under similar conditions, and we find that the images do indicate a structural change when going from subcritical to supercritical conditions. Under subcritical conditions we observe a well-defined liquid/gas interface, surface wave structure, and formation of ligaments and voids. Under supercritical conditions the interface transitions into a continuous, turbulent mixing layer. Images of this layer include the cellular structure characteristic of gas jets. These changes are consistent with experimental literature on cryogenic supercritical jets and with DNS modeling of supercritical mixing layers.

Keywords: Sprays; Supercritical; Ballistic imaging

1. Introduction

The conventional paradigm for Diesel engine combustion begins with injection of an intact stream of liquid fuel into the surrounding high pressure charge of air. The surface of the stream rapidly breaks up via 'primary breakup' mechanics to produce primary drops that break up further (or collide and coalesce in regions of high drop density). The smallest drops then vaporize and mix with the air to produce a combustible gas-phase fuel/air mixture which is spatially and temporally varying.

The atomization process just described does indeed occur in laboratory settings when the air pressures and temperatures are not fully representative of the combustion chamber in a modern compression-ignition engine. Recently, however, Dahms et al. [1,2] have rekindled[1] speculation that the pressure and temperature in Diesel engine combustion chambers at the time of injection can

* Corresponding author.
E-mail address: mark.linne@chalmers.se (M. Linne).

[1] See e.g., [3] J. Bellan, Progress in Energy and Combustion Science, 26 (2000) 329–366. and the citations therein.

http://dx.doi.org/10.1016/j.proci.2014.06.109
1540-7489/

exceed supercritical conditions for the liquid/gas mixtures at locations that would normally be called the spray formation region. Such states could significantly change the conventional description of mixture formation in such an engine.

Supercritical conditions are known to occur during fuel and oxidizer injection into a rocket motor. Bellan [3] reviewed activity in that area up to the year 2000, and related work has continued up to the current time. Cheroudi et al. [4], for example, studied cryogenic jets at subcritical and supercritical conditions. They point out that under supercritical conditions the "sharp distinction between liquid and gas phases disappears". The well-defined and very thin liquid/gas interface (termed a "jump condition" by Dahms et al.) disappears and is replaced by a more gradual, continuous distribution of density. This material is called a 'fluid' by Bellan [3], to distinguish the single, supercritical phase from the original combination of condensed-phase fuel and ideal gas. Under supercritical conditions, transport properties are both pressure and temperature dependent. The solubility of the two materials grows significantly and surface tension goes nearly to zero, meaning that well defined drops are not identifiable; neither is the liquid/gas interface of the core. Thermal conductivity and mass diffusivity can vary much more strongly, and the latent heat of vaporization goes almost to zero owing to the practical absence of surface tension.

Cheroudi et al. studied injection of liquid nitrogen into gaseous nitrogen using shadowgraphy. They injected the liquid into a chamber held at 300 K (the critical Temperature for N_2 is $T_c = 126.2$ K). The chamber pressure was varied from well below the critical pressure to well above it; they investigated reduced pressures ($P_r \equiv P/P_c$) in the range $0.23 < P_r < 2.74$ (for N_2 the critical pressure is $P_c = 3.4$ MPa). A clear change in spray structure was observed near $P_r = 1$. At low P_r the jet images indicated a well-defined liquid/gas interface, formation of surface waves, stripping of ligaments and formation of easily identifiable drops. For $P_r > 1$ they observed that the formerly obvious drops and ligaments had disappeared and the jet had become somewhat more transparent. The well-defined edges disappeared and the sides of the jet looked more like a gas jet even though there were clearly denser regions in the core. Cheroudi et al. characterized the spray divergence angle under various operating conditions and showed that for high P_r the jet angle had the characteristics of a gas jet, not a spray.

Dahms et al. [1] reported experiments using an engine combustion network (ECN, [5]) single-hole Bosch injector in the pre-burn type spray chamber at Sandia National Labs. They ran an experimental condition at 29 bar gas pressure and 440 K temperature, producing a gas density of 22.8 kg/m^3, and the fuel was pure *n*-dodecane at a fuel temperature of around 90 °C. They used a backlit shadowgram arrangement and applied a long distance microscope to observe the near field of the spray. When looking very late in the process (after the needle had seated again) they were able to observe distinct drops and ligaments, albeit with some degradation of resolution caused by index variations across the chamber. Next, they operated at a nonreacting "Spray A" condition, which includes a chamber pressure of 60 bar and chamber temperature of 900 K (achieving the same gas density as before)[2]. The Spray A conditions ($T = 900$ K and $P = 60$ bar) exceed the critical conditions for pure dodecane ($T_c \cong 658.1$ K, $P_c \cong 18.17$ bar). Under these conditions the flowfield exhibited no distinct interfaces; there were no obvious drops or ligaments.

Dahms et al. [2] have recently published a detailed description of a model for this jet. They apply a Knudsen number criterion to argue that the Spray A chamber condition can produce jets that are transitionally supercritical and hence produce a thick, diffusion dominated border instead of a well-defined liquid/gas interface. They predict that under light-load, medium-load, and highly-boosted conditions the Diesel jet should encounter supercritical conditions in an operating compression ignition engine. A more classical spray would be found only under very light loads.

A transitionally supercritical jet is expected to have condensed liquid in the core (along the centerline) very near the nozzle where the liquid temperature reflects more nearly the rail temperature than the gas condition. Moving radially outwards, the fuel is heated and it enters a fairly broad single-fluid-phase, diffusion-dominated region. Dahms et al. argued that the former sharp liquid/gas interface thickens and loses its jump-condition structure owing to growth of the interface, reduction of the gas mean free path, and reduction of the surface tension. The injected liquid is postulated to diffuse into the surrounding gas; it would not evaporate from a distinct surface, and so the thickened interface would become a turbulent mixing layer. This edge would appear similar to what one observes at the edge of a turbulent gas jet mixing into a background gas.

Bellan and co-workers [6–9] have described the development and use of a direct numerical simulation (DNS) for supercritical mixing layers of various kinds. Their work is mostly related to rocket chambers but they do discuss the Diesel issue. For DNS in such a case, one must choose how to describe transport of heat and mass within the mixing layer. Bellan and co-workers devote significant effort to support their approach to heat and

[2] See http://www.sandia.gov/ecn/ for a complete description of the Spray A condition.

mass transport, but it is a complex, coupled problem. The critical properties depend upon the mixture, the mixture depends upon transport, transport coefficients depend upon the state, and the fluid state depends upon temperature which also depends on transport. Temperature and mass fractions vary within the mixing layer. Even counter-gradient diffusion can occur in specific mixtures [7]. Because their solution is a DNS approach, the Reynolds numbers were low but the results indicate that a turbulent mixing layer with continuous density gradients should stand between the compressed liquid core and the ideal gas that lies far beyond the shear layer.

Here, we report initial experimental results aimed at observing the thickened turbulent mixing layer, applying ballistic imaging [10] to the same ECN injector studied by Dahms et al. under similar conditions.

2. Experiments

The measurements reported here were carried out in the steady flow spray research chamber at Chalmers University. This optically accessible chamber can reach 90 bar back pressure and 900 K gas temperature. The electronically heated gas flow is quite slow relative to the velocity of a fuel jet but rapid enough to evacuate the chamber within minutes. The injector was mounted in the top of the chamber with the spray pointing downward. The Bosch ECN injector has a single, 84 μm diameter hole on centerline. The injector is cooled so that the fuel in the tip never exceeds 130 °C at the Spray A condition in this facility. The electrically heated air flows into the chamber through an annulus surrounding the injector, flowing downward until it is exhausted at the base. Oblong quartz windows allow optical access to the entire jet.

Before performing other ECN experiments, it is necessary to confirm that the spray reproduces accepted liquid and flame liftoff lengths in the chamber being used; to confirm that the specific conditions of interest have been reached. We followed the standard procedures as listed at the ECN web page. Pure dodecane was used as the fuel. In the Chalmers case the incoming air was not diluted with nitrogen; the oxygen level was 21%. Most of the other ECN work is performed at 15% O_2 (to emulate exhaust gas recirculation) but there have been a few experiments with normal air. The injector tip temperature was also 40 °C higher than most other ECN experiments. Our liquid lengths are 7.7 mm, within 4% of the accepted number and the liftoff length was 9 mm. The lift-off length was 40% shorter than that measured at 15% 0_2 ambient gas composition in a similar chamber at Caterpillar, Inc., but that difference is to be expected given the additional oxygen in our experiment.

To investigate further the changes in jet structure noted by Dahms et al., we set up a single-shot ballistic imaging (BI) instrument around the spray chamber. Ballistic imaging [10] is a laser-based optical technique (see Fig. 1) that can image larger liquid structures that are buried inside a turbid medium like an optically dense spray. The main point is that larger liquid structures refract light (e.g., as one uses to create a shadowgram or schlieren image) but the image can be corrupted by light that is strongly scattered off axis by small drops. BI preserves the refracted light that contains the images of larger liquid structures (termed "useful imaging light") meanwhile rejecting light that was scattered off axis by droplets and other background light (termed "corrupted image light"). BI preserves useful imaging light by segregating it based on intrinsic signatures: (1) useful imaging light lies on the laser beam axis while corrupted light scatters strongly off-axis (one can use careful optical design to reject corrupted elements while preserving high quality elements, similar to spatial filtering but strong spatial filtering can degrade image spatial resolution), (2) useful imaging light is cleanly polarized while corrupted light is depolarized (the polarizers in Fig. 1 remove un-polarized light), and (3) useful imaging light travels the shortest path and exits first (the optical Kerr effect (OKE) time gate in Fig. 1 is a very fast shutter with adjustable time delay). Detail on the OKE time gate is provided in Ref. [10] and the sources cited therein.

The system used here begins with a mode-locked Ti: Sapphire oscillator (Spectra-Physics Mai Tai) emitting ~80 fs pulses at 82 MHz repetition rate with an average power of around 1.5 W. The oscillator seeds a chirped-pulse regenerative amplifier (Spectra-Physics Spitfire). This device emits amplified pulses at 1 kHz repetition rate, with a pulse width on the order of 100 fs, at a central wavelength in the vicinity of 800 nm, and pulse energy around 4 mJ. The pulse energy is well in excess of that required for ballistic imaging and so the total energy delivered to the experiment was controlled with a polarization rotator/polarizer combination. The laser beam was launched 5 m across the laboratory to the chamber, but because the oscillator has active beam pointing control the BI instrument was stable over each day. At the spray chamber, the beam was split into an imaging beam that passed through the spray and a switching beam that activated the OKE gate in Fig. 1. The energy in both beams was controlled at the experiment by polarization rotator/polarizer combinations. Finally, the switching beam passed through a polarization rotator (rotated 45°, because the OKE gate relies on polarization switching) and an adjustable delay line so that the switching pulse landed at the CS_2 cell (the Kerr-active medium) in the OKE gate at the same time as the imaging pulse.

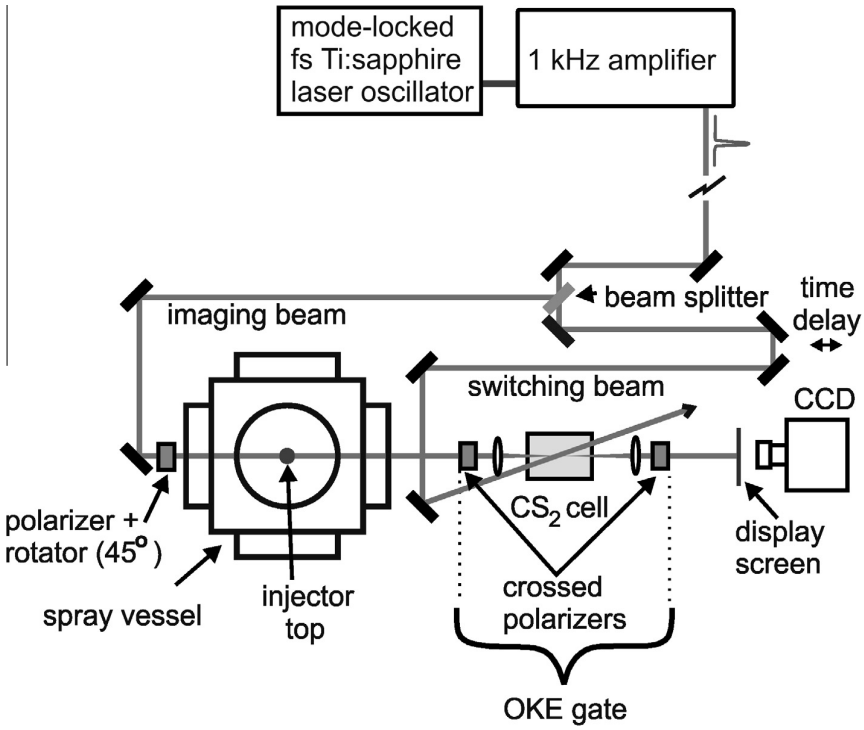

Fig. 1. Ballistic imaging in the spray chamber.

After passing through the chamber windows and the spray, the image beam entered the OKE gate which is effectively a very fast shutter (~1.5 ps shutter time when using CS_2 as the Kerr active medium). In BI, the OKE gate is activated by the switching beam as it passes through the CS_2 cell, and the timing of this shutter relative to the image pulse is set by the optical time delay line. The image beam was then directed onto a frosted glass display screen and the image was captured by an Andor iXon electron multiplying CCD camera (1004 × 1002 active pixels). The shutter speed for the camera is slow (~1 ms), but the effective shutter for the imaging system is the OKE gate, which is quite fast. This camera has on-chip electron multiplying gain and we used gain values from 10 to 16 here. Based on prior work discussed in Ref. [10] the spatial resolution of this BI instrument is known to be 20–25 μm.

In the past it has been speculated that window birefringence in pressurized chambers or engines could defeat the OKE switching process, but that does not happen. The OKE gate starts with a polarizer. If some of the image light is depolarized by window birefringence, those corrupted elements are rejected at this first polarizer and then the rest of the OKE gate performs as usual. The maximum possible window rotation would reduce the useful imaging light entering the gate by half. While that loss is regrettable, it remains possible to acquire images using on-chip gain, or alternatively an image intensifier if one has such a camera instead.

A frequently overlooked aspect of BI is that the OKE gate is not required under all conditions (as discussed in Ref. [10]). Presence of an OKE gate does not identify the BI technique; BI is essentially any shadowgram technique that uses optical components to reject corrupted image elements. The OKE gate is just one of several possible optical components which can be used separately or combined, depending on the imaging problem. Sprays with low optical depth (e.g., few drops) do not require an OKE gate, for example; the optical design and the polarizers segregate useful imaging light, contributing to image fidelity. Very dense sprays do require the OKE gate.

Two ECN-related cases were evaluated here. The first, a low temperature case (LTC), used a chamber pressure of 30 bar ($P_r = 1.6$ for pure dodecane) and temperature of 445 K ($T_r \equiv T/T_c = 0.7$ for pure dodecane) for a gas charge density of around 23 kg/m^3. The second was a high temperature case ("Spray A") with a chamber pressure of 60 bar ($P_r = 3.2$ for pure dodecane) and temperature of 900 K ($T_r = 1.4$ for

pure dodecane) at the same density. Note that these reduced quantities are based on critical properties for pure dodecane and they do not reflect the critical properties of the undetermined mixture existing at the boundary between air and fuel. The low temperature case, for example, uses a pressure that is above the critical pressure of dodecane, but the mixing layer of the jet will entrain gas and the mixture is known to have a critical pressure roughly twice that of the pure fuel. LTC and Spray A are the same conditions discussed by Dahms et al. in Ref. [1]. In addition, images were acquired at two different times: at 0.8 ms after start of injection (asoi, i.e., during the steady jet period, similar to Dahms et al.) and 1.64 asoi (just after the fuel has shut off, e.g., the late injection case presented by Dahms et al.).

3. Results and discussion

Figure 2 contains ballistic images of the LTC spray taken 0.8 ms asoi (steady period). This was the first time that BI had been performed on a spray at pressures and temperatures characteristic of a modern Diesel engine. One can see that the image background contains some schlieren (refractive) structures caused by thermal mixing layers (the cooled injector holder is located just inside the hot air supply, creating thermal mixing layers). Despite this fact, image processing makes it possible to extract the spray core images. Here, edge detection was used to separate the core area from the background and then the intensity/contrast of the background was manually adjusted to allow the spray to stand out more in a visual way. This is not a recommended procedure for numerous images but there are experimental means to eliminate the background problem in future work and we plan to apply them. In Fig. 2 one can see a liquid core structure that features a sharp liquid/gas interface, ligaments stripping from the surface and some evidence for voids inside the core structure. As described by Linne [10], the drop cloud surrounding the core is not in evidence because BI rejects drop signatures.

The core region in Fig. 2 grows with distance downstream. Considering mass conservation, it is clear that the image does not represent a contiguous liquid stream. There must be voids inside the core. Linne et al. [11] report evidence of voids and broken liquid in a Diesel spray issuing into air at 1 bar back pressure, and one can detect small evidence for voids in Fig. 2. Moreover, X-ray radiography produces images of the liquid mass in a spray [10]. Results from such measurements on the same injector (see e.g., Kastengren et al. [12]) indicate that the liquid mass fraction is never 100%. Although those results were for somewhat

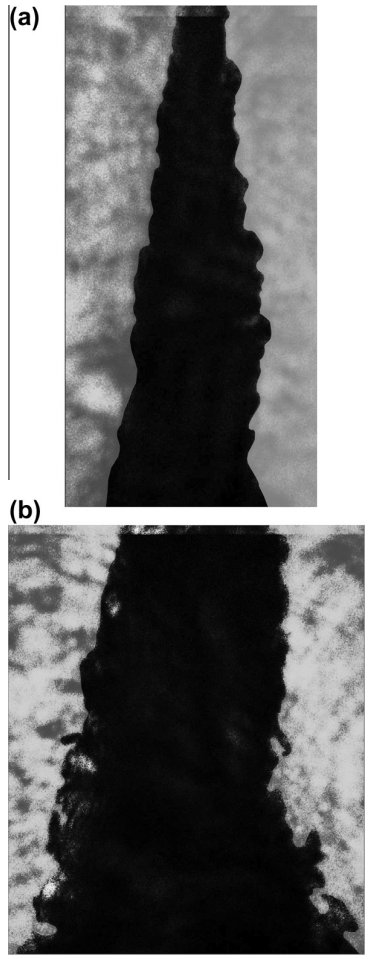

Fig. 2. BI of the jet at the LTC taken 0.8 ms after start of injection (steady region): (a) from 1 mm below the injector to 5 mm below, (b) from 5–9 mm below.

different conditions, they do confirm this observation. The rest of the core remains black, especially on centerline for reasons provided in Ref. [10].

Figure 3 contains a BI of the jet at the Spray A case taken 0.8 ms asoi (similar to Fig. 2a but at higher temperature and pressure). The background thermal mixing layers are different in this case. Here a very short pre-burn was used to disturb the schlieren structures because they generated even worse interference than before. The pre-burn was possible because the jet ignites at 900 K. The pre-burn did not disturb the experiment significantly as the chamber contains a very large volume of gas and it has an open inlet and exhaust. The change in pressure due to the pre-burn was negligible while the local temperature was probably increased somewhat. Our goal in

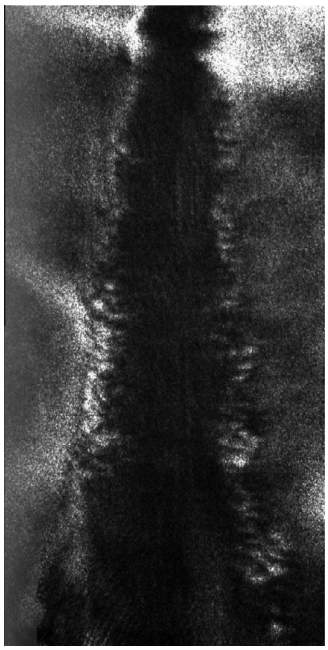

Fig. 3. BI of the jet at the Spray A condition taken 0.8 ms after start of injection (steady region), between 1 and 5 mm.

this part was to observe T_r and P_r both well above one, however, so this small change in temperature can also be considered negligible. Despite these background interferences, a clear change in the spray structure can be detected; the edge is now defined by a cellular structure.

Cellular structure is emphasized in Fig. 4a, which contains an image of the same jet (Spray A) taken 1.64 ms asoi (just after the fuel has shut off). That jet image has been cropped to remove the bottom 1 mm because it suffered from the background gas beam steering problem; a very bright schlieren spot made it impossible to detect inner structure there. One can see, however, that this jet exhibits no evidence of a liquid/gas interface (e.g., ligaments or trailing drops). It has the cellular structure characteristic of shadowgrams or schlieren images of a gas jet (see e.g., Fig 4b for just one example) and the sinuous shape indicates that this jet has low relative momentum. This same sinuous structure has been reported for low momentum, steady supercritical jets related to rocket combustors [3].

Returning to the jet in Fig. 3, one can see that the edges of the jet are similar to the jet of Fig. 4a, but the core (on axis) is different. That core has new liquid arriving steadily, and the fuel inside the injector has a temperature around 130 °C. The centerline would thus be expected to contain condensed liquid with fairly high momentum. As one moves radially off centerline, however, the gas heats the fluid and it undergoes a conversion of states. As argued by Dahms et al., this edge is a fairly broad single phase, diffusion dominated region. The thickened interface caused by a transition to a supercritical state would become a turbulent mixing layer. This edge does indeed appear similar to what one observes at the edge of a turbulent gas jet mixing into a gas.

Another point of evidence for supercriticality for this single-component fuel and air mixture would be that surface tension is significantly reduced (that is just one of the contributors to this the thickened interface of the jet core). Dahms et al. note that evidence for drops and ligaments disappears in their experiments at the Spray A condition.

As discussed above, the OKE gate in Fig. 1 is necessary only for high density (high number of small drops) sprays. As the density decreases one can achieve equally good or better resolution without the OKE gate even though the spray has drops. This happens because even without the OKE gate, the system uses a carefully designed optical system (it does some spatial filtering) and it incorporates polarizers. We thus decided to disable the OKE gate and observe the effect. The BI beam was located low in the spray (between 5 and 9 mm, similar to Fig. 2b but at the Spray A condition). The image in Fig. 5 represents this case, taken 0.8 ms asoi. The fact that this image is even clearer than the others implies that there were very few drops, if they existed at all. The BI setup is capable of imaging this process clearly because it controls what photons are accepted; broadly steered light that could corrupt the image is rejected.

At the top of the image in Fig. 5, one can see the dark, high-density core region transitioning continuously into a cellular structure, in the vertical direction moving downwards. The cellular image structure is generated simply by optical path length differences from one region to its neighbor, caused by turbulence in a fairly uniform field of fluid (uniform when compared to a multiphase flow). These OPL differences steer light into some regions and away from others, as a random micro-lens array would. This image thus indicates a thickened interface with a turbulent mixing layer.

To emphasize the correlation between the Spray A images and a gas jet, Fig. 6a contains the cellular portion of Fig. 3 (from the right hand side), Fig. 6b. contains the central portion of Fig. 4a, and Fig. 6c contains a cut from the right hand side of Fig. 4b (the gas jet schlieren image). These images share the same basic cellular structure (if we look just at the side of Fig. 3), and it is remarkably different from the liquid/gas interface one encounters when the gas conditions are below the critical point for the jet.

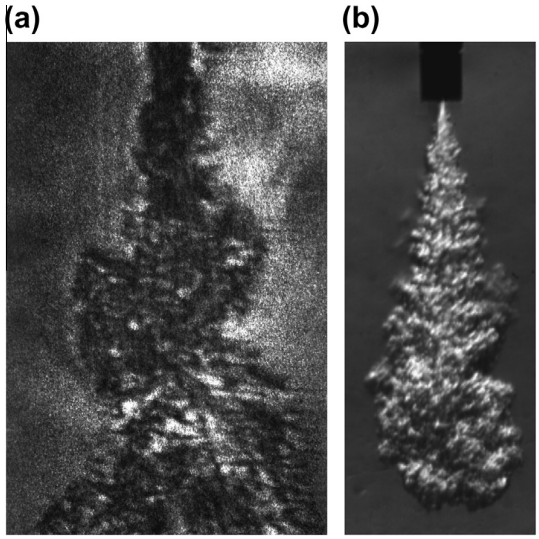

Fig. 4. (a) Diesel jet at the Spray A condition taken 1.64 ms after start of injection (just after shutoff), between 1 and 4 mm, (b) schlieren image of a He gas jet into room temperature air at 6 bar (previously unpublished image, acquired within a different project at Chalmers University).

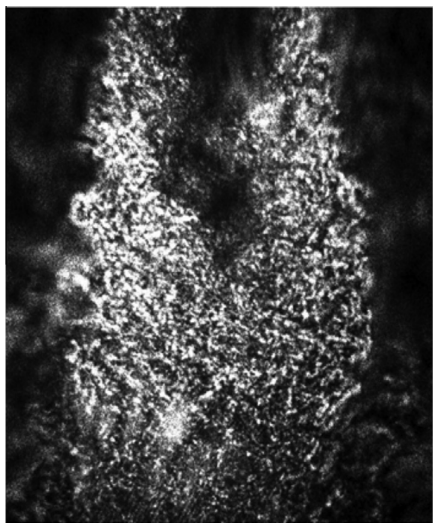

Fig. 5. Image with OKE gate disabled, taken at the Spray A condition, 0.8 ms after start of injection (steady region). Note the disappearance of the core as it transitions downwards.

The DNS predictions of Bellan and co-workers [6–9] are instructive. They studied low Re cases (Re $\sim$ 600) and these experiments use high Re flows (Re $\sim$ 65,000). Masi et al. [7] argue that in this regime the results are not as sensitive to Re as they are in sub-critical cases, but it is not possible to compare their images directly with ours. Despite this fact their images of 2-D density fields in a supercritical turbulent mixing layer are consistent with our experimental images as far as they go.

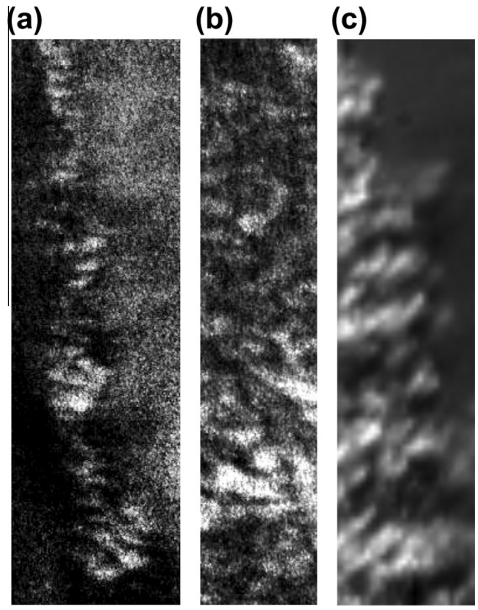

Fig. 6. Comparison of the edge of the jet from Fig. 2, the center of the jet in Fig. 4a, and the edge of the jet in Fig. 4b showing that they share the same cellular structure.

The results presented here do not prove conclusively that the Spray-A condition generates a transitionally supercritical jet, but they support the hypothesis.

4. Conclusions

This work has shown that a clear change of jet structure occurs when a Diesel fuel jet is injected into gas at conditions that are supercritical for the liquid, when compared to subcritical cases. The subcritical case is characterized by a well-defined liquid/gas interface, surface waves, ligaments, and ultimately drop production (although drops were not a subject of investigation here). At supercritical conditions the interface has been replaced by a thickened turbulent mixing layer with the cellular structure of a gas jet. No ligaments were observed and it is likely there were no drops.

While this work is not fully conclusive, it supports the hypothesis posed by the authors cited above. Future work will focus on improvement of the BI image quality using known techniques, magnification of the mixing layer (i.e., produce much clearer and detailed images similar to Fig. 6a), and corresponding drop measurements via phase Doppler interferometry (PDI). Gas conditions will varied across a matrix of subcritical and supercritical conditions. PDI is expected to detect the presence of defined drops at subcritical conditions and the signal is expected to degrade to an undetectable case when genuinely supercritical conditions are reached. These results can then be correlated with observations of the jet shear layers.

Acknowledgments

The authors would like to acknowledge financial support from the Swedish Research Council, the Swedish Energy Agency, and the Knut and Alice Wallenberg Foundation.

References

[1] R.N. Dahms, J. Manin, L.M. Pickett, J.C. Oefelein, *Proc. Combust. Inst.* 34 (2013) 1667–1675.
[2] R.N. Dahms, J.C. Oefelein, *Phys. Fluids* 25 (2013).
[3] J. Bellan, *Prog. Energy Combust. Sci.* 26 (2000) 329–366.
[4] B. Chehroudi, D. Talle, E. Coy, *Phys. Fluids* 14 (2002) 850–861.
[5] L.M. Pickett, C.L. Genzale, G. Bruneaux, L.-M. Malbec, L. Hermant, C. Christiansen, J. Schramm, *SAE Int. J. Engines* 3 (2010) 156–181.
[6] J. Bellan, *Combust. Sci. Technol.* 178 (2006) 253–281.
[7] E. Masi, J. Bellan, K.G. Harstad, N.A. Okong'o, *J. Fluid Mech.* 721 (2013) 578626.
[8] R.S. Miller, K.G. Harstad, J. Bellan, *J. Fluid Mech.* 436 (2001) 1–39.
[9] N. Okong'o, K. Harstad, J. Bellan, *AIAA J.* 40 (2002) 914–925.
[10] M. Linne, *Prog. Energy Combust. Sci.* 39 (2013) 403–440.
[11] M. Linne, M. Paciaroni, T. Hall, T. Parker, *Exp. Fluids* 40 (2006) 836–846.
[12] A. Kastengren, C.F. Powell, K. Fezzaa, Z. Liu, S. Moon, X. Zhang, in: SAE technical paper series, paper no. 2011–01-0383, 2011.

Paper III

Combustion and Flame 162 (2015) 2937–2953

Contents lists available at ScienceDirect

Combustion and Flame

journal homepage: www.elsevier.com/locate/combustflame

Distributed reactions in highly turbulent premixed methane/air flames Part I. Flame structure characterization

Bo Zhou [a], Christian Brackmann [a], Qing Li [b], Zhenkan Wang [a], Per Petersson [a], Zhongshan Li [a,*], Marcus Aldén [a], Xue-song Bai [b]

[a] Division of Combustion Physics, Lund University, P.O. Box 118, S221 00 Lund, Sweden
[b] Department of Energy Science, Lund University, P.O. Box 118, S221 00 Lund, Sweden

ARTICLE INFO

Article history:
Received 20 October 2014
Received in revised form 19 December 2014
Accepted 22 December 2014
Available online 16 March 2015

Keywords:
PLIF
Distributed reaction zone regime
Turbulent premixed flames
LDV
Flame/turbulence interaction
Borghi diagram

ABSTRACT

Simultaneous planar laser-induced fluorescence (PLIF) measurements of a series of reactive scalars and Rayleigh scattering measurements of temperature, i.e. CH/CH_2O/OH, HCO/CH_2O/OH and T/CH_2O/OH, and laser Doppler anemometry (LDA) measurements are carried out to characterize the flame/turbulence interaction in various regimes of turbulent combustion, including the laminar flamelet regime, the thin reaction zone (TRZ) regime, and the distributed reaction zone (DRZ) regime. A series of turbulent premixed methane/air jet flames with different jet speeds and equivalence ratios are studied. The jet Reynolds number ranges from 6000 to 40,000 and the Karlovitz number (*Ka*) of the studied flames varies from 25 to 1470. It is shown that in the TRZ regime CH/HCO layer remain thin but the layer of CH_2O and temperature gradient are broadened owing to the rapid turbulence transport. In the DRZ regime the CH and HCO layers are also broadened owing to the rapid transport of reactive species such as OH radicals from the high temperature regions where these radicals are formed to the low temperature region. In the DRZ regime CH and HCO are found to coexist with OH or CH_2O owing to the rapid turbulence eddy interaction, which differs fundamentally from that in the TRZ regime and the laminar flamelet regime. For the present investigated flames, the temperature range for the distributed reaction to occur is found to be between 1100 K and 1500 K. It is shown that the structures of flames in different regimes can affect the turbulence field differently. In the DRZ regime the temperature gradient is lower than that in the laminar flamelet and the TRZ regimes, which results in a lower peak of turbulence intensity owing to the retarded velocity gradient across the flames and thereby a lower rate of turbulence production.

1. Introduction

Combustion in most practical applications operates at highly turbulent conditions. The interaction between turbulence and chemical reactions has been one of the most important research subjects in the combustion community over the last a few decades. For premixed turbulent combustion, several authors have proposed a regime diagram to delimit the various combustion regimes on the basis of scaling analysis, e.g. [1–3]; a review on the regime diagram of turbulent premixed flames can be found in Lipatnikov and Chomiak [4] where a list of different versions of the regime diagram is given. In the regime diagram modified by Peters [3], a non-dimensional parameter, the Karlovitz number (*Ka*), was introduced to classify the regimes. The *Ka* is defined as the ratio of the time scale of the chemical reactions to the smallest time scale of turbulence (the Kolmogorov time scale). In the wrinkled and corrugated flamelet regimes, it is argued that the thickness of flame front (δ_L) is thinner than the Kolmogorov length scale (η). As such, turbulence can only wrinkle the flame front so that the instantaneous flame front can be modeled locally as a laminar flamelet. As turbulence becomes stronger, i.e. η becomes smaller, the thin reaction zone (TRZ) regime is approached, in which η is smaller than the flame thickness (δ_L) but still larger than the length scale of the thin fuel-consumption layer (known as the inner layer that has a thickness δ_r on the order of one tenth of δ_L [5]). The Karlovitz number in the thin reaction zone regime is therefore in the range $1 < Ka < 100$. In this regime, the preheat zone can be distorted and broadened by small eddies while the inner layer of the reaction zone remains thin and intact. The aforementioned regimes have the important common characteristic that the major heat release is confined to a thin reaction zone that separates the unburned reactants from the burned products and the internal

* Corresponding author.
E-mail address: Zhongshan.li@forbrf.lth.se (Z. Li).

http://dx.doi.org/10.1016/j.combustflame.2014.12.021
0010-2180/

structure of the thin reaction zone is barely distorted by turbulence eddies. This leads to the "flamelet" concept being widely applicable as validated by experimental observations [6–11] and direct numerical simulations (DNS) [12,13].

However, a spontaneous question is that to which extent the flamelet concept will still be valid as the Kolmogorov scale becomes smaller than δ_r (i.e. $Ka > 100$) so that small eddies could distort and consequently broaden the reaction zone [14,15]. Evidence from experiments [16–19] as well as numerical simulations [20,21] has shed light on the limit of the flamelet concept. Moreover, it is also highly questioned whether the flame can be sustained at $Ka > 100$ [4,22], since it has been observed that the flame may be shredded [23] or quenched [24–26] before being broadened due to high levels of stretch and heat loss exerted by intense turbulence. Due to the aforementioned reasons, the regime with $Ka > 100$ is referred to as the distributed or broken reaction zone regime, depending on whether a flame can be sustained.

Recently, we have experimentally observed a broad spatial distribution of short-lived CH and HCO radicals in flames established on a piloted jet burner (LUPJ, abbreviated from Lund University Piloted Jet burner) [27], indicating distributed reactions. In the LUPJ, a laminar pilot coflow flame is used to prevent the turbulent jet flames from quenching, thus allowing for well-stabilized jet flames with Ka significantly higher than one hundred. Similar burners have also been employed by other groups to generate high Ka flames [18,28]. It can be concluded that flames like the ones employed in the present study do not necessarily extinguish at high Ka if properly protected by a hot coflow. For this reason, the present paper prefers to use the term "distributed reaction zone (DRZ)" regime instead of the "broken reaction zone" regime.

Theoretical predictions of combustion in the DRZ regime have been presented in several pioneering works [29–31]. In short, it has been characterized by: (1) the elimination of the sharp interfaces between the unburnt and the products owing to the rapid turbulence-dominated mixing; (2) the relatively broadened heat-release region with reduced local burning rate; and consequently (3) the reduced maximum flame temperature and homogenized temperature field. The first feature calls for a revision of the current flamelet combustion models for numerical simulations of turbulent premixed combustion. There is no obvious flamelet generated manifolds, and the concepts of displacement speeds of the flame fronts and the flame surface density may no longer be valid. Finite rate chemistry may have to be used in the numerical simulations, which requires greater computer resources for the multi-scale physical and chemical processes involved. The second and third features could be of benefit to reduce the thermal NO_x emission as its production is strongly temperature dependent. To our knowledge, the DRZ regime is fairly unexplored in the existing literature [32,33]. The need to systematically investigate the basic structures and dynamics of premixed flames in the DRZ regime is clear, and examining the similarity/difference among the flames in the various regimes is one of the present focuses.

The present work is an extension of our recent work on the DRZ regime combustion [27]. Here, a wider range of flames with varying degree of turbulence and equivalence ratios are considered. Reactive scalars (i.e. OH, CH_2O, CH and HCO) and temperature (T) have been captured instantaneously by three series of simultaneous imaging measurements which include planar laser-induced fluorescence (PLIF) of OH/CH_2O in combination alternatively with CH PLIF, HCO PLIF or planar Rayleigh scattering temperature measurements. For the T/CH_2O/OH measurements, quantifications of CH_2O and OH concentrations have been made based on data from the corresponding laminar flames and the instantaneous temperature field. In addition, the flow fields of the flames were measured using laser Doppler anemometry (LDA). One goal of this work is to clarify the dependences of reactive scalars on the jet speed (U_0) and equivalence ratio (Φ). The other goal is to obtain a dataset from the statistical analysis of the PLIF, the Rayleigh thermometry and the LDA measurements for model development and validation in the DRZ regime.

2. Experimental details

2.1. Laser diagnostics

The LUPJ burner consists of a porous sintered-brass plate (61 mm in diameter) with a center jet 1.5 mm (d) in diameter. A flat laminar CH_4/air flame with the exit flow velocity of 0.3 m/s and $\Phi = 0.9$ was stabilized on the porous-plug surface. Details about the investigated flames will be given in Section 2.2. Other details about the burner configuration are referred to Ref. [34].

The experimental system for simultaneous multi-scalar two dimensional imaging has been described in detail in our previous work [27] and only a brief description is given here. For Rayleigh scattering thermometry, an s-polarized 355-nm Nd:YAG laser was employed together with a bandpass filter (355 ± 5 nm) for detection. Formaldehyde (CH_2O) was excited using the same laser, and the signal was detected at wavelengths above 400 nm. The OH radicals were excited at the $Q_1(8)$ transition in the $A^2\Sigma^+$–$X^2\Pi$ (1-0) band, and the off-resonance fluorescence centered at 309 nm was detected. An alexandrite laser was employed for the excitation of CH at 387 nm and HCO at 259 nm, respectively, following the excitation–detection strategies detailed in Refs. [34,35] with special care to ensure an interference-free detection [34–36]. The thickness of the combined laser sheets was measured to be 100 μm and an imaging spatial resolution for PLIF and Rayleigh measurements of around $70 \times 70\ \mu m^2$ was determined from the finest resolvable pattern on a resolution target (USAF-1951). Other experimental parameters and further information about the imaging qualities and the signal-to-noise ratios (SNR) of measured scalars can be found in Ref. [27]. Based on species concentrations estimated from CHEMKIN simulations (see Section 4.2 for details) and the achieved experimental SNRs, the detection limits are evaluated to be ~100 ppm for OH, 40 ppm for CH_2O, 3 ppm for HCO and 0.1 ppm for CH.

To measure the axial velocity component and its fluctuations a calibrated LDA system (Dantec, Flow Explorer DPSS & BSA F80 processor unit) was employed. A diode pumped solid state laser is used to generate beams at 532 nm with average powers of 300 mW. The laser beam is split into two beams, one of which is shifted in frequency with 80 MHz enabling detection of instantaneous stagnation and reversal flows. The incident laser beams were focused using a 300 mm lens above the center of the jet exit, giving a physical ellipsoidal probe volume of 80 (width) × 80 (height) × 700 (length) μm^3. This optical setup allows for the detection of velocities up to around 300 m/s. The signal, burst of scattered light from seeding particles crossing the fringes, is collected in a back-scatter mode with the signal receiving optics incorporated in the LDA probe. The data acquisition was performed at temporal equidistant intervals with a sampling interval (typically 100 μs) of at least twice the estimated integral timescale of the investigated jet conditions. This approach was used to avoid over-sampling the velocity information, to eliminate velocity bias and also to reduce bias effects due to a non-uniform seeding density in the jet and the coflow. The maximum number of independent acquired samples was set to 10^4. A fluidized-bed seeder was used to seed 0.5-μm diameter Al_2O_3 particles into the main jet air flow which was then mixed with the fuel stream before entering the burner. The LDA measurements have been focused on the stoichiometric turbulent flames. Lean flames ($\Phi = 0.4$) with jet speeds of 66, 330 and 418 m/s as well as a non-reacting case with the jet speed of 165 m/s were also performed for reference. Pointwise LDA measurements were started from 4 mm up to 120 mm height above the burner surface (x) with a 3 mm interval between

two adjacent measurement points. Exceptions were made for flames with jet speeds of 330 m/s (LUPJ1-330) and 418 m/s (LUPJ1-418), where only a fraction of the velocity profiles was obtained as the maximum flow velocities exceed the maximum detectable velocity range of the LDA system. In addition, velocity profiles along the radial (r) direction were measured at a few axial positions (x).

The uncertainty of the LDA measurement is a combination of random and fixed errors. At the same spatial positions, the reproducibility of the mean axial velocity (U) and its root-mean-square (rms, v') velocities was 5% (random error), mainly attributed to the mismatch of spatial relocation. The fixed errors are attributed from (1) the finite probe volume which introduces spatial averaging effect and (2) the non-uniform seeding as only the jet flows are seeded. Dibble et al. [37] has shown that an unseeded coflow has a negligible effect on the profiles of mean/rms axial velocity at $x/d > 30$ with a similar burner configuration. The fixed errors are expected to be more significant near the jet exit where the velocity gradient is large. The total error near the jet exit $\sim x/d = 10$ is estimated to be about 20% for the mean axial velocity and 15% for the rms of the axial velocity fluctuations. The turbulent quantities (see Section 3) of reacting jet flows are characterized at $x/d \geqslant 20$ to avoid the uncertainty introduced from the fixed errors.

2.2. Investigated flames

To systematically characterize the variations of the flame structures at various Ka numbers, 21 flame cases are considered, covering laminar flames, turbulent flames at the TRZ regime and the DRZ regime. The flames are named as LUPJα–β, where α represents the equivalent ratio Φ of the jet flow and β represents the jet flow speed U_0 in m/s, as summarized in Tables 1 and 2. The laminar flame cases with a constant center jet exit speed (U_0) but different equivalence ratios are summarized in Table 1. The small jet diameter and the pilot coflow flame ensure stable laminar CH_4/air jet flames including the ultra-lean flame condition ($\Phi = 0.4$), which is below the normal flammability limit. Numerical simulations for an ideal free-propagation planar flame configuration were performed using the CHEMKIN software and the GRI 3.0 chemical kinetic mechanism [38] with full transport properties to obtain the laminar flame speed (S_L) and the laminar flame thickness (δ_L) for the investigated laminar flames, where δ_L was defined as $\frac{T_p - T_u}{|\nabla T|_{max}}$ with T_p and T_u being the temperature of products and unburnt reactants, respectively. Numerical simulation of the laminar flame with $\Phi = 0.4$ is not feasible since the mixture is below the flammability limit for the planar freely propagating flame condition. For comparison, S_L was also determined experimentally using the relation $S_L = U_0 \times \sin\theta$, where θ is the half angle of the flame cone, and δ_L was experimentally obtained from the temperature fields measured using Rayleigh scattering thermometry as listed in Table 1. It is apparent that the pilot coflow flame has a direct heating effect on the laminar jet flame, which, as expected, significantly increases the laminar flame speeds, especially for the leaner case. To account for the impact of the pilot coflow, the experimentally measured laminar speeds and flame thicknesses were adopted in the calculations of Ka and other non-dimensional parameters shown in Table 2.

The characteristic quantities of the investigated turbulent flames are listed in Table 2. The turbulence intensity (v') and the integral length scale (l_0) were estimated from the LDA data, which will be discussed in Section 3. The formulations/explanations of some other quantities are given in the footnotes of Table 2. The investigated turbulent flames span over a wide range of Ka from the TRZ regime to the DRZ regime in the Borghi diagram. This gives the possibility to investigate the boundary between the TRZ regime

Table 1
Quantities for the investigated laminar flames.

Flame code	Φ	U_0 (m/s)	$S_{L,\,exp}$ (cm/s)	$S_{L,\,CHEM}$ (cm/s)	$\delta_{L,\,exp}$ (mm)	$\delta_{L,\,CHEM}$ (mm)
LUPJ1-11	1.0		42.5	37.5	0.48	0.44
LUPJ2-11	0.7	11	33.2	19.2	0.60	0.66
LUPJ3-11	0.4		21.4		0.85	

Table 2
Quantities for the investigated turbulent flames.

Flame code	Φ	U_0 (m/s)	Re_{jet} [a]	Re_t [b]	l_0 (mm)	η (μm)	v'/S_L	Ka_{20} [c]	Ka_{30} [d]	Ka_{50} [e]	Da_{30} [f]	Imaging data [g]	LDA data
LUPJ1-66	1.0	66	6306	95		96	16	37	25	14	0.39		√
LUPJ2-66	0.7			97		95	20	59	40	22	0.25		×
LUPJ3-66	0.4			138		73	40	136	135	72	0.09		√
LUPJ1-110	1.0	110	10,510	190		57	31	71	70	46	0.20		√
LUPJ2-110	0.7			195		56	40	115	113	74	0.12		×
LUPJ3-110	0.4			214		53	62	264	261	171	0.06		×
LUPJ1-165	1.0	165	15,764	238		49	39	112	98	73	0.16		√
LUPJ2-165	0.7			244		48	50	181	158	118	0.10		×
LUPJ3-165	0.4			267		45	77	417	365	271	0.04		×
LUPJ1-220	1.0	220	21,019	317	2.9	39	52	152	151	100	0.12	√	√
LUPJ2-220	0.7			325		38	66	246	244	162	0.07		×
LUPJ3-220	0.4			356		32	103	567	561	373	0.03		×
LUPJ1-330	1.0	330	31,529	476		26	78	327	277	212	0.08		√
LUPJ2-330	0.7			487		26	99	530	448	344	0.05		×
LUPJ3-330	0.4			534		24	154	1220	1031	791	0.02		√
LUPJ1-418	1.0	418	39,936	603		22	98	467	394	302	0.06		√
LUPJ2-418	0.7			617		21	126	756	639	490	0.04		×
LUPJ3-418	0.4			676		20	196	1739	1470	1127	0.02		√

[a] Jet Reynolds number, $Re_{jet} = (U_0 \times d)/\nu$, where ν is the kinematic viscosity of flow at 298 K.
[b] Turbulent Reynolds number, $Re_t = (v' \times l_0)/(S_L \times \delta_L)$.
[c] Karlovitz number: $Ka = \{(v'/S_L)^3 \times (\delta_L/l_0)\}^{1/2}$, Ka_{20}, evaluated at $x/d = 20$, $r = 0$.
[d] Ka_{30}, evaluated at $x/d = 30$, $r = 0$.
[e] Ka_{50}, evaluated at $x/d = 50$, $r = 0$.
[f] Damköhler number: $Da = Re_t^{1/2}/Ka$, Da_{30}, evaluated at $x/d = 30$, $r = 0$.
[g] Imaging data includes three series of simultaneous measurements, i.e. (1) qualitative CH/CH_2O/OH; (2) qualitative HCO/CH_2O/OH; and (3) quantitative T/CH_2O/OH.

and the DRZ regime for CH_4/air flames as will be elaborated in the following sections.

Photographs of the investigated flames are shown in Fig. 1 to provide an overall impression of the flame structures. It can be seen that all the turbulent jet flames comprise of: (1) an inner core with triangular shape as marked by a dark region above the jet exit; and (2) a relatively homogeneous bluish luminescence brush region on the top of the inner core. The bluish color can be attributed to CH^* emission and the maroon color surrounding the center jet flames attributed to the emission of hot water vapor in the product gas of the pilot flame. With increasing jet speed, both the height of the inner core and the luminescence brush increased gradually. On the other hand, the height for which the hot coflow merged with the jet flame was gradually reduced as shown by the shortened maroon-colored region. This indicates an increasing entrainment of the ambient cold air to the flame as the jet speed increases. The equivalence ratio appears not to influence the air entrainment to a noticeable level in Fig. 1. Further discussion on this will be given in Section 3.

The intensity of flame chemiluminescence appears to change significantly with the equivalence ratio but not obviously with the jet speed. For flames with the same jet speed, the height of the luminescence region decreased visually with the equivalence ratio. Nevertheless, Dunn et al. [18] have previously used flame chemiluminescence to indicate extinction and re-ignition.

3. Flow-field characterization

In this section, results from the LDA flow-field measurements are presented. In Fig. 2, the axial variation of the local mean axial velocity component (U) normalized by the inlet jet speed (U_0) is shown. All normalized axial velocity profiles coincide and can be fitted into one single profile, independent of the inlet jet speed. An exception was found for flame LUPJ1-66 (i.e. the stoichiometric flame with a center jet exit velocity of 66 m/s) whose Reynolds number is considered to be moderate and therefore the turbulent flow was not fully developed. Figure 3 shows the rms of the axial velocity fluctuations (u'), also referred to as the turbulence velocities. The quantity was normalized by U_0 and plotted as a function of x/d. Similar to the observations by Dunn et al. [18], the normalized turbulence velocity (u'/U_0, which is referred here to as the turbulence intensity) of the selected flames increases along the axial direction, peaks in the range of $20 \leqslant x/d \leqslant 40$, and the peak turbulence intensities are in the range 8–12%, with the lower jet velocity flames having higher turbulence intensities in general. The flame LUPJ1-66 is again exceptional due to its non-fully developed turbulence. Without the loss of generality, turbulence velocities at $x/d = 30$ (i.e. within the range of the peak turbulence intensities) have been used in the calculation of the turbulent characteristic

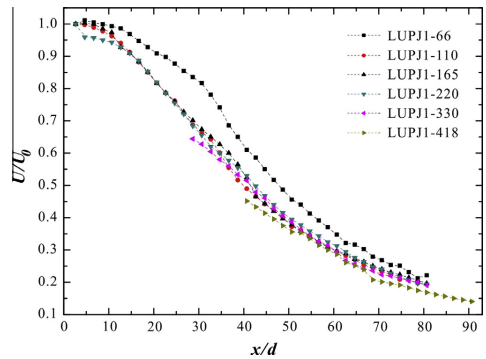

Fig. 2. Axial variation of the mean of axial velocity component (U) normalized by $U_0 = U(x/d = 0, r = 0)$ for the selected flames.

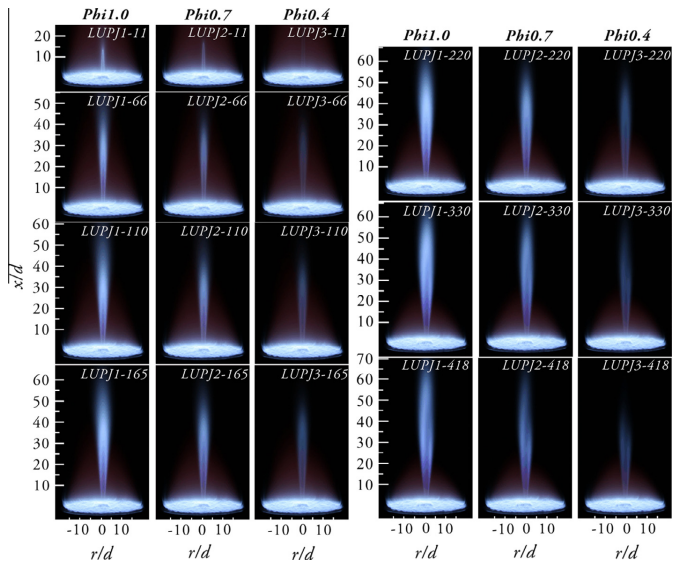

Fig. 1. Photographs (100 ms exposure time) of chemiluminescence for the investigated flames.

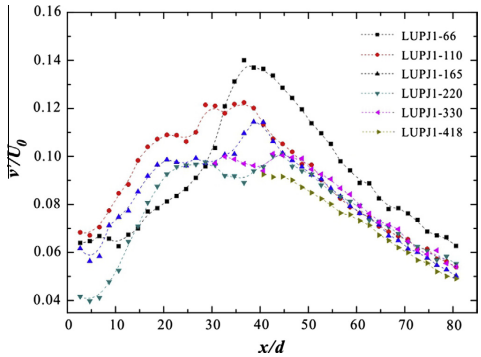

Fig. 3. Axial variation of the axial rms velocity (v') normalized by U_0 for the selected flames.

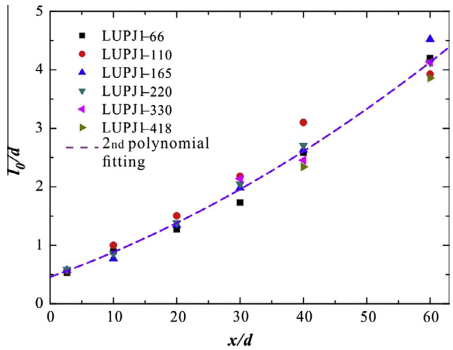

Fig. 4. Axial variation of the integral length scale l_0.

quantities listed in Table 2. For the lean flames where LDA measurements were not performed, the same turbulence intensities of the corresponding stoichiometric flames were adopted. For the flame LUPJ1-418, velocity data at $x/d = 30$ is not available and a turbulence intensity of 10% has been assumed.

It is noteworthy that the turbulence intensity profiles show two local peaks along the burner axis for all the selected flames except LUPJ1-66. The bimodal structure, however, has not been found in the LDA measurement of the non-reacting jet flow at the center jet velocity of 165 m/s condition (for brevity the isothermal flow results are not shown). A similar observation of the bimodal structure has been reported by Dunn et al. [18]. The first peak is likely due to the turbulence production in the strong shear layer of the inner jet flow/coflow hot gas. With increasing jet speed, the second peak in the turbulence intensity profiles appear to shift downstream of the flow, which is consistent with the observation of a downstream-shifted luminescence brush in the flame photographs shown in Fig. 1. The second peak always resides inside the region of the luminescence brush of the corresponding flame. This suggests that the second peak of the rms velocity is due to the high temperature gradient across the flames at the upstream location of the second peak (which gives rise to the high velocity gradient and thereby high production rate of turbulence). Further downstream, due to the absence of the high temperature gradient and thus the absence of turbulence production, the intensity of turbulence decreases due to dissipation of turbulence. This is consistent with the observation that with increasing jet speed, hence a broadened temperature layer (to be discussed in detail later), the temperature and velocity gradients across the flame become lower and the peak turbulence intensity is therefore lower.

In order to quantify *Ka*, *Da*, and turbulent Reynolds numbers, the integral scale (l_0) is required. In the present study, radial profiles of the axial velocity component have been acquired at several axial locations. At a given axial location (x/d), l_0 was approximated by the half-width at half-maximum (HWHM) of the radial profile of axial velocity. Figure 4 shows that l_0 is independent of jet speed, and it increases nearly linearly with x/d, and it is basically equal to half of the jet diameter (d) at the jet exit. A second-order polynomial fitting of l_0 has been applied, giving an expression of $l_0/d = 3.74 \times 10^{-4}(x/d)^2 + 0.039(x/d) + 0.46$. The value of l_0 at $x/d = 30$ is presented in Table 2. In addition to the *Ka* estimated at $x/d = 30$ (i.e. Ka_{30}), the *Ka* numbers at $x/d = 20$ and 50 (i.e. Ka_{20} and Ka_{50}) have also been estimated to show the spatial variance of *Ka* which will be discussed later. In general, the *Ka* peaks around $20 < x/d < 30$, and then decreases with increasing x/d due to the increased l_0 and decreased turbulence intensity downstream. The value of Ka_{30} is adopted as a characteristic *Ka* for the investigated flames in the following text since $x/d = 30$ approximately corresponds to the middle of the peak turbulence intensity range for investigated flames and also to the location where CH/HCO layer start to appear broadened (to be discussed in Section 4.3.1). Moreover, Table 2 shows that the investigated turbulent flames have a turbulent Reynolds number ranging from 100 to 400, and a Kolmogorov length ranging from 20 μm to 100 μm, which is on the same order of magnitude but slightly finer than our experimental resolution.

4. High-resolution multi-scalar and temperature imaging

In this section, simultaneous imaging of temperature and reactive scalars is presented. A description of the data processing (Section 4.1) is followed by discussions of the laminar flames (Section 4.2) and the turbulent flames (Section 4.3).

4.1. Image processing

Simultaneous imaging measurements were carried out with the following combinations: (1) CH/CH_2O/OH; (2) HCO/CH_2O/OH; and (3) T/CH_2O/OH. Each combination dataset consists of 500 single-shot frames for each scalar. All PLIF images have been flat-field corrected and processed with a 2×2 pixels median filter to reduce noise. For the T/CH_2O/OH series, the Rayleigh signal was evaluated using the cross-section data reported by Sutton et al. [39], and the effects of temperature-dependent quenching and Boltzmann fraction on the OH and the CH_2O PLIF signals were taken into account.

In the present study, the laser spectral power density for OH excitation was estimated to be 0.18 GW/cm^2/cm^{-1}, which resides in the upper limit of the linear LIF regime [40]. Given an incident laser power (E) in the linear LIF regime, the OH number density (N) could be expressed as [41],

$$N = N_{ref}\left[\frac{S}{S_{ref}}\cdot\frac{f_{ref}}{f}\cdot\frac{E_{ref}}{E}\cdot\frac{Q}{Q_{ref}}\cdot\frac{[g(\upsilon_0)]_{ref}}{g(\upsilon_0)}\right], \quad (1)$$

where S is the detected LIF signal, Q the quenching rate, f the Boltzmann factor and $g(\upsilon_0)$ the spectral overlap. The subscript "*ref*" indicates the quantities measured at a reference condition, which in this case is the data acquired in the laminar flame LUPJ1-11 with the same excitation–detection system. The LIF signal from the coflow flame burnt gas region was used as S_{ref} for OH, and the CHEMKIN simulation of the free-propagation planar flame with

the GRI 3.0 mechanism was used to estimate the OH concentration at equilibrium state (N_{ref}). The major species of the combustion products from the simulation were regarded as collisional quenching partners of the OH radicals. The temperature dependent quenching rate (Q) was calculated using the expression given by Paul [42] and the quenching cross-section data were taken from [43]. The Boltzmann factor (f) as a function of temperature has been simulated using the LIFBASE software [44]. The ratio of the line overlap factors in Eq. (1) has been assumed to be unity as $g(\upsilon_0)$ barely changes with temperature in atmospheric flames.

Linearity of CH_2O LIF signal excited at 355 nm even with high incident laser power has been shown by Brackmann et al. [45]. Therefore, Eq. (1) is also applicable for CH_2O quantification. However, literature on models and experimental data for the quenching rate of CH_2O LIF are limited. Metz et al. [46] have shown that the CH_2O fluorescence lifetime is inversely linearly proportional to temperature up to 800 K, suggesting a relation of $Q \propto T$, which is consistent with several experimental observations in flames [47–49]. Therefore, the relation of $Q \propto T$ was adopted for $T < 800$ K and constant quenching rate $Q = Q\ (T = 800\ \text{K})$ was assumed for $T > 800$ K due to the lack of experimental data. The estimated temperature-dependent quenching rate Q might impose the major uncertainty on the quantification of CH_2O LIF signal.

The Boltzmann factor f for broadband excitation at 355 nm was computed using the PGOPHER software [50]. The CH_2O LIF signal was then quantified by relating the peak LIF signal measured for the reference flame (LUPJ1-11) with the peak CH_2O concentration from the CHEMKIN simulation.

4.2. Laminar flames

Prior to the measurements in turbulent flames, measurements have been performed in the laminar flames (for conditions see Table 1). The laminar piloted jet flames show excellent stability and therefore the reactive scalars and the temperature measured from different series can be spatially correlated. Figure 5 shows an example of imaging of measured quantities in the flame LUPJ1-11 as an average of 100 frames. A typical laminar flame structure is clearly observed; HCO and CH show a nearly identical thin reaction zone, located downstream of the thin preheat zone (marked by CH_2O [8]) and upstream of the oxidization zone and the post-flame zone (marked by OH). The temperature field also shows a thin layer with a high spatial gradient in the vicinity of the thin preheat/reaction zones. These observations demonstrate the spatial resolution and fidelity of the present PLIF measurements. A slight asymmetry of the OH PLIF image is due to the absorption of the incident laser by OH radicals from the pilot coflow flame, resulting in at most a 15% signal deviation from the left to the right side of the image. Profiles of the temperature and the LIF signals of reactive scalars along the short line shown in the CH image in Fig. 5 are plotted as solid curves in Fig. 6(a). The dashed curves are the normalized OH and CH_2O profiles with corrections for quantification. It can be seen that the corrections have a negligible influence on the OH LIF profile, while the CH_2O LIF profile is slightly shifted downstream. Results of the CHEMKIN flame simulation, obtained with the burner-stabilized model are plotted in Fig. 6(b) for comparison. Since the experimental flame is stretched and

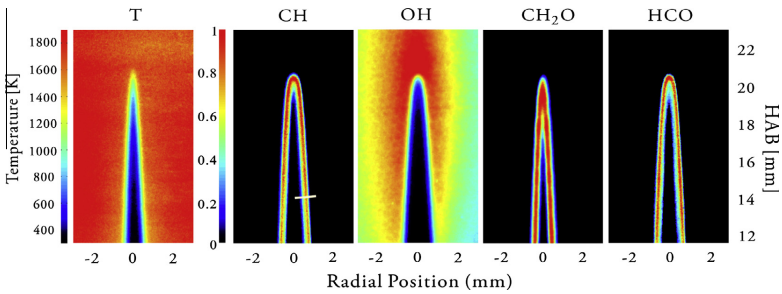

Fig. 5. Example of (quasi-simultaneous) imaging of temperature (Rayleigh scattering) and species (laser-induced fluorescence) for LUPJ1-11.

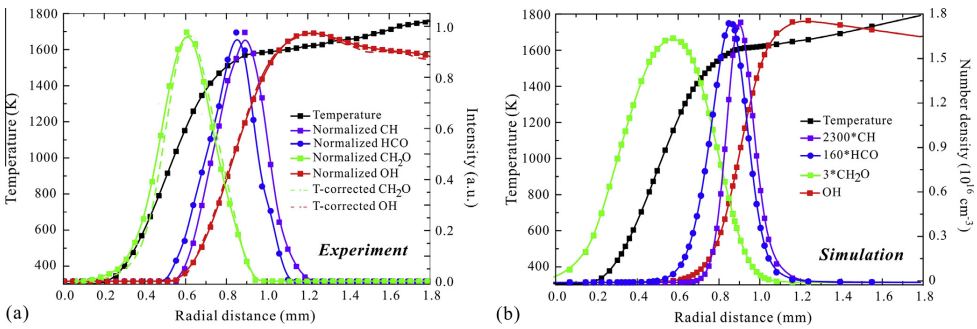

Fig. 6. Comparison of species and temperature profiles from experimental data (a) and CHEMKIN simulation (b) for the laminar stoichiometric flame LUPJ1-11.

supported by a hot coflow, the temperature field is different from that of a planar adiabatic flame. To allow for more relevant comparison between the numerical results and the experiments, the experimental temperature profile (the black curve in Fig. 6(a)) is used as an input in the numerical simulations. The simulated species profiles are shown to be in a reasonable agreement with the experimental data. The locations and shapes of species profiles are correctly reproduced: the inner layer (marked by HCO/CH) resides in the temperature region where temperature gradient starts to be flattened, and the peak of HCO appears slightly prior to the peak of CH. It appears that the thickness of the HCO/CH layer might be experimentally overestimated due to the finite spatial resolution and the slight broadening from the image averaging. On the other hand, the measured CH_2O profile appears to be thinner than the one simulated, likely due to the difference in the practical and the idealized flame configurations employed in the experiments and the flame simulations, respectively. Overall, the experimental data obtained in the laminar flames and the associated CHEMKIN flame simulations are in fairly good agreement, which provides good confidence for the measurements of the turbulent flames to be discussed below.

4.3. Turbulent flames

In the following, the variations of the turbulent flame structures with changes in the jet speed (Section 4.3.1) and equivalence ratio (Section 4.3.2) will be discussed. Special observations of the flames in the DRZ regime will be presented in Section 4.3.3.

4.3.1. Jet speed dependence

4.3.1.1. CH/CH_2O/OH and HCO/CH_2O/OH series. CH and HCO radicals, both known as short-lived combustion intermediates, have been shown to be good markers of the reaction zone. For the laminar flamelet and the thin reaction zone regimes the CH and HCO layers are known to remain thin [33]. Figures 7 and 8 present groups of single-shot images taken from the CH/CH_2O/OH and HCO/CH_2O/OH measurement series, respectively, of the stoichiometric flames with various jet speeds. Both CH and HCO show a transition from the flamelet mode (e.g. LUPJ1-66) to the broadened reaction zone mode (e.g. LUPJ1-165). It is seen that when the jet speed is increased further, i.e. LUPJ1-330/418, the CH/HCO layers become more broadened. Readers are referred to Supplement 1 for Figs. 7 and 8 with CH_2O iso-intensity contours to facilitate comparison of the degree of overlap between the measured scalars. In the following, we refer the distributed reaction to that with a broadened CH and HCO layers.

The CH_2O layer and the CH/HCO layers were shown to have a similar thickness in laminar flames (cf. Figs. 5 and 6). However, in turbulent flames the layer of CH_2O becomes broadened even at rather low speed, e.g. the stoichiometric flame with the jet speed of 66 m/s (LUPJ1-66, cf. Figs. 7A and 8A). In this flame the CH/HCO layer remains thin. The thickening of the CH_2O layer indicates that turbulence starts to disturb the preheat zone of the flame. Therefore, one may refer the flames with thin CH/HCO layers but broadened CH_2O layer to the thin-reaction zone regime flames.

It is of interest to investigate the transition between the TRZ regime and the DRZ regime, especially, at which *Ka* the turbulence eddies start to distort the thin inner layer (i.e. the CH/HCO layers) as the jet speed increases or the equivalence ratio varies. For the stoichiometric flames, the first observation of broadened CH and HCO layers starts at the top of the flame LUPJ1-165 (cf. Figs. 7(B) and 8(B), at $x/d = 30$, $r = 0$), which can hardly be attributed to three-dimensional effect as the broadening is so significant. At this flame height the flame has a characteristic Ka_{30} of 98 (see Table 2, Ka_{30} estimated at $x/d = 30$, $r = 0$), which is rather close to the boundary of $Ka = 100$ for the DRZ regime predicted by Peters [3]. It should be pointed out that the value of *Ka* varies along the flame height. For flame LUPJ1-165 the value of *Ka* at $x/d = 20$ is about 112 and at $x/d = 50$ it is about 73. With a higher Ka value of 112 the CH/HCO layers in the flame LUPJ1-165 at $x/d = 20$ are not significantly broadened owing to the small turbulence length scale that limits the broadening of the reaction layers, whereas with a lower *Ka* value of 73 at $x/d = 50$, the CH/HCO layers are more broadened, which is likely due to a history effect of the upstream flame broadening. Thus, one can expect that the boundary the TRZ/DRZ regimes in the present jet flames is not merely a function of the local *Ka* number but also depends on the local length scales of turbulence as well as the history effect of the upstream state of the flame. The boundary for the flames with leaner equivalence ratios will be discussed in Section 4.3.2.

Key features observed for the flames in the DRZ regime (some has been discussed in [27]) will be briefly summarized in the following together with a tentative qualitative explanation. One of the striking features among the flames LUPJ1-165/330/418 is the progressive broadening of the CH/HCO layer along the axial direction, which is partially associated with the progressive increase of the integral length scale as shown in Fig. 4. The thickness of the distorted inner layer is limited within the length scale of the large energy containing eddies l_0. Therefore, even though the inner layer is strongly distorted by the turbulence eddies, it is still virtually thin if l_0 is small. This explains the observation that at $x/d = 10$ the high *Ka* number flames, such as LUPJ1-330/418, are shown to have rather thin CH/HCO layers, since l_0 is on the same order of magnitude as the CH/HCO layer thickness.

Other features of the flames LUPJ1-330/418 are summarized as the following: (1) OH and CH_2O are located at mutually exclusive regions; (2) CH/HCO is able to penetrate deeper into the OH region than CH_2O; (3) CH/HCO can markedly overlap with CH_2O. The stronger CH/HCO signals generally correspond to the regions where CH_2O signal is weak, and vice versa. This is consistent with the nature of fuel oxidation chemistry, which proceeds sequentially from CH_4 through methyl radicals (CH_3), formaldehyde (CH_2O) and then formyl radicals (HCO), no matter whether the reaction is distributed or flamelet-like [51]. At high *Ka* conditions CH, HCO and CH_2O can widely coexist in space. However, owing to the rapid reaction rates in reactions associated with the OH radicals, OH radicals tend not to coexist together with, for example, CH_2O, at an appreciable level. As shown in Figs. 7(B–D) and 8(B–D), OH radicals are merely found to coexist with CH_2O at a low/moderate level of signals. For the same reason, the OH radicals of high concentration (signifying the post-flame region) are only visually manifested itself in patchy regions of no CH_2O, as also observed by Dunn et al. [18] and Temme et al. [28], while OH radicals of low concentration (which could be even lower than the OH PLIF detection limit ~100 ppm) might overlap with CH_2O. According to the GRI 3.0 kinetic mechanism [38], CH is formed primarily via the reaction:

$$H + CH_2 \rightarrow CH + H_2, \quad (R1)$$

while HCO is formed mainly through the reactions:

$$H + CH_2O \rightarrow HCO + H_2, \quad (R2)$$

$$OH + CH_2O \rightarrow HCO + H_2O. \quad (R3)$$

Therefore, the appearance of an appreciable CH/HCO signals indicates the presence of OH and/or H radicals and less amount of CH_2O.

4.3.1.2. T/CH_2O/OH series. Examples of quantitative T/CH_2O/OH measurements in the stoichiometric flames with various jet speeds are displayed in Fig. 9. Contours of CH_2O (iso-intensity lines at 10% of the maximum signal) have been superimposed on the temperature fields for comparison. At the lower axial position (i.e. $7 < x/$

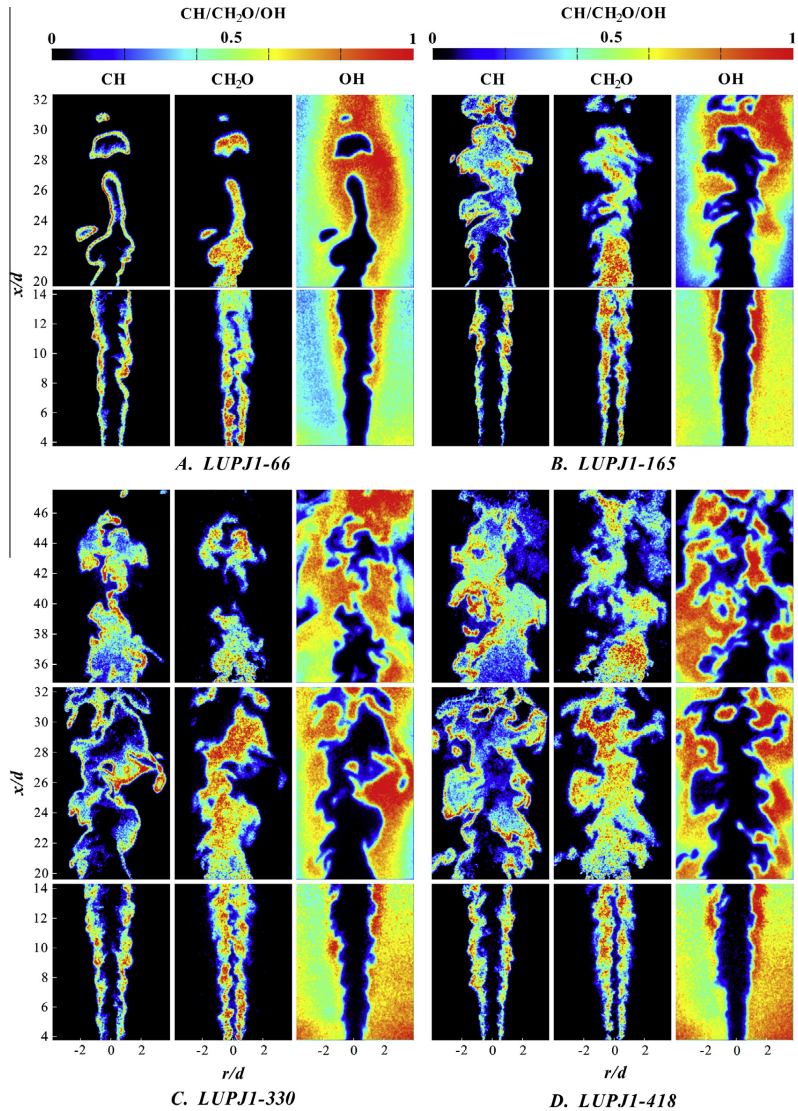

Fig. 7. Illustration of jet speed dependence from $CH/CH_2O/OH$ images for the selected flames (A) LUPJ1-66; (B) LUPJ1-165; (C) LUPJ1-330; (D) LUPJ1-418.

$d < 16$), the thermal layer (i.e. the layer with temperature gradient) is relatively thin for all the studied flames, and it becomes thicker with increasing jet speed. It is worth noting that the CH_2O contours show similarity to the thermal layer. High level CH_2O is seen only in the region where temperature is relatively low. Along the axial direction, the thermal layer thickness is continuously increasing as indicated by the vitiated temperature gradient. There are more hot regimes ($T > 1250$ K, corresponding to orange and red in the colormap) being included inside the CH_2O contours as the jet speed increases, indicating the increasingly rapid transport of heat by turbulence eddies. A slightly reduced temperature of the coflow flame at $20 < x/d < 33$ is also noticeable for the flames LUPJ1-220/418, implying an increased influence of the cold ambient air entrainment at high jet speeds as also evidenced by the flame emission photos in Fig. 1. Further downstream ($37 < x/d < 49$), the turbulent mixing with the ambient air further reduces the maximum flame temperature to ~1500 K, with reduced temperature gradient. Since all the selected turbulent flames reside in either

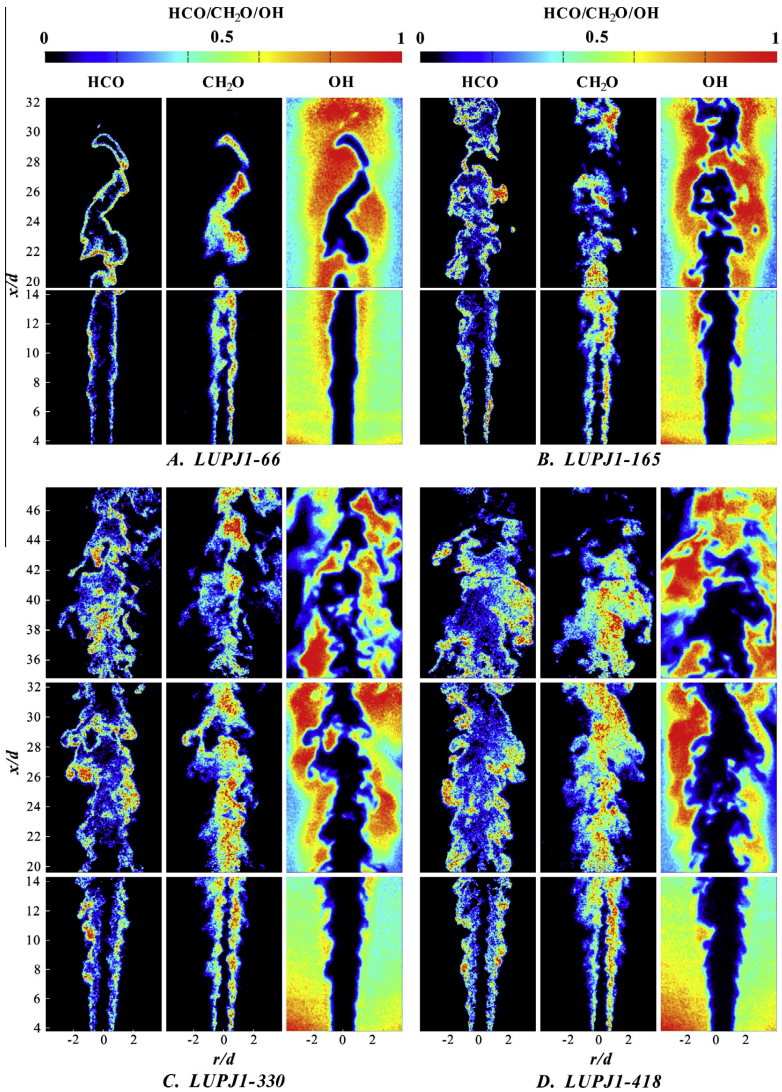

Fig. 8. Illustration of jet speed dependence from HCO/CH_2O/OH images for the selected flames (A) LUPJ1-66; (B) LUPJ1-165; (C) LUPJ1-330; (D) LUPJ1-418.

the TRZ regime or the DRZ regime, the thermal layer can be distorted by the penetration of turbulence eddies, and consequently heat can be transported far ahead of the inner layer toward the preheat zone as also evidenced by other experimental observations [52–54].

The temperature field has direct impacts on the turbulence field. First, with high temperature gradient, the density gradient and hence the velocity gradient is high, resulting in a high production rate of turbulence. From Fig. 9, it is seen that the region with high temperature gradient ranges from the burner exit to x/d about 30 for the low speed flames to slightly above $x/d = 30$ for the 330 m/s and 418 m/s flames. This region of the flame corresponds to the region of increasing turbulence intensity shown in Fig. 3. Thereafter, due to the lack of the temperature gradient and hence the velocity gradient, turbulence starts to decay along the axial direction due to viscous dissipation. In non-reacting flows, due to the lack of the temperature gradient the decay of turbulence starts at much lower x/d. Secondly, owing to gas expansion, turbulence eddies are greatly weakened after passing through the flame front due to the dilation effect [55,56]. The dilation effect is expected to

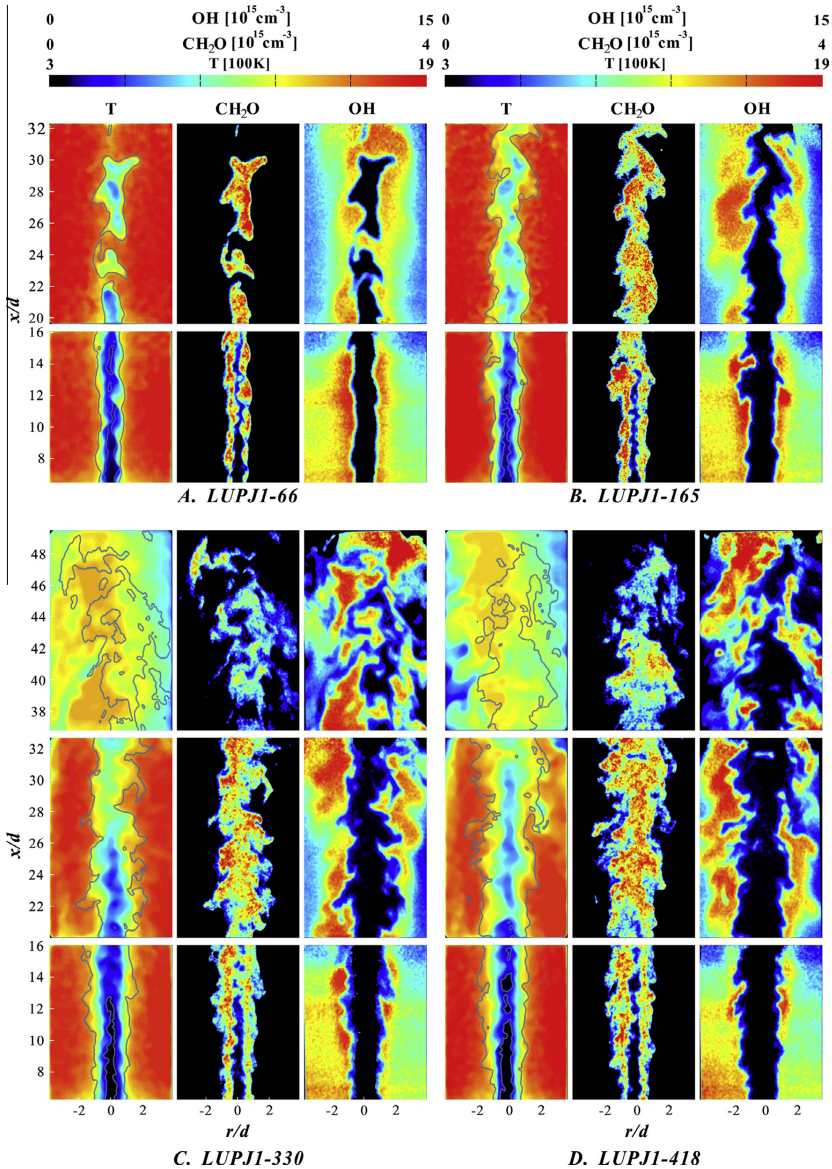

Fig. 9. Illustration of jet speed dependence from $T/CH_2O/OH$ images for the selected flames (A) LUPJ1-66; (B) LUPJ1-165; (C) LUPJ1-330; (D) LUPJ1-418. Iso-intensity (10% of maximum) contours of CH_2O were superimposed on the temperature fields for comparison.

be reduced at downstream locations ($x/d > 37$) where a relatively homogeneous temperature field is found.

To quantify the effect of turbulence on the flames, joint probability density functions (JPDF) of OH concentration/temperature for the selected flames at several axial locations are presented in Fig. 10. The colormap in the JPDF plots denotes the probabilities with red being the maximum and black being the minimum in logarithmic scale. The white dashed curves are the mean OH concentration weighted by its probabilities as a function of temperature, while the red dashed curves show the OH/temperature

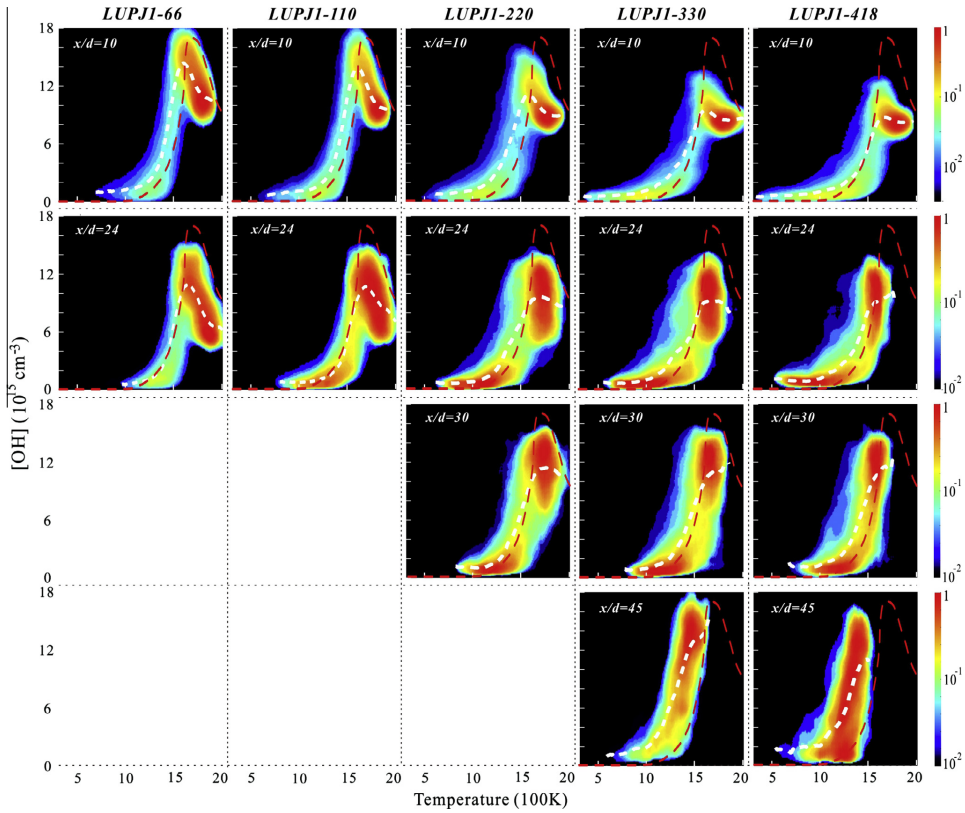

Fig. 10. JPDF of OH concentration and temperature for five selected flames (LUPJ1-66, LUPJ1-110, LUPJ1-220, LUPJ1-330 and LUPJ1-418) at four axial locations (x/d = 10, 24, 30 and 45). Colormap is presented in logarithmic scale. The white dashed curves represent the mean OH concentration weighted by the probability and the red dashed curves represent the OH/T correlation measured from the corresponding laminar flame, LUPJ1-11. (For interpretation of the references to color in this figure legend, the reader is referred to the web version of this article.)

correlation from the experimental measurement of the laminar flame (LUPJ1-11) as shown in Fig. 6(a). In the laminar flame, the OH concentration peaks approximately in the reaction zone, which is known as the super-equilibrium OH. Then, the OH concentration decreases to an equilibrium value in the post-flame zone. The OH concentration is shown to be negligibly low in the region with temperature below 1200 K. In contrast to this, a striking feature shown in Fig. 10 for all the selected turbulent flames is that a substantially high amount of OH can be found in the lower temperature region. At x/d = 10 (Fig. 10 top row), with increasing jet speed, it can be seen that OH can be found in regions of temperature below 600 K and the possibility of finding OH in the temperature range of 900 K < T < 1400 K is also enhanced. This observation is consistent with recent direct numerical simulation (DNS) studies of high *Ka* number methane/air premixed flames [57,58], where it was shown that rapid transport by the turbulence eddies can effectively bring reactive radicals (e.g. H) from the high temperature reaction zone to the low temperature zone (~500 K) where H can react with O_2 through the third body recombination reaction $H + O_2 + M = HO_2 + M$, giving rise to an appreciable amount of heat release in the low temperature zone. Subsequently, with increasing jet speed (hence increasing turbulence level) the peak (super-equilibrium) concentration of radicals (e.g. H and OH) is decreased due to the rapid transport of these radicals to low temperature regions. This can be seen clearly in Fig. 10.

At further downstream locations (x/d > 10), owing to the increase of turbulence intensity along the axial direction (until x/d about 40, Fig. 3) transport of radicals by turbulence eddies becomes even faster, which results in a higher probability of having OH radicals at the low temperature. At x/d = 10, the distribution of OH JPDF shows certain similarity to the laminar flame as indicated by the red dashed curve. However, such a similarity is no longer obvious at downstream locations of the highly turbulent flames (LUPJ1-220/330/418), indicating a strong turbulent perturbation of the post-flame zone and the flame front. Near the flame tip (x/d = 45) where the temperature field is rather homogeneous, OH appears to spread over a wide range of concentrations confined mostly in the temperature range from 1000 K to 1500 K with nearly equal probabilities due to the lack of a distinct flame front.

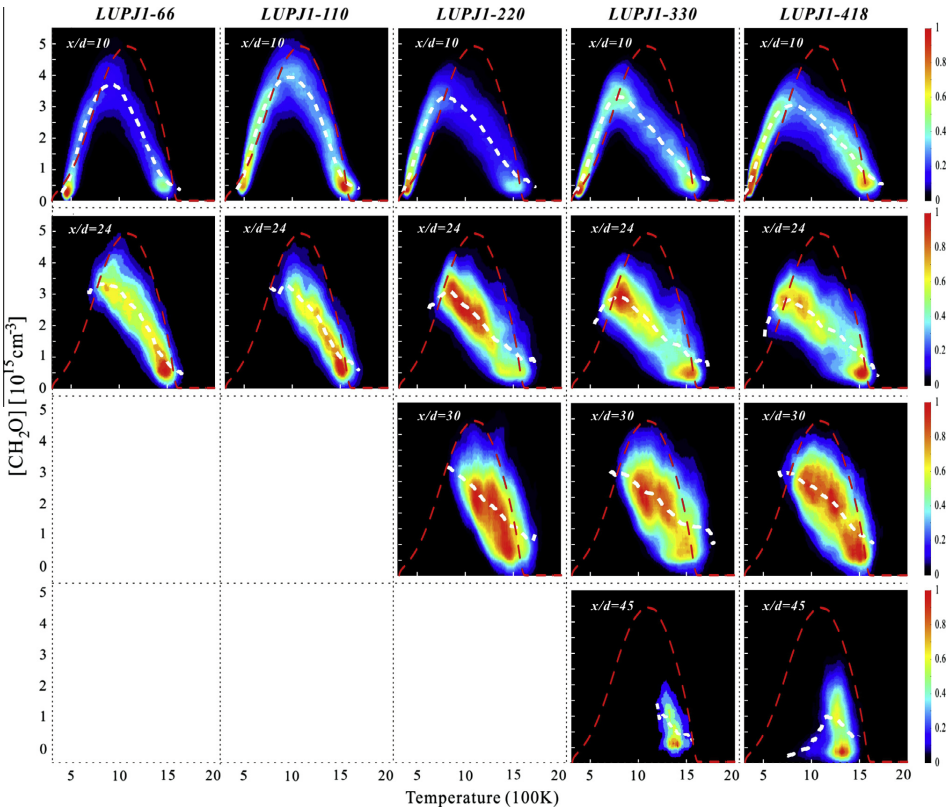

Fig. 11. JPDF of CH_2O concentration and temperature for five selected flames (LUPJ1-66, LUPJ1-110, LUPJ1-220, LUPJ1-330 and LUPJ1-418) at four axial locations (x/d = 10, 24, 30 and 45). Colormap is presented in linear scale. The white dashed curves represent the mean CH_2O concentration weighted by the probability and the red dashed curves represent the CH_2O/T correlation measured from the corresponding laminar flame, LUPJ1-11. (For interpretation of the references to color in this figure legend, the reader is referred to the web version of this article.)

In Fig. 11, JPDF plots are presented for CH_2O concentration versus temperature. Note that the colormap in Fig. 11 is linear. The experimentally determined CH_2O/T profile (red curve) from the laminar LUPJ1-11 flame is plotted for comparison. At x/d = 10, the qualitative structures from measurements of the laminar and the turbulent flames are the same. The CH_2O concentration rises with temperature first and reaches its peak value at around 1000 K for the flames LUPJ1-66/110 and 800 K for the flames LUPJ1-220/330/418. Subsequently, the CH_2O concentration decreases with increasing temperature. This is analogous to the process of fuel decomposition reactions that produce CH_2O (seen as the rising branch of CH_2O JPDF profiles), which is then followed by the oxidization of CH_2O at high temperature (seen as the decreasing branch of CH_2O JPDF profiles). The shift of the temperature of the peak CH_2O concentration toward lower temperature with increasing jet speed indicates that the fuel decomposition has been accelerated by the enhanced transport of radicals with stronger turbulence. This is consistent with the decrease in the peak of CH_2O and the decrease of the slopes of the decreasing branch of CH_2O JPDF profiles as jet speed increases. At downstream locations of all the selected flames, the consumption branch of the CH_2O JPDF profiles at high temperatures remains a similar trend, although the distribution departures from the corresponding laminar profile. Contrarily, the rising branch at low temperatures in the CH_2O JPDF profiles due to fuel decomposition is greatly reduced or in some region has even completely disappeared. This is owing to that the dominant fuel decomposition process has been completed at the upstream locations where CH_2O is generated. Then, CH_2O is transported by the flow to the downstream locations. Using a simultaneous four species (OH, CH, CH_2O and toluene as the fuel tracer) PLIF measurements under similar flame conditions, Sjoholm et al. [59] showed that the fuel is mainly located in the inner region enclosed by the CH_2O, and less amounts of fuel exists at the downstream ($x/d > 20$) overlapping with the distributed CH_2O. This suggests that the disappearance of the rising branch in the CH_2O JPDF profiles is attributed to the absence of fuel in the downstream locations.

It is interesting to note that the high concentration of CH_2O is mostly located within the area delimited by the red curve; the chance of finding CH_2O at $T > 1600$ K is low as CH_2O will be quickly consumed at high temperatures. At x/d = 45, CH_2O mostly exists within the temperature range from 1100 K to 1500 K. Note that

most OH radials also exist in the same temperature range at the same axial location as shown in Fig. 10. There is a small fraction of probability to find CH_2O in the low temperature region ($T < 1100$ K) for the flame LUPJ1-418, which is not observed in the flame LUPJ1-330. This difference is associated with specific observations for flame LUPJ1-418 and will be discussed in Section 4.3.3. For further details, the averaged radial profiles of CH_2O, OH and temperature for the flames with different jet speeds are presented in Supplement 2 as a reference.

It has been shown in Figs. 7 and 8 that distributed HCO/CH radicals can be substantially overlapped with CH_2O at $x/d > 35$. Therefore, it is expected that distributed HCO/CH radicals exist in the same temperature range (1100–1500 K) as CH_2O. In a flame similar to LUPJ1-165 but with a smaller pilot flame (20 mm in diameter), Li et al. [8] has demonstrated that the top of the flame can be completely quenched due to significant heat loss by the ambient air entrainment, which is contrary to the observation of a broadened reaction zone at the top of the flame in LUPJ1-165

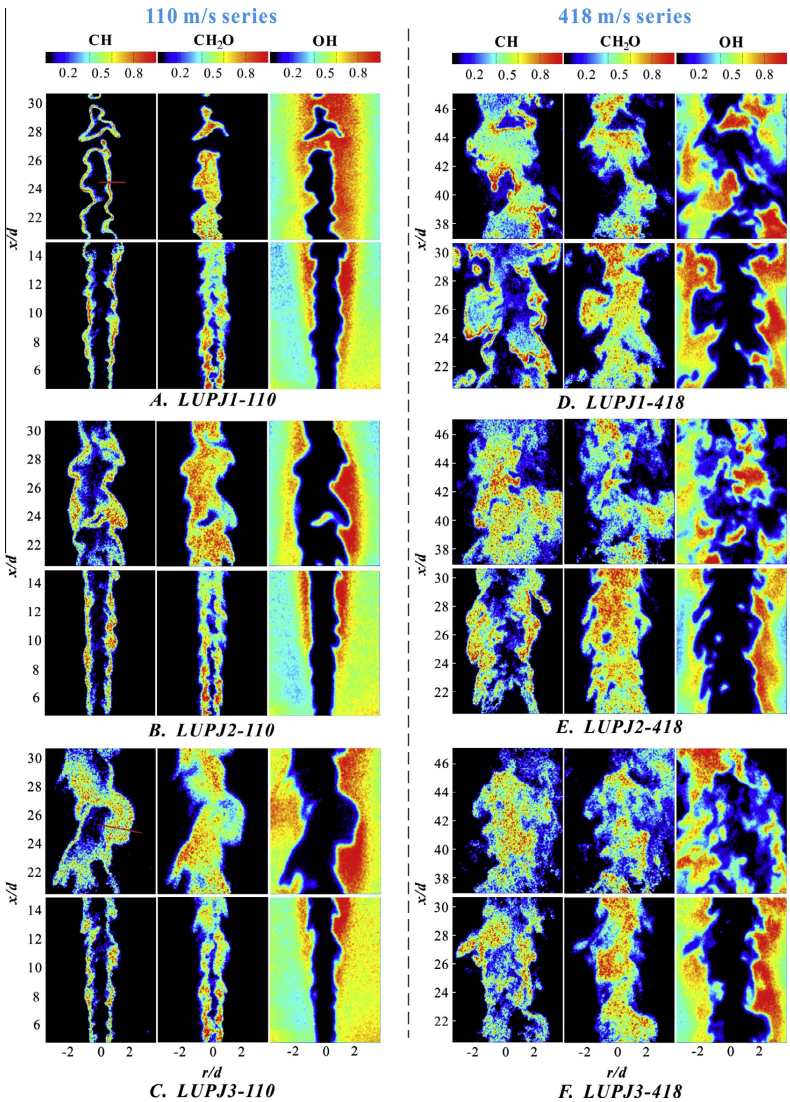

Fig. 12. Examples of equivalence ratio dependence for two given jet speeds, 110 m/s (left column) and 418 m/s (right column) from the CH/CH_2O/OH series.

(cf. Figs. 7(B) and 8(B)). This difference indicates that temperature is important in promoting the distributed reactions. Within the temperature range from 1100 K to 1500 K, the temperature is above the cross-over temperature which sustains the flame from extinction, while being sufficiently low so that the oxidization reactions do not proceed as quickly as that in a laminar flame.

4.3.2. Equivalence ratio dependence

As noted in Tables 1 and 2, S_L decreases and δ_L increases when reducing the equivalence ratio from stoichiometric to fuel lean conditions. It is expected that the penetration of turbulence eddies into the inner layer becomes easier at fuel lean conditions. Snapshots of simultaneous PLIF of CH/CH_2O/OH in an axial symmetric plane in turbulent flames for two given jet speeds, 110 m/s and 418 m/s, are shown in Fig. 12. For the 110 m/s series shown in Fig. 12(A–C), as the equivalence ratio varies from 1.0 to 0.4 and Ka_{30} from 70 to 261, the inner layer marked by CH is first thin (LUPJ1-110, cf. Fig. 12(A)) and then gradually broadened (LUPJ2/3-110, Fig. 12(B and C)). The flame LUPJ2-110 displayed in Fig. 12(B) shows the onset of a distorted CH layer with corresponding Ka_{30} = 113. As shown in Fig. 12(C), the CH layer in the flame LUPJ3-110 is significantly broadened, while it can also still remain thin in some part at the same axial location, suggesting significant variation of the length scale of turbulence in space. Profiles of the measured species along the red short lines across the flame front, as indicated in Fig. 12(A) and (C), are plotted in Fig. 13. As expected, flame LUPJ1-110 shows a typical flamelet structure similar to the one measured in a laminar flame (cf. Fig. 6). However, the flame LUPJ3-110 shows a distributed reaction where the CH region is significantly broader than that in a laminar flame. Consistent with the JPDF plots discussed in the previous section, a small amount of OH radicals was found in the CH_2O region due to turbulence eddy transport. In all flames, the reaction zone broadening appears to be accompanied with the transport of a small amount of OH radicals into the unburned regions. In addition, it is noteworthy that the flame LUPJ3-66 (data not shown) also exhibits a broadened CH layer similar to the flame LUPJ3-110 with corresponding Ka_{30} = 135.

For the 418 m/s flame series shown in Fig. 12(D–F), all presented flames show features of the distributed reaction zone. A noticeable difference among them is found at the interface where OH and CH_2O overlap. For the flame LUPJ1-418, the interface generally corresponds to a strong CH signal with a relative sharp gradient, indicating relatively intensive local reactions that produce CH. However, such local strong CH signal is less clear for flames LUPJ2-418 and LUPJ3-418, for which the CH signals are rather smoothly distributed with no obvious appearance of sharp CH gradients. This difference is attributed to the decreased Damköhler (Da) number, and therefore the reduced reactivity among those flames. Similar distributions from the HCO/CH_2O/OH datasets have been observed, and examples of simultaneous HCO/CH_2O/OH PLIF measurements can be found in Supplement 3. In addition, averaged radial profiles of CH_2O, OH as well as temperature for the flames with 110 m/s jet speed and various equivalence ratios can be found in Supplement 4.

To summarize, all the studied flame conditions listed in Tables 1 and 2 are plotted in the turbulent Reynolds number versus equivalence ratio diagram in Fig. 14. Based on the observation of the broadened HCO/CH layer in flames as shown in Figs. 7, 8 and 12, it appears that for all studied cases the critical Ka_{30} number above which the HCO/CH layer becomes broadened is rather close to the value of 100. This is shown in Fig. 14 by the dashed iso-line of Ka = 100 that separates the TRZ and the DRZ regimes. This is consistent with the dimensional scaling of Peters [3]. On the other hand, as discussed in Section 4.3.1.1, one should also note that, apart from the local Ka number, the local length scales of turbulence as well as the streamwise history effect in practical flames will also influence the determination of the boundary between the TRZ and DRZ regime. Thus caution has to be taken when interpreting the boundary of Ka = 100.

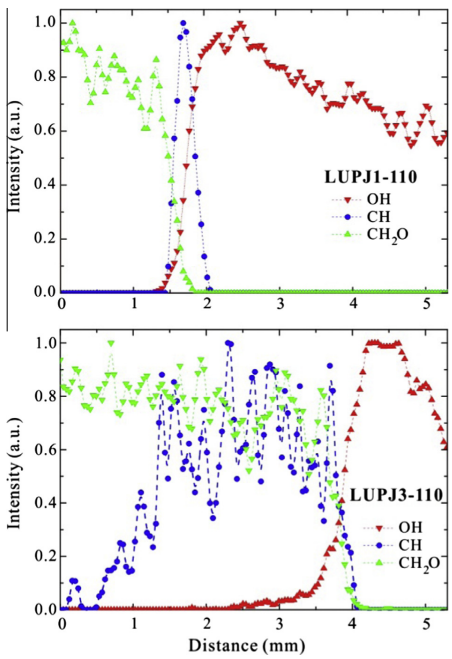

Fig. 13. Profiles of measured species across the flame front for flames LUPJ1-110 and LUPJ3-110. Note the clear CH broadening observed for flame LUPJ3-110 burning under distributed reaction conditions.

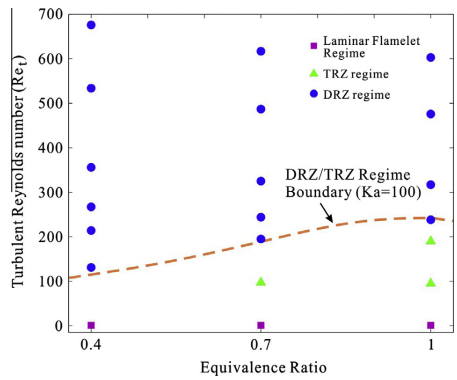

Fig. 14. Turbulent Reynolds number versus Equivalence ratio diagram for all studied flames. An iso-intensity line of Ka = 100 is shown as a boundary that separates the TRZ and the DRZ regimes.

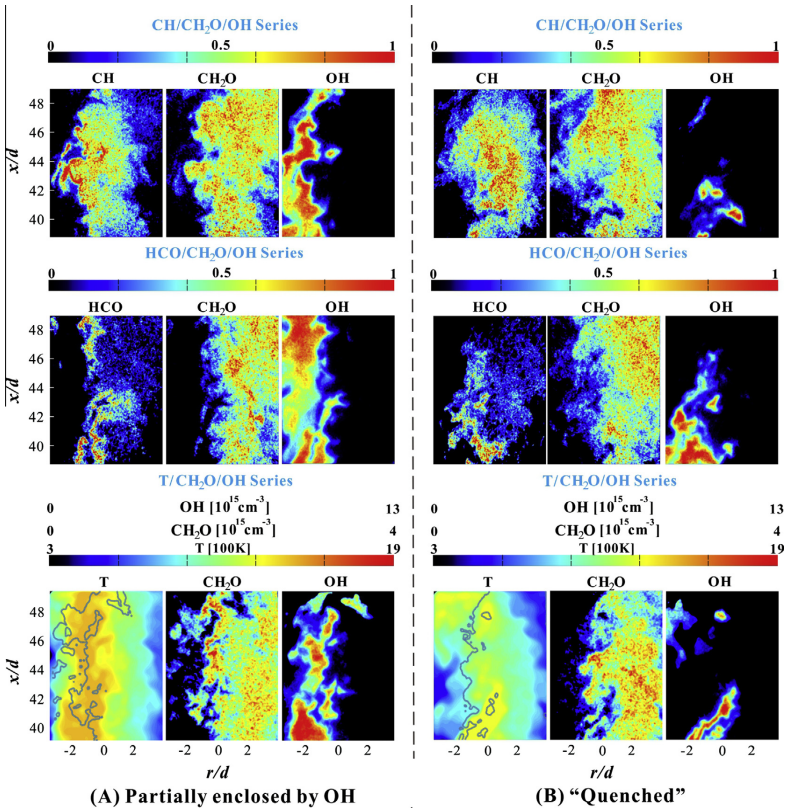

Fig. 15. Examples of simultaneous images of HCO/CH_2O/OH, CH/CH_2O/OH and *T*/CH_2O/OH series measured on the top of flame LUPJ1-418 with (A) flame partially enclosed by OH and (B) "quenched". Iso-intensity (10% of maximum) contours of CH_2O were superimposed on the temperature fields for comparison. Note the distributed CH, HCO and CH_2O exist when OH is quenched.

4.3.3. Flame tip structures

From the flamelet point of view, a local quenching of a flame can be experimentally verified by the observation of a broken reaction zone. A global quenching could be identified as the absence of, e.g. OH radicals, which is likely associated with complete termination of high temperature chemical reactions. However, for cases in the DRZ regime, the definition of "flame quenching" appears to be unclear. Some indications similar to "flame quenching" are observed, specifically at the top of the flames with the 418 m/s jet speed. For example, in the flames LUPJ1/2/3-418 illustrated in Figs. 7(D), 8(D) and 12(D–F), distributed CH, HCO and CH_2O were mostly fully enclosed by OH radicals. In contrast, due to the cold-air entrainment, it is shown in Fig. 15 that the top of the flame can also occasionally either be (A) partially enclosed by OH and (B) nearly absent of OH (termed as "quenched" in the figure). Note that the local *Ka* number might change significantly under such conditions due to the cold-air entrainment. From the CH/CH_2O/OH, HCO/CH_2O/OH and *T*/CH_2O/OH series shown in Fig. 15, one can see that the overall temperature of case (B) was found to be lower than the one of case (A) due to the stronger cold ambient air entrainment in case (B). It is not surprising that in both cases CH_2O is always leaking through the region without OH due to the lack of consumption mechanisms when the temperature is low [8]. This corresponds to the observed small portion of CH_2O at the lower temperature region in the JPDF plot (LUPJ1-418, $x/d = 45$) of Fig. 11. However, it is interesting to note that CH/HCO radicals can survive and appear distributed in both cases. Unlike CH_2O, CH and HCO are expected to be rapidly oxidized through reactions with, for example O_2, which is expected to exist widely in space. Analysis of chemical kinetics shows that the CH/HCO radicals can be completely oxidized by O_2 within the order of magnitude of ten nanoseconds. Such a short resident time prohibits any significant transport by turbulence or diffusion. Therefore, the CH/HCO radicals must be generated locally through reactions. Both HCO and CH radicals can appear in a large area where OH radicals are almost invisible, while the HCO radicals appear to be more concentrated on the OH/CH_2O interface than the CH radicals. According to the different reaction paths discussed in Section 4.3.1, the CH radicals are generated mainly through reaction R(1) that involves H radicals, while reaction R(2) that involves H radicals only partially contributes to the generation of HCO radicals. An appreciable amount of HCO is generated through R(3) that involves OH.

Therefore, it is expected that OH and H radicals might have different spatial distributions at least at the top of the flames LUPJ1/2/3-418 when "local quenching" happens; H radicals might still exist when OH radicals are low or absent, and H radicals could also be spread wider in space than OH radicals. Without OH radicals, H radicals will still contribute to the generation of CH and HCO. When OH radicals are available at some locations, the reaction R(3) will be predominantly responsible for the generation of HCO radicals. This issue remains to be explored in future experiments and numerical simulations.

5. Concluding remarks

The present paper reports an experimental investigation of a series of premixed methane/air flames with different jet speeds and equivalence ratios, covering the laminar flamelet regime, the thin reaction zone (TRZ) regime, and the distributed reaction zone (DRZ) regime. Three series of simultaneous laser-induced planar measurements of reactive scalars and temperature, i.e. CH/CH_2O/OH, HCO/CH_2O/OH and T/CH_2O/OH, have been performed. The flow field of the investigated flames was characterized using LDA (laser Doppler anemometry) measurements. The jet speed and equivalence ratio dependences of the flame behavior have been investigated. The major findings of the observation specifically for the flames in the DRZ regime are summarized in the following:

- It is observed that in the DRZ regime short-lived radicals, CH and HCO, can exist widely in space where OH is almost disappeared. This suggests a potentially different distribution of radicals such as OH, H and O than they are in the flamelet and the thin reaction zone regimes. OH radicals, and likely also other radicals such as H and O, are shown to be transported by turbulence eddies into the low temperature regions, which is responsible for the significant broadening of the reaction zone as marked by the observed broad distributions of CH/HCO. The results are consistent with recent direct numerical simulation studies of high Ka number flames [57,58].
- The term "local quenching" in the distributed reaction zone regime appears to be more reaction and radical specific. This could be explained by the increased availability of radicals through turbulent mixing which enhances/activates reactions that were spatially restricted in the flamelet manifolds.
- Temperature appears to be important for sustaining combustion in the DRZ regime. In the present studied flames, the observation of distributed reactions (marked by distributed HCO and CH) can be assigned to a temperature range approximately from 1100 K to 1500 K.
- Reducing the equivalence ratio from stoichiometry to fuel lean decreases the laminar flame speed and promotes the occurrence of distributed reaction to happen with lower jet speed (i.e. lower turbulence level). This is consistent with the effect of temperature on the onset of DRZ regime.
- The present results have shown a boundary for the DRZ regime to occur, which is rather close to $Ka = 100$. However, care has to be taken when interpreting this boundary. In the present cases the turbulence quantities at the location of peak turbulence intensity ($x/d = 30$) has been used to evaluate the Karlovitz number and other flame parameters. It is found that Karlovitz number peaks at $20 < x/d < 30$ and then decreases along the flame height along with an increase of the shear layer thickness of the jet. The broadening of the CH/HCO layers, thus the boundary of the DRZ regime is not only merely a function of the local Karlovitz number but also depends on the length scales of the shear layer and the history effect of upstream flame broadening.

Acknowledgments

The authors acknowledge financial support from the Swedish Energy Agency through CECOST (Centre for Combustion Science and Technology) and the Swedish-Chinese collaboration project (Project No. 33305-1), the Swedish Research Council, the Knut & Alice Wallenberg foundation and the European Research Council Advanced Grant the DALDECS program.

Appendix A. Supplementary material

Supplementary data associated with this article can be found, in the online version, at http://dx.doi.org/10.1016/j.combustflame.2014.12.021.

References

[1] R. Borghi, Prog. Energy Combust. Sci. 14 (1988) 245–292.
[2] N. Peters, Proc. Combust. Inst. 21 (1988).
[3] N. Peters, Turbulent Combustion, Cambridge University Press, Cambridge, 2000.
[4] A.N. Lipatnikov, J. Chomiak, Prog. Energy Combust. Sci. 28 (2002) 1–74.
[5] K. Seshardri, N. Peters, Combust. Flame 81 (1990) 96–118.
[6] I.G. Shepherd, R.K. Cheng, T. Plessing, C. Kortschik, N. Peters, Proc. Combust. Inst. 29 (2002) 1833–1840.
[7] L.P.H. de Goey, T. Plessing, R.T.E. Hermanns, N. Peters, Proc. Combust. Inst. 30 (2005) 859–866.
[8] Z.S. Li, B. Li, Z.W. Sun, X.S. Bai, M. Aldén, Combust. Flame 157 (2010) 1087–1096.
[9] K. Yamamoto, S. Isii, M. Ohnishi, Proc. Combust. Inst. 33 (2011) 1285–1292.
[10] K.H.H. Goh, P. Geipel, F. Hampp, R.P. Lindstedt, Proc. Combust. Inst. 34 (2013) 3311–3318.
[11] D. Veynante, J.M. Duclos, J. Piana, Proc. Combust. Inst. 25 (1994).
[12] R. Sankaran, E.R. Hawkes, J.H. Chen, T.F. Lu, C.K. Law, Proc. Combust. Inst. 31 (2007) 1291–1298.
[13] J.A. van Oijen, G.R.A. Groot, R.J.M. Bastiaans, L.P.H. de Goey, Proc. Combust. Inst. 30 (2005) 657–664.
[14] R.W. Bilger, Prog. Energy Combust. Sci. 26 (2000) 367–380.
[15] S.B. Pope, Proc. Combust. Inst. 34 (2013) 1–31.
[16] F.T.C. Yuen, Ö.L. Gülder, Proc. Combust. Inst. 32 (2009) 1747–1754.
[17] M.J. Dunn, A.R. Masri, R.W. Bilger, R.S. Barlow, Flow Turbul. Combust. 85 (2010) 621–648.
[18] M.J. Dunn, A.R. Masri, R.W. Bilger, Combust. Flame 151 (2007) 46–60.
[19] B. Coriton, J.H. Frank, A.G. Hsu, M.D. Smooke, A. Gomez, Proc. Combust. Inst. 33 (2011) 1647–1654.
[20] J. Savre, H. Carlsson, X.S. Bai, Flow Turbul. Combust. 90 (2013) 325–341.
[21] A.J. Aspden, M.S. Day, J.B. Bell, J. Fluid Mech. 680 (2011) 287–320.
[22] S.S. Shy, C.C. Liu, W.T. Shih, Combust. Flame 157 (2010) 341–350.
[23] D.J. Micka, J.F. Driscoll, Combust. Flame 159 (2012) 1205–1214.
[24] Y.C. Chen, N. Peters, G.A. Schneemann, N. Wruck, U. Renz, M.S. Mansour, Combust. Flame 107 (1996) 223–244.
[25] Y.C. Chen, M.S. Mansour, Appl. Phys. B – Lasers Opt. 64 (1997) 599–605.
[26] W. Meier, X.R. Duan, P. Weigand, Proc. Combust. Inst. 30 (2005) 835–842.
[27] B. Zhou, C. Brackmann, Z.S. Li, M. Alden, X.-S. Bai, Proc. Combust. Inst. 35 (2015) 1409–1416.
[28] J.E. Temme, T.M. Wabel, A.W. Skiba, J.F. Driscoll, 52nd Aerospace Sciences Meeting, 2014.
[29] S.B. Pope, M.S. Anand, Proc. Combust. Inst. 20 (1985) 403–410.
[30] K.N.C. Bray, Proc. R. Soc. – Math. Phys. Sci. 451 (1995) 231–256.
[31] F.A. Williams, Combustion Theory, Addison-Wesley, 1985.
[32] R.W. Bilger, S.B. Pope, K.N.C. Bray, J.F. Driscoll, Proc. Combust. Inst. 30 (2005) 21–42.
[33] J.F. Driscoll, Prog. Energy Combust. Sci. 34 (2008) 91–134.
[34] B. Zhou, J. Kiefer, J. Zetterberg, Z.S. Li, M. Aldén, Combust. Flame 161 (2014) 1566–1574.
[35] Z.S. Li, J. Kiefer, J. Zetterberg, M. Linvin, A. Leipertz, X.S. Bai, M. Aldén, Proc. Combust. Inst. 31 (2007) 727–735.
[36] J. Kiefer, F. Ossler, Z.S. Li, M. Aldén, Combust. Flame 158 (2011) 583–585.
[37] R.W. Dibble, V. Hartmann, R.W. Schefer, W. Kollmann, Exp. Fluids 5 (1987) 103–113.
[38] Gregory P. Smith, David M. Golden, Michael Frenklach, Nigel W. Moriarty, Boris Eiteneer, Mikhail Goldenberg, C. Thomas Bowman, Ronald K. Hanson, Soonho Song, William C. Gardiner, V.V. Lissianski Jr., Z. Qin. http://www.me.berkeley.edu/gri_mech/.
[39] J.A. Sutton, J.F. Driscoll, Opt. Lett. 29 (2004) 2620–2622.
[40] M.J. Dunn, A.R. Masri, Appl. Phys. B – Lasers Opt. 101 (2010) 445–463.
[41] C.D. Carter, R.S. Barlow, Opt. Lett. 19 (1994) 299–301.
[42] P.H. Paul, J. Phys. Chem. 99 (1995) 8472–8476.
[43] M. Tamura, P.A. Berg, J.E. Harrington, J. Luque, J.B. Jeffries, G.P. Smith, D.R. Crosley, Combust. Flame 114 (1998) 502–514.

[44] J. Luque, D.R. Crosley, in: SRI International Report MP 99-009, 1999.
[45] C. Brackmann, J. Nygren, X. Bai, Z.S. Li, H. Bladh, B. Axelsson, I. Denbratt, L. Koopmans, P.E. Bengtsson, M. Aldén, Spectrochim. Acta Part a – Mol. Biomol. Spectrosc. 59 (2003) 3347–3356.
[46] T. Metz, X. Bai, F. Ossler, M. Aldén, Spectrochim. Acta Part a – Mol. Biomol. Spectrosc. 60 (2004) 1043–1053.
[47] D.I. Shin, T. Dreier, J. Wolfrum, Appl. Phys. B – Lasers Opt. 72 (2001) 257–261.
[48] Y. Yamasaki, A. Tezaki, Appl. Phys. B – Lasers Opt. 80 (2005) 791–795.
[49] C. Brackmann, J. Bood, M. Aldén, G. Pengloan, O. Andersson, Combust. Sci. Technol. 178 (2006) 1165–1184.
[50] C.M. Western, University of Bristol Research Data Repository, 2014.
[51] F.A. Williams, Prog. Energy Combust. Sci. 26 (2000) 657–682.
[52] I.B. Ozdemir, N. Peters, Exp. Fluids 30 (2001) 683–695.
[53] C. Kortschik, T. Plessing, N. Peters, Combust. Flame 136 (2004) 43–50.
[54] B. Bohm, J.H. Frank, A. Dreizler, Proc. Combust. Inst. 33 (2011) 1583–1590.
[55] C.J. Mueller, J.F. Driscoll, D.L. Reuss, M.C. Drake, M.E. Rosalik, Combust. Flame 112 (1998) 342–358.
[56] A.M. Steinberg, J.F. Driscoll, Combust. Flame 156 (2009) 2285–2306.
[57] H. Carlsson, R. Yu, X.-S. Bai, Int. J. Hydrogen Energy 39 (2014) 20216–20232.
[58] A.J. Aspden, M.S. Day, J.B. Bell, Proc. Combust. Inst. 35 (2015) 1321–1329.
[59] J. Sjoholm, J. Rosell, B. Li, M. Richter, Z.S. Li, X.S. Bai, M. Alden, Proc. Combust. Inst. 34 (2013) 1475–1482.

Paper IV

SAE INTERNATIONAL

2015-24-2454
Published 09/06/2015

High-Speed Particle Image Velocimetry Measurement of Partially Premixed Combustion (PPC) in a Light Duty Engine for Different Injection Strategies

Zhenkan Wang and Slavey Tanov
Lund University

Hua Wang
Dantec Dynamics A/S

Mattias Richter, Bengt Johansson, and Marcus Alden
Lund University

CITATION: Wang, Z., Tanov, S., Wang, H., Richter, M. et al., "High-Speed Particle Image Velocimetry Measurement of Partially Premixed Combustion (PPC) in a Light Duty Engine for Different Injection Strategies," SAE Technical Paper 2015-24-2454, 2015, doi:10.4271/2015-24-2454.

Abstract

It has been proven that partially premixed combustion (PPC) has the capability of high combustion efficiency with low soot and NOx emissions, which meet the requirements of increasingly restricted emission regulations. In order to obtain more homogenous combustion and longer ignition delay in PPC, different fuel injection strategies were employed which could affect the fuel air mixing and control the combustion. In the present work, a light duty optical diesel engine was used to conduct high speed particle image velocimetry (PIV) for single, double and triple injections with different timings. A quartz piston and a cylinder liner were installed in the Bowditch configuration to enable optical access. The geometry of the quartz piston crown is based on the standard diesel combustion chamber design for this commercial passenger car engine, including a re-entrant bowl shape. The severe image distortions caused by the optical piston shape are minimized through recordings of reference targets and an image dewarping algorithm. To the authors knowledge this is the first time the flow field inside such realistic re-entrant piston bowl has been mapped through high speed PIV. PRF 70 was used as fuel in these measurements. The in-cylinder flow field was evaluated and investigated with high temporal and spatial resolution to provide additional understanding of the fuel air mixing process. Formation of the vortices and turbulence enhance the air fuel interaction. The vector field of 40 consecutive cycles, mean velocity, and turbulence kinetic energy were calculated and evaluated. All the results based on PIV experiment also provide a quantitative dataset being useful for model validation of the computational fluid dynamics (CFD) simulation of this PPC engine.

Introduction

Partially premixed combustion (PPC) or premixed charge compression ignition (PCCI) has been investigated and developed for several years since it has potential for high brake efficiency in combination with very low soot and NOx emissions that meet the requirements of the restricted emission regulations nowadays [1,2,3,4,5,6,7,8,9,10,11,12,13,14,15,16,17].

The gasoline like fuel, which has a high resistance to auto-ignition, could be used in a compression ignition (CI) diesel engine to reduce the soot and NOx [3, 4, 5, 9, 17, 18, 19, 20, 21, 22, 23, 24, 25, 26]. Peak combustion temperature will be low due to the exhaust gas recirculation (EGR) which leads to low NOx emission whereas the dominant premixed combustion makes less soot [27]. In our previous studies [5, 7, 10, 11, 14, 19, 25, 28, 29], by using optimal research octane number (RON) fuel, EGR and injection strategies, high engine performance and low emissions could be achieved with PPC. The long ignition delay (ID) in PPC engines is very crucial. Controllable ID in PPC is one of the distinguished advantages compared to HCCI and it is the key to control the combustion phasing as well. The ignition delay is defined as the time difference or the crank angle between start of the final fuel injection and start of combustion (SOC) [36]. ID is affected by many parameters in the engine, such as injection strategies, EGR rate, intake temperature, intake pressure, compression ratio, fuel type, engine speed and load etc.

If every engine parameter is kept constant except injection strategies, the ignition delay could be controlled by different start of injection (SOI) timings or multiple injections with large amount of EGR in PPC [4, 28, 30,31,32,33,34,35,36]. This is because the mixing process of fuel and air is affected by different injection strategies and this in turn can have an effect on the ID.

In other words, long ID could enhance the fuel air mixing, since there is more time available for mixing of fuel and air. For example, different SOI timings and multiple injection strategies which affects the turbulent mixing rates were investigated by Y. Hanho and R. Reitz [22, 23, 31]. F. Zhang *et al.* have demonstrated lower emissions by using different multiple injection strategies with dieseline fuel in a PPCI engine as a consequence of the higher volatility fuel which enhances the fuel air mixing and promotes the premixed combustion [37]. N. Dronniou *et al.* utilized and optimized multiple injection strategies together with high level of EGR to largely decrease the soot emission without the side effects of increasing NOx and fuel consumption [30]. G. Kalghatgi also pointed out that multiple injection strategies combined with optimal SOI timings and injector geometry resulting in better mixture can reduce fuel consumption, noise and the emissions such as NOx, soot, CO and HC [4]. In addition, triple injections were investigated and used to aggravate the premix and to reduce soot emissions in PPC by Y. Ra [12], G. Kalghatgi [20], V. Manente [29], and M. Sellnau [35, 38].

In order to aid the understanding of mixture preparation in PPC, particle image velocimetry (PIV) was employed. Particle image velocimetry (PIV) as a non-intrusive laser diagnostics is a prominent option and mature tool for mapping flow fields. It is based on Mie-scattering of light from seeding particles and recording of two sequenced images from which the velocity vector fields can be calculated by cross-correlation [39]. PIV was first used to investigate flow fields in the 1980s. For instance, R. Adrian *et al* used pulsed laser velocimetry (PLV), an early stage of the PIV method, to measure the velocity of particles in a turbulent flow [40]. In recent engine measurements, PIV was frequently applied to get the 2D in-cylinder flow structures [41,42,43,44,45,46,47,48,49,50]. One of the first applications in engine velocity measurement by PIV was conducted by D. Reuss *et al.* [41]. H. Nordgren *et al.* investigated swirl flow structure in horizontal plane in the combustion chamber of a diesel engine by PIV [52]. G. Valentino *et al.* used PIV to study the swirl flow structures correlated with the emissions for different injection strategies, in which the swirling structure changed significantly due to the injection strategies [53]. L. Hildingsson *et al.* investigated in-cylinder mixing process which is important in PRE-mixed lean Diesel Combustion (PREDIC) due to both high EGR levels and limited time available for the mixing [46, 54]. P. Miles *et al.* studied velocity field in a light duty direct-injection diesel engine together with simulations for both motored and fired engine conditions. Both large-scale structures in the vertical plane and the distribution of angular momentum were obtained [55]. They also managed to show a very evident agreement between experiment and simulations.

Regarding the PIV measurement in PPC engines, P. Miles *et al.* measured vertical plane velocity fields which describes the bulk flow structures in a light duty diesel engine with re-entrant optical piston bowl shape to evaluate the fuel air mixture and the production of emissions [56]. The measured velocity fields also indicate the locations of heat release [57]. F. Perini *et al.* made up a model and validated it with PIV experiment in different horizontal planes to study the mixture preparation for PPC in a light duty diesel engine [58]. The PIV performed in their research work was based on a traditional 10 Hz PIV system.

However, the averaged flow field obtained from many cycles at a specific CAD with widely used 10-Hz double-cavity Nd:YAG laser could contain the fluctuation of cycle-to-cycle variations (CCV) as well. And CCV is common and inevitable in internal combustion engines [59,60,61,62,63,64]. For example, D. Towers used high speed PIV to quantitatively study the cyclic variability [64]. Lately, cycle-to-cycle variations were observed in an optical engine through Proper orthogonal decomposition (POD) by K. Bizon *et al.* [65]. CCV in a diesel engine with multiple injection strategies were also investigated by K. Bizon *et al.* [66, 67, 68].

Thus the best way to investigate or avoid the effect of CCV in the optical engine is to use high speed imaging to obtain a full data set, covering the desired CAD range, from a single cycle.

M. Reeves and D. Towers studied cycled-resolved 2-D flow field and CCV by means of high speed PIV and high speed digital cameras [64, 69]. C. Fajardo *et al.* used 355 nm wavelength laser to perform UV PIV in a fired spray-guided spark-ignition direct-injection (SIDI) engine with cycle-resolved flow field [70]. P. Abraham *et al.* improved dynamic range of velocity and spatial resolution while using high speed PIV to study in-cylinder flow [71]. Other recent examples where high speed PIV was employed to obtain the in-cylinder flow field in internal combustion engines can be found in reference [72, 73, 74].

In light duty diesel engines the turbulence created by fuel injection and by bulk flow structures enhances small-scale mixing [75]. This also applies to the PPC engines in which the injection strategies and piston bowl geometry will affect the ID according to the turbulence and mixing level generated.

However the complexity of mixing processes affecting ID and the emissions in PPC or PCCI has not been explored so much. In this work, cycle-resolved high speed PIV will be utilized in a light duty optical PPC engine with different injection strategies. The geometry of the quartz piston crown is based on the standard diesel combustion chamber designed for this passenger car engine, including a re-entrant bowl shape.

The objective of the paper is to investigate the influence of different injection strategies on in-cylinder flow field and fuel air interaction and mixing with this kind of combustion chamber design. It is obvious that triple injections is quite different from double or single injections, but the magnitude in e.g. induced turbulence is not well known. In this paper, the differences between injection strategies and their effects on the in-cylinder flow and air fuel interaction will be investigated.

To the authors' knowledge, this is the first time high speed PIV has been implemented in a PPC engine with such realistic piston bowl shape. The in-cylinder flow field in the combustion chamber with high temporal and spatial resolution was investigated to aid the understanding of the fuel air mixing. Ensemble average flow field and cycle-resolved fluctuations of instantaneous velocity, namely turbulence, was evaluated and compared for different injection strategies as well.

The measurements in this paper were performed with fuel injection but without combustion. This was achieved by means of ultra-high EGR levels. Some related PIV results with combustion cases can be

found in a companion paper by S. Tanov *et al.* [76]. All the results based on PIV experiments also provide quantitative validation and prominent support to computational fluid dynamics (CFD) modeling of PPC engines.

Experiment Setup

Optical Engine

The high speed PIV measurement was employed in a Volvo D5 light duty optical diesel engine. Detailed engine configuration and information could be found in the literature [3, 46, 47, 54, 56, 77, 78, 79]. The specification of the engine is shown in Table 1. The original engine was modified to a Boditch-design single-cylinder engine with 480 cm^3 displacement. The stock cylinder head was retained almost unaltered with only minor modifications of the cooling system, such as water and oil recirculation. In order to enable the optical access inside the piston bowl region, a quartz piston and cylinder liner replaced the metal ones in this engine. The injection system contains a Bosch common rail fuel injection system and a 5-hole Solenoid Bosch injector with a spray-angle of 140°.

A blended fuel, PRF 70, consisting of 30% n-heptane and 70% iso-octane in volume percentage was used in the experiment to achieve suitable ignition delay for PPC. However, in order to have only injection events without any combustion, the EGR level was set to very high. This was achieved by an external burner providing CO_2 as the EGR source. As a result, the O_2 concentration was below 8% to ensure no ignition in the engine. Results obtained with combustion can be found in a related work by S. Tanov *et al.* [76].

A high speed camera was also used to visualize possible chemiluminescence inside the combustion chamber as a double-check. No chemiluminescence signal was detected after the injection or during the expansion stroke.

Table 1. Engine specifications.

Engine type	Light-duty diesel engine
Number of valves	4
Bore	81 mm
Stroke	92.3 mm
Connecting rod	147 mm
Displacement	480 cm^3
Compression ratio	1:11.3
Swirl ratio	2.6
Engine speed	800 rpm
Fuel type	PRF 70
Common rail pressure	500 bar
Injector type	5-hole Solenoid, 140° VCO
Injector orifice diameter	159 µm
Intake temperature, T_{in}	80 °C ± 2 °C
Intake pressure, P_{in}	1.14 bar ± 0.02 bar
Intake O_2	< 8 vol. %
Cooling water temperature	70 °C ± 1 °C

The diameter of the optical piston bowl is 42 mm. The geometry of the quartz piston crown is based on the standard diesel combustion chamber design for this passenger car engine, including a re-entrant bowl shape. The re-entrant piston bowl geometry and combustion chamber configuration were described in previous studies [46, 56, 57]. By using the re-entrant piston bowl, the investigation and results are relevant to a realistic environment similar to the production engine.

PIV System

Figure 1 and Figure 2 illustrate the high speed PIV experimental setup which is similar to the one used by P. Miles *et al.* for performing 10 Hz PIV measurements [46, 56, 57]. In this high speed PIV measurement, a commercial diode-pumped double-cavity Nd:YLF high speed laser (model type: DualPower 30-1000) was utilized. It was synchronized with the engine speed at every 2 crank angle degrees (CADs) by a cyclic synchronization timing box. The pulse energy of the PIV laser was about 11 mJ/pulse for each cavity, measured by a power meter. A diverging laser sheet with 25 mm height and less than 1 mm thickness in the field of view was generated by light sheet optics. Concerning the out-of-plane motion by the swirl, the laser sheet should not be too thin. However, a thick laser sheet would create some perspective errors [80]. The upper edge of the laser sheet was aligned with the roof of combustion chamber as shown in Figure 2. The injector nozzle used had 5 holes. Thereby the laser sheet was hitting one of the spray plumes as shown in the top-view of Figure 2. All the measurements in this work were made with a vertical laser sheet which is the tumble plane.

A high speed CMOS camera (SpeedSense 710) was placed at another side of the optical liner, perpendicular to the laser sheet, to capture the PIV images as shown in Figure 1 and Figure 2. Because of the symmetric feature of the combustion chamber, the field of view was set to cover only half of the piston bowl area and squish region. The camera, which was synchronized with the laser through the use of a cyclic synchronization timing box, can get double frames for every 2 CADs. The resolution of the camera was set to 1040 * 440 pixels to achieve a frame rate that match the frequency of the engine.

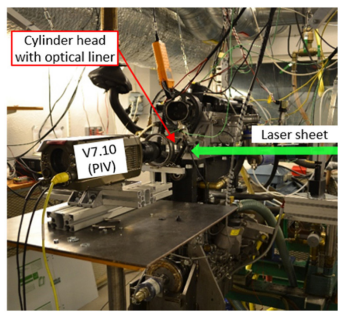

Figure 1. Picture of PIV experiment setup.

The time difference between two laser pulses was 20 µs. It's a trade-off between more accurate vectors in the full range of anticipated velocities and the time interval as pointed out by P. Miles *et al.* [46]. Hence, after enough trials, the out-of-plane motion was proved to show less impact within this time interval and the maximum particle displacement was less than one quarter of the interrogation window size. The latter is important since the error rises if the displacement increases too much [81].

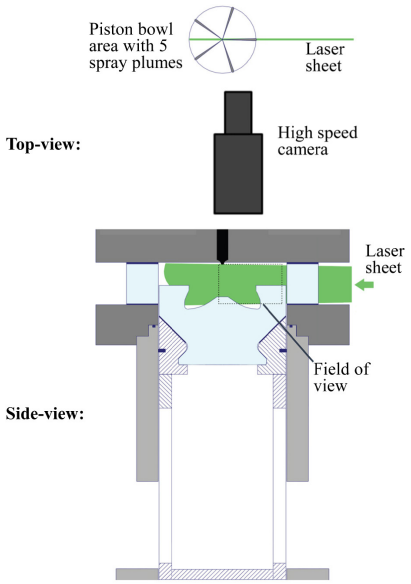

Figure 2. schematic diagram of PIV experiment setup.

A Nikon (AF Nikkor) f=105 mm visible-light lens with an extension ring (Nikkor PK-13) were mounted on the high speed camera used for capturing the PIV images. In order to compromise between the distortion/de-focusing effects caused by the re-entrant piston bowl shape and the signal to noise ratio, the aperture of camera lens was set to f#16. The geometrical distortion can be compensated in post-processing by image dewarping as discussed in a later section. The long readout time for the first frame of the camera can cause background interference on the second frame [48, 82]. However, in this experiment the exposure time was 66 µs for the first image and about 350 µs for the second image. Providing this short exposure time during the measurement, the background interference was largely limited. Therefore no additional filter or mechanical shutter was used.

Titanium dioxide (TiO_2) powder from Struers Company was used as PIV seeding particles. It was dried in the oven over 24 hours at 110 °C to prevent them from aggregating. The diameter of the TiO_2 particle is around 2.5 µm and its density is 4260 kg/m^3. For the thermodynamic conditions near top dead center (TDC), the particle time constant (τ) is roughly 40 µs. Under such conditions, τ is slightly larger than Kolmogorov time scale which indicates the seeding particles are able to follow the flow structure and the turbulence. The seeding particles were supplied by an aluminium cylindrical container with tangential inlet flow which generate strong swirl and turbulent flow inside to get uniform seeding particles in the air. The outlet of the container was connected to the intake manifold where seeding particles were mixed together with intake air and EGR. The EGR was supplied by the exhaust gas from an external burner burning conventional (MKI) diesel at stoichiometric conditions to produce mainly CO_2 and water vapour. Due to the water vapour in the EGR, static electricity of the particles was reduced. As a result, the chance of adhesion to the internal surfaces of the optical engine, such as piston bowl and cylinder liner was alleviated. The flow rate of seeding was controlled by a Bronkhorst mass flow controller (MFC) with 13 ln/min which was found to be an optimal value for this engine speed.

Operation Conditions

Besides the bulk flow structures, spray injection also influences the in-cylinder turbulence which leads to the changing of ID. Therefore, the impact on the flow field was investigated for several different injection strategies in this study.

Table 2. High speed PIV measurement conditions for different injection strategies.

Case	Injection strategy	SOI (bTDC)	Injection duration (µs)
S16	Single	16	600
S24	Single	24	600
D53-17	Double	53/17	600/390
D35-17	Double	35/17	600/390
D45-24	Double	45/24	600/390
D52-14	Double	52/14	600/390
D52-20	Double	52/20	600/390
T63-30-17	Triple	63/30/17	470/360/350
T63-30-12	Triple	63/30/12	470/360/350
Motored	No injection	-	-

Table 2 depicts 10 cases including no injection (motored case), single, double and triple injections at different SOI timings in this study. These conditions were found to have very low COV of IMEP for PPC mode under different injection strategies with combustion event. The engine was heated to a cooling water temperature of 70 °C and the intake pressure and temperature were 1.14 bar and 80 °C, respectively. These settings mimic the conditions prevailing when the engine was operated with combustion. For each case, 40 consecutive cycles were recorded and evaluated. The engine thermal conditions were kept constant throughout the measurements, as shown in Table 1.

Post Processing

Image Dewarping

The application of a re-entrant piston bowl, inevitably results in severe image distortions. However, the geometrical distortions could be minimized through the recording of reference targets and careful dewarping of the PIV images. By using Matlab software with local-weighted-mean algorithm, two images with and without distortion were compared and the distorted image were corrected accordingly. P. Miles *et al.* performed such distortion correction successfully and detailed information can be found in reference [56, 57]. An example of a recorded image before and after distortion correction can be seen in the appendix, Figure 29 and companion paper by S. Tanov *et al.* [76].

PIV Vector Evaluation

After the correction of the distorted images, the flow field vectors were calculated by a commercial PIV software provided by Dantec Dynamics [39]. This adaptive PIV could iteratively adjust IA size, shape and orientation according to the result of iterations [81]. The IA size could

vary from 64 * 64 pixels to 16 * 16 pixels in order to adapt large range of particle movement. Due to severe distortion in the bottom area of the piston bowl it was impossible to perform the corrections in this region. Hence, a mask was used when calculating the velocity vectors and all the vectors outside of the mask were set to zero.

As mentioned above, the laser sheet was aligned with one spray plume. When the spray appears in the interested evaluation area, it's possible to use the fuel droplets scattering to calculate the PIV result [81], and to derive the flow field of spray.

Results and Discussion

Turbulence plays an important role in internal combustion engines, as it influences the flame front propagation speed [60]. Since high speed PIV experiment was performed in a light duty PPC engine for different injection strategies which includes single, double and triple injections at different SOI timings, two kinds of evaluation will be conducted to investigate the in-cylinder flow field and turbulence in the combustion chamber. The first evaluation is ensemble average method in which the averaged velocity can be firstly obtained based on 40 cycles and the fluctuation of mean velocity, namely turbulence, could be calculated and evaluated afterwards.

In order to consider the cycle to cycle variations of the engine, ensemble average and turbulence calculated based on it cannot perfectly represent the in-cylinder flow feature of turbulence, because the turbulence by the calculation with ensemble average contains not only the information about the turbulence of the in-cylinder flow but also the content of cyclic variability. The other evaluation is cycle-resolved average method in which the CCV is excluded when calculating the turbulence. The turbulence kinetic energy (TKE) as a representative of turbulence according to Tennekes and Lumley [83], is calculated and discussed. Since the PIV data was collected every 2 CADs, the interval for all data analysis is 2 CADs correspondingly.

Ensemble Average and Turbulence

In this study, PIV measurement data from 40 consecutive cycles were obtained. Hence, the ensemble average analysis could be calculated based on these 40 cycles. The definition of ensemble average $\overline{U}_{EA}(\theta)$ is

$$\overline{U}_{EA}(\theta) = \frac{1}{N}\sum_{i=1}^{N} U(\theta, i) \tag{1}$$

Where U means instantaneous velocity, θ indicates the CAD, i is the operator which means cycle index and N is the number of cycles.

The turbulence, which is based on the ensemble averaged velocity discussed above, could be the expressed by the standard deviation of the instantaneous velocity relative to the ensemble average velocity.

$$u'_{EA}(\theta) = \sqrt{\frac{1}{N}\sum_{i=1}^{N}[U(\theta, i) - \overline{U}_{EA}(\theta)]^2} \tag{2}$$

The fluctuation could be treated as the extent for distribution of instantaneous velocity from each cycle around mean velocity and that is indicated as turbulence.

Motored case

As mentioned above, there was no injection in the motored case. Figure 3 represents the ensemble averaged results of motored cycles with every 2 CAD interval. The direction of the vector illustrates the direction of the flow and the color of the vector indicates the magnitude of the flow speed in Figure 3. They are the same for all other flow field figures in the paper. From 20 CAD before top dead center (bTDC) to 10 CAD bTDC, the direction of mean flow field was towards upward, which means the flow in the piston bowl was driven by the piston motion. At 8 CAD bTDC, part of the in-cylinder flow inside piston goes into the squish volume. Due to the squish-swirl flow interaction, a clockwise vortex was observed in the re-entrant piston bowl from 6 CAD bTDC to TDC. This is very close to what P. Miles *et al.* found in a direct injection (DI) diesel engine with similar re-entrant bowl shape piston [57, 84].

After TDC position the vortex was mitigated and moving to the upper position of the piston bowl area. The flow direction is kind of arbitrary. That means the small-scale turbulence was enhanced while large-scale flow structure such as bulk flow structure was weakened. At 8 CAD after top dead center (aTDC), one clockwise vortex coexisted with another counter-clockwise vertical structure in the piston bowl. At 14 CAD aTDC, the reverse-squish flow emerged. Due to no combustion and no volume expansion in this case, reverse-squish flow maintained very little amount as expected. The main flow structure followed piston motion when piston was descending during expansion stroke.

In general, the results of ensemble averaged flow field indicate that the PIV measurements and evaluation show good agreement with the previous study by P. Miles *et al.* [57] under similar conditions.

Cycle-resolved average and turbulence

By means of the high speed measurement, it's possible to resolve the turbulence in one cycle, and hence obtain cycle-resolved results. In such case, the impact from cycle to cycle variations could be prevented during the calculation.

Cycle-resolved turbulence could be expressed as equation (3).

$$u'(\theta, i) = \sqrt{\frac{1}{M}\sum_{j=1}^{M}\left[U\left(\theta + \frac{2j - M - 1}{2}\Delta\theta \cdot F, i\right) - \overline{U}(\theta, i)\right]^2} \tag{3}$$

Where U is instantaneous velocity, θ indicates the CAD, i means cycle index, $\Delta\theta$ is the CADs between each piston positions involved in the calculation, and j is an operator.

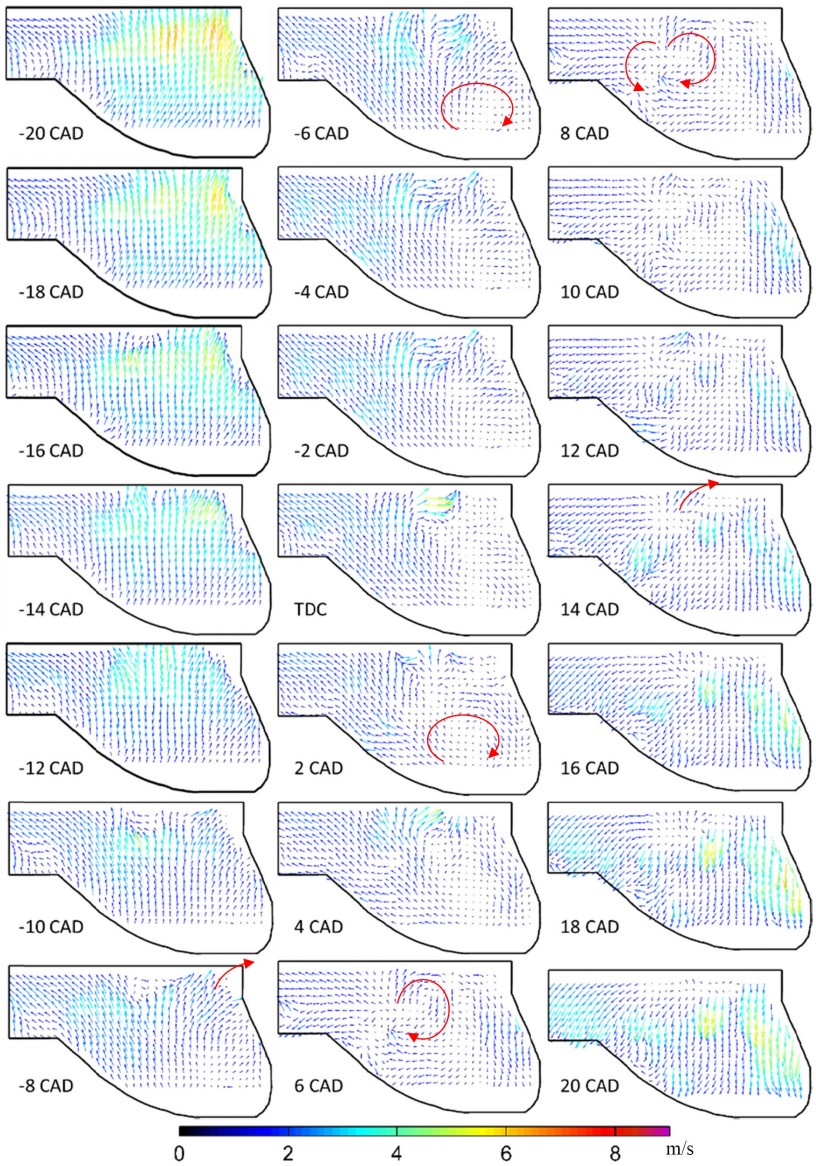

Figure 3. ensemble averaged flow field of motored case.

In equation (3) the number of total steps between CADs should be even. That means the number of total different CAD positions involved in the calculation, namely M, should be odd. For example, four steps are chosen for calculation so that the velocity of −2, −1, 0, +1, +2 CAD, these five piston positions will be calculated to get the turbulence at 0 CAD position. Here M equals to five and $\Delta\theta$ is 1 CAD.

F is used to separate odd number and even number of M. The expression is

$$F = \frac{(-1)^{M+1} + 1}{2} \tag{4}$$

M should be an odd number and hence F equals to 1.

In equation (3), $\overline{U}(\theta, i)$ is the sine weighted moving averaged (SWMA) velocity of the instantaneous velocities in M*$\Delta\theta$ CADs. M*$\Delta\theta$ CADs are the window size of the calculation.

$$\overline{U}(\theta, i) = \frac{1}{M}\sum_{j=1}^{M} \frac{C(j)}{C(j)^G} \cdot U(\theta + \frac{2j - M - 1}{2}\Delta\theta \cdot F, i) \tag{5}$$

In equation (5), G is another function to separate odd number and even number.

$$G = \frac{(-1)^M + 1}{2} \tag{6}$$

C(j) is the weight factor in equation (5). Here it is sine weighted.

$$C(j) = \frac{\sin(\frac{j}{M+1}\pi)}{\sum_{j=1}^{M}\sin(\frac{j}{M+1}\pi)} \qquad j = 1,2,\cdots,M \tag{7}$$

$$\sum C(j) = 1 \tag{8}$$

The averaged velocity in equation (5) considers the influence of turbulence in upstream and downstream because turbulence is not an independent event. It cannot suddenly appear and disappear.

Total number of step(s) calculated for averaged velocity is equal to *M* - 1. Namely, $\frac{M-1}{2}$ steps before the center point whose instantaneous velocity is *U*(*θ*, *i*) and the same amount of steps after the center point were gathered together and averaged by SWMA method to obtain the cycle-resolved averaged velocity at θ CAD in cycle number i.

In our case, $\Delta\theta$ is 2 CAD and M is 5. That means instantaneous velocities of 5 CAD positions including 2 steps before *U*(*θ*, *i*), 2 steps after *U*(*θ*, *i*) and *U*(*θ*, *i*) itself were used totally to calculate the average velocity in these 5 piston positions (window size is 10 CADs) for $\overline{U}(\theta, i)$ at θ CAD and cycle number i.

The mean value of cycle-resolved SWMA velocity at each CAD for all the cycles could be expressed as

$$\overline{U}_c(\theta) = \frac{1}{N}\sum_{i=1}^{N} \overline{U}(\theta, i) \tag{9}$$

For an IA, the turbulence of horizontal and vertical directions could be express as ${u'}_{x,y}$ and ${v'}_{x,y}$, respectively. They could be derived by equation (3). x and y indicate the position of different interrogation areas in the piston bowl.

The TKE in an IA could be express as

$$TKE_{x,y} = \frac{1}{2}\left({u'}_{x,y}{}^2 + {v'}_{x,y}{}^2\right) \tag{10}$$

The averaged TKE, $\overline{TKE}$, hence could be extracted from the individual TKE of all the cycles.

$$\overline{TKE} = \frac{1}{N}\sum_{i=1}^{N} TKE_i \tag{11}$$

Where N is the number of total cycles.

The same as calculating the velocity vector in PIV flow vector evaluation, the mask was used in TKE calculation as well.

Motored case

Mean velocity of cycle-resolved averaged velocity, $\overline{U}_c(\theta)$ for motored case is similar to ensemble averaged velocity at different CADs. Because there was no combustion event in the experiment, CCV was very low. More information of motored case $\overline{U}_c(\theta)$ is provided in the Appendix.

Different SOI timings

The ensemble averaged flow field and cycle-resolved TKE of 9 cases under different injection strategies were investigated to study the turbulence and flow field in the PPC engine. All these injection strategies were performed in a fired PPC light duty diesel engine as well. However, as mentioned earlier this paper will only focus on the results obtained without combustion.

Single injection cases

Figure 4 describes the averaged TKE of motored case and single injection cases from −20 CAD bTDC to 20 CAD aTDC. It's evident that the motored case has the lowest TKE as expected.

Before TDC, the TKE of the motored case increased with CAD and it reached the maximum value near TDC. That is because the squish flow interacted with the swirl flow inside the cylinder. When the piston is moving upward and approaching TDC, the flow in the squish volume is compressed and pushed into the piston bowl. The kinetic energy increasing ratio is $(B/D)^2$ as described by J. Heywood [60]. B is the bore diameter and D represents the piston bowl diameter. The re-entrant shape of piston bowl redirected the flow which was squeezed by the shrink of squish volume and generated a bulk flow structure inside piston bowl. With the ascending of piston, the bulk flow structure broke down and turbulence increased.

From TDC to 10 CAD aTDC, the large-scale flow structure such as swirl flow has been broken down and the turbulence starts to dissipate with the descending motion of the piston. And the reverse-squish flow is another source of decreasing the TKE as well. After 10 CAD, the turbulence level keeps almost constant with the piston motion.

TKE of single injection cases, case S16 and case S24, have much higher value than that of motored case in Figure 4. At 20 CAD bTDC and 18 CAD bTDC, TKE of case S16 has the same level as motored case.

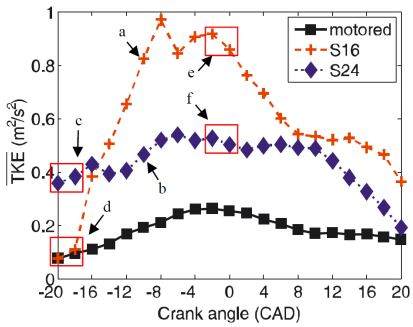

Figure 4. cycle-resolved averaged TKE of motored case, S16 case and S24 case.

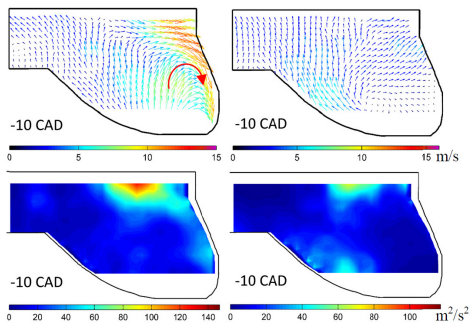

Figure 5. ensemble averaged flow field and cycle-resolved averaged TKE for case S16 (left column, point a in Figure 4) and case S24 (right column, point b in Figure 4).

The point a, b, c, d, e and f in Figure 4 are presented into ensemble averaged flow field and cycle-resolved averaged TKE for both case S16 and case S24 as shown in Figure 5, 6, 7.

For case S16, SOI of the injection occurred at 16 CAD bTDC. The spray plume entered directly into the piston bowl region and impinged on the wall of piston bowl as it was observed by Mie-scattering recorded with high speed PIV camera. The spray itself carries a lot of flow momentum and TKE during the injection event. It also introduces a great deal of turbulence via air entrainment, turbulent diffusion and evaporation of volatile fuel [84]. Thus, after the injection event in case S16, TKE increased rapidly and attained the maximum value at 8 CAD bTDC. The TKE of case S16 is fairly higher than that of case S24 and motored case. The amount of TKE caused by the injection was dominant during the compression stroke.

The bulk flow structure generated by the injection created a clockwise vertical vortex in the piston bowl as shown in Figure 5 as point a in Figure 4. It moved the low angular momentum fluid from the central part of the piston bowl toward the bowl periphery. Similar findings were reported by P. Miles *et al.* [84]. In Figure 5, the TKE of case S16 at 10 CAD bTDC is much higher than that of case S24 at the same piston position. The area of high TKE values in case S16 has the same spatial distribution as the bulk flow structure as shown in the left column in Figure 5.

Nevertheless, for case S24, because of its early SOI time (SOI at 24 CAD bTDC), there was not bulk flow structure at 10 CAD bTDC as shown in the right column of Figure 5. However, due to the squish-swirl interaction and injection-swirl interaction, the TKE of case S24 at 10 CAD bTDC was still higher than motored case in Figure 4. The area of large turbulence locates at upper part of the piston bowl area and bottom part of the piston bowl near the piston pip. The bulk flow structure of case S24 when observed at 20 CAD bTDC and 18 CAD bTDC (Figure 4 point d) are presented in Figure 6. Similar to case S16, the area of high TKE values has the same spatial position of bulk flow structure for case S24.

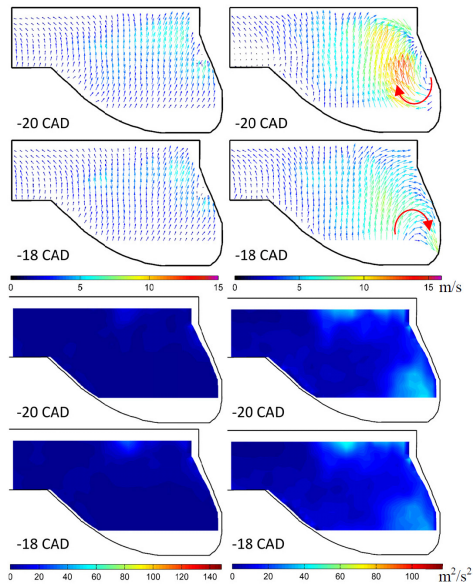

Figure 6. ensemble averaged flow field and cycle-resolved averaged TKE for case S16 (left column, point c in Figure 4) and case S24 (right column, point d in Figure 4).

For this injection timing, observations by Mie-scattering reveled that, part of the spray plume was just hitting on the lip of the piston bowl rim and the rest impinged on the top surface of the piston, i.e. in the

squish volume. This would bring out two issues. One is that some momentum and energy was lost by the impingement which is not as good as for case S16 where the re-entrant piston bowl shape could redirect the spray plume and preserve most of the injection energy. The second issue is that because the spray penetrated a long distance due to the high injection pressure and relatively low in-cylinder pressure, it reached the squish volume and pushed more low angular moment flow towards to the periphery of the cylinder. With the moving of the piston closer to TDC, the high angular momentum flow of fuel and air mixture in the squish volume will enter into the piston bowl following the squish flow that will have higher velocity and generate more turbulence. The swirl ratio of the engine is 2.6 and that keeps the swirl flow inside the cylinder.

The TKE of case S24 decreased a little at 14 and 12 CAD bTDC. That is because the high turbulence flow created by the spray went into squish volume with the ascending motion of piston.

When the piston was approaching TDC, the squish-swirl interaction was more complicated. The centrifugal force exerting on the in-cylinder flow pushed it to the periphery of the piston bowl meanwhile the bulk flow structure brought the in-cylinder flow to the center part of piston bowl. That could explain a count-clockwise vortex occurred together with a clockwise vortex in case S16 while case S24 only had one clockwise vortex near TDC as shown in Figure 7 which represents point e and f in Figure 4. An assumption could be that the bulk flow structure of case S16 is stronger than case S24 and that intensity just pushed the flow to the bottom of piston bowl and deflected the flow nearly towards the upward direction at mean time the centrifugal force pushed this flow along the radial direction and those two motions created the counter-clockwise vortex and clockwise vortex at the same time. In spite of the centrifugal force caused by swirl motion, the flow near the piston pip had too less radius of gyration leading to too little centrifugal force on this amount of flow, so that the flow cannot pierce towards the radial direction and it just followed the direction of bulk flow structure in Figure 7. More detailed investigation of the interaction between swirl and bulk flow was summarized by P. Miles *et al.* [84].

The high TKE occurred at the interface between the counterclockwise vortex and the clockwise vortex in case S16, i.e. in the shear layer between them, and in the shear layer between the tangential flow and the bulk flow.

After the TDC position, the TKE of case S16 decreased quickly due to the turbulence dissipation and reverse-squish flow as shown in Figure 4. The TKE of case S24 had a little increase and then it dropped down after 10 CAD aTDC. Because the TKE introduced by fuel injection in case S16 is much higher than case S24, it remains higher in case S16 than in case S24 also during the expansion stroke.

Comparison between Single and Double Injection Cases

Figure 8 illustrates the TKE versus CAD of case S24 and case D45-24, which represents the single and double injection cases, respectively. Apparently, case D45-24 has less TKE than case S24 as expected. If less fuel was injected into the engine, less amount of turbulence would be generated by the injection event. The injection duration for case S24 was 600 μs while that of second injection in case D45-24 was merely 390 μs although they had same SOI timing. As mentioned above, SOI at 24 CAD bTDC for case S24 led to bifurcating of the spray plume. Part of the spray went into the squish volume while the rest entered into the piston bowl. The second injection of case D45-24 was performed under the same circumstances.

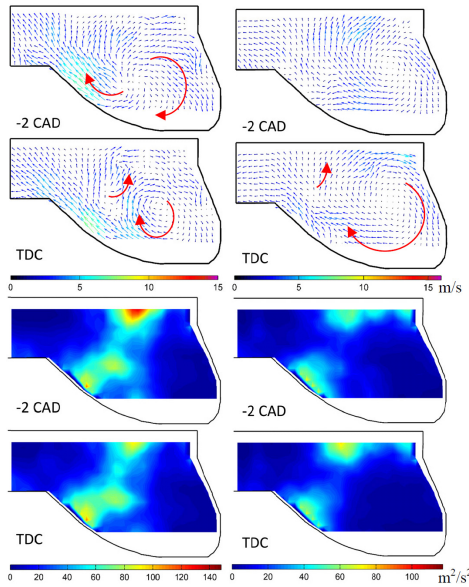

Figure 7. ensemble averaged flow field and cycle-resolved averaged TKE for case S16 (left column, point e in Figure 4) and case S24 (right column, point f in Figure 4).

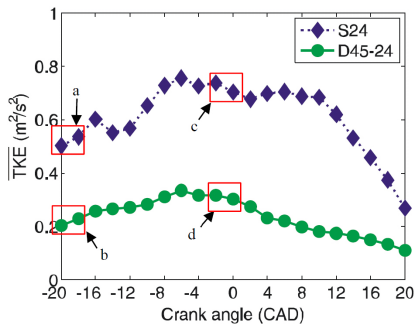

Figure 8. cycle-resolved averaged TKE of case S24 and case D45-24.

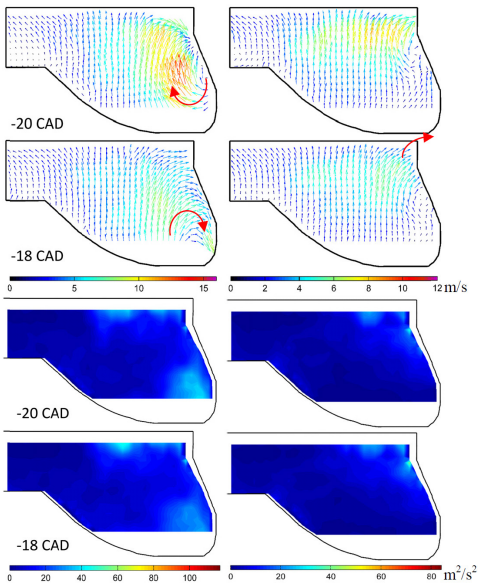

Figure 9. ensemble averaged flow field and cycle-resolved averaged TKE for case S24 (left column, point a in Figure 8) and case D45-24 (right column, point b in Figure 8).

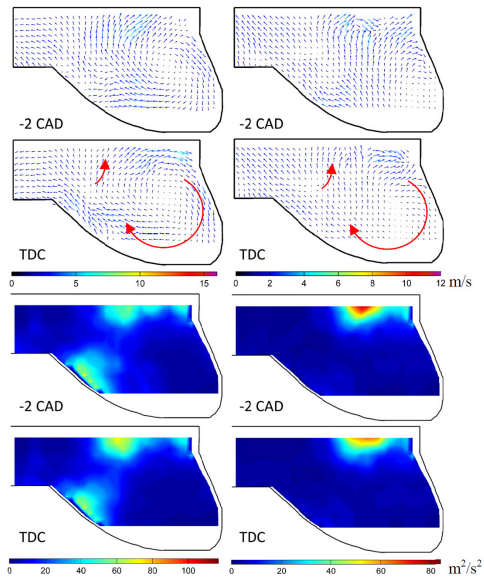

Figure 10. ensemble averaged flow field and cycle-resolved averaged TKE for case S24 (left column, point c in Figure 8) and case D45-24 (right column, point d in Figure 8).

The point a, b, c and d in Figure 8 are extended into ensemble averaged flow field and cycle-resolved averaged TKE for both case S24 and case D45-24 as shown in Figure 9 and Figure 10.

However, due to the lower amount of fuel being injected into the piston bowl for the second injection of case D45-24, the bulk flow structure at 20 CAD bTDC and 18 CAD bTDC was not as strong as for case S24. In Figure 9, the area of high level TKE covered the region of flow structure caused by injection event for case D45-24 which was similar to case S24. Due to less fuel amount, the spray could not penetrate the full distance to the squish volume and therefore it wasn't able to push more low angular moment flow towards the periphery of the cylinder. Hence, case D45-24 did not obtain a rapid increase of TKE as case S24 from 12 to 6 CAD bTDC. The flow field of case D45-24 near TDC looks similar to case S24 as shown in Figure 10. They possess counter-clockwise vertical structure.

Different Injection Durations

Although case D45-24 had double injections and the duration of first injection was 600 µs which is the same as injection duration of single injection in case S24, the TKE level of case D45-24 was still far lower than case S24 in the entire range of 20 CAD bTDC to 20 CAD aTDC. TKE level of case D45-24 was similar to motored case because fuel injection had nearly no influence on the turbulence at this moment.

Thus, it could be concluded that the first injection of case D45-24 at 45 CAD bTDC has very little influence on the turbulence near TDC position. In another word, although the first injection had very large amount of fuel, the turbulence created by it will be consumed and dissipated promptly.

Case S24 and second injection of case D45-24 had same SOI timing but the turbulence of them was different. Thus, the amount of fuel injected at 24 CAD bTDC dominates the TKE level near TDC when it's a double injection strategy.

Comparison between 1st Injections of Double Injection Cases

Figure 11 presents the cycle-resolved TKE for case D53-17 and case D35-17. They had same SOI timing and the same amount of fuel in their second injection. As pointed out in the previous section, the first injection of case D45-24 had very limited influence on the TKE near TDC positions. However, when the SOI timing of the first injection retarded to 35 CAD bTDC, the injection event would raise the TKE level during ascending motion of piston before TDC as shown in Figure 11. The trace sustained quite a few CADs.

Nevertheless, after TDC the TKE levels of case D53-17 and case D35-17 were very close to each other. That means the turbulence created by the first injection was wiped out since they have same second injection. Thus, too early SOI timing of first injection like case D53-17 and case D35-17 has no influence on the turbulence level after TDC. As a result, the second injection of the double injection strategy plays a main role of the TKE level near TDC.

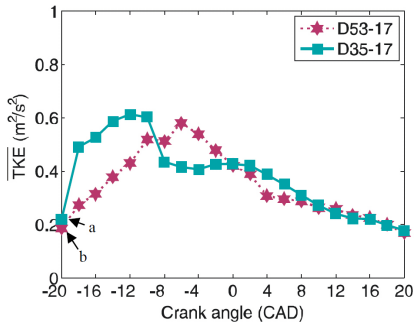

Figure 11. cycle-resolved averaged TKE of case D53-17 and case D35-17.

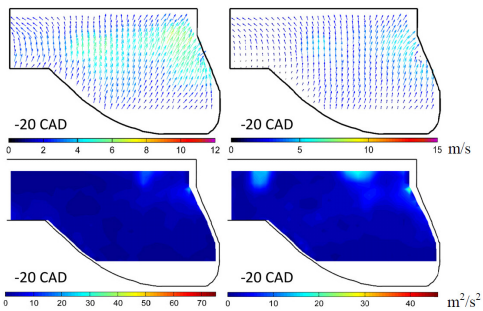

Figure 12. ensemble averaged flow field and cycle-resolved TKE for case D53-17 (left column, point a in Figure 11) and case D35-17 (right column, point b in Figure 11).

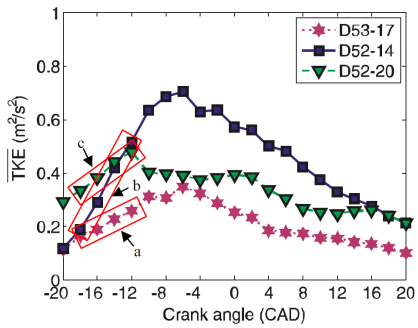

Figure 13. cycle-resolved averaged TKE of case D53-17, case D52-14 and case D52-20.

The shape of TKE in 40 CADs range for case D53-17 resembled case S16 because they had very similar SOI between single injection for case S16 and 2nd injection for case D53-17. The whole amount of fuel inside piston bowl was redirected by the re-entrant shape of the bowl. Due to different amounts of fuel injection, they had several times difference in quantity. But the shape of TKE between case D53-17 and case D35-17 before TDC is quite different. The first injection of case D35-17 affected the TKE level before TDC.

The point a and b in Figure 11 are extended into ensemble averaged flow field and cycle-resolved averaged TKE for both case D53-17 and case D35-17 as shown in Figure 12.The directions of velocity vectors were the similar, mostly pointing upward, as rising of the piston.

Comparison between 2nd Injections of Double Injection Cases

Since too early time of first injection hardly has the effect on the turbulence near TDC, case D53-17, case D52-14 and case D52-20 represented different SOI timings of second injection for double injection strategies in the paper. The cycle-resolved averaged TKE of them is illustrated in Figure 13. As discussed above, the TKE level near TDC depends on the second injection and fuel amount, which means the fuel injection inside the piston bowl mainly control the turbulence in the range of 20 CADs before and after TDC. For case D53-17, SOI timing of 2nd injection was at 17 CAD bTDC while it was 14 CAD bTDC for case D52-14. With later SOI timing, the turbulence imparted by the fuel injection could be retained and TKE level became high as shown in Figure 13. That could explain although the injection duration for case D53-17 and case D52-14 was the same, TKE of case D52-14 was higher than case D53-17 after the SOI.

Surprisingly, SOI time of 2nd injection for case D52-20 was only 3 CADs earlier than case D53-17, but the TKE of case D52-20 was higher than case D53-17. As mentioned before, it was found that for SOI at 24 CAD bTDC in case S24, the spray was hitting on the lip of the piston bowl rim. It's the same for SOI at 20 CAD bTDC in case D52-20 as observed during the experiment. Although SOI of case S24 was at 24 CAD bTDC, the injection duration of it was 1.5 times longer than case D52-20. The moment of the spray was higher and it lasted longer time. Regarding the SOI time and fuel amount between case S24 and case D52-20, it is possible to assume that the fuel entering into the piston bowl in case S24 could be the same magnitude as case D52-20, which leads them to encounter similar circumstances. The TKE of case D52-20 and case S24 have similar shape from 20 CAD bTDC to 12 CAD bTDC. With the injection of fuel, the turbulence increases and the high TKE area covered the turbulence region introduced by the injection event as shown in Figure 14 which represents point a, b and c in Figure 13. Therefore, TKE level of case D52-20 was high at the beginning.

Comparison between 3rd Injections of Triple Injection Cases

Although for case D35-17 SOI of first injection at 35 CAD bTDC retained the influence of TKE level from 20 CAD bTDC until TDC position, the influence disappeared if the injection of fuel amount was very tiny. Thus, TKE level of case D53-17 was close to that of case T63-30-17, which had a second injection at 30 CAD bTDC, as shown in Figure 15. From 20 CAD bTDC to 10 CAD bTDC, the TKE curve of case D53-17 overlaps fairly well with that of case T63-30-17 because both cases had same SOI timing and very similar injection duration for the last injection, namely the second injection for case D53-17 and the third injection for case T63-30-17. Because the fuel amount of case D53-17 was slightly higher than case T63-30-17, the turbulence generated by injection was kept a little longer time than case T63-30-17 and the TKE level of case D53-17 was higher than case

T63-30-17 from 10 CAD bTDC until TDC. After TDC, the turbulence created by injection event extinguished completely and TKE curves of case D53-17 and case T63-30-17 converged together again.

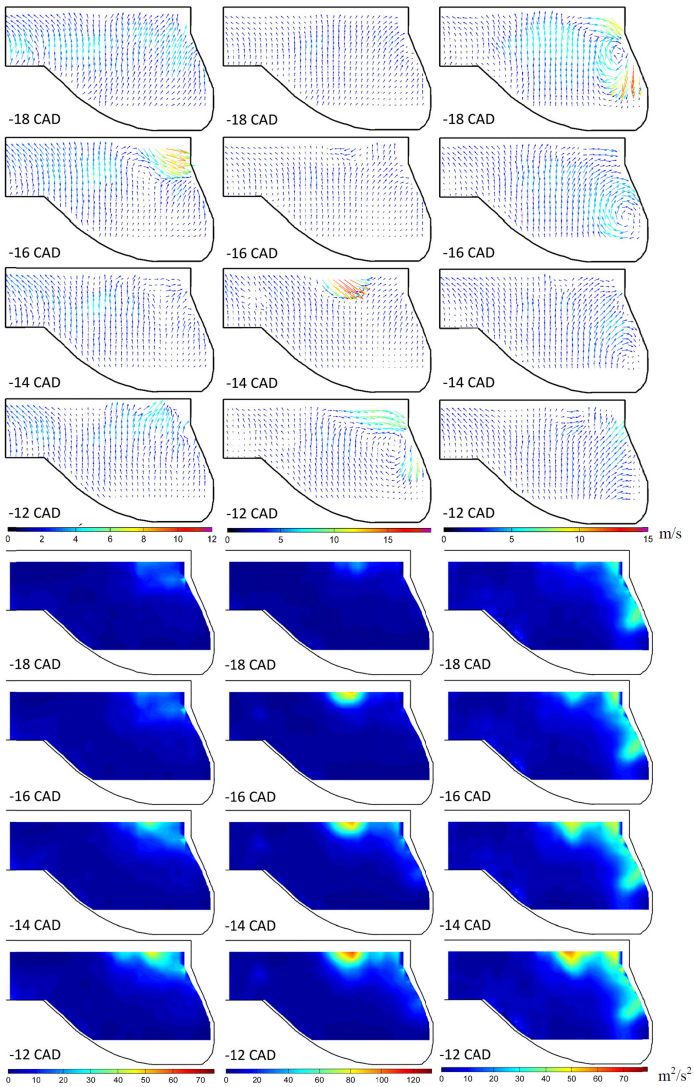

Figure 14. ensemble averaged flow field and cycle-resolved TKE for case D53-17 (left column, point a in Figure 13), case D52-14 (middle column, point b in Figure 13) and case D52-20 (right column, point c in Figure 13.

In Figure 15 the TKE level of case T63-30-12 rose dramatically and reached to the maximum TKE among these three cases. However, after 6 CAD bTDC the TKE decreased quickly to the same level of case D53-17. That is because the injection of fuel amount was too less and the turbulence introduced by it was not dominant source contributing to TKE in the piston bowl. Squish-swirl interaction also influence and control the TKE.

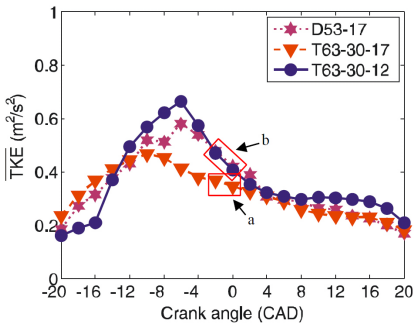

Figure 15. cycle-resolved averaged TKE of case D53-17, case T63-30-17 and case T63-30-12.

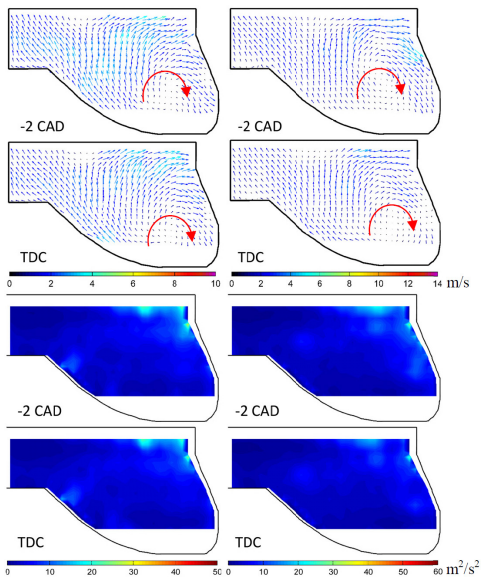

Figure 16. ensemble averaged flow field and cycle-resolved TKE for case T63-30-17 (left column, point a in Figure 15) and case T63-30-12 (right column, point b in Figure 15).

Another evidence could support that explanation is that the flow field and distribution of TKE were very similar to each other between case T63-30-17 and case T63-30-12 as shown in Figure 16. Large-scale bulk flow structure brought about a clockwise vortex inside piston bowl for both cases.

It can be concluded that if too little amount of fuel is injected into the piston bowl that will only influence the turbulence before TDC and such influence will disappear after TDC. The later the SOI, the higher TKE could be obtained before TDC. If SOI was after 17 CAD bTDC, the peak TKE occured near 8 CAD bTDC.

The ignition timing or SOC for PPC is usually near TDC, therefore turbulence after TDC is of less importance and a detailed investigation of this is not within the scope of this paper. With combustion event, the flow field and TKE will be different.

Summary and Conclusions

Cycle-resolved high speed PIV was successfully employed in a light duty optical PPC engine with a re-entrant piston bowl shape for different injection strategies. The re-entrant piston bowl shape is based on the standard diesel combustion chamber design for this passenger car engine. The severe distortions caused by the optical piston shape could be minimized through the recordings of reference targets and careful dewarping of result images. The adaptive PIV method employed in the commercial software which changes the IA size, orientation and shape automatically by the iteration was used to evaluate the flow field.

The ensemble averaged flow field, cycle-resolved mean velocity and TKE of 10 cases were calculated and evaluated, including motored, single, double and triple injection cases. With cycle-resolved evaluation, cycle-to-cycle variation (CCV) could be minimized. The strong interactions between injection and large-scale bulk flow caused by the re-entrant piston bowl shape were observed and discussed. Other interactions such as squish-swirl interaction and swirl-injection interaction also influence the turbulence and TKE in the combustion chamber for this engine. Formation of the vortices and turbulence enhance the air fuel interaction. The result of ensemble averaged flow field for motored case was analyzed and discussed. It has very good agreement with previous study, performed in a similar engine, by P. Miles *et al.* [57].

- For single injection strategies, if the SOI happens after 17 CAD bTDC, the TKE is proportional to the fuel amount injected into the piston bowl. The larger amount of fuel injection increases TKE rapidly as expected. The turbulence created by the injection event is dominant.
- For double injection strategies, the first injection at 45 CAD bTDC has very little influence on the turbulence at 20 CAD bTDC. SOI timing of first injection like 35 CAD bTDC has no influence on the turbulence level after TDC. The second injection of the double injection strategies play a main role of TKE level if the whole spray enters into the piston bowl.
- For double and triple injection strategies, regarding the last injection, if a too small amount of fuel was injected into piston bowl that will only affect the turbulence before TDC and such influence will disappear after TDC. Similar to single injection strategy, the later the SOI, the higher TKE could be obtained and

the more turbulence will be retained before TDC for both double and triple injection strategies, if same amount of fuel is injected.

- For all cases, if SOI begins after 17 CAD bTDC, the peak TKE will occur near 8 CAD bTDC. The turbulence created by the last injection is proportional to the fuel amount of that injection when the spray plume enters into the piston bowl. First and second injection has limited effect and the turbulence created by them will be almost dissipated before SOI of last injection if they happen very early.
- The part of the spray injected into the top-land region, penetrating into the squish volume, could push low angular momentum flow in the center part of the cylinder outwards to help increasing the kinetic energy, and consequentially to maintain high TKE level near TDC.
- Even with 350 μs injection duration, we observed by the Mie-scattering light of the spray that the spray plume still hit on the periphery of piston bowl which could lose the kinetic energy of the injection. Therefore, spray targeting should also be considered because there would be an optimal spray angle and SOI time for this re-entrant piston bowl shape to deflect the spray plume and fuel air mixture flow, and to preserve the TKE introduced by the injection event as much as possible.
- High level of TKE occurs and overlaps at the same spatial position of spray plumes generated by the injection event. Shear layer of two flow vortexes in the flow field also create high TKE level.
- Finally, the results generated constitute an experimental database which provides quantitative validation data to the ongoing computational fluid dynamics (CFD) modeling of PPC.

REFERENCES

1. Hardy, W. and Reitz, R., "A Study of the Effects of High EGR, High Equivalence Ratio, and Mixing Time on Emissions Levels in a Heavy-Duty Diesel Engine for PCCI Combustion," SAE Technical Paper 2006-01-0026, 2006, doi:10.4271/2006-01-0026.
2. Lee, S. and Reitz, R., "Spray Targeting to Minimize Soot and CO Formation in Premixed Charge Compression Ignition (PCCI) Combustion with a HSDI Diesel Engine," SAE Technical Paper 2006-01-0918, 2006, doi:10.4271/2006-01-0918.
3. Noehre, C., Andersson, M., Johansson, B., and Hultqvist, A., "Characterization of Partially Premixed Combustion," SAE Technical Paper 2006-01-3412, 2006, doi:10.4271/2006-01-3412.
4. Kalghatgi, G., Risberg, P., and Ångström, H., "Partially Pre-Mixed Auto-Ignition of Gasoline to Attain Low Smoke and Low NOx at High Load in a Compression Ignition Engine and Comparison with a Diesel Fuel," SAE Technical Paper 2007-01-0006, 2007, doi:10.4271/2007-01-0006.
5. Manente, V., Johansson, B., and Tunestal, P., "Partially Premixed Combustion at High Load using Gasoline and Ethanol, a Comparison with Diesel," SAE Technical Paper 2009-01-0944, 2009, doi:10.4271/2009-01-0944.
6. Kokjohn, S., Hanson, R., Splitter, D., and Reitz, R., "Experiments and Modeling of Dual-Fuel HCCI and PCCI Combustion Using In-Cylinder Fuel Blending," *SAE Int. J. Engines* 2(2):24-39, 2010, doi:10.4271/2009-01-2647.
7. Hildingsson, L., Kalghatgi, G., Tait, N., Johansson, B., and Harrison, A., "Fuel Octane Effects in the Partially Premixed Combustion Regime in Compression Ignition Engines," SAE Technical Paper 2009-01-2648, 2009, doi:10.4271/2009-01-2648.
8. Dec, John E. "Advanced compression-ignition engines-understanding the in-cylinder processes." Proceedings of the Combustion Institute 32, no. 2 (2009): 2727-2742.
9. Manente, V., Zander, C., Johansson, B., Tunestal, P., Cannella, W., "An Advanced Internal Combustion Engine Concept for Low Emissions and High Efficiency from Idle to Max Load Using Gasoline Partially Premixed Combustion," SAE Technical Paper 2010-01-2198, 2010, doi:10.4271/2010-01-2198.
10. Manente, V., Tunestal, P., Johansson, B., and Cannella, W., "Effects of Ethanol and Different Type of Gasoline Fuels on Partially Premixed Combustion from Low to High Load," SAE Technical Paper 2010-01-0871, 2010, doi:10.4271/2010-01-0871.
11. Manente, V., Johansson, B., Tunestal, P., and Cannella, W., "Influence of Inlet Pressure, EGR, Combustion Phasing, Speed and Pilot Ratio on High Load Gasoline Partially Premixed Combustion," SAE Technical Paper 2010-01-1471, 2010, doi:10.4271/2010-01-1471.
12. Ra, Y., Loeper, P., Andrie, M., Krieger, R. et al., "Gasoline DICI Engine Operation in the LTC Regime Using Triple-Pulse Injection," *SAE Int. J. Engines* 5(3):1109-1132, 2012, doi:10.4271/2012-01-1131.
13. Kaiadi, M., Johansson, B., Lundgren, M., and Gaynor, J., "Sensitivity Analysis Study on Ethanol Partially Premixed Combustion," *SAE Int. J. Engines* 6(1):120-131, 2013, doi:10.4271/2013-01-0269.
14. Shen, M., Tuner, M., Johansson, B., and Cannella, W., "Effects of EGR and Intake Pressure on PPC of Conventional Diesel, Gasoline and Ethanol in a Heavy Duty Diesel Engine," SAE Technical Paper 2013-01-2702, 2013, doi:10.4271/2013-01-2702.
15. Won, H., Peters, N., Pitsch, H., Tait, N., and Kalghatgi, G., "Partially Premixed Combustion of Gasoline Type Fuels Using Larger Size Nozzle and Higher Compression Ratio in a Diesel Engine," SAE Technical Paper 2013-01-2539, 2013, doi:10.4271/2013-01-2539.
16. Reitz, Rolf D. "Directions in internal combustion engine research." Combustion and Flame 160, no. 1 (2013): 1-8.
17. Leermakers, C., Bakker, P., Somers, L., de Goey, L. et al., "Commercial Naphtha Blends for Partially Premixed Combustion," *SAE Int. J. Fuels Lubr.* 6(1):199-216, 2013, doi:10.4271/2013-01-1681.
18. Kalghatgi, G., Risberg, P., and Ångström, H., "Advantages of Fuels with High Resistance to Auto-ignition in Late-injection, Low-temperature, Compression Ignition Combustion," SAE Technical Paper 2006-01-3385, 2006, doi:10.4271/2006-01-3385.
19. Manente, V., "Gasoline Partially Premixed Combustion". PhD thesis, Lund Institute of Technology, Lund University, Sweden, 2010.
20. Kalghatgi, G., Hildingsson, L., and Johansson, B. "Low NOx and low smoke operation of a diesel engine using gasoline like fuels." Journal of Engineering for Gas Turbines and Power 132, no. 9 (2010): 092803.

21. Kalghatgi, G., Hildingsson, L., Harrisona, A.J., Johansson, B., "Autoignition quality of gasoline fuels in partially premixed combustion in diesel engines," Proceedings of the Combustion Institute, Volume 33, Issue 2, Pages 3015-3021, 2011, doi:10.1016/j.proci.2010.07.007.
22. Hanson, R., Kokjohn, S., Splitter, D., and Reitz, R., "An Experimental Investigation of Fuel Reactivity Controlled PCCI Combustion in a Heavy-Duty Engine," *SAE Int. J. Engines* 3(1):700-716, 2010, doi:10.4271/2010-01-0864.
23. Dempsey, A. and Reitz, R., "Computational Optimization of Reactivity Controlled Compression Ignition in a Heavy-Duty Engine with Ultra Low Compression Ratio," *SAE Int. J. Engines* 4(2):2222-2239, 2011, doi:10.4271/2011-24-0015.
24. Chang, J., Kalghatgi, G., Amer, A., and Viollet, Y., "Enabling High Efficiency Direct Injection Engine with Naphtha Fuel through Partially Premixed Charge Compression Ignition Combustion," SAE Technical Paper 2012-01-0677, 2012, doi:10.4271/2012-01-0677.
25. Solaka, H., Aronsson, U., Tuner, M., and Johansson, B., "Investigation of Partially Premixed Combustion Characteristics in Low Load Range with Regards to Fuel Octane Number in a Light-Duty Diesel Engine," SAE Technical Paper 2012-01-0684, 2012, doi:10.4271/2012-01-0684.
26. Kalghatgi, G., "Developments in internal combustion engines and implications for combustion science and future transport fuels." Proceedings of the Combustion Institute 35, no. 1 (2015): 101-115.
27. Petersen, B., Ekoto, I., and Miles, P., "An Investigation into the Effects of Fuel Properties and Engine Load on UHC and CO Emissions from a Light-Duty Optical Diesel Engine Operating in a Partially Premixed Combustion Regime," *SAE Int. J. Engines* 3(2):38-55, 2010, doi:10.4271/2010-01-1470.
28. Lewander, M., Ekholm, K., Johansson, B., Tunestål, P. et al., "Investigation of the Combustion Characteristics with Focus on Partially Premixed Combustion in a Heavy Duty Engine," *SAE Int. J. Fuels Lubr.* 1(1):1063-1074, 2009, doi:10.4271/2008-01-1658.
29. Manente, V., Johansson, B., Tunestal, P., Sonder, M., and Serra, S. "Gasoline partially premixed combustion: high efficiency, low NOx and low soot by using an advanced combustion strategy and a compression ignition engine." International Journal of Vehicle Design 59, no. 2 (2012): 108-128.
30. Dronniou, N., Lejeune, M., Balloul, I., and Higelin, P., "Combination of High EGR Rates and Multiple Injection Strategies to Reduce Pollutant Emissions," SAE Technical Paper 2005-01-3726, 2005, doi:10.4271/2005-01-3726.
31. Yun, Hanho, and Reitz Rolf D.. "Combustion optimization in the low-temperature diesel combustion regime." International Journal of Engine Research 6, no. 5 (2005): 513-524.
32. Hanson, R., Splitter, D., and Reitz, R., "Operating a Heavy-Duty Direct-Injection Compression-Ignition Engine with Gasoline for Low Emissions," SAE Technical Paper 2009-01-1442, 2009, doi:10.4271/2009-01-1442.
33. Hildingsson, L., Johansson, B., Kalghatgi, G., and Harrison, A., "Some Effects of Fuel Autoignition Quality and Volatility in Premixed Compression Ignition Engines," *SAE Int. J. Engines* 3(1):440-460, 2010, doi:10.4271/2010-01-0607.
34. Benajes, J., Novella, R., Garcia, A., Domenech, V., and Durrett, R., "An Investigation on Mixing and Autoignition using Diesel and Gasoline in a Direct-Injection Compression-Ignition Engine Operating in PCCI Combustion Conditions," *SAE Int. J. Engines* 4(2):2590-2602, 2011, doi:10.4271/2011-37-0008.
35. Sellnau, M., Sinnamon, J., Hoyer, K., and Husted, H., "Full-Time Gasoline Direct-Injection Compression Ignition (GDCI) for High Efficiency and Low NOx and PM," *SAE Int. J. Engines* 5(2):300-314, 2012, doi:10.4271/2012-01-0384.
36. Solaka, H., Tuner, M., and Johansson, B., "Analysis of Surrogate Fuels Effect on Ignition Delay and Low Temperature Reaction during Partially Premixed Combustion," SAE Technical Paper 2013-01-0903, 2013, doi:10.4271/2013-01-0903.
37. Zhang, F., Xu, H., Zhang, J., Tian, G. et al., "Investigation into Light Duty Dieseline Fuelled Partially-Premixed Compression Ignition Engine," *SAE Int. J. Engines* 4(1):2124-2134, 2011, doi:10.4271/2011-01-1411.
38. Sellnau, M., Sinnamon, J., Hoyer, K., and Husted, H., "Gasoline Direct Injection Compression Ignition (GDCI) - Diesel-like Efficiency with Low CO2 Emissions," *SAE Int. J. Engines* 4(1):2010-2022, 2011, doi:10.4271/2011-01-1386.
39. http://www.dantecdynamics.com/particle-image-velocimetry
40. Adrian, R., Yao, C., Development of pulsed laser velocimetry (PL V) for measurement of turbulent flow. In Proc. Symp. Turbul., pp. 170-186., 1984
41. Reuss, D., Adrian, R., Landreth, C., French, D. et al., "Instantaneous Planar Measurements of Velocity and Large-Scale Vorticity and Strain Rate in an Engine Using Particle-Image Velocimetry," SAE Technical Paper 890616, 1989, doi:10.4271/890616.
42. Reuss, D., Kuo, T., Khalighi, B., Haworth, D. et al., "Particle Image Velocimetry Measurements in a High-Swirl Engine Used for Evaluation of Computational Fluid Dynamics Calculations," SAE Technical Paper 952381, 1995, doi:10.4271/952381.
43. Reuss, D., "Cyclic Variability of Large-Scale Turbulent Structures in Directed and Undirected IC Engine Flows," SAE Technical Paper 2000-01-0246, 2000, doi:10.4271/2000-01-0246.
44. Funk, C., Sick, V., Reuss, D., and Dahm, W., "Turbulence Properties of High and Low Swirl In-Cylinder Flows," SAE Technical Paper 2002-01-2841, 2002, doi:10.4271/2002-01-2841.
45. Deslandes, W., Dupont, A., Baby, X., Charnay, G. et al., "PIV Measurements of Internal Aerodynamic of Diesel Combustion Chamber," SAE Technical Paper 2003-01-3083, 2003, doi:10.4271/2003-01-3083.
46. Hildingsson, L., Hultqvist, A., and Miles, P. C., "The Effect of Swirl and Injection Phasing on Flow Structures and Mixing in an HSDI Diesel Engine," THIESEL, 2006.
47. Colban, W., Ekoto, I., Kim, D., and Miles, P. C., "In-Cylinder PIV Measurements in an Optical Light-Duty Diesel at LTC Conditions," THIESEL, 2008.
48. Petersen, B. and Miles, P., "PIV Measurements in the Swirl-Plane of a Motored Light-Duty Diesel Engine," SAE Int. J. Engines 4(1):1623-1641, 2011, doi:10.4271/2011-01-1285.

49. Karhoff, D., Bücker, I., Dannemann, J., Klaas, M. et al., "Experimental Analysis of Three-Dimensional Flow Structures in Two Four-Valve Combustion Engines," SAE Technical Paper 2011-24-0044, 2011, doi:10.4271/2011-24-0044.
50. Heim, D. and Ghandhi, J., "A Detailed Study of In-Cylinder Flow and Turbulence using PIV," *SAE Int. J. Engines* 4(1):1642-1668, 2011, doi:10.4271/2011-01-1287.
51. Binjuwair, S., Ibrahim, S., Wigley, G., and Pitcher, G., "In-Cylinder Flow Structure Analysis by Particle Image Velocimetry Under Steady State Condition," SAE Technical Paper 2012-01-1975, 2012, doi:10.4271/2012-01-1975.
52. Nordgren, H., Hildingsson, L., Johansson, B., Dahlén, L. et al., "Comparison Between In-Cylinder PIV Measurements, CFD Simulations and Steady-Flow Impulse Torque Swirl Meter Measurements," SAE Technical Paper 2003-01-3147, 2003, doi:10.4271/2003-01-3147.
53. Valentino, G., Allocca, L., and Marchitto, L., "PIV Investigation of High Swirl Flow on Spray Structure and its Effect on Emissions in a Diesel-Like Environment," SAE Technical Paper 2011-01-1286, 2011, doi:10.4271/2011-01-1286.
54. Hildingsson, Leif. "Laser Diagnostics of HCCI and Partially Premixed Combustion". PhD thesis, Lund Institute of Technology, Lund University, Sweden, 2006.
55. Miles, P., Megerle, M., Sick, V., Richards, K. et al., "The Evolution of Flow Structures and Turbulence in a Fired HSDI Diesel Engine," SAE Technical Paper 2001-01-3501, 2001, doi:10.4271/2001-01-3501.
56. Miles, P.C., Collin, R., Hildingsson, L., Hultqvist, A. Andersson, Ö., "Combined measurements of flow structure, partially oxidized fuel, and soot in a high-speed, direct-injection diesel engine," Proceedings of the Combustion Institute, 31 II, pp. 2963-2970. doi:10.1016/j.proci.2006.07.231
57. Miles Paul C., Hildingsson Leif, Hultqvist. Anders, "The influence of fuel injection and heat release on bulk flow structures in a direct-injection, swirl-supported diesel engine", Experiments in Fluids, Volume 43, Number 2-3, Page 273, 2007
58. Perini, F., Zha K., Sahoo D., Busch S., Miles P. C., and Reitz R. D., "Effects of in-cylinder non-uniformities on mixture preparation in a light-duty Diesel engine operating a light-load Partially Premixed Combustion strategy.", THIESEL, 2014
59. Heywood, J. B., "Fluid motion within the cylinder of internal combustion engines-The 1986 freeman scholar lecture." Journal of fluids engineering 109, no. 1 (1987): 3-35.
60. Heywood, J. B., Internal combustion engine fundamentals. Vol. 930. New York: Mcgraw-hill, ISBN 007028637X, 1988.
61. Dec, J., "Soot Distribution in a D.I. Diesel Engine Using 2-D Imaging of Laser-induced Incandescence, Elastic Scattering, and Flame Luminosity," SAE Technical Paper 920115, 1992, doi:10.4271/920115.
62. Johansson, Bengt. "On Cycle to Cycle Variations in Spark Ignition Engines." Doctoral theses, Lund Institute of Technology, Sweden, 1995.
63. Johansson, B., "Cycle to Cycle Variations in S.I. Engines - The Effects of Fluid Flow and Gas Composition in the Vicinity of the Spark Plug on Early Combustion," SAE Technical Paper 962084, 1996, doi:10.4271/962084.
64. Towers, D. P., and Towers, C. E., "Cyclic variability measurements of in-cylinder engine flows using high-speed particle image velocimetry." Measurement Science and Technology 15, no. 9 (2004): 1917.
65. Bizon, K., Continillo G., Mancaruso E., Merola, S. S., and Vaglieco B. M. "POD-based analysis of combustion images in optically accessible engines." Combustion and flame 157, no. 4 (2010): 632-640.
66. Bizon, K., Continillo G., Leistner K. C., Mancaruso E., and Vaglieco B. M. "POD-based analysis of cycle-to-cycle variations in an optically accessible diesel engine." Proceedings of the Combustion Institute 32, no. 2 (2009): 2809-2816.
67. Bizon, K., Lombardi, S., Continillo, G., Mancaruso, E., and Vaglieco, B. M. "Analysis of Diesel engine combustion using imaging and independent component analysis." Proceedings of the Combustion Institute 34, no. 2 (2013): 2921-2931.
68. Bizon, K., Continillo, G., Lombardi, S., Mancaruso, E. et al., "Independent Component Analysis of Combustion Images in Optically Accessible Gasoline and Diesel Engines," SAE Technical Paper 2013-24-0045, 2013, doi:10.4271/2013-24-0045.
69. Reeves, M., Towers, D. P., Tavender, B., and Buckberry, C. H. A high-speed all-digital technique for cycle-resolved 2-D flow measurement and flow visualisation within SI engine cylinders. Optics and Lasers in Engineering, 1999, 31.4: 247-261.
70. Fajardo, Claudia, and Volker Sick. "Flow field assessment in a fired spray-guided spark-ignition direct-injection engine based on UV particle image velocimetry with sub crank angle resolution." Proceedings of the combustion institute 31, no. 2 (2007): 3023-3031.
71. Abraham, P., Reuss, D., and Sick, V., "High-Speed Particle Image Velocimetry Study of In-Cylinder Flows with Improved Dynamic Range," SAE Technical Paper 2013-01-0542, 2013, doi:10.4271/2013-01-0542.
72. Müller, S., Arndt, S., and Dreizler, A., "Analysis of the In-Cylinder Flow Field / Spray Injection Interaction within a DISI IC Engine Using High-Speed PIV," SAE Technical Paper 2011-01-1288, 2011, doi:10.4271/2011-01-1288.
73. Disch, C., Kubach, H., Spicher, U., Pfeil, J. et al., "Investigations of Spray-Induced Vortex Structures during Multiple Injections of a DISI Engine in Stratified Operation Using High-Speed-PIV," SAE Technical Paper 2013-01-0563, 2013, doi:10.4271/2013-01-0563.
74. Zeng, W., Sjöberg, M., and Reuss, D., "Using PIV Measurements to Determine the Role of the In-Cylinder Flow Field for Stratified DISI Engine Combustion," *SAE Int. J. Engines* 7(2):615-632, 2014, doi:10.4271/2014-01-1237.
75. Miles, P.C., "In-Cylinder Turbulent Flow Structure in Direct-Injection, Swirl-Supported Diesel Engines," Ch. 4 in Flow and Combustion in Reciprocating Engines, Arcoumanis, C. and Kamimoto, T., eds. Springer-Verlag, Berlin-Heidelberg, pp 173-256, 2009.
76. Tanov, S., Wang, Z., Wang, H., Richter, M. and Johansson, B., "Effects of Injection Strategies on Fluid Flow and Turbulence in Partially Premixed Combustion (PPC) in a Light Duty Engine", SAE Technical Paper 2015-24-2455, 2015, in press.

77. Borgqvist, P., Tunestal, P., and Johansson, B., “Comparison of Negative Valve Overlap (NVO) and Rebreathing Valve Strategies on a Gasoline PPC Engine at Low Load and Idle Operating Conditions,” *SAE Int. J. Engines* 6(1):366-378, 2013, doi:10.4271/2013-01-0902.
78. Borgqvist, P., Tuner, M., Mello, A., Tunestal, P. et al., “The Usefulness of Negative Valve Overlap for Gasoline Partially Premixed Combustion, PPC,” SAE Technical Paper 2012-01-1578, 2012, doi:10.4271/2012-01-1578.
79. Tanov, S., Collin, R., Johansson, B., and Tuner, M., “Combustion Stratification with Partially Premixed Combustion, PPC, using NVO and Split Injection in a LD - Diesel Engine,” *SAE Int. J. Engines* 7(4):1911-1919, 2014, doi:10.4271/2014-01-2677.
80. Prasad, A. K., “Stereoscopic particle image velocimetry,” Experiments in Fluids 29 (2): 103-116, 2000, doi:10.1007/s003480000143.
81. Dantec Measurement Technology A/S, “FlowMap Particle Image Velocimetry Instrumentation - Installation & User's guide”, Publication no.: 9040U3624, 2000
82. Zha, K., Busch, S., Miles, P., Wijeyakulasuriya, S. et al., “Characterization of Flow Asymmetry During the Compression Stroke Using Swirl-Plane PIV in a Light-Duty Optical Diesel Engine with the Re-entrant Piston Bowl Geometry,” SAE Int. J. Engines 8(4):2015, doi:10.4271/2015-01-1699.
83. Tennekes, H., & Lumley, J. L. “A first course in turbulence”. MIT press, Cambridge, ISBN 0262200198, 1972.
84. Miles, P. C., RempelEwert B. H., and Reitz R. D. “Squish-swirl and injection-swirl interaction in direct-injection diesel engines.” In Sixth international conference on engines for automobile, ICE2003, Sept, pp. 14-19. 2003.

Contact Information

Zhenkan Wang
PhD student
Combustion Physics Division
Physics Department, Lund University, Sweden
zhenkan.wang@forbrf.lth.se

Acknowledgments

This research was performed at Lund University. The authors would like to acknowledge the Swedish Energy Agency and KCFP (Project number 50286) for financial support. The research leading to these results has also received funding from the People Programme (Marie Curie Actions) of the European Union's Seventh Framework Programme FP7/2007-2013/ under REA grant agreement number 607214. The authors would like to thank Dantec Dynamic for the technical support as well.

Definitions/Abbreviations

aTDC - after top dead center

B - bore diameter

bTDC - before top dead center

C - weight factor

CAD - crank angle degree

CCV - cycle to cycle variation

CFD - computational fluid dynamics

CI - compression ignition

D - piston bowl diameter

DI - direct injection

EGR - exhaust gas recirculation

F - judgment for even or odd number

G - judgment for even or odd number

i - cycle index

IA - interrogation area

ID - ignition delay

j - operator

M - steps for SWMA velocity

MFC - mass flow controller

MK - modulated kinetics

N - numbers of cycles

RON - research octane number

PIV - particle image velocimetry

PLV - pulsed laser velocimetry

POD - proper orthogonal decomposition

PPC - partially premixed combustion

PPCI - premixed charge compression ignition

PREDIC - premixed lean diesel combustion

SIDI - spark-ignition direct-injection

SOC - start of combustion

SOI - start of injection

SWMA - sine weighted moving averaged

TDC - top dead center

TiO_2 - titanium dioxide

TKE - turbulence kinetic energy

$\overline{TKE}$ - averaged turbulence kinetic energy

U - instantaneous velocity

$\overline{U}_{EA}$ - ensemble averaged velocity

u'_{EA} - ensemble averaged turbulence

u' - cycle-resolved turbulence

$\overline{U}$ - cycle-resolved SWMA velocity

$\overline{U}_c$ - mean value of cycle-resolved SWMA velocity

θ - CAD

$\Delta\theta$ - how many CADs between two steps

APPENDIX

Ensemble Averaged Flow Field for All Cases

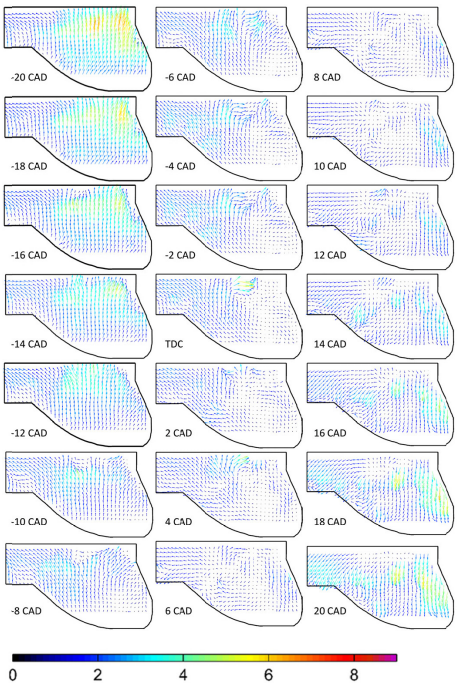

Figure 17. ensemble averaged flow field of motored case.

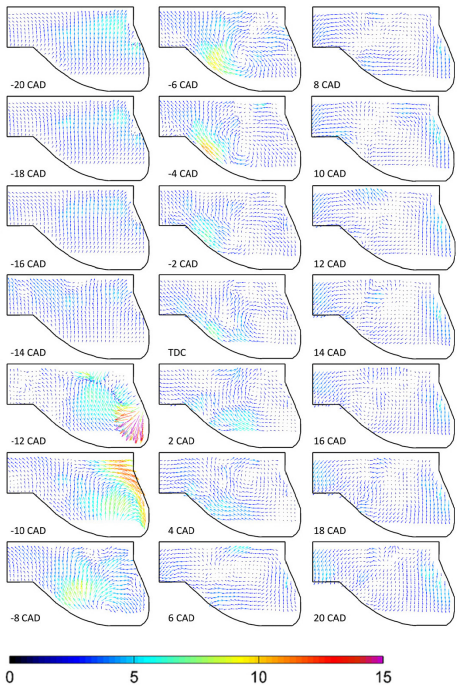

Figure 18. ensemble averaged flow field of case S16.

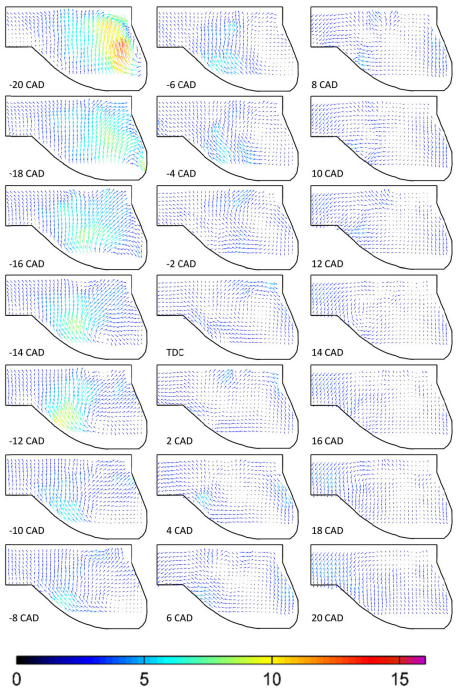

Figure 19. ensemble averaged flow field of case S24.

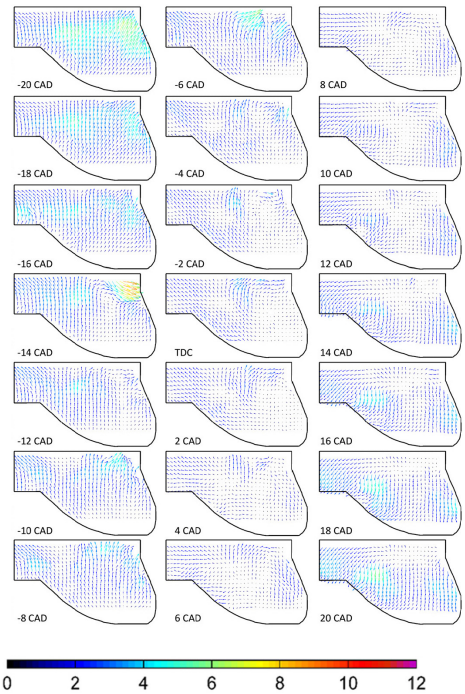

Figure 20. ensemble averaged flow field of case D53-17.

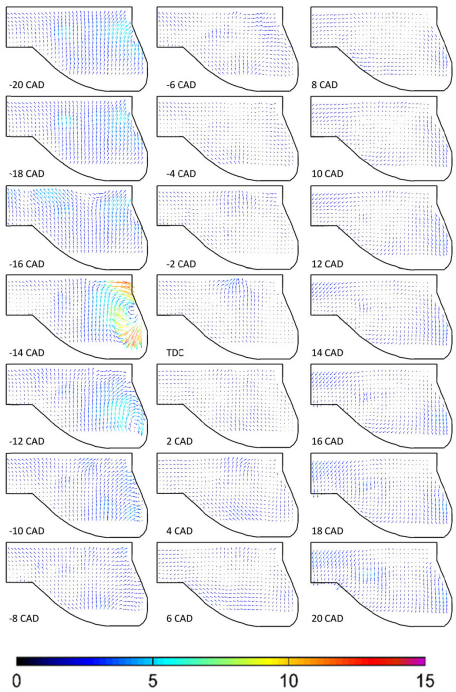

Figure 21. ensemble averaged flow field of case D35-17.

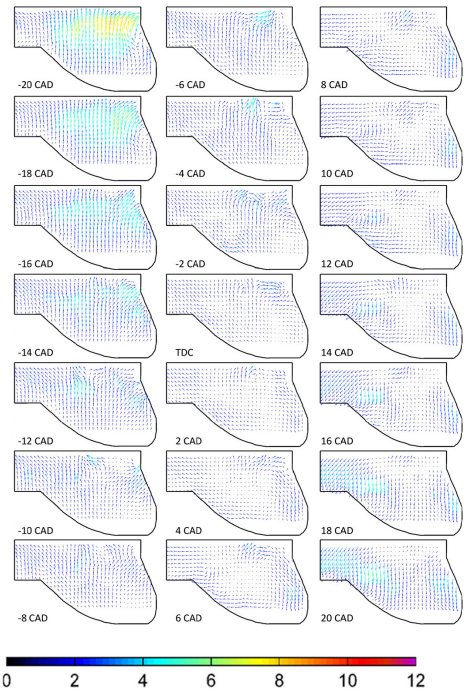

Figure 22. ensemble averaged flow field of case D45-24.

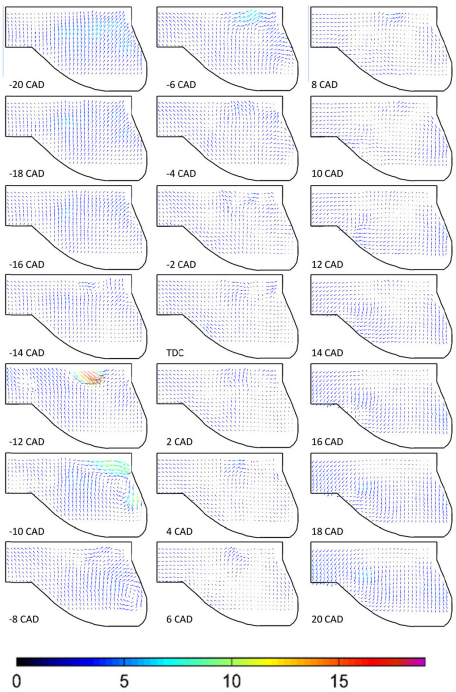

Figure 23. ensemble averaged flow field of case D52-14.

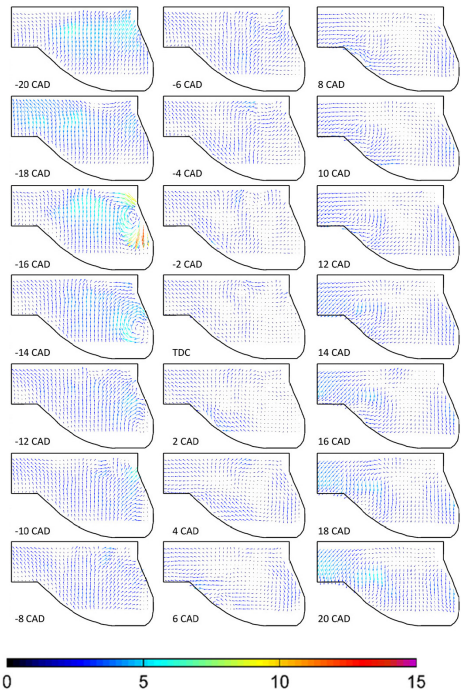

Figure 24. ensemble averaged flow field of case D52-20.

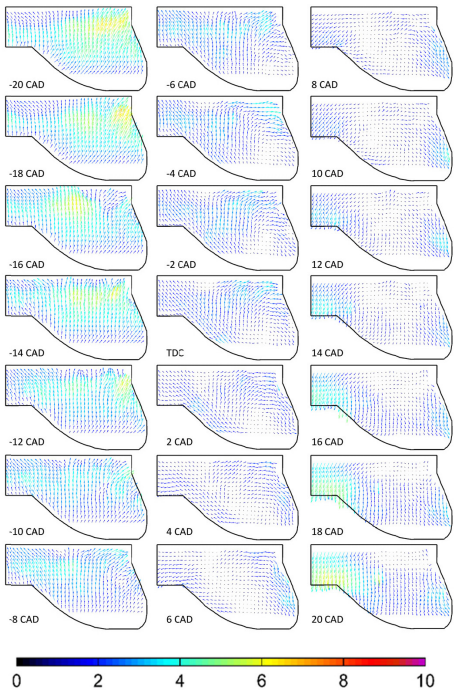

Figure 25. ensemble averaged flow field of case T63-30-17.

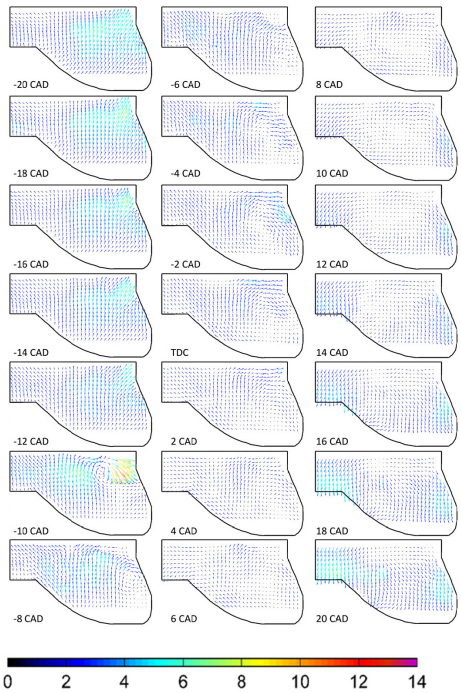

Figure 26. ensemble averaged flow field of case T63-30-12.

Mean Velocity of Cycle-Resolved SWMA Flow Field for Motored Case

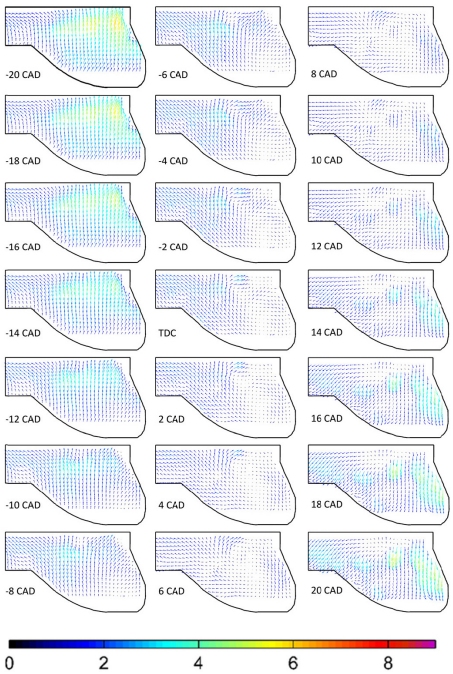

Figure 27. Mean velocity of cycle-resolved SWMA flow field for motored case.

Raw PIV Result with Piston in the Field-Of-View

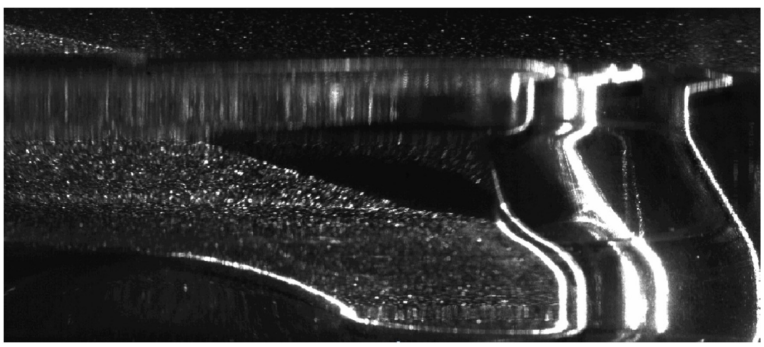

Figure 28. Raw PIV image with piston in the field-of-view before any post-processing.

Image Distortion and Correction

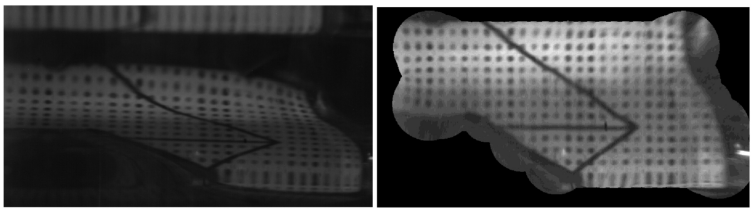

Figure 29. Target image before dewarping (left) and after dewarping (right).

ISSN 0148-7191

http://papers.sae.org/2015-24-2454

Paper V

Published 03/28/2017

doi:10.4271/2017-01-0748
saeeng.saejournals.org

Transition from HCCI to PPC: Investigation of Fuel Distribution by Planar Laser Induced Fluorescence (PLIF)

Zhenkan Wang, Sara Lonn, Alexios Matamis, Oivind Andersson,
Martin Tuner, Marcus Alden, and Mattias Richter
Lund University

ABSTRACT

In a previous study, in order to investigate the effect of charge stratification on combustion behavior such as combustion efficiency and combustion phasing which also largely affects the emissions, an experiment was conducted in a heavy-duty compression ignition (CI) metal engine. The engine behavior and emission characteristics were studied in the transition from HCCI mode to PPC mode by varying the start of injection (SOI) timing. To gain more detailed information of the mixing process, in-cylinder laser diagnostic measurements, namely fuel-tracer planar laser induced fluorescence (PLIF) imaging, were conducted in an optical version of the heavy-duty CI engine mentioned above. To the authors' best knowledge, this is the first time to perform fuel-tracer PLIF measurements in an optical engine with a close to production bowl in piston combustion chamber, under transition conditions from HCCI to PPC mode. Results show that four mixing schemes can be distinguished as the SOI timings are varied during the transition. They are linked to the results presented in the reference paper, where emissions were varied in different zones. For SOI at -100 crank angle degree (CAD), fuel distribution is homogeneous as expected. With other SOI timings, a significant part of the fuel mixture was trapped in the squish region and crevice area before start of combustion (SOC) as shown by PLIF results. The observations in the reference metal engine paper were confirmed by this measurement. Results are also in good agreement with computational fluid dynamics (CFD) simulations performed for this engine.

CITATION: Wang, Z., Lonn, S., Matamis, A., Andersson, O. et al., "Transition from HCCI to PPC: Investigation of Fuel Distribution by Planar Laser Induced Fluorescence (PLIF)," *SAE Int. J. Engines* 10(4):2017, doi:10.4271/2017-01-0748.

INTRODUCTION

Homogeneous charge compression ignition (HCCI) and partially premixed combustion (PPC) have attracted interest as both of them share the capability of producing low NOx and soot emissions without adverse effects on engine efficiency. In PPC mode the combustion phasing can be controlled by the injection timing, that in turn affects the ignition delay (ID) which is defined as the time between start of fuel injection and start of combustion (SOC) [1]. This is not possible to replicate in HCCI conditions as they, per definition require early fuel injection and feature a combustion process that is mainly controlled by chemical kinetics.

For PPC, there is a measurable time interval between end of injection and start of combustion leading to the gas mixture being partially premixed before the combustion process. In PPC mode, the stratification feature brings out different combustion behavior. In order to understand the change in engine behavior and emission characteristics, there is a need for further understanding of the mixture preparation in the transition from HCCI mode to PPC mode.

The start of combustion process during the transition was studied in terms of finding the relation between start of injection (SOI) and SOC and the location of initial ignition sites [2]. Moreover, the variation of combustion and emissions were investigated in this transition by Shen et al. [3]. In their work, the influence of SOI on the combustion efficiency and emissions was studied. As expected, in pure HCCI mode, small changes in SOI timing will not affect the engine combustion and emission behavior. But as the level of fuel stratification increases, it can affect combustion behavior significantly. It has the potential to achieve better combustion efficiency along with lower emissions, or they can both deteriorate, depending on the degree of mixing in different zones. Therefore, the transition from HCCI to PPC mode needs further investigation.

Recently, this transition behavior was investigated by varying the SOI timing in a single cylinder heavy duty diesel engine by Li et al. [4]. In order to keep CA 50 (the crank angle at which 50% of the fuel energy has been released) constant during the sweep in SOI timing, different intake temperatures were required. Plausible explanations based on the change in mixture formation for different SOI timings were presented. On basis of the required intake temperatures and the resulting emissions the swept SOI range was divided into five zones where the mixing process and stratification were expected to be significantly different. Furthermore, it was claimed that due to fuel trapping in the squish volume and crevices, emissions such as CO and total hydrocarbon (THC) increase tremendously in a segment of the transition in those studies. Nonetheless, the experiments were done in a full metal heavy-duty compression ignition (CI) engine. To

gain more detailed information of the mixing process, in-cylinder laser diagnostic measurement is essential. Therefore, to bring this investigation a step further, fuel-tracer planar laser induced fluorescence (PLIF) imaging was conducted in an optical version of the heavy-duty CI engine mentioned above.

Fuel-tracer laser induced fluorescence is commonly used to measure the fuel distribution in the combustion chamber in order to study the in-cylinder fuel injection process and mixture formation [5, 6, 7, 8, 9, 10]. Some PLIF experiments have been performed in HCCI/PPC engines. For example, Seyfried et al. [11] investigated the effect of turbulence on mixing process by using different geometry of the combustion chamber in an HCCI engine by high speed fuel-tracer PLIF. Results showed that the mixing process influences the heat release rate.

Hence, a homogeneity index was calculated and evaluated for different mixture formations. Later, Persson et al. [12] used a similar system and method to study the homogeneity level of fuel distribution under different amount of fuel in a direct injected, spark assisted compression ignition (SACI) engine. Tang et al. [13] performed a quantitative fuel-tracer PLIF measurement in a PPC engine to get the overall fuel stratification under different double injection strategies.

To the authors' best knowledge, this is the first time to perform fuel-tracer PLIF measurements in an optical engine with a close to production bowl in piston combustion chamber, under transition conditions from HCCI to PPC combustion. The measurements covered PLIF imaging at different crank angle degrees (CADs) to understand how the in-cylinder mixture formation is affected by SOI timing.

EXPERIMENTAL SETUP

The fuel tracer-PLIF experiments were conducted in a Scania D13 heavy duty optical engine. The optical engine was modified from a conventional 6-cylinder diesel engine into a single-cylinder one. The cylinder liner and the piston were extended according to the Bowditch design as shown in figure 1 and 2. The quartz piston geometry was similar to the metal piston used in the reference engine [4]. There are three quartz windows (25×55 mm) placed at right angles between them on a spacer mounted between the cylinder head and the engine block, providing large optical access into the combustion chamber for a wide range of CADs around top dead center (TDC).

The fuel used in this set of experiments was PRF 81, which contains 81% of isooctane and 19% of n-heptane per volume, together with 10% (volume) of acetone as a PLIF fuel tracer. More information about acetone used as a fuel-tracer for PLIF measurements in optical engines can be found in reference. [10, 11, 12, 14, 15, 16, 17, 18, 19, 20]. During the measurement campaign, fresh fuel and acetone blends were used every day.

Limited pressure dependence of acetone PLIF signal at pressures relevant for the compression stroke in internal combustion engines (ICE) has been reported [19]. But the temperature dependence will generate some uncertainties to the performed measurements.

A Nd:YAG (Continuum Powerlite DLS 9010) laser was used combined with a second harmonic generator and a fourth harmonic generator, in order to excite acetone at a wavelength of 266 nm. A Pellin Broca prism was placed at the exit of the laser system to separate the 532 nm and 266 nm wavelength laser beams that were overlapped. The laser energy at 266 nm was measured and set to 60±1 mJ. It was tested that with higher laser fluence, damage to the quartz piston is highly possible.

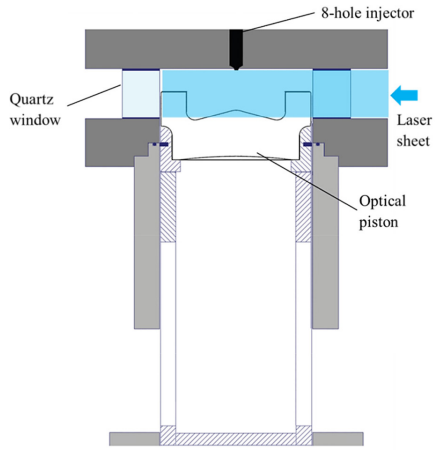

Figure 1. Experimental setup from side view

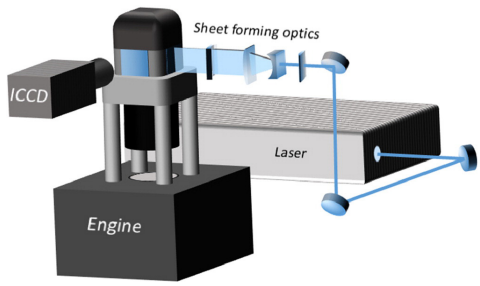

Figure 2. Isometric view of the experimental setup

In the experiment, four cylindrical lenses formed a 28 mm wide and less than 1 mm thick laser sheet to create a 2D fluorescence field. The focal lengths of the four cylindrical lenses were, -40 mm, -75 mm, +310 mm and +500 mm. The Gaussian wings of the laser sheet were then trimmed down resulting in a final height of 25 mm. The laser sheet entered through one of the quartz window and it was placed at the center of the piston bowl, passing through two opposing spray plumes as shown in figure 3.

An ICCD camera (PI-MAX II) was positioned perpendicular to the laser sheet to detect the PLIF signal through the quartz window and an achromatic Bernard-Halle quartz lens (f=+100 mm, f#=2) was

mounted in front of the camera. Two long pass filters were used in front of the camera lens. Each of them was a 20 mm optical path length quartz cuvette, containing the liquid N,N-dimethyl-formamide, that will prevent almost all undesired scattered laser light from entering the ICCD camera. A transmission curve for this filter can be found in reference [21].

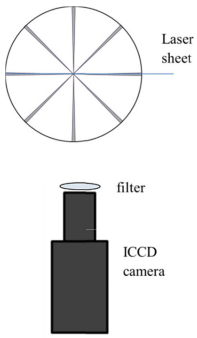

Figure 3. Experimental setup from top view (piston bowl area with 8 spray plumes)

Table 1. Engine specifications.

Engine type	Heavy-duty diesel engine
Number of valves	4
Bore	130 mm
Stroke	160 mm
Connecting rod	255 mm
Displacement	2124 cm^3
Engine speed	1200 rpm
Fuel type	PRF 81
PLIF fuel tracer	Acetone
Common rail pressure	800 bar
Injector type	8-hole Solenoid, 120°
Injection duration	900 µs
Intake temperature, T_{in}	75-150 °C
Intake pressure, P_{in}	1.5 bar
Intake O^2	21 vol. %

The exposure time of the camera was set to 100 ns. Since little soot was produced in PPC mode and with such a short exposure time, the chemiluminescence signal from the combustion was very low and contributed to the background noise. The original resolution of the camera is 1024×1024. However, due to the limitation of the quartz window size, the resolution was clipped down to 1024*680, which is corresponding to 97×64 mm field of view.

Due to the bowl-in-piston design, some undesired reflections and dark patches are formed in the PLIF images, especially on the exit side. Therefore, only the entrance side of the images was processed and analyzed.

OPERATING CONDITIONS

The engine speed and combustion phasing were kept constant at 1200 rpm and CA50 was achieved at +3 CAD after top dead center (ATDC) for all the conditions. In the below text, the position of the piston which is before TDC of the combustion stroke will be indicated with a '-' sign in front of CAD and after TDC will be a '+' sign. A skip-fire strategy was employed, where one out of ten cycles was fired and the other nine were motored, in order to maintain realistic surface temperatures. This approach reduces the possibility of window failures due to thermal load and resulting mechanical stresses. The laser was triggered by the combustion TDC signal, providing a repetition rate of 10 Hz. The trigger signal of the engine was sent out at different CADs in order to facilitate the following of the evolution of the mixing process for different SOI timings. Table 2 summarizes the operating conditions including different SOI and trigger timings. 50 images were recorded for each CAD of each SOI for statistical data analysis.

Table 2. operating conditions.

Single injection								
SOI	**-100**	**-70**	**-54**	**-46**	**-35**	**-30**	**-20**	**-15**
Case name	case100	case70	case54	case46	case35	case30	case20	case15
PLIF imaging CAD	-95							
	-90							
	-85							
	-80							
	-75							
	-70							
	-65	-65						
	-60	-60						
	-55	-55						
	-50	-50	-50					
	-45	-45	-45					
	-40	-40	-40	-40				
	-35	-35	-35	-35				
	-30	-30	-30	-30	-30			
	-25	-25	-25	-25	-25	-25		
	-20	-20	-20	-20	-20	-20		
	-15	-15	-15	-15	-15	-15	-15	
	-10	-10	-10	-10	-10	-10	-10	-10
	-5	-5	-5	-5	-5	-5	-5	-5
	0	0	0	0	0	0	0	0
	3	3	3	3	3	3	3	

IMAGE POST-PROCESSING

Background images recorded during motored cycles were subtracted from the raw PLIF images. Due to the dome-shaped piston bowl the images acquired were optically distorted. MATLAB (The Matworks, Massachusetts, USA) was used for correction of distorted images. An example of a recorded image before and after distortion correction can be seen in the appendix, figure 16. Detailed information on image correction for a similar piston bowl shape can be found in reference [22, 23, 24, 25].

The distortion corrected PLIF images were compensated for vertical variations in the energy distribution of the laser sheet. The PLIF intensity variations due to time averaged variations in the energy distribution of the laser sheet can be obtained by using pure acetone in the combustion chamber and record the corresponding PLIF image.

Figure 4 represents an example after image post-processing at -5 CAD for case46. The yellow box in the upper image of the figure indicates the area above the piston and the squish volume; the blue box shows half of the piston bowl; in the red box is the area where the mixture preparation has been studied because reliable illumination can be maintained for the investigated CAD range. The region between the blue box and the red one is masked because of insufficient illumination and severe image distortion due to the curvature of the piston bowl.

It should be mentioned that laser attenuation was not accounted for, since with high laser energy and low acetone concentration, the attenuation by acetone can be considered negligible [5]. However, due to the laser absorption by intermediates of the combustion process and soot particles, it is still possible to have a degree of extinction in the measurements.

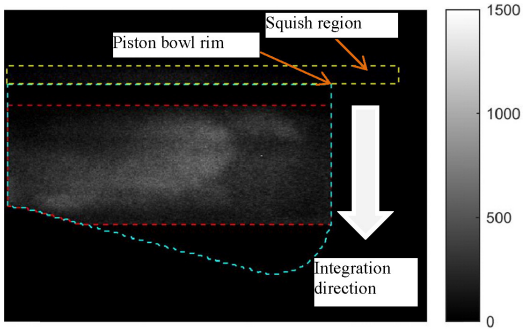

Figure 4. Instantaneous PLIF image after post-processing for case46 at -5 CAD

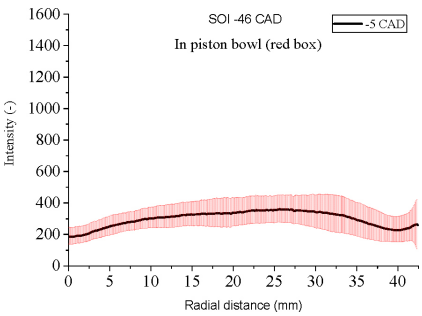

Figure 5. Averaged intensity (black line) and the standard deviation (red envelope) in vertical direction at different radial position inside the piston bowl calculated by PLIF images of 50 cycles for case46 at -5 CAD

Case46 at -5 CAD is taken as an example. First, the mean intensity at a specific radial position in the piston bowl is calculated along the vertical direction (sum of the intensity along the vertical direction and then it is normalized by the pixel numbers). Therefore, the mean intensity is independent on the pixel numbers.

The averaged tracer PLIF intensity profile along the radial direction can be hence calculated together with its standard deviation for 50 cycles. In figure 5, the black line is the averaged intensity over 50 cycles along the radial direction of the piston bowl. The red envelope filling around the averaged intensity is the standard deviation of 50 cycles.

The calculation and data analysis for the region above piston is the same as those for the region inside the piston bowl as described above.

RESULTS AND DISCUSSION

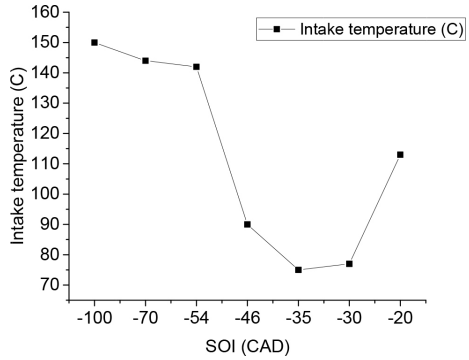

Figure 6. Intake temperatures versus SOI timings.

Figure 6 presents the required intake temperature to keep constant CA50 for the various SOI timings investigated. The profile of the intake temperatures has a similar shape as for the reference engine [4]. This indicates that the in-cylinder conditions from the previous metal engine studies could be approximately replicated in the optical engine. The peak pressure and CA50 were tuned to be the same as those in the metal engine to keep the in-cylinder conditions as close as possible.

1. Instantaneous PLIF Image

The instantaneous PLIF images for all the cases at different CADs from -95 CAD to +3 CAD can be found in the appendix. The images were post-processed as described in the previous section. 5 grayscale ranges (from 8000 to 800) were used in order to present better contrast. The indicators, G1 to G5, at the bottom right corner of each image, show the grayscale bin applied.

After evaluating the images, it becomes apparent that for SOI timings of -15 and up to -35 CAD, all of the fuel is injected inside the piston bowl and most of the mixture formation takes place in that volume. The case of SOI at -35 CAD is the first case where some of the gas mixture appears in the top-land volume of the piston, noticeable at -20 CAD. In case46, the fuel plume interacts with the piston bowl rim at position -35 CAD and some fuel is delivered in the piston top-land and the squish region. As the piston moves towards TDC though, the signal drops in the squish region, indicating that the gas either moves to the piston bowl or dissipates below the noise level. For SOI of -54

CAD a significant part of the fuel mixture is distributed in the squish region as shown in appendix figure 17, from position -45 CAD to -35 CAD. This leads to fuel being deposited in the crevice region and greater heat loses from the surface to volume ratio, contributing to high CO and THC emissions, as demonstrated in the reference engine [4]. For even earlier SOI, as in case70 and case100, the outcome is very similar, requiring high inlet temperatures in order to achieve combustion as the mixture inside the piston bowl is relatively lean. The majority of the mixing takes place above the piston and gradually enters the bowl when the piston ascends towards TDC.

These results are also in good agreement with the computational fluid dynamics (CFD) results shown in reference [4]. According to the modelling results, fuel was trapped on the piston top-land and in the squish volume for SOI from -80 CAD to -50 CAD.

From the PLIF imaging (see figure 7), four mixing schemes can be identified as the SOI timings are varied during this HCCI to PPC transition.

Scheme 1: When SOI is retarded beyond -35 CAD, most of the fuel is injected inside the piston bowl and that is where all the mixing process takes place. The earlier the injection, the more homogeneous it can become before the onset of combustion.

Scheme 2: When SOI is at -46 CAD or -54 CAD, the injection hits on the rim of the piston bowl. It splits the mixture moving into two directions: inside the piston bowl and towards the squish region as arrows show in figure 7. The mixing processes at these two places interact with each other and finally combine together inside the piston bowl due to piston motion and squish flow. During the mixing process, part of the fuel mixture also dissipates into the crevice areas above the ring pack. This leads to poor combustion efficiency and high emissions [26].

Scheme 3: When SOI is at -70 CAD, no fuel is injected directly into the piston bowl. Therefore, the majority of the mixing takes place above the piston. Due to limited mixing time, the still stratified gas mixture then enters the piston bowl for further mixing before ignition.

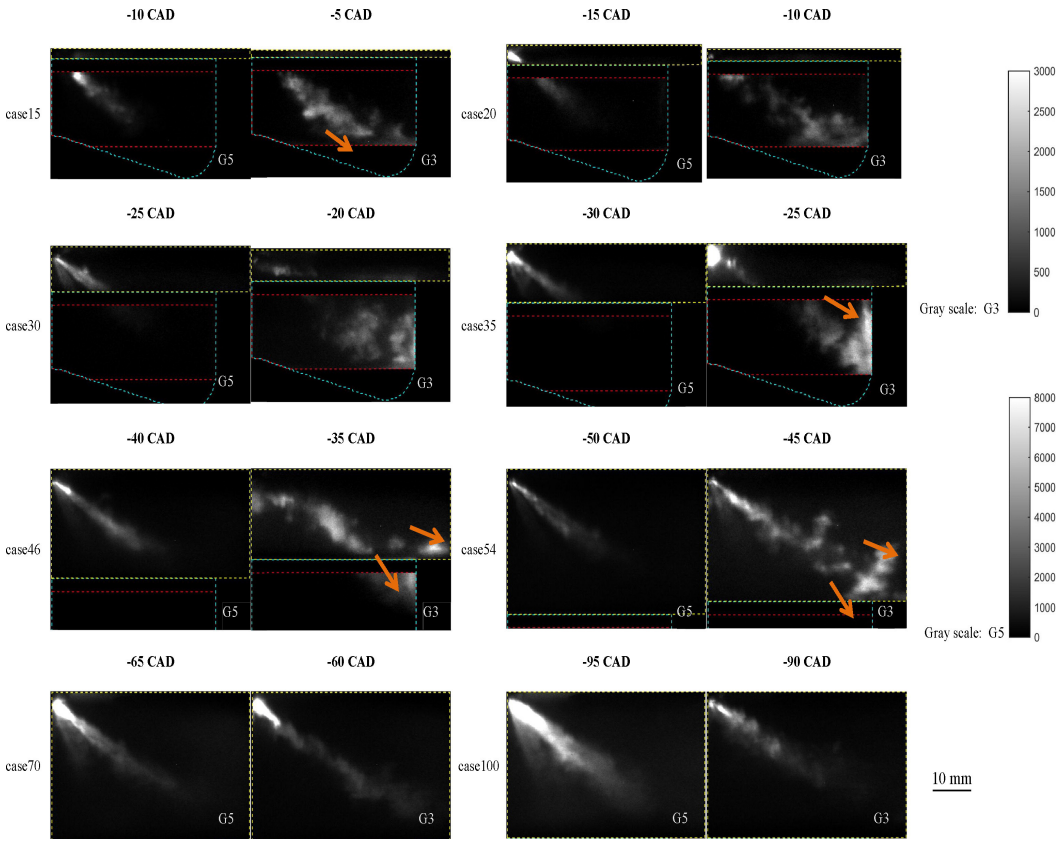

Figure 7. Instantaneous PLIF images at 5 CADs and 10 CADs after SOI for all cases

Scheme 4: When SOI is more advanced than -100 CADs, plenty of time is available for mixing before the mixture enters the piston bowl. A more uniform gas mixture will form and lead to HCCI combustion.

During +3 CAD, 0 CAD (TDC) and -5 CAD, some 'holes' were observed in PLIF images such as in case20 and case30. This is not only because of non-uniform fuel distribution in the piston bowl, but also due to the combustion process which consumes fuel in the combustion chamber. For case100, the PLIF image faded homogenously while the piston was ascending which means combustion close to HCCI.

The discussion above is based on instantaneous PLIF images. Due to cycle-to-cycle variation of the engine, more analysis with statistical data will be presented.

2. Two Different Fuel Distributions in Scheme-1

Figure 8 shows the PLIF images and the averaged intensity at different radial positions inside the piston bowl for two cases. Due to different injection timings, the fuel impinges at different locations of the piston bowl. This could lead to a clockwise vortex (case35), when the injection hits the vertical wall of the piston bowl, or a counterclockwise vortex (case20), when that hits the bottom of the piston bowl. Therefore, an assumption could be made, that two kinds of fuel distribution exist for scheme-1 mixing process. For case20, with the piston ascending, the gas mixture diffuses towards the periphery of the piston bowl by the momentum of the injection and a vortex is created. Thus, the intensity near the piston bowl wall increases dramatically as the arrows indicate in figure 8(a).

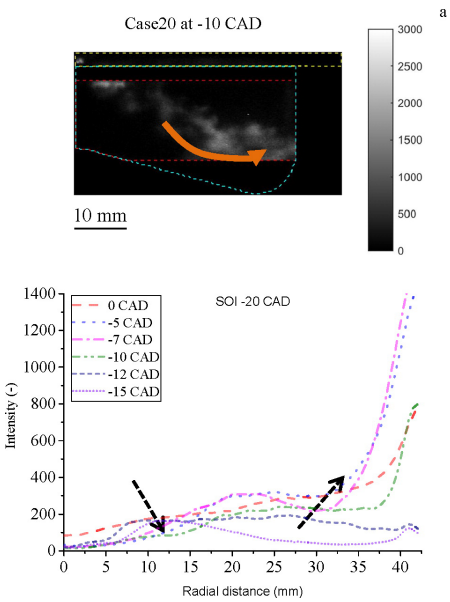

Figure 8(a). Averaged intensity at different radial positions inside piston bowl for case20 at different CADs

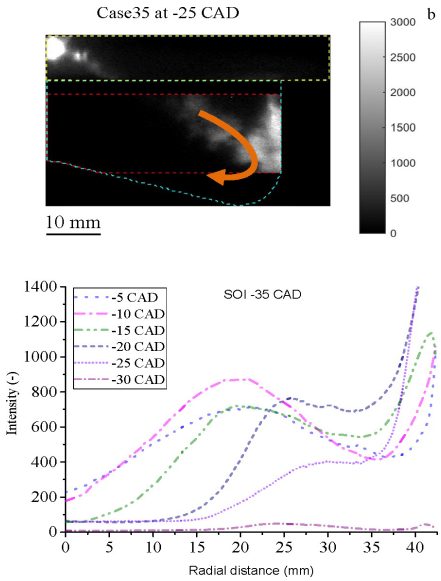

Figure 8(b). Averaged intensity at different radial positions inside piston bowl for case35 at different CADs

On the contrary, for case35, the intensity near the center of the piston increases over time, as shown in figure 8(b) due to the clockwise vortex generated by the injection event and the piston bowl geometry. In order to confirm this assumption, a study on in cylinder flows, such as PIV measurements is needed.

3. Fuel Distributions for Mixing Schemes Inside Piston Bowl

Figure 9 summarizes the intensity profile at different radial positions inside the piston bowl for all cases at different CADs. The arrows in the figure depict the trend of the fuel distribution from SOI at -100 CAD to SOI at -15 CAD.

For case15, due to limited mixing time, the fuel distribution is highly stratified spatially. Thus in figure 9(a) the intensity curve is relatively flat as it is a 2D PLIF measurement. The fuel was aggregated together instead of distributing in space.

For case35, intensity maxima are found both at 20 mm (which is the middle point between the center and the periphery of the piston bowl) and at the periphery of the piston bowl at -10 CAD and -5 CAD as shown in the figure 9(d).

In case30 and case20, the intensity near the center is lower than that of case46 and case54 and more fuel is close to the wall of the piston bowl, as pointed out in figure 9(b) and (c). The fuel distribution is more stratified for case30 than case35. Thus, when SOI is before -35 CAD, the later the injection, the more stratified it can become before the onset of combustion.

For case54 and case46, the intensity close to the center is very high as pointed out in figure 9(e) and (f). Therefore, more fuel is distributed near the center of the piston bowl. At -5 CAD, the intensity curve becomes relatively flat, indicating a more even the fuel distribution.

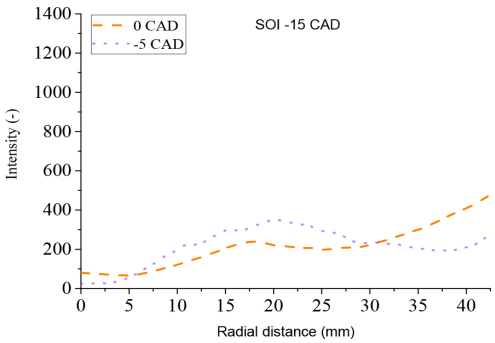

a.

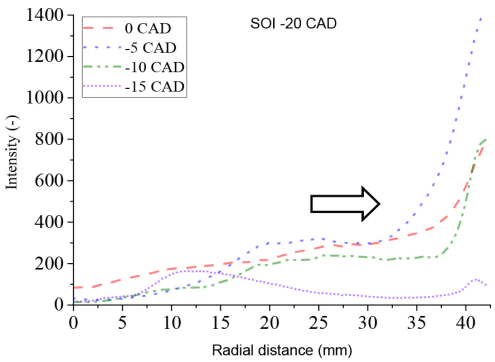

b.

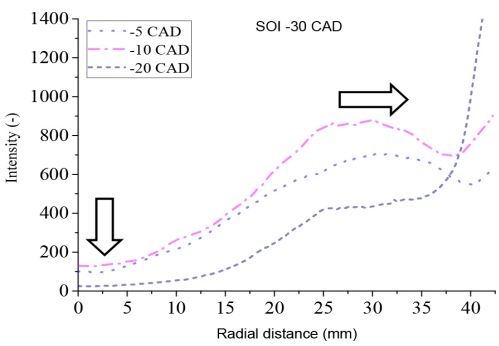

c.

Figure 9.

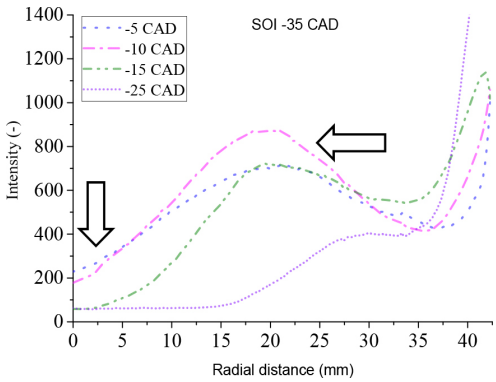

d.

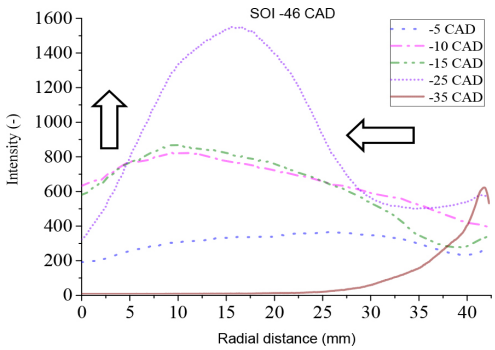

e.

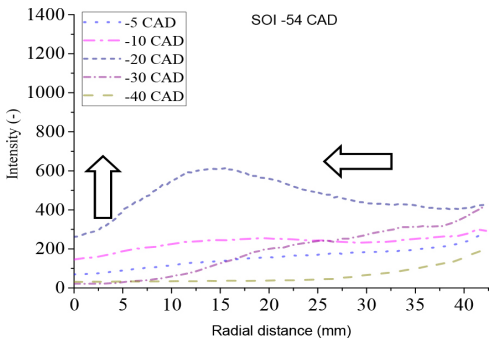

f.

Figure 9. (cont.) Averaged intensity in vertical direction at different radial positions inside piston for all cases at different CADs. (a-h represent different SOI timings).

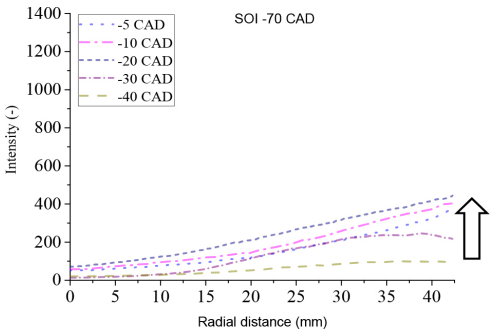

g.

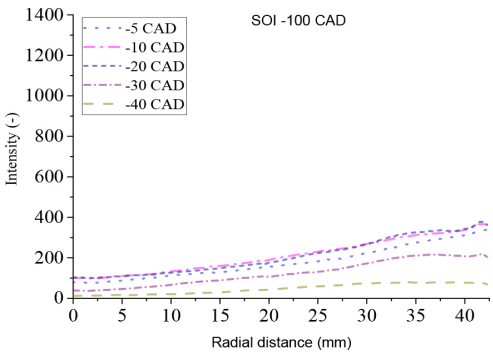

h.

Figure 9. (cont.)Averaged intensity in vertical direction at different radial positions inside piston for all cases at different CADs. (a-h represent different SOI timings).

For case100 and case70, fuel is located close to the periphery of the piston bowl. It increases first and then decreases slightly over time, as shown in figure 9(g) and (h). The fuel distribution along radial direction is relatively homogeneous before SOC.

Due to varied SOI timings, the fuel distributes at different locations inside the piston. The geometry of the combustion chamber, coupled with the spray angle and fuel penetration will lead to differences in fuel distribution.

4. Fuel Distributions at a Certain Time after SOI

In figure 10, the intensity of the PLIF signal at different radial distances is shown, at approximately 15 CADs after SOI. This illustrates the fuel distribution inside the piston bowl, for four different SOI cases given the same mixing time. One noticeable fact is that despite the cylinder pressure being higher for late injections (SOI at -30 and -35 CAD), the fuel is distributed further away from the center of the piston. For SOI at -46 CAD, the first peak in fuel concentration is found in the region of 18-20 mm while for further radial distances, namely closer to the periphery of the bowl, the intensity increases but not acutely, demonstrating good homogeneity in the bowl volume.

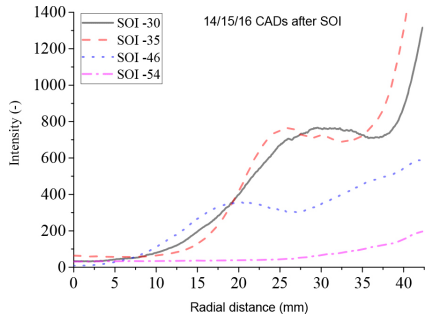

Figure 10. Integrated intensity, averaged in the vertical direction, versus radial distance inside piston bowl, for case30, case35, case46, and case54, at 15 CADs after SOI.

For later SOI, like -35 CAD and -30 CAD, this first peak is at 25 and 30 mm respectively. Close to the edge of piston bowl, in both cases the intensity increases substantially, indicating that a big part of the mixture is present. In a sense, the slope of this curve can be a prime indicator of fuel stratification. This is also verified in case54 where higher homogeneity is apparent from the small slope of the curve and the fuel distribution does not vary substantially in the radial direction. The intensity of case54 is low which indicates lean mixture. Therefore, a transition of fuel homogeneous distribution to a stratified one after a certain time of SOI could be found between case54 and case35.

5. Fuel Distributions at a Certain CAD

Figure 11 and 12 show that fuel is transported along different radial directions at -15 and -10 CAD, which is close to the onset of combustion. For case30 and case35, the gas mixture moves towards the center of the piston bowl resulting in the PLIF intensity to decrease near the edge of the bowl, while the opposite happens in case46.

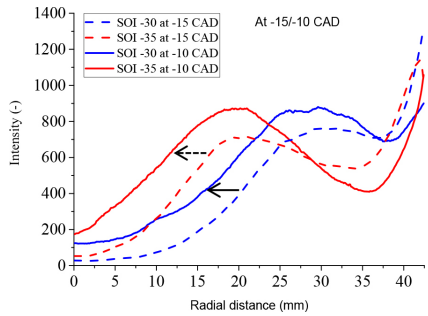

Figure 11. Averaged intensity at different radial positions inside the piston bowl at -15 CAD and -10 CAD for case30 and case35.

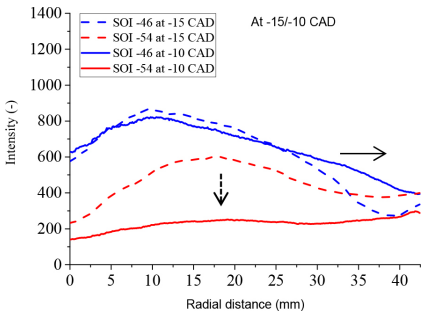

Figure 12. Averaged intensity at different radial positions inside the piston bowl at -15 CAD and -10 CAD for case46 and case54.

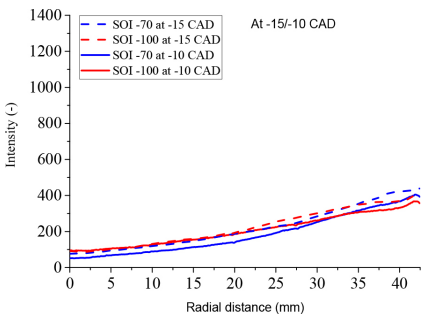

Figure 13. Averaged intensity at different radial positions inside the piston bowl at -15 CAD and -10 CAD for case70 and case100.

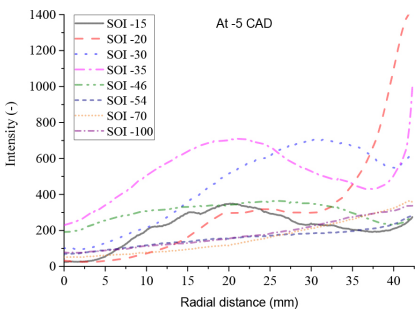

Figure 14. Averaged intensity at different radial positions inside the piston bowl at -5 CAD.

For case54, the fuel distribution became more homogeneous which probably leads to a homogeneous combustion in the piston bowl after -10 CAD as shown in figure 12.

For case70 and case100, there is not much difference in fuel distribution between -15 CAD and -10 CAD in figure 13, as fuel and air are already mixed well.

The gas mixture is homogeneously distributed in the piston bowl for case46, case54, case70 and case100. The later three cases are very similar in intensity at -5 CAD as shown in figure 14.

The gas mixture for case46, case54, case70 and case 100 is evenly distributed inside the piston bowl, indicating that homogeneous combustion will occur. In mixing scheme-2, more fuel was inside the piston bowl for case46 than case54, as the intensity of case46 is higher while remaining relatively homogeneous. Therefore, case54 needs higher intake temperature (see figure 6) which leads to higher in-cylinder temperature around TDC in order to keep the same combustion phasing (CA 50 at +3 CAD). Fuel distribution is more stratified for SOI timing later than -46 CAD. This fuel stratification leads to higher local combustion temperatures which as a result produce higher NOx emissions. Thus, an increase in NOx emissions can be found in the experimental data of the reference engine.

6. Interaction of Mixing Process between Regions Above and Inside Piston Bowl

The correlation between the fuel distribution above the piston and that inside the piston bowl can be found in figure 15. The lower plot in each sub-figure describes the fuel distribution inside the piston bowl, namely, the red box shown in figure 4. Similarly, the upper plot indicates the region above the piston, or the yellow box shown in figure 4.

For case35, fuel is injected inside the piston bowl (scheme-1) as shown in figure 7. As a result, the fuel above piston is distributed only from the center of the cylinder to 30 mm radial distance (figure 15a). The gas mixture rarely reaches the squish volume as pointed out by the arrow in figure 15(a). Therefore, the CO and THC emissions are very low as less fuel was trapped in the squish and crevice regions [4]. Although less time is available for evaporation and mixing, more fuel is consumed in the piston bowl which leads to higher NOx emissions, since the combustion temperature is higher compared to other cases (in figure 15) with leaner mixtures in the piston bowl.

As the majority of fuel is injected inside the piston bowl for case46 (scheme-2), the intensity above the piston is lower at -35 CAD compared to other cases with earlier SOI timing as shown in figure 15. With the piston ascending, fuel above the piston diffuses into the piston bowl resulting in a small decrease of the intensity profile above piston, despite that the influence on fuel distribution in the piston bowl is limited. However, the fuel distributed in the squish region can also be transported to crevice areas as well. Thus, the emission results showed that the CO and THC emissions are very high and NOx is low.

For case54, fuel is mainly injected in the squish region as shown in figure 7. It is obvious that in the area above the piston, there is a sharp decrease of intensity around 42 mm to 53 mm radial distance from -15 CAD to -10 CAD as pointed out in upper plot of figure 15(c). A reasonable assumption is that the gas mixture in the squish volume was pushed towards both, piston bowl and crevice area by the squish flow. This can be an indication of substantial fuel trapping in the squish volume and crevice area, leading to worse CO and THC emissions for case54.

In the region above the piston, the fuel distribution of case70 before -20 CAD is more stratified than case100 because all the fuel is injected towards the cylinder liner with less evaporating and mixing time. While the piston moves towards TDC, more fuel enters into the piston bowl. The fuel distribution inside the piston bowl was affected by the mixture above it from -40 CAD to -35 CAD judging by a large increase of intensity in the piston bowl. The mixing process makes fuel distribute more homogeneously above the piston over time as well.

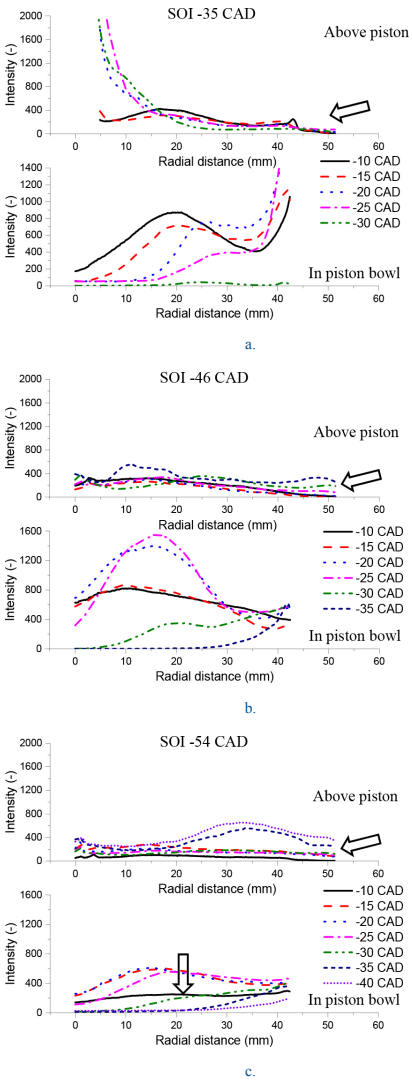

Figure 15.

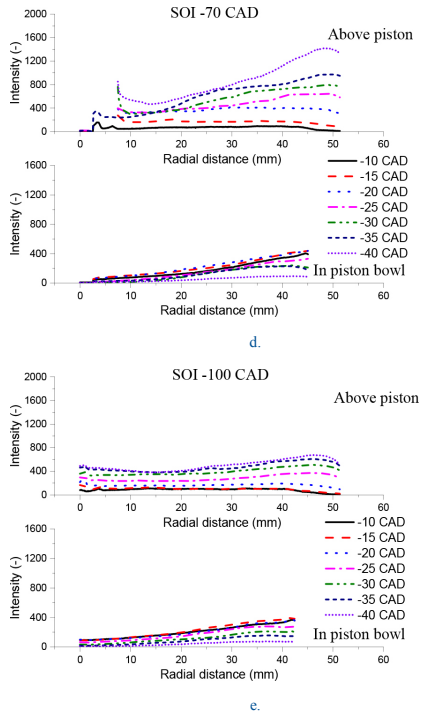

Figure 15. (cont.) Averaged intensity at different radial positions above (upper plot) and inside (lower plot) piston bowl at different CADs. (a-e represent different SOI timings).

For case100 (scheme-4), the fuel distribution along the radial direction is quite even in the region above the piston due to plenty of mixing time. With the piston ascending, more fuel above the piston bowl is transported into it. Since it is quite homogeneous, there is limited impact on the fuel distribution inside the piston bowl. The higher intensity at the right side of the curve in the upper plot of figure 15(e) could be due to both the swirl pushing more gas mixture to the periphery and laser extinction.

Due to lack of data for SOI between -46 CAD and -35 CAD, it can only be assumed that a transition of mixing scheme may be happening at a certain time of SOI between them.

SUMMARY/CONCLUSIONS

Fuel-tracer PLIF measurements were employed in a heavy-duty optical engine in order to obtain better knowledge about the mixing process in the transition from HCCI to PPC mode. The operating conditions were kept the same as the reference metal engine for comparison. Intake temperature was varied for different SOI, which has a similar profile as the reference condition. PLIF images were recorded at different timings for 8 cases. With post-processing, the

fuel distribution of both above and inside the piston along the radial direction was obtained as well. By comparing the data the following conclusions can be drawn.

1. From the PLIF imaging, four mixing schemes can be distinguished as the SOI timings are varied during the transition. It is linked to the results presented in the reference engine where emissions were measured in different zones.

   In short, scheme-1, all the fuel is injected inside the piston; scheme-2, some fuel is injected in the piston bowl; scheme-3, all the fuel is injected above the piston or in the squish region with limited mixing time; scheme-4, all the fuel is injected towards the cylinder liner with plenty of mixing time.
2. A shift of fuel distribution in the piston bowl was found with varied SOI timings. Fuel distribution inside the piston was relatively even and close to the periphery of the bowl for case70 and case100 after -40 CAD; more fuel was distributed close to the center of the piston bowl with the piston ascending until -10 CAD for case54 and case46; The fuel distribution moves close to the periphery of the piston bowl for SOI timing later than -35 CAD.
3. In scheme-1 mixing process, due to different injection timing the fuel was injected at different locations of the piston bowl where two kinds of fuel distribution exist possibly by the bulk-structure flow.
4. A certain time after SOI, case54 has more homogeneous distribution compared to other cases in scheme-1 and scheme-2 mixing. It reaches a homogeneous distribution at -10 CAD and achieves a similar homogeneous distribution as cases in scheme-3 and scheme-4 in the piston bowl at -5 CAD which is shortly before the onset of combustion. It is assumed that homogeneous combustion will occur for case54. Case46 comes to homogeneous fuel distribution at -5 CAD with higher PLIF intensity than case54, which indicates it is leaner for case54. Therefore, case54 needs higher intake temperature which leads to higher in-cylinder temperature around TDC in order to keep the same combustion phasing (CA50 at +3 CAD).

   Case46 exhibits higher PLIF intensity when it becomes homogeneous fuel distribution compared to case70 and case100. This indicates that the later ones have leaner mixture in the bowl and therefore require higher intake temperature, namely higher in-cylinder temperature near TDC, in order to keep the same combustion phasing (CA50 at +3 CAD).
5. The fuel distribution is more stratified for SOI timing later than -46 CAD. This fuel stratification leads to higher local combustion temperatures which as a result produce higher NOx emissions as measured by the reference engine.
6. In scheme-3 and scheme-4, the gas mixture is well mixed and homogeneously distributed in the piston bowl before SOC.
7. For SOI earlier than -100 CAD or later than -35 CAD, the fuel distribution above the piston has limited influence on the mixing process inside the piston bowl. For case46 and case54, a significant part of the fuel mixture was trapped in the squish region and crevice area before SOC. This is the main reason for high CO and THC emissions. The assumption in the reference metal engine paper was confirmed by this measurement.
8. Results are in good agreement with the CFD simulations in the reference paper[4]. Therefore, the measurements also provide prominent support to the modeling of PPC engines.

   Due to lack of data for SOI between -46 CAD and -35 CAD, it can only be assumed that a transition of mixing scheme is happening between them. More detailed experiments are needed to identify the boundary conditions between the four mixing schemes. For example, better resolution of CADs for varied SOI between the two cases. Lastly, some additional measurements are needed to prove that case54 has a relatively homogeneous combustion in scheme-2.

REFERENCES

1. Solaka, H., Tuner, M., and Johansson, B., "Analysis of Surrogate Fuels Effect on Ignition Delay and Low Temperature Reaction during Partially Premixed Combustion," SAE Technical Paper 2013-01-0903, 2013, doi:10.4271/2013-01-0903.
2. Lundgren, M., Rosell, J., Richter, M., Andersson, Ö. et al., "Optical study on combustion transition from HCCI to PPC with gasoline compression ignition in a HD engine," SAE Technical Paper 2016-01-0768, 2016, doi:10.4271/2016-01-0768.
3. Shen, M., Lonn, S., and Johansson, B., "Transition from HCCI to PPC Combustion by Means of Start of Injection," SAE Technical Paper 2015-01-1790, 2015, doi:10.4271/2015-01-1790.
4. Li, C., Yin, L., Shamun, S., Tuner, M. et al., "Transition from HCCI to PPC: the Sensitivity of Combustion Phasing to the Intake Temperature and the Injection Timing with and without EGR," SAE Technical Paper 2016-01-0767, 2016, doi:10.4271/2016-01-0767.
5. Reuss, D. and Sick, V., "Inhomogeneities in HCCI Combustion: An Imaging Study," SAE Technical Paper 2005-01-2122, 2005, doi:10.4271/2005-01-2122.
6. Musculus, M., "Multiple Simultaneous Optical Diagnostic Imaging of Early-Injection Low-Temperature Combustion in a Heavy-Duty Diesel Engine," SAE Technical Paper 2006-01-0079, 2006, doi:10.4271/2006-01-0079.
7. Musculus, M., Lachaux, T., Pickett, L., and Idicheria, C., "End-of-Injection Over-Mixing and Unburned Hydrocarbon Emissions in Low-Temperature-Combustion Diesel Engines," SAE Technical Paper 2007-01-0907, 2007, doi:10.4271/2007-01-0907.
8. Sahoo, D., Petersen, B., and Miles, P., "Measurement of Equivalence Ratio in a Light-Duty Low Temperature Combustion Diesel Engine by Planar Laser Induced Fluorescence of a Fuel Tracer," *SAE Int. J. Engines* 4(2):2312-2325, 2011, doi:10.4271/2011-24-0064.
9. Petersen, B., Miles, P., and Sahoo, D., "Equivalence Ratio Distributions in a Light-Duty Diesel Engine Operating under Partially Premixed Conditions," *SAE Int. J. Engines* 5(2):526-537, 2012, doi:10.4271/2012-01-0692.
10. Sjöholm, J., Chartier C., Kristenson E., Berrocal E., Gallo Y., Richter M., Andersson Ö., Aldén M., and Johansson B.. "Quantitative in-cylinder fuel measurements in a heavy duty diesel engine using Structured Laser Illumination Planar Imaging (SLIPI)." COMODIA 2012, MD2 3 (2012).
11. Seyfried, H., Olofsson, J., Sjöholm, J., Richter, M. et al., "High-Speed PLIF Imaging for Investigation of Turbulence Effects on Heat Release Rates in HCCI Combustion," SAE Technical Paper 2007-01-0213, 2007, doi:10.4271/2007-01-0213.
12. Persson, H., Sjöholm, J., Kristensson, E., Johansson, B. et al., "Study of Fuel Stratification on Spark Assisted Compression Ignition (SACI) Combustion with Ethanol Using High Speed Fuel PLIF," SAE Technical Paper 2008-01-2401, 2008, doi:10.4271/2008-01-2401.
13. Tang, Q., Liu, H., Li, M., and Yao, M., "Study on the Double Injection Strategy of Gasoline Partially Premixed Combustion under a Light-Duty Optical Engine," *SAE Int. J. Engines* 9(4):2185-2193, 2016, doi:10.4271/2016-01-2299.
14. Fansler, T., French, D., and Drake, M., "Fuel Distributions in a Firing Direct-Injection Spark-Ignition Engine Using Laser-Induced Fluorescence Imaging," SAE Technical Paper 950110, 1995, doi:10.4271/950110.
15. Grossman, F., Monkhouse, P. B., Ridder, M., Sick, V., Wolfrum, J., "Temperature and pressure dependence of the laser induced fluorescence of gas-phase acetone and 3-pentanone", Applied Physics B, Vol. 62, No. 3, pp. 249-253, 1996.

16. Thurber, M. C., Hanson, R. K., "Pressure and composition dependences of acetone laser-induced fluorescence with excitation at 248, 266, and 308 nm", Applied Physics B, Vol. 69, No. 3, pp. 229-240, 1999
17. Richter, M., Engström, J., Franke, A., Aldén, M. et al., "The Influence of Charge Inhomogeneity on the HCCI Combustion Process," SAE Technical Paper 2000-01-2868, 2000, doi:10.4271/2000-01-2868.
18. Hultqvist, A., Christensen, M., Johansson, B., Richter, M. et al., "The HCCI Combustion Process in a Single Cycle - Speed Fuel Tracer LIF and Chemiluminescence Imaging," SAE Technical Paper 2002-01-0424, 2002, doi:10.4271/2002-01-0424.
19. Schulz, C., Sick, V., "Tracer-LIF diagnostics: quantitative measurement of fuel concentration, temperature and fuel/air ratio in practical combustion systems", Progress in Energy and Combustion Science, Vol. 31, No. 1, pp. 75-121, 2005.
20. Chartier, C., Sjoholm, J., Kristensson, E., Andersson, O. et al., "Air-Entrainment in Wall-Jets Using SLIPI in a Heavy-Duty Diesel Engine," *SAE Int. J. Engines* 5(4):1684-1692, 2012, doi:10.4271/2012-01-1718.
21. Aronsson, U., Chartier, C., Andersson, Ö., Egnell, R. et al., "Analysis of the Correlation Between Engine-Out Particulates and Local Φ in the Lift-Off Region of a Heavy Duty Diesel Engine Using Raman Spectroscopy," *SAE Int. J. Fuels Lubr.* 2(1):645-660, 2009, doi:10.4271/2009-01-1357.
22. Miles, P.C., Collin, R., Hildingsson, L., Hultqvist, A., Andersson, Ö., "Combined measurements of flow structure, partially oxidized fuel, and soot in a high-speed, direct-injection diesel engine, " Proceedings of the Combustion Institute, 31 II, pp. 2963-2970. doi: 10.1016/j.proci.2006.07.231.
23. Miles Paul C., Hildingsson Leif, Hultqvist. Anders, "The influence of fuel injection and heat release on bulk flow structures in a direct-injection, swirl-supported diesel engine", Experiments in Fluids, Volume 43, Number 2-3, Page 273, 2007.
24. Wang, Z., Tanov, S., Wang, H., Richter, M. et al., "High-Speed Particle Image Velocimetry Measurement of Partially Premixed Combustion (PPC) in a Light Duty Engine for Different Injection Strategies," SAE Technical Paper 2015-24-2454, 2015, doi:10.4271/2015-24-2454.
25. Tanov, S., Wang, Z., Wang, H., Richter, M. et al., "Effects of Injection Strategies on Fluid Flow and Turbulence in Partially Premixed Combustion (PPC) in a Light Duty Engine," SAE Technical Paper 2015-24-2455, 2015, doi:10.4271/2015-24-2455.
26. Aronsson, U., Andersson, Ö., Egnell, R., Miles, P. et al., "Influence of Spray-Target and Squish Height on Sources of CO and UHC in a HSDI Diesel Engine During PPCI Low-Temperature Combustion," SAE Technical Paper 2009-01-2810, 2009, doi:10.4271/2009-01-2810.

CONTACT INFORMATION

Zhenkan Wang
PhD student
Combustion Physics Division
Physics Department, Lund University
Lund, 22363, Sweden
zhenkan.wang@forbrf.lth.se

ACKNOWLEDGMENTS

This research was performed at Lund University. The authors would like to acknowledge the Competence Centre for the Combustion Processes, KCFP and the Swedish Energy Agency (Project number 22485-3) for the financial support.

DEFINITIONS/ABBREVIATIONS

ATDC - after top dead center

CAD - crank angle degree

CFD - computational fluid dynamics

CI - compression ignition

HCCI - homogeneous charge compression ignition

ICE - internal combustion engine

ID - ignition delay

PLIF - planar laser induced fluorescence

PPC - partially premixed combustion

SACI - spark assisted compression ignition

SOC - start of combustion

SOI - start of injection

TDC - top dead center

APPENDIX

DISTORTION CORRECTION

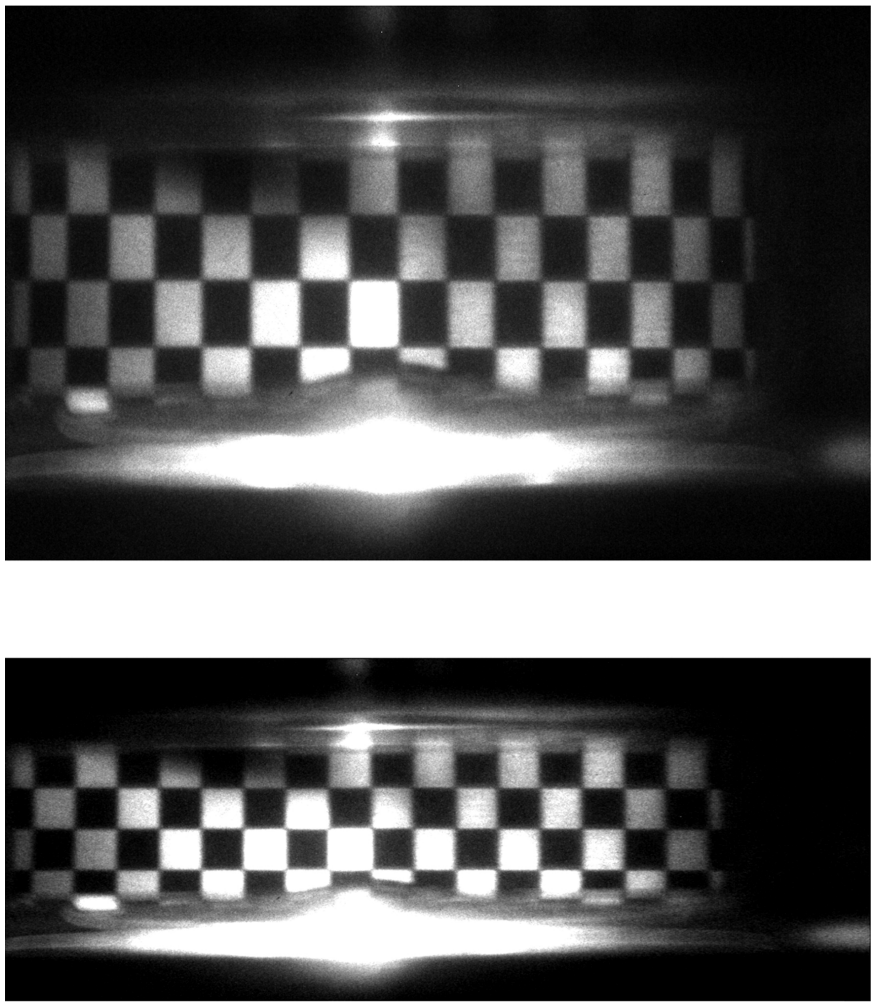

Figure 16. Recorded grid image before (upper) and after (lower) distortion correction.

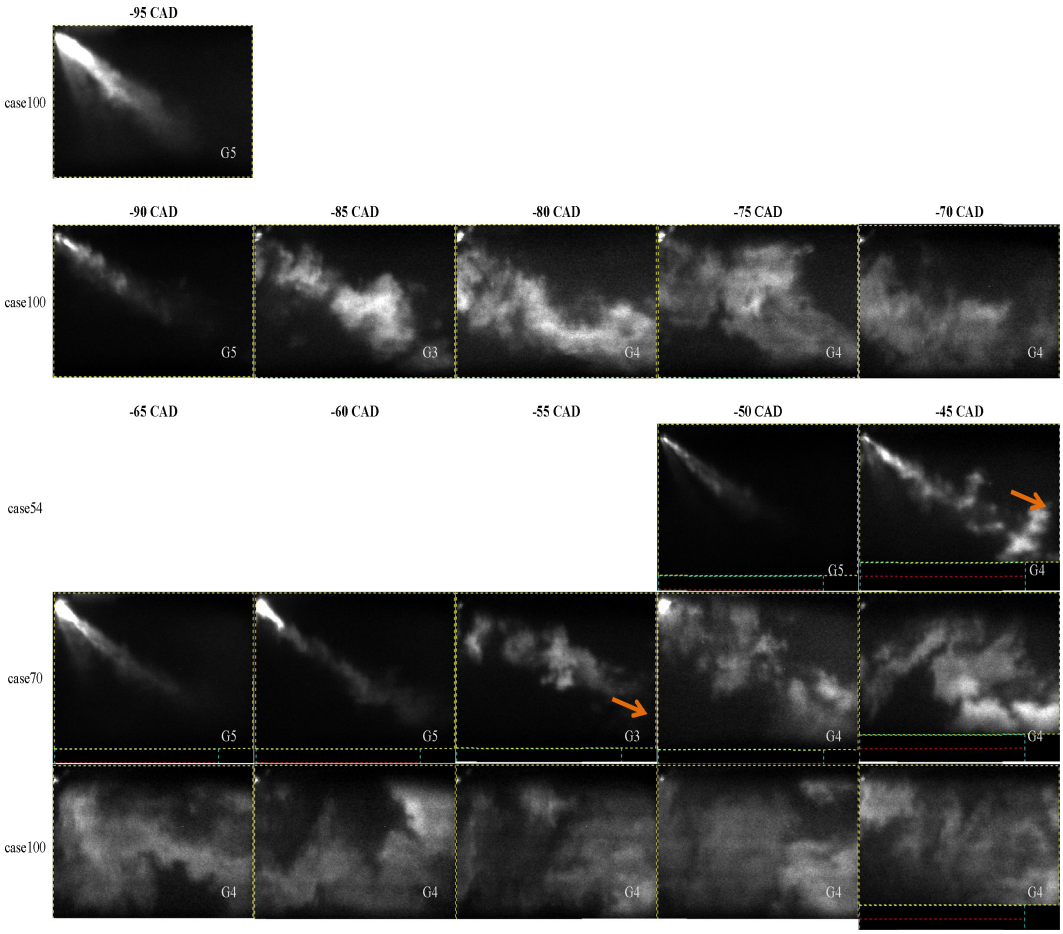

Figure 17.

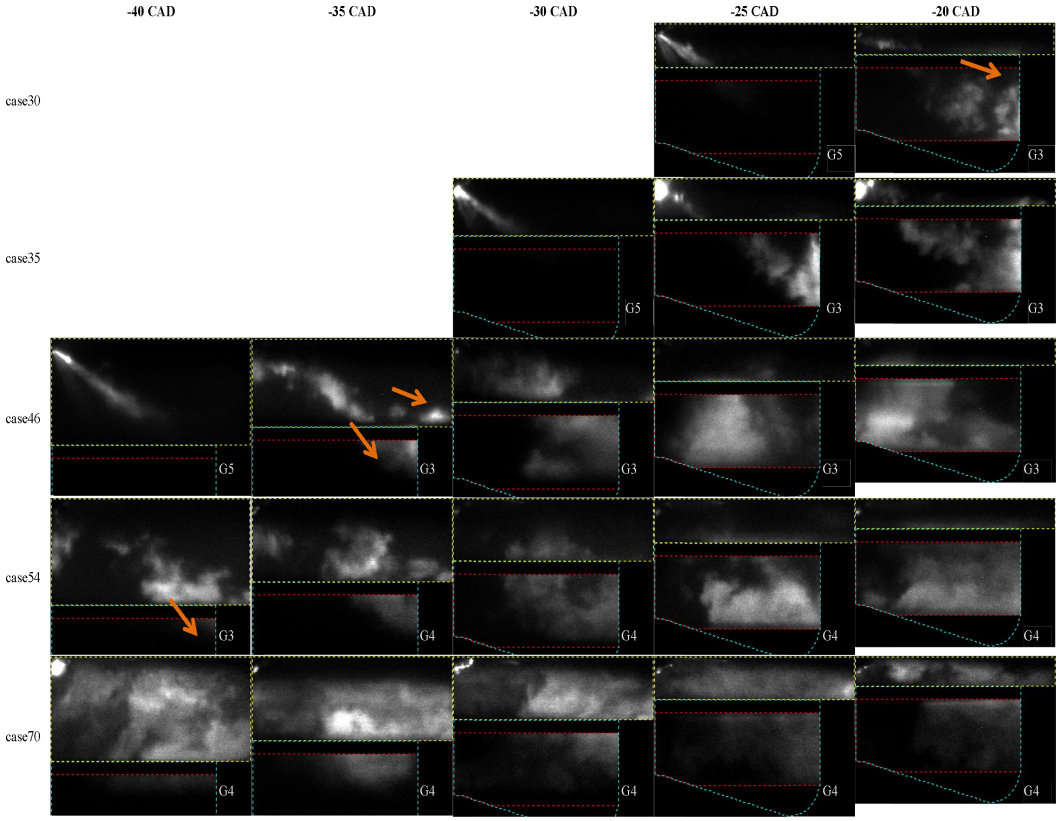

Figure 17. (cont.) Instantaneous PLIF images for all cases

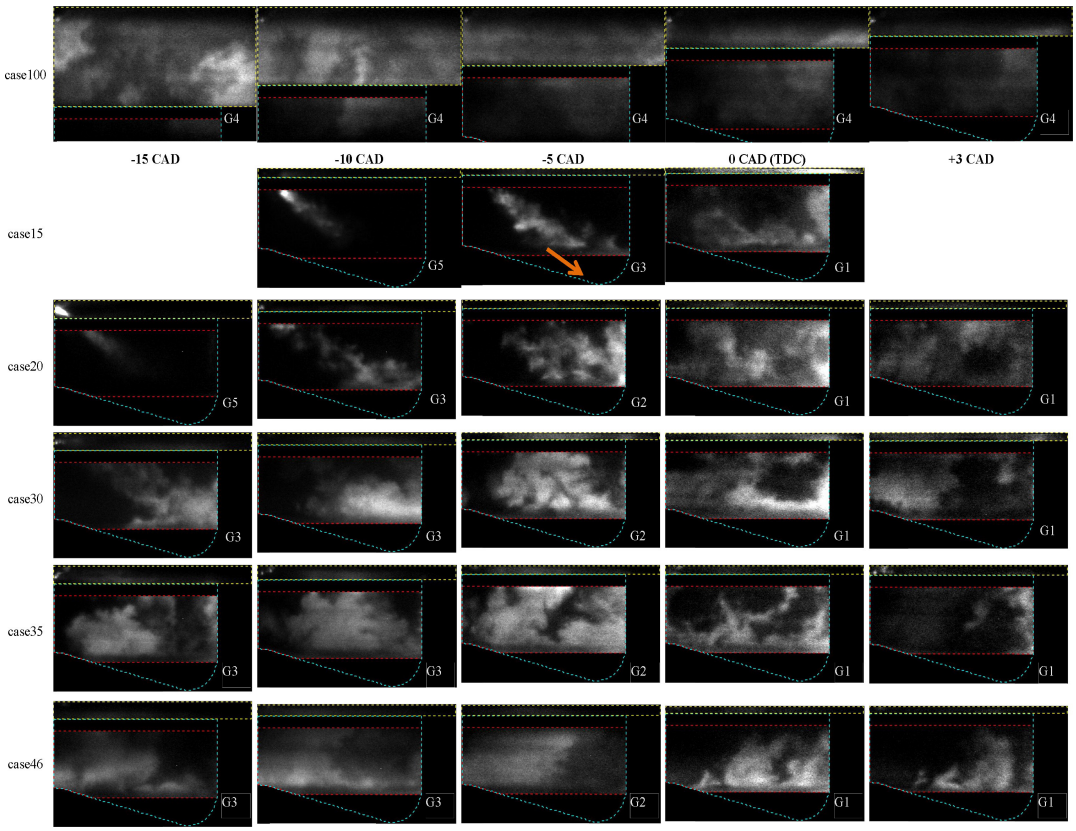

Figure 17. (cont.) Instantaneous PLIF images for all cases

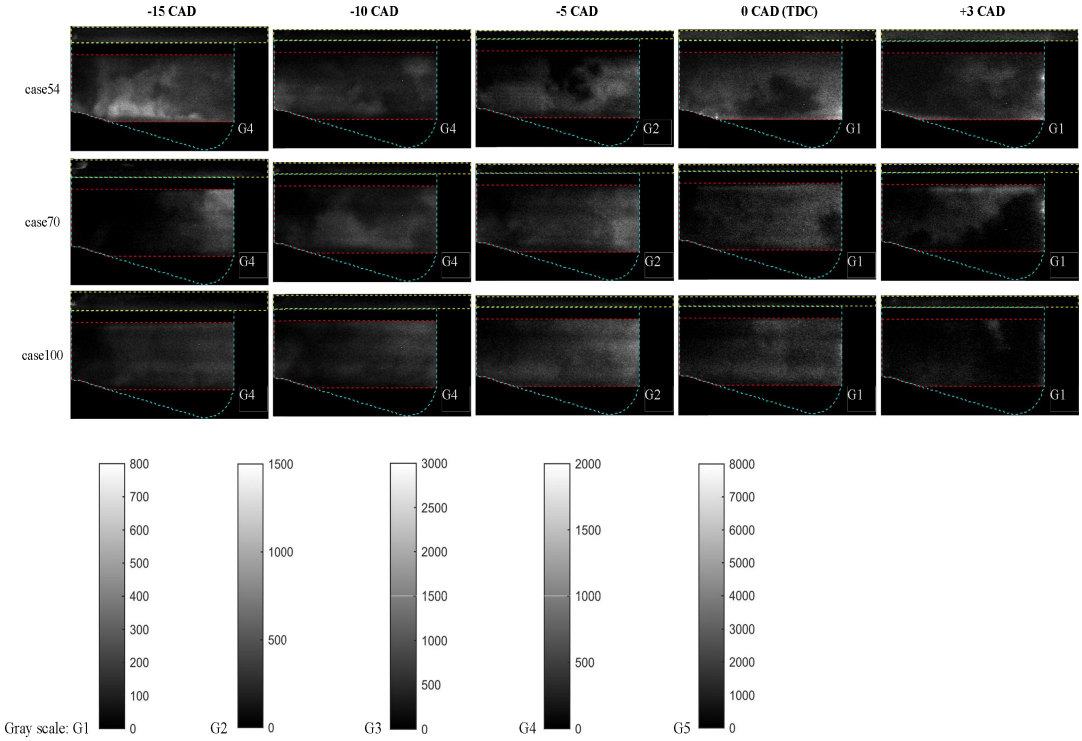

Figure 17. (cont.) Instantaneous PLIF images for all cases

Paper VI

Ultra-high-speed PLIF imaging for simultaneous visualization of multiple species in turbulent flames

ZHENKAN WANG,* PANAGIOTA STAMATOGLOU, ZHEMING LI, MARCUS ALDÉN, AND MATTIAS RICHTER

Division of Combustion Physics, Physics Department, Lund University, Box 118, Lund 22100, Sweden
**zhenkan.wang@forbrf.lth.se*

Abstract: In order to obtain more detailed characteristics and information in highly turbulent flames, for a better understanding of the transient behavior of eddies in such flames, a measurement technique with sufficient temporal resolution is requested. However, the probing of species distributions relevant in combustion (*e.g.* OH, CH_2O) with ultra-high-speed laser diagnostics still remains a challenge. Nd:YAG clusters commercially available can generate only 4-8 pulses, although with high laser energy. Systems based on a diode-pumped solid-state Nd:YAG laser combined with a dye laser produce only about 100 μJ pulse energy at ultra-high repetition rates (≥50 kHz). Even more comprehensive information on the flame structure can be gained if simultaneous recording of multi-species is performed. In the present work, the development of the first ultra-high-speed diagnostic technique capable of simultaneous probing of hydroxyl radicals and formaldehyde distributions at a repetition rate of 50 kHz is outlined. This has been achieved by employing a burst laser pumped optical parametric oscillator system for the simultaneous detection of CH_2O excited at 355 nm and OH-radicals excited at 283 nm, where the interference of scattering laser light can be avoided. The applicability of the proposed technique was demonstrated in a highly turbulent jet flame. Moreover, the presented improvement in terms of the number of consecutive images recorded with ultra-high-speed planar laser induced fluorescence imaging is significant. Due to the high temporal resolution, the movement of CH_2O pocket enclosed by OH at the flame tip can be clearly captured. The transport velocity of the CH_2O pocket was calculated and found to be in good agreement with previous LDV results.

OCIS codes: (120.4820) Optical systems; (120.1740) Combustion diagnostics; (300.2530) Fluorescence, laser-induced; (190.4970) Parametric oscillators and amplifiers; (110.6915) Time imaging.

References and links

1. W. Lempert, P. F. Wu, R. Miles, B. Zhang, J. Lowrance, V. Mastrocola, and W. Kosonocky, "Pulse-burst laser system for high-speed flow diagnostics," in Proceedings of 34th Aerospace Sciences Meeting and Exhibit, AIAA Paper 96–0179 (1996).
2. W. Lempert, P. F. Wu, and R. Miles, "Filtered rayleigh scattering measurements using a MHz rate pulse-burst laser system," in *Proceedings of 35th Aerospace Sciences Meeting and Exhibit* (1997), paper 97–0500 (1997).
3. P. F. Wu, W. Lempert, and R. Miles, "Megahertz pulse-burst laser and visualization of shock-wave/boundary-layer interaction," AIAA J. **38**(4), 672–679 (2000).
4. C. F. Kaminski, J. Hult, and M. Aldén, "High repetition rate planar laser induced fluorescence of OH in a turbulent non-premixed flame," Appl. Phys. B **68**(4), 757–760 (1999).
5. J. Nygren, J. Hult, M. Richter, M. Aldén, M. Christensen, A. Hultqvist, and B. Johansson, "Three-dimensional laser induced fluorescence of fuel distributions in an HCCI Engine," Proc. Combust. Inst. **29**, 679–685 (2002).
6. B. Thurow, N. Jiang, and W. Lempert, "Review of ultra-high repetition rate laser diagnostics for fluid dynamic measurements," Meas. Sci. Technol. **24**, 012002 (2013).
7. K. N. Gabet, R. A. Patton, N. Jiang, W. Lempert, and J. A. Sutton, "High-speed CH_2O PLIF imaging in turbulent flames using a pulse-burst laser system," Appl. Phys. B **106**, 569–575 (2012).
8. M. N. Slipchenko, J. D. Miller, S. Roy, J. R. Gord, S. A. Danczyk, and T. R. Meyer, "Quasi-continuous burst-mode laser for high-speed planar imaging," Opt. Lett. **37**(8), 1346–1348 (2012).
9. J. B. Michael, P. Venkateswaran, J. D. Miller, M. N. Slipchenko, J. R. Gord, S. Roy, and T. R. Meyer, "100 kHz thousand-frame burst-mode planar imaging in turbulent flames," Opt. Lett. **39**(4), 739–742 (2014).

10. J. D. Miller, M. Slipchenko, T. R. Meyer, N. Jiang, W. R. Lempert, and J. R. Gord, "Ultrahigh-frame-rate OH fluorescence imaging in turbulent flames using a burst-mode optical parametric oscillator," Opt. Lett. **34**(9), 1309–1311 (2009).
11. I. Boxx, C. M. Arndt, C. D. Carter, and W. Meier, "High-speed laser diagnostics for the study of flame dynamics in a lean premixed gas turbine model combustor," Exp. Fluids **52**, 555–567 (2012).
12. R. Wellander, M. Richter, and M. Aldén, "Time-resolved (kHz) 3D imaging of OH PLIF in a flame," Exp. Fluids **55**, 1746 (2014).
13. S. Hammack, C. Carter, C. Wuensche, and T. Lee, "Continuous hydroxyl radical planar laser imaging at 50 kHz repetition rate," Appl. Opt. **53**(23), 5246–5251 (2014).
14. A. A. Konnov, "Implementation of the NCN pathway of prompt-NO formation in the detailed reaction mechanism," Combust. Flame **156**, 2093–2105 (2009).
15. J. Sjöholm, E. Kristensson, M. Richter, M. Aldén, G. Göritz, and K. Knebel, "Ultra-high-speed pumping of an optical parametric oscillator (OPO) for high-speed laser-induced fluorescence measurements," Meas. Sci. Technol. **20**, 025306 (2009).
16. N. Jiang, R. A. Patton, W. Lempert, and J. A. Sutton, "Development of high-repetition rate CH PLIF imaging in turbulent nonpremixed flames," Proc. Combust. Inst. **33**, 767–774 (2011).
17. B. Zhou, C. Brackmann, Z. Li, M. Aldén, and X.-S. Bai, "Simultaneous multi-species and temperature visualization of premixed flames in the distributed reaction zone regime," Proc. Combust. Inst. **35**, 1409–1416 (2015).
18. J. Sjöholm, J. Rosell, B. Li, M. Richter, Z. Li, X.-S. Bai, and M. Aldén, "Simultaneous visualization of OH, CH, CH_2O and toluene PLIF in a methane jet flame with varying degrees of turbulence," Proc. Combust. Inst. **34**, 1475–1482 (2013).
19. B. Zhou, Q. Li, Y. He, P. Petersson, Z. Li, M. Aldén, and X.-S. Bai, "Visualization of multi-regime turbulent combustion in swirl-stabilized lean premixed flames," Combust. Flame **162**, 2954–2958 (2015).
20. B. Zhou, *Advanced laser-based multi-scalar imaging for flame structure visualization towards a deepened understanding of premixed turbulent combustion* (Doctoral Thesis, Lund University 2015).
21. B. Böhm, C. Heeger, R. L. Gordon, and A. Dreizler, "New perspectives on turbulent combustion: multi-parameter high-speed planar laser diagnostics," Flow Turbul. Combus. **86**, 313–341 (2011).
22. Z. Li, J. Rosell, M. Aldén, and M. Richter, "Simultaneous burst imaging of dual species using planar laser-induced fluorescence at 50 kHz in turbulent premixed flames," Appl. Spectrosc. **71**(6), 1363–1367 (2017).
23. B. Zhou, C. Brackmann, Q. Li, Z. Wang, P. Petersson, Z. Li, M. Aldén, and X.-s. Bai, "Distributed reactions in highly turbulent premixed methane/air flames," Combust. Flame **162**, 2937–2953 (2015).
24. B. Zhou, C. Brackmann, Z. Wang, Z. Li, M. Richter, M. Aldén, and X.-S. Bai, "Thin reaction zone and distributed reaction zone regimes in turbulent premixed methane/air flames: scalar distributions and correlations," Combust. Flame **175**, 220–236 (2017).
25. J. Rosell, X.-S. Bai, J. Sjoholm, B. Zhou, Z. Li, Z. Wang, P. Pettersson, Z. Li, M. Richter, and M. Alden, "Multi-species PLIF study of the structures of turbulent premixed methane/air jet flames in the flamelet and thin-reaction zones regimes," Combust. Flame **182**, 324–338 (2017).
26. J. Luque and D. R. Crosley, "LIFbase: database and spectral simulation (Version 2.0.60, 2008)," Sri. Int. Report MP. 99–009 (2008).
27. B. Halls, P. Hsu, N. Jiang, E. Legge, J. Felver, M. N. Slipchenko, S. Roy, T. R. Meyer, and J. R. Gord, "kHz-rate four-dimensional fluorescence tomography using an ultraviolet-tunable narrowband burst-mode optical parametric oscillator," Optica **4**, 897–902 (2017).
28. C. Brackmann, J. Nygren, X. Bai, Z. Li, H. Bladh, B. Axelsson, I. Denbratt, L. Koopmans, P.-E. Bengtsson, and M. Aldén, "Laser-induced fluorescence of formaldehyde in combustion using third harmonic Nd:YAG laser excitation," Spectrochim. Acta A Mol. Biomol. Spectrosc. **59**(14), 3347–3356 (2003).
29. A. D'Anna and A. Violi, "A kinetic model for the formation of aromatic hydrocarbons in premixed laminar flames," in Proceedings of 27th Symposium on Combustion, 425–433 (1998).

1. Introduction

Turbulent combustion commonly occurs in most practical advanced combustors nowadays, such as internal combustion engines (ICE) and gas turbines. Comprehensive understanding of turbulent combustion calls for more advanced modelling and diagnostic techniques. Eddies in the flow field of a turbulent flame can form, interact and propagate rapidly. The time-scales of both turbulence and chemical reactions span widely from nanoseconds to seconds. For a better understanding of the transient behavior (small integral time-scales) of wrinkled structures and eddies in highly turbulent flames, sufficient temporal resolution is needed. However, that still remains challenging experimentally.

During the last two decades, the field of high speed diagnostics has seen significant development. Initially, burst-mode lasers were introduced. These are based on sequential amplification of a high repetition rate seed laser [1–3]. Soon after, Nd:YAG clusters were developed that can produce bursts with short pulse separation (theoretically with no minimum

time limitation between pulses) making them capable of resolving very small time scales, *e.g.* 125 μs [4] and 10 μs [5], while maintaining pulse energies similar to what is normally found in 10 Hz systems. The architecture of complete parallel systems in the YAG clusters implies that they can be faster than the burst-mode systems but their main drawback is the limited number of pulses. However, the burst mode systems allow for high temporal resolution under prolonged time scales [6]. In several studies as mentioned below burst-mode systems have been used for the investigation of turbulent flames.

Using a burst-mode YAG-laser, probing of species distributions relevant in combustion, *e.g.* CH_2O excited at 355 nm can be achieved through planar laser induced fluorescence (PLIF). Gabet *et al.* demonstrated the visualization of CH_2O in a turbulent CH_4-air flame with excellent signal-to-noise ratio [7]. Taking it one step further, Slipchenko *et al.* developed a burst-mode laser and one of the applications exhibited the detection of CH_2O in a CH_4-air diffusion flame at 20 kHz repetition rate [8]. This approach has later been improved by Michael *et al.* [9] to facilitate imaging of CH_2O at 100 kHz.

Besides CH_2O species, OH is also an important radical in combustion, and its formation is commonly employed as a marker of the reaction zone in a flame. However, excitation of OH radicals cannot be accessed directly by the harmonics from the commonly employed Nd:YAG laser systems. This could present a challenge for ultra-high-speed diagnostics since although the pump lasers might be available, rapid high energy pumping of dye-lasers has proven to be problematic [4]. Albeit there has been a significant development of dye-lasers since then, there are no reports demonstrating that dye-lasers operate efficiently in combination with high-energy and high-repetition-rate pump lasers. The first ultra-high-speed (50 kHz and above) OH measurement was conducted by Miller *et al.* [10] in a H_2-air diffusion flame. They used the output of a seeded optical parametric oscillator (OPO), mixed with residuals at 532 nm from the pump source, to achieve laser radiation at around 313 nm. This was used to probe the P2(10) line in the (0,0) vibrational band of OH. Although this excitation scheme is favored by a high fluorescence yield, scattering light from the laser prohibits such a diagnostic approach from being employed in practical combustion systems with confined combustion chambers, such as ICE.

An alternative excitation scheme commonly employed for the detection of OH radicals is to probe the (1,0) vibrational transition, at approximately 284 nm. The red-shifted fluorescence, at 308 nm, facilitates the spectral filtering of the spurious laser radiation. High speed OH PLIF can be achieved by using a diode-pumped solid-state (DPSS) Nd:YAG laser combined with a dye laser, which has been reported in, for example, premixed CH_4-air flames [11, 12]. Nevertheless, the detection of OH radicals at repetition rates higher than 20 kHz by means of this laser system significantly has disadvantage of the low pulse energy (about 100 μJ) available, leading to low signal-to-noise ratio (SNR). Hammack *et al.* demonstrated OH-PLIF imaging in a Henchen burner and a DC transient-arc plasmatron at 50 kHz repetition rate with a DPSS and a dye laser [13]. However, in a CH_4-air turbulent flame, the OH concentration is very low, *.e.g.* several thousand ppm calculated by numerical simulation with modeling provided in [14].

Experience from earlier work, where dye-lasers were pumped using the high energy output from the Multi-YAG system [4], indicates that such technology would not be favorable for the applications of burst-mode laser system. For ultra-high-speed OH detection, the combination of a burst-mode YAG-laser and an OPO could be a viable solution for providing a decent compromise between pulse energy and repetition rate. Sjöholm *et al.* have successfully demonstrated the utilization of a YAG-cluster/OPO combination to excite the A-X (1,0) vibration band of the OH molecule at 282.97 nm with 8-pulses per burst, and to detect the fluorescence of OH through the A-X (0,0) transition around 308 nm [15]. Another example is that Jiang *et al.* employed a burst-mode laser system in combination with an OPO at 10 kHz repetition rate to investigate the presence of CH in a DLR Flame A [16].

It has been demonstrated extensively that multi-scalar detection plays an important role in the understanding of turbulent flame structures [17–20]. Further comprehension of the flame structure can be gained due to detailed information that simultaneous recording of multi-species provide. Naturally, different species represent different characteristics of the flame. The highest gradient of OH is a well-established marker of the flame front as mentioned before. CH_2O is mostly present in the preheat zone and is, hence, often used as a marker of that zone. Furthermore, simultaneous measurement of OH and CH_2O has been proposed to provide a good qualitative measure of the heat release rate [21] which is an important quantity for studying turbulent combustion. For these reasons, simultaneous ultra-high-speed OH and CH_2O measurements can provide both scalar and temporal information on the evolution of the pre-heat zone and flame topology. This can potentially aid the understanding of turbulent flames and thus be useful for model validation. At present, this combination of multiple scalars, probed at such ultra-high repetition rates, has not yet been accomplished according to the authors' best knowledge.

This work aims at developing the first ultra-high-speed diagnostic technique capable of simultaneous probing of hydroxyl radicals and formaldehyde distributions in a highly turbulent flame at a repetition rate of 50 kHz. This has been achieved by employing a burst laser pumped OPO system. The output from such high speed multi-scalar measurements can bring out new insights to the interaction between turbulence and chemical reactions.

Moreover, 100 consecutive images were recorded in the present work. Therefore, this brings the possibility of following events that occur over longer sequences than in the previous work by Sjöholm and Li *et al.* with 8 images [18, 22], and Miller *et al.* who presented 28 pulses [10].

The novelty of the present study and the difference compared to previous studies are as follows. Firstly, the OH-PLIF is performed utilizing the 283.93 nm Q1(9) transition, which has less temperature dependence. Secondly, a 310 nm band-pass filter is used in order to suppress most of the scattered light at 283.93 nm, which facilitates measurements also in confined combustion chambers. The latter cannot be achieved by exciting at 309 nm due to lower SNR. Thirdly, the sequence of 100 images (simultaneous CH_2O/OH) is significantly longer than reported in previous work [10, 22]. This would be highly beneficial, for example, in ICE applications where the entire combustion phase in a single cycle can be captured.

2. Experimental setup

Figure 1 illustrates the experimental setup for simultaneous multi-species visualization in a premixed turbulent jet flame. The burner is a hybrid porous-plug/jet type burner (LUPJ burner), described in more detail in [17, 18, 23–25]. Its main parts are a porous sintered stainless steel plug with a diameter of 61 mm and a 1.5 mm-diameter nozzle in the center for the creation of a jet flame. Premixed CH_4 and air mixture were fed through the center nozzle to create the jet flame which was stabilized by a reacting co-flow in the form of a premixed CH_4-air flat-flame above the porous plug. The gas flows were regulated by six mass flow controllers (Bronkhorst), all calibrated at 300 Kelvin with higher than 98.5% accuracy. Various conditions were studied by altering the flow speed in the jet and co-flow as well as the air-fuel ratio as shown in Table 1. The turbulent Reynolds numbers, Kolmogorov length scales and Karlovitz numbers of the jet flame are depict in Table 2. Detailed calculation is presented in the previous study [23].

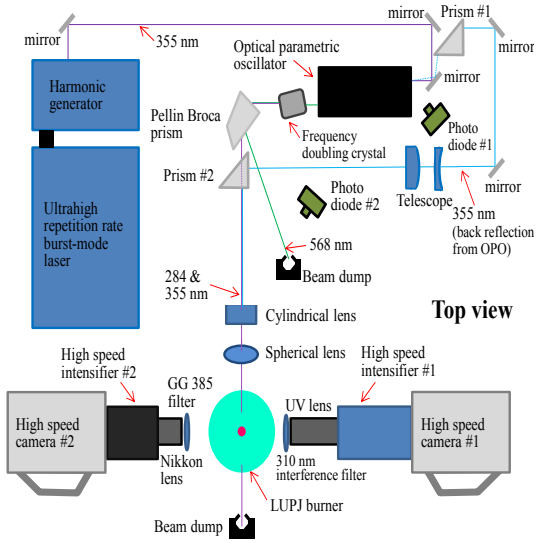

Fig. 1. Schematic diagram of experimental setup for ultra-high-speed simultaneous OH and CH_2O PLIF imaging.

Table 1. Flow conditions

Case	1	2	3
Jet flow speed(m/s)	66	66	110
Equivalence ratio of jet flow	1	0.3	1
Co-flow flow speed (m/s)	0.3	0.1	0.3
Equivalence ratio of co-flow	0.9	0.9	0.9

Table 2. Quantities for the jet flames at 45 mm height above the burner (HAB) [23]

Jet flow speed(m/s)	Turbulent Reynolds number	Kolmogorov length scale (μm)	Karlovitz number
66	95	96	25
110	190	57	70

The laser system used in the experiment to pump an OPO (GWU, PremiScan/ MB) is a state-of-the-art ultra-high-speed laser (QuasiModo by Spectral Energies, LLC), which is similar but not identical to the one developed by Slipchenko *et al.* [8]. In short, the laser system is a hybrid-pumped burst-mode laser with two diode-pumped amplifiers followed by five flashlamp-pumped amplifiers. Two 4-mm flashlamp-pumped amplifiers serve as a double-pass for the laser beam in order to increase the gain. The beam is being further amplified after passing through three flashlamp-pumped amplifiers. In the future, the system will be equipped with one extra 12-mm amplifier which will result in an energy output twice as high as for the present configuration.

The measured output energy of this laser is approximately 210 mJ/pulse at 1064 nm and 50 kHz repetition rate. The maximum burst duration is 10 ms which refers to 500 consecutive laser pulses per burst, at 50 kHz. However, a burst duration of 2 ms was used in the presented work with a 10 seconds separation between the bursts, in order to avoid thermal lensing effects in the amplifiers. The pulse duration was set to 15 ns at full width at half maximum (FWHM) and the spectral bandwidth was below 0.03 cm^{-1} at 1064 nm.

A third harmonic generator (THG) crystal (KDP type) was utilized in order to produce radiation at 355 nm. The peak output energy after the THG was measured at 80 mJ/pulse. The beam size was reduced to approximately 4 mm in diameter, using a telescope before the β-barium borate (BBO) crystal, in order to increase the power density and consequently the

conversion efficiency of the OPO. The output wavelength of the OPO signal beam was measured by a wavemeter (GWU, LambdaScan) and the desired wavelength was selected before frequency doubling in a KDP type crystal.

In the present work an OH excitation scan from 282.3 nm to 284.5 nm was performed initially. The emission from the A-X (0, 0) transition was collected at around 308 nm, through an interference filter (λ_T = 310 ± 10 nm) mounted in front of a CMOS camera (Photron SA-Z) equipped with a lens coupled high speed intensifier (Lavision HS-IRO).

In Fig. 2 the excitation scan is presented together with a fitted curve generated by LIFBASE [26]. In the LIFBASE simulation the settings were selected based on a 0.06 nm resolution Gaussian profile and 1600 K flame temperature. After comparing the OH excitation scan with the LIFBASE simulation, an experimental resolution of approximately 0.06 nm could be estimated. The specific transition at 283.93 nm ($A^2\Sigma^+$-$X^2\Pi$, 1-0 transition) was selected because of its high population and limited dependence on the flame temperature in the 1500-2500 K range. Furthermore, it is spectrally well separated from other transitions lines. Further information on this specific transition line can be found in [27].

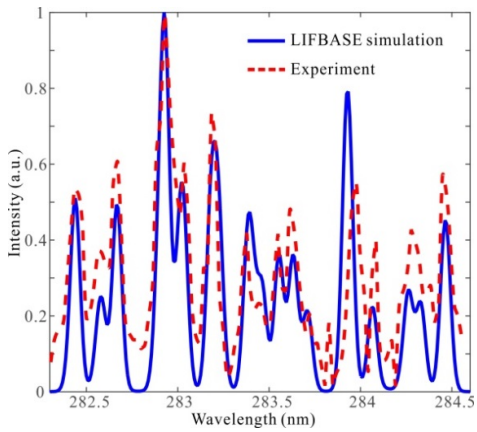

Fig. 2. Excitation scan from 282.3 nm to 284.5 nm covering the major part of the A–X (1–0) transition of the OH molecule.

The OH excited wavelength will be expressed as 284 nm instead of 283.93 nm below.

In Fig. 1, after the doubling crystal, a Pellin Broca prism was used to separate 284 nm from 568 nm. The 284 nm beam was then formed into a laser sheet by a cylindrical lens (f = –40 mm) in combination with a spherical lens (f = 200 mm). The resulting pulse energy of the 284 nm at 50 kHz was about 350 μJ/pulse, which is sufficient for getting good SNR in this application. The shot-to-shot variation in pulse energy is less than 10%.

CH_2O was excited in several rotational transitions at 355 nm [28]. For this purpose the residuals of the OPO pump beam were collected by a prism (#1) as shown in Fig. 1. A telescope in the 355 nm beam path was used to locate the focal points of both 284 nm and 355 nm beams at the center of the burner with only one set of sheet forming optics. The 355 nm beam was redirected, along the same direction as the 284 nm beam, by another prism (#2) which was positioned just below the 284 nm beam path. The height of the 284 nm and the 355 nm laser sheets were around 23 mm and 14 mm respectively and the thickness of both was coarsely measured to be less than 200 μm.

Two high speed cameras in combination with two high speed intensifiers were mounted opposite to each other in order to capture both OH and CH_2O fluorescence simultaneously. For detecting the former species, a CMOS Photron Fastcam SA-Z (see Fig. 1: High speed camera #1) was used in combination with a high speed intensified (LaVision HS-IRO). For the CH_2O imaging, a CMOS Photron Fastcam SA-X2 (see Fig. 1: High speed camera #2) was

employed which was also combined with a high speed intensifier (Lambert HS IRO 2 stage). The resolution had to be reduced due to the limited read-out speed of both cameras at 50 kHz. In the present work, the resolution of the CMOS cameras was reduced to 1024 x 400 and 640 x 384, respectively. The exposure gate-width of both high speed intensifiers was set to 100 ns to make sure that any temporal jittering in the laser/detector system would not affect the results. At 100 ns exposure time, background signals caused by the chemiluminescence of the flame were proved to be negligible. Both image intensifiers were operated in the middle of their respective gain range. The parameters of camera lens and filters utilized for the cameras are described in Table 3.

Table 3. Parameters of the optical setup

Species	OH	CH_2O
Camera pixels	1024 x 400	640 x 384
Intensifier	LaVision HS-IRO	Lambert HS IRO 2 stage
Intensifier gain	55	700
Camera lens	B. Halle lens, f# = 2, f = 100 mm	Nikkon f# = 1.2, f = 50 mm
Field of view	27 mm x 10 mm	17 mm x 10 mm
Optical filter	Interference filter, $\lambda_T = 310 \pm 10$ nm	long pass filter, GG 385
Intensifier gate	100 ns	100 ns
λ_{laser}	283.93 nm	355 nm
Laser energy	0.35 mJ	6 mJ

The residual 355 nm and the OPO output at 568 nm were monitored using fast photo diodes (PDs). By observing the signal of PDs, the gate of intensifiers and the exposure timing of cameras on an oscilloscope, accurate timing could be achieved for the image acquisition. By carefully aligning the two cameras the corresponding field of view (FOV) which is 27 mm x 27 mm measuring at full chip could be made virtually identical. A transparent grid object was used to generate reference images for both cameras. Hence, pixel to pixel correspondence between images recorded by the two cameras could be achieved through image registration.

3. Results and discussion

As a 2ms burst contains 100 pulses in the experiment, thermal load on the BBO crystal of the OPO is quite high leading to potential problems. Due to the increased thermal load of the BBO in longer bursts, optimal phase matching conditions cannot be maintained throughout the full duration of the burst. This causes a decrease in the conversion efficiency for subsequent pulses and, hence, a steady drop in available laser energy at 284 nm. One might expect a similar behavior from the pump source at 355 nm, but this was verified to show only a marginal drift in pulse energy during a burst. It was also noted that the output wavelength from the OPO was drifting shot-by-shot after a ‘cold start’. After being ‘warming-up’ by the burst laser, the wavelength shift stabilized and it could be compensated by adjusting the angle of the BBO.

To demonstrate the applicability of the proposed diagnostics, a practical application of this ultra-high-speed imaging technique in a turbulent jet flame is described below. 100 consecutive images of both species in the turbulent flame were captured with a 20-μs interval between successive images, corresponding to a 50 kHz data acquisition rate.

The SNR was calculated based on dividing the average value of the signal by the standard deviation of the background noise from the region where laser radiation is present but there is no fluorescence signal. Figure 3 shows the raw images of OH and CH_2O signals prior to post-processing. One solid line and one dashed line were selected for both OH and CH_2O at different heights above the burner for SNR calculation. Figure 4 contains plotted signal profiles of OH and CH_2O along the red lines, respectively. The averaged value of the signal is marked as I_s and I'_s while the standard deviation of the background noise is indicated as I_n

and I'_n. The region for signal or noise calculation is illustrated as the width of the arrows in Fig. 4. The resulting SNR for OH and CH_2O were calculated to be around 40 and 18, respectively.

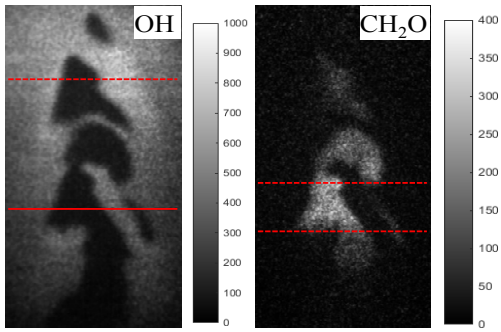

Fig. 3. Raw images of OH signal (left) and CH_2O (right) without post-processing.

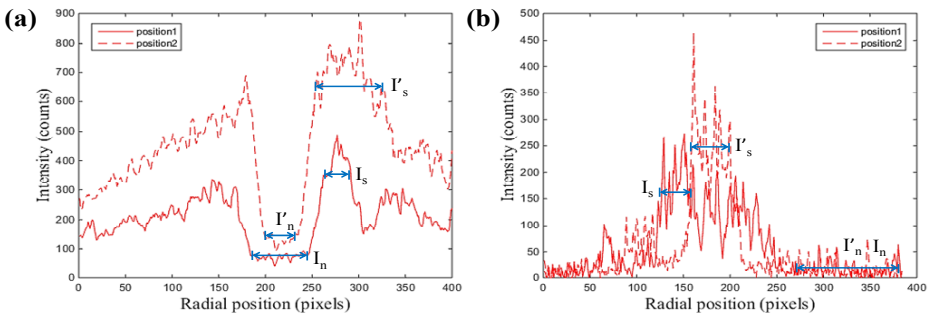

Fig. 4. (a) OH and (b) CH_2O PLIF signal profiles. The locations of the profiles are marked with a solid line and a dashed line on the single shot OH and CH_2O PLIF images as shown in Fig. 3, respectively.

It is worth pointing out that both CH_2O and Polycyclic aromatic hydrocarbon (PAH) mark the fuel-rich regions of the flame. However, from numerical simulations, the CH_2O concentration in CH_4-air flames is about one thousand ppm at stoichiometric condition while PAH concentration is much lower (<10 ppm) [29]. Furthermore, a PLIF measurement was conducted in a CH_4-air flame at stoichiometric condition with 266 nm and 355 nm wavelengths respectively to check the contribution of PAH fluorescence on the CH_2O signal. The results show that the PAH fluorescence is barely detected, which is as low as the background noise, while the CH_2O signal is well distinguished. Therefore, the influence of PAH on CH_2O signal is considered to be negligible in this experiment. PAH can also be excited by 284 nm laser beam. Any possible cross talk was evaluated by blocking one laser at the time, which revealed no detectable cross talk as well. For high PAH concentration flames, preferred solution can be delaying the OH excitation beam significantly (on the order to 50 ns) with respect to the CH_2O excitation beam to avoid the resulting cross talk.

The first case in Table 1 is presented in Fig. 5, where the red region indicates the OH distribution. The green region, which is enclosed by the OH distribution, represents the distribution of CH_2O, a species commonly used as a marker of low temperature reactions in the preheat zone. In the post-processing, both OH and CH_2O images have been normalized by their maximum value. In Fig. 5 one can notice the strong spatial correlation between the distributions of these two species. The number in the upper right corner of each sub-image indicates the number of the frame in a consecutive sequence of images. For the conditions prevailing, the time scale, τ ($\tau = (\nu/\varepsilon)^{0.5}$), at 45 mm height above the burner (HAB) is about

0.05 ms for a jet speed of 66 m/s and it is around 0.02 ms for 110 m/s. In addition, the integral time scale, τ_0 ($\tau_0 = l_0/u$), is approximately 0.44 ms and 0.22 ms, respectively. Thus, the temporal resolution achieved is capable of following the turbulent development of this jet flame.

For brevity, only a couple of consecutive OH and CH_2O images are presented in the "results and discussion" section. But additional data are available in the appendix and supplementary materials (see Visualization 1, Visualization 2, and Visualization 3).

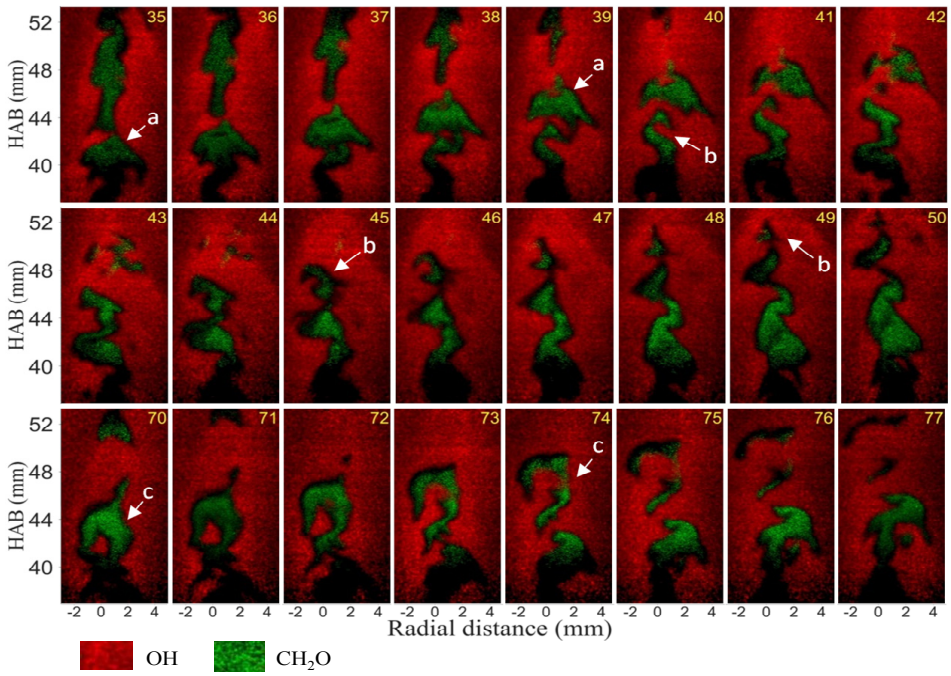

Fig. 5. Simultaneous OH (red), and CH_2O (green) PLIF images measured in case 1 (ϕ_{jet} = 1, U_{coflow} = 0.3 m/s) at 45 mm HAB.

It is worth mentioning that in some situations, 100 images of OH and CH_2O are critically useful for the combustion characterization within a specific time domain. For example, in the homogeneous charge compression ignition (HCCI) and partially premixed combustion (PPC) engines, the duration of the main combustion phase is less than 15 crank angle degrees which corresponds to 2 ms at 1200 rpm (100 images at 50 kHz). Furthermore, in turbulent combustion studies, the chance of capturing extinction and re-ignition events can be significantly increased when more consecutive images are available.

In Fig. 5, the CH_2O signal is absent from the upper and lower part of the imaged area, because of the limitation in laser energy and the non-uniform energy distribution in the residual OPO pump beam. However, this does not mean that there is no CH_2O present in the flame.

The CH_2O was transported downstream the jet flame by convection, *e.g.* several flame structures (spatial structure a, b and c) in the sub-images of Fig. 5 (start from No. 35, No. 40 and No. 70) can be observed and followed as the combustion process progress. The temporal resolution is sufficient to visualize the process in which the CH_2O region was disconnected into small pockets at the 'neck' point of the flame. Later, the CH_2O pocket was deformed into thin and long ligaments due to the turbulence straining and shearing, while being consumed.

These results are in good agreement with the results obtained by Sjöholm *et al.* [18] and Zhou *et al.* [23]. In those publications single-shot imaging captured at 10 Hz shows that the

CH_2O is usually an extended thin ligament at the tip of the flame. However, with the utilization of this ultra-high-speed diagnostics, the development of highly turbulent flame structures can be visualized and investigated for a better understanding of turbulent combustion processes.

In case 2, the equivalence ratio of the jet flow was reduced to 0.3 and the co-flow speed was decreased to one-third of the previous case (case 1), leading to local extinction as shown in Fig. 6. As a consequence, the jet flame became unstable because less heat was supplied by the surrounding co-flow flame as well as leaner combustion for the jet flow and local quenching of OH could be identified. For instance, from sub-images No. 33 to No. 42,

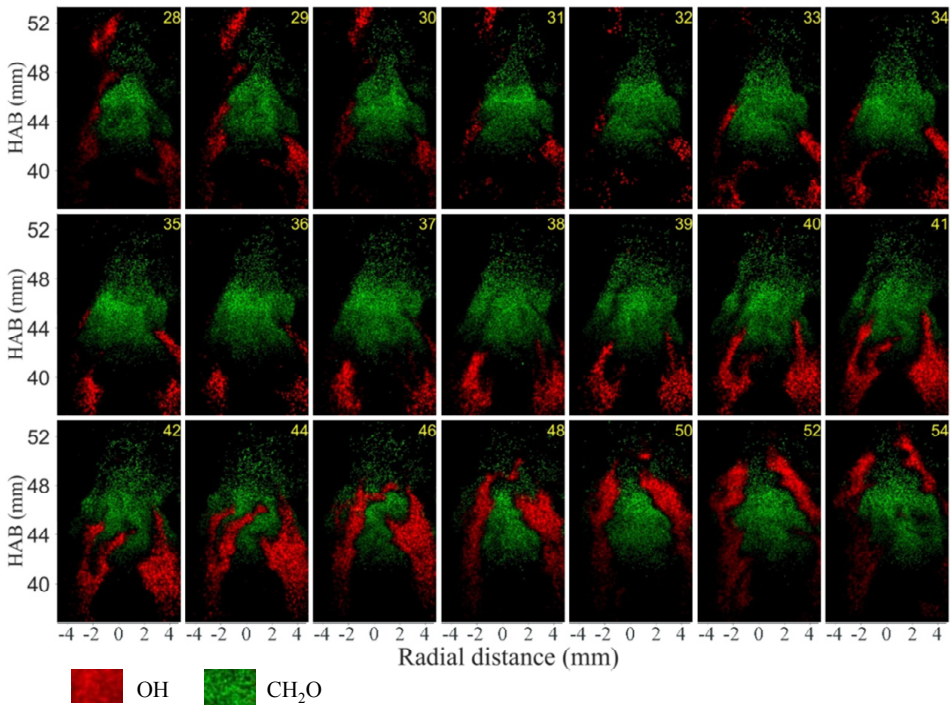

Fig. 6. Simultaneous OH (red), and CH_2O (green) PLIF images measured in case 2 (ϕ_{jet} = 0.3, U_{coflow} = 0.1 m/s) at 45 mm HAB where quenching of OH occurs.

OH was hardly observed at the height above 44 mm HAB while CH_2O distributed in this domain. It is evident that starting from No. 44 (Fig. 6), re-ignition occurs at the flame-tip as indicated by the OH layer propagating to a higher position.

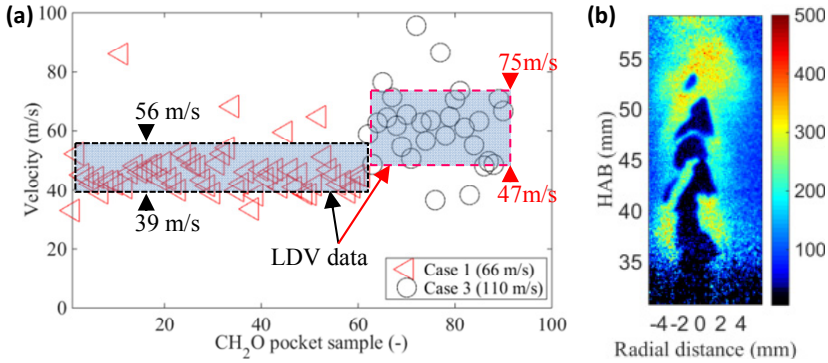

Fig. 7. (a). Comparison between LDV data and CH_2O pocket imaging velocimetry at case 1 and case 3 conditions; (b) OH PLIF image at case 1 condition.

Figure 7(a) illustrates the comparison between the velocity of CH_2O pockets and the velocity data measured by laser Doppler velocimetry (LDV) in a previous study [23]. The grey box represents the data from LDV and red triangle and black circle symbols indicate the data calculated from 66 m/s and 110 m/s PLIF images, respectively. The pocket was evaluated by the OH PLIF image due to the large FOV as shown in Fig. 7(b). The velocity of the CH_2O pocket was calculated by the movement of the centroid of a CH_2O pocket between two frames (Δt = 20 μs). The result of CH_2O pocket imaging velocimetry and LDV data are in very good agreement for both case 1 and case 3, as shown in Fig. 7(a). Therefore, by using such ultra-high-speed diagnostics, proper data evaluation and analysis can provide complementary velocity information in a turbulent jet flame.

4. Summary and conclusion

According to the literature survey performed by the authors, this is the first time that simultaneous PLIF imaging of two species relevant to combustion studies has been conducted at such high repetition rate, 50 kHz, including 100 consecutive images. Furthermore, the ability to extract more than 30 pulses from an OPO being pumped at 50 kHz is also being demonstrated for the first time. The OH radicals were excited in the Q1(9) transition at 283.93 nm generated by 355 nm pumping of an OPO followed by frequency doubling of the signal beam. Formaldehyde distributions were accessed through excitation at 355 nm utilizing the residuals of the OPO pumping beam. By applying a 2 ms long burst at 50 kHz, a pulse train of 100 individual pulses could be generated from the burst laser. The peak output energy was 80 mJ/pulse at 355 nm and after frequency conversion in the OPO this resulted in approximately 350 μJ/pulse at 284 nm and 6 mJ/pulse remaining at 355 nm. Using appropriate filters in front of two intensified CMOS detectors the feasibility of this ultra-high-speed diagnostics technique could be successfully demonstrated in a premixed turbulent jet flame featuring flow velocities in excess of 60 m/s. Even at these high velocities the demonstrated diagnostics approach was capable of following the temporal evolution of the reacting flow.

Appendix

In the appendix, a series of consecutive OH and CH_2O PLIF images (Figs. 8-11) are presented.

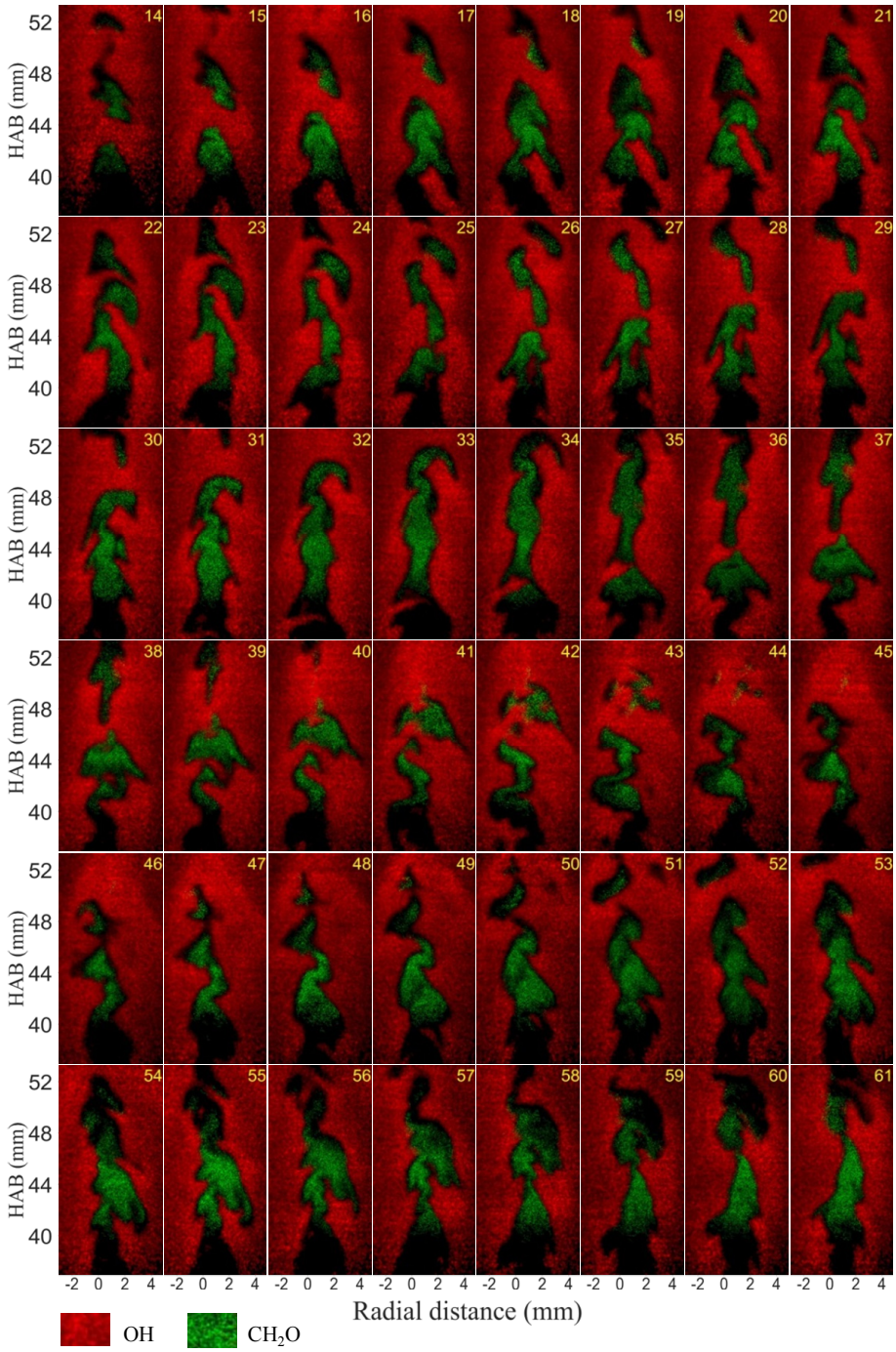

Fig. 8. Simultaneous OH (red) and CH_2O (green) PLIF images measured in case 1 (part 1).

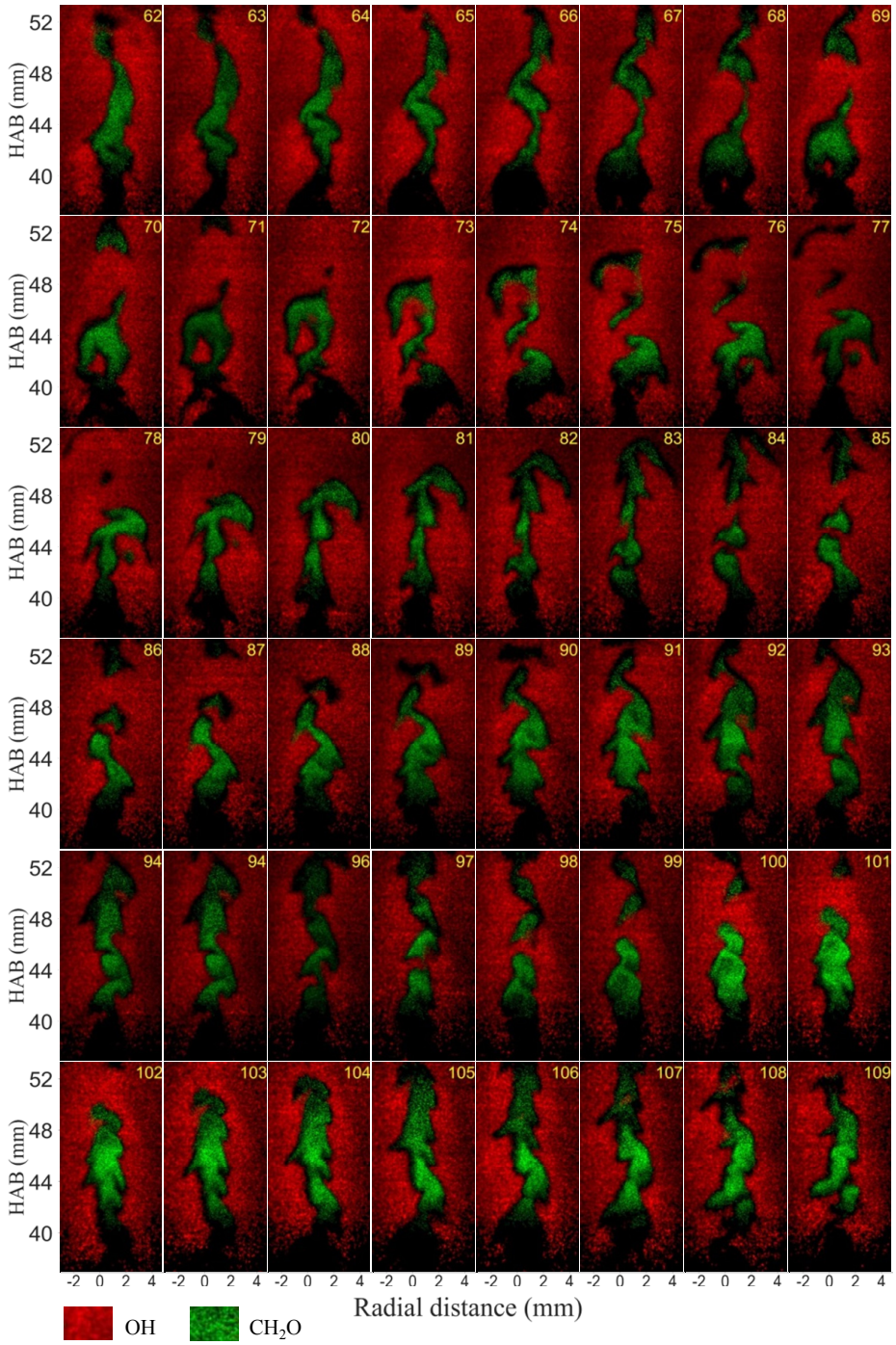

Fig. 9. Simultaneous OH (red) and CH_2O (green) PLIF images measured in case 1 (part 2).

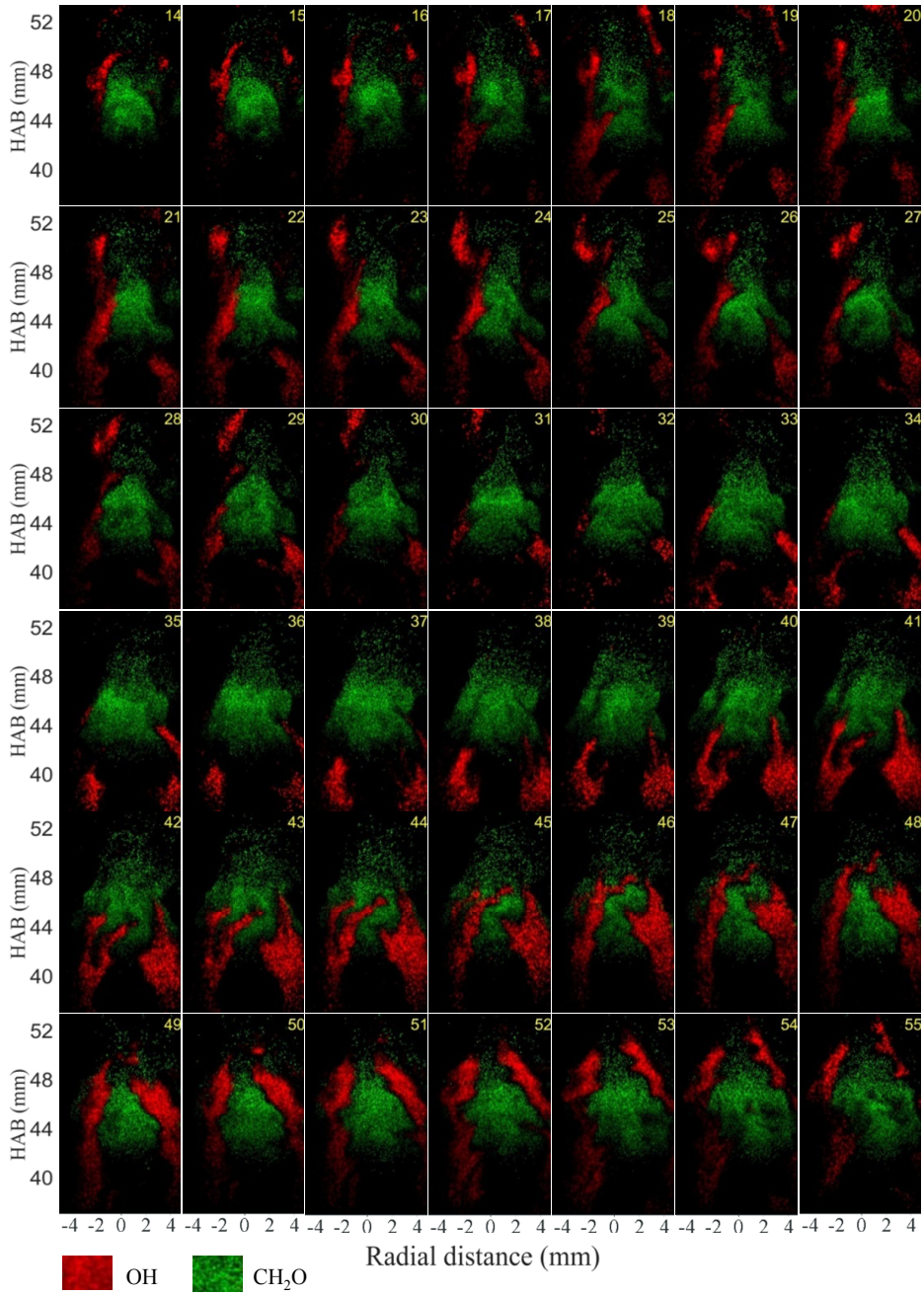

Fig. 10. Simultaneous OH (red) and CH_2O (green) PLIF images measured in case 2 (part 1).

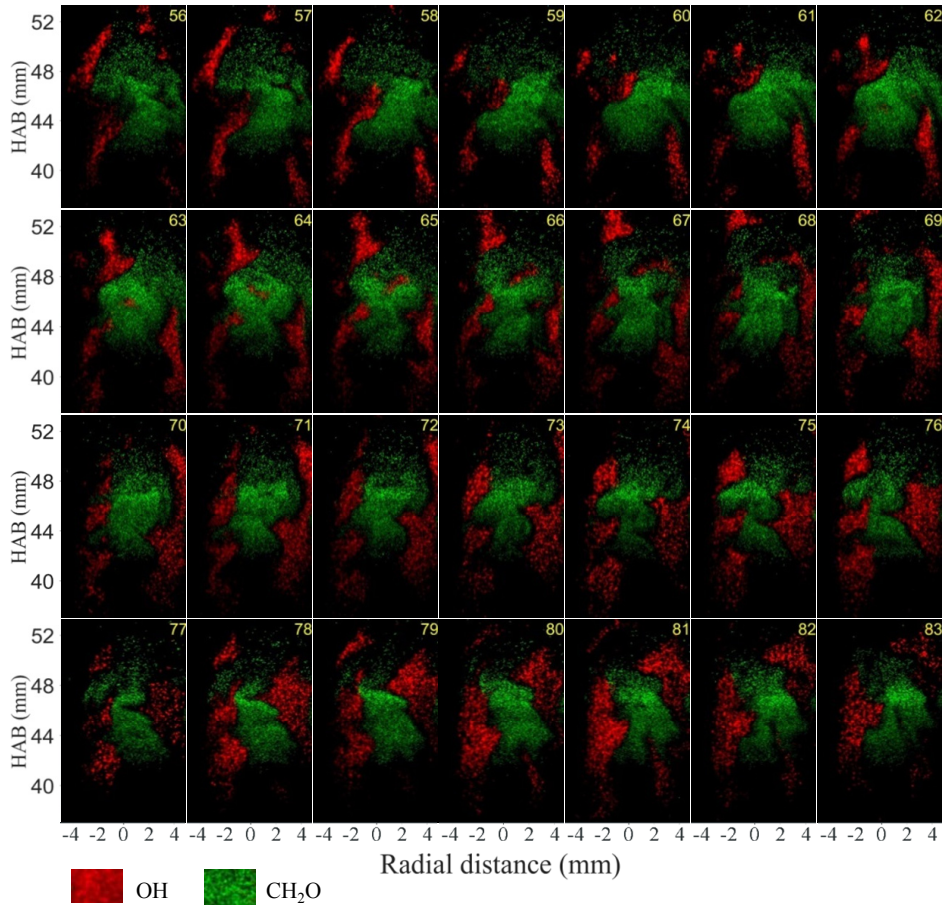

Fig. 11. Simultaneous OH (red) and CH_2O (green) PLIF images measured in case 2 (part 2).

Funding

Energimyndigheten.

Acknowledgments

The financial support from CECOST and KCFP through the STEM (Swedish Energy Agency) are gratefully acknowledged. The authors would also like to thank Prof. Xuesong Bai, Prof. Alexander Konnov, Dr. Mikhail Slipchenko and Dr. Jason Mance for their valuable help and contribution.

Paper VII

2018-01-0904

Ultra-high speed fuel tracer PLIF imaging in a heavy-duty optical PPC engine

Author, co-author (Do NOT enter this information. It will be pulled from participant tab in MyTechZone)
Affiliation (Do NOT enter this information. It will be pulled from participant tab in MyTechZone)

Abstract

In order to meet the requirements in the stringent emission regulations, more and more research work has been focused on homogeneous charge compression ignition (HCCI) and partially premixed combustion (PPC) or partially premixed compression ignition (PCCI) as they have the potential to produce low NOx and soot emissions without adverse effects on engine efficiency. The mixture formation and charge stratification influence the combustion behavior and emissions for PPC/PCCI, significantly. An ultra-high speed burst-mode laser is used to capture the mixture formation process from the start of injection until several CADs after the start of combustion in a single cycle. To the authors' best knowledge, this is the first time that such a high temporal resolution, *i.e.* 0.2 CAD, PLIF could be accomplished for imaging of the in-cylinder mixing process. The capability of resolving single cycles allows for the influence of cycle-to-cycle variations to be eliminated. This ability to study individual cycles aids the understanding of the mixture formation process as well as the cycle-to-cycle variations. Strong air entrainment at the boundary layer can be clearly observed and followed as the mixing process progresses. The formation of eddies created by the shear force and their rotational motion can be continuously observed during the mixing process. The interaction between two adjacent spray plumes in the recirculation zone is well captured and studied. In addition, the mixing process resulting in the stratified fuel charge being located in the recirculation zone before the SOC while the areas along the original spray axis are leaned out after the end of injection, can be followed in one time sequence. Moreover, the auto-ignition position and early flame development can be studied, from the high-speed chemiluminescence imaging, together with the fuel distribution in the combustion chamber.

Introduction

Homogeneous charge compression ignition (HCCI) and partially premixed combustion (PPC) have been investigated for more than a decade, as both of them share the capability of producing low NOx and soot emissions without adverse effects on engine efficiency [1-4]. In HCCI engines, the fuel mixture is homogeneously distributed in the combustion chamber before the start of combustion and the charge is usually highly diluted in order to keep the pressure rise rate at acceptable levels. In principle, as long as it is sufficient, the mixing process doesn't play a role on HCCI. Ignition occurs all over the combustion chamber simultaneously in HCCI while it occupies a small portion of the combustion chamber in PPC. Moreover, there is a prolonged time delay between the end of injection (EOI) and the start of combustion (SOC) leading to the mixture being partially premixed before the combustion process in PPC. Therefore, on the contrary to HCCI, the degree of mixing of fuel and air before the onset of combustion is crucial for the combustion behavior and emission production in the PPC mode. The ignition delay (ID) and combustion duration are largely dependent on the stratification level of the fuel distribution. In order to understand the influence of stratified fuel distribution on the combustion performance, it is important to visualize the fuel distribution with high temporal resolution.

Fuel-tracer laser induced fluorescence (LIF) is commonly used to measure the fuel distribution in the combustion chamber in order to study the in-cylinder fuel injection process and mixture formation [5-12]. However, due to cycle-to-cycle variation (CCV) of the internal combustion engine (ICE), the fuel distribution varies tremendously for the same crank angle degree (CAD) in different cycles. Measurements performed by employing commonly-used laser systems, *i.e.* Nd:YAG and excimer laser at low repetition rates ($\leqslant$ 100 Hz), cannot follow and capture the mixture formation within a single cycle, *e.g.* with the engine running at 1200 rpm. In order to avoid averaging effects caused by the cycle-to-cycle variations, it is preferable to use a high-speed imaging technique capable of capturing a full injection sequence within a single engine cycle and thus generate truly cycle-resolved data.

There remain difficulties with PLIF in engines, including temperature dependence of the signal, non-uniform temperature fields partly due to evaporative cooling of fuel, and *etc.* These are inherent problems and not specific to high-speed imaging. Therefore they are beyond the scope of this paper.

One approach to reach ultra-high speed ($\geqslant$10 kHz) fuel tracer planar laser induced fluorescence (PLIF) in the engine is to use a cluster of Nd: YAG lasers. For example, John Hult *et al.* [13,14] employed a multi-YAG system to create 8 consecutive images with 0.5 CAD temporal resolution (at 1200 rpm) in a HCCI engine for the investigation of fuel distribution. However, to follow the mixing process in detail from the injection event all the way through the combustion process requires significantly more image frames to be recorded. Although YAG-clusters are modular and can be extended, they quickly reach a limit where cost and space are no longer favorable.

Another option is to use a quasi-continuous diode pumped solid state (DPSS) laser which operates at high repetition rates and generates much more than 8 pulses per sequence. It is demonstrated that commercially available DPSS lasers work well for PLIF imaging in

laboratory burners under atmosphere condition [15-18]. However, the application of such lasers in combustion engines imposes a great challenge, due to the combination of low pulse energies, high temperature and high pressure atmosphere. In spite of the mentioned difficulties, there are some excellent examples of successful application of high-speed diagnostics in engines performed using DPSS-lasers as excitation source [19-21].

For instance, Smith *et al.* utilized a frequency tripled Nd: YAG laser (Quantronix Hawk) to obtain more than 20 fuel tracer PLIF images in a gasoline spark ignition (SI) engine at 12 kHz for visualizing cycle-resolved fuel distribution [19]. In their study, the fuel tracer was biacetyl which can be excited by 355 nm radiation. This is favorable due to the higher pulse energies available, compared to 266 nm where most commonly used tracers are excited. A drawback that must be considered though is the possible health risk associated with the use of this tracer. Furthermore, the significantly lower pulse energy, compared to what is common in conventional 10 Hz probing, is here partly compensated for by a relatively limited field of view.

Except the various work by Sick *et al.* there are very few examples of high-speed 2D fuel-tracer PLIF imaging performed in engines using DPSS-lasers. This is mainly due to the low pulse energies available from theses excitation sources. It is also why there is a lack of reports where commonly used tracer, *e.g.* acetone, 3-pentanone or toluene have been used in combination with this type of lasers. At present the trade-off between pulse energy and repetition rate, typical of DPSS-lasers, causes a too weak LIF signal when the laser repetition rate is high enough for single-cycle-resolved measurements [17,22].

In addition, high temperature and high pressure toughen the challenge to employ fuel-tracer PLIF in the compression ignition (CI) engines. The peak pressure and temperature in SI engines are typically lower than those in CI engines. In other words, due to temperature- and pressure- quenching, the LIF signal is weaker in CI engines with the same excitation energy.

Burst-mode laser has recently been developed to create a series of pulses in a certain amount of time [23-28], which allows for high temporal resolution as well as significantly increasing the maximum number of frames in a sequence. Moreover, the pulse energies are comparable to what is commonly seen for 10 Hz laser systems such as conventional high power Nd:YAG lasers. Due their size and complexity, high power burst laser systems have mostly been limited to stationary applications in optical laboratories. However, Jiang *et al.* [29,30] and Miller *et al.* [31] have managed to apply burst-mode laser systems for NO and CH_2O PLIF measurements in supersonic continuous-flow wind tunnels and a model scramjet cavity combustor.

The aim of this paper is to report and demonstrate the application of an ultra-high speed laser technique for capturing the mixture formation process from the start of injection (SOI) to the start of the combustion, and to do this with a field of view that allows for global features to be studied. To the authors' best knowledge, this is the first time that the fuel distribution could be studied with such a high temporal resolution in an IC engine.

Experimental work

Figure 1 illustrates the experimental setup of this study, including an optical engine, a laser sheet, a high speed camera and a long pass filter. More detailed introduction of these systems will follow.

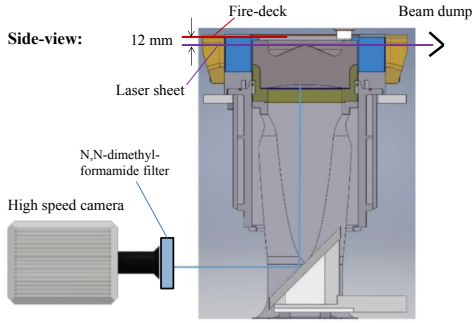

Figure 1. Experimental setup.

Optical engine

Experiments were conducted in a 6-cylinder Volvo heavy-duty engine modified for optical access on cylinder one. While the remaining five cylinders are balanced with tungsten weights, compared to the traditional single cylinder optical engines, this design requires no balancing shafts. The layout is based on the traditional Bowditch design with three side windows to the combustion chamber and a hollow piston extension with a quartz piston in a titanium retainer. The cylinder linear is of a drop-down type, and the piston and windows are therefore easy to clean when needed. More detailed information on this can be found in [32,33].

The windows and piston are manufactured in quartz, Suprasil 2B. All quartz components are glued into its respective retainer. A 45-degree mirror is mounted inside the extended liner to reflect the fluorescence light from the combustion chamber through the optical piston to the camera. The engine specifications are presented in Table 1.

Exhaust gas recirculation (EGR) was used as diluent to reduce the oxygen concentration and prolong the ignition delay, which allow for more mixing before the onset of combustion. The EGR in this study was generated by an external diesel furnace operated at stoichiometric conditions. A condenser was used to remove most of the water from the EGR.

Table 1. Engine specifications

Displaced volume	2123 cm^3
Stroke	153 mm
Bore	131 mm
Connecting Rod	255 mm
Compression ratio	16:1
Number of Valves	4
Swirl	Close to zero
Fuel system	Delphi F2 common rail external pump
Orifices	6
Nozzle diameter	212 µm
Included spray angle	150 deg.

Operating conditions

Table 2 shows the operating conditions for this study. In order to have comparable data sets, all the parameters were the same as in [32]. The experiment was carried out at 1200 rpm with a constant load of 7 bar gross indicated mean effective pressure (IMEPg). The intake oxygen level was kept at 16% as it is suitable for trade-off between NOx and low particulate matter (PM) emissions with research octane number (RON) 87 gasoline [34].

Table 2. Operating conditions

Engine speed [RPM]	1200
IMEPg [bar]	7
Intake O2 concentration [%]	16
Intake Temperature [˚C]	108
Intake Pressure [bar]	2.1
Fuel Pressure [bar]	1500
Cooling water temperature [˚C]	87
Oil temperature [˚C]	92

The fuel in the experiment consisted of 13% n-heptane and 87% iso-octane (PRF 87) to represent RON 87 gasoline fuel. Acetone was chosen as the fluorescent tracer of the fuel (10% by volume). At pressures relevant to the injection and combustion events in PPC engines, the pressure dependence of the acetone PLIF signal levels off. However there is still a temperature dependence that varies with the excitation wavelength, as reported in [35]. The spectral footprint of acetone fluorescence allows detection without the use of an image intensifier, which is fragile and can easily be damaged by intense reflections. High-speed image intensifiers are also prone to saturation due to the nonlinear response in the micro channel plate [36,37]. Further information about acetone and its use as a fuel-tracer for PLIF measurements in optical engines can be found in [10,14,38-45], which imply that the tracer does not influence the combustion process itself. Although adding acetone increases the octane number, and consequently increases the ignition delay and the time for mixing process, quantitative analysis is beyond the scope of this study.

Figure 2 shows the injection signal together with the pressure trace in motored and combusting case, respectively. The pressure traces are averaged by about 200 and 25 cycles for motored case and combusting case, respectively. The fuel flow was measured to be close to 77 mg/stroke with an injection duration of 930 µs.

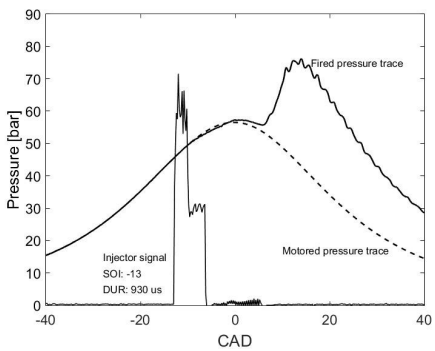

Figure 2. The injection signal together with the pressure trace in motored case (dashed line) and combusting case (solid line) versus CAD, respectively.

Optics

A burst-mode laser (Quasimodo, Spectral Energies) was used in this study. Detailed description of the laser can be found in reference [24,46,47]. A brief introduction will be provided here. A laser pulse train of 1064 nm wavelength is produced, at a maximum duration of 10 ms, at ultra-high repetition rates, *e.g.* 36 kHz. The pulse energy is amplified by several diode-pumped amplifiers and flashlamp-pumped amplifiers mounted in series. Then the wavelength is converted to 532 nm through a frequency doubling crystal. After sequential doubling in a fourth harmonic generator (FHG), 50 mJ per pulse of 266 nm wavelength is generated at 36 kHz. The pulse duration of the laser was around 15 ns. A photodiode was used to monitor the pulse energy fluctuation throughout the burst.

A laser sheet was formed by a cylindrical lens (with the focal length of -50 mm) and a spherical lens (with the focal length of +500 mm). The width of the laser sheet was 65 mm which is approximately equal to the width of the windows mounted on the spacer between the cylinder head and the extended liner. Most of the surface of the combustion chamber in the engine was painted black to reduce any laser reflections.

A high speed CMOS camera (Photron Fastcam SAZ) was used to capture the fluorescence signal with an objective (f=105 mm, f#=1.8) mounted in front of the camera, where f and f# represent the focal length and the focal ratio, respectively. The extension ring between the objective lens and the camera chip was 20 mm in width. The camera and laser were synchronized with the engine by a pulse generator (DG535). The exposure time of the camera was set to 250 ns for mitigation of the background luminosity. The camera was running at 36 kHz with a pixel resolution of 640x848. The corresponding field of view was 65 mm x 86 mm. Usually, for high-speed CMOS cameras, the pixel resolution is reduced with increasing repetition rate. This results in a trade-off between the field of view and the spatial resolution. Since the spray pattern in the combustion chamber is essentially symmetric this field of view showing 3 spray plumes was chosen.

A long pass filter, which contains liquid N,N-dimethyl-formamide, was placed in front of the camera lens, and prevented almost all undesired scattered laser light from entering the camera lens. A transmission curve for this filter can be found in [44].

Due to the curvature of the liner windows (a concave surface towards the inner-side of the combustion chamber), the laser sheet was expanded in the horizontal direction (~70 mm). The slightly divergent sheet illuminated almost the whole piston bowl area in the combustion chamber.

The laser pulse burst started just before the SOI and it continued until the SOC. Thus, the whole fuel mixing process was captured in a sequence of about 90 frames, which were collected in one fired cycle. After about 5 CAD after top dead center (ATDC), the chemiluminescence (laser was off) of the combustion was recorded by the high speed camera continuously with 0.2 CAD temporal resolution, as well.

Image post-processing

Background subtraction

Background images were recorded during the motored cycles, without fuel injection. The first step of post-processing is to subtract the background image recorded at each corresponding CAD.

Distortion correction

Due to the dome-shaped piston bowl, the recorded image is distorted. The correction of the distortion is made in MATLAB (The Matworks, Massachusetts, USA). Further information can be found in the reference [12,48].

Normalization

After all the post-processing described above, the image is applied with a grey scale color bar. The higher intensity indicates higher fuel concentration and vise versa. A false color scale is used for the images showing the natural luminosity of the combustion. The higher intensity implies more intense natural luminosity from the flame. The intensities of PLIF images and combustion luminosity images are normalized to the maximum intensity of each individual image.

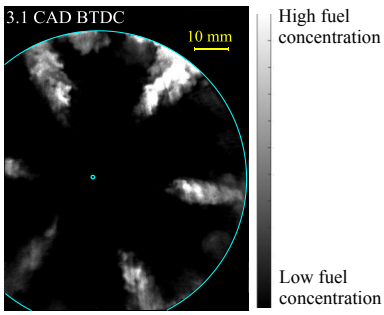

Figure 3. An example of PLIF image after post-processing at 3.1 CAD BTDC.

Figure 3 displays an example of a PLIF image after post-processing. The image represents the fuel distribution at 3.1 CAD before top dead center (BTDC), which is shown in the upper left corner of the figure. The big blue circle outlines the piston bowl rim. The small solid blue circle indicates the injector tip. The dimension scale of the image is shown in the upper right corner of the figure. It is worth mentioning that since the laser sheet is horizontally placed at 12 mm beneath the fire-deck and the spray's included angle is 150 degrees, there is a distance between the injector tip (small blue circle) and the fuel distribution at the laser sheet plane.

Signal to noise ratio

Figure 4(a) shows a raw PLIF image (prior to post-processing) recorded at 3.7 CAD BTDC, *i.e.* several CADs after the EOI. The area between the two thin red lines, shown in the figure, is selected for the calculation of the signal-to-noise ratio (SNR). The signal intensity is averaged along the radial direction as a function of each polar (or azimuthal) angle in clockwise direction and is then plotted in Fig. 4(b).

The same procedure is applied for a background image which was obtained when the engine was motored without fuel injection and the laser was turned on. Figure 5 presents the PLIF image and the intensity plot of the background. The SNR ratio is then calculated by dividing the highest PLIF signal to the average intensity of the background image. As a result, the SNR value is above 200.

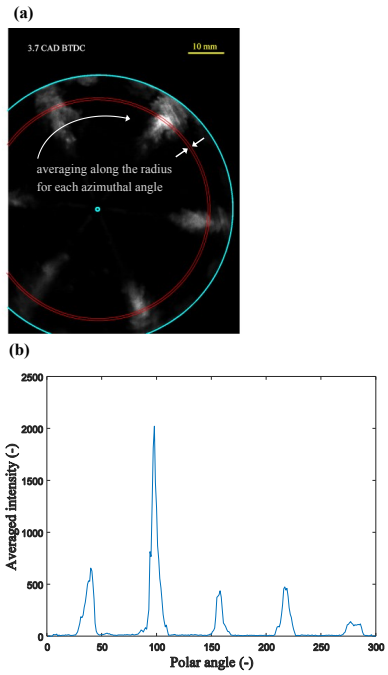

Figure 4. (a) Selection of the area for SNR calculation; (b) averaged intensity versus polar angle at 3.7 CAD BTDC.

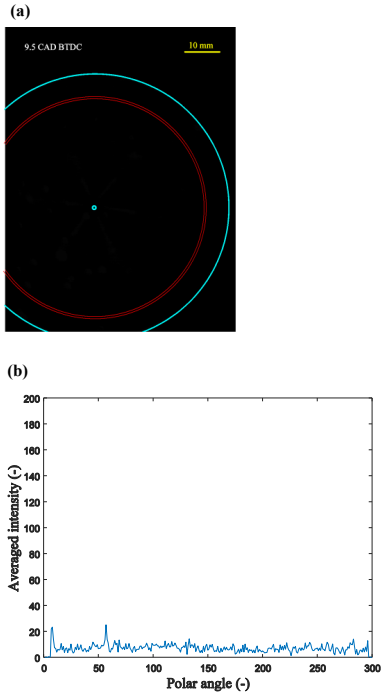

Figure 5. (a) Selection of the area for SNR calculation; (b) averaged intensity versus polar angle from the background image.

Results and discussions

More than 90 sequential PLIF images are obtained from 11.5 CAD BTDC (before SOI) to 5.5 CAD ATDC (after SOC) within one engine cycle. The entire mixing process, from the injection through the ignition delay to the onset of combustion, can be investigated in the resulting image series. Due to the space limitation, not all the images are displayed in this section. More results can be found in the appendix (see Fig. 12) where full sequence of images is available and a movie (cycle No. 1) is provided through a web link. By looking at the movie, one can visualize a clear view on the transition of the fuel distribution not only in spatial but also in high temporal resolution. The development and movement of the mixture gas are well captured in one engine cycle. That is the significant advantage and merit of this technique. The influence of cycle-to-cycle variations, which traditionally introduce an averaging effect on the results, can be eliminated completely.

Spray impinging and merging

In this example, the injection pressure is 1500 bar and the in-cylinder pressure at the SOI is around 60 bar. The ultra-high speed PLIF imaging is capable of following the fuel penetration as the spray spreads with an extremely high speed, *e.g.* > 100 m/s. The formation and development of large eddies can be observed distinctly in the movie (from 8.3 CAD BTDC to 1.1 CAD BTDC) at the boundary layer of the spray. The counter rotating vortices, as red arrows shown in Fig. 6, relates to air entrainment. Thus, the dynamic features of the fuel mixing process are well captured by this single-cycle resolved PLIF imaging approach. The development of the mixing layer between air and fuel is for example hard to observe by conventional low repetition rate (10 Hz and one image per cycle) techniques.

Around 7 CAD BTDC, the fuel impinges on the piston bowl wall and is redirected afterwards. The spray is split into two parts, which subsequently proceed further circumferential movement along the piston's bowl as the green arrows show in Fig. 6. Shear forces appear between the piston bowl wall and the boundary layer of the spray during the circumferential movement. Interestingly, the rotational direction (*e.g.* counter-clockwise for spray part No. 1) of the eddies created by this shear force is the opposite of that generated by the aforementioned air entrainment, which is the same as the fuel rotational direction (see supplementary movie cycle No. 1) as illustrated in Fig. 7. The counter-clockwise rotating vortices, generated by the air-entrainment into the main jet, and the close-to-wall shear forces present after the wall impingement, enhance the turbulence in the recirculation zone where the adjacent sprays encounter each other. This can be seen in the movie from 6.1 CAD BTDC to 2.5 CAD BTDC. In this experiment, no swirl is produced in the combustion chamber.

Once two adjacent spray plumes merge together, which occurs at around 2 CAD BTDC as highlighted in Fig. 8, the transport of the fuel mixture is re-directed towards the center of the piston bowl. It is apparent that the rotational directions of the downstream eddies from two adjacent spray plumes are opposite to each other, *i.e.* clockwise and counter-clockwise, as can be seen in the movie from 5.1 CAD BTDC to 2.3 CAD BTDC. This confirms the importance of this recirculation region where the interaction between two adjacent sprays promotes the turbulent mixing. Augment of velocity gradient increases the turbulence of the mixture, dramatically. As a result the mixing process is enhanced in this spatial region during the merging event. Then the mixture area is growing and moving further towards the center of the piston bowl before SOC as indicated by the green arrow in figure 8(b).

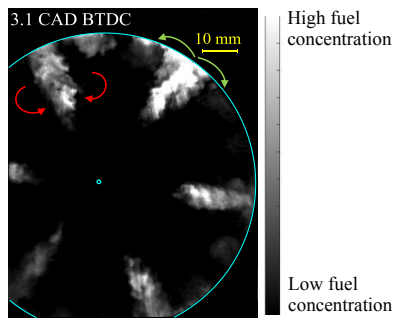

Figure 6. Air entrainment at the shear layer of the spray plume at 3.1 CAD BTDC. Spray plume is split into two parts after impingement on the piston bowl wall.

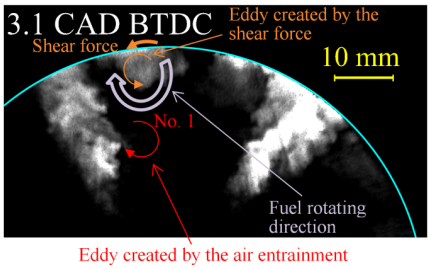

Figure 7. Fuel rotating direction is clockwise though shear force between the piston bowl wall and the boundary layer of the spray makes counter-clockwise eddies.

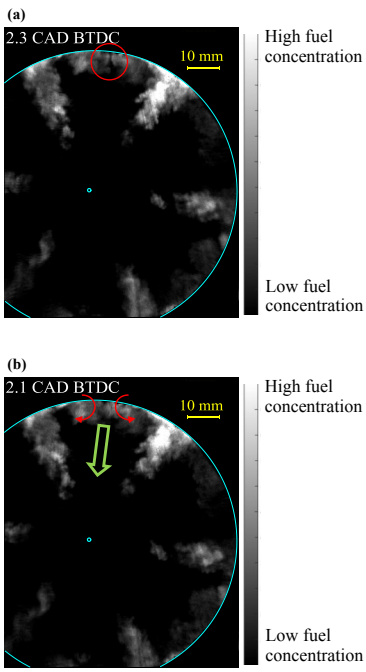

Figure 8. (a) Two adjacent sprays merge together around 2.3 CAD BTDC; (b) the merged mixture gas is pushed towards the center of the piston bowl afterwards.

As the fuel injection event lasts for about 7 CADs (930 μs injection duration of the electrical driving signal), the strong momentum of the spray makes it to continuously impinge on the bowl wall. This contributes to an increase in turbulence and causes significant expansion as the gaseous spray plume is split into parts that propagate along the bowl rim into the recirculation zone.

Spray propagation velocity

Figure 9 shows the extension of the fuel spray plume in the laser sheet plane at 9.1 CAD BTDC and at 6.9 CAD BTDC, respectively. They were obtained by applying a threshold just above the background noise. By observing the movie in the supplementary material, the evolution of the spray boundary is well captured. The distance between two frames hence can be obtained, which results in the velocity information of the spray. For instance, once the laser sheet plane and spray axis are co-aligned, the velocity of the spray tip can be obtained through this technique.

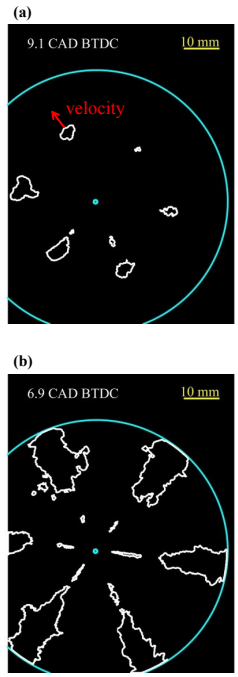

Figure 9. Boundary layer of the spray at 9.1 CAD BTDC (a) and at 6.9 CAD BTDC (b).

Fuel distribution at the start of combustion

Interestingly, Fig.10 demonstrates that, at the onset of combustion, the majority of the fuel mixture (green arrow) is not located at the same position as the spray plumes during the injection event (marked by the yellow contour). One can see that the stratified fuel mixture is located in the recirculation zone where two adjacent sprays impinge and merge together before the SOC. Apparently, under operating conditions with prolonged ignition delays, the region where the fuel is located during the injection event (yellow contour in figure 10(b)) contains almost no fuel at the start of combustion. While the fuel gathers in the recirculation zone, the areas along the original spray axis are leaned out after the end of injection. This behavior, here

captured within a single cycle, most likely constitutes yet another proof of the entrainment wave following immediately after the end of injection, as first described by Musculus *et. al.* [49].

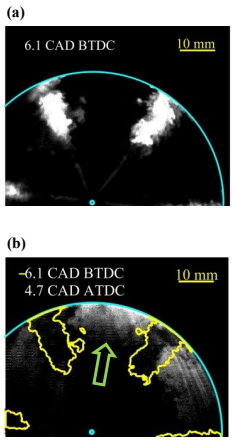

Figure 10. (a) Fuel distribution during the injection event at 6.1 CAD BTDC; (b) fuel distribution before SOC at 4.7 CAD ATDC together with the boundary layer of fuel distribution at 6.1 CAD BTDC (yellow lines).

Comparing the current chemiluminescence images of the combustion event in this study with the corresponding ones from a recent study by Lundgren *et al.* [33], the ignition always takes place in the recirculation zone while the area along the spray axis shows no chemiluminescence signal. An interesting follow up study of this detected leaning-out along the spray axis, would be to perform high-speed PIV in order to resolve the flow motion within a single cycle.

This is a unique feature of the PPC type combustion, in which the long ignition delay, here in combination with the proposed entrainment wave, allows the fuel mixture to end up in the recirculation zone prior to ignition. Regardless of the specific outcome in this example, such detailed findings are not possible to retrieve from single-shot measurements since cycle-to-cycle variations will introduce an averaging effect that partly smears the gradients of the single-cycle fuel distribution as discussed above.

Auto-ignition positions

Another advantage of this technique is that the position of the auto-ignition can be captured almost simultaneously with the fuel distribution. Due to cycle-to-cycle variation and strong turbulence in the cylinder, the auto-ignition timing and position are variable and predicting them a priori is not easy. Hence, it is very difficult to obtain such simultaneous results with the commonly-used 10 Hz lasers. The long burst duration of this ultra-high speed techniques makes the measurement far more feasible.

Figure 11 illustrates the start and development of auto-ignition regions (yellow and red lines) together with the fuel distribution. After 5.5 CAD ATDC, the development of auto-ignition sites and the following flame 'propagation' can be observed by chemiluminescence images as the laser has been turned off. It can be seen that the auto-ignition sites are distributed in the recirculation zone. Therefore, the fuel concentration at these locations before the onset of combustion could be probed.

It is fully feasible to record cycle-resolved PLIF images from multiple cycles between window cleanings. A supplementary movie (cycle No. 2) based on cycle-resolved data from another engine cycle is shown in the appendix.

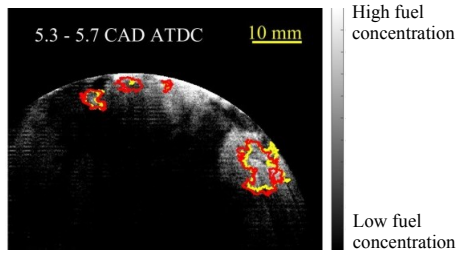

Figure 11. Fuel distribution at 5.3 CAD ATDC together with boundary layer of auto-ignition positions at 5.5 CAD ATDC (yellow) and 5.7 CAD ATDC (red), respectively.

Summary/Conclusions

Ultra-high speed fuel-tracer PLIF imaging is successfully performed in an optical heavy-duty diesel engine. About 90 consecutive PLIF images are obtained from one engine cycle. The fuel distribution can be imaged in a relatively large field of view (~70 x 80 mm) inside the combustion chamber with high temporal resolution, *i.e.* 0.2 CAD. Due to their size and complexity, high power burst laser systems have until recently been mainly limited to stationary applications in optical laboratories. To the best knowledge of the authors, this report is the first to demonstrate the applicability of ultra-high speed burst lasers in an internal combustion engine. The combination of high pulse energies (50 mJ at 266 nm) and high repetition rate (36 kHz) brings unique advantages. The temporally resolved fuel distribution can be captured and studied within one single cycle. This capability eliminates the influence from cycle-to-cycle variations that is inherent to conventional 10 Hz diagnostics. The time scale between the laser pulses is smaller than the integral time scale (~ms) and comparable to the Taylor time scale in the engine. The SNR is better than 200 in areas with high fuel concentration after the EOI. For PLIF measurements performed under in-cylinder conditions and at such high repetition rates, this is a significant number.

The eddies created by the shear force and their rotational motion can be continuously observed. The interaction between two adjacent spray plumes is well captured. Although the fuel is initially distributed along the original spray axis during the injection event, this region experiences significant leaning-out after the end of injection. On the contrary, the fuel concentration in the recirculation regions increases at the same time. Single-cycle data of the fuel distribution indicate that the mixing process in the recirculation zone is of major importance for the operation in PPC mode, especially after the EOI. Thus, new piston geometries, aimed at the utilization of spray momentum to promote turbulence and enhance the mixing in the recirculation zone, might provide improved performance.

Moreover, auto-ignition positions can be studied together with the fuel distribution in the combustion chamber by this technique. The luminosity of the auto-ignition and the fluorescence signal of the fuel-tracer by PLIF prior to SOC can be captured. It is also possible to obtain the fuel movement and propagation speed of the spray tip along the spray axis with such a high repetition rate, as discussed in the paper.

With a careful calibration measurement, the cycle-resolved equivalence ratio in the combustion chamber could be measured as well. In addition to this, the results also provide qualitative data for cycle-resolved large eddy simulation in computational fluid dynamics (CFD) modeling. Both single-shot imaging at 10 Hz and high speed techniques provide different types of data and thus complement each other.

The burst-mode laser is a useful tool for the laser diagnostics in internal combustion engines, as both repetition rate and laser energy are competently high. Transient behaviors, *e.g.* mixing process and auto-ignition, can be captured with a cycle-resolved resolution in a very short time that can be covered by a sufficient long burst duration. Additionally, no intensifier is needed for this measurement which can largely reduce the risk of damaging the intensifier and camera. Furthermore, it is fully feasible to record cycle-resolved PLIF images from multiple cycles between window cleanings. The benefit of applying the high-speed burst system for in-cylinder laser diagnostics is the greatly reduced acquisition time; this is especially valuable under sooty conditions where window fouling can be a major obstacle.

References

1. G. T. Kalghatgi, P. Risberg, and H.-E. Ångström, 'Advantages of Fuels with High Resistance to Auto-Ignition in Late-Injection, Low-Temperature, Compression Ignition Combustion', *SAE Technical Paper* 2006-01-3385, 2006.
2. G. T. Kalghatgi, P. Risberg, and H.-E. Ångström, 'Partially Pre-Mixed Auto-Ignition of Gasoline to Attain Low Smoke and Low Nox at High Load in a Compression Ignition Engine and Comparison with a Diesel Fuel', *SAE Technical Paper* 2007-01-0006, 2007.
3. V. Manente, B. Johansson, and P. Tunestal, 'Partially Premixed Combustion at High Load Using Gasoline and Ethanol, a Comparison with Diesel' *SAE Technical Paper* 2009-01-0944, 2009.
4. C. Li, L. Yin, S. Shamun, M. Tuner, B. Johansson, R. Solsjo, and X.-S. Bai, 'Transition from HCCI to PPC: The Sensitivity of Combustion Phasing to the Intake Temperature and the Injection Timing with and without EGR', *SAE Technical Paper* 2016-01-0767, 2016.
5. D. L. Reuss, and V. Sick, 'Inhomogeneities in HCCI Combustion: An Imaging Study', *SAE Technical Paper* 2005-01-2122, 2005.
6. M. P. B. Musculus, 'Multiple Simultaneous Optical Diagnostic Imaging of Early-Injection Low-Temperature Combustion in a Heavy-Duty Diesel Engine', *SAE Technical Paper* 2006-01-0079, 2006.
7. M. P. B. Musculus, T. Lachaux, L. M. Pickett, and C. A. Idicheria, 'End-of-Injection over-Mixing and Unburned Hydrocarbon Emissions in Low-Temperature-Combustion Diesel Engines', *SAE Technical Paper* 2007-01-0907, 2007.
8. D. Sahoo, B. Petersen, and P. C. Miles, 'Measurement of Equivalence Ratio in a Light-Duty Low Temperature Combustion Diesel Engine by Planar Laser Induced Fluorescence of a Fuel Tracer', *SAE International Journal of Engines,* 4, 2312-25, 2011-24-0064, 2011.
9. B. Petersen, P. C. Miles, and D. Sahoo, 'Equivalence Ratio Distributions in a Light-Duty Diesel Engine Operating under Partially Premixed Conditions', *SAE International Journal of Engines,* 5, 526-37, 2012-01-0692, 2012.
10. J. Sjoholm, C. Chartier, E. Kristensson, E. Berrocal, Y. Gallo, M. Richter, O. Andersson, M. Alden, and B. Johansson, ' Quantitative in-Cylinder Fuel Measurements in a Heavy Duty Diesel Engine Using Structured Laser Illumination Planar Imaging (SLIPI)', *The Proceedings of the International symposium on diagnostics and modeling of combustion in internal combustion engines,* 2012.8, 500-05, 2012.
11. S. Kokjohn, R. D. Reitz, D. Splitter, and M. Musculus, 'Investigation of Fuel Reactivity Stratification for Controlling PCI Heat-Release Rates Using High-Speed Chemiluminescence Imaging and Fuel Tracer Fluorescence', *SAE International Journal of Engines,* 5, 248-69, 2012-01-0375, 2012.
12. Z. Wang, S. Lonn, A. Matamis, O. Andersson, M. Tuner, M. Alden, and M. Richter, 'Transition from HCCI to PPC: Investigation of Fuel Distribution by Planar Laser Induced Fluorescence (PLIF)', *SAE International Journal of Engines,* 10, 1465-81, 2017-01-0748, 2017.
13. J. Hult, M. Richter, J. Nygren, M. Aldén, A. Hultqvist, M. Christensen, and B. Johansson, 'Application of a High-Repetition-Rate Laser Diagnostic System for Single-Cycle-Resolved Imaging in Internal Combustion Engines', *Applied Optics,* 41, 5002-14, 2002.
14. A. Hultqvist, M. Christensen, B. Johansson, M. Richter, J. Nygren, J. Hult, and M. AldJn, 'The HCCI Combustion Process in a Single Cycle - Speed Fuel Tracer LIF and Chemiluminescence Imaging', *SAE Technical Paper*, 2002-01-0424, 2002.
15. I. Boxx, C. Heeger, R. Gordon, B. Böhm, M. Aigner, A. Dreizler, and W. Meier, 'Simultaneous Three-Component PIV/OH-PLIF Measurements of a Turbulent Lifted, C3H8-Argon Jet Diffusion Flame at 1.5kHz Repetition Rate', *Proceedings of the Combustion Institute,* 32, 905-12, 2009.
16. A. M. Steinberg, I. Boxx, C. M. Arndt, J. H. Frank, and W. Meier, 'Experimental Study of Flame-Hole Reignition Mechanisms in a Turbulent Non-Premixed Jet Flame Using Sustained Multi-KHz PIV and Crossed-Plane OH PLIF', *Proceedings of the Combustion Institute,* 33, 1663-72,2011.
17. V. Sick, 'High Speed Imaging in Fundamental and Applied Combustion Research', *Proceedings of the Combustion Institute,* 34, 3509-30, 2013.
18. R. Wellander, M. Richter, and M. Aldén, 'Time-Resolved (KHz) 3D Imaging of OH PLIF in a Flame', *Experiments in Fluids,* 55(6):1764, 2014.
19. J. D. Smith, and V. Sick, 'Crank-Angle Resolved Imaging of Biacetyl Laser-Induced Fluorescence in an Optical Internal Combustion Engine', *Applied Physics B,* 81, 579-84, 2005.
20. J. D. Smith, and V. Sick, 'Quantitative, Dynamic Fuel Distribution Measurements in Combustion-Related Devices Using Laser-Induced Fluorescence Imaging of Biacetyl in Iso-Octane', *Proceedings of the Combustion Institute,* 31, 747-55,2007.
21. B. Peterson, and V. Sick, 'Simultaneous Flow Field and Fuel Concentration Imaging at 4.8 kHz in an Operating Engine', *Applied Physics B,* 97, 887-95, 2009.
22. V. Sick, M. C. Drake, and T. D. Fansler, 'High-Speed Imaging for Direct-Injection Gasoline Engine Research and Development', *Experiments in Fluids,* 49, 937-47, 2010.

23. N. Jiang, M. Webster, W. R. Lempert, J. D. Miller, T. R. Meyer, C. B. Ivey, and P. M. Danehy, 'MHz-Rate Nitric Oxide Planar Laser-Induced Fluorescence Imaging in a Mach 10 Hypersonic Wind Tunnel', *Applied Optics,* 50, A20-A28, 2011.
24. M. N. Slipchenko, J. D. Miller, S. Roy, J. R. Gord, S. A. Danczyk, and T. R. Meyer, 'Quasi-Continuous Burst-Mode Laser for High-Speed Planar Imaging', *Optics Letters,* 37, 1346-48, 2012.
25. B. Thurow, N. Jiang, and W. Lempert, 'Review of Ultra-High Repetition Rate Laser Diagnostics for Fluid Dynamic Measurements', *Measurement Science and Technology,* 24, 012002, 2013.
26. M. J. Papageorge, T. A. McManus, F. Fuest, and J. A. Sutton, 'Recent Advances in High-Speed Planar Rayleigh Scattering in Turbulent Jets and Flames: Increased Record Lengths, Acquisition Rates, and Image Quality', *Applied Physics B,* 115, 197-213, 2013.
27. M. N. Slipchenko, J. D. Miller, S. Roy, T. R. Meyer, J. G. Mance, and J. R. Gord, '100 KHz, 100 ms, 400 J Burst-Mode Laser with Dual-Wavelength Diode-Pumped Amplifiers', *Opt Lett,* 39, 4735-8, 2014.
28. S. Roy, J. D. Miller, M. N. Slipchenko, P. S. Hsu, J. G. Mance, T. R. Meyer, and J. R. Gord, '100-Ps-Pulse-Duration, 100-J Burst-Mode Laser for KHz-MHz Flow Diagnostics', *Opt Lett,* 39, 6462-5, 2014.
29. N. Jiang, M. Webster, W. Lempert, J. Miller, T. Meyer, and P. Danehy, 'Mhz-Rate No PLIF Imaging in a Mach 10 Hypersonic Wind Tunnel', in *48th AIAA Aerospace Sciences Meeting Including the New Horizons Forum and Aerospace Exposition* (American Institute of Aeronautics and Astronautics, 2010).
30. N. Jiang, J. Bruzzese, R. Patton, J. Sutton, R. Yentsch, D. V. Gaitonde, W. R. Lempert, J. D. Miller, T. R. Meyer, R. Parker, T. Wadham, M. Holden, and P. M. Danehy, 'No PLIF Imaging in the Cubrc 48-Inch Shock Tunnel', *Experiments in Fluids,* 53, 1637-46, 2012.
31. J. D. Miller, S. J. Peltier, M. N. Slipchenko, J. G. Mance, T. M. Ombrello, J. R. Gord, and C. D. Carter, 'Investigation of Transient Ignition Processes in a Model Scramjet Pilot Cavity Using Simultaneous 100 KHz Formaldehyde Planar Laser-Induced Fluorescence and CH * Chemiluminescence Imaging', *Proceedings of the Combustion Institute,* 36, 2865-72, 2017.
32. M. Lundgren, J. Rosell, M. Richter, Ö. Andersson, B. Johansson, A. Arne, and M. Alden, 'Optical Study on Combustion Transition from HCCI to PPC with Gasoline Compression Ignition in a HD Engine', *SAE Technical Paper*, 2016-01-0768, 2016.
33. M. O. Lundgren, Z. Wang, A. Matamis, O. Andersson, M. Richter, M. Tuner, M. Alden, and A. Arne, 'Effects of Post-Injections Strategies on UHC and CO at Gasoline PPC Conditions in a Heavy-Duty Optical Engine', *SAE Technical Paper*, 2017-01-0753, 2017.
34. M. Shen, 'Particulate Matter Emissions from Partially Premixed Combustion with Diesel, Gasoline and Ethanol' , Doctoral Degree Thesis (Lund University, Faculty of Engineering, Department of Energy Sciences, Division of Combustion Engines), 2016.
35. C. Schulz, and V. Sick, 'Tracer-LIF Diagnostics: Quantitative Measurement of Fuel Concentration, Temperature and Fuel/Air Ratio in Practical Combustion Systems', *Progress in Energy and Combustion Science,* 31, 75-121, 2005.
36. V. Weber, J. Brübach, R. L. Gordon, and A. Dreizler, 'Pixel-Based Characterisation of CMOS High-Speed Camera Systems', *Applied Physics B,* 103, 421-33, 2011.
37. R. Wellander, 'Multi-Dimensional Quantitative Laser-Based Diagnostics-Development and Practical Applications', Doctoral Degree Thesis, *Lund reports on combustion physics,* 177, 2014.
38. T. D. Fansler, D. T. French, and M. C. Drake, 'Fuel Distributions in a Firing Direct-Injection Spark-Ignition Engine Using Laser-Induced Fluorescence Imaging', *SAE Technical Paper*, 950110, 1995.
39. F. Grossmann, P. B. Monkhouse, M. Ridder, V. Sick, and J. Wolfrum, 'Temperature and Pressure Dependences of the Laser-Induced Fluorescence of Gas-Phase Acetone and 3-Pentanone', *Applied Physics B,* 62, 249-53, 1996.
40. M. C. Thurber, and R. K. Hanson, 'Pressure and Composition Dependences of Acetone Laser-Induced Fluorescence with Excitation at 248, 266, and 308 nm', *Applied Physics B,* 69, 229-40, 1999.
41. M. Richter, J. Engström, A. Franke, M. Aldén, A. Hultqvist, and B. Johansson, 'The Influence of Charge Inhomogeneity on the HCCI Combustion Process', *SAE Technical Paper*, 2000-01-2868, 2000.
42. H. Seyfried, J. Olofsson, J. Sjöholm, M. Richter, M. Aldén, A. Vressner, A. Hultqvist, and B. Johansson, 'High-Speed PLIF Imaging for Investigation of Turbulence Effects on Heat Release Rates in HCCI Combustion', *SAE Technical Paper*, 2007-01-0213, 2007.
43. H. Persson, J. Sjöholm, E. Kristensson, B. Johansson, M. Richter, and M. Aldén, 'Study of Fuel Stratification on Spark Assisted Compression Ignition (SACI) Combustion with Ethanol Using High Speed Fuel PLIF', *SAE Technical Paper*, 2008-01-2401, 2008).
44. U. Aronsson, C. Chartier, Ö. Andersson, R. Egnell, J. Sjöholm, M. Richter, and M. Aldén, 'Analysis of the Correlation between Engine-out Particulates and Local Φ in the Lift-Off Region of a Heavy Duty Diesel Engine Using Raman Spectroscopy', *SAE International Journal of Fuels and Lubricants,* 2, 645-60, 2009.
45. C. Chartier, J. Sjoholm, E. Kristensson, O. Andersson, M. Richter, B. Johansson, and M. Alden, 'Air-Entrainment in Wall-Jets Using SLIPI in a Heavy-Duty Diesel Engine', *SAE International Journal of Engines,* 5, 1684-92, 2012-01-1718 , 2012.
46. J. B. Michael, P. Venkateswaran, J. D. Miller, M. N. Slipchenko, J. R. Gord, S. Roy, and T. R. Meyer, '100 KHz Thousand-Frame Burst-Mode Planar Imaging in Turbulent Flames', *Opt Lett,* 39, 739-42, 2014.
47. Z. Wang, P. Stamatoglou, Z. Li, M. Aldén, and M. Richter. "Ultra-high-speed PLIF imaging for simultaneous visualization of multiple species in turbulent flames." *Opt. Express* 25, No. 24: 30214-30228, 2017.
48. S. Lonn, A. Matamis, M. Tuner, M. Richter, and O. Andersson, 'Optical Study of Fuel Spray Penetration and Initial Combustion Location under Ppc Conditions', *SAE Technical Paper*, 2017-01-0752, 2017.
49. M. P. B. Musculus, and K. Kattke, 'Entrainment Waves in Diesel Jets', *SAE International Journal of Engines,* 2, 1170-93, 2009-01-1355, 2009.

Contact Information

Zhenkan Wang
PhD student
Combustion Physics Division
Physics Department, Lund University
Lund, 22363, Sweden
zhenkan.wang@forbrf.lth.se

Acknowledgments

This research was performed at Lund University. The authors would like to acknowledge Swedish Energy Agency through Competence Centre for the Combustion Processes (KCFP) and Centre for Combustion Science and Technology (CECOST), and Volvo AB for the financial support. All the technical support from the lab technicians is appreciated.

Definitions/Abbreviations

ATDC	after top dead center
BTDC	before top dead center
CAD	crank angle degree
CCV	cycle-to-cycle variation
CFD	computational fluid dynamics
CI	compression ignition
DPSS	diode pumped solid state
EGR	exhaust gas recirculation
EOI	end of injection
FHG	fourth harmonic generator
HCCI	homogeneous charge compression ignition
ICE	internal combustion engine
ID	ignition delay
IMEP	indicated mean effective pressure
LIF	laser induced fluorescence
PCCI	partially premixed compression ignition
PDF	probability density function
PLIF	planar laser induced fluorescence
PM	particulate matter
PPC	partially premixed combustion
RON	research octane number
SI	spark ignition
SNR	signal to noise ratio
SOC	start of combustion
SOI	start of injection
TDC	top dead center

Appendix

All PLIF and chemiluminescence images are presented in Fig. 12.

Movies and their links are provided as below:

Fuel-tracer PLIF and HSV natural luminosity images (cycle No. 1)

https://www.dropbox.com/s/2nvj61idjk4nwvn/m36ksingle_60-7.avi?dl=0

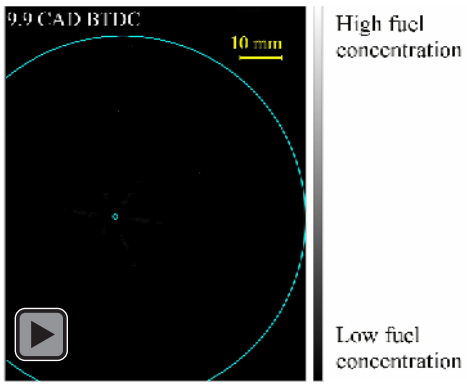

Fuel-tracer PLIF and HSV natural luminosity images (cycle No. 2)

https://www.dropbox.com/s/7yevlvlh8u97tjj/comblaser2.avi?dl=0

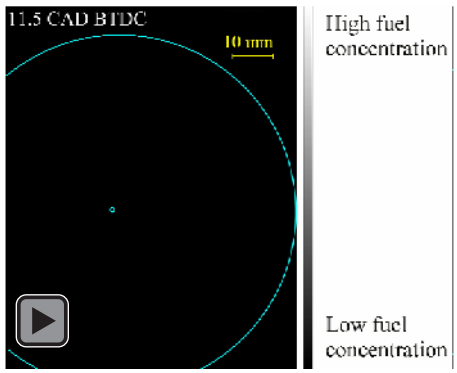

Boundary of fuel-tracer PLIF and HSV natural luminosity images

https://www.dropbox.com/s/ca4niihnvj2wgu9/m36ksingle_60-9.avi?dl=0

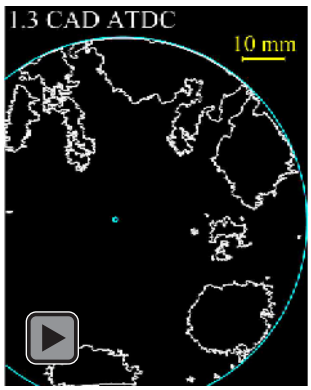

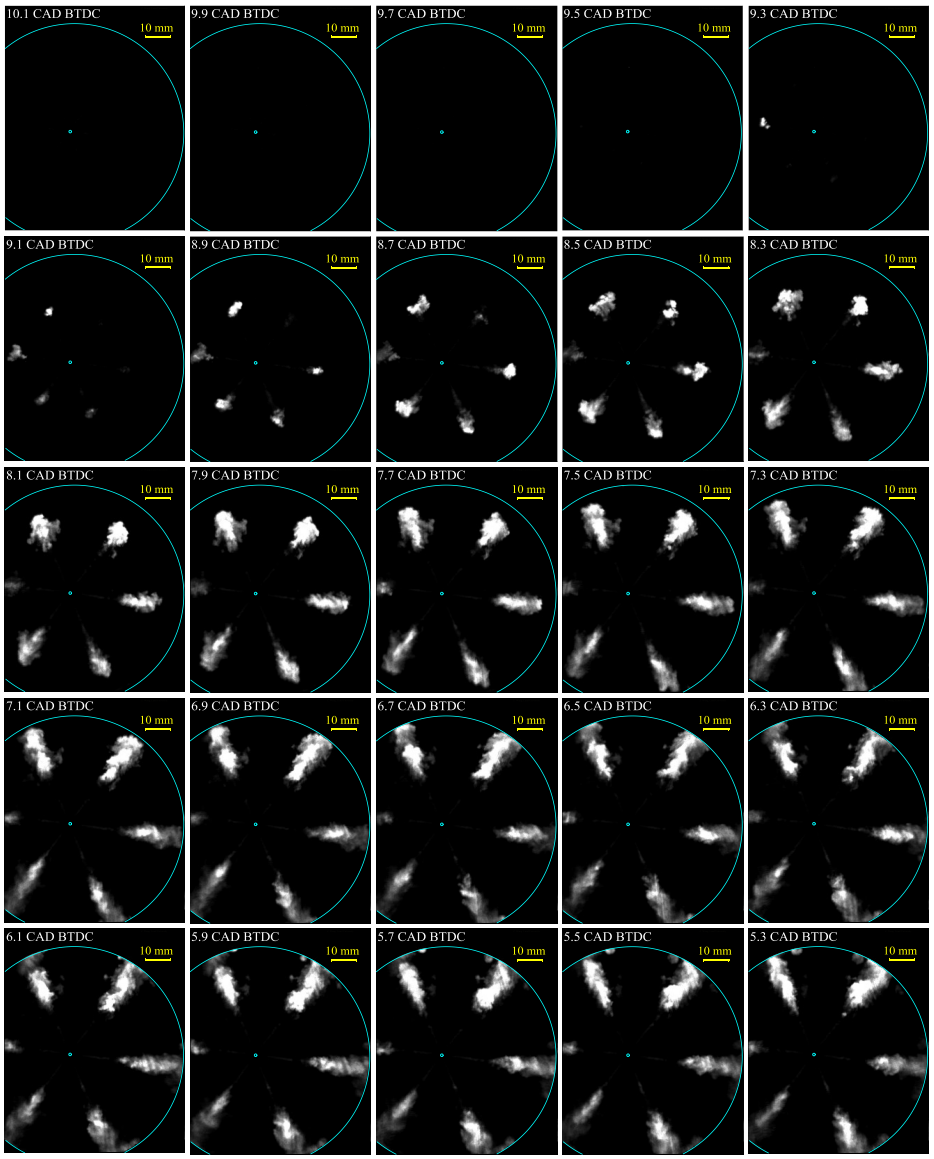
10.1 CAD BTDC
10 mm
9.9 CAD BTDC
10 mm
9.7 CAD BTDC
10 mm
9.5 CAD BTDC
10 mm
9.3 CAD BTDC
10 mm
9.1 CAD BTDC
10 mm
8.9 CAD BTDC
10 mm
8.7 CAD BTDC
10 mm
8.5 CAD BTDC
10 mm
8.3 CAD BTDC
10 mm
8.1 CAD BTDC
10 mm
7.9 CAD BTDC
10 mm
7.7 CAD BTDC
10 mm
7.5 CAD BTDC
10 mm
7.3 CAD BTDC
10 mm
7.1 CAD BTDC
10 mm
6.9 CAD BTDC
10 mm
6.7 CAD BTDC
10 mm
6.5 CAD BTDC
10 mm
6.3 CAD BTDC
10 mm
6.1 CAD BTDC
10 mm
5.9 CAD BTDC
10 mm
5.7 CAD BTDC
10 mm
5.5 CAD BTDC
10 mm
5.3 CAD BTDC
10 mm

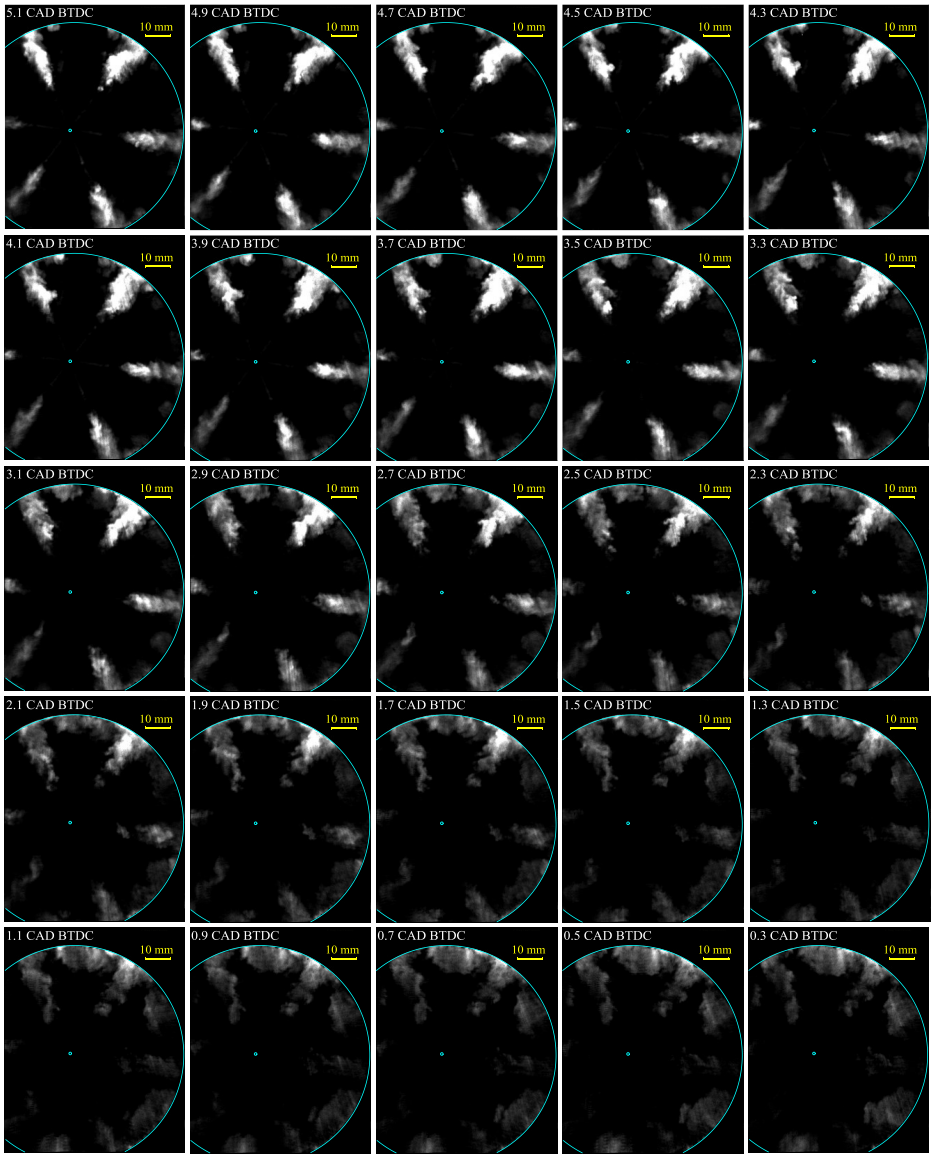
5.1 CAD BTDC
10 mm
4.9 CAD BTDC
10 mm
4.7 CAD BTDC
10 mm
4.5 CAD BTDC
10 mm
4.3 CAD BTDC
10 mm
4.1 CAD BTDC
10 mm
3.9 CAD BTDC
10 mm
3.7 CAD BTDC
10 mm
3.5 CAD BTDC
10 mm
3.3 CAD BTDC
10 mm
3.1 CAD BTDC
10 mm
2.9 CAD BTDC
10 mm
2.7 CAD BTDC
10 mm
2.5 CAD BTDC
10 mm
2.3 CAD BTDC
10 mm
2.1 CAD BTDC
10 mm
1.9 CAD BTDC
10 mm
1.7 CAD BTDC
10 mm
1.5 CAD BTDC
10 mm
1.3 CAD BTDC
10 mm
1.1 CAD BTDC
10 mm
0.9 CAD BTDC
10 mm
0.7 CAD BTDC
10 mm
0.5 CAD BTDC
10 mm
0.3 CAD BTDC
10 mm

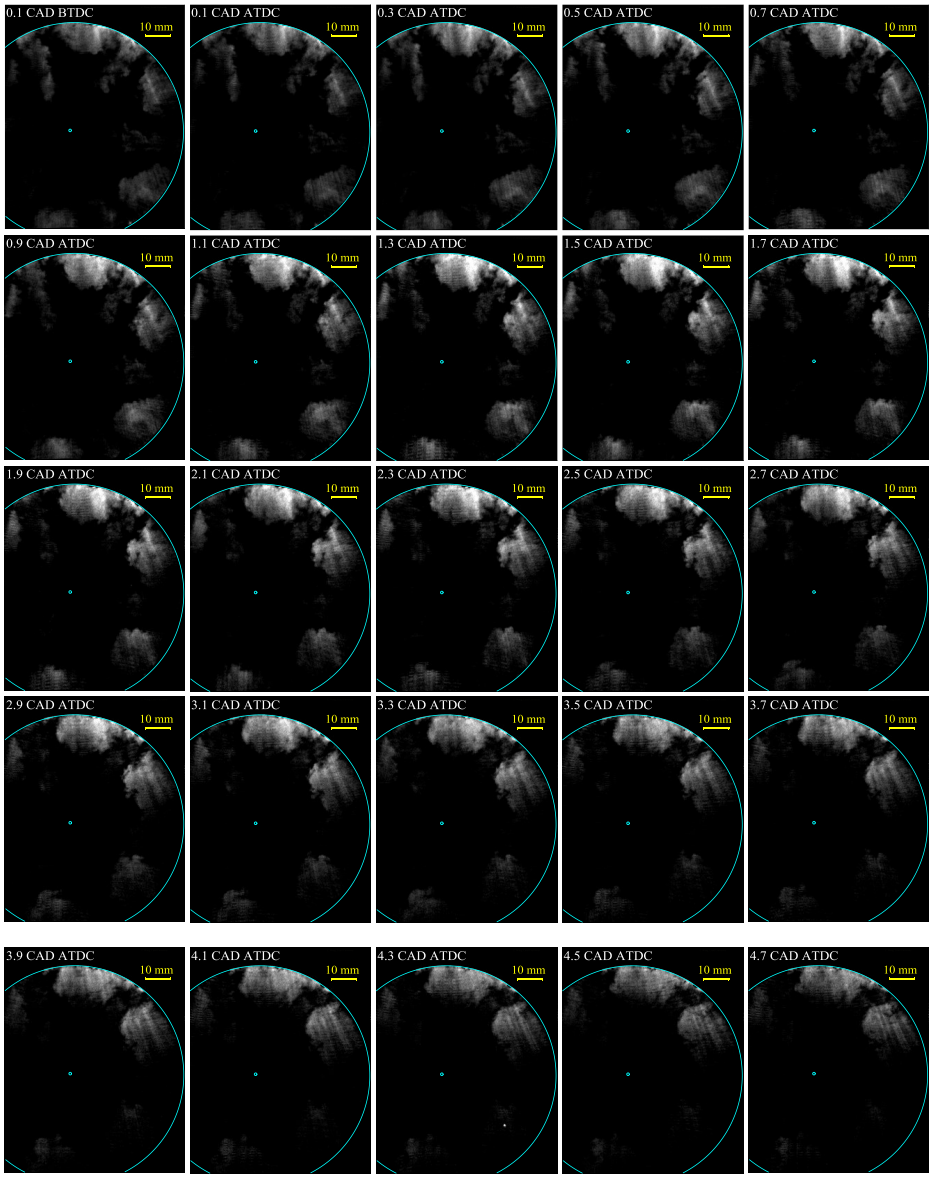
0.1 CAD BTDC
10 mm
0.1 CAD ATDC
10 mm
0.3 CAD ATDC
10 mm
0.5 CAD ATDC
10 mm
0.7 CAD ATDC
10 mm
0.9 CAD ATDC
10 mm
1.1 CAD ATDC
10 mm
1.3 CAD ATDC
10 mm
1.5 CAD ATDC
10 mm
1.7 CAD ATDC
10 mm
1.9 CAD ATDC
10 mm
2.1 CAD ATDC
10 mm
2.3 CAD ATDC
10 mm
2.5 CAD ATDC
10 mm
2.7 CAD ATDC
10 mm
2.9 CAD ATDC
10 mm
3.1 CAD ATDC
10 mm
3.3 CAD ATDC
10 mm
3.5 CAD ATDC
10 mm
3.7 CAD ATDC
10 mm
3.9 CAD ATDC
10 mm
4.1 CAD ATDC
10 mm
4.3 CAD ATDC
10 mm
4.5 CAD ATDC
10 mm
4.7 CAD ATDC
10 mm

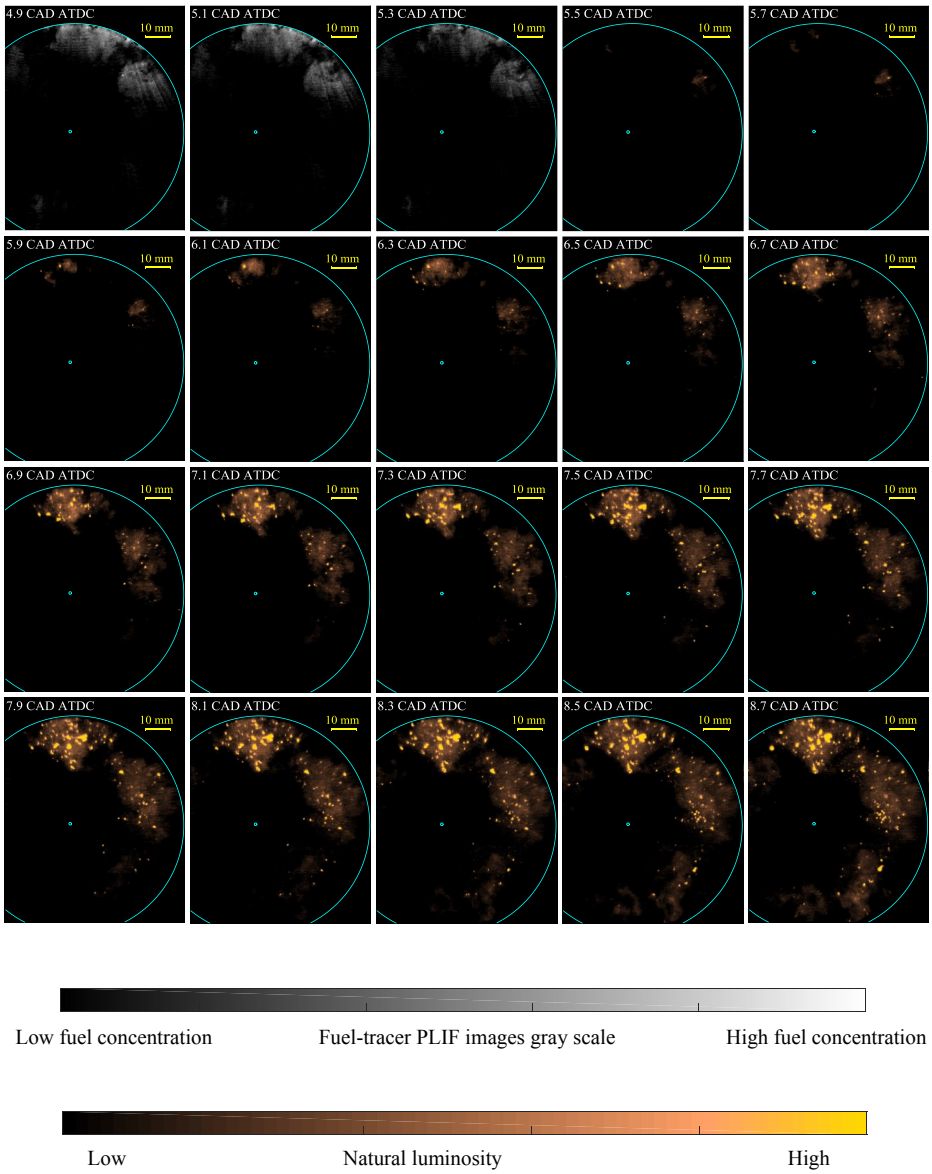

Figure 12. Full sequence of fuel distribution from SOI to EOI and sequential autoignition.

Paper VIII

Elsevier Editorial System(tm) for
Proceedings of The Combustion Institute
Manuscript Draft

Manuscript Number:

Title: Simultaneous 36 kHz PLIF/Chemiluminescence imaging of fuel, CH2O and combustion in a PPC engine

Article Type: 11. Internal Combustion Engines

Keywords: PPC; Autoignition; Ultra-high speed diagnostics; Burst-mode laser; Planar laser induced fluorescence.

Corresponding Author: Mr. Zhenkan Wang, M.D.

Corresponding Author's Institution: Combustion Physics

First Author: Zhenkan Wang, M.D.

Order of Authors: Zhenkan Wang, M.D.; Panagiota Stamatoglou, M.D.; Marcus Lundgren , Ph.D.; Ludovica Luise , M.D.; Bianca Vaglieco , Ph.D.; Arne Andersson , Ph.D.; Marcus Aldén , Ph.D.; Öivind Andersson , Ph.D.; Mattias Richter , Ph.D.

Abstract: The requirements on high efficiency and low emissions of internal combustion engines (ICEs) raise the research focus on advanced combustion concepts, e.g. premixed-charge compression ignition (PCCI), partially premixed compression ignition (PPCI), (reactivity controlled compression ignition) RCCI, partially premixed combustion (PPC) etc. In the present study, an optically accessible engine is operated in PPC mode, featuring compression ignition of a diluted, stratified charge of gasoline-like fuel injected directly into the cylinder. A high-speed, high-power burst-mode laser system in combination with a high-speed CMOS camera is employed for diagnostics of the autoignition process which is critical for the combustion phasing and efficiency of the engine. To the authors' best knowledge, this work demonstrates for the first time the application of the burst-system for simultaneous fuel tracer planar laser induced fluorescence (PLIF) and chemiluminescence imaging in an optical engine, at 36 kHz repetition rate. In addition, high-speed formaldehyde PLIF and chemiluminescence imaging are employed for investigation of autoignition events with a high temporal resolution (5 frames/CAD). The development of autoignition together with fuel or CH2O distribution are simultaneously visualized using a large number of consecutive images. Prior to the onset of combustion the majority of both fuel and CH2O are located in the recirculation zone, where the first autoignition also occurs. The ability to record, in excess of 100 PLIF images, in a single cycle brings unique possibilities to follow the in-cylinder processes without the averaging effects caused by cycle-to-cycle variations.

Simultaneous 36 kHz PLIF/Chemiluminescence imaging of fuel, CH_2O and combustion in a PPC engine

Zhenkan Wang[a,*], Panagiota Stamatoglou[a], Marcus Lundgren[b], Ludovica Luise[c], Bianca Maria Vaglieco[c], Arne Andersson[d], Marcus Aldén[a], Öivind Andersson[b], Mattias Richter[a]

[a] *Division of Combustion Physics, Lund University, P.O. Box 11, S221 00 Lund, Sweden*

[b] *Division of Combustion Engines, Lund University, P.O. Box 11, S221 00 Lund, Sweden*

[c] *Istituto Motori- CNR Naples, Via Marconi, 4 - 80125 Napoli, Italy*

[d] *Volvo Group Trucks Technology, Powertrain Engineering, Sweden*

[*]*Email:* zhenkan.wang@forbrf.lth.se*;*

Corresponding Author:

Zhenkan Wang
Division of Combustion Physics,
Lund University, P.O. Box 118
SE-221 00 Lund, Sweden
Email: zhenkan.wang@forbrf.lth.se
Tel: +46 46 222 4962
Fax: +46 46 222 4542

Colloquium: Internal Combustion Engines (alternate colloquia: **Diagnostics)**

Total word count (method 1): 3368 (main text)+ 542 (reference)+ 84(table)+ 1795 (figure) = 5789
Main text: 753 (Introduction) +518 (Experimental setup)+1802 (Results and discussions)+252 (Conclusion)+43 (Acknowledgement)=3368
References: (29 refs+2)*2.3*7.6=542
Table.1: (9 line+2)*7.6=84
Figure 1: (66+10)*2.2+12=179
Figure 2: (40+10)*2.2+27=137
Figure 3: (96.7+10)*2.2+39=274
Figure 4: (91.7+10)*2.2+12=236
Figure 5: (37.5+10)*2.2+27=132
Figure 6: (36+10)*2.2+38=139
Figure 7: (91.1+10)*2.2+16=238
Figure 8: (93+10)*2.2+18=245
Figure 9: (82.2+10)*2.2+12=215

Color Reproduction: Agree to pay color reproduction charges.

Abstract

The requirements on high efficiency and low emissions of internal combustion engines (ICEs) raise the research focus on advanced combustion concepts, e.g. premixed-charge compression ignition (PCCI), partially premixed compression ignition (PPCI), (reactivity controlled compression ignition) RCCI, partially premixed combustion (PPC) etc. In the present study, an optically accessible engine is operated in PPC mode, featuring compression ignition of a diluted, stratified charge of gasoline-like fuel injected directly into the cylinder. A high-speed, high-power burst-mode laser system in combination with a high-speed CMOS camera is employed for diagnostics of the autoignition process which is critical for the combustion phasing and efficiency of the engine. To the authors' best knowledge, this work demonstrates for the first time the application of the burst-system for simultaneous fuel tracer planar laser induced fluorescence (PLIF) and chemiluminescence imaging in an optical engine, at 36 kHz repetition rate. In addition, high-speed formaldehyde PLIF and chemiluminescence imaging are employed for investigation of autoignition events with a high temporal resolution (5 frames/CAD). The development of autoignition together with fuel or CH_2O distribution are simultaneously visualized using a large number of consecutive images. Prior to the onset of combustion the majority of both fuel and CH_2O are located in the recirculation zone, where the first autoignition also occurs. The ability to record, in excess of 100 PLIF images, in a single cycle brings unique possibilities to follow the in-cylinder processes without the averaging effects caused by cycle-to-cycle variations.

Keywords: PPC; Autoignition; Ultra-high speed diagnostics; Burst-mode laser; Planar laser induced fluorescence.

1. Introduction

Stricter demands on the efficiency and emissions of internal combustion engines (ICEs) increase the interest in low temperature combustion concepts. These are based on combustion processes that are largely kinetically controlled. Dilution is used to limit the combustion temperature, thus moderating the burn rate and reducing emissions of nitrogen oxides and particulates. Dilution also reduces the heat losses, which in combination with adequate burn rates, has been demonstrated to enable remarkable engine efficiencies [1]. In the present study, an optically accessible engine was operated in partially premixed combustion (PPC) mode, featuring compression ignition of a diluted, stratified charge of gasoline-like fuel injected directly into the cylinder.

Understanding the autoignition process allows control of the combustion phasing and efficiency in PPC engines. High-speed diagnostics are critical for this purpose, due to the stochastic cycle-to-cycle variability in ignition location and timing. Autoignition has been studied in PPC engines using high-speed chemiluminescence imaging [2, 3]. While this technique provides line-of-sight averaged information about where and when the charge ignites, it does not reveal the underlying causes. A more detailed overview of the autoignition process requires high-speed laser diagnostics to couple the initial flame location(s) to simultaneous information about distributions of fuel and relevant ignition precursors, such as formaldehyde.

Planar laser induced fluorescence (PLIF) is a technique used to investigate in-cylinder species distributions and combustion propagation. Since most of the research fuels are not fluorescent, a tracer is added to the fuel mixture. The most common tracers being used in previous studies are: acetone [4-11], 3-Pentanone [4, 7, 12], biacetyl [13] and toluene [14,

15]. A detailed review on ketones and the dependence of the LIF signal on temperature, pressure and mixture can be found in [16].

Initially, fuel tracer PLIF experiments were conducted with 10-Hz Nd:YAG lasers and statistical analysis was employed to address cycle-to-cycle variations (CCV) [4-6, 14]. Fuel tracer PLIF in combination with chemiluminescence imaging has been used to acquire information about the leading edge of the vapor jet and the location of ignition, simultaneously [17].

The presence of CCV and the need to temporally resolve events within a single cycle have led to the application of high-repetition rate laser diagnostic for cycle-resolved imaging in ICEs. An approach based on the application of laser clusters in combination with multiple CCD detectors was first successfully demonstrated by Hult *et al.* [7] at up to 14.4 kHz. High-speed fuel tracer LIF [18] combined with chemiluminescence [8] as well as high-speed PLIF for cycle-resolved formaldehyde visualization [19] were investigated using this technique. The cluster of four YAG lasers combines both high-repetition and high pulse energy but is limited to only 8 images within one engine cycle. Hult *et al.* also reported that the beam profile deteriorates when the pulse separation decreases [7].

Smith and Sick used biacetyl as a tracer to image the fuel distribution in a direct-injection gasoline engine at 12 kHz repetition rate from a DPSS YAG-laser with a 100 ns pulse duration [13]. The high repetition rate reduced the available energy per pulse to a few hundreds of microjoules at 355 nm, resulting in a limited field of view (FOV) or a low signal-to-noise ratio compared to conventional 10 Hz systems. The development of burst-mode laser systems has facilitated the acquisition of multiple images at high repetition rates and high pulse energy. For a thorough description of the development of burst lasers, including the pioneering work by Lempert *et al.*, please see [20]. Due to their size and complexity, most applications of burst-mode lasers have been restricted to dedicated optical laboratories, see for

example the recent study by Michael *et al.*, where PLIF imaging of formaldehyde was performed at 100 kHz in a lifted jet diffusion flame [21]. There are a few exceptions though, *e.g.* Miller *et al.* [22] conducted high-speed CH_2O PLIF in a supersonic scramjet combustor facility. The laser system employed in the current work was developed by Slipchenko *et al.* with some modifications [23, 24]. To the authors' best knowledge, this work demonstrates for the first time the application of burst-system for simultaneous fuel tracer PLIF and chemiluminescence imaging in an optical engine, at 36 kHz repetition rate. In addition, high-speed formaldehyde PLIF and chemiluminescence imaging are employed for investigation of autoignition events with a high temporal resolution (5 frames/crank angle degree, CAD). A state-of-the-art laser system is employed in this study in combination with a high-speed CMOS camera in order to achieve high pulse energies at high repetition rates for generation of a large number of consecutive images.

2. Experimental details

2.1 Optical engine and operating conditions

The work was conducted in a Volvo heavy-duty engine modified for optical access through applying a Bowditch design. The combustion system of this engine is non-swirling and features a common-rail system with a centrally mounted 6-hole injector. More detailed information on the engine hardware can be found in reference [2, 25].

Table 1.
Operating conditions

Engine speed [RPM]	1200
Engine load (IMEPg) [bar]	7
Fuel pressure [bar]	1500
Intake temperature [˚C]	108
Intake pressure [bar]	2.1
Intake O_2 concentration [%]	16 (combusting)
Intake O_2 concentration [%]	< 8 (non-combusting)

The operating conditions for this experiment are similar to the ones applied in previous studies conducted in this engine [25], see Table 1.

The fuel was primary reference fuel (PRF) 87, *i.e.* a mixture of 13% n-heptane and 87% iso-octane. To this 10% v/v of acetone was added as a fuel tracer. At elevated pressures the fluorescence from acetone depends mainly on temperature [16]. Due to the unknown local temperature variations no attempt to quantify the fuel concentrations was made in this study.

2.2 Fuel tracer PLIF

Planar laser induced fluorescence and chemiluminescence were used to simultaneously investigate the fuel distribution and the characteristic of the early phase of combustion. The laser source was an Nd:YAG based burst system operating at a repetition rate of 36 kHz, with an output of 50 mJ per pulse at 266 nm. A horizontal 65 mm wide laser sheet was formed by a cylindrical (-50 mm) and a spherical (500 mm) lens and positioned 12 mm below the injector tip. At such repetition rates this represents a significant increase in illuminated area compared to what would be feasible with a conventional kHz DPSS YAG-laser. The fluorescence was collected from beneath, through the optical piston. The position of the laser sheet and the FOV are illustrated in Fig. 1.

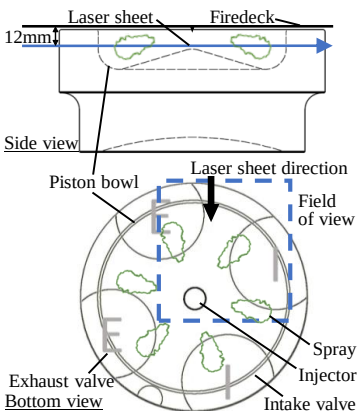

Figure 1. Field of view for fuel tracer and CH_2O PLIF imaging.

The fluorescence was detected by a high-speed CMOS camera (Photron Fastcam SA-Z) operating at 72 kHz in order to capture both fuel-tracer PLIF and chemiluminescence (every second image) from the combustion. The resolution of the detector at this frame rate was 512x480 pixels, corresponding to a 65x60 mm^2 FOV. A Nikon (f=105 mm, f#=1.8) camera lens was employed for signal collection. A quartz cuvette containing liquid N,N-dimethylformanide was used as long-pass filter to discriminate against spurious radiation at 266 nm.

2.3 CH_2O PLIF

The 355 nm output from the burst system was used to excite CH_2O and partially oxidized fuel. The available energy was 180 mJ per pulse and the beam was directed through the same set of optical components (lens position was adjusted accordingly) as for the fuel tracer PLIF. A Nikon (f=85 mm, f#=1.4) camera lens was used for signal collection in combination with a long-pass (GG385) filter for suppression of scattered radiation. Also in these experiments the laser system was operated at 36 kHz whereas the detector was running at 72 kHz to enable quasi-simultaneous detection of chemiluminescence. The acquisition time was set to capture in excess of 150 consecutive images from the start of injection to a few CADs after the start of combustion (SOC) within a single engine cycle. Both formaldehyde and acetone PLIF were conducted without image intensifier.

2.4 Post-processing

The image post-processing includes background subtraction, distortion correction and normalization. More detailed description can be found in [11].

3. Results and discussion

3.1 Fuel tracer PLIF

More than 100 sequential PLIF images where recorded within one engine cycle. The entire mixing process from injection, through ignition delay, to the onset of combustion can be investigated in the resulting image series. Due to the space restriction only a fraction of the image series can be shown here. More results, including full movies, can be found in the supplementary material (SM1, SM2). By looking at the movie SM1, a unique view of the in-cylinder mixing process in high spatial and temporal resolution is provided. The charge motion and distribution are well captured within one engine cycle. This ability to truly resolve single-cycles constitutes the most significant advantage of this technique. The influence of cycle-to-cycle variations, which traditionally introduce an averaging effect on the results, can thus be avoided.

In the beginning of the mixing process, the fuel spray is introduced with very high velocity, *e.g.* > 100 m/s [26]. This provides a strong momentum that drives air entrainment into the evaporating spray. This process is captured by ultra-high speed PLIF imaging. In movie SM1, the formation and development of large eddies, created by aerodynamic forces, can be directly observed. Around 7 CAD before top dead center (BTDC), the gaseous fuel impinges on the piston bowl wall. The spray is here split into two parts, which subsequently proceed further in a circumferential movement along the piston bowl perimeter. In spite of the counteracting sheer force at the bowl wall, the eddies created upstream keep their initial rotational direction (introduced through air entrainment) when entering the recirculation zone between two adjacent spray plumes.

Thus the rotational directions of the down-stream eddies in two adjacent spray plumes are opposite each other when they collide in the recirculation zone. The turbulence is significantly enhanced here when two adjacent spray interact with each other, which confirms the importance of this recirculation region for gasoline PPC. Through momentum driven mixing

the charge in the recirculation zone expands and moves further towards the center of the piston bowl before SOC.

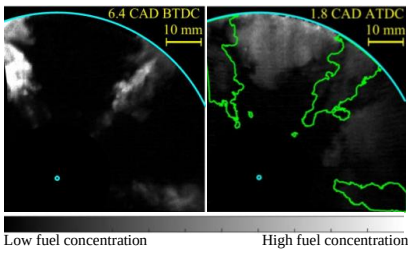

Figure 2. Fuel distribution before SOC at 1.8 CAD ATDC together with the outer boundary of fuel distribution at 6.4 CAD BTDC (green lines) in one cycle.

The entrainment wave, first described by Musculus *et al.* [27], following immediately after the end of injection enhances the mixing process resulting in further reduction of the fuel concentration along the spray axis. This can be directly observed in the present experiment. Fuel distributions at 6.4 CAD BTDC and at 1.8 CAD after top dead center (ATDC) (just before ignition occurs) in the same engine cycle are displayed in Fig. 2. It is evident that after the end of injection (EOI), the majority of the charge ends up in the recirculation zone before the onset of combustion while the area along the spray axis is highly leaned out by the momentum of the jet in combination with the entrainment wave. The green boundary in Fig. 2 represents the envelop of the fuel distribution during the injection event (at 6.4 CAD BTDC).

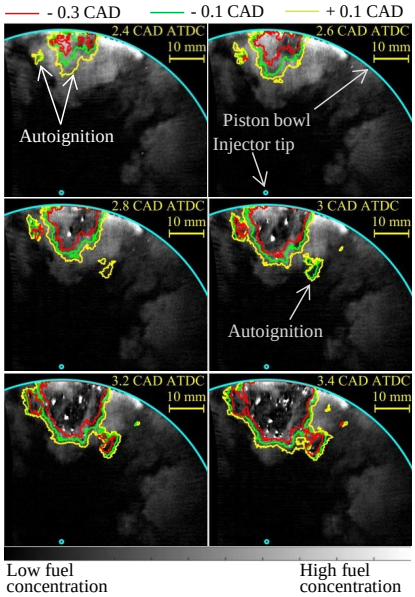

Figure 3. Fuel distribution after SOC together with envelop of autoignition zones. Red, green and yellow lines indicate envelop of flame luminosity at 0.3 CAD, 0.1 CAD before the PLIF image and 0.1 CAD after the PLIF image, respectively.

In order to obtain the spatial relation between autoignition and fuel distribution, the outer boundary of simultaneously recorded chemiluminescence is imposed on the fuel PLIF images as shown in Fig. 3. The red, green and yellow lines indicate the envelop of the flame at 0.3 CAD, 0.1 CAD before the recording of the fuel PLIF image and 0.1 CAD after it, respectively. The timing of the fuel PLIF image is indicated in the upper right corner of the image. Given the uncertainty of the line-of-sight averaged chemiluminescence, one can still see that the initial autoignition (left image in the upper row of Fig. 3) is located close to the bowl rim in the center of the recirculation zone where most of the mixture resides after the ignition delay. It is also interesting to see that following autoignition sites occur at the periphery of the fuel distribution in the recirculation zone. In the single-cycle resolved imaging it can be seen how, under PPC conditions with such long ignition delay, the early

combustion progress through sequential autoignition rather than conventional flame propagation.

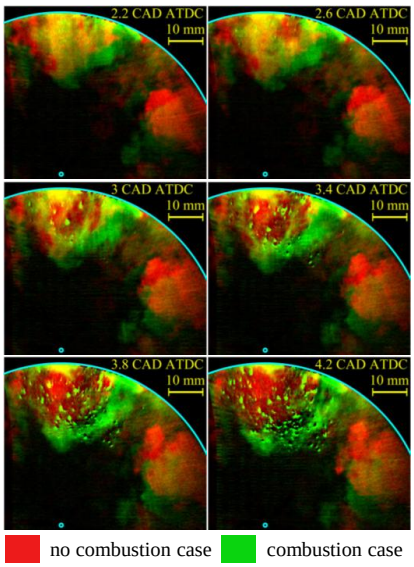

Figure 4. Fuel distribution for combusting case (green) and non-combusting case (red).

From the recorded image series it can be seen that the expansion of the flame kernels pushes the surrounding fuel in the recirculation zone away tangentially and towards the center of the piston bowl. A comparison of the fuel distributions in a combusting case (green) and a non-combusting case (red) is illustrated in Fig. 4. During the ignition delay the fuel distributions of two cases show a similar spatial spread. However, after the onset of combustion the remaining unburnt fuel in the combusting case is distributed over a larger area compared to the non-reacting case. In order to be feasible, the tracking of this process in time requires single-cycle resolved data.

3.2 CH_2O PLIF

The laser radiation at 355 nm excites not only CH_2O but also partially oxidized fuel such as PAHs. Hence, the fluorescence collected by the camera comes from both CH_2O and PAHs if present. However, since PAH and CH_2O are both formed from fuel at elevated temperatures during the initial phase of combustion and are later consumed by the high temperature reactions, this cross-talk should not jeopardize the results.

In movie SM2, the formation and development of large eddies can be observed at the boundary of the CH_2O distribution, similar to the fuel mixing process discussed earlier. As a product of low temperature combustion, or first stage ignition, the CH_2O distribution essentially overlaps with the fuel mixture distribution [28] when sufficient temperatures are reached.

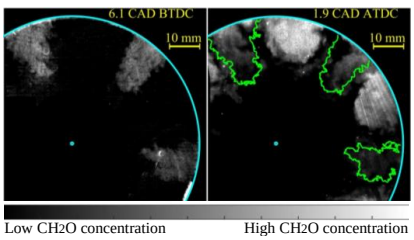

Figure 5. CH_2O distribution before SOC at 1.9 CAD ATDC together with the outer boundary of CH_2O distribution at 6.1 CAD BTDC (green lines) in one cycle.

Figure 5 shows the CH_2O distribution during the injection event and 0.1 CAD before SOC respectively. The green line represents the outer boundary of the CH_2O distribution at 6.1 CAD BTDC. As expected the CH_2O and fuel distributions follows a similar pattern, *i.e.* also the CH_2O gathers in the recirculation zone where it is being pushed towards the center of the piston bowl before the SOC, while less CH_2O is located along the spray axis.

A unique feature of gasoline-like PPC is the long ignition delay, compared to diesel PPC. In the present study it can be seen how the CH_2O being formed in the autoignition process,

persists until the high temperature combustion starts consuming it. Whereas the fuel, or rather the fuel tracer, is being decomposed slightly earlier.

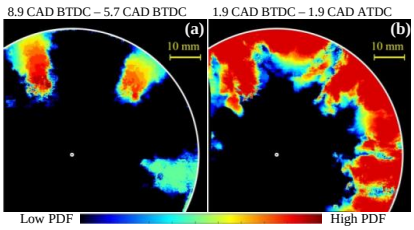

Figure 6. (a). Probability density function (PDF) of the CH_2O distribution during the injection from 8.9 CAD BTDC to 5.7 CAD BTDC; (b). PDF of the CH_2O distribution before SOC from 1.9 CAD BTDC to 1.9 CAD ATDC.

Cycle-averaged PDF plots are normally generated using a conventional 10 Hz laser and acquisition system by lumping together data recorded at the same CADs in different cycles. The PDF shown in Fig. 6 is instead generated by lumping together data from a short CAD interval in one single cycle. One benefit of applying the high-speed burst system for generating fuel/ CH_2O distribution PDFs, through this approach, is the greatly reduced acquisition time. This is especially valuable under sooty conditions where window fouling can be a major obstacle. It should be mentioned though, that cycle-averaged and CAD-averaged PDFs do not show the same thing and are thus not directly comparable.

As can be seen from Fig. 6, the CH_2O is essentially distributed along the periphery of the piston bowl before the onset of combustion. This lack of fuel/CH_2O closer to the center of the combustion chamber indicates poor air utilization. A possible solution for improved mixing, through promoting mixture motion towards the center, is the “wave” piston bowl geometry introduced by Volvo [29]. A follow-up study to investigate the impact of this novel geometry is thus planned for.

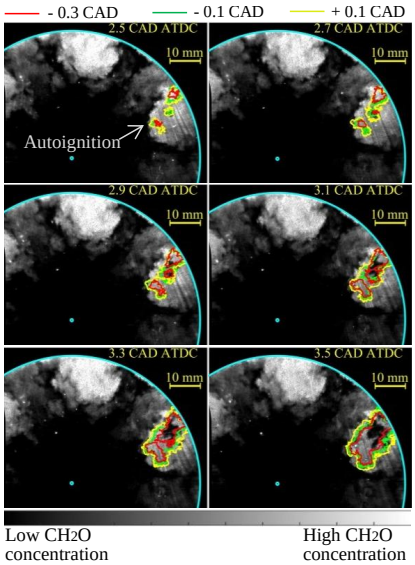

Figure 7. CH_2O distribution after SOC together with envelop (curve notation, see Fig.4) of autoignition zones.

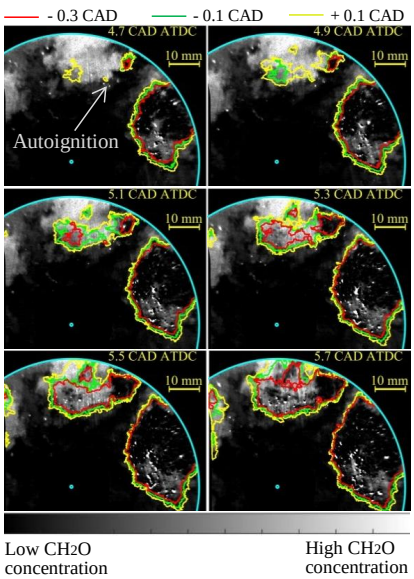

Figure 8. CH_2O distribution during sequential autoignition events with envelop (curve notation, see Fig.4) of the autoignition positions.

Similar to Fig. 3, the outer boundary of chemiluminescence is overlaid on the CH_2O PLIF image and presented in Fig. 7 and Fig. 8 from 0.3 CAD ASOC to 3.7 CAD ASOC. The initial autoignition (images in the top row of Fig. 7) is again located in the recirculation zone. The obvious difference between the chemiluminescence boundary and the 'holes' in CH_2O distribution in the recirculation zone (in the bottom row of Fig. 7) is a result of the PLIF images showing true two-dimensional cross-sections whereas the chemiluminescence signal is integrated along the line of sight. The outer border of the chemiluminescence thus represents the largest possible extent of the three-dimensional flame as viewed by the camera.

In Fig. 8 it can be seen how the flame approaches the boundary of the CH_2O distribution in the recirculation zone that ignited first. The steep gradient of the charge causes the flame expansion speed to reduce significantly and finally come to a halt when there is no more fresh charge to consume. Also here it becomes obvious that there is a lack of combustible species and ignition precursors in the center of the combustion chamber. In addition, in Fig. 8 the sequential autoignition of the upper recirculation zone can be studied. Here the expansion speed of the chemiluminescence boundary is significantly faster than the corresponding expansion in the recirculation zone that ignited first. The consumption of CH_2O in the upper recirculation zone, indicated by the growing holes in the CH_2O distribution, is lagging the growth indicated by the chemiluminescence. This is a consequence of the 3D flame being initiated outside the plane imaged in the PLIF series.

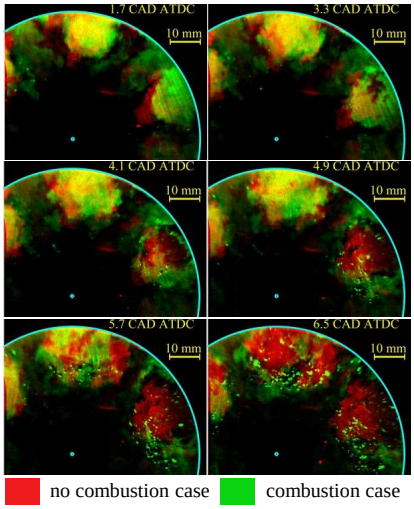

Figure 9. CH_2O distribution for combusting case (green) and non-combusting case (red).

Figure 9 shows how the expanding hot gases in the early flame kernel pushes the CH_2O in the recirculation zone along the tangential direction (towards the spray axis) and towards the center of the piston bowl. This pattern is similar to the charge movement shown in Fig. 4, but since CH_2O is present also slightly after the fuel (tracer) has decomposed, the push from the burnt gases is even more pronounced here.

It's well known that the evaporative cooling effect plays an important role in the autoignition process. During the injection event the leading edge of the spray is heated as it propagates towards the recirculation zone while the wake along the spray axis has relatively cold environment due to the cooling effect from the spray vaporization. In addition, entrainment wave leans out the equivalence ratio along the spray axis after EOI. Consequently, the mixture in the recirculation zone is more likely to be ignited first.

At the early phase of injection in PPC, the velocity of the leading edge of the spray is too high and due to the early injection timing the local temperature is not high enough for autoignition to occur. However, after impingement of neighboring sprays in the recirculation zone, the flow velocity becomes low and the mixture is further heated which results in favorable

condition for autoignition. The ignition precursor CH_2O is formed in the recirculation zone well before the SOC. Once ignition occurs, the reaction front propagation speed is very high and is driven by sequential autoignition and hot gas expansion.

Whether the initial autoignition occurs in the center or at the periphery of the recirculation zone is a competition between the local equivalence ratio and temperature. Equivalence ratio is higher inside recirculation zone while temperature is higher at the periphery due to less vaporization and more heat exchange with the hot ambient air.

Summary

The present study constitutes the first application of a high-speed, high-power burst-mode laser system for diagnostics in an optical engine. Due to size and complexity, high power burst-laser systems have until recently been mainly limited to stationary applications in optical laboratories. To the authors' best knowledge, this is the first time to achieve a combination of simultaneous fuel tracer PLIF and chemiluminescence imaging as well as CH_2O PLIF and chemiluminescence imaging in an optical engine, at 36 kHz repetition rate, *i.e.* temporal resolution of 0.2 CAD at 1200 rpm. The development of autoignition together with fuel or CH_2O distribution are visualized simultaneously. It is observed that the equivalence ratio of fuel along the spray axis decreases rapidly after the EOI, which is consistent with the occurrence of the entrainment wave proposed by Musculus *et.al.* [27]. Prior to the onset of combustion the majority of both fuel and CH_2O are located in the recirculation zone, where the first autoignition also occurs.

The ability to record in excess of 100 PLIF images in a single cycle brings unique possibilities to follow the in-cylinder processes without the averaging effects caused by cycle-to-cycle variations. The cinematic results from single-cycle events reveals details about the charge mixing and development, such as eddies formation and transport that cannot be accessed

through conventional 10 Hz imaging. Fast and stochastic processes such as the sequential autoignition found in combustion concepts featuring long ignition delays, *e.g.* HCCI and PPC, can now be studied in single-cycle events with high temporal resolution.

Acknowledgement

The authors would like to acknowledge Swedish Energy Agency through Competence Centre for the Combustion Processes (KCFP) and Centre for Combustion Science and Technology (CECOST), and Volvo AB (VEV project) for the financial support. Thanks to the technicians for their technical support.

References

[1] V. Manente, B. Johansson, P. Tunestal, SAE International, 2009-01-0944, (2009).
[2] M. Lundgren, J. Rosell, M. Richter, Ö. Andersson, B. Johansson, A. Arne, M. Alden, SAE International, 2016-01-0768, (2016).
[3] S. Lonn, A. Matamis, M. Tuner, M. Richter, O. Andersson, SAE International, 2017-01-0752, (2017).
[4] F. Grossmann, P.B. Monkhouse, M. Ridder, V. Sick, J. Wolfrum, Applied Physics B, 62 (1996) 249-253.
[5] M.C. Thurber, R.K. Hanson, Applied Physics B, 69 (1999) 229-240.
[6] M. Richter, J. Engström, A. Franke, M. Aldén, A. Hultqvist, B. Johansson, SAE International, 2000-01-2868, (2000).
[7] J. Hult, M. Richter, J. Nygren, M. Aldén, A. Hultqvist, M. Christensen, B. Johansson, Appl. Opt., 41 (2002) 5002-5014.
[8] A. Hultqvist, M. Christensen, B. Johansson, M. Richter, J. Nygren, J. Hult, M. Aldén, SAE International, 2002-01-0424, (2002).
[9] C. Chartier, J. Sjoholm, E. Kristensson, O. Andersson, M. Richter, B. Johansson, M. Alden, SAE International Journal of Engines, 5 (2012) 1684-1692.
[10] J.D. Miller, J.B. Michael, M.N. Slipchenko, S. Roy, T.R. Meyer, J.R. Gord, Applied Physics B, 113 (2013) 93-97.
[11] Z. Wang, S. Lonn, A. Matamis, O. Andersson, M. Tuner, M. Alden, M. Richter, SAE International Journal of Engines, 10 (2017) 1465-1481.
[12] N. Graf, J. Gronki, C. Schulz, T. Baritaud, J. Cherel, P. Duret, J. Lavy, SAE International, 2001-01-1924, (2001).
[13] J.D. Smith, V. Sick, Applied Physics B, 81 (2005) 579-584.
[14] D.L. Reuss, V. Sick, SAE International, 2005-01-2122, (2005).
[15] S. Kokjohn, R.D. Reitz, D. Splitter, M. Musculus, SAE International Journal of Engines, 5 (2012) 248-269.
[16] C. Schulz, V. Sick, Progress in Energy and Combustion Science, 31 (2005) 75-121.
[17] M.P.B. Musculus, SAE International, 2006-01-0079, (2006).
[18] H. Persson, J. Sjöholm, E. Kristensson, B. Johansson, M. Richter, M. Aldén, SAE International, 2008-01-2401, (2008).
[19] J. Olofsson, H. Seyfried, M. Richter, M. Aldén, A. Vressner, A. Hultqvist, B. Johansson, K. Lombaert, SAE International, 2005-01-0641 (2005).

[20] B. Thurow, N. Jiang, W. Lempert, Measurement Science and Technology, 24 (2013) 012002.
[21] J.B. Michael, P. Venkateswaran, J.D. Miller, M.N. Slipchenko, J.R. Gord, S. Roy, T.R. Meyer, Opt. Lett., 39 (2014) 739-742.
[22] J.D. Miller, S.J. Peltier, M.N. Slipchenko, J.G. Mance, T.M. Ombrello, J.R. Gord, C.D. Carter, Proceedings of the Combustion Institute, 36 (2017) 2865-2872.
[23] M.N. Slipchenko, J.D. Miller, S. Roy, J.R. Gord, S.A. Danczyk, T.R. Meyer, Opt. Lett., 37 (2012) 1346-1348.
[24] Z. Wang, P. Stamatoglou, Z. Li, M. Aldén, M. Richter, Opt. Express, 25 (2017) 30214-30228.
[25] M.O. Lundgren, Z. Wang, A. Matamis, O. Andersson, M. Richter, M. Tuner, M. Alden, A. Arne, SAE International, 2017-01-0753, (2017).
[26] R. Payri, J.M. García, F.J. Salvador, J. Gimeno, Fuel, 84 (2005) 551-561.
[27] M.P.B. Musculus, K. Kattke, SAE International Journal of Engines, 2 (2009) 1170-1193.
[28] G. Särner, M. Richter, M. Aldén, L. Hildingsson, A. Hultqvist, B. Johansson, SAE International, 2005-01-3869, (2005).
[29] Volvo, https://www.dieselnet.com/news/2016/09volvo.php, (2016).

Figure captions

Figure 1. Field of view for fuel tracer and CH_2O PLIF imaging.

Figure 2. Fuel distribution before SOC at 1.8 CAD ATDC together with the outer boundary of fuel distribution at 6.4 CAD BTDC (green lines) in one cycle.

Figure 3. Fuel distribution after SOC together with envelop of autoignition zones. Red, green and yellow lines indicate envelop of flame luminosity at 0.3 CAD, 0.1 CAD before the PLIF image and 0.1 CAD after the PLIF image, respectively.

Figure 4. Fuel distribution for combusting case (green) and non-combusting case (red).

Figure 5. CH2O distribution before SOC at 1.9 CAD ATDC together with the outer boundary of CH2O distribution at 6.1 CAD BTDC (green lines) in one cycle.

Figure 6. (a). Probability density function (PDF) of the CH2O distribution during the injection from 8.9 CAD BTDC to 5.7 CAD BTDC; (b). PDF of the CH2O distribution before SOC from 2.0 CAD BTDC to 1.8 CAD ATDC.

Figure 7. CH2O distribution after SOC together with envelop (curve notation, see Fig.4) of autoignition zones.

Figure 8. CH2O distribution during sequential autoignition events with envelop (curve notation, see Fig.4) of the autoignition positions.

Figure 9. CH_2O distribution for combusting case (green) and non-combusting case (red).

Tables

Table 1.
Operating conditions

Engine speed [RPM]	1200
Engine load (IMEPg) [bar]	7
Fuel pressure [bar]	1500
Intake temperature [˚C]	108
Intake pressure [bar]	2.1
Intake O_2 concentration [%]	16 (combusting)
Intake O_2 concentration [%]	< 8 (non-combusting)

Paper IX

Elsevier Editorial System(tm) for
Proceedings of The Combustion Institute
Manuscript Draft

Manuscript Number:

Title: Structure and burning velocity of turbulent premixed methane/air jet flames in thin-reaction zone and distributed reaction zone regimes

Article Type: 5. Turbulent Flames

Keywords: planar laser-induced fluorescence; distributed reaction zone regime; turbulent flame speed; flame structures

Corresponding Author: Professor Xue-Song Bai,

Corresponding Author's Institution: Lund University

First Author: Z. Wang

Order of Authors: Z. Wang; B. Zhou; S. Yu; C. Brackmann; Z. Li; M. Richter; M. Alden; Xue-Song Bai

Abstract: A series of turbulent premixed methane/air jet flames are studied using simultaneous planar laser diagnostic imaging of OH/CH/temperature and CH/OH/CH2O. The Karlovitz number of the flames ranges from 25 to 1500, and the turbulence intensity ranges from 16 to 200. These flames can be classified as highly turbulent flames in the thin reactions zone (TRZ) regime and distributed reaction zone (DRZ) regime. The aims of this study are to investigate the structural change of the preheat zone and the reaction zone as the Karlovitz number and turbulent intensity increase, to study the impact of the structural change of the flame on the propagation speed of the flame, and to evaluate the turbulent burning velocity computed in different layers in the preheat zone and reaction zone. It is found that for all investigated flames the preheat zone characterized with planar laser-induced fluorescence (PLIF) of CH2O is broadened by turbulent eddies. The thickness of the preheat zone increases with the turbulent intensity and it can be on the order of integral length of turbulence at high Karlovitz numbers. The reaction zone characterized using the overlapping layer of OH and CH2O PLIF signals is not significantly broadened by turbulence eddies; however, CH radicals are found to be broadened significantly by turbulence. The turbulent burning velocity is shown to monotonically increase with turbulent intensity and Karlovitz number. The increase in turbulent burning velocity is mainly due to the enhanced turbulent heat and mass transfer in various layers of the flame, while the contribution of flame front wrinkling to the turbulent burning velocity is rather minor.

Structure and burning velocity of turbulent premixed methane/air jet flames in thin-reaction zone and distributed reaction zone regimes

Zhenkan Wang[1*], Bo Zhou[1], Senbin Yu[2], Christian Brackmann[1],
Zhongshan Li[1], Mattias Richter[1], Marcus Aldén[1], Xue-Song Bai[2]

[1]Division of Combustion Physics, Lund University, P.O. Box 11, S221 00 Lund, Sweden
[2]Division of Fluid Mechanics, Lund University, P.O. Box 11, S221 00 Lund, Sweden

Corresponding author:
Xue-Song Bai
Division of Fluid Mechanics, Lund University, P.O. Box 11, S221 00 Lund, Sweden
xue-song.bai@energy.lth.se

Colloquium: turbulent flames

Total word count (method 1): 3435 (main text)+ 385 (reference)+ 502(table)+ 45(equation)+1347 (figure) = 5714
Main text: 680 (Introduction) +845 (Experimental setup)+1639 (Results and discussions)+239 (Conclusion)+32 (Acknowledgement)=3435
References: (20 refs+2)*2.3*7.6=385
Table.1: (31 line+2)*7.6=502
Figure 1: (64.3+10)*2.2*2+22=349
Figure 2: (44+10)*2.2*2+52=290
Figure 3: (47+10)*2.2+25=150
Figure 4: (51.3+10)*2.2+25=236
Figure 5: (52.4+10)*2.2+65=202
Figure 6: (73.6+10)*2.2+12=196
Equation 1: (1+2)*7.6*1=23
Equation 2: (1+2)*7.6*1=23

Color Reproduction: Agree to pay color reproduction charges.

Abstract

A series of turbulent premixed methane/air jet flames are studied using simultaneous planar laser diagnostic imaging of OH/CH/temperature and CH/OH/CH_2O. The Karlovitz number of the flames ranges from 25 to 1500, and the turbulence intensity ranges from 16 to 200. These flames can be classified as highly turbulent flames in the thin reactions zone (TRZ) regime and distributed reaction zone (DRZ) regime. The aims of this study are to investigate the structural change of the preheat zone and the reaction zone as the Karlovitz number and turbulent intensity increase, to study the impact of the structural change of the flame on the propagation speed of the flame, and to evaluate the turbulent burning velocity computed in different layers in the preheat zone and reaction zone. It is found that for all investigated flames the preheat zone characterized with planar laser-induced fluorescence (PLIF) of CH_2O is broadened by turbulent eddies. The thickness of the preheat zone increases with the turbulent intensity and it can be on the order of integral length of turbulence at high Karlovitz numbers. The reaction zone characterized using the overlapping layer of OH and CH_2O PLIF signals is not significantly broadened by turbulence eddies; however, CH radicals are found to be broadened significantly by turbulence. The turbulent burning velocity is shown to monotonically increase with turbulent intensity and Karlovitz number. The increase in turbulent burning velocity is mainly due to the enhanced turbulent heat and mass transfer in various layers of the flame, while the contribution of flame front wrinkling to the turbulent burning velocity is rather minor.

Keywords: planar laser-induced fluorescence; distributed reaction zone regime; turbulent flame speed; flame structures

1. Introduction

Turbulent flames in practical combustion devices are often highly turbulent, which, within the context of the regime diagram [1], typically falls into the thin reaction zone (TRZ) regime and the distributed reaction zone (DRZ) regime. In the TRZ regime, the small turbulence eddies can enter and consequently broaden the preheat zone of the flame while the reaction zone is not influenced and remains as a thin layer [2-4]. In contrast, flames in the DRZ regime are hypothetically characterized as reactions taking place volumetrically (i.e. distributed reactions) due to the small-eddy penetration into the reaction zone, a scenario being fundamentally different from the thin flamelet-like reaction zones in the TRZ regime. Due to the distributed reactions, the combustion processes in the DRZ regime may proceed with a relatively uniform temperature distribution and a reduced maximum temperature, which can be a merit for, e.g., NO_x reduction in practical combustion devices.

Experimental studies of distributed reactions in turbulent flames are relatively rare, which is partly due to the difficulties in realization of distributed reactions in laboratory flames and the limitations in diagnostic methods available. There is also no common consensus regarding experimental quantification of the reaction zones. The overlapping region of OH radicals and CH_2O, obtained from simultaneous planar laser induced fluorescence (PLIF) of OH and CH_2O, may be used to denote the heat release zone [5]. Alternatively, PLIF of HCO may be used to denote the reaction zone since HCO is the product of the OH and CH_2O reaction [3]. Driscoll [4] suggested that the distributed reaction zone regime might be characterized using PLIF of CH radicals. This is because CH radicals are short-lived, which prohibits it being transported an appreciable distance from where it is produced, and its presence in space should therefore be attributed to the formation reactions locally. Very recently, a number of experiments using PLIF of CH or HCO have been carried out for

high speed turbulent premixed jet flames [6-12]. In the experimental study of pilot flame stabilized methane/air jet flames, Zhou et al. [11] showed that with Karlovitz number (Ka) greater than 100, significant spread of CH-PLIF signals could be observed, where Ka is the ratio between the chemical time scale and the Kolmogorov time scale. While this critical Ka of CH broadening coincides very well with the hypothetical boundary of DRZ/TRZ regimes [1], it is however not always the case in other flames. In the experimental study of Wabel et al. [6-9] of methane/air jet flames with a large jet diameter and a lower jet velocity than that of Zhou et al. [10,11], no significant broadening of CH PLIF signal could be observed at high Ka numbers. Therefore, there is a need to perform further investigations under high Ka conditions.

Apart from the structural change of the reaction layers, the propagation of high Ka flames has caused the attention of many research groups. As stressed by Bradley [13], one important quantity for characterization of the propagation of turbulent premixed flames is the turbulent burning velocity (S_T). In the flamelet regimes, the Damköhler's hypothesis [14] suggests that S_T is proportional to the flame surface area due to wrinkling, which has been evidenced in both experiments [15] and direct numerical simulation (DNS) studies [16,17]. In the TRZ regime, S_T is however affected by both the increased wrinkling and the enhanced heat and mass diffusion in the broadened preheat zone. In the DRZ regime, in addition to the flame wrinkling and the enhanced heat and mass transfer in the preheat zone, the broadening of the reaction zone may also affect the turbulent burning velocity. At extremely high Ka, S_T may even decrease with increasing turbulent velocity, u' [1,13]. It is useful to correlate S_T with key turbulent parameters such as the turbulent intensity; however, the results have been controversial since S_T is rather sensitive to experiment devices and evaluation methods [4,13]. In this study, S_T under a large range of flame conditions is computed using different methods and

correlation of S_T with the structural changes of flames at TRZ and DRZ regimes is examined.

2. Experiment setup and apparatus

The experimental system employed is shown in Fig. 1a. In the present study, detailed flame structures were visualized using simultaneous laser-diagnostic imaging of temperature/CH/OH with an imaging size of ~23×23 mm^2 to allow for directly correlating the temperature with the reaction zone marker CH. Additionally, simultaneous measurements of OH and CH_2O were also performed with a larger imaging size of ~55×55 mm^2 to allow for analysis of global flame quantities. Snap-shot images of CH, OH, and CH_2O and temperature were acquired through PLIF and Rayleigh Scattering Thermometry (RST), respectively, following the excitation-detection strategies described in our previous work [10]. High imaging quality and signal fidelity for each measured scalar has been ensured [10,11]. For all scalars measured, the camera gates were set to less than 50 ns and proper optical filters (cf. [10] for details) were employed for background rejection. The signal-to-noise ratios (SNRs) were estimated to be better than 17 for CH-PLIF, 32 for OH-PLIF under stoichiometric flame conditions, and 24 for temperature at room temperature air. The imaging resolution is better than 70×70 μm^2 (for ~23×23 mm^2 imaging size) and the thickness of the combined laser sheet was measured to be 100 μm. In particular, special attention has been paid to the CH detection as CH is the key radical for determining distributed reactions; the CH LIF emission spectra were examined in both laminar and turbulent flames to ensure interference-free detection. Furthermore, additional supports for a high-quality and high-fidelity CH measurement as reported in our previous study [10] are as follows: (1) HCO-PLIF (another reaction zone marker [3]) exhibited similar distributed features to that of the CH-PLIF; (2) CH-PLIF images exhibit clearly spatial correlations as well as

(anti-) correlation of signal intensities at both large and small scales with other scalars (e.g. CH_2O and OH) that were measured simultaneously with CH using independent detection system.

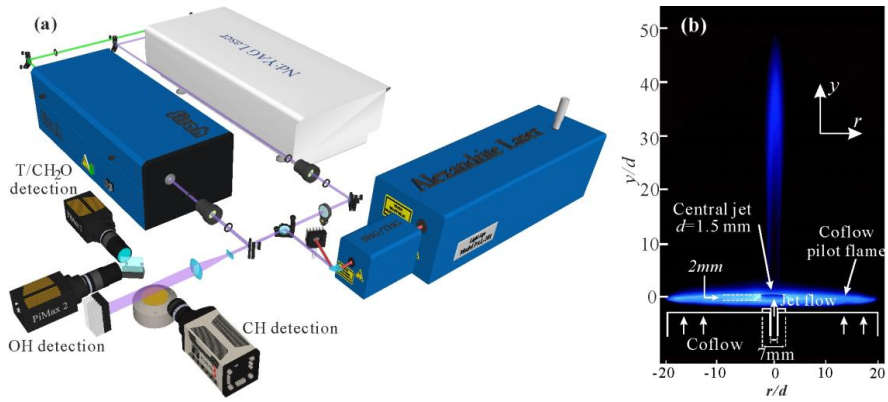

Figure 1. (a) Experimental setup for simultaneous T/CH/OH imaging measurements, and (b) schematic plot of the burner with photograph of a flame.

As shown in Fig. 1b, the burner consists of a porous-plug laminar flame burner (61 mm in diameter) and a central jet 1.5 mm in diameter (d). The jet is made of a stainless tube of thickness 2 mm and an outer diameter of 7 mm to prevent direct mixing between the jet and the coflow at the jet exit. A flat laminar CH_4/air flame with the exit flow velocity of 0.3 m/s at 300 K and equivalence ratio Φ=0.9 was stabilized on the porous-plug burner, providing a hot environment to sustain the central jet methane/air flames. The coflow condition was deliberately kept the same to ensure the same ambient environment for all jet flames studied. The jet inlet velocity (U_0) was varied systematically from 11 to 418 m/s and equivalence ratio, Φ, from 0.4 to 1, to cover a wide range of flames residing in both the laminar flame regime and the turbulent TRZ/DRZ regimes. The characteristic quantities of the investigated flames are summarized in Table 1. The flames were

referred to as Lund University Piloted Jet (LUPJ) premixed flames and labeled as LUPJα-β, where α and β represent the values of the Φ and U_0 of the flame, respectively.

The laminar flame speed (S_L) at different Φ given in Table 1 was determined experimentally using the relation $S_L=U_0\times\sin\theta$, where θ is the half angle of the flame cone determined from the inner boundary of the OH-PLIF field of a laminar flame at a jet velocity of 11 m/s. At this speed, the OH/CH2O/CH layers are smooth and of perfectly conical shape. The difference of using the OH, CH2O or CH layer to determine θ is small since the CH and CH2O layers are thin and coincide with the inner boundary of the OH layer [11]. The laminar flame thickness δ_L is defined as $\delta_L = \frac{T_p - T_u}{|\nabla T|_{max}}$ where the temperature of products (T_p) and unburnt reactants (T_u) and the maximum temperature gradient $|\nabla T|_{max}$ were measured using RST in the corresponding laminar flames. The value of S_L for the stoichiometric laminar flame (LUPJ10-11) determined from experiment is about 10% higher than the value reported in the literature. This is due to the back-support from the pilot flame. Note that the laminar flame Φ=0.4 is below the lean flammability limit while with the back-support of the pilot flame the value of S_L for Φ=0.4 is 21.4 cm/s. The use of experimentally determined S_L and δ_L is to enable consistently scaling the analysis of the turbulent statistical quantities for all range of Φ and to account for the effects of the pilot flame and burner configuration [11].

For the studied turbulent flames listed in Table 1, the characteristic integral length scale (l_0) and the turbulent intensity (u') were determined at axial location y/d=30 from our previous flow field measurements [11] which showed that both l_0 and u' have rather minor dependence on Φ. Following the formulations of Peters [1] as given in the footnotes of Table 1, the jet/turbulent Reynolds number (Re_{jet}/Re_t), the Kolmogorov length scale (η) and the Karlovitz number (Ka) for the investigated flames were estimated. The heights (H) of the studied LUPJ turbulent flames were determined from

the isosurface of averaged binarized OH images.

Table 1.

Experimental cases and key parameters. The laminar flame speed (S_L) and thermal thickness (δ_L) are determined based on the measurement on LUPJ flames at jet velocity of 11 m/s [11]. [a)] Jet Reynolds number, $Re_{jet}=U_0 d/\nu$ (ν is the kinematic viscosity at 298 K); [b)] Turbulent Reynolds number, $Re_t=(u' l_0)/(S_L \delta_L)$; [c)] Kolmogorov length scale, $\eta=l_0 Re_t^{-3/4}$; [d)] Karlovitz number: $Ka=(u'/S_L)^{3/2}\times(\delta_L/l_0)^{1/2}$.

Flame cases	Φ	S_L (cm/s)	δ_L (mm)	U_0 (m/s)	Re_{jet} [a]	Re_t [b]	l_0 (mm)	η [c] (μm)	u'/S_L	l_0/δ_L	Ka [d]
LUPJ10-66	1.0	42.5	0.48	66	6306	95	2.9	96	16	6.0	25
LUPJ07-66	0.7	33.2	0.60			97		95	20	4.8	40
LUPJ06-66	0.6	31.5	0.62			99		93	21	4.7	44
LUPJ04-66	0.4	21.4	0.85			107		89	31	3.4	92
LUPJ10-110	1.0	42.5	0.48	110	10510	190		57	31	6.0	70
LUPJ07-110	0.7	33.2	0.60			195		56	40	4.8	113
LUPJ06-110	0.6	31.5	0.62			199		56	42	4.7	125
LUPJ04-110	0.4	21.4	0.85			214		53	62	3.4	261
LUPJ10-165	1.0	42.5	0.48	165	15764	238		49	39	6.0	98
LUPJ07-165	0.7	33.2	0.60			244		48	50	4.8	158
LUPJ06-165	0.6	31.5	0.62			248		47	52	4.7	174
LUPJ04-165	0.4	21.4	0.85			267		45	77	3.4	365
LUPJ10-220	1.0	42.5	0.48	220	21019	317		39	52	6.0	151
LUPJ07-220	0.7	33.2	0.60			325		38	66	4.8	244
LUPJ06-220	0.6	31.5	0.62			331		38	70	4.7	268
LUPJ04-220	0.4	21.4	0.85			356		36	103	3.4	561
LUPJ10-330	1.0	42.5	0.48	330	31529	476		26	78	6.0	277
LUPJ07-330	0.7	33.2	0.60			487		26	99	4.8	448
LUPJ06-330	0.6	31.5	0.62			496		26	105	4.7	496
LUPJ04-330	0.4	21.4	0.85			534		24	154	3.4	1031
LUPJ10-418	1.0	42.5	0.48	418	39936	603		22	98	6.0	394
LUPJ07-418	0.7	33.2	0.60			617		21	126	4.8	639
LUPJ06-418	0.6	31.5	0.62			629		21	133	4.7	707
LUPJ04-418	0.4	21.4	0.85			676		20	196	3.4	1470

3. Results and discussion

3.1 Flame structure

Figure 2 shows instantaneous multi-scalar images acquired in LUPJ flames of U_0=165 m/s for equivalence ratios Φ=1.0 and 0.6. For illustration, the CH and OH images were normalized by their maximal intensities. The broadened/distributed CH layer in both flames can clearly be observed. It can be seen that distributed CH appears more prominently in the low-temperature regions; however, there are regions where CH signals are found at high intensity along with high temperature and high OH signals, indicated by the windows marked with the dashed boxes. The arrows in Fig. 2 mark regions where both the CH and T are low.

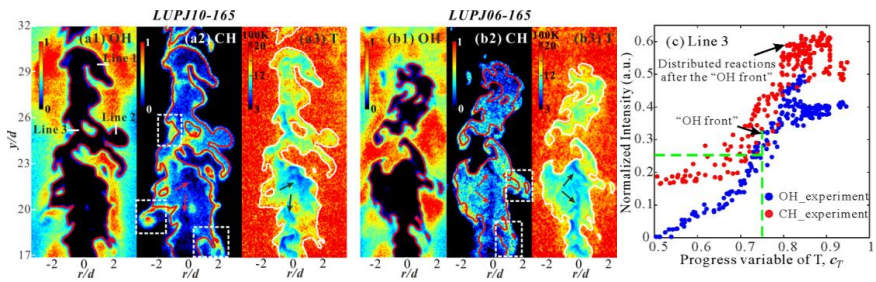

Figure 2. Simultaneous T/CH/OH image for the flames (a1-a3) LUPJ10-165 and (b1-b3) LUPJ06-165, and (c) intensities of OH- and CH-PLIF and normalized temperature along line-3 indicated in (a1). The iso-surface of 25% of OH PLIF intensity was superimposed onto the images. Dashed boxes highlight the presence of CH signals at high-temperature regions.

DNS studies [18,19] indicated that distributed reactions in high Ka flames are facilitated by the turbulent transport of radicals, e.g., H and OH, from the high-temperature region to the low-temperature region where radical recombination reactions can take place. As seen in Fig. 2,

although regions of high OH signals are frequently associated with high temperatures, there are OH signals in low-temperature regions. Note that in Fig.2 OH intensity lower than 25% of its maximum (as separated by the red iso-lines) is not visible due to the choice of color scale. Fig. 2c shows the normalized OH and CH PLIF intensities along line-3 in Fig.2a, as a function of the local normalized temperature $c_T=\frac{T-T_u}{T_p-T_u}$. T_p is set to the measured mean temperature of the coflow flame (1850K) and T_u =300K. It is shown that both OH and CH signals can appear simultaneously over a wide range of c_T values ($0.5<c_T<0.9$). The intensities of both OH and CH increase with temperature.

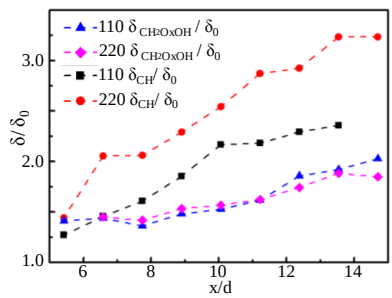

Figure 3. Mean thickness of CH layer and the overlapping layer of OH and CH_2O along the flame height for two flames, LUPJ10-110 and LUPJ10-220.

The broadening of CH layers can be compared with the layer of the “heat release marker”, i.e., the overlapping region of OH-PLIF and CH_2O-PLIF. Figure 3 shows the statistical mean thickness of the CH layer and the overlapping region of OH and CH_2O along the flame height for two LUPJ10 flame cases. The mean thickness of these layers is computed at a given flame height for each PLIF image and then ensemble-averaged using about 300 images. The thickness of the layers has been normalized with the corresponding thickness of the laminar flame of U_0=11 m/s. The thickness of the CH layer increases with flame height as well as with U_0 and Ka. Within the range of flame height

shown in the figure, the CH layer of the LUPJ10-220 flame is broadened to about 3 times of that of the laminar flame. On the contrary, the broadening of the overlapping layer of OH and CH_2O is not sensitive to U_0 and Ka, and the mean thickness of this 'heat release' layer is still considerably thinner than the CH layer.

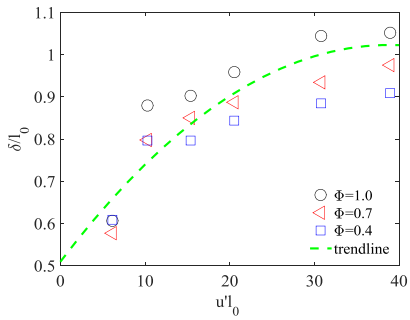

Figure 4. Thickness of the CH_2O layer at $\frac{x}{d} = 10$ for the flames listed in Table 1. l_0 is the integral length, determined from the experiments [11].

The CH_2O layer may be used as the preheat zone marker [20]. Figure 4 shows that the statistical mean thickness of the CH_2O layer at $\frac{x}{d} = 10$ increases with U_0 and Ka. The mean thickness is computed in a similar way as that of CH layer or the overlapping layer of OH and CH_2O. All flames show a significant broadening of the CH_2O layer in comparison with the laminar flames ($u' = 0$) at the corresponding equivalence ratio. The broadening increases along the flame height (for brevity the figure is not shown here). The increase of the mean thickness of the CH_2O layer with U_0 and Ka may be explained as follows: as the jet velocity increases, the turbulent eddy diffusivity ($u'l_0$) increases, which in turn leads to the increase of eddy transfer in the preheat zone. It is interesting to note that at high jet velocity, the broadening of the preheat zone saturates to the level of integral length. The

preheat zone appears not to be thicker than the integral eddies.

3.2 Turbulent burning velocity

Turbulent burning velocity can be defined in different ways, for example, a global consumption speed of the flame ($S_{T,c}$) can be defined as [15,6],

$$S_{T,c} = \dot{m}_{in}/(\rho_u \bar{A}_f), \quad (1)$$

where $\dot{m}_{in}$ is the mass flow rate of the jet, ρ_u is the density of the unburned mixture, and $\bar{A}_f$ is the characteristic area of the mean flame front. Alternatively, an area-averaged local displacement speed on a given surface of the mean flame can be defined as,

$$S_{T,d} = \int s_d dA \,/\bar{A}_f, \quad (2)$$

where s_d is the local displacement speed on the given surface and $\bar{A}_f$ is the total area of the surface. Integration of Eq. (2) is done for the entire surface. For a statistical stationary flame the local displacement speed on a surface of the mean flame is equal to the local mean flow velocity normal to surface, v_n, owing to the mass conservation law. It can be shown that $S_{T,d} = \frac{\int s_d dA}{\bar{A}_f} = \frac{\rho \int v_n dA}{\rho \bar{A}_f} = \dot{m}_{in}/(\rho \bar{A}_f) = S_{T,c}\theta$, where ρ is the mean density on the given surface and $\theta = \rho_u/\rho$ is the ratio of density of the unburned mixture to the density on the given surface, which is proportional to the ratio of the temperature on the surface to that of the unburned mixture. The calculation of $S_{T,d}$ requires information on the mean flow velocity on the flame surface and information on the mean flame surface position, whereas $S_{T,c}$ only requires the information on the mean flame surface position and the mass flow rate of the jet.

It is clear that $S_{T,d}$ and $S_{T,c}$ are equal if the mean flame surface in Eqs. (1) and (2) is defined in the preheat zone, where $\theta = \rho_u/\rho \sim 1$. In a one-dimensional unstretched laminar flame, the

laminar flame speed S_L is defined as the displacement speed in the beginning of the preheat zone. Following the same analogy, the turbulent burning velocity should also be defined at the beginning of the preheat zone. A convenient choice is to use the temperature field, i.e, small value of c_T (e.g. 0.1) to compute the mean flame surface area for Eq. (1). Equivalently, one can use the mean reaction progress variable defined based on the mean CH_2O field. Experimental data of $S_{T,c}$ reported in the literature are often based on the mean flame surface area defined at the OH layer [4]. For statistically planar flames, the mean surface area defined in different layers of the flame is the same; thus, $S_{T,c}$ determined using different layers is identical. For jet flames the situation is very different. In the TRZ and DRZ regimes the preheat zone is thickened by turbulence, in particular at the flame tip. This will make the mean flame surface area defined in the OH layer much larger than that defined in the CH_2O layer, which will result in an underestimated $S_{T,c}$.

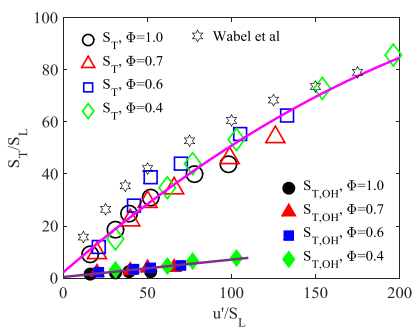

Figure 5. Turbulent burning velocity normalized with the corresponding laminar flame speed ($S_{T,c}/S_L$) as a function of turbulent intensity, u'/S_L, for a series of the turbulent flames listed in Table 1. Two mean flame surface areas are used, a CH_2O based reaction progress variable $c_{CH2O} = 0.5$, and a OH based reaction progress variable $c_{OH} = 0.2$. The data of Wabel et al. [6] are also shown for comparison.

Figure 5 shows the global consumption speed determined from both the CH_2O layer and the OH layer, for the various flames listed in Table 1. It is seen that $S_{T,c}$ defined using $c_{\mathrm{CH2O}} = 0.5$ is about 4-6 times of that determined using $c_{\mathrm{OH}} = 0.2$. The results are compared with the experimental data of Wabel et al. [6], obtained at high turbulent intensity, u'/S_L up to 160. $S_{T,c}$ reported by Wabel et al. [6] was determined using Eq. (1) with the mean area defined at $c_{\mathrm{OH}} = 0.2$ and $c_{\mathrm{OH}} = 0.5$. They reported a difference of $S_{T,c}$ computed using the two iso-surfaces by a factor 2, indicating the relative lower sensitivity of $S_{T,c}$ to the definition of the mean surface area than the present flames. It is worth noting that the flame in Wabel et al. [6] is much shorter than the present flames and the jet has a much larger diameter, about 10 times of that of the current flames. This makes the area defined in different layers of the flames of Wabel et al. [6] less sensitive to the definition of the mean flame surface.

The turbulent burning velocity in the present series of flames determined using $c_{\mathrm{CH2O}} = 0.5$ is consistent with the data of Wabel et al. [6]. It is expected that $S_{T,c}$ of Wabel et al. would be higher than the present data at a given u'/S_L, if it were evaluated at $c_{\mathrm{CH2O}} = 0.5$ (the same as the present flames). This difference is expectable and it is attributed to the difference of jet diameter and integral length scales. Despite the differences, the present data shows a similar trend of the turbulent burning velocity in the TRZ and DRZ regimes as that of Wabel et al. [6]; $S_{T,c}$ increases monotonically with the turbulent intensity, first linearly until u'/S_L~40, and then it increases at a slower rate, which is known as the bending of turbulent burning velocity at high turbulent intensities [1]. Similar to the results of Wabel et al. [6], there is no 'flatten-out' tendency of $S_{T,c}$ within the present range of turbulence intensity. $S_{T,c}$ from all four equivalence ratios and jet velocities falls nicely into a

non-dimensional profile of $S_{T,c}/S_L$ as a function of u'/S_L.

In the laminar flamelet regime the increase of $S_{T,c}/S_L$ is proportional to the wrinkle ratio of area (a ratio of the wrinkled turbulent flame surface area to that of the mean flame surface area) [14]. Figure 6 shows the winkled area ratio determined in the CH_2O and OH layers. Since the PLIF imaging is limited to two-dimensional (2D) information, only 2D wrinkle ratio is computed, which is known to be smaller than the 3D wrinkle ratio. The wrinkle ratio in both the OH layer and the CH_2O layer is about 1.3 – 1.5, which is significantly smaller than the value of $S_{T,c}/S_L$. Similar results are reported in the work of Wabel et al. [6] at high Ka conditions.

One may speculate that low wrinkle ratio is due to the low PLIF resolution. In Fig. 6 the wrinkle ratios obtained with two different OH-PLIF image resolutions are compared. Clearly, with higher resolution the wrinkle ratio is larger. Nevertheless, the wrinkle ratio is by far smaller than the value of $S_{T,c}/S_L$, and the winkle ratio flattens out at high u'/S_L, which is different from the profile of $S_{T,c}/S_L$. The implication of the small wrinkle ratio in comparison to $S_{T,c}/S_L$ is that the propagation of the present high Ka flames is not by area wrinkling, rather it is attributed to the turbulent heat and mass transfer in the broadened preheat and reaction zones.

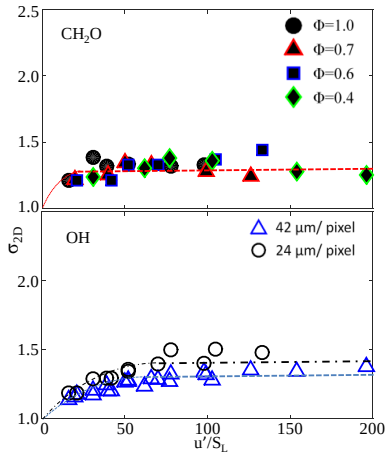

Figure 6. Two-dimensional flame surface wrinkle ratio computed from $c_{\mathrm{CH2O}} = 0.5$ and $c_{\mathrm{OH}} = 0.2$.

4. Concluding remarks

A series of turbulent methane/air premixed jet flames with different jet speeds and equivalence ratios were studied using simultaneous OH/CH/T and CH/OH/CH_2O planar imaging measurements. Simultaneous OH/CH/T measurements, reported for the first time, directly correlate the temperature with CH-PLIF and OH-PLIF. It was found that CH and OH PLIF overlap in a wide range of temperature at high Karlovitz number conditions. The reaction zone characterized using CH-PLIF signal shows increased broadening with increasing jet velocity or Karlovitz number. The heat release zone characterized by the overlapping region of OH-PLIF and CH_2O-PLIF is however not as significantly broadened as the CH layer. The broadening of this heat release rate is not sensitive to the jet velocity. The preheat zone characterized with the CH_2O-PLIF signal shows increased broadening with increasing turbulent eddy viscosity ($u'l_0$). The broadening of this layer at high Ka flames is on the order of the turbulent integral length scale. The turbulent burning velocity is shown

to increase monotonically with the turbulence intensity (u'/S_L). At very high turbulent intensity, $u'/S_L \sim 200$, the turbulent burning velocity is about 60 times of that of the corresponding laminar flame. In the thin-reaction zone and distributed reaction zone regimes, the governing mechanism of enhanced flame propagation is attributed to the turbulent eddy transfer of heat and mass in the preheat zone and reaction zone, while the contribution of flame front wrinkling to the turbulent burning velocity is rather minor.

Acknowledgements

The authors gratefully acknowledge financial support from VR (Swedish Research Council) and the Swedish Energy Agency via the CECOST programme and the European Research Council Advanced Grant through the TUCLA program.

References

[1] N. Peters, Turbulent Combustion, Cambridge University Press, Cambridge, 2000.

[2] L.P.H. de Goey, T. Plessing, R.T.E. Hermanns, N. Peters, Proc. Combust. Inst. 30 (2005) 859-866.

[3] B. Zhou, J. Kiefer, J. Zetterberg, Z.S. Li, M. Alden, Combust. Flame 161 (2014) 1566-1574.

[4] J.F. Driscoll, Prog. Energy Combust. Sci. 34 (2008) 91-134.

[5] P.H. Paul, H.N. Najm, Symp. (Int.) Combust. 27 (1998) 43-50.

[6] T. M. Wabel, A. W. Skiba, J. F. Driscoll, Proc. Combust. Inst. 36 (2017) 1801-1808.

[7] T. M. Wabel, A. W. Skiba, J. E. Temme, J. F. Driscoll, Proc. Combust. Inst. 36 (2017) 1809-1816.

[8] A. W. Skiba, T. M. Wabel, C. D. Cater, S. D. Hammack, J. E. Temme, L. Tonghun, J. F. Driscoll, Proc. Combust. Inst. 36 (2017) 4593-4601

[9] T. M. Wabel, A. W. Skiba, J. F. Driscoll, Combust. Flame 188 (2017) 13-27.

[10] B. Zhou, C. Brackmann, Z.S. Li, M. Alden, X.-S. Bai, Proc. Combust. Inst. 35 (2014) 1409-1416.

[11] B. Zhou, C. Brackmann, Q. Li, Z. Wang, P. Petersoon, Z. Li, M. Alden, X.-S. Bai, Combust. Flame 162 (2015) 2937-2953.

[12] B. Zhou, Q. Li, Y. He, P. Pertersson, ZS.Li, M. Alden, X.S. Bai, Combust. Flame 162 (2015) 2954-2958.

[13] D. Bradley, Proceedings of the Combustion Institute 24 (1992).

[14] G. Damkohler, Z Elktrochem Angew P 46 (1940) 601-626.

[15] S.A. Filatyev, J.F. Driscoll, C.D. Carter, J.M. Donbar, Combust. Flame 141 (2005) 1-21.

[16] A.Y. Poludnenko, E.S. Oran, Combust. Flame 158 (2011) 301-326.

[17] J.B. Bell, M.S. Day, J.F. Grcar, Proc. Combust. Inst. 29 (2002) 1987-1993.

[18] A.J. Aspden, M.S. Day, J.B. Bell, Proc. Combust. Inst. 35 (2014) 1321-1329.

[19] H. Carlsson, R.X. Yu, X.S. Bai, Int. J. Hydrogen Energy 39 (2014) 20216-20232.

[20] Z.S. Li, B. Li, Z.W. Sun, et al., Combust. Flame 157 (2010) 1087–1096.

Figure captions

Figure 1. (a) Experimental setup for simultaneous T/CH/OH imaging measurements, and (b) schematic plot of the burner with photograph of a flame.

Figure 2. Simultaneous T/CH/OH image for the flames (a1-a3) LUPJ10-165 and (b1-b3) LUPJ06-165, and (c) intensities of OH- and CH-PLIF and normalized temperature along line-3 indicated in (a1). The iso-surface of 25% of OH PLIF intensity was superimposed onto the images. Dashed boxes highlight the presence of CH signals at high-temperature regions.

Figure 3. Mean thickness of CH layer and the overlapping layer of OH and CH_2O along the flame height for two flames, LUPJ10-110 and LUPJ10-220.

Figure 4. Thickness of the CH_2O layer at $\frac{x}{d} = 10$ for the flames listed in Table 1. l_0 is the integral length, determined from the experiments [11].

Figure 5. Turbulent burning velocity normalized with the corresponding laminar flame speed ($S_{T,c}/S_L$) as a function of turbulent intensity, u'/S_L, for a series of the turbulent flames listed in Table 1. Two mean flame surface areas are used, a CH_2O based reaction progress variable $c_{CH2O} = 0.5$, and a OH based reaction progress variable $c_{OH} = 0.2$. The data of Wabel et al. [6] are also shown for comparison.

Figure 6. Two-dimensional flame surface wrinkle ratio computed from $c_{CH2O} = 0.5$ and $c_{OH} = 0.2$.

Table

Table 1.

Experimental cases and key parameters. The laminar flame speed (S_L) and thermal thickness (δ_L) are determined based on the measurement on LUPJ flames at jet velocity of 11 m/s [11]. [a)] Jet Reynolds number, $Re_{jet}=U_0 d/\nu$ (ν is the kinematic viscosity at 298 K); [b)] Turbulent Reynolds number, $Re_t=(u'l_0)/(S_L\delta_L)$; [c)] Kolmogorov length scale, $\eta=l_0 Re_t^{-3/4}$; [d)] Karlovitz number: $Ka=(u'/S_L)^{3/2}\times(\delta_L/l_0)^{1/2}$.

Flame cases	Φ	S_L (cm/s)	δ_L (mm)	U_0 (m/s)	Re_{jet} [a]	Re_t [b]	l_0 (mm)	η [c] (μm)	u'/S_L	l_0/δ_L	Ka [d]
LUPJ10-66	1.0	42.5	0.48	66	6306	95	2.9	96	16	6.0	25
LUPJ07-66	0.7	33.2	0.60			97		95	20	4.8	40
LUPJ06-66	0.6	31.5	0.62			99		93	21	4.7	44
LUPJ04-66	0.4	21.4	0.85			107		89	31	3.4	92
LUPJ10-110	1.0	42.5	0.48	110	10510	190		57	31	6.0	70
LUPJ07-110	0.7	33.2	0.60			195		56	40	4.8	113
LUPJ06-110	0.6	31.5	0.62			199		56	42	4.7	125
LUPJ04-110	0.4	21.4	0.85			214		53	62	3.4	261
LUPJ10-165	1.0	42.5	0.48	165	15764	238		49	39	6.0	98
LUPJ07-165	0.7	33.2	0.60			244		48	50	4.8	158
LUPJ06-165	0.6	31.5	0.62			248		47	52	4.7	174
LUPJ04-165	0.4	21.4	0.85			267		45	77	3.4	365
LUPJ10-220	1.0	42.5	0.48	220	21019	317		39	52	6.0	151
LUPJ07-220	0.7	33.2	0.60			325		38	66	4.8	244
LUPJ06-220	0.6	31.5	0.62			331		38	70	4.7	268
LUPJ04-220	0.4	21.4	0.85			356		36	103	3.4	561
LUPJ10-330	1.0	42.5	0.48	330	31529	476		26	78	6.0	277
LUPJ07-330	0.7	33.2	0.60			487		26	99	4.8	448
LUPJ06-330	0.6	31.5	0.62			496		26	105	4.7	496
LUPJ04-330	0.4	21.4	0.85			534		24	154	3.4	1031
LUPJ10-418	1.0	42.5	0.48	418	39936	603		22	98	6.0	394
LUPJ07-418	0.7	33.2	0.60			617		21	126	4.8	639
LUPJ06-418	0.6	31.5	0.62			629		21	133	4.7	707
LUPJ04-418	0.4	21.4	0.85			676		20	196	3.4	1470

Paper X

Elsevier Editorial System(tm) for Fuel
Manuscript Draft

Manuscript Number: JFUE-D-18-00143

Title: Investigation of OH and CH2O distributions at ultra-high repetition rates by planar laser induced fluorescence imaging in highly turbulent jet flames

Article Type: VSI: Clean Air 2017

Keywords: Burst-mode laser; Ultra-high-speed diagnostics; Turbulent jet flame; Planar laser induced fluorescence; OH; CH2O

Corresponding Author: Mr. Zhenkan Wang, M.D.

Corresponding Author's Institution: Combustion Physics

First Author: Zhenkan Wang, M.D.

Order of Authors: Zhenkan Wang, M.D.; Panagiota Stamatoglou, M.D.; Bo Zhou, Ph.D.; Marcus Aldén, Ph.D.; Xuesong Bai, Ph.D.; Mattias Richter, Ph.D.

Abstract: For better understanding of the transient behavior of the eddy/flame interaction in highly turbulent premixed flames, measurement techniques with sufficient temporal resolution are required. Using a burst-mode laser pumped optical parametric oscillator system, the present work demonstrated an ultra-high-speed diagnostic, for the first time, capable of visualizing hydroxyl radicals (OH) and formaldehyde (CH2O) distributions in a highly turbulent flame at repetition rates up to 140 kHz (i.e. with a temporal resolution of 7.1 μs) to access the Kolmogorov time scales of flames in the distributed/broken reaction zone regime (Ka ≥100). More than 100 consecutive images were recorded in the present work for OH Planar laser induced fluorescence (PLIF) measurement at 100 kHz. Systematic temporal and spatial evolution of the flame structure is clearly resolved over long sequences, e.g. 1.2 ms for OH PLIF and 10 ms for CH2O PLIF respectively. The Kolmogorov time scale for all the cases at x/d=10 and x/d=30 are estimated with the minimum Kolmogorov time scale of 7.5 μs, indicating that nearly all time-scales of the flow are resolved with the present experimental setup. The axial velocity of the CH2O structure at its outer layer at different x/d positions, UCH2O, is obtained. The velocity UCH2O is compared with the LDV results, which shows a good agreement. By comparing UCH2O with the local axial velocity, different mechanisms responsible for the large-scale wrinkle structures in the reaction zone and the propagation of CH2O structure along the flame height are discussed. Frequency spectrum, autocorrelation function and power spectral density based on the CH2O radial fluctuation are discussed. Quantitative analysis of the ultra-high-speed diagnostics data further augments the understanding of turbulent combustion down to Kolmogorov scale experimentally.

Suggested Reviewers: James Gord Dr.
Researcher, Air Force Research Laboratory, Aerospace Systems Directorate
james.gord@us.af.mil
Dr. James Gord is very familiar with the topic and burst-mode laser systems.

Investigation of OH and CH_2O distributions at ultra-high repetition rates by planar laser induced fluorescence imaging in highly turbulent jet flames

Zhenkan Wang*, Panagiota Stamatoglou*, Bo Zhou, Marcus Aldén*, Xuesong Bai*** and Mattias Richter***

* Department of Physics, Combustion Physics, Lund University, Box 118, Sweden

** Combustion Research Facility, Sandia National Laboratories, Livermore, CA 94551, USA

*** Department of Energy Sciences, Lund University, Box 118, Sweden

E-mail: zhenkan.wang@forbrf.lth.se

Abstract

For better understanding of the transient behavior of the eddy/flame interaction in highly turbulent premixed flames, measurement techniques with sufficient temporal resolution are required. Using a burst-mode laser pumped optical parametric oscillator system, the present work demonstrated an ultra-high-speed diagnostic, for the first time, capable of visualizing hydroxyl radicals (OH) and formaldehyde (CH_2O) distributions in a highly turbulent flame at repetition rates up to 140 kHz (*i.e.* with a temporal resolution of 7.1 μs) to access the Kolmogorov time scales of flames in the distributed/broken reaction zone regime (Ka ≥100). More than 100 consecutive images were recorded in the present work for OH Planar laser induced fluorescence (PLIF) measurement at 100 kHz. Systematic temporal and spatial evolution of the flame structure is clearly resolved over long sequences, *e.g.* 1.2 ms for OH PLIF and 10 ms for CH_2O PLIF respectively. The Kolmogorov time scale for all the cases at x/d=10 and x/d=30 are estimated with the minimum Kolmogorov time scale of 7.5 μs, indicating that nearly all time-scales of the flow are resolved with the present experimental setup. The axial velocity of the CH_2O structure at its outer layer at different x/d positions, U_{CH2O}, is obtained. The velocity U_{CH2O} is compared with the LDV results, which shows a good agreement. By comparing U_{CH2O} with the local axial velocity, different mechanisms responsible for the large-scale wrinkle structures in the reaction zone and the propagation of CH_2O structure along the flame height are discussed. Frequency spectrum, autocorrelation function and power spectral density based on the CH_2O radial fluctuation are discussed. Quantitative analysis of the ultra-high-speed diagnostics data further augments the understanding of turbulent combustion down to Kolmogorov scale experimentally.

Key words: *Burst-mode laser; Ultra-high-speed diagnostics; Turbulent jet flame; Planar laser induced fluorescence; OH; CH_2O*

1. Introduction

Recent advance of high speed diagnostic techniques allows measurements of flame structures with sufficient spatiotemporal resolution, which is highly desirable for understanding the flame dynamics *e.g.* the interaction between the flames and eddies at various length and time scales.

As one of the high speed diagnostic methods, Nd:YAG clusters were developed for producing bursts with short pulse separation while maintaining pulse energies comparative to conventional 10 Hz systems. This makes them be capable of resolving very small time scales down to tens of microsecond levels [1-3]. However, the architecture of complete parallel systems in the YAG clusters implies that they can perform at ultra-high repetition rates while being limited by the number of pulses that are required to track the flow temporal evolution. In addition, Hult *et al.* reported that the beam profile of the laser cluster system degrades as the pulse separation time decreases [4].

As another alternative technique for high speed diagnostic, the burst-mode laser system allows for measurements of high temporal resolution with a prolonged sequence [5]. The first burst-mode laser system was developed by Lempert *et al.* in 1996 [6], and the system development was described by Thurow et al. [5]. More recently, Slipchenko *et al.* have developed a burst-mode laser system that is able to create a series of pulses in a short time period, *e.g.* 10 ms. Planar Laser Induced Fluorescence (PLIF) measurements of formaldehyde (CH_2O) have been demonstrated using such a system in a lifted CH_4-air diffusion flame at 20 kHz [7]. Later on, Michael *et al.* improved the system to conduct CH_2O PLIF measurements in a lifted jet diffusion flame at 100 kHz [8] followed by the work of Miller *et al.* who used CH_2O PLIF imaging to capture the transient features of ignition in scramjet pilot cavities [9]. CH_2O PLIF imaging provides the spatial information on pre-heat zone of a premixed flame [10]. In addition to CH_2O imaging, quantitative scalars such as temperature measured by Rayleigh scattering [11] and coherent anti-Stokes Raman scattering (CARS) spectroscopy [12], and velocity field acquired

using particle image velocimetry (PIV) [13,14] in turbulent flames have been realized at 100 kHz with burst-mode laser systems.

OH radical is an important species in combustion chemistry. The sharp OH gradient has been taken as a reliable marker of the flame front. However, excitation of OH cannot be accessed directly from the Nd:YAG laser. The first ultra-high-speed (≥ 50 kHz) OH measurement was reported by Miller *et al.* in a Mach 1 hydrogen–air diffusion flame to track localized extinction events [15]. An optical parametric oscillator (OPO) pumped by 532 nm output of the burst Nd:YAG laser system was used to access the OH $P_2(10)$ transition of the (0,0) vibrational band at 313 nm. The detection of OH LIF signals at the same excitation wavelength limited its application to any practical combustion system where surface scattering can dominantly prevail.

A common alternative excitation scheme for OH LIF is to probe the (1,0) vibrational transition, at approximately 283 nm. The red-shifted fluorescence, at 308 nm, can be spectrally separated from the spurious laser radiation using a spectral filter. A diode-pumped solid-state (DPSS) Nd:YAG laser combined with a dye laser has been demonstrated for ultra-high-speed OH PLIF measurement in a Henchen burner and a DC transient-arc plasmatron at 50 kHz [16]. Besides the DPSS Nd:YAG laser and dye laser system, Wang *et al.* employed a burst-mode laser pumped OPO system, which is operated at 50 kHz, for the excitation of OH at 284 nm in turbulent flames in the thin reaction zone regime with the Karlovitz number (Ka) of 25-70 [17]. To sufficiently resolve the dynamics of small-scale turbulence in flames with even higher turbulence intensities, *i.e.* Ka>=100 in distributed/broken reaction zone regime, measurements with even higher repetition rate are required.

This work aims at measuring instantaneous hydroxyl radicals and formaldehyde distributions at ultra-high repetition rates up to 140 kHz such that the Kolmogorov time scale in highly turbulent flames can be properly resolved. In addition, flame spatiotemporal evolution is studied by longer consecutive images than that of Sjöholm and Li *et al.* [18,19] with a maximum of 8 images obtained, and that of Miller *et al.* who presented 28 pulses [15]. This unique diagnostic feature of the present work allows for quantitative analysis of the flame spatiotemporal dynamics which is crucial for understanding of turbulent combustion but poorly available in literature.

2. Experimental setup

Figures 1 and 2 illustrate the experimental setup for CH_2O and OH PLIF imaging in a premixed turbulent jet flame, respectively. A hybrid porous-plug/jet type burner, Lund University Piloted Jet (LUPJ) burner, with a 1.5 mm-diameter nozzle in the center was utilized for the creation of a jet flame in this study. The premixed methane/air jet flame was stabilized by a reacting co-flow above the porous sintered stainless steel plug burner that has a diameter of 61 mm. The reacting co-flow was generated from a premixed methane/air flat-flame at 0.9 equivalence ratio and 0.3 m/s flow speed. Eight mass flow controllers (Bronkhorst) were used in order to control the gas flow rate. They had been calibrated at 300 Kelvin with higher than 98.5% accuracy. More detailed description of the LUPJ burner can be found in Refs. [20-24].

Different jet velocity conditions were studied as shown in Table 1. In all studied flames the equivalence ratio of the jet flow was kept at 1.0. Table 2 and Table 3 list the turbulent Reynolds numbers, Karlovitz numbers, Kolmogorov length/time scales and integral time scales in the different jet flame cases. The method for computing these parameters is identical to that in Ref. [21].

The laser system used in the experiment is a state-of-the-art ultra-high-speed burst-mode laser (QuasiModo Spectral Energies, LLC), originally developed by Slipchenko *et al.* [7] and here employed with modifications. A detailed description about the laser system can be found in Ref. [17]; here only a brief discussion of the system is presented. The laser system is a hybrid-pumped burst-mode laser with diode-pumped amplifiers followed by flashlamp-pumped amplifiers. The pulse duration was set to 15 ns at full-width of half maximum (FWHM) of the pulse profile and the spectral bandwidth was below 0.03 cm^{-1} at 1064 nm.

2.1 CH_2O PLIF imaging

CH_2O can be excited in several rotational transitions at 355 nm [25]. A second harmonic generator and a third harmonic generator (KDP type) were utilized in order to produce radiation at 355 nm. The 355 nm beam was then formed into a laser sheet of 24 mm height by a cylindrical lens (f=-75 mm) in combination with a spherical lens (f=+300 mm) as shown in Fig. 1. The resulting pulse energy of the 355 nm laser at 140 kHz was about 25 mJ/pulse.

A high speed CMOS camera (Photron Fastcam SA-Z) was used in combination with a high speed intensifier (LaVision HS-IRO) for the CH_2O PLIF measurement. The exposure gate-width of the high speed intensifier was set to 40 ns. The intensifier was operated in the middle of its respective gain range. An objective lens (Nikkor f#1.2, f=50 mm) and a GG385 long-pass filter were mounted in front of the intensifier and camera while the resolution of the CMOS camera was reduced to 640 x 184 pixels at 140 kHz.

2.2 OH PLIF imaging

An OPO (GWU, PremiScan/ MB) was used for the generation of excitation radiation of OH radicals in the flame. The pump beam size was reduced to approximately 4 mm in diameter, using a telescope before the β-barium borate (BBO) crystal, in order to increase the power density and consequently the conversion efficiency of the OPO. The output wavelength of the OPO signal beam was measured by a wavemeter (GWU, LambdaScan) and the desired wavelength was selected before frequency doubling in a KDP type crystal as shown in Fig. 2. OH excitation scan is not presented here for brevity. More information can be found in Ref. [17].

After the OH excitation scan, laser radiation was tuned to 283.93 nm ($A^2\Sigma^+$-$X^2\Pi$, 1-0 transition) because of its high number density and limited dependence of the flame temperature in the 1500-2500 K range [26]. Furthermore, it is spectrally well separated from other transitions lines. The OH excited wavelength will be expressed as 284 nm instead of 283.93 nm below. The emission from the A-X (0, 0) transition was collected at around 308 nm, through a bandpass filter (λ_T=310±10 nm) and an UV lens (B. Halle lens, f#=2, f= 100 mm) mounted in front of a high speed intensifier (Lavision HS-IRO) and a CMOS camera (Photron Fastcam SA-Z).

A Pellin-Broca prism was used to separate 284 nm from 568 nm after the doubling crystal as shown in Fig. 2. A 20 mm high laser sheet was formed by a cylindrical lens (f=-40 mm) and a spherical lens (f=+200 mm). The resulting pulse energy of the 284 nm laser at 100 kHz was about 150 μJ/pulse, which is sufficient for obtaining good SNR in this application.

The resolution of the CMOS camera for OH PLIF measurement was set to 600 x 240 pixels at 100 kHz. The parameters of the optical setup and filters utilized for the cameras are depicted in Table 3.

3. Results and discussion

To demonstrate the applicability of the proposed diagnostics, a practical application of this ultra-high-speed imaging technique in a turbulent jet flame is described below. More than 100 consecutive images of OH PLIF in the turbulent flame are captured with 10 μs intervals between successive images. In addition, CH_2O PLIF images are obtained in the flame at 140 kHz data acquisition rates corresponding to 7.1 μs time interval between successive laser pulses. The burst duration for OH PLIF and CH_2O PLIF is about 1.2 ms and 10 ms, respectively.

Signal-to-noise ratio (SNR) is first determined. The SNR is calculated based on dividing the averaged value of signal by the standard deviation of the background noise from the region where laser radiation is present but there is no fluorescence signal. Figures 3 and 4 show the raw images of CH_2O and OH signals prior to post-processing and the signal profiles along a red line marked in the PLIF images. The resulting SNR for CH_2O and OH are calculated to be 25 and 30, respectively.

In the following post-processing, both OH and CH_2O images have been normalized by their maximum value. The number in the lower left corner of each sub-image represents the number of the frame in a consecutive sequence of images.

Figure 5 illustrates a sequence of CH_2O PLIF images taken in the LUPJ220 flame, with 7.1 μs temporal resolution. Only part of the whole consecutive images is displayed here for brevity. More images can be found in the appendix. The red lines mark the outer boundary of the CH_2O region. This boundary typically coincides with the inner boundary of the OH PLIF region; thus, it marks the location of the heat release layer in the reaction zone. It is clear that there are large and small-scale wrinkles in the heat release layer. The arrows shown in the figure indicate the temporal evolution of a large-scale wrinkle of the heat release layer. It can be seen that from image No. 149 to No. 153 the large-scale wrinkle structure is slightly moving downstream along the flame height. The jet velocity is about 200 m/s whereas the large-scale wrinkle structure moves about 2.5 mm within 5 frames (corresponding to 35.5 μs), which is at a speed about 70 m/s. Obviously this large-scale wrinkle structure does not follow the convective flow motion of the jet flame; rather it is likely a result of the large-scale flow vortex in the jet shear layer interacting with the flame. With the present ultra-high-speed diagnostics, the temporal evolution of the flame is clearly captured. Indeed, with the current temporal resolution of 7.1 μs, flame structures at this jet

speed (220 m/s) would propagate a distance of approximately 1.5 mm/frame and could be tracked in detail during the time sequence before exiting the 20 mm field of view. The Kolmogorov time scale for this case (220 m/s) at x/d=10 is about 10 μs, which means that nearly all time-scales of the flow can be tracked with the present experimental setup. It is seen that the life time of the large-scale wrinkle structure indicated by the arrows is about 50 ms (7 frames, from image No. 149 to 156), which is about half of the integral time scale at these flame heights.

Figure 6 presents a sequence of OH-PLIF images taken in the LUPJ220 flame. The red lines mark the inner boundary of the OH layer, which corresponds to the outer boundary of the CH_2O region and it therefore indicates also the heat release layer. The images were taken at HAB from 40 mm to 57 mm. The arrows mark a large-scale wrinkle structure of the heat release layer, which moves along the flame height downstream 6 mm within 5 frames (35.5 μs), which is at a speed about 140 m/s. This speed is on the same order of magnitude of the mean axial velocity at these flame heights; thus, the large-scale wrinkle structure is likely moving due to the convective transport of large unburned fuel pockets. The Kolmogorov time scale for LUPJ220 at x/d=30 is 7.5 μs. Thus, the present experimental setup can capture almost all turbulent time scales in the present flame. The life time of the wrinkle structure indicated by the arrows is much longer than that shown in Fig. 5, *i.e.*, the structure can be seen in all 10 frames (71 ms); the large-scale structure from the right side of the conical flame merges with the left side of the flame at frame 70. Table 4 summarizes the integral time scales and Kolmogorov time scales for all the cases.

By tracking the wrinkled CH_2O structure in the LUPJ66 flame at x/d=10 to 20, its displacement can be obtained as shown in Fig. 7. The horizontal axis shows the time and the vertical axis indicates the position of the structure. The wrinkled structure is extracted from CH_2O outer boundary and it moves towards downstream of the jet. More than 10 structures (as shown in different color in Fig. 7) at different time and different x/d positions are followed and used for the calculation of propagation speed, which is implied by the slope. The dash line represents the linear fitting of the structure positions with least square method as shown in the figure. Apparently, the slope of the fitted line is the velocity of the CH_2O outer layer. It can be seen that the slope closer to the burner surface is slightly steeper than the slope at downstream positions as expected.

Figure 8 presents normalized axial velocity of the CH_2O structure at their outer layer at different x/d positions. The velocity calculated from Fig. 7 is normalized by the inlet jet speed (U_0) and compared with the LDV results

[21]. As seen, the velocity at which the large wrinkle structures moves downstream is on the same order of magnitude of the mean flow velocity in the LUPJ66 flame. The speed is slightly lower at higher height above of the burner (x/d), which corresponds well with the decay of the axial velocity along the flame height.

A mean axial velocity of the large-scale wrinkle structures at the outer CH_2O boundary at x/d=10 – 20 has been calculated for all four flames studied. Figure 9 shows the comparison between the mean axial velocity of CH_2O structures (U_{CH2O}) and the local axial velocity (U) of the mean flow along the burner axis for all cases as shown in Table 1. The dashed line in Fig. 9 represents U. It can be seen that U_{CH2O} is similar to U for the LUPJ66 case and it becomes much smaller than U with increasing jet speed. The large-scale wrinkle structures in the reaction zone/distributed reaction zone regime can be due to different mechanisms: (a) large-scale coherent flow structure in the shear layer (generated due to Kelvin-Helmholtz instability) that wrinkles the flame front, (b) large scale unburned fuel or CO/CH_2O pockets that are separated by the flow from the main stream of the fuel/CO/CH_2O region, and (c) flame wrinkling by the large turbulence eddies (on the integral length scale). The second mechanism would give rise to a speed of the structure on the order of the local mean axial velocity, while wrinkled structures due to the first and the third mechanisms would travel downstream at a slower speed than that of the mean axial velocity. The life time of the large-scale structures from the different mechanisms is expected to be different, with the first and the second mechanism having the longest lifetime while the third mechanism having the shortest lifetime.

Figure 10 shows the radial position of CH_2O at its outer boundary at x/d=10 HAB versus time for LUPJ66 case. It is expected that the fluctuation of the CH_2O structure in the radial direction with time is due to all flow scales including large coherent structures, pocket motion of the unburned fuel pocket, and all turbulent time scales, from integral time to Kolmogorov time. When an eddy or a flow structure passes the CH_2O outer boundary at x/d=10, it will make the CH_2O outer boundary move towards the center of the burner or away from the center. The zero value of the vertical axis represents the mean position of the CH_2O outer layer. The positive value and negative value indicate a displacement distance between the instantaneous CH_2O radial position and its mean position. The largest fluctuation is about half of the integral scale, l_0, which is approximately 0.9d.

Figure 11 shows the frequency spectrum of the CH_2O radial fluctuation from fast Fourier transform (FFT) of the CH_2O instantaneous position in Fig. 10 at x/d=10 for all cases as shown in Table 1. The highest frequency is 70 kHz, which is half of the laser repetition rate, due to the Nyquist limit. Because the size of the eddies in the flame covers a large range, the spectrum has no dominant frequency. Namely, high amplitude happens at many different frequencies. For example, the amplitude keeps about 0.02 for LUPJ66 at frequency below 20 kHz. Interestingly, the amplitude is low at higher frequency for LUPJ66 while it becomes higher with increasing inlet jet speed. For instance, the amplitude in LUPJ220 at frequency beyond 30 kHz is obviously larger than that in LUPJ66. This corresponds well to the fact that at higher jet velocity the Kolmogorov eddies become smaller and the time scales become shorter. Thus, it is concluded that the high frequency fluctuation of the CH_2O outer layer is due to the small-scale turbulence eddies that distort the flame.

The autocorrelation function R(τ) at a given position x can be defined as,

$$R(\tau) = \frac{\frac{1}{N}\sum_{i=1}^{N} f(x,t_i)\cdot f(x,t_i+\tau)}{\sqrt{\frac{1}{N}\sum_{i=1}^{N}[f(x,t_i)]^2}\cdot\sqrt{\frac{1}{N}\sum_{i=1}^{N}[f(x,t_i+\tau)]^2}} \quad (1)$$

where N represents the number of samples; f is the instantaneous radial position of CH_2O outer boundary at x/d=10; t_i defines a time in the time series and τ indicates the time lag or the time-distance. It can be noted that R depends only on the time lag and its value must lie in the range between −1 and 1, with 1 indicating perfect correlation while −1 indicating perfect anti-correlation.

Since the laser repetition rate for CH_2O PLIF measurement in this study is 140 kHz, the smallest time lag τ is around 7.1 μs. Figure 12 shows the autocorrelation function versus τ. The blue circle is the calculated autocorrelation coefficient at different τ and red solid curve is the curve fitting by an exponential decay function, $\rho(t) = e^{-\frac{t}{\tau_0}}$, where τ_0 represents the characteristic time beyond which the fluctuations are uncorrelated. By definition, when τ is zero, the autocorrelation coefficient equals to unity. The autocorrelation coefficient decays very fast with increasing of τ as shown in the figure. It can be deduced that the position of CH_2O at its outer layer has autocorrelation within only 2-3 times of the laser pulse interval, *i.e.*, with τ_0 about 14-21 μs, which means that

the information from eddies is preserved only in this short period of time. As discussed earlier, when a large-scale wrinkle structure is tracked along the axial position as it moves downstream the lifetime of the large scales can be more than half of the integral time scale of turbulence. Thus, the radial fluctuation of the CH_2O outer layer is not a good indicator of the large-scale flame/flow interaction, but rather the fluctuations are mainly due to the small-scale turbulent eddy/flame interaction.

Figure 13 presents the autocorrelation function at x/d=10 for all the cases as shown in Table 1 and only the fitted curves by the exponential decay function are plotted. With increasing inlet jet speed U_0, the autocorrelation coefficient decays faster due to higher turbulence intensity. It can be seen that the autocorrelation function of LUPJ165 overlaps with LUPJ220.

Figure 14 shows the power spectral density (PSD) of the CH_2O fluctuation based on the instantaneous radial position of the CH_2O outer boundary at x/d=10 at different frequencies. The black dots correspond to the samples captured during 10 ms in the experiment. Hence, the minimum PSD frequency is 100 Hz. The maximum frequency is limited to 70 kHz by Nyquist limit. The PSD was calculated using 300-samples Welch rectangular windowing with 75% overlap. More detailed information can be found in Ref. [14]. The variance is reduced by selecting this Welch windowing scheme. The solid red line represents the curve fitting of the PSD while the dashed black line indicates -5/3 slope. It is obvious that in the high frequency range, *e.g.* >10 kHz, the PSD distribution follows -5/3 Kolmogorov law as the large eddies break down from integral scale and cascade into smaller scale afterwards. It can also be seen that a "flat" PSD in the low frequency range represents that the large structures, *i.e.* beyond integral scale, have similar power without energy transfer. Therefore, the PSD from the large structures starts to decrease towards smaller eddies at integral scale, *i.e.* about 100 μs (10 kHz), which is similar to the calculated integral time scale in Table 4. The smaller scale fluctuations have a low PSD indicating a smaller scale fluctuation in the radial direction.

4. Summary and conclusions

According to the literature survey performed by the authors, this is the first time that ultra-high repetition rates CH_2O and OH PLIF, at 140 kHz and 100 kHz respectively, have been applied for combustion studies. The present work demonstrates the ultra-high-speed diagnostic technique capable of probing of hydroxyl radicals and

formaldehyde distributions in a highly turbulent flame and distributed/broken reaction zone regime (Ka ≥100) with sufficient temporal resolution to approach the Kolmogorov time scale. This has been achieved through employing a burst-mode laser pumped optical parametric oscillator system. OH was excited at 284 nm where interference from scattered laser light can be avoided through spectral filtering. In addition, more than 100 consecutive images were recorded in the present work for OH PLIF at 100 kHz. Systematic temporal and spatial evolution of the flame structure is clearly resolved over long sequences, *e.g.* 1.2 ms for OH PLIF and 10 ms for CH_2O PLIF respectively. The resulting SNR for CH_2O and OH are calculated to be 25 and 30, respectively.

The Kolmogorov time scale for all the cases at x/d=10 and x/d=30 are calculated and the minimum value is 7.5 μs, which means that nearly all time-scales of the flow can be tracked with the present experimental setup. Normalized axial velocity of the CH_2O structure at its outer layer at different x/d positions, U_{CH2O}, is obtained. The velocity U_{CH2O} is compared with the LDV results, which shows a good agreement. By comparing U_{CH2O} with the local axial velocity (U), the large-scale wrinkle structures in the reaction zone can be due to different mechanisms, *i.e.* (a) large-scale coherent flow structure in the shear layer (generated due to Kelvin-Helmholtz instability) that wrinkles the flame front; (b) large scale unburned fuel or CO/CH_2O pockets that are separated by the flow from the main stream of the fuel/CO/CH_2O region; (c) flame wrinkling by the large turbulence eddies (on the integral length scale). The competition among the mechanisms makes the propagation of CH_2O structure along the flame height faster or slower. The fluctuation of CH_2O outer layer in radial direction is calculated covering the whole record length for all the cases. Frequency spectrum, autocorrelation function and power spectral density of the CH_2O radial fluctuation are calculated and presented as well. These results show that the radial fluctuation of the CH_2O outer layer is not a good indicator of the large-scale flame/flow interaction, but rather the fluctuations are mainly due to the small-scale turbulent eddy/flame interaction. Furthermore, in the high frequency range, *e.g.* >10 kHz, the PSD distribution follows -5/3 Kolmogorov law while the PSD from the large structures starts to decrease towards smaller eddies at integral scale which is similar to the calculated value. In this paper, quantitative analysis of the ultra-high-speed diagnostics data further augments the understanding of turbulent combustion down to Kolmogorov scale experimentally.

5. Reference

[1] C. F. Kaminski, J. Hult, and M. Aldén, 'High Repetition Rate Planar Laser Induced Fluorescence of OH in a Turbulent Non-Premixed Flame', Applied Physics B, 68, 757-60(1999).
[2] J. D. Miller, S. R. Engel, T. R. Meyer, T. Seeger, and A. Leipertz, 'High-Speed CH Planar Laser-Induced Fluorescence Imaging Using a Multimode-Pumped Optical Parametric Oscillator', Optics Letters, 36, 3927-29(2011).
[3] J. Nygren, J. Hult, M. Richter, M. Aldén, M. Christensen, A. Hultqvist, and B. Johansson, 'Three-Dimensional Laser Induced Fluorescence of Fuel Distributions in an HCCI Engine', Proceedings of the Combustion Institute, 29, 679-85(2002).
[4] J. Hult, M. Richter, J. Nygren, M. Aldén, A. Hultqvist, M. Christensen, and B. Johansson, 'Application of a High-Repetition-Rate Laser Diagnostic System for Single-Cycle-Resolved Imaging in Internal Combustion Engines', Applied Optics, 41, 5002-14(2002).
[5] B. Thurow, N. Jiang, and W. Lempert, 'Review of Ultra-High Repetition Rate Laser Diagnostics for Fluid Dynamic Measurements', Measurement Science and Technology, 24, 012002(2013).
[6] W. Lempert, P. F. Wu, R. Miles, B. Zhang, J. Lowrance, V. Mastrocola, and W. Kosonocky, 'Pulse-Burst Laser System for High-Speed Flow Diagnostics', in 34th Aerospace Sciences Meeting and Exhibit (American Institute of Aeronautics and Astronautics, 1996).
[7] M. N. Slipchenko, J. D. Miller, S. Roy, J. R. Gord, S. A. Danczyk, and T. R. Meyer, 'Quasi-Continuous Burst-Mode Laser for High-Speed Planar Imaging', Optics Letters, 37, 1346-48(2012).
[8] J. B. Michael, P. Venkateswaran, J. D. Miller, M. N. Slipchenko, J. R. Gord, S. Roy, and T. R. Meyer, '100 kHz Thousand-Frame Burst-Mode Planar Imaging in Turbulent Flames', Optics Letters, 39, 739-42(2014).
[9] J. D. Miller, S. J. Peltier, M. N. Slipchenko, J. G. Mance, T. M. Ombrello, J. R. Gord, and C. D. Carter, 'Investigation of Transient Ignition Processes in a Model Scramjet Pilot Cavity Using Simultaneous 100 kHz Formaldehyde Planar Laser-Induced Fluorescence and CH * Chemiluminescence Imaging', Proceedings of the Combustion Institute, 36, 2865-72(2017).
[10] B. O. Ayoola, R. Balachandran, J. H. Frank, E. Mastorakos, and C. F. Kaminski, 'Spatially Resolved Heat Release Rate Measurements in Turbulent Premixed Flames', Combustion and Flame, 144, 1-16(2006).
[11] J. H. Frank, B. Coriton, A. J. Ruggles, S. E. Bisson, B. D. Patterson, and E. Huang, 'Probing the Spatial and Temporal Structure of Turbulent Combustion with Tomographic PIV and High-Speed Imaging', in Conference on Lasers and Electro-Optics (San Jose, California: Optical Society of America, 2017), paper SF2M.5.
[12] S. Roy, P. S. Hsu, N. Jiang, M. N. Slipchenko, and J. R. Gord, '100-kHz-Rate Gas-Phase Thermometry Using 100-ps Pulses from a Burst-Mode Laser', Optics Letters, 40, 5125-28(2015).
[13] J. D. Miller, N. Jiang, D. Thul, M. Slipchenko, J. Mance, T. R. Meyer, S. Roy, and J. R. Gord, '100- kHz Burst-Mode Particle Image Velocimetry: Space-Time Correlations and Considerations for Spatial and Temporal Resolution', in 54th AIAA Aerospace Sciences Meeting (American Institute of Aeronautics and Astronautics, 2016).
[14] J. D. Miller, N. Jiang, M. N. Slipchenko, J. G. Mance, T. R. Meyer, S. Roy, and J. R. Gord, 'Spatiotemporal Analysis of Turbulent Jets Enabled by 100- kHz, 100-ms Burst-Mode Particle Image Velocimetry', Experiments in Fluids, 57(2016).
[15] J. D. Miller, M. Slipchenko, T. R. Meyer, N. Jiang, W. R. Lempert, and J. R. Gord, 'Ultrahigh-Frame-Rate OH Fluorescence Imaging in Turbulent Flames Using a Burst-Mode Optical Parametric Oscillator', Optics Letters, 34, 1309-11(2009).
[16] S. Hammack, C. Carter, C. Wuensche, and T. Lee, 'Continuous Hydroxyl Radical Planar Laser Imaging at 50 kHz Repetition Rate', Applied Optics, 53, 5246-51(2014).
[17] Z. Wang, P. Stamatoglou, Z. Li, M. Aldén, and M. Richter, 'Ultra-High-Speed Plif Imaging for Simultaneous Visualization of Multiple Species in Turbulent Flames', Optics Express, 25, 30214-28(2017).
[18] J. Sjöholm, E. Kristensson, M. Richter, M. Aldén, G. Göritz, and K. Knebel, 'Ultra-High-Speed Pumping of an Optical Parametric Oscillator (OPO) for High-Speed Laser-Induced Fluorescence Measurements', Measurement Science and Technology, 20, 025306(2009).
[19] Z. Li, J. Rosell, M. Alden, and M. Richter, 'Simultaneous Burst Imaging of Dual Species Using Planar Laser-Induced Fluorescence at 50 kHz in Turbulent Premixed Flames', Applied Spectroscopy, 71, 1363-67(2017).
[20] B. Zhou, C. Brackmann, Z. Li, M. Aldén, and X.-S. Bai, 'Simultaneous Multi-Species and Temperature Visualization of Premixed Flames in the Distributed Reaction Zone Regime', Proceedings of the Combustion Institute, 35, 1409-16(2015).
[21] B. Zhou, C. Brackmann, Q. Li, Z. Wang, P. Petersson, Z. Li, M. Aldén, and X.-s. Bai, 'Distributed Reactions in Highly Turbulent Premixed Methane/Air Flames', Combustion and Flame, 162, 2937-53(2015).
[22] B. Zhou, Advanced Laser-Based Multi-Scalar Imaging for Flame Structure Visualization Towards a Deepened Understanding of Premixed Turbulent Combustion, Doctoral Thesis, Lund University, (2015).
[23] B. Zhou, C. Brackmann, Z. Wang, Z. Li, M. Richter, M. Aldén, and X.-S. Bai, 'Thin Reaction Zone and Distributed Reaction Zone Regimes in Turbulent Premixed Methane/Air Flames: Scalar Distributions and Correlations', Combustion and Flame, 175, 220-36(2017).

[24] J. Rosell, X.-S. Bai, J. Sjoholm, B. Zhou, Z. Li, Z. Wang, P. Pettersson, Z. Li, M. Richter, and M. Alden, 'Multi-Species PLIF Study of the Structures of Turbulent Premixed Methane/Air Jet Flames in the Flamelet and Thin-Reaction Zones Regimes', Combustion and Flame, 182, 324-38(2017).
[25] C. Brackmann, J. Nygren, X. Bai, Z. Li, H. Bladh, B. Axelsson, I. Denbratt, L. Koopmans, P.-E. Bengtsson, and M. Aldén, 'Laser-Induced Fluorescence of Formaldehyde in Combustion Using Third Harmonic Nd:YAG Laser Excitation', Spectrochimica Acta Part A: Molecular and Biomolecular Spectroscopy, 59, 3347-56(2003).
[26] B. R. Halls, P. S. Hsu, N. Jiang, E. S. Legge, J. J. Felver, M. N. Slipchenko, S. Roy, T. R. Meyer, and J. R. Gord, 'kHz - Rate Four-Dimensional Fluorescence Tomography Using an Ultraviolet-Tunable Narrowband Burst-Mode Optical Parametric Oscillator', Optica, 4, 897(2017).

6. Acknowledgements

The financial support from CECOST and KCFP through the STEM (Swedish Energy Agency) are gratefully acknowledged. The authors would also like to thank Dr. Mikhail Slipchenko and Dr. Jason Mance for their valuable help and contribution.

Figures and tables

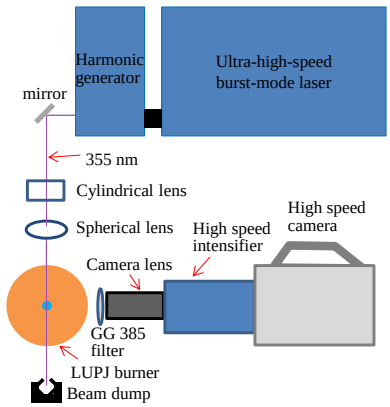

Figure 1. Schematic diagram of experimental setup for ultra-high-speed CH_2O PLIF imaging.

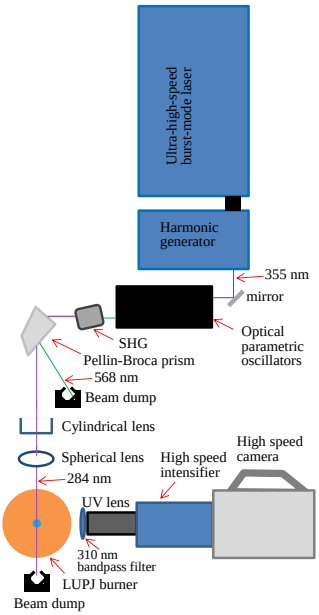

Figure 2. Schematic diagram of experimental setup for ultra-high-speed OH PLIF imaging.

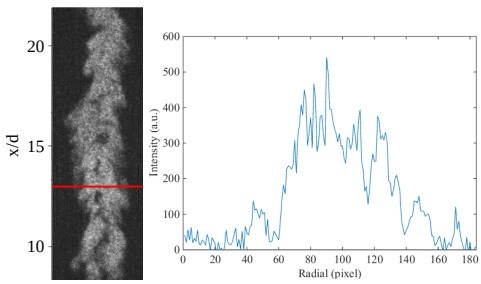

Figure 3. Raw CH_2O PLIF image for the LUPJ110 flame prior to post-processing and its signal profile along the red marked line.

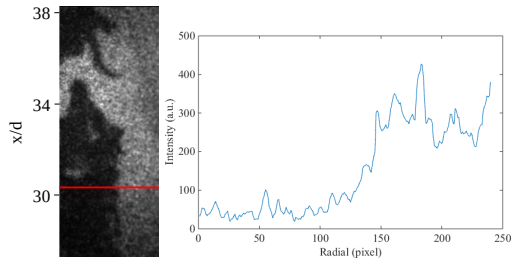

Figure 4. Raw OH PLIF image for the LUPJ220 flame prior to post-processing and its signal profile along the red marked line.

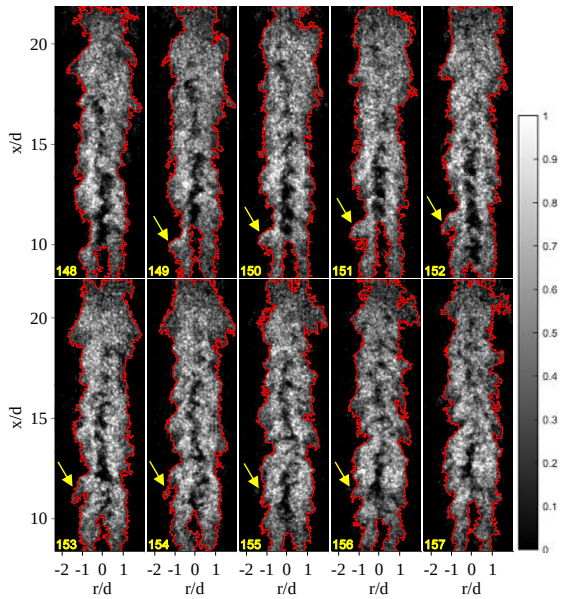

Figure 5. Temporal evolution of the CH_2O PLIF images measured for the LUPJ220 flame.

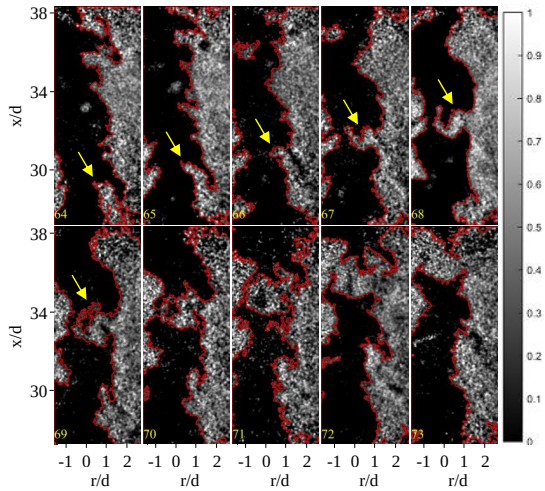

Figure 6. Temporal evolution of OH PLIF images measured for the LUPJ220 flame.

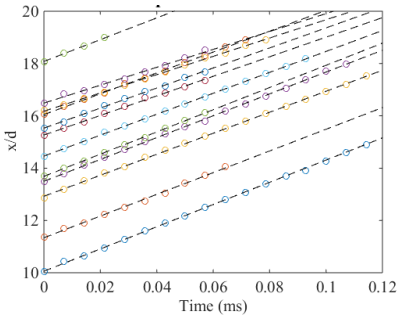

Figure 7 Axial positions of large-scale wrinkle structures in the CH_2O outer layer of the LUPJ66 flame at different time; the slope indicates the velocity at which the large scale wrinkle structure travels in the axial direction downstream.

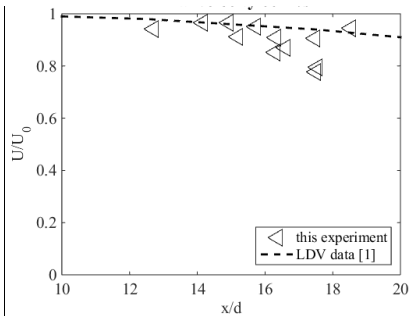

Figure 8 Normalized axial velocity of the CH_2O structure at its outer layer in Fig. 7 at different x/d positions in LUPJ66 flame and comparison with LDV data [21].

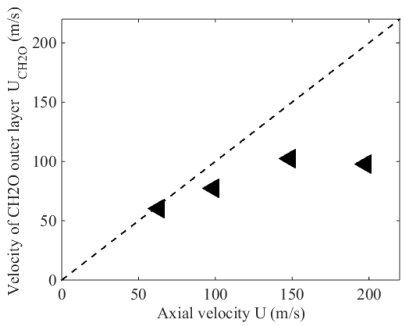

Figure 9 Comparison between the mean axial velocity of CH_2O structure (U_{CH2O}) and the local mean axial velocity component (U)

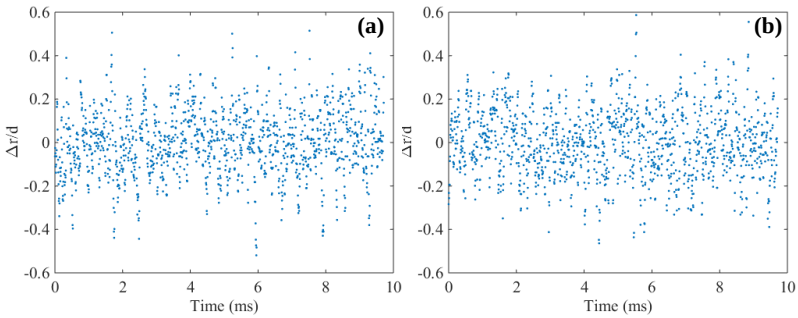

Figure 10 Temporal evolution of the radial position of CH_2O outer layer on the left side (a) and the right side (b) of the conical flame at x/d=10.

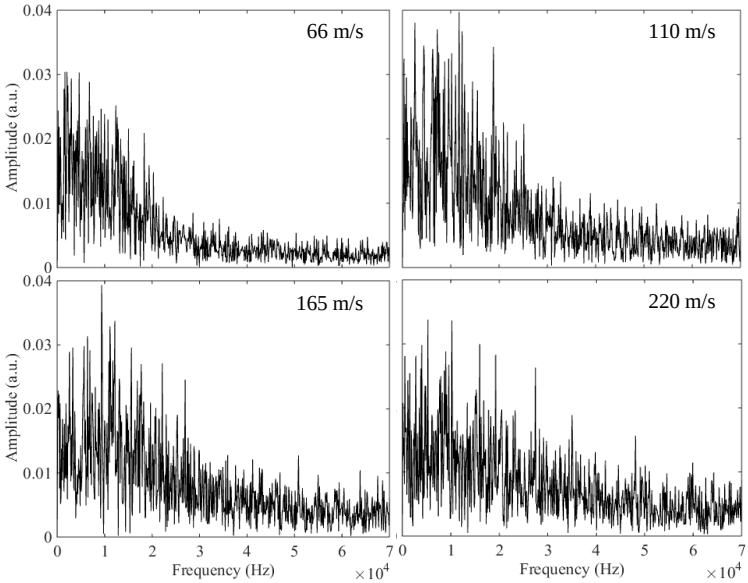

Figure 11 Amplitude of CH_2O radial positions in Fig. 10 versus different frequency (*i.e.* frequency spectrum).

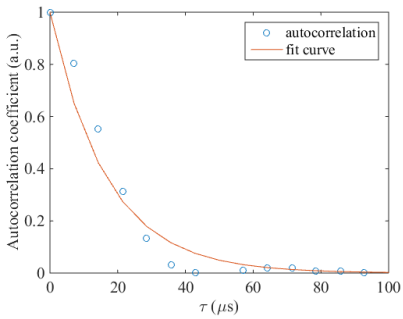

Figure 12 Autocorrelation function at x/d=10 versus time lag, τ, for the LUPJ66 flame.

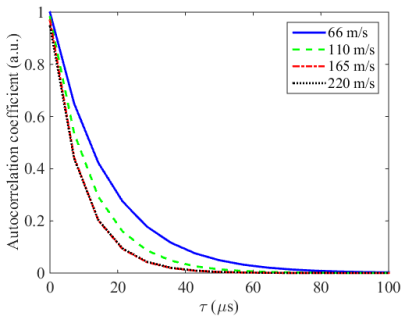

Figure 13 Autocorrelation function at x/d=10 versus time lag, τ, for all the cases as shown in Table 1.

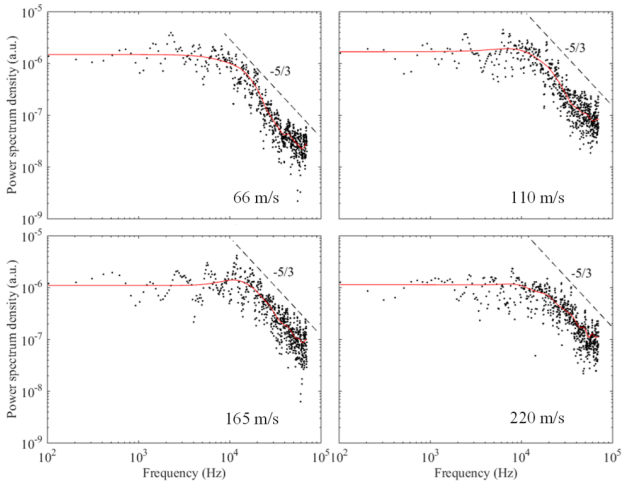

Figure 14 Power density spectrum of CH_2O radial position in Fig. 10 with comparison of Kolmogorov's -5/3 law.

Table 1. Flow conditions.

Cases	LUPJ66	LUPJ110	LUPJ165	LUPJ220
Jet flow speed (m/s)	66	110	165	220
Equivalence ratio of jet flow	1.0	1.0	1.0	1.0
Co-flow flow speed (m/s)	0.3			
Equivalence ratio of co-flow	0.9			

Table 2. Quantities for the jet flames at x/d=30 and Ka number calculated at x/d=30 and x/d=10, based on the LDA data of Ref. [21].

Jet flow speed(m/s)	Turbulent Reynolds number	Kolmogorov length scale (μm)	Karlovitz number[1]	Karlovitz number[2]
66	95	96	25	22
110	190	57	70	51
165	238	49	98	85
220	317	39	151	117

[1] Ka number calculated at x/d=30;

[2] Ka number calculated at x/d=10.

Table 3. Parameters of the optical setup.

Species	OH	CH_2O
Camera pixels	600 x 240	640 x 184
Intensifier gain	55	50
Camera lens	B. Halle lens, f#=2, f= 100 mm	Nikkon f#=1.2, f=50 mm
Field of view	18 mm x 7mm	20 mm x 6 mm
Optical filter	Interference filter, λ_T=310±10 nm	GG 385
Intensifier gate	100 ns	40 ns
λ_{laser}	283.93 nm	355 nm
Laser energy	~ 0.15 mJ	25 mJ

Table 4. Time scale of the studied cases.

Cases	LUPJ66	LUPJ110	LUPJ165	LUPJ220
Integral time scale at x/d=10 (μs)	288	161	115	93
Integral time scale at x/d=30 (μs)	447	223	179	134
Kolmogorov time scale at x/d=10 (μs)	52	22	13	10
Kolmogorov time scale at x/d=30 (μs)	46	16	11	7.5

Appendix

Sequences of CH_2O PLIF images and OH PLIF images captured in the LUPJ220 flame are presented in the appendix.

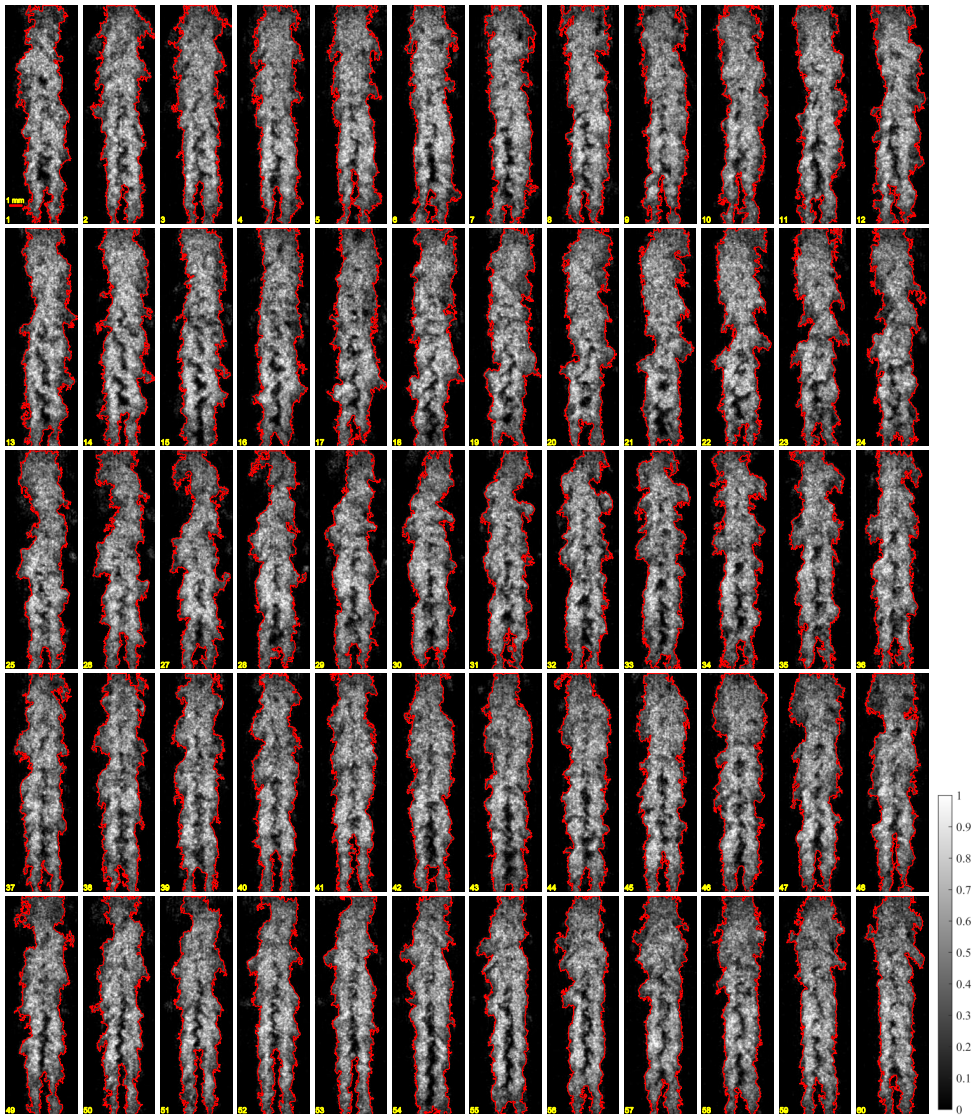

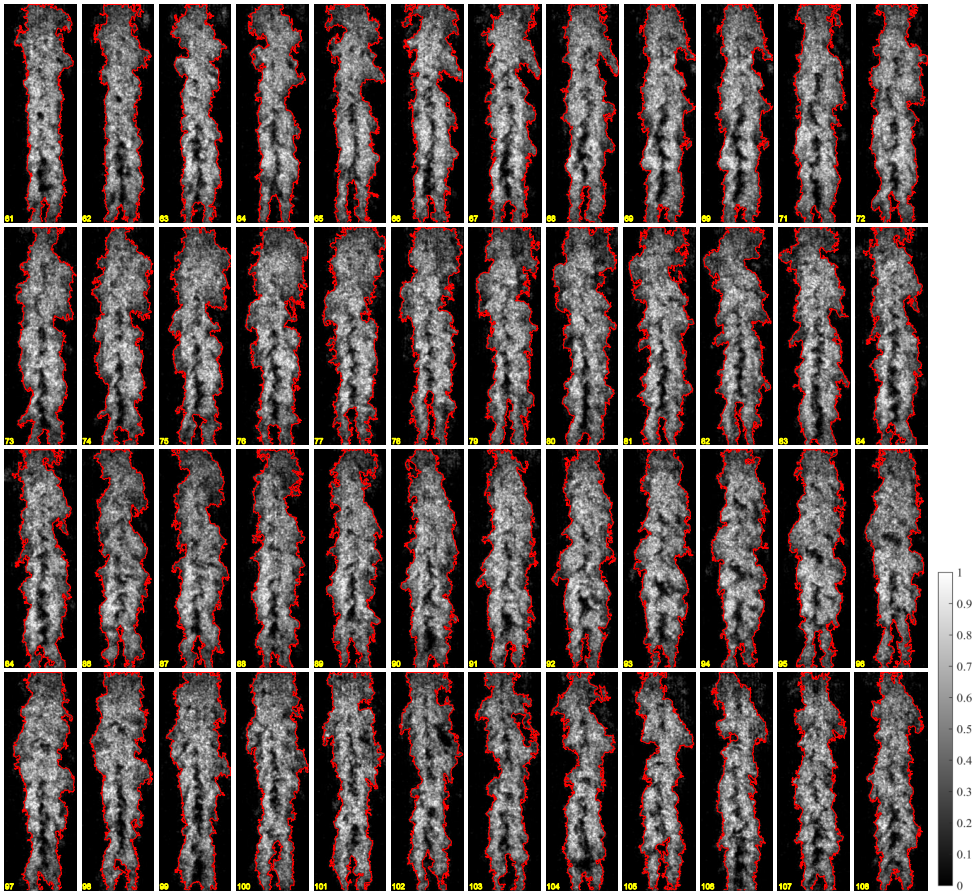

Figure 15. Temporal evolution of the CH_2O PLIF images measured for the LUPJ220 flame (220 m/s) at 140 kHz repetition rate.

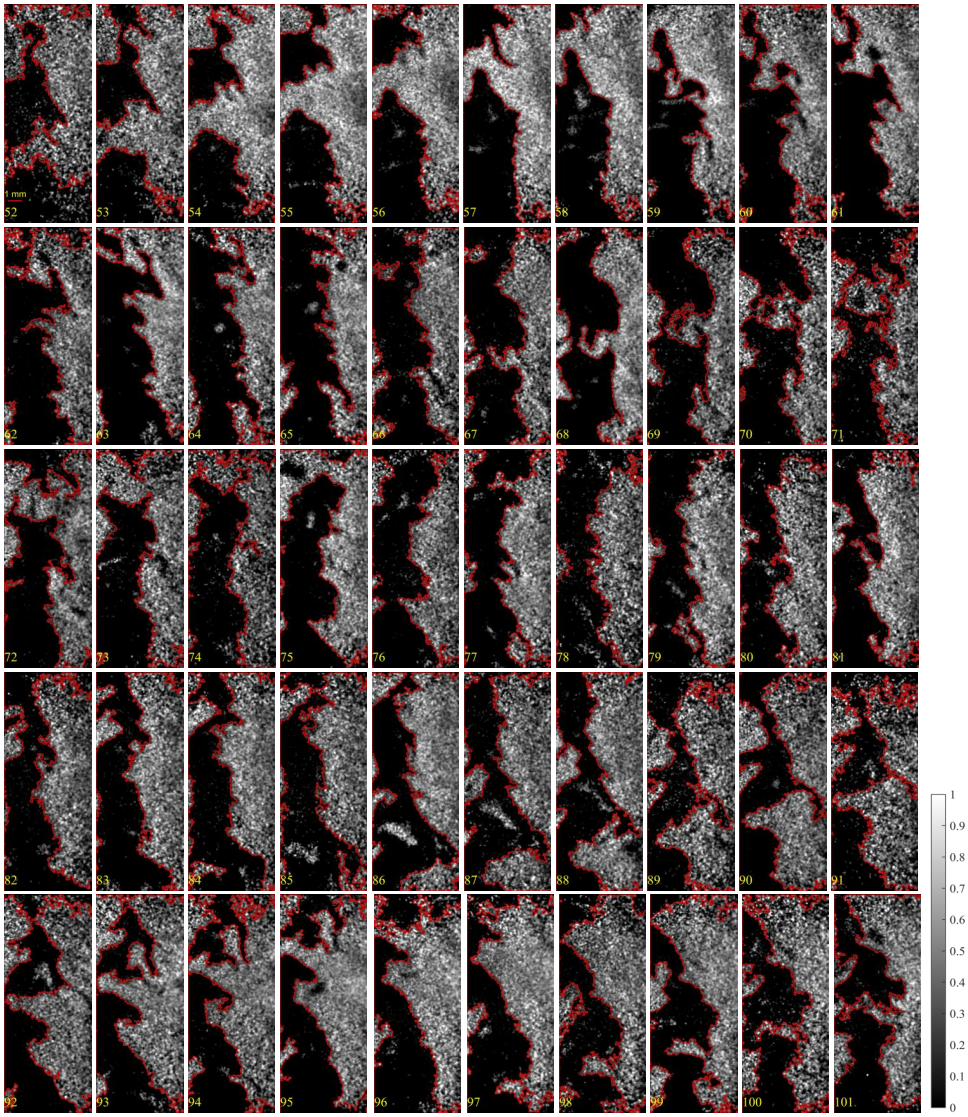
1 mm
52
53
54
55
56
57
58
59
60
61
62
63
64
65
66
67
68
69
70
71
72
73
74
75
76
77
78
79
80
81
82
83
84
85
86
87
88
89
90
91
92
93
94
95
96
97
98
99
100
101
1
0.9
0.8
0.7
0.6
0.5
0.4
0.3
0.2
0.1
0

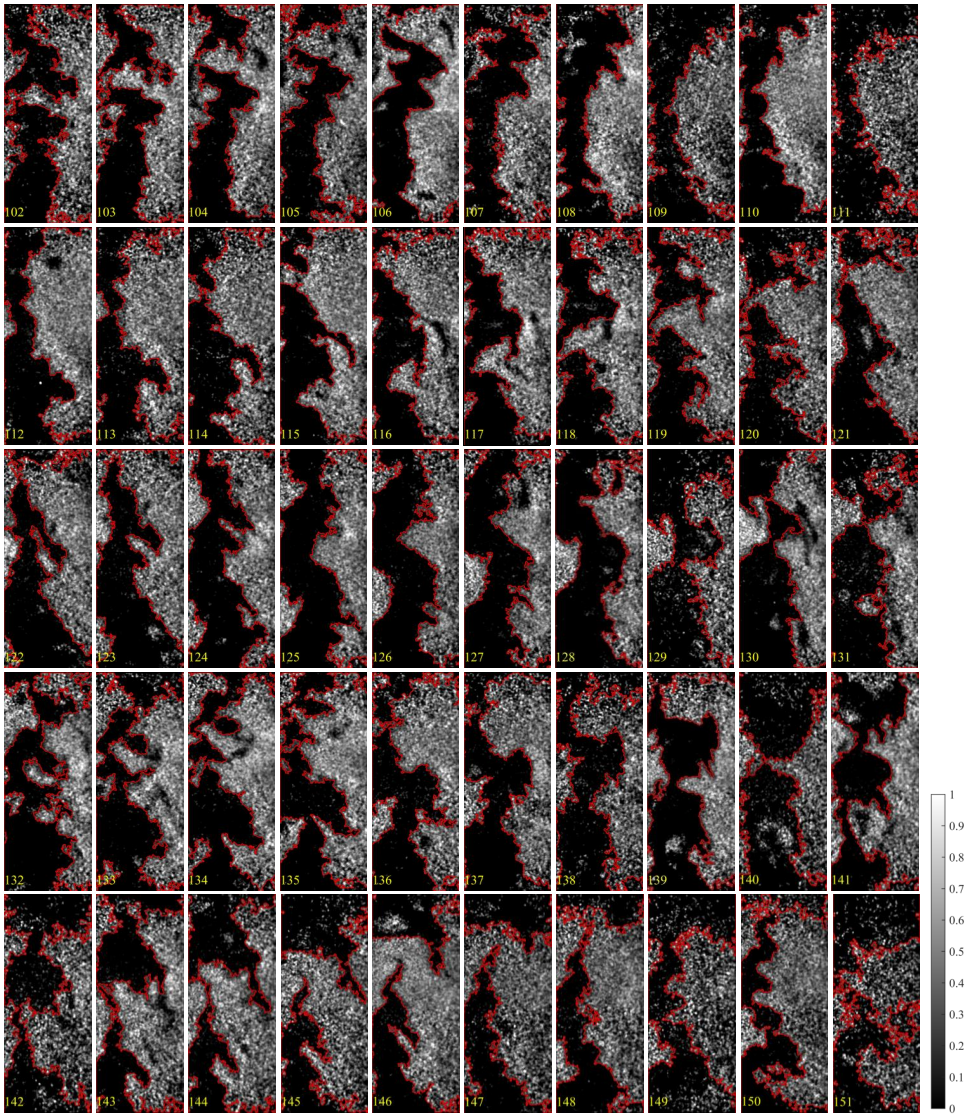
102
103
104
105
106
107
108
109
110
111
112
113
114
115
116
117
118
119
120
121
122
123
124
125
126
127
128
129
130
131
132
133
134
135
136
137
138
139
140
141
142
143
144
145
146
147
148
149
150
151
1
0.9
0.8
0.7
0.6
0.5
0.4
0.3
0.2
0.1
0

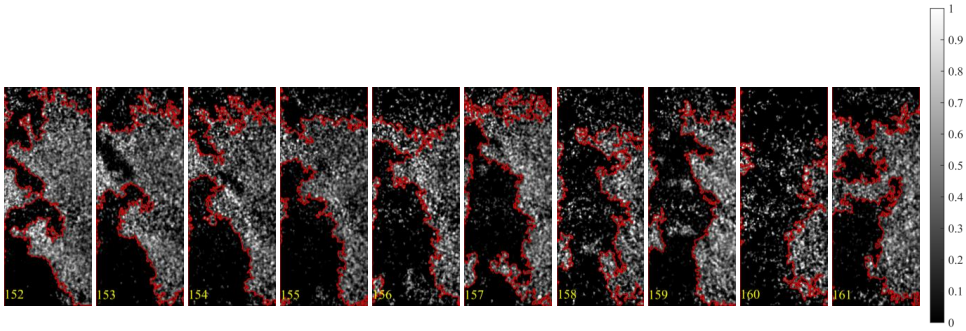

Figure 16. Temporal evolution of the OH PLIF images measured for the LUPJ220 flame (220 m/s) at 100 kHz repetition rate.

Paper XI

Title: PLIF imaging at 27 kHz of OH radicals - applications in pulsed plasma discharges

1. Introduction

In the past two decades, the amount of research has increased over the last two decades for non-thermal atmospheric-pressure discharges. Non-thermal plasmas have higher electron number density than gas temperature and does thus favor formation of reactive species, *such as* OH, O, O_3 and etc. rather than gas heating. These reactive species are studied in diverse measurements and applications covering different fields such as surface treatment [1-3], medical treatment [4-9], water process and chemical synthesis [10-13], gas treatment and pollution control [14-27], assisted ignition and combustion enhancement [28-39] etc.

The hydroxyl radical (OH) is one of the most important species for non-thermal plasmas due to its high reactivity [13, 40] and hence, the detection of OH is of major importance as it plays an important role in non-thermal plasmas in all the applications mentioned above. OH is believed to be produced in the gliding arc primarily due to electron-induced dissociation of water vapour in open air [41, 42].

$$H_2O + e \rightarrow OH + H + e \quad (1)$$

During the electron discharge, the voltage and current peaks are extremely high, *e.g.* 8 kV and 0.2 A, respectively [2, 43]. Optical imaging diagnostics methods can be used to detect hydroxyl radicals. Further, selective visualization of OH radicals provides high temporal- and spatial resolution using laser excitation schemes that in addition are nonintrusive. Planar laser-induced fluorescence (PLIF) is one of the best analytical techniques for measuring transient species, such as OH radical, in atmospheric-pressure discharges. Time resolution of such data is related to the laser pulse duration, which for conventional nanosecond laser systems is about 10 ns. Ground-state OH radicals are not detectable with for example optical emission spectroscopy (OES) that only can be used to detect species that has been excited by electron induced chemistry. Recently, time-resolved OH radical distributions and densities

have been measured in pulsed discharges by employing laser-induced fluorescence [13, 27, 30, 31, 40, 44-64].

The non-thermal plasma discharge has many different forms, such as a corona, a dielectric barrier, and a gliding arc [65]. Among these, the gliding arc discharge has an advantage due to its simplicity, low-cost and the potential to provide a high-power non-thermal plasma volume at atmospheric pressure [66]. The gliding arc is a thin, string-like plasma column that repeatedly ignites in the narrowest gap between the diverging electrodes, glides up along the electrodes, and extinguishes in a turbulent gas flow [44] as shown in figure 1 derived from reference [67].

In our previous study, OH-PLIF imaging has been successfully applied to characterize a gliding arc in detail [3, 67, 68]. However, the large-scale motion of the gliding arc is caused by convection in a turbulent jet flow which leads to dynamic feature of the radicals produced by gliding arc discharge [2,43, 69-71]. Therefore, capturing the dynamic features of the OH radical can be often challenging with the commonly-used 10 Hz dye laser systems utilized in aforementioned OH PLIF study.

It has been shown that high-speed photography is an effective way to capture evolution processes of a gliding arc as well as to investigate the arc dynamics [43, 69-77]. Up to now, there mainly are three types of high-speed laser systems, *i.e.* multi-YAG laser system [78], diode-pumped solid-state (DPSS) Nd:YAG laser system [79-81] and burst mode laser system. With the development of the burst mode laser system [82-84], it has become more popular than other high speed laser systems because of its advantage of high pulse energy and high repetition rate.

In this work, high speed observations of the ground-state OH radical in AC gliding arc discharge are studied with the use of a burst mode laser system combined with an optical parametric oscillator (OPO). The decay of OH radical concentration in post glow discharge is consequently obtained. To authors' best knowledge, it is first time to report high-speed OH PLIF imaging in non-thermal plasma discharges at ultra-high repetition rate (>20 kHz). Better understanding of pulsed discharge characteristics is achieved

by the PLIF measurement at 27 kHz repetition rate in this study. Thus, the aim of this paper is to employ the high-speed PLIF technique to capture the dynamic features of OH radicals in a gliding arc discharge. The following is a brief outline of this paper:

Section II provides an introduction to the experimental setup. First, the optical system is described in detailed including the state-of-the-art burst mode laser system, OPO, image acquiring system and associated device. Secondly, the discharge system is introduced including the electrodes, the power supply and the feeding gas together with the current and voltage measurement system.

Section III shows the procedure for post processing the OH PLIF data.

Section IV presents the main results concerning the evolution of the OH distribution and the analysis of OH intensity changes. A series of OH PLIF images at 27 kHz are shown as well. The decay rate and increase rate of OH radical in post discharge are compared and discussed.

Section V summarizes the work.

2. Experimental setup

2.1 Burst mode laser

Figure 2 shows the layout of the burst mode laser used in this study. A single mode (spectral linewidth <100 MHz) laser (IPS 1064SU0120PA) produces a continuous wave (CW) laser beam at 1064 nm (see figure 3(a)). The laser beam is guided through optical fibers to an acousto-optic modulator (AOM) and two fiber amplifiers. The AOM slices the CW laser into a pulse train as shown in figure 3(b). The gate time of AOM is 10 ns which creates pulses of 10 ns width. However, using the first order of diffraction of the AOM cannot block all the background noise. Furthermore, the background noise, which is located between two pulses, is not coherent. When that light passes through the next stages of amplifiers it will consume the gain that is used for amplifying the coherent light. This is usually defined as amplified spontaneous emission (ASE). An electro-optic modulator (EOM) is employed to suppress the ASE, which will be discussed later. The repetition rate of the laser pulse is adjustable and is controlled by the

AOM. For instance, the repetition rate can cover from 10 kHz up to 1000 kHz. However, a consequence of higher repetition rates is a decrease in laser pulse energy, as the total burst power is nearly constant. The AOM-frequency in this particular study is set to generate a 27 kHz pulse train in this particular study.

In this burst mode laser, there are four amplification stages including two diode-pumped amplifiers and six flashlamp-pumped amplifiers. After the AOM, the pulse train is guided by optical fibers and several mirrors towards the first amplification stage. In this stage, the pulse train is amplified by two 2.8-mm-diameter Nd:YAG-rod diode-pumped amplifiers (A1 and A2 in figure 2). An optical relay including two convex spherical lenses is placed between the amplifiers. A spatial filter is positioned at the focus point of the lens to reduce high spatial frequency noise and to produce a uniform Gaussian beam profile. After the diode-pumped amplifiers, a Faraday-rotation optical isolator is used to prevent any back reflected light entering into the amplifiers, being amplified again and damaging the upstream optical components afterwards. The pulse energy after the first amplification stage is below 1 mJ at 27 kHz.

After the isolator, there is a double-pass of the laser beam including another optical isolator and the EOM. This configuration enables a dramatic reduction of the ASE as shown in figure 3(c).

The gate width of the EOM is around 1 μs, whereas the envelope of the EOM waveform in a burst is adjustable as well, providing freedom to control the pulse energy distribution within a burst so that it is as uniform as possible. For example, if the pulse energy is higher at the beginning of the burst, the voltage of the EOM can be lower for these initial pulses to achieve small pulse energy variation throughout the burst.

After the double-pass of the isolator and EOM, another optical relay and spatial filter are utilized to reduce the noise. An optical isolator is utilized before the pulse train passes through the second amplification stage. In this stage, two 4-mm-diameter flashlamp-pumped amplifiers A3 and A4 are used in a double-pass configuration. An optical relay is placed between the amplifiers. A spatial filter is installed in a vacuum tube to prevent any ionization by the laser at the focus point of the lens. Due to

higher and higher laser pulse energy, spatial filters in downstream optics are also placed in vacuum tubes. After the double-pass of two amplifiers, the pulse train is guided by a beam splitter to the next amplification stage. The pulse energy is around 14 mJ at 27 kHz after this amplification stage.

Two xenon flashlamps are exerted to optically pump an Nd:YAG gain medium in each flashlamp-pumped amplifier in this laser system. The amplifier employs water cooling system to remove the heat created by the flashlamps. However, the burst duration is at an order of several milliseconds. Therefore, even with thermal management, the huge amounts of heat cannot transfer promptly and sufficiently during the burst, which can result in some undesired effects *e.g.* thermal lensing. In order to compensate for the thermal lensing effect, amplifier A3 is rotated 90 degrees compared to amplifier A4. Another approach to mitigate the adverse effect is to setup a sufficiently long time interval between the two bursts, *e.g.* ≥20 seconds, as shown in figure 3(d).

Another set of optical relay and spatial filter (with vacuum tube), and an optical isolator are used before the pulse train passes through two 9.5-mm-diameter flashlamp-pumped amplifiers, A5 and A6. After the amplification by A5 and A6, similar to the previous stage, optical relay, spatial filter (with vacuum tube) and isolator are used before the pulse train enters into the next amplification stage. The pulse energy is approximately 220 mJ at 27 kHz after amplifier A6.

Two 12.7-mm-diameter flashlamp-pumped amplifiers are employed in the last amplification stage. The last set of optical relay and spatial filter (with vacuum tube) are placed after the amplifiers A7 and A8. The usage of this spatial filter is mainly to block the back reflection light as the size of the pinhole is fairly large, ≥3 mm. The output of the burst mode laser is about 540 mJ per pulse at 27 kHz.

Figure 3 illustrates the production of a pulse train from the master oscillator to the EOM. Each pulse in a burst is comparable to that produced by commonly-used 10 Hz Nd: YAG laser. The 1064-nm-wavelength laser is then converted to 355 nm by second- and third harmonic generation. The optical setup for frequency conversion is not shown in this paper as it is similar to commonly-used 10 Hz Nd: YAG lasers.

2.2 OPO

Figure 4 illustrates the OPO (GWU, PremiScan/ MB) system in this study. A telescope is used to reduce the size of the laser beam in order to have higher laser irradiance and better conversion efficiency. A 355 nm wavelength laser is used as a pumping beam and is guided by two mirrors into a resonator cavity, including two resonator mirrors and a beta barium borate (BBO) crystal. Detailed information of the resonator mirror and BBO crystal is described in reference [85]. The angle of the BBO crystal controls the output wavelength which is tuned to 568 nm. By adjusting the resonator mirrors, the optimal output achieved is around 15 mJ/ pulse. A UV filter is used only to absorb the residual 355 nm laser. The offset of the beam path caused by rotating the BBO crystal is controlled with a compensator. After the resonator cavity, the 568 nm wavelength laser and idler laser (947 nm) beams are separated by a dichroic mirror. The idler beam is terminated with a beam dump. A beam splitter is used for the 568 nm laser before the OPO outlet. After the beam splitter, a fraction of the 568 nm laser enters a wavemeter (GWU, LambdaScan) for monitoring the output wavelength. Several neutral density filters are used to reduce the laser power in order to protect the wavemeter.

Figure 5 shows the top view of the experimental setup. The majority of the output from the OPO at 568 nm enters a potassium dihydrogen phosphate (KDP) type second-harmonic-generation crystal which doubles the frequency. A Pellin–Broca prism is employed to separate 284 nm and 568 nm laser beams as shown in figure 5. A laser sheet is formed by a cylindrical lens (f=-50 mm) and a spherical lens (f=+300 mm). The height of the laser sheet is about 40 mm and the thickness is approximately 200 μm at the focus. The laser sheet is focused between two electrodes where the gliding arc discharge is generated as seen in figure 5. A description of the discharge system will be introduced later in this section. In the experiment, the plane which contains the two electrodes has an angle of 45 degrees to direction of propagation of the laser. The laser sheet covers the area from 84 mm to 120 mm above the Teflon plate. The laser energy is monitored using a beam splitter, a 3 inches spherical lens (f=+200 mm) and a photodiode (Thorlabs, PDA10A).

2.3 Detection system

A CMOS high-speed camera (Photron, Fastcam SA-Z) in combination with a high-speed intensifier (LaVision HS-IRO) were used to detect the LIF from OH radicals. A 31-mm-width extension ring is placed between the intensifier and an UV lens (B. Halle, f#=2, f= 100 mm) to obtain a 52 × 36 mm field of view.

After an excitation scan, the laser is tuned to a specific transition ($A^2\Sigma^+$-$X^2\Pi$, 1-0) at 283.93 nm. The OH laser induced fluorescence from A-X (0, 0) transition is then collected at around 308 nm through an interference filter (λ_I=310±10 nm) mounted in front of the B. Halle lens.

The camera and intensifier are synchronized through a high speed controller box (LaVision, standard # 1108075) at 27 kHz. The resolution of the high speed camera is reduced to 832 × 568 pixels (each pixel measuring 63 × 63 μm) at this repetition rate.

In the experiment, the intensifier gate duration is set to 50 ns, which was assessed to be sufficient to block the background noise such as glow discharge luminosity. When the laser is turned off, no OH* chemiluminescence from the plasma column is detected.

2.4 Gliding arc discharge system

A schematic diagram of the gliding arc discharge system is shown in figure 6. Similar configurations are detailed in references [2, 27, 43, 44, 67-70, 86, 87].

The pulsed discharge is driven by an AC power supply at a frequency of 35 kHz (Generator 9030E, SOFTAL Electronic GmbH, Germany), corresponding to a full cycle period of 28 μs. The power supply is triggered in a burst mode by a programmable pulse generator (BNC 575). The time duration of the high-voltage burst is set to 81.5 ms, which is enough to make the gliding arc propagate into the field-of-view. In addition, afterglow studies can be performed in this setup since the burst discharge is synchronized with the high-speed camera. Details about synchronization, data acquisition, plasma ignition and burst-mode operation for this setup were described by Sun *et al.* [44].

A current monitor (Pearson Electronics, model 6585) and a voltage probe (Tektronix P6015A) are employed for current and voltage measurements of the discharge. The current and voltage signals together with the photodiode signal (represents laser pulse), the high-speed intensifier gate and the triggers for the pulsed discharge are recorded simultaneously by two four-channel oscilloscopes (PicoScope 4424, PS and Rigol DS4024) at a sample rate of 2 GHz.

The input power to the gliding arc is approximately 800 W. The effective electrical circuit driving the gliding arc discharge is shown in figure 6. The high voltage output of the power supply is connected to one electrode and the other electrode is grounded. Both the grounded and high voltage electrode are made of hollow stainless steel tubes with an outer diameter of 3 mm, where cooling water can be circulated. The electrodes are fixed on a Teflon plate with a closest gap separation of approximately 5 mm.

An air jet is ejected from a circular channel (with a diameter of 3 mm) that is located in the center of the Teflon plate. The jet flow is controlled by mass flow controllers which provide a mass flow corresponding to 5 standard liters per minute. The gliding arc discharge is first established at the narrowest gap between the two diverging electrodes and starts elongating and propagating upwards due to the jet flow. The relative humidity of the compressed air is 36% and the amount of water vapour is 8 g/m^3, which are the same as our previous study [67].

2.5 Timing

Figure 7 represents the temporal relation between the pulsed discharge system and the data-acquisition system. The gliding arc discharge system starts at 0 ms and is stopped at 81.5 ms as the high voltage (blue) is turned off and hence the current (red) drops to zero. The synchronized laser and camera starts operating at 80.7 ms, which is 0.8 ms before the high voltage is turned off, and continues to collect data for about 2.7 ms (green).

A more detailed description of the synchronization scheme is illustrated in figure 8. The voltage and current are oscillating in phase at 35 kHz while the interval between two consecutive camera gate signals is approximately 37 μs (27 kHz).

The data that is acquired with this setup is able to capture OH signal for 0.8 ms with the gliding discharge running as well as the decay of the OH distribution in the post glow discharge regime.

2.6 Post-processing

The procedure of post-processing for the OH PLIF images is done in MATLAB©.A background image is recorded without the presence of plasma while the laser is on. The background image is subtracted from each OH PLIF image as the first step in the post-processing procedure. The processing also included compensation for vertical variations in the energy distribution of the laser sheet in OH PLIF images. This is carried out by using a Bunsen burner with a CH_4 and air premixed flame to record the corresponding PLIF image. The OH PLIF image of the flame and the intensity along the laser sheet is shown in figure 9. In the figure, the intensity is a sum of all the intensities at each pixel along the horizontal direction and it is then normalized by the maximum intensity along the laser sheet, *i.e.* vertical direction. The compensation of energy variations was achieved by normalizing each OH PLIF image in the plasma discharge by the laser sheet energy distribution, *i.e.* the intensity curve in figure 9. As a last step, each image is normalized by the laser pulse energy measured by the photodiode, although the pulse to pulse variation is very small [83, 88].

3. Results and discussion

Figure 10 represents an OH PLIF image of the gliding arc after post-processing. A toroidal shape can be observed because ground state OH is mostly located at outer layer of the plasma column, which has good agreement with our previous studies [44, 67]. Inside the hollow the excited state OH, *i.e.* OH*, predominately exists, rather than ground state OH because of the higher temperature which was

measured by Zhu *et al.* [87] and because ionization of the OH is present in the core of the discharge. OH* is mainly generated by electron impact dissociation of water [89]. As a result, the OH PLIF signal inside torus is very weak, *i.e.* similar to the background. The time information and dimension scale are indicated in the bottom-left and bottom-right corner of the figure, respectively. The intensity is normalized to the maximum among all the OH PLIF images. A greyscale bin ranging from 0 to 100 is displayed to the right side of the image.

The SNR is calculated based on dividing the average value of the signal by the standard deviation of the background noise. In order to obtain SNR, the OH PLIF image has not been conducted any post-processing. A red solid line passes the center of the OH torus as shown in figure 11 and the intensity profile along it is displayed in figure 12 where the region for signal or noise calculation is marked by double-arrowed lines. The SNR for the OH PLIF image is about 55.

The OH layer thickness is calculated by full width at half maximum (FWHM) of the OH PLIF intensity and the OH* thickness is deduced from the distance between two sides of the OH layer as shown in figure 12. The changing of OH layer and OH* layer thickness with time will be shown and discussed in the end of this section.

Figure 13 shows a number of high speed OH PLIF images including before and during the post discharge. The dynamic feature of OH distribution can be captured solely by high speed PLIF imaging. In the first two subfigures, t=0.37 ms and t= 0.741 ms, the toroidal structure of OH distribution is clearly observed. After switching off the plasma at approximately t=0.8 ms, the hollow structure gradually turns to a solid circle as seen from last five subfigures (from t=0.926 ms to t=2.222 ms) in Figure 13. A possible explanation can be that once the power supply of discharge is turned off, the balance between producing excited state OH and consuming OH* ,*e.g.* quenching, collapses. As a consequence, consumption of OH* becomes more dominant due to a lack of support of energy from glow discharge and chemical reactions. More OH* becomes ground state OH, which can be excited by the laser and emits fluorescence light. The results from OH chemiluminescence show that plenty of OH* exist inside

the hollow structure of OH PLIF image, where the plasma column is before switching off the power supply, and the decay time of OH* is quite long, *e.g.* >1 ms [86]. It can also been seen that after the ground-state OH radical is formed at the outer layer of plasma column, the life time of OH is quite long, *e.g.* > 2 ms, in this study. More consecutive high speed OH PLIF images and an animation are included in the appendix section of this paper.

In order to obtain the relation between OH distribution and time, the intensity profile across the center of the toroidal structure is calculated as shown in figure 14. The intensity profile along the blue line of the OH PLIF image is illustrated in figure 14(a). Afterwards, the intensity profile at different time is plotted in figure 14(b) where the horizontal axis indicates the time from 0 ms to 2.7 ms and vertical axis means the position of OH PLIF intensity which is displayed by pseudo color scale. In the center of figure 14(b) where the plasma column is located, the OH PLIF intensity keeps constantly low until t=0.8 ms. Similarly, the OH PLIF intensity at outer layer of plasma column remains almost steady during that period. After t=0.8 ms, the intensity drops at outer layer of plasma column while it increases rapidly in plasma column. Since the OH PLIF intensity is roughly (assuming same quenching rate) proportional to the number density of OH radical in a plasma [45, 50], OH concentration is increasing in plasma column while it is decreasing at outer layer of plasma column during post discharge.

In order to obtain quantitative result, the averaged intensity in plasma column and at outer layer of plasma column, *i.e.* at the cross section of either side of the torus, is calculated based on figure 14. Figure 15 shows how they change with the time and the intensity is normalized to unity. The circle, square and triangle symbols indicate the experimental results while the solid and dashed lines represent the corresponding curve fittings.

An exponential function $I = I_0 e^{-\frac{t}{\tau}}$ is used for fittings of the intensity decay (or the increase of intensity). I and I_0 are instantaneous intensity and initial intensity, respectively. t means time and τ is the exponential time constant which represents the lifetime. According to calculations, the lifetime of OH at

outer layer of plasma column is around 3 ms from the exponential fitting (solid line) during post discharge. In the same period, τ for the increment of OH intensity in plasma column (dashed line) is approximately -1 ms. That means the growth rate is 1 ms^{-1}, *i.e.* the rate for producing OH radicals is 3 times faster in plasma column than the OH extinction outside plasma column from t=0.8 ms to t= 2.1 ms. The decay of OH number density attributes to the depletion reactions and diffusion effect of turbulence while the production of OH by radical chemistry and ionic reactions as well as OH* relaxation into OH by quenching contributes to the increase of OH. A plausible conclusion is made that the impacts causing the increment of OH number density are dominant rather than the destructions leading to reduction of OH number density in plasma column region. In addition, owing to low diffusion rate by the turbulence, even though the OH number density is rising in plasma column, it is still declining at the outer layer of the plasma column as depletion reactions dominate.

Because the OH* is used up at about t=2.1 ms as its chemiluminescence disappeared, OH number density is not able to be escalated by OH* relaxation. After that time, the intensity in plasma column and around it converges to the same level and the decay rate of OH number density also becomes the same as shown in figure 15.

Figure 16 presents that the thickness of the OH layer and thickness between two OH layers, *i.e.* OH* layer, alter with the time. The calculation is presented in previous section and two exponential curve fittings display in figure 16. Before plasma switches off at t=0.8 ms, the OH layer thickness keeps about 2.3 mm and OH* layer thickness remains around 3.7 mm.

Comparing with figure 15, during the post discharge the increasing rate of the OH layer thickness (τ= -2 ms) is 1.5 times higher than the decreasing rate of the OH intensity at outer layer of the plasma column, while the decay rate of OH* layer thickness (τ=0.5 ms) is half of the increasing rate of OH intensity in the plasma column. When the OH layer thickness reaches approximately 4 mm at about t=2 ms, the OH* layer thickness is close to zero. Namely, the OH* relaxes into OH completely and the torus shape of OH distribution becomes a solid circle as shown in figure 13. In addition, the changing of OH laver

thickness implies that the decay rate of OH in the middle of OH layer is faster than that in the edge of OH layer. In other words, the decay rate of OH is higher in high OH concentration zone.

4. Summary and conclusion

This paper demonstrates high speed laser technique is very useful for the investigation of pulsed discharge. By using burst mode laser system combined with optical parametric oscillator, the dynamic feature of the gliding arc discharge is successfully studied which cannot be obtained by commonly-used 10 Hz laser system. The changing of OH radical distribution during post discharge is captured at 27 kHz, *e.g.* the deformation of the OH PLIF intensity from toroidal shape to a filled circle is observed. In addition, the decay rate of OH distribution at outer layer of plasma column and the increasing rate of that in plasma column are calculated. The results show that the decay time of OH at outer layer of the plasma column is about 3 ms while the increasing rate in plasma column is 3 times faster than it, which is partially contributed from the relaxation of OH* into OH. Furthermore, the thickness of OH layer and the thickness between two OH layers, *i.e.* OH* layer altering with the time is obtained. During the post discharge, the OH layer thickness rises from 2.3 mm to 4 mm while the OH* layer declines from 3.7 mm to zero when OH distribution becomes a solid circle.

It's the first time that burst mode laser system is applied for high-speed OH PLIF imaging in pulsed plasma discharges at tens of kHz repetition rate. In this paper, the optical system is described in detail including the state-of-the-art burst mode laser system, OPO and image acquiring system. The signal to noise ratio achieves 55.

5. Reference

[1] Y. Kusano, K. Norrman, J. Drews, F. Leipold, S. V. Singh, P. Morgen, A. Bardenshtein, and N. Krebs, 'Gliding Arc Surface Treatment of Glass-Fiber-Reinforced Polyester Enhanced by Ultrasonic Irradiation', *Surface and Coatings Technology,* 205, S490-S94(2011).

[2] Y. Kusano, M. Salewski, F. Leipold, J. Zhu, A. Ehn, Z. Li, and M. Aldén, 'Stability of Alternating Current Gliding Arcs', *The European Physical Journal D,* 68(2014).

[3] Y. Kusano, J. J. Zhu, A. Ehn, Z. S. Li, M. Aldén, M. Salewski, F. Leipold, A. Bardenshtein, and N. Krebs, 'Observation of Gliding Arc Surface Treatment', *Surface Engineering,* 31, 282-88(2015).
[4] M. G. Kong, G. Kroesen, G. Morfill, T. Nosenko, T. Shimizu, J. van Dijk, and J. L. Zimmermann, 'Plasma Medicine: An Introductory Review', *New Journal of Physics,* 11, 115012(2009).
[5] M. Laroussi, 'Low-Temperature Plasmas for Medicine?', *IEEE Transactions on Plasma Science,* 37, 714-25(2009).
[6] M. Laroussi, A. Fridman, P. Favia, and M. R. Wertheimer, 'Second Special Issue on Plasma Medicine', *Plasma Processes and Polymers,* 7, 193-93(2010).
[7] D. B. Graves, 'The Emerging Role of Reactive Oxygen and Nitrogen Species in Redox Biology and Some Implications for Plasma Applications to Medicine and Biology', *Journal of Physics D: Applied Physics,* 45, 263001(2012).
[8] J. Van der Paal, S. Aernouts, A. C. T. van Duin, E. C. Neyts, and A. Bogaerts, 'Interaction of O and OH Radicals with a Simple Model System for Lipids in the Skin Barrier: A Reactive Molecular Dynamics Investigation for Plasma Medicine', *Journal of Physics D: Applied Physics,* 46, 395201(2013).
[9] Y. F. Yue, S. Mohades, M. Laroussi, and X. Lu, 'Measurements of Plasma-Generated Hydroxyl and Hydrogen Peroxide Concentrations for Plasma Medicine Applications', *IEEE Transactions on Plasma Science,* 44, 2754-58(2016).
[10] F. Tochikubo, Y. Furuta, S. Uchida, and T. Watanabe, 'Study of Wastewater Treatment by OH Radicals Using DC and Pulsed Corona Discharge over Water', *Japanese Journal of Applied Physics,* 45, 2743-48(2006).
[11] P. Bruggeman, and C. Leys, 'Non-Thermal Plasmas in and in Contact with Liquids', *Journal of Physics D: Applied Physics,* 42, 053001(2009).
[12] B. R. Locke, and K.-Y. Shih, 'Review of the Methods to Form Hydrogen Peroxide in Electrical Discharge Plasma with Liquid Water', *Plasma Sources Science and Technology,* 20, 034006(2011).
[13] S. Kanazawa, H. Kawano, S. Watanabe, T. Furuki, S. Akamine, R. Ichiki, T. Ohkubo, M. Kocik, and J. Mizeraczyk, 'Observation of OH Radicals Produced by Pulsed Discharges on the Surface of a Liquid', *Plasma Sources Science and Technology,* 20, 034010(2011).
[14] A. Czernichowski, 'Gliding Arc: Applications to Engineering and Environment Control', in *Pure and Applied Chemistry* (1994), p. 1301.
[15] S. Brethes-Dupouey, R. Peyrous, and B. Held, 'Removal of H2S in Air by Using Gliding Discharges', *Eur. Phys. J. AP,* 11, 43-58(2000).
[16] A. Khacef, J. M. Cormier, and J. M. Pouvesle, 'Non Thermal Plasma NOx Remediation: From Binary Gas Mixture to Lean-Burn Gasoline and Diesel Engine Exhaust', in *Journal of Advanced Oxidation Technologies* (2005), p. 150.
[17] C. M. Du, J. H. Yan, and B. Cheron, 'Decomposition of Toluene in a Gliding Arc Discharge Plasma Reactor', *Plasma Sources Science and Technology,* 16, 791-97(2007).
[18] J. Van Durme, J. Dewulf, C. Leys, and H. Van Langenhove, 'Combining Non-Thermal Plasma with Heterogeneous Catalysis in Waste Gas Treatment: A Review', *Applied Catalysis B: Environmental,* 78, 324-33(2008).
[19] L. Yu, X. Tu, X. Li, Y. Wang, Y. Chi, and J. Yan, 'Destruction of Acenaphthene, Fluorene, Anthracene and Pyrene by a Dc Gliding Arc Plasma Reactor', *J Hazard Mater,* 180, 449-55(2010).
[20] J. C. Whitehead, 'Plasma Catalysis: A Solution for Environmental Problems', *Pure and Applied Chemistry,* 82(2010).
[21] A. Gutsol, A. Rabinovich, and A. Fridman, 'Combustion-Assisted Plasma in Fuel Conversion', *Journal of Physics D: Applied Physics,* 44, 274001(2011).
[22] K. Gutsol, T. Nunnally, A. Rabinovich, A. Fridman, A. Starikovskiy, A. Gutsol, and A. Kemoun, 'Plasma Assisted Dissociation of Hydrogen Sulfide', *International Journal of Hydrogen Energy,* 37, 1335-47(2012).
[23] Z. Bo, E. Wu, J. Yan, Y. Chi, and K. Cen, 'Note: Gliding Arc Discharges with Phase-Chopped Voltage Supply for Enhancement of Energy Efficiency in Volatile Organic Compound Decomposition', *Rev Sci Instrum,* 84, 016105(2013).
[24] X. Tu, and J. C. Whitehead, 'Plasma Dry Reforming of Methane in an Atmospheric Pressure Ac Gliding Arc Discharge: Co-Generation of Syngas and Carbon Nanomaterials', *International Journal of Hydrogen Energy,* 39, 9658-69(2014).
[25] W. Piavis, S. Turn, and S. M. Ali Mousavi, 'Non-Thermal Gliding-Arc Plasma Reforming of Dodecane and Hydroprocessed Renewable Diesel', *International Journal of Hydrogen Energy,* 40, 13295-305(2015).
[26] I. Stasiulaitiene, D. Martuzevicius, V. Abromaitis, M. Tichonovas, J. Baltrusaitis, R. Brandenburg, A. Pawelec, and A. Schwock, 'Comparative Life Cycle Assessment of Plasma-Based and Traditional Exhaust Gas Treatment Technologies', *Journal of Cleaner Production,* 112, 1804-12(2016).
[27] J. Gao, J. Zhu, A. Ehn, M. Aldén, and Z. Li, 'In-Situ Non-Intrusive Diagnostics of Toluene Removal by a Gliding Arc Discharge Using Planar Laser-Induced Fluorescence', *Plasma Chemistry and Plasma Processing,* 37, 433-50(2016).
[28] A. Y. Starikovskii, 'Plasma Supported Combustion', *Proceedings of the Combustion Institute,* 30, 2405-17(2005).
[29] S. M. Starikovskaia, 'Plasma Assisted Ignition and Combustion', *Journal of Physics D: Applied Physics,* 39, R265-R99(2006).

[30] T. Ombrello, X. Qin, Y. Ju, A. Gutsol, A. Fridman, and C. Carter, 'Combustion Enhancement Via Stabilized Piecewise Nonequilibrium Gliding Arc Plasma Discharge', *AIAA Journal,* 44, 142-50(2006).
[31] A. Fridman, A. Gutsol, S. Gangoli, Y. Ju, and T. Ombrello, 'Characteristics of Gliding Arc and Its Application in Combustion Enhancement', *Journal of Propulsion and Power,* 24, 1216-28(2008).
[32] T. Ombrello, Y. Ju, and A. Fridman, 'Kinetic Ignition Enhancement of Diffusion Flames by Nonequilibrium Magnetic Gliding Arc Plasma', *AIAA Journal,* 46, 2424-33(2008).
[33] I. V. Adamovich, I. Choi, N. Jiang, J. H. Kim, S. Keshav, W. R. Lempert, E. Mintusov, M. Nishihara, M. Samimy, and M. Uddi, 'Plasma Assisted Ignition and High-Speed Flow Control: Non-Thermal and Thermal Effects', *Plasma Sources Science and Technology,* 18, 034018(2009).
[34] W. Sun, M. Uddi, T. Ombrello, S. H. Won, C. Carter, and Y. Ju, 'Effects of Non-Equilibrium Plasma Discharge on Counterflow Diffusion Flame Extinction', *Proceedings of the Combustion Institute,* 33, 3211-18(2011).
[35] W. Sun, M. Uddi, S. H. Won, T. Ombrello, C. Carter, and Y. Ju, 'Kinetic Effects of Non-Equilibrium Plasma-Assisted Methane Oxidation on Diffusion Flame Extinction Limits', *Combustion and Flame,* 159, 221-29(2012).
[36] A. Starikovskiy, and N. Aleksandrov, 'Plasma-Assisted Ignition and Combustion', *Progress in Energy and Combustion Science,* 39, 61-110(2013).
[37] Y. Ju, and W. Sun, 'Plasma Assisted Combustion: Dynamics and Chemistry', *Progress in Energy and Combustion Science,* 48, 21-83(2015).
[38] M. G. D. Giorgi, A. Sciolti, S. Campilongo, E. Pescini, A. Ficarella, L. M. Martini, P. Tosi, and G. Dilecce, 'Plasma Assisted Flame Stabilizationin a Non-Premixed Lean Burner', *Energy Procedia,* 82, 410-16(2015).
[39] I. V. Adamovich, and W. R. Lempert, 'Challenges in Understanding and Predictive Model Development of Plasma-Assisted Combustion', *Plasma Physics and Controlled Fusion,* 57, 014001(2015).
[40] R. Ono, and T. Oda, 'OH Radical Measurement in a Pulsed Arc Discharge Plasma Observed by a LIF Method', *IEEE Transactions on Industry Applications,* 37, 709-14(2001).
[41] T. J. Dolan, 'Electron and Ion Collisions with Water Vapour', *Journal of Physics D: Applied Physics,* 26, 4(1993).
[42] Y. Itikawa, and N. Mason, 'Cross Sections for Electron Collisions with Water Molecules', *Journal of Physical and Chemical Reference Data,* 34, 1-22(2005).
[43] J. Zhu, J. Gao, Z. Li, A. Ehn, M. Aldén, A. Larsson, and Y. Kusano, 'Sustained Diffusive Alternating Current Gliding Arc Discharge in Atmospheric Pressure Air', *Applied Physics Letters,* 105, 234102(2014).
[44] Z. W. Sun, J. J. Zhu, Z. S. Li, M. Aldén, F. Leipold, M. Salewski, and Y. Kusano, 'Optical Diagnostics of a Gliding Arc', *Optics Express,* 21, 6028-44(2013).
[45] R. Ono, and T. Oda, 'Measurement of Gas Temperature and OH Density in the Afterglow of Pulsed Positive Corona Discharge', *Journal of Physics D: Applied Physics,* 41, 035204(2008).
[46] R. Ono, and T. Oda, 'Dynamics of Ozone and OH Radicals Generated by Pulsed Corona Discharge in Humid-Air Flow Reactor Measured by Laser Spectroscopy', *Journal of Applied Physics,* 93, 5876-82(2003).
[47] R. Ono, and T. Oda, 'Measurement of Hydroxyl Radicals in an Atmospheric Pressure Discharge Plasma by Using Laser-Induced Fluorescence', in *Conference Record of 1998 IEEE Industry Applications Conference. Thirty-Third IAS Annual Meeting (Cat. No.98CH36242)* (1998), pp. 1777-83 vol.3.
[48] R. Ono, and T. Oda, 'OH Radical Measurement in a Pulsed Arc Discharge Plasma Observed by a LIF Method', *IEEE Transactions on Industry Applications,* 37, 709-14(2001).
[49] O. Ryo, and O. Tetsuji, 'Dynamics and Density Estimation of Hydroxyl Radicals in a Pulsed Corona Discharge', *Journal of Physics D: Applied Physics,* 35, 2133(2002).
[50] C. Zheng, X. Shen, X. Gao, Z. Li, X. Zhu, Z. Luo, and K. Cen, 'Planar Laser-Induced Fluorescence Diagnostics for Spatiotemporal OH Evolution in Pulsed Corona Discharge', *IEEE Transactions on Plasma Science,* 41, 485-93(2013).
[51] Y. Nakagawa, R. Ono, and T. Oda, 'Density and Temperature Measurement of OH Radicals in Atmospheric-Pressure Pulsed Corona Discharge in Humid Air', *Journal of Applied Physics,* 110, 073304(2011).
[52] J. P. Jiang, Z. Y. Luo, L. Zhao, J. Y. Xuan, M. X. Fang, and X. Gao, 'Detection of OH Radicals Generated in Wire–Plate Pulsed Corona Discharge by Lif', *IEEE Transactions on Plasma Science,* 43, 1747-57(2015).
[53] L. Magne, S. Pasquiers, N. Blin-Simiand, and C. Postel, 'Production and Reactivity of the Hydroxyl Radical in Homogeneous High Pressure Plasmas of Atmospheric Gases Containing Traces of Light Olefins', *Journal of Physics D: Applied Physics,* 40, 3112-27(2007).
[54] T. Verreycken, R. M. van der Horst, A. H. F. M. Baede, E. M. Van Veldhuizen, and P. J. Bruggeman, 'Time and Spatially Resolved Lif of OH in a Plasma Filament in Atmospheric Pressure He–H2o', *Journal of Physics D: Applied Physics,* 45, 045205(2012).

[55] G. Dilecce, P. F. Ambrico, M. Simek, and S. De Benedictis, 'Lif Diagnostics of Hydroxyl Radical in Atmospheric Pressure He-H2O Dielectric Barrier Discharges', *Chemical Physics,* 398, 142-47(2012).
[56] F. Tochikubo, S. Uchida, and T. Watanabe, 'Study on Decay Characteristics of OH Radical Density in Pulsed Discharge in Ar/H2O', *Japanese Journal of Applied Physics,* 43, 315-20(2004).
[57] G. Dilecce, L. M. Martini, P. Tosi, M. Scotoni, and S. De Benedictis, 'Laser Induced Fluorescence in Atmospheric Pressure Discharges', *Plasma Sources Science and Technology,* 24, 034007(2015).
[58] S. Kanazawa, H. Tanaka, A. Kajiwara, T. Ohkubo, Y. Nomoto, M. Kocik, J. Mizeraczyk, and J.-S. Chang, 'LIF Imaging of OH Radicals in Dc Positive Streamer Coronas', *Thin Solid Films,* 515, 4266-71(2007).
[59] G. Dilecce, and S. De Benedictis, 'Laser Diagnostics of High-Pressure Discharges: Laser Induced Fluorescence Detection of OH in He/Ar–H2o Dielectric Barrier Discharges', *Plasma Physics and Controlled Fusion,* 53, 124006(2011).
[60] Q. Xiong, A. Y. Nikiforov, L. Li, P. Vanraes, N. Britun, R. Snyders, X. P. Lu, and C. Leys, 'Absolute OH Density Determination by Laser Induced Fluorescence Spectroscopy in an Atmospheric Pressure Rf Plasma Jet', *The European Physical Journal D,* 66(2012).
[61] S. Yonemori, Y. Nakagawa, R. Ono, and T. Oda, 'Measurement of OH Density and Air–Helium Mixture Ratio in an Atmospheric-Pressure Helium Plasma Jet', *Journal of Physics D: Applied Physics,* 45, 225202(2012).
[62] J. Voráč, P. Dvořák, V. Procházka, J. Ehlbeck, and S. Reuter, 'Measurement of Hydroxyl Radical (OH) Concentration in an Argon Rf Plasma Jet by Laser-Induced Fluorescence', *Plasma Sources Science and Technology,* 22, 025016(2013).
[63] X. Pei, Y. Lu, S. Wu, Q. Xiong, and X. Lu, 'A Study on the Temporally and Spatially Resolved OH Radical Distribution of a Room-Temperature Atmospheric-Pressure Plasma Jet by Laser-Induced Fluorescence Imaging', *Plasma Sources Science and Technology,* 22, 025023(2013).
[64] I. Choi, Z. Yin, I. V. Adamovich, and W. R. Lempert, 'Hydroxyl Radical Kinetics in Repetitively Pulsed Hydrogen–Air Nanosecond Plasmas', *IEEE Transactions on Plasma Science,* 39, 3288-99(2011).
[65] A. Fridman, *Plasma Chemistry*. New York, NY, USA: Cambridge Univ. Press, 2008
[66] A. Fridman, S. Nester, L. A. Kennedy, A. Saveliev, and O. Mutaf-Yardimci, 'Gliding Arc Gas Discharge', *Progress in Energy and Combustion Science,* 25, 211-31(1999).
[67] J. Zhu, Z. Sun, Z. Li, A. Ehn, M. Aldén, M. Salewski, F. Leipold, and Y. Kusano, 'Dynamics, OH Distributions and UV Emission of a Gliding Arc at Various Flow-Rates Investigated by Optical Measurements', *Journal of Physics D: Applied Physics,* 47, 295203(2014).
[68] J. Zhu, Y. Kusano, and Z. Li, 'Optical Diagnostics of a Gliding Arc Discharge at Atmospheric Pressure', in *Atmospheric Pressure Plasmas: Processes, Technology and Applications* (Nova Science Publishers, Incorporated, 2016).
[69] J. Zhu, J. Gao, A. Ehn, M. Aldén, Z. Li, D. Moseev, Y. Kusano, M. Salewski, A. Alpers, P. Gritzmann, and M. Schwenk, 'Measurements of 3D Slip Velocities and Plasma Column Lengths of a Gliding Arc Discharge', *Applied Physics Letters,* 106, 044101(2015).
[70] J. Zhu, J. Gao, A. Ehn, M. Aldén, A. Larsson, Y. Kusano, and Z. Li, 'Spatiotemporally Resolved Characteristics of a Gliding Arc Discharge in a Turbulent Air Flow at Atmospheric Pressure', *Physics of Plasmas,* 24, 013514(2017).
[71] F. Mitsugi, T. Ohshima, H. Kawasaki, T. Kawasaki, S. I. Aoqui, T. Baba, and S. Kinouchi, 'Gas Flow Dependence on Dynamic Behavior of Serpentine Plasma in Gliding Arc Discharge System', *IEEE Transactions on Plasma Science,* 42, 3681-86(2014).
[72] X. Tu, L. Yu, J. H. Yan, K. F. Cen, and B. G. Chéron, 'Dynamic and Spectroscopic Characteristics of Atmospheric Gliding Arc in Gas-Liquid Two-Phase Flow', *Physics of Plasmas,* 16, 113506(2009).
[73] X. Tu, H. J. Gallon, and J. C. Whitehead, 'Dynamic Behavior of an Atmospheric Argon Gliding Arc Plasma', *IEEE Transactions on Plasma Science,* 39, 2900-01(2011).
[74] F. Mitsugi, J. Furukawa, T. Ohshima, H. Kawasaki, T. Kawasaki, S.-i. Aoqui, and H. D. Stryczewska, 'Observation of Dynamic Behavior of Gliding Arc Discharge', *The European Physical Journal Applied Physics,* 61, 24308(2013).
[75] S.-i. Aoqui, F. Mitsugi, H. Kawasaki, S. Kinouchi, and T. B. T. Ikegami, 'Analysis of Atmospheric Serpentine Plasma Phenomenon Using a High-Speed Camera', 21st International Symposium on Plasma Chemistry (ISPC 21), (2013).
[76] N. Balcon, N. Benard, P. Braud, A. Mizuno, G. Touchard, and E. Moreau, 'Prospects of Airflow Control by a Gliding Arc in a Static Magnetic Field', *Journal of Physics D: Applied Physics,* 41, 205204(2008).
[77] S. P. Gangoli, A. F. Gutsol, and A. A. Fridman, 'A Non-Equilibrium Plasma Source: Magnetically Stabilized Gliding Arc Discharge: I. Design and Diagnostics', *Plasma Sources Science and Technology,* 19, 065003(2010).
[78] C. F. Kaminski, J. Hult, and M. Aldén, 'High Repetition Rate Planar Laser Induced Fluorescence of OH in a Turbulent Non-Premixed Flame', *Applied Physics B,* 68, 757-60(1999).
[79] I. Boxx, C. M. Arndt, C. D. Carter, and W. Meier, 'High-Speed Laser Diagnostics for the Study of Flame Dynamics in a Lean Premixed Gas Turbine Model Combustor', *Experiments in Fluids,* 52, 555-67(2012).

[80] R. Wellander, M. Richter, and M. Aldén, 'Time-Resolved (kHz) 3D Imaging of OH PLIF in a Flame', *Experiments in Fluids,* 55(2014).
[81] S. Hammack, C. Carter, C. Wuensche, and T. Lee, 'Continuous Hydroxyl Radical Planar Laser Imaging at 50 kHz Repetition Rate', *Appl Opt,* 53, 5246-51(2014).
[82] B. Thurow, N. Jiang, and W. Lempert, 'Review of Ultra-High Repetition Rate Laser Diagnostics for Fluid Dynamic Measurements', *Measurement Science and Technology,* 24, 012002(2013).
[83] J. D. Miller, M. Slipchenko, T. R. Meyer, N. Jiang, W. R. Lempert, and J. R. Gord, 'Ultrahigh-Frame-Rate OH Fluorescence Imaging in Turbulent Flames Using a Burst-Mode Optical Parametric Oscillator', *Optics Letters,* 34, 1309-11(2009).
[84] Z. Wang, P. Stamatoglou, Z. Li, M. Aldén, and M. Richter, 'Ultra-High-Speed PLIF Imaging for Simultaneous Visualization of Multiple Species in Turbulent Flames', *Optics Express,* 25, 30214-28(2017).
[85] G. Anstett, G. Göritz, D. Kabs, R. Urschel, R. Wallenstein, and A. Borsutzky, 'Reduction of the Spectral Width and Beam Divergence of a BBO-OPO by Using Collinear Type-Ii Phase Matching and Back Reflection of the Pump Beam', *Applied Physics B,* 72, 583-89(2014).
[86] J. Zhu, "Optical Diagnostics of Non-thermal Plasmas and Plasma-assisted Combustion," Doctoral Degree, Division of Combustion Physics, Lund University, Lund Report on Combustion Physics, 2015.
[87] J. Zhu, A. Ehn, J. Gao, C. Kong, M. Aldén, M. Salewski, F. Leipold, Y. Kusano, and Z. Li, 'Translational, Rotational, Vibrational and Electron Temperatures of a Gliding Arc Discharge', *Optics Express,* 25, 20243(2017).
[88] M. N. Slipchenko, J. D. Miller, S. Roy, J. R. Gord, S. A. Danczyk, and T. R. Meyer, 'Quasi-Continuous Burst-Mode Laser for High-Speed Planar Imaging', *Optics Letters,* 37, 1346-48(2012).
[89] S. Teodoru, Y. Kusano, and A. Bogaerts, 'The Effect of O2 in a Humid O2/N2/NOx Gas Mixture on NOx and N2O Remediation by an Atmospheric Pressure Dielectric Barrier Discharge', *Plasma Processes and Polymers,* 9, 652-89(2012).

Figures:

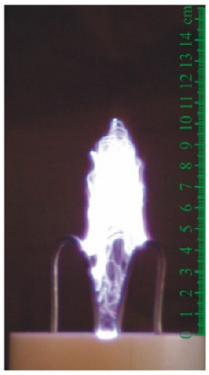

Figure 1. A photo of gliding arcs operated at flow rates of 42 SLM (standard litres per minute), derived from reference [67].

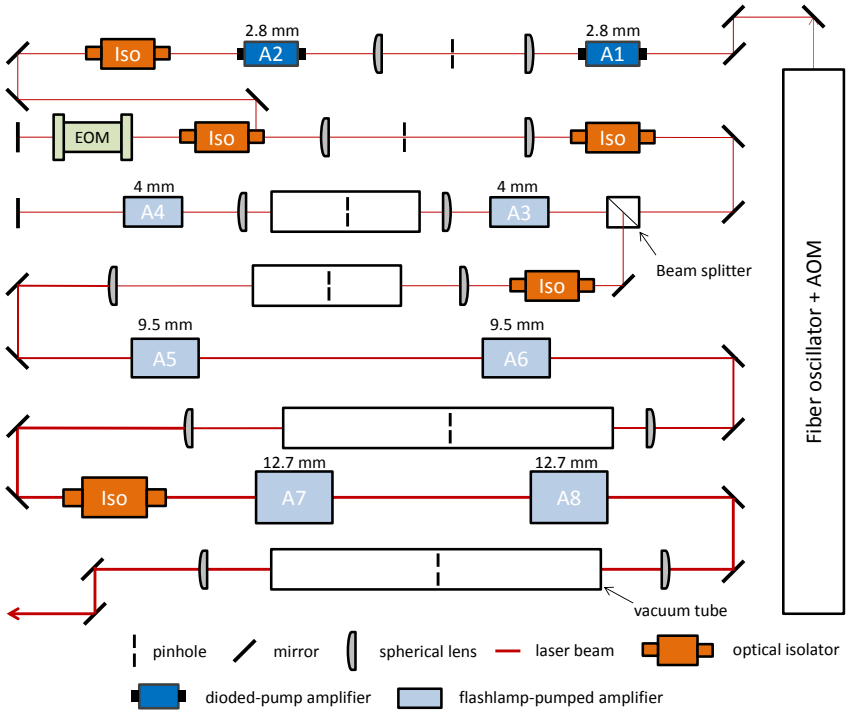

Figure 2. Layout of burst mode laser for fundamental wavelength at 1064 nm.

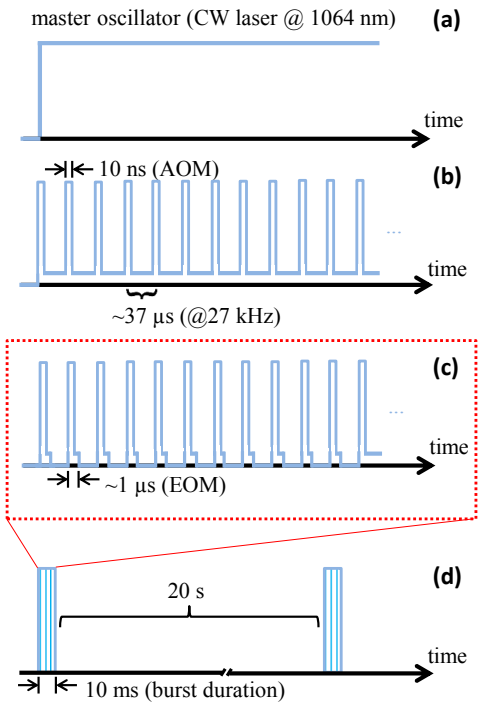

Figure 3. Pulse train producing strategy for fundamental wavelength at 1064 nm.

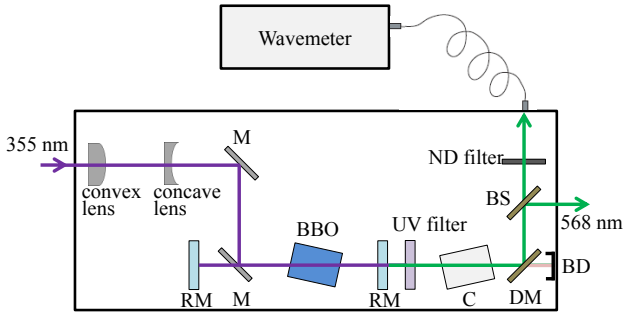

BBO: beta barium borate (BBO) crystal
BS: beam splitter
BD: beam dump
C: compensator
DM: dichroic mirror
M: HR 355 nm mirror
ND filter: neutral density filter
RM: resonator mirror

Figure 4. Schematic sketch of the optical parametric oscillators (OPO).

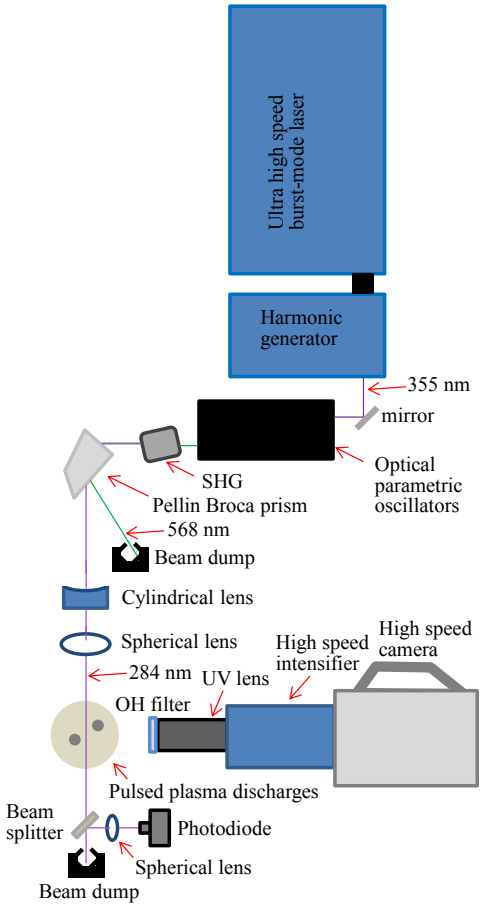

Figure 5. Experimental setup of OH PLIF imaging for pulsed gliding arc discharge.

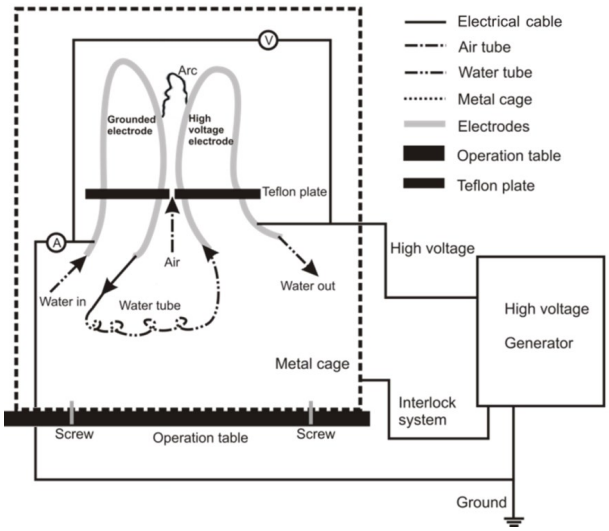

Figure 6. Schematic diagram of gliding arc discharge system.

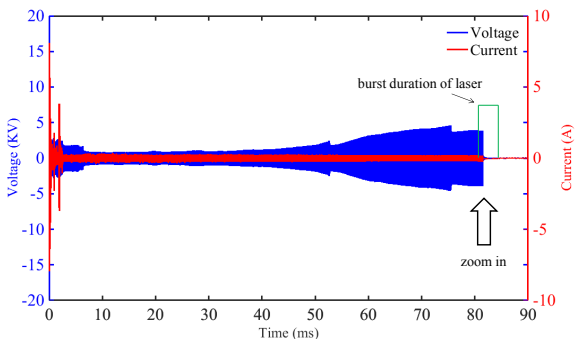

Figure 7. Current and voltage waveform of pulsed discharge together with the burst duration of laser/camera.

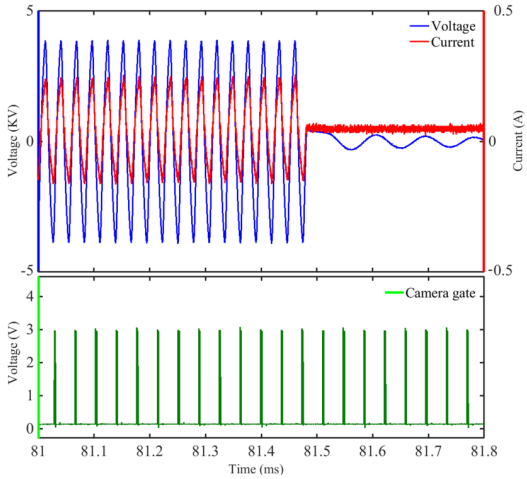

Figure 8. Zoom in to figure 6 for current and voltage waveform together with camera gate.

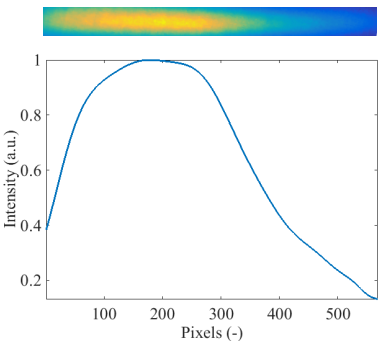

Figure 9. Correction for variations in the energy distribution of the laser sheet.

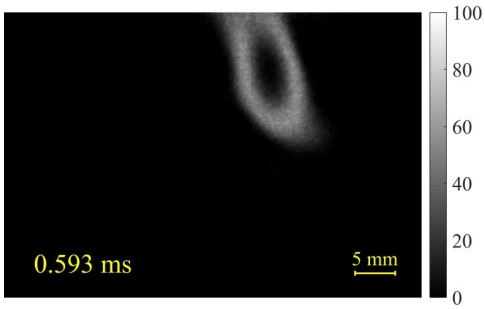

Figure 10. OH PLIF of gliding arc after post processing (an example).

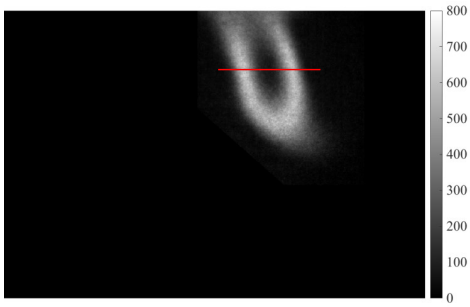

Figure 11. Raw OH PLIF image without post processing for SNR calculation.

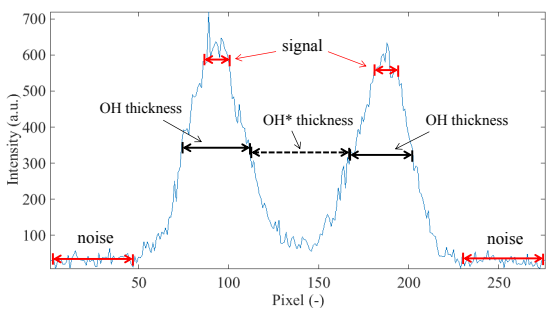

Figure 12. Cross section of OH PLIF signal. The location of the signal profile is marked with a red solid line in Figure 9.

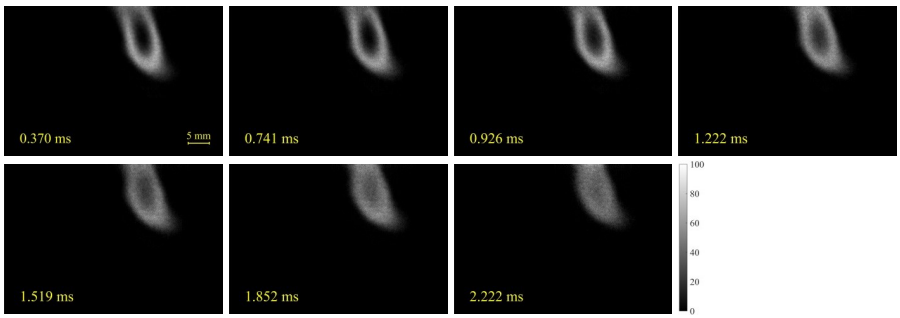

Figure 13. OH PLIF images versus time. The distribution of OH radicals looks like a torus.

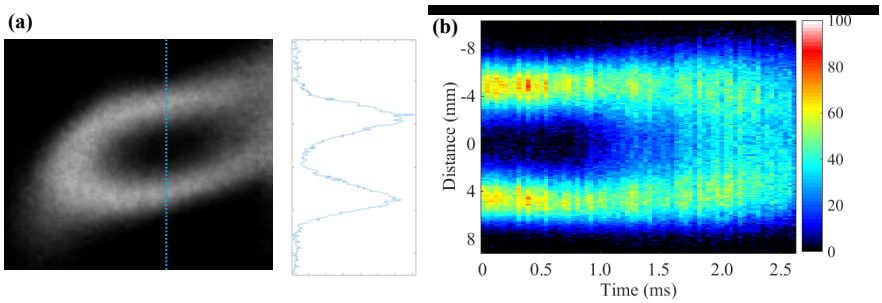

Figure 14. The signal profile of OH PLIF across the center of the plasma column (a) versus time (b).

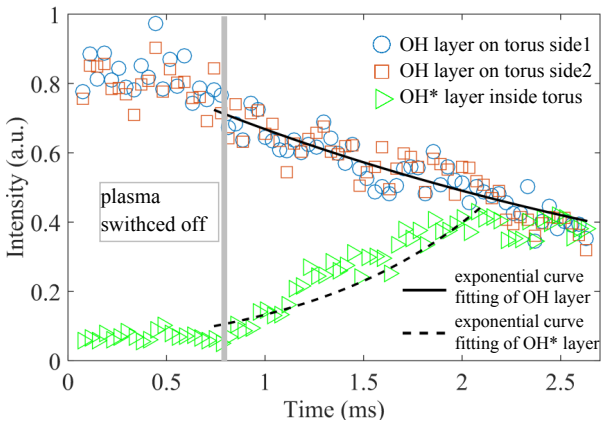

Figure 15. Intensity of OH PLIF on both sides of the torus and inside torus versus time. The circle, square and triangle markers show the experimental results while the solid and dashed lines indicate the corresponding exponential fittings. The intensity is obtained as shown in figure 13.

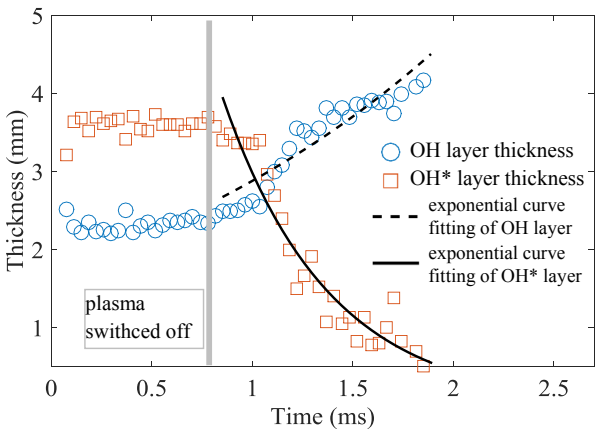

Figure 16. Thickness of OH layer and thickness between two OH layer, *i.e.* OH* layer versus time. The circle and square markers present the experimental results while the solid and dashed lines indicate the corresponding exponential fittings. The thickness is obtained by calculating the full width at half maximum of the OH PLIF intensity shown in figure 11.

Appendix

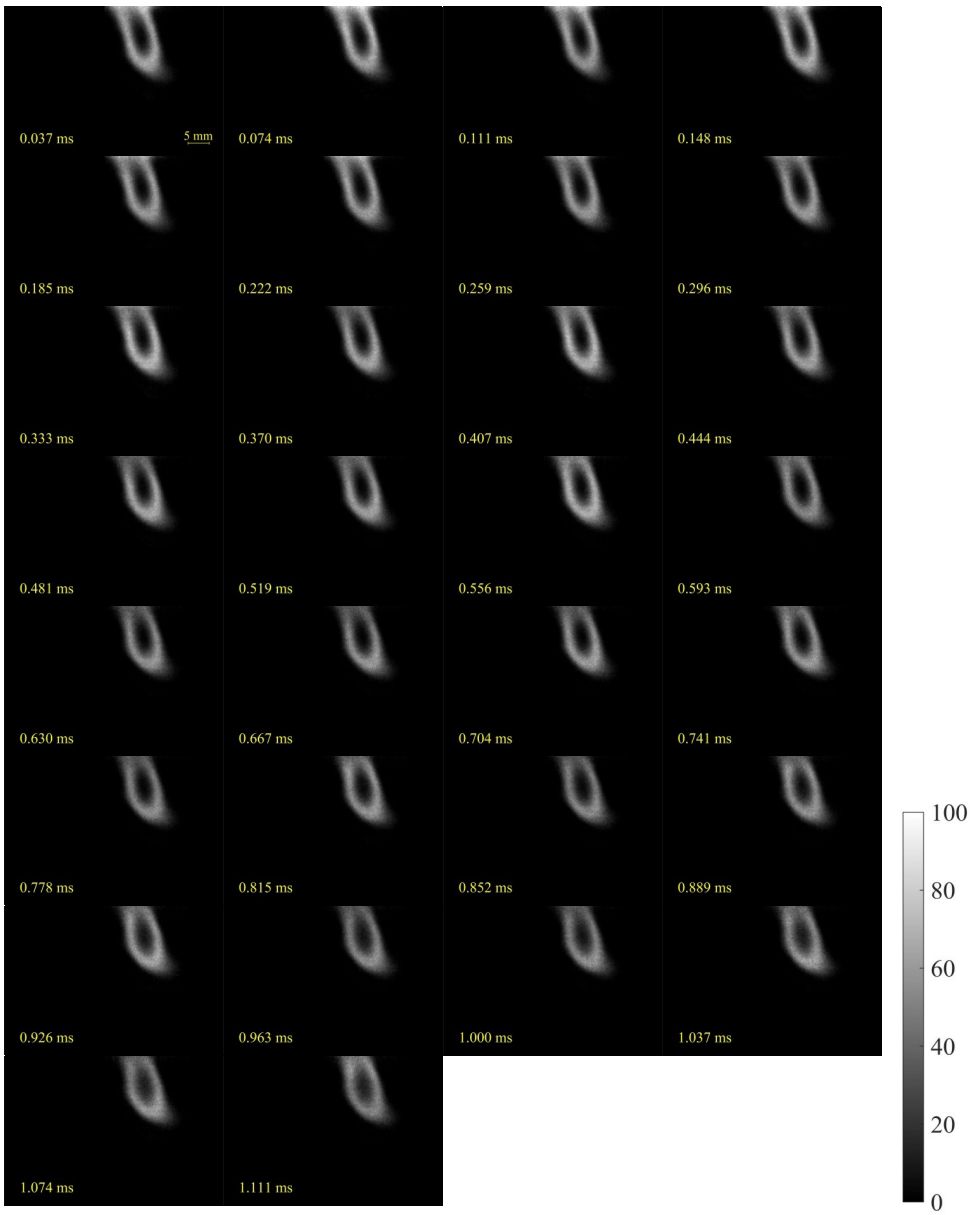
0.037 ms
5 mm
0.074 ms
0.111 ms
0.148 ms
0.185 ms
0.222 ms
0.259 ms
0.296 ms
0.333 ms
0.370 ms
0.407 ms
0.444 ms
0.481 ms
0.519 ms
0.556 ms
0.593 ms
0.630 ms
0.667 ms
0.704 ms
0.741 ms
0.778 ms
0.815 ms
0.852 ms
0.889 ms
0.926 ms
0.963 ms
1.000 ms
1.037 ms
1.074 ms
1.111 ms
100
80
60
40
20
0